



IntechOpen

Desalination and Water Treatment

Edited by Murat Eyvaz and Ebubekir Yüksel



DESALINATION AND WATER TREATMENT

Edited by **Murat Eyvaz** and **Ebubekir Yüksel**

Desalination and Water Treatment

<http://dx.doi.org/10.5772/intechopen.72352>

Edited by Murat Eyvaz and Ebubekir Yüksel

Contributors

Magdi Ali, German Eduardo Devora-Isiordia, Gustavo Adolfo Fimbres-Weihs, Jesús Álvarez-Sánchez, María Araceli Correa Murrieta, María Del Rosario Martínez Macías, Fadi Alnaimat, James Klausner, Bobby Mathew, Bao The Nguyen, Adil Charef, M'barek Feddaoui, Abderrahman Nait Alla, Monssif Najim, Cliff Dansoh, Jesús Manuel Epalza, Oscar Darío Guarín Villamizar, Jhoan Sebastian Jaramillo Peralta, Bouchra Lamrini, El-Khadir Lakhal, Konstantin Ivanovich Popov, Maxim Oshchepkov, Florentina Bunea, Gabriel Dan Ciocan, German Devora Isiordia, Reyna Guadalupe Sánchez-Duarte, Sergio Pérez Sicaïros, Griselda Romero-López, Liu Bin, Woo Chang Hwa, Saad Alami Younssi, Majda Breida, Brahim Achiou, Alberto M. Pernía, Miguel J. Prieto, Juan A. Martín-Ramos, Pedro J. Villegas Saiz, Francisco J. Álvarez-González, Clint Sutherland, Abeni Macarno, Beverly Chittoo, Muhammad Wakil Shahzad, Hisham Maddah, Mohammed Shihon, Manish Kumar Thimmaraju, Sreepada Divya

© The Editor(s) and the Author(s) 2018

The rights of the editor(s) and the author(s) have been asserted in accordance with the Copyright, Designs and Patents Act 1988. All rights to the book as a whole are reserved by INTECHOPEN LIMITED. The book as a whole (compilation) cannot be reproduced, distributed or used for commercial or non-commercial purposes without INTECHOPEN LIMITED's written permission. Enquiries concerning the use of the book should be directed to INTECHOPEN LIMITED rights and permissions department (permissions@intechopen.com). Violations are liable to prosecution under the governing Copyright Law.



Individual chapters of this publication are distributed under the terms of the Creative Commons Attribution 3.0 Unported License which permits commercial use, distribution and reproduction of the individual chapters, provided the original author(s) and source publication are appropriately acknowledged. If so indicated, certain images may not be included under the Creative Commons license. In such cases users will need to obtain permission from the license holder to reproduce the material. More details and guidelines concerning content reuse and adaptation can be found at <http://www.intechopen.com/copyright-policy.html>.

Notice

Statements and opinions expressed in the chapters are those of the individual contributors and not necessarily those of the editors or publisher. No responsibility is accepted for the accuracy of information contained in the published chapters. The publisher assumes no responsibility for any damage or injury to persons or property arising out of the use of any materials, instructions, methods or ideas contained in the book.

First published in London, United Kingdom, 2018 by IntechOpen

eBook (PDF) Published by IntechOpen, 2019

IntechOpen is the global imprint of INTECHOPEN LIMITED, registered in England and Wales, registration number:

11086078, The Shard, 25th floor, 32 London Bridge Street

London, SE19SG – United Kingdom

Printed in Croatia

British Library Cataloguing-in-Publication Data

A catalogue record for this book is available from the British Library

Additional hard and PDF copies can be obtained from orders@intechopen.com

Desalination and Water Treatment

Edited by Murat Eyvaz and Ebubekir Yüksel

p. cm.

Print ISBN 978-1-78923-758-0

Online ISBN 978-1-78923-759-7

eBook (PDF) ISBN 978-1-83881-679-7

We are IntechOpen, the world's leading publisher of Open Access books Built by scientists, for scientists

3,750+

Open access books available

115,000+

International authors and editors

119M+

Downloads

151

Countries delivered to

Our authors are among the
Top 1%

most cited scientists

12.2%

Contributors from top 500 universities



WEB OF SCIENCE™

Selection of our books indexed in the Book Citation Index
in Web of Science™ Core Collection (BKCI)

Interested in publishing with us?
Contact book.department@intechopen.com

Numbers displayed above are based on latest data collected.
For more information visit www.intechopen.com



Meet the editors



Dr. Murat Eyvaz is an assistant professor at the Environmental Engineering Department, Gebze Technical University. He received his BSc degree in Environmental Engineering from the Kocaeli University in Turkey in 2004. He completed his MSc and PhD degrees in 2013 in Environmental Engineering from the Gebze Institute of Technology (former name of GTU). He completed his postdoctoral research from the National Research Center on Membrane Technologies in 2015. His research interests are water and wastewater treatment, electrochemical processes, filtration systems/membrane processes, spectrophotometric and chromatographic analyses. He has coauthored numerous journal articles and conference papers and has taken part in many national projects. He serves as an editor in 30 journals and a reviewer in 100 journals indexed in SCI, SCI-E and other indexes.



Prof. Ebubekir Yüksel is a faculty member at the Environmental Engineering Department, Gebze Technical University. He received his bachelor degree in Civil Engineering from the İstanbul Technical University in 1992. He completed his graduate work (MSc degree in 1995 and PhD degree in 2001) from the İstanbul Technical University. His research interests are applications in water and wastewater treatment facilities, electrochemical treatment process and filtration systems at laboratory and pilot scale, watershed management, flood control, deep sea discharges, membrane processes, spectrophotometric analyses, chromatographic analyses and geographic information systems. He has coauthored numerous journal articles and conference papers and has taken part in many national projects. He has produced more than 25 peer-reviewed publications in journals indexed in SCI, SCI-E and other indexes.

Contents

Preface XIII

Section 1 Desalination Applications 1

Chapter 1 **Using Desalination to Improve Agricultural Yields: Success Cases in Mexico 3**

Germán Eduardo Dévora-Isiordia, María del Rosario Martínez-Macías, Ma. Araceli Correa-Murrieta, Jesús Álvarez-Sánchez and Gustavo Adolfo Fimbres-Weihs

Chapter 2 **Activated Carbon Cloth for Desalination of Brackish Water Using Capacitive Deionization 17**

Hisham A. Maddah and Mohammed A. Shihon

Chapter 3 **Energy Recovery in Capacitive Deionization Technology 37**

Alberto M. Pernía, Miguel J. Prieto, Juan A. Martín-Ramos, Pedro J. Villegas and Francisco J. Álvarez-González

Chapter 4 **Computational Study of Liquid Film Condensation with the Presence of Non-Condensable Gas in a Vertical Tube 55**

Adil Charef, M'barek Feddaoui, Abderrahman Nait Alla and Monssif Najim

Chapter 5 **Distilled Water Production by Vacuum Heat Pump 77**

Liu Bin, Cai Ling, Li Tianyin and Sajid Muhammad

Section 2 Renewable Energy in Desalination 93

Chapter 6 **Renewable Energy-Driven Desalination Hybrids for Sustainability 95**

Muhammad Wakil Shahzad, Doskhan Ybyraiyemkul, Muhammad Burhan and Kim Choon Ng

- Chapter 7 **Solar Desalination 127**
Fadi Alnaimat, James Klausner and Bobby Mathew
- Chapter 8 **Factors Affecting the Yield of Solar Distillation Systems and Measures to Improve Productivities 151**
Bao The Nguyen
- Chapter 9 **The Use of Renewable Energy for the Provision of Power to Operate Reverse Osmosis Desalination Facilities at Massawa 177**
Cliff Dansoh
- Section 3 Membrane Applications 199**
- Chapter 10 **Research Trend of Membranes for Water Treatment by Analysis of Patents and Papers' Publications 201**
Chang Hwa Woo
- Chapter 11 **Alumina Membranes for Desalination and Water Treatment 221**
Saad Alami Younssi, Majda Breida and Brahim Achiou
- Chapter 12 **Development, Characterization, and Applications of Capsaicin Composite Nanofiltration Membranes 255**
Jesús Álvarez-Sánchez, Griselda Evelia Romero-López, Sergio Pérez-Sicairos, German Eduardo Devora-Isiordia, Reyna Guadalupe Sánchez-Duarte and Gustavo Adolfo Fimbres-Weihs
- Section 4 Water Treatment Applications 269**
- Chapter 13 **Automatic Control Technologies to Enhance Water 271**
Magdi Osman Ali Hamed
- Chapter 14 **A Survey of Deep Learning Methods for WTP Control and Monitoring 293**
Bouchra Lamrini and El-Khadir Lakhal
- Chapter 15 **Fluorescent Markers in Water Treatment 311**
Maxim Oshchepkov and Konstantin Popov

- Chapter 16 **Desalination of Water 333**
Manish Thimmaraju, Divya Sreepada, Gummadi Sridhar Babu,
Bharath Kumar Dasari, Sai Kiran Velpula and Nagaraju Vallepu
- Chapter 17 **Experimental Study of Standard Aeration Efficiency in a
Bubble Column 349**
Florentina Bunea and Gabriel Dan Ciocan
- Chapter 18 **Extraction and Use of Plant Biopolymers for Water
Treatment 369**
Jesús Epalza, Jhoan Jaramillo and Oscar Guarín
- Chapter 19 **Artificial Neural Network-Genetic Algorithm Prediction of
Heavy Metal Removal Using a Novel Plant-Based Biosorbent
Banana Floret: Kinetic, Equilibrium, Thermodynamics and
Desorption Studies 385**
Clint Sutherland, Abeni Marcano and Beverly Chittoo

Preface

The need for fresh water is increasing with the rapid growth of the world's population. In countries and regions with available water resources, it is necessary to ensure the health and safety of the water supply. However, in countries and regions with limited freshwater resources, priority is given to water supply plans and projects, among which the desalination strategy stands out. In the desalination process, membrane and thermal processes are used to obtain fresh water from salty water, which is in abundant amounts in the sea. High energy requirement, brine (concentrate) disposal and greenhouse gas emissions are still the main challenges for desalination. Therefore, it is necessary to combine renewable energy sources with desalination facilities and to develop concentrate management. This book will outline valuable scientific contributions to the new desalination and water treatment technologies to obtain high quality water with low negative environmental impacts and cost.

This book consists of four sections. In the first section, some case studies related to the desalination processes used for various purposes are included. In the second section, studies using renewable energy in desalination systems are discussed. In the third section, research utilizing membranes in different characteristics is presented and in the last section, research on current technologies used in water treatment applications and water treatment facilities is stated.

Asst. Prof. Murat Eyvaz and Prof. Ebubekir Yüksel
Department of Environmental Engineering
Gebze Technical University
Turkey

Desalination Applications

Using Desalination to Improve Agricultural Yields: Success Cases in Mexico

Germán Eduardo Dévora-Isiordia,
María del Rosario Martínez-Macías,
Ma. Araceli Correa-Murrieta,
Jesús Álvarez-Sánchez and
Gustavo Adolfo Fimbres-Weihs

Additional information is available at the end of the chapter

<http://dx.doi.org/10.5772/intechopen.76847>

Abstract

Water scarcity is a global problem, motivating growth and development of new technologies for water treatment, reuse and desalination. For many arid regions in Mexico, especially in the northwest, agriculture is an important economic activity. The Yaqui Valley in Sonora, Mexico, faces problems related to aquifer overexploitation and saline intrusion, which have increased salt concentration in well water to 2000–9000 mg/L total dissolved solids (TDS) and led to soil salinization and low crop yields. This work evaluates the effect of TDS in irrigation water on crop yield. A 150 m³/d desalination plant was used, consisting of 12 SWC4B-MAX membrane modules, with 98% rejection and 75% recovery. Two crops were irrigated with control (4000 mg/L) and desalinated water (200 mg/L). Sorghum (*Sorghum*) had yields of 7.9 and 8.8 ton/ha, whereas tomatillo (*Physalis philadelphica*) had yields of 30.82 and 35.88 ton/ha, respectively. Evidently, the desalination process influences agricultural yields.

Keywords: reverse osmosis, irrigation, crop yields, desalination

1. Introduction

Constant population growth, soil erosion, scarcity and excessive consumption of fresh water represent the most important reasons for the constant development and innovation of new technologies to provide water in large quantities and good quality [1]. Water scarcity exists

when demand exceeds freshwater supply in a given area [2]. The three main features that characterize water scarcity are: the physical shortage of available water to meet demand; the level of infrastructure development that controls storage, distribution and access; and the institutional capacity to provide the required water services [3]. In Mexico, there is a chronic shortage of water, especially in the northern part of the country, where precipitation volumes are notably lower than the potential evapotranspiration [4].

Considering that 97% of the water available on Earth has a salinity level exceeding 35 g/L, the desalination process is a viable option in the short term, which has had a significant growth in the recent past [2]. At the beginning of the modern development of desalination, before the 1970s, desalination methods consisted of thermal processes and their operation was such that they evaporated the fluid and collected the condensate. Known thermal processes include thermal vapor compression (TVC), multi-stage flash (MSF) and multi-effect distillation (MED) [5]. However, because evaporation processes require large amounts of energy for their operation, the use of semi-permeable membranes through reverse osmosis (RO) has become the main technology in use, accounting for 65% of the installed capacity of desalination plants. This installed RO capacity grows at a rate of 4 million m³/d each year [4].

The use of desalination to produce clean water as well as industrial and agricultural water has gained popularity among the sectors that require this resource [3]. The agricultural sector is the most important consumer of water resources, so RO desalination technology for crop irrigation has been successfully implemented in several countries, mainly in arid regions such as Israel [6] and Spain, where more desalinated water is currently provided for agricultural use than for domestic use [7, 8]. Likewise, several nations such as China, Chile and Australia offer specialized advice on the different techniques and technologies of desalination focused on agricultural crops [1], making the RO process the most used to tackle water scarcity in that sector [1, 2]. Therefore, desalination technologies enable the possibility to make optimal use of hydrological resources, both of the product (permeate) water and the retentate (brine).

The characteristics of irrigation water are directly linked to the quality of the crops harvested, as high salinity is intolerable for most crops established for food production. The agricultural sector benefits from the supply of higher volumes of better quality water [7]. However, the volume of global desalinated water currently accounts for only 1% of the world's supply. Of this value, only 2% of desalinated water is used for agricultural purposes [9, 10].

The state of Sonora, located in northwestern Mexico, ranks second in irrigation crops in the country. About 95% of the state is considered semi-arid and is characterized by a climate of high temperatures and low rainfall per year. Those conditions, combined with the overexploitation and lack of recharge into aquifers, have led to a decrease in the levels of available water [3], especially for agriculture. Several regions in the state present high salinity in well water, ranging from 2000 to 9000 mg/L of total dissolved solids (TDS), which are attributed to saline intrusion effects, causing soil salinization and decreasing the yields of vegetable and grain crops [8]. In this context, the objective of this study is to evaluate the performance of two typical crops (Sorghum and Tomatillo) under brackish water irrigation, by comparing their yield using water with different salinity levels, in order to determine the salinity-yield effect.

2. Methodology

2.1. Location of the study area

This study took place near Cd. Obregon, Sonora, Mexico, in field 1814 (**Figure 1**), located in the Yaqui Valley, with geographic coordinates 27° 11' 21.7" N, 109° 52' 15.6" W [8].

2.2. Configuration of the desalination process

A 150 m³/d capacity RO desalination plant was used, consisting of 12 Hydranautics 8 × 40" SWC4 membrane modules with a permeate flow rate of 27.3 m³/d, 99.8% salt rejection, spiral wound configuration, polyamide composite membrane and 440 ft² active membrane area. The plant uses a 40 hp high pressure pump (Grundfos). The pressure levels in the membrane modules and cartridge filters, as well as the process flow rates, were all monitored. In determining the water production cost of the RO process, the costs of electricity, labor, chemicals and maintenance were considered.

2.3. Brackish well pump

The water supplied to the desalination process was sourced from a brackish well adjacent to the study area, with an average salinity of 4000 mg/L TDS. The brackish water was pumped from the well by a 3 hp triphasic pump (Grundfos).

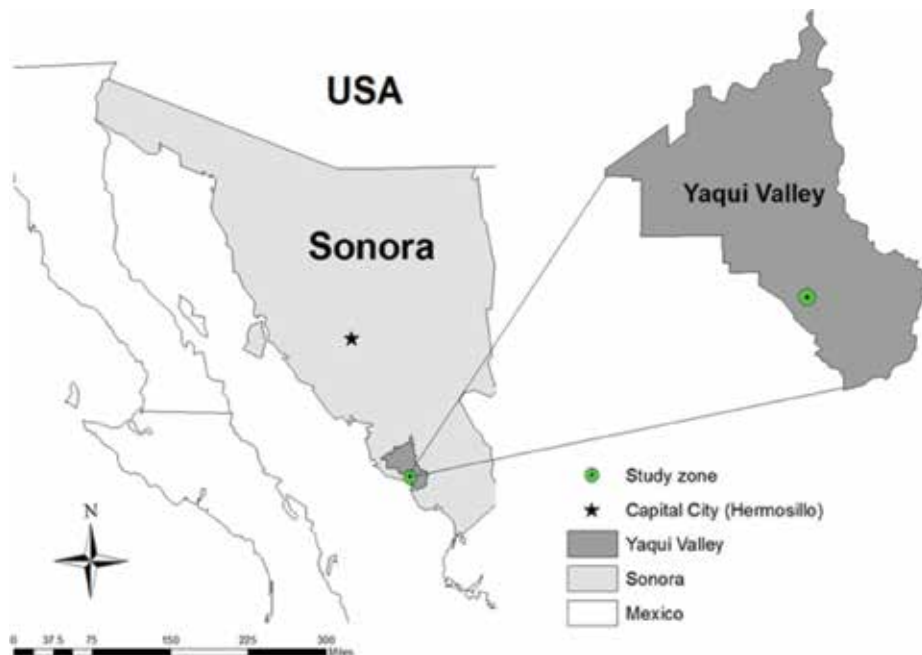


Figure 1. Study area, Sonora, Mexico.

2.4. Physical and chemical pretreatment system

The desalination plant has a physical pretreatment system consisting of a multimedia filter and 6 cartridge filters. The multimedia filter (63" × 90") has a capacity of 100 ft³ and consists of anthracite, turbidex, zeolite, and gravel. This filter removes suspended particles up to 50 μm in diameter. Subsequently, the cartridge filters remove particles of up to 5 μm in size.

For chemical pretreatment, a 0.25 hp diaphragm pump was used for the supply of antiscalant. In order to prevent salt precipitation on the surface of the membranes and, thus, prevent an increase in operating pressure. A 0.20 hp diaphragm pump was also used for the supply of H₂SO₄ at 30%, to regulate pH at the inlet of the RO membrane modules, maintaining a value of 7.0 ± 0.1.

2.5. Water and soil quality

Water quality was measured using a multiparametric measuring device (YSI 556 MPS). The concentration of salts in the feed, product and retentate of the RO process were determined. In addition, electrical conductivity (μS/cm), TDS (mg/L), pH and temperature (°C) were also measured. A visible spectrophotometer (SPECTRUM PROVE 300) was used to determine the concentration of different minerals in the water.

Soil quality was determined via pH and electrical conductivity (μS/cm) measurements. The damage caused by salinity in the agricultural soil was assessed at the beginning, during and at the end of the project, by determining parameters such as Sodium Adsorption Ratio (SAR) and Exchangeable Sodium Percentage (ESP). These parameters measure soil damage caused by sodium buildup.

2.6. Experimental design

To assess the effect of salt concentration in irrigation water on crop yield, two different experiments were conducted with sorghum and tomatillo (*Physalis philadelphica*). The experiments occurred in different agricultural cycles and different years (2014 and 2016). The first crop was chosen because it has a high tolerance to salt concentration in water. The second crop was chosen because it is not very tolerant to salinity in water. An experimental planting area of 1 ha was used. The field was divided into two sections of 0.5 ha each (**Figure 2**). The first section was irrigated with well water containing 4000 mg/L TDS on average. The second section was irrigated with treated water from the desalination process, with an average of 200 mg/L TDS.

A drip irrigation system was used with a flow rate of 1 L/h, using 16 mm diameter irrigation belts. The treated water for irrigation was generated by mixing the permeate from the RO plant with raw well water, in order to reach an average salinity of 200–285 mg/L TDS. The following formula was used to calculate the mixtures:

$$C_1 V_1 + C_2 V_2 = C_3 V_3 \quad (1)$$



Figure 2. Satellite photograph of the study area and experimental sections.

where:

C_1 = salt concentration in the feed water from the well, in mg/L of TDS.

V_1 = volume of well feed water, in liters (L).

C_2 = salt concentration in the permeate water, in mg/L of TDS.

V_2 = volume of permeate water, in liters (L).

C_3 = required salt concentration for irrigation, in mg/L of TDS.

V_3 = volume of required irrigation water in liters (L).

The water mixtures were stored in three tanks, each being 5000 L in size. The water was homogenized by an electric stirrer that was placed in the tank hatch.

2.7. Irrigation control sensors

Electronic sensors (Watermak 200) and manual tensiometers were installed to monitor soil moisture (matric potential), in order to determine the optimal moment to water the soil. The matric potential is a measure of the force or tension of soil moisture with which water is retained. It is the product of adhesion or attraction between the surface of soil particles and water; and cohesion or attraction between water molecules. The water retention process, which depends on the surface tension characteristics of the water in the soil, as well as on the

contact angle between water and soil particles, is the main mechanism of water retention in light and middle soils within certain moisture intervals, and in heavy soils. In this context, a matric potential between 30 and 40 kPa indicates that the soil needs irrigation, whereas a matric potential between 0 and 10 kPa indicates that the soil is saturated [11].

3. Results and discussion

3.1. Desalination process operating parameters

The results obtained during the operation of the desalination process are shown in **Table 1**.

The pumping equipment pressure is within the desired range as it averages 37.33 psi, very close to the acceptable minimum of 30 psi. This indicates that the water level of the well is adequate, as well as the power and flow rate of the pump used to draw fluid from the well. With respect to the multimedia filter, an average pressure drop of 7.33 psi is observed, which is acceptable for operation. This suggests that the multimedia filter is removing 50 μm particles without clogging in its filter media. On the other hand, the cartridge filter had an average pressure drop of 6.33 psi, which suggests that the removal of 5 μm suspended particles is occurring without any problem, and that the membrane system should be operating as intended. The flow rate supplied from the desalination process to irrigation, for both study years was in the range of 1.5–1.7 L/s.

3.2. Process water field parameters

Measurements at the desalination plant show that when the feed water presents about 3900 mg/L TDS, the permeate and retentate currents have 285 and 11,200 mg/L TDS, respectively. There is an increase in temperature of 0.32 and 1.2°C in the permeate and retentate respectively, considering that the temperature in the feed water is 24.69°C (**Table 2**).

Parameter	Units	Min	Max	Sample			Mean
				1	2	3	
Well discharge pressure	psi	30	80	40	36	36	37.33
Multimedia filter inlet pressure	psi	30	70	38	33	33	34.66
Multimedia filter outlet pressure	psi	20	60	30	26	26	27.33
Multimedia filter pressure drop	psi	8	12	8	7	7	7.33
Cartridge filter inlet pressure	psi	20	40	33	29	28	30.00
Cartridge filter outlet pressure	psi	20	40	32	28	28	29.33
Cartridge filter pressure drop	psi	5	10	6	6	7	6.33

Table 1. Operation of the desalination process.

Sample	pH	Temperature (°C)	Electrical conductivity ($\mu\text{S}/\text{cm}$)	Total dissolved solids (mg/L)
Feed	7.68	24.69	6096.00	3901.40 \pm 222.55
Permeate	6.16	25.01	446.00	285.00 \pm 51.20
Retentate	8.08	25.89	17,496.00	11,197.44 \pm 1389.01

Table 2. Water characterization at the 150 m³/d desalination plant.

The analysis of the RO desalination plant shows that it works as intended, since the concentration of salts in the produced water decreased significantly with respect to the feed water. Observed salt rejection was 92% compared to the salinity level of the brackish well, this through the action of semi-permeable membranes. On the other hand, the temperature of the retentate and permeate flows was always higher than the feed rate, due to the friction that occurs during pumping in RO, as well as the friction within the membrane modules. Care should be taken to ensure that the temperature does not exceed 45°C in the feed water, as this can shorten the working life of the equipment. Operating at high temperatures would increase permeate flow and decrease rejection (increased salt passage) as the diffusivity of both water and salt in the membrane increases with temperature. However, if temperature is increased significantly, changes in the polymer structure of the membrane can also occur, which could cause irreversible damage to the membrane.

3.3. Physical-chemical parameters of process water

The results of physical-chemical analysis of the water in the feed, permeate and retentate, are presented (Table 3). These were obtained using standard analytical techniques and a PROVE-300-Merck spectrophotometer.

These data are consistent with the data characterized by field parameters for both experimentation years [8, 11]. It can be observed that the presence of sodium in the permeate is 80.06 mg/L, which does not interfere with the adsorption of the nutrients in the irrigation water when adding fertilizers to the crop. However, special care must be taken in the dosage of nutrients by means of fertilizers in the irrigation water, since fertilizers can present high acidity and salinity, which inhibits the adsorption of nutrients.

3.4. Soil parameters of the agricultural field

The reduction of pH in RO permeate water is caused by the removal of carbonates and bicarbonates from the feed. Brackish well water usually contains bicarbonates (calcium, sodium, magnesium) and carbonates (calcium), which raise the pH of the water. Soil measurements of all physical-chemical parameters, SAR and ESP, at the beginning and end of the experiment are shown in Figure 3.

Taking chlorine and sodium ions as reference, as they are the major indicators of salts present in a sample, there is an evident increase in salinity (greater than 600 and 610% on average) attributed to brackish water irrigation for sorghum and tomatillo (*Physalis philadelphica*) in the

Water type	Ca	Mg	Na	K	NO ₃	HCO ₃	Cl	SO ₄	TDS
Feed	65.55	146.32	1079.66	72.74	28.76	33.83	1969.45	445.74	3842.05
Permeate	4.86	10.85	80.06	5.39	2.13	2.51	146.04	33.05	284.91
Retentate	190.70	425.90	3143.70	211.70	83.60	98.50	5733.80	1297.60	11,185.90

Table 3. Water quality assessment via physical-chemical parameters, in mg/L.

study area. On the other hand, under desalinated irrigation, the concentration of the sodium ion is reduced to 96%, which can be directly attributed to the salt removal by the RO process [11, 12].

Moreover, the SAR and ESP at the beginning and end of the experiment did not show significant changes in the samples irrigated with desalinated water, mainly due to the ease of internal soil drainage [13]. However, brackish irrigation samples show an average increase of 230% in SARs and 610% in ESP.

3.5. Desalinated water production cost

The economic data of the desalination process are shown in **Table 4**.

The economic evaluation of the process shows that the cost of producing desalinated water is \$0.338 USD/m³ very similar to that reported by the International Desalination Association [11, 14, 15], which is \$0.368 USD/m³, both for brackish water. To determine the viability of this desalination technology applied to agriculture, farmers should look for high-yield crops so that the cost-benefit effect is profitable, such as vegetables (e.g., tomatoes, chiles), and using drip irrigation systems [16].

3.6. Crop yields

3.6.1. Sorghum (2014)

There was a notable difference in the height of the plants, with the part irrigated with desalinated water being 10–15 cm higher on average. In addition, the plants irrigated with brackish water showed what appeared to be burned tips on the leaves of the plants: This is due to the excess of salts that are concentrated in the crop by the effect of brackish water from the well and possibly the addition of fertilizers. Although the latter was not reflected in burnt tips on the leaves of the plants irrigated with desalinated (**Figure 4**).

In all cases, the average height observed for the sorghum irrigated with desalinated water was higher compared to the average height of the crop irrigated with brackish water. This is directly attributed to soil management and the concentration of salts in the water, and therefore in the soil. These results in salt increase coincide with those reported by other authors [17, 18], who state that high salinity directly affects nutrient assimilation and germination in sorghum crops.

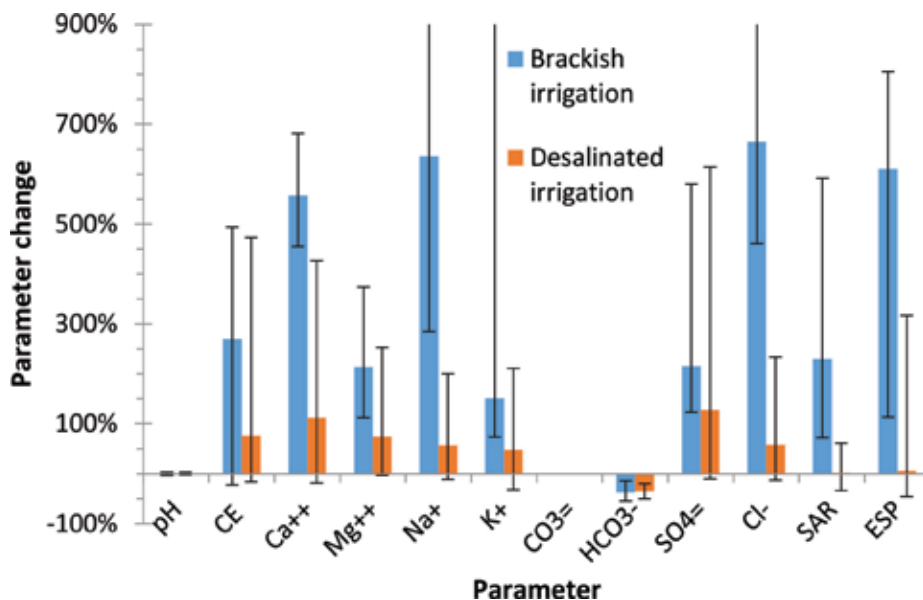


Figure 3. Physical-chemical parameters in the agricultural field soil.

Concept	Cost (USD \$/m ³)
Energy cost	0.207
High pressure pumps	
Dosage pumps	
General energy	
Labor costs	0.095
Operating personnel	
Technical assistance	
Chemical costs	0.0043
Antiscalant	
RO Clean	
Sulfuric acid	
Maintenance costs	0.031
Piping and accessories	
Soldering	
Total	0.338

Table 4. Operating costs.

At the time of harvest, it was verified that parameters such as the height (m), the number of panicles per m² and weight per panicle (g) were higher in all cases when using water with lower salt concentration. This led to an increase of 1 ton/ha (10.2%) of sorghum for the desalinated irrigation compared to irrigation with brackish water (**Table 5**). ANOVA analyses show a direct relationship in height and number of fruits, with respect to the salinity of water irrigated, with a 95% reliability.

Sorghum harvesting had a single cut, producing 7.9 ton/ha for the area irrigated with brackish water (4000 mg/L TDS), while the area irrigated with desalinated water (200–285 mg/L) yielded 8.8 ton/ha. Yield in tons shows a difference of 10.2%, demonstrating a higher profit margin when using desalinated water (**Figure 5**).

The results in **Figure 5** are similar to those of a previous study [17, 18] where the effect of saltwater irrigation on sorghum cultivation was verified. That study determined a direct relationship between seedling weight, stem diameter, delayed germination effect, and crop yield.

3.6.2. Tomatillo (*Physalis philadelphica*) (2016)

A difference in plant height was observed as a result of a lower salt concentration in the irrigation water. The plants irrigated with desalinated water were 5–6 cm smaller on average than those irrigated with brackish water. This decrease in height was due to greater weight and diameter in the products. These results coincide with other investigations that use water with different concentrations of salts to observe significant differences [16].

Some of the parameters found were similar, such as stem diameter, plant height, germination and yield per cut. Nonetheless, there was an improvement when irrigating with lower salinity water [16, 18]. In addition, the tomatillo (*Physalis philadelphica*) crop was harvested in three

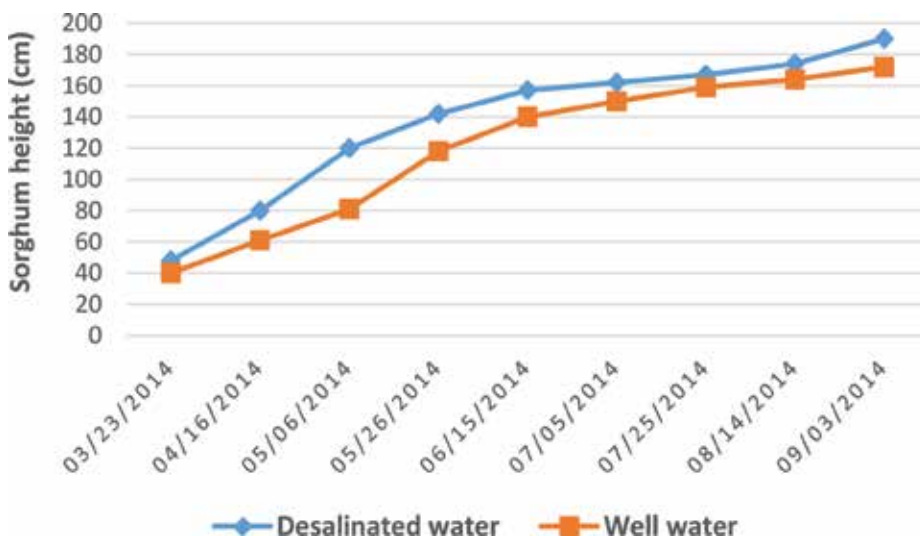


Figure 4. Behavior of the mean height of the sorghum crop.

Parameter	Desalinated irrigation	Brackish water irrigation	α 95%
Height (m)	1.7	1.5	X
Number of panicles per m ²	29.0	28.0	
Weight per panicle (g)	30.0	29.0	
Yield (Ton/ha)	8.8	7.9	

Table 5. Behavior of the sorghum crop parameters.

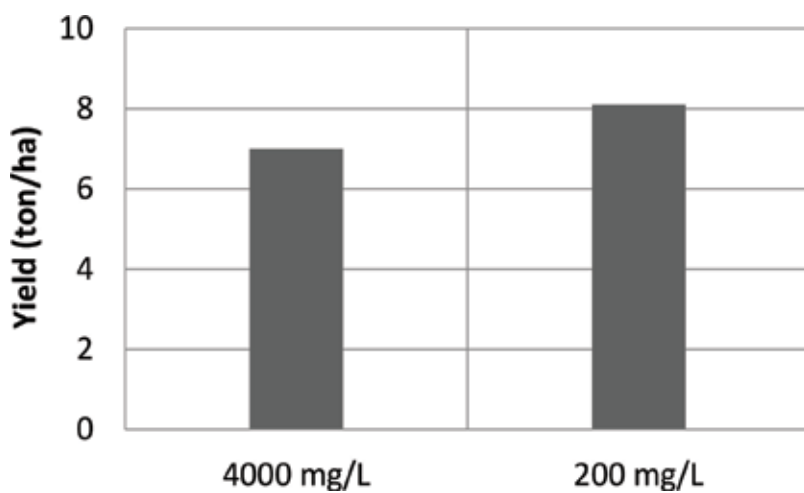


Figure 5. Dependence of sorghum crop yield with salinity in irrigation water.

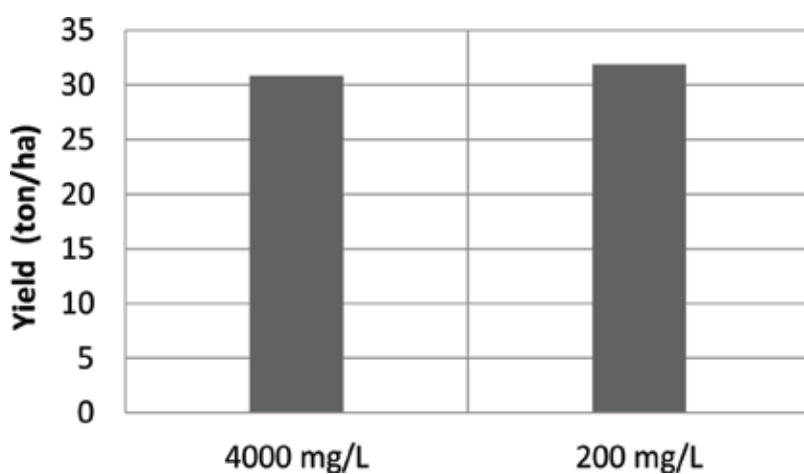


Figure 6. Dependence of tomatillo crop yield with salinity in irrigation water.

cuts. The average yield for the area irrigated with brackish water was 30.82 ton/ha, while the section irrigated with desalinated water yielded 35.88 ton/ha (**Figure 6**).

4. Conclusions

The use of desalinated water for agricultural irrigation increased the productivity of sorghum and tomatillo (*Physalis philadelphica*) crops. This means that wells with high salinity in the region can be utilized for irrigation through the use of desalination systems. In this sense, public and private investments in desalination in the rural sector are viable in the short term.

Cations and anions from the well water were successfully removed by the use of SWC4 membranes in an RO system. The operating parameters of the desalination process, such as pressure drop through the membrane modules, multimedia filter and cartridge filters, were below the limits and within the correct operating standards, which ensured a flow rate of 1.5–1.7 L/s of permeate, as well as a high rejection above 92%.

The total cost of producing the desalinated water was 0.338 USD $\$/\text{m}^3$. The cost of using electrical energy to operate the high pressure pump represented 70% of the total cost. Clearly, desalination processes need to incorporate renewable energy generation processes to reduce their environmental impact. In this energetic context, it is concluded that vegetables such as tomatillo have a higher profit in the market, compared to the sale of grains such as sorghum. This research project and other authors reaffirm that for the economic viability of desalination applied to agriculture, there must be a coupling of desalinated water using irrigation tapes for crops of high commercial value, with renewable energy such as solar photovoltaic.

The performance of the *Physalis philadelphica* and Sorghum are greatly improved by using tapes and sensory equipment, to apply irrigation as required and to decrease the concentration of salts in the irrigation water. It is concluded that the objective of the project has been satisfactorily achieved. Finally, it is concluded that with the use of desalination, producers will not need to worry about planting crops that support or tolerate the concentration of salts from their wells, since they will be able to establish high yield and high commercial value crops. Notably, the cost of production is a success factor in places where desalination is applied, such as agriculture and others. It is also necessary to continue investigating the incorporation of electric energy from renewable sources.

Acknowledgements

The authors acknowledge funding granted by Fundación PRODUCE Sonora, A. C., and the Instituto Tecnológico de Sonora, for the realization of this research project. Special thanks also to Alejandro Méndez, who facilitated the agricultural land and the use of the brackish well for the desalination plant operation.

Author details

Germán Eduardo Dévora-Isiordia¹, María del Rosario Martínez-Macías¹,
Ma. Araceli Correa-Murrieta¹, Jesús Álvarez-Sánchez¹ and Gustavo Adolfo Fimbres-Weihs^{2*}

*Address all correspondence to: gustavo.fimbres@itson.edu.mx

¹ Departamento de Ciencias del Agua y Medio Ambiente, Instituto Tecnológico de Sonora, Cd. Obregón, Sonora, México

² CONACYT-ITSON, Departamento de Ciencias del Agua y Medio Ambiente, Instituto Tecnológico de Sonora, Cd. Obregón, Sonora, México

References

- [1] Burn S, Hoang M, Zarzo D, Olewniak F, Elena C, Bolto B, Barron O. Desalination techniques. A review of the opportunities for desalination in agriculture. *Desalination*. 2015; **364**:2-16. DOI: 10.1016/j.desal.2015.01.041
- [2] Val S. Frenkel. Seawater desalination: Trends and technologies. In: Michael S, editor. *Desalination, Trends and Technologies*. Croatia: IntechOpen; 2011. DOI: 10.5772/13889, ISBN: 978-953-307-311-8
- [3] Hallack-Alegría M, Watkins DJ. Annual and warm season drought intensity–duration–frequency analysis for Sonora, Mexico. *Journal of Climate*. 2006;**20**:1897-1909. DOI: 10.1175/JCLI4101.1
- [4] Dévora-Isiordia GE, Gonzalez ER, Saldivar CJ. Diseño de procesos de desalinización de aguas subterráneas salobres mediante simulación química de electrodiálisis reversible, con propósitos de consumo humano. *Revista Latinoamericana de Recursos Naturales*. 2009;**5**(1):31-41
- [5] Nikolay V. Energy use for membrane seawater desalination current status and trends. *Desalination*. 2017;**431**:2-14. DOI: 10.1016/j.desal.2017.10.033
- [6] Shaffer DL, Yip NY, Gilron J, Elimelech M. Seawater desalination for agriculture by integrated forward and reverse osmosis: Improved product water quality for potentially less energy. *Journal of Membrane Science*. 2012;**415-416**:1-8. DOI: 10.1016/j.memsci.2012.05.016
- [7] Quist-Jensen CA, Macedonio F, Drioli E. Membrane technology for water production in agriculture: Desalination and wastewater reuse. *Desalination*. 2015;**364**:17-32. DOI: 10.1016/j.desal.2015.03.001
- [8] Dévora-Isiordia GE, Robles A, Fimbres GA, Álvarez J. Comparación de métodos de descarga para vertidos de salmueras, provenientes de una planta desalinizadora en

- Sonora, México. *Revista Internacional de Contaminación Ambiental*. 2017;**33**:45-54. DOI: 10.20937/RICA.2017.33.esp02.04
- [9] Dévora-Isiordia GE, Lopez-Mercado ME, Fimbres-Weihs G, Alvarez-Sanchez J, Astorga-Trejo S. Desalination by reverse osmosis and its use in agriculture in Valle del Yaqui, Sonora, Mexico. *Tecnología y Ciencias del Agua*. 2016;**7**(3):155-169
- [10] Zarzo D, Prats D. Desalination and energy consumption. What can we expect in the near future? *Desalination*.**427**:1-9. DOI: 10.1016/j.desal.2017.10.046
- [11] López ME. Evaluación de una planta desalinizadora de ósmosis inversa para su empleo en la agricultura [thesis]. Ciudad Obregón, Sonora, México: Instituto Tecnológico de Sonora; 2013
- [12] Liang W, Ma X, Wan P, Liu L. Plant salt-tolerance mechanism: A review. *Biochemical and Biophysical Research Communications*. 2018;**495**:268-291. DOI: 10.1016/j.bbrc.2017.11.043
- [13] Gasca C, Menjivar J, Torrente-Trujillo A. Cambios en el Porcentaje de Sodio Intercambiable (PSI) y la Relación de Adsorción de Sodio (RAS) de un suelo y su influencia en la actividad y biomasa microbiana. *Acta Agronómica*. 2011;**60**:27-38
- [14] Pankratz T, IDA. Market profile. In: *Desalination Yearbook*. United Kingdom: International Desalination Association; 2009. pp. 91-125
- [15] Pankratz T, IDA. Market profile. In: *Desalination Yearbook*. United Kingdom: International Desalination Association; 2017. pp. 34-46
- [16] Martinez-Alvarez V, Martin-Gorriz B, Soto-Garcia M. Seawater desalination for crop irrigation—A review of current experiences and revealed key issues. *Desalination*. 2016;**381**:58-70. DOI: 10.1016/j.desal.2015.11.032
- [17] Almodares A, Hadi MR, Dosti B. Effects of salt stress on germination percentage and seedling growth in sweet sorghum cultivars. *Journal of Biological Sciences*. 2007;**7**(8):1492-1495. DOI: 10.3923/jbs.2007.1492.1495
- [18] Bafeel SO. Physiological parameters of salt tolerance during germination and seedling growth of Sorghum bicolor cultivars of the same subtropical origin. *Saudi Journal of Biological Sciences*. 2014;**21**:300-304. DOI: 10.1016/j.sjbs.2014.05.005

Activated Carbon Cloth for Desalination of Brackish Water Using Capacitive Deionization

Hisham A. Maddah and Mohammed A. Shihon

Additional information is available at the end of the chapter

<http://dx.doi.org/10.5772/intechopen.76838>

Abstract

Capacitive deionization (CDI) is an emerging technology that is currently being widely explored for brackish water desalination. The theory behind the CDI technology depends on ion electrosorption at the surface of a pair of electrically charged porous carbon electrodes. Salt ions are removed upon applying an electrical low voltage of 1.2 V between two electrodes. Activated carbon cloth (ACC) electrodes have a significant potential for energy-efficient CDI water desalination due to the high surface area and salt storage capacity in which salt ions will be temporarily immobilized. The current state of the art of CDI technology is critically reviewed and evaluated to understand and summarize CDI background, phenomenon, advantages, operating conditions, performance metrics and equations, carbon electrode materials, cell architectures and CDI designs. We also provide a review study to evaluate the performance and feasibility of utilizing ACC-CDI systems for brackish water desalination.

Keywords: CDI, brackish water, treatment, activated carbon cloth, ACC, salt, desalination

1. Introduction

Water has always been prioritized as the most vital element for human existence since it makes up to 70% of human total body weight. Expected life quality and life span of any human are directly related to the presence of fresh water for drinking and other daily uses [1, 2]. Recent studies showed that both worldwide demand for drinking water and production of wastewater are increasing dramatically. By the year of 2025, it is expected that there will be 1.8 billion people suffering from fresh water shortage due to the high amounts of wastewater

produced from industrial wastes. Hence, improving water purification technologies is important to secure fresh water for the coming generations [3–6].

Today, there are numerous water and wastewater treatment technologies that are commercially selected and utilized based on both water feed characteristics and required water product quality. For example, high saline water (seawater) is usually treated in advanced reverse osmosis (RO) membrane desalination plants; a membrane consists of a porous layer of polymeric or metal material that allows the passage of fluid with restrictions to salt particles. Pressure-driven membrane technology has no side pollution effects and requires a small footprint for installation. However, membrane processes require applying low/high pressures to pump water for filtration and thereby increasing energy consumption and water production cost [4–6]. In contrast, low saline water (e.g., groundwater, surface water and brackish water) is better treated with industrial emerging technologies, which are different from membranes to reduce energy costs, such as electro dialysis (ED) and capacitive deionization (CDI) [7, 8].

2. Capacitive deionization

2.1. Historical background

In 1960s, the concept of capacitive deionization (CDI) was introduced at the University of Oklahoma by G.W. Murphy as an alternative water treatment method and was called “electrochemical demineralization of water.” Activated carbon powder (charged electrode sheets) and flow-through electrode architecture were selected for the first designed CDI system to treat saline water. Carbon electrodes were capable of capturing salt ions as a result of the static electrical force and the physical adsorption [9–11]. Murphy and Caudle combined mass balance and transport equations to obtain a model which described the salt concentration as function of time [12]. It was believed that ion removal is attributed to specific chemical groups present on the surface which are reduced or oxidized (faradaic reactions) and create ionic bond with salts [13].

Evans studied the mechanism of “electrochemical demineralization,” which is the CDI process, and carried out the mass balance analysis to explain the fundamental idea behind ion removal. Evans’ explanation analysis was similar to Murphy’s findings and it was added that the concentration of surface groups determines the salt removal efficiency [14].

However, Murphy’s and Evans’s classical views on water desalination by porous electrodes are no longer valid and have been replaced by the common electric double layer theory (EDL) which describes the capacitive storage of ions in electrode pores [9, 10].

In 1968, a commercialization study on CDI, a demineralization unit, was initiated by Reid et al. to sustain the CDI process for long-term operation and without losing electrode adsorption capacity over time. Furthermore, it was demonstrated that the CDI unit is effective for the removal of other ions besides sodium and chloride which include calcium, magnesium, sulfate, nitrate and phosphate ions [13].

In 1970s, Johnson et al. [15] proposed a reversible electrosorption model for electrode regeneration by removing the applied electric potential to release the captured ions back to a concentrate flow. Salt adsorption mechanism was investigated to be a result of the EDL theory which was known as “potential-modulated ion sorption.” A porous electrode model and electrode charge voltage dependence were developed to conclude that electrode capacity depends on the EDL electrical capacity, the available surface area and the applied cell voltage. Johnson and Newman indicated that CDI is economically feasible only if stable electrodes can be produced [9, 10, 15, 16].

In 1990s, CDI technology captured the attention of scientific scholars and many released publications were about developing an effective carbon electrode with large internal surface area and good conductivity for better water deionization. The summarized timeline of CDI development is shown in **Figure 1** [13].

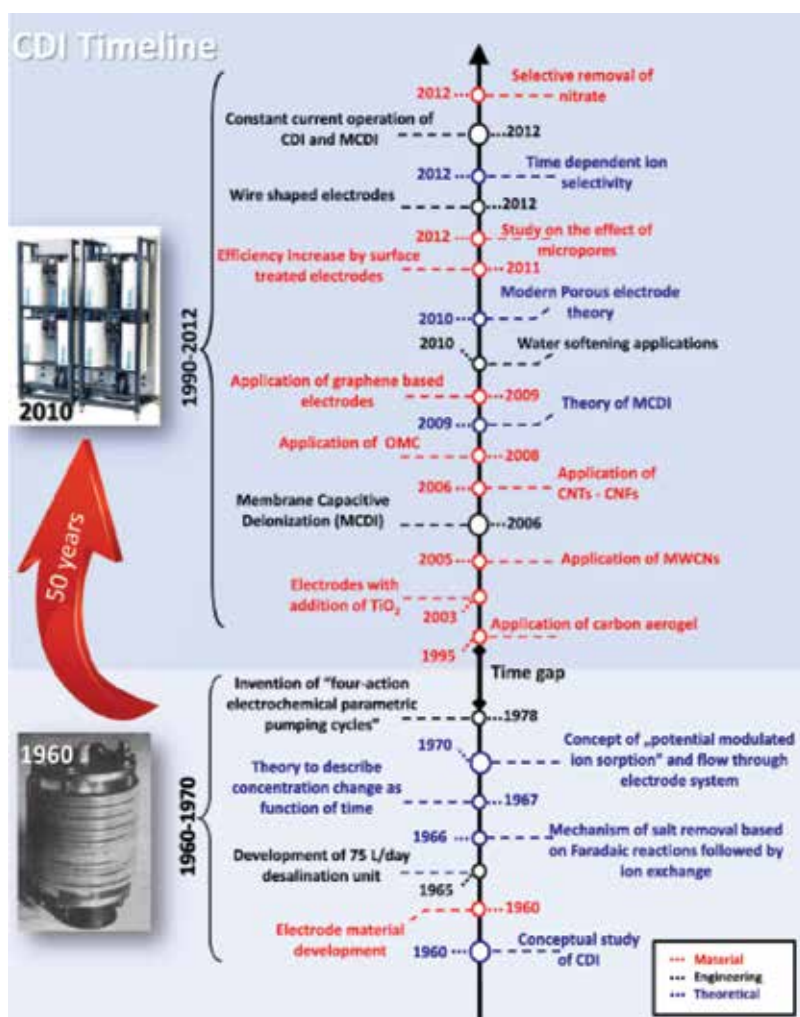


Figure 1. Timeline of scientific developments of CDI, indicating milestones since the inception of CDI in 1960 [13].

2.2. Fundamental concept

The fundamental concept of CDI technology is simply associated with electrosorption of ions at the surface of a pair of electrically charged electrodes (high porous carbon materials) [17]. The electrosorption phenomenon can be understood by the classical EDL theory which explains the charge-voltage and salt-voltage characteristics of the cell that strongly depends on electrodes properties. Basically, it is approximated that charge transfer along the cell is only attributed to electronic charge (in the carbon electrode) and ionic charge (in the aqueous phase), while surface charge from chemical adsorption/carbon redox chemistry is neglected [18]. In other words, there will be no voltage drop across the EDL if the material is not charged since the two components of charge sum up to zero, and only local voltage differences relative to a reference electrode play a role and not absolute potentials [13, 17, 18].

The concept of the EDL dates back to Helmholtz, in the nineteenth century, who assumed that there should be a condensed layer of counterions that directly compensates the surface charge, meaning that all surface charges are directly charge compensated by countercharges adsorbed to the surface [19]. If this holds, ion/charge transport in CDI would be ideally described by Helmholtz-model which states that one full salt molecule (one cation at the cathode and one anion at the anode) would be removed for every electron transferred from one electrode to the other giving us unity charge efficiency.

Unfortunately, porous CDI electrodes do not condense ions right next to their surface; instead, ions remain diffusively distributed in a layer close to the surface. Hence, Gouy-Chapman (GC) described that there must be a diffuse layer combined by an inner stern (or compact) layer in between the electrodes (the carbon matrix) and the diffuse layer. Structure of the EDL according to the Gouy-Chapman-Stern (GCS) theory for a single planar EDL is shown in **Figure 2** [20–22].

Diffuse layer observations show that ion concentrations progressively decay with increasing distance from the surface. The characteristic distance for the counterion concentration and potential to decay by a factor of $e^{-2.7}$ is known as the Debye length (λ_D). It was estimated that the diffuse layer starts to fade away after 2 or 3 times the Debye length. The Debye length of a sodium chloride (NaCl) solution of 10 mM ionic strength is approximately 3.1 nm at 20°C. GCS theory assumes that there is no overlapping of the diffuse layer extending from one surface with a nearby surface. However, micropores (<2 nm) in activated carbon particles are generally less than the Debye length, thus the EDL overlap situation occurs [13].

Based on the EDL concept, CDI desalination occurs when putting a charged carbon electrode in contact with ionic solution, and then counterions will occupy the electrode-electrolyte interface in the pores inside the carbon particles due to the presence of the Coulomb force which forms the EDL. It should be noted that ions are not only removed by the electrical adsorption, but there will be a contribution from the physical adsorption effect. However, the regeneration step takes place when there is reduction in the applied potential (charge) and/or reversed polarity which results in the removal of Coulomb force and/or reversing the force effect (i.e., there will be a repulsion force between held ions and charge) and therefore releasing the held ions back to the concentrate solution. Desalination/regeneration steps form one complete CDI treatment cycle [9].

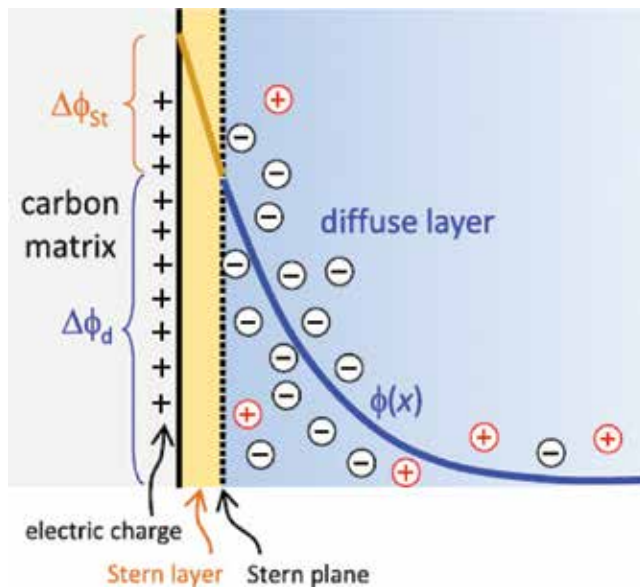


Figure 2. Structure of the electrical double layer (EDL) according to the Gouy-chapman-stern (GCS) theory for a single planar EDL [13].

2.3. Advantages

Effective water desalination at lower costs is considered as one of the grand technological challenges of the twenty-first century. Common commercial technologies such as reverse osmosis, electro dialysis, thermal distillation and multistage flash distillation have been developed to achieve efficient desalination. However, the latter technologies consume a lot of energy and may not be a cost-effective manner for water desalination. Recently, CDI has gained much attention as a desalination technology alternative for brackish water (which has low or moderate salt content) due to its simple design, low energy consumption, economical feasibility, high efficiency, safety and environmental friendliness [23–27].

CDI does not involve membranes and therefore it is a low-pressure process of deionization which does not require energy for pumping water or any other means (except for a fairly low applied voltage). Moreover, CDI stores applied potential as a capacitive energy and one may recover this energy again to further reduce power consumption and operating expenses [27, 28]. In other words, electrode discharge step (regeneration) can be recovered and utilized to charge a neighboring cell (electrosorption) for ion rejection [13]. Possibility of electrode fouling during the desalination-regeneration cycles is relatively low, hence, making this technology more attractive for desalting water. CDI does not have additional contaminants (e.g., chemicals) released from the process which makes CDI technology environmentally friendly [29].

From previous discussed advantages, CDI becomes very suitable in providing fresh water and agricultural water with low cost and without pollution [26, 30]. Despite that CDI may not

be capable of treating sea water (high saline water); it is still efficient to remove salt concentrations up to 10 g/L. Accordingly, water shortage problems in arid areas and contaminated brackish water-rich regions can be overcome with the advantageous CDI technology [13].

CDI technology does not require expensive designed parts/materials for the construction phase. Materials required to build a CDI cell are commercially available and cheap which include, but not limited to, a pair of porous electrodes (e.g., carbon), a porous separator between the two electrodes, a conductive rod material (e.g., graphite) to be attached to both electrodes and connected to a potentiostat (to transfer a typical applied potential of 1–1.4 V) and a designed acrylic support/reservoir with an inlet and outlet [17].

2.4. Operating conditions

Since this chapter is related to using activated carbon cloth (ACC) as an electrode in the CDI cell, the reported operating conditions in this section are for ACC-CDI systems. Laxman et al. and Myint et al. have investigated the use of ACC (Zorflex FM-100) for CDI brackish water desalination. Zorflex ACC thickness was about 1.0 mm, electrode area was 8.4 cm² and specific surface area was approximately 1100 m²/g. The ACC was grafted/coated with zinc oxide (ZnO) micro/nanomaterials (nanoparticles, nanorods, microspheres and microspheres) by a simple and low-temperature hydrothermal method to enhance salt removal from the improved electrode conductivity [29, 31, 32].

Based on the literature data for ACC-CDI systems, studied feed water, NaCl solution concentration should be between 100 and 1000 ppm (typically a salt concentration between 5 and 50 mM and/or 0.5 and 5 mS/cm) and applied potential must be in the range 0.6–1.6 V DC (typically 1.2 V to avoid water hydrolysis at 1.23 V). The system should be operated under room temperature and normal atmospheric pressure with a flowrate of 2 mL/min (and may reach up to 1–4 L/min). Flowrate values could be changed/increased and might not have much effect on salt adsorption. Desalination/regeneration time should be approximately 25 min (typically 10 min for desalination and 10 min for regeneration, or charge–discharge cycle can have any duration/time, from very short ~4 min, with little adsorption, to very long >90 min, depending on when equilibrium concentration becomes steady with time). Salt rejections could reach up to 25 and 35% for plain ACC and ACC deposited with ZnO nanorods, respectively, and electrode electrosorptive capacity could reach up to 8.1 mg/g [17, 31, 32].

2.5. Performance metrics and equations

2.5.1. Desalination (salt removal) efficiency

It is defined as how much salt ions can be removed from brackish water in a CDI cell; see Eq. (1).

$$R (\%) = \frac{C_0 - C_f}{C_0} \times 100 \quad (1)$$

where C_0 and C_f are the initial and final (or equilibrium) concentration in ppm “mg/L” (or conductivity in $\mu\text{S/cm}$) of saline (NaCl) solution. Regeneration efficiency can also be calculated

from the abovementioned equation and multiplying the result by (-1) to have a positive number since C_f will be much higher than C_0 (due to flushing/cleaning the system with DI water) [29, 32].

2.5.2. Charge efficiency

It is defined as the ratio of adsorbed salt over charge and calculated from Eq. (2) by multiplying the total adsorbed salts on the electrodes (mol/g) by Faraday's constant (C/mol) and then divided by the total amount of charge density transferred for adsorption cycle (C/g). Charge efficiency is used to analyze static electrode CDI cycles as an integral property and it must be less than unity (or approaching one for the ideal case). Charge efficiency is a function of the applied potential during charging/discharging and initial salt concentration. Increasing charging and discharging voltages and decreasing feed concentrations will result in higher charge efficiency. Higher values of charge efficiency lead to lower energy consumption [17, 24, 25].

$$\Lambda = \frac{\Gamma \times F}{\Sigma} = \frac{(SAC/M) \times F}{\int I dt} \quad (2)$$

where Γ is the deionization capacity upon applying a cell voltage (mol/g), F is the Faraday's constant (96485.33 C/mol), Σ is the total charge transferred (C/g) and is calculated through integrating the current over time per electrode mass to give an estimate on the total amount of charge delivered in Coulombs per gram of electrode during the adsorption cycle, SAC is the salt adsorption capacity (see Section 2.5.3) and is calculated from Eq. (3) with the unit (mg/g), M is the molar mass of NaCl (58.4 g/mol), I is the measured current density (A/g, where A = Amperes = C/s), t is the charging time (s) and $\int I dt = C/g$, where C = Coulomb. Current is generally higher in magnitude during charging when compared to discharging. The above equation is valid for any CDI system, symmetric or asymmetric cells with/without redox reactions as long as the current and salt rejection are measured from experiment [17, 24, 25].

2.5.3. Salt adsorption capacity

Salt adsorption capacity (SAC) is defined as the amount of ions in milligram electroadsorbed per gram of electrodes; see Eq. (3). This is also known as "specific salt adsorption capacity" and gives information on the electrosorption capacity of both electrodes of a cell's charge-discharge cycle. One may calculate the maximum salt adsorption capacity (mSAC), which is also known as equilibrium salt adsorption capacity (eqSAC), when the measured conductivity of the cell effluent no longer changes over time [17].

$$SAC (mg/g) = \frac{(C_0 - C_f)V}{m} \quad (3)$$

where C_0 and C_f are the initial and final (or equilibrium) concentrations of NaCl solution (mg/L), m refers to the total mass of the two carbon electrodes when dry (g) and V represents the volume of NaCl solution (L). However, if the effluent was discharged, the amount of ion adsorption per unit mass of carbon electrodes can be calculated from Eq. (4) [17, 23, 27];

$$SAC \text{ (mg/g)} = \frac{C_f Q t}{m} \quad (4)$$

where C_f represents the final ion concentration of NaCl solution (mg/L), Q is the flow rate of the solution (L/min), t is the electrosorption time (min) and m is the mass of the two carbon electrodes (g) [17, 23, 27, 31, 33, 34].

2.5.4. Average salt adsorption rate

This metric gives information on the rate of salt sorption, and is usually in the units (mg/g/min) with the (min) referring to the charging time, (mg) referring to the mass of salt removed, (g) referring to the mass of the two electrodes together and average salt adsorption rate (ASAR) is calculated from Eq. (5).

$$ASAR = \frac{SAC}{t} \quad (5)$$

where t stands for the deionization time (min) and SAC refers to the salt adsorption capacity (mg/g). Zhao et al. reported the highest value of ASAR which is 2.3 mg/g/min for a membrane CDI cell architecture (see Section 4.3) with sub-equilibrium charging times and 300-mm-thick electrodes [17, 27, 35, 36].

Kim-Yoon proposed KY diagrams which combine two CDI metrics, salt adsorption capacity (SAC) and salt adsorption rate (ASAR), in a single plot. KY diagram can be used in optimization studies for CDI cells. For example, KY was plotted for a flow by CDI cell with static film electrodes (Kuraray YP50F-activated carbon powder) as a function of the charging voltage as shown in **Figure 3**, and the discharge voltage was set to zero for all experiments. Calculations were carried out at varied half-cycle time (HCT; the charging and discharging steps were of the same duration) and the charging voltage was set between 0.9 and 1.3 V. Dividing SAC by ASAR is equal to twice the half-cycle time (HCT) and optimum operational values are shown by black circles [17, 27, 35, 36].

2.5.5. Specific capacitance

It is defined as the cell or electrode charge storage capacity, expressed in Farads per gram (F/g), and is estimated from capacitive charge and the applied cell voltage as in Eq. (6) and/or Eq. (7). The specific capacitance is often referred to a single electrode capacitance. Capacitance and desalination (salt removal) are not equivalent but are linked by the charge efficiency (see Section 2.5.2). Cyclic voltammetry measurements should be performed on the working electrode using a potentiostat with a specific scan rate (mV/s) and a potential window (e.g., -0.4 V to +0.4 V), to obtain voltammogram diagrams and then calculate the specific electrode capacitance from obtained data and given Equations [17, 27, 29, 31].

$$C_s = \int_{E_1}^{E_2} \frac{i(E)dE}{[2(E_2 - E_1)mv]} \quad (6)$$

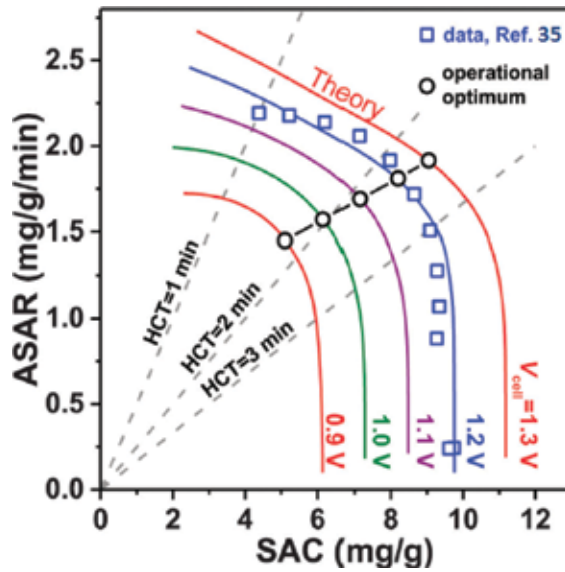


Figure 3. Kim-Yoon plot for (ASAR) in a flow by CDI cell vs. (SAC) as a function of charging voltage.

$$C_s = \frac{i(E)}{mv} \tag{7}$$

where E_1 & E_2 are the potential ranges (V), m is the electrode mass (g), v is the scan rate (mV/s), $i(E)$ is the instantaneous current and power delivered during the scan (A).

2.5.6. Langmuir isotherm

Adsorption data of the electrolyte with respect to carbon electrode in CDI systems can be simulated by the Langmuir isotherm (1918) as in Eq. (8), by plotting C_e/q_e vs. C_e .

$$\frac{C_e}{q_e} = \frac{1}{q_m K_L} + \frac{C_e}{q_m} \tag{8}$$

where C_e is the equilibrium concentration of salt ions (mg/L), q_e represents the amount of electroadsorbed ions at equilibrium per unit weight of carbon electrode (mg/g), q_m is the maximum adsorption capacity (mg/g) with respect to the complete surface monolayer coverage and K_L (L/mg) is the Langmuir constant related to the adsorption energy [33].

3. Carbon electrode materials for CDI

Carbon is a large chemical family and represents a wide range of materials that are mainly composed by the carbon element. Among them, graphite and diamond are the two with crystal

structures and are not property adsorption materials because of the lack of surface area. Others are normally referred to as amorphous carbon. Earlier studies in the last few decades showed that carbon electrodes are promising in CDI cells because of their very high specific surface area, and thereby resulting in better electrosorption and higher salt rejections. Common carbon electrodes, which are utilized for CDI, are activated carbon, activated carbon powder, activated carbon cloth, carbon aerogel, carbon nanotubes, carbon nanofibers, ordered mesoporous carbon and graphene [9, 13].

3.1. Selected parameters for an ideal electrode

1. High specific surface area; it allows for high electrical capacity and high ion capacity to hold considerable quantity of ions (high adsorption). However, not the entire surface area calculated from experimental methods may be available to ions [9, 13, 29].
2. High electrical conductivity; it offers higher ion capacity [9, 31]; one may increase electrical conductivity by coating the electrode surface with dielectric materials. Myint et al. studied the CDI electrode made of nano/micro-sized zinc oxide/ACC to achieve better performance. Metallic or metal-like (e.g., metal oxide; titania) electronic conductivity guarantees that the whole electrode surface of all particles is charged with low-voltage gradients within the carbon. Low energy dissipation and low heating are achieved by having a high electronic conductivity [29, 31, 32]. Jia et al. reported that titania-modified-ACC increased adsorption sites on the electrode surface and showed good reversibility [9].
3. High stability: high physical, chemical and electrochemical electrodes' stability over a wide range of pH values, and the ability to tolerate frequent voltage changes is important to ensure longevity and system stability [9, 37].
4. High and improved hydrophilicity: good wetting behavior, by introducing hydrophilicity, ensures that the whole pore volume participates in the CDI process [9, 13].
5. Lower spacing between the two electrodes and large spacer electrostatic permittivity (short distances between EDLs) [9]. Laxman et al. added an ion exchange membrane in CDI cells to achieve better surface energy and stability [31].
6. Fast ion mobility within the pore network: bottlenecks or very small pores cause diffusional limitations and limit the kinetics. This concerns the porosity within carbon particles as well as the pore structure of the entire CDI electrode, considering, for example, interparticle distances and electrode thickness [13].
7. Low costs and scalability: low costs are important for large-scale applications [9, 13].
8. High bio-inertness: for long-term operation biofouling needs to be avoided in surface or brackish water treatment [13].
9. Low contact resistance between the current collector and the porous electrode to avoid a large voltage drop; thus, a low interfacial resistance is required from the electrode to the current collector [9, 13].
10. Good processability, moldable into film electrodes based on compacted powders, fibers or monoliths [13].

Non-composites		Composites	
Electrode	Specific surface area (m ² /g)	Electrode	Specific surface area (m ² /g)
ACC*	1200–1980	ACC/titania*	~ 1890
AC powder*	730–3073	AC/titania*	~ 546
AC nanofiber*	670–712	AC/Graphene*	~ 779
Graphene	220–406.4	Graphene/mesoporous carbon	~ 685.2
Carbon aerogels	113–1100	Graphene/mesoporous	~ 400.4
Carbon nanofiber	~ 186	Graphene/CNT*	222.1–479.5
CNT*	129.2–359.6	CNT/carbon nanofiber*	~ 211
OMC*	~ 844	CNT/micro/mesoporous carbon*	526–990

*ACC: Activated Carbon Cloth; AC: Activated Carbon; CNT: Carbon Nanotubes; OMC: Ordered Mesoporous Carbon.

Table 1. Specific surface area of various carbon non-composite and composite electrodes, as measured and reported from several previous studies reported by Jia et al. [9].

3.2. Specific surface area of various electrodes

As discussed earlier, higher specific surface area is the most important parameter in selecting an ideal carbon electrode for the CDI cell to ensure the maximum adsorption. Hence, **Table 1** shows the specific area of various carbon non-composites and composite electrodes [9].

4. Cell architectures and CDI designs

4.1. Flow between electrodes

In this architecture, CDI contains a pair of porous carbon electrodes parted by a spacer where feed water flows (feed water flows perpendicular to the applied electric field direction (see **Figure 4A**)). Flow between electrodes, which is also known as flow by electrodes, is the oldest and most used CDI architecture and was widely employed in various experiment works, including, but not limited to, removing salt from numerous feed waters, inspecting novel electrode materials performance and performing fundamental studies of salt sorption on porous electrodes. Traditional CDI design has advantages over newer designs due to its simplicity (no membranes or flow electrodes), which can potentially lower the system cost and reduce fouling issues [17, 38–42].

4.2. Flow-through electrodes

This architecture is defined as a CDI cell, with a pair of porous carbon electrodes parted by a thinner spacer, in which the feed goes directly through the electrodes and parallel to the applied electric field direction (**Figure 4B**). Flow-through electrodes system is used in a three-electrode cell to study fundamental performance parameters such as charge efficiency. Flow-through electrodes allow faster cell charging relative to flow-between systems. The primary

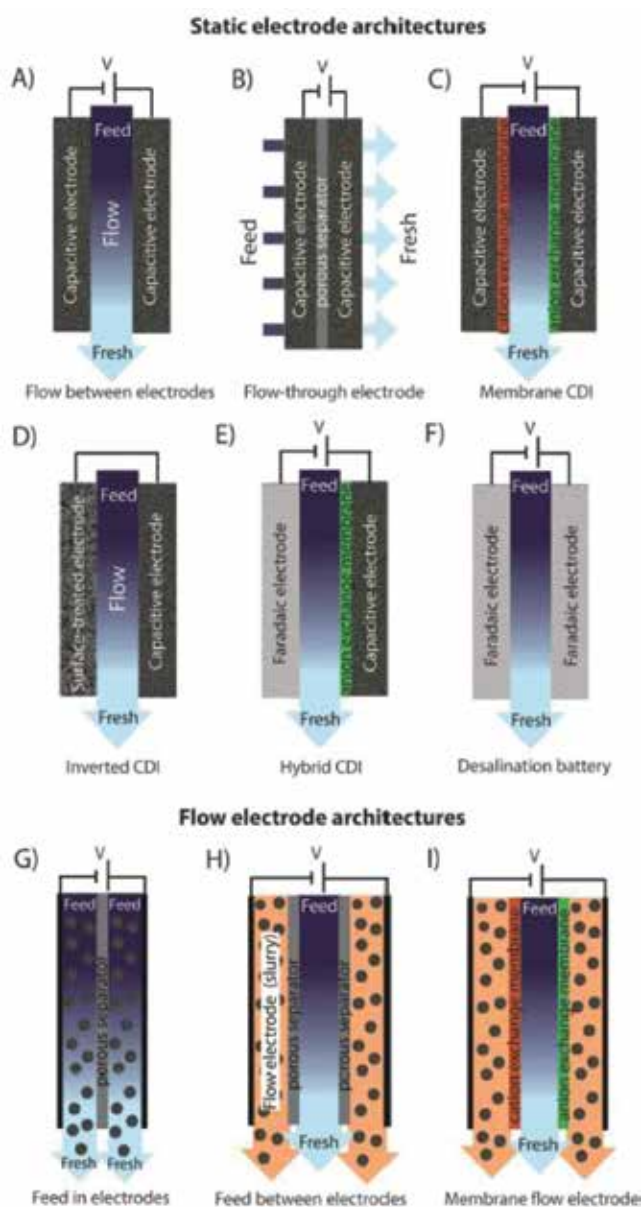


Figure 4. CDI architectures using static electrodes, including (A) flow between electrodes, (B) flow-through electrode, (C) membrane CDI and (D) inverted CDI. (E) and (F) show architectures which utilize static electrodes that depart from purely capacitive behavior, including (E) hybrid CDI and (F) a desalination battery. (G)–(I) show CDI architectures with flow electrodes, including systems with (G) feed-in electrodes, (H) feed-between electrodes and (I) membrane flow electrode CDI [17].

benefit of this architecture is to remove (or decrease) the separator layer which also serves as the feed flow channel, thus allowing a less separator thickness (from normally 200–500 μm to about 10 μm). The reduction of spacer thickness between electrodes allows for more compact

cells with lesser cell ionic resistance and faster desalination due to diffusion timescale reduction governing the removal of salt from the electrodes [17, 38, 42, 43].

4.3. Membrane CDI

This architecture uses ion exchange membranes on the separator side of each electrode (**Figure 4C**). As in electro dialysis cells, the feed water channels in membrane CDI (MCDI) cells are bounded by an anion exchange membrane (AEM) and a cation exchange membrane (CEM). The main benefit of the addition of membranes to the CDI cell is to improve the charge efficiency (which is linked to the efficiency of cell energy). Membranes may be tailored to have selectivity between different ions of the same charge sign which offers an additional level of tunability for complex multi-ion systems. The benefit of charging a CDI cell with constant current rather than constant voltage is that constant current allows for constant cell effluent concentration, which was first demonstrated on an MCDI cell which has the well-established advantage of improving the system's charge efficiency and sorption capacity because of the addition of ion exchange membranes, but this added a significant membrane cost as compared to other cell components [17, 13, 41–45].

4.4. Inverted-CDI

In this architecture, the flow between electrode CDI cell is modified by using a surface-treated carbon ^Anode (negative surface charge via a chemical surface treatment), leading to the case of inverted-CDI (I-CDI, **Figure 4D**). Inverted cell demonstrates inverted behavior, whereby cell charging results in desorption of ions and cell discharging results in ion electrosorption [17, 46].

4.5. Hybrid CDI

A hybrid cell architecture combines a battery electrode (sodium manganese oxide) and a capacitive electrode (porous carbon) in a single desalination cell (**Figure 4E**). Hybrid systems enable high salt adsorption of ~ 31 mg/g as compared to traditional capacitive CDI cells which achieve up to about ~15 mg/g [17, 47–49].

4.6. Desalination battery

In this architecture, CDI cell utilizes two battery electrodes (**Figure 4F**) for better salt adsorption. The Faradaic reactions in electrodes are tuned to consume a single species (such as chloride or sodium) and may not be able to significantly remove (or affect) other present species [17, 47].

4.7. Carbon flow electrodes

In this design, feed water is pumped through electrode compartments for salinity treatment (**Figure 4G–I**). Carbon flow electrodes (FCDI) have two major benefits: first, feed water flowing through a single cell can be desalinated continuously, as the active carbon particle discharge (formation of brine) can occur as a separate process downstream of the cell, and a second major benefit is that FCDI can effectively increase the capacitance available for better

desalination than that of static electrode CDI systems. Therefore, FCDI can desalinate higher salinity streams than static CDI systems. Subsequently, FCDI has to evolve gradually to be economically suitable for sea water desalination [17, 47, 50].

5. ACC-CDI performance analysis

Removal efficiency of the CDI cells has been reviewed and analyzed with respect to many parameters (operating conditions). The effect of the feed flow rate and the initial ionic concentration on the removal efficiency is shown in **Figure 5**. It was found that salt rejections decrease at high flow rate; this is because the separation process requires high contact time between the electrode surface and the salt solution. Furthermore, high feed concentrations would result in reduced removal efficiency but would increase electroadsorption capacity (SAC) since high amounts of salts will fill up more carbon pores and yield in higher adsorbed salts per electrode mass. Removal efficiency decreases at higher salt concentrations because it would

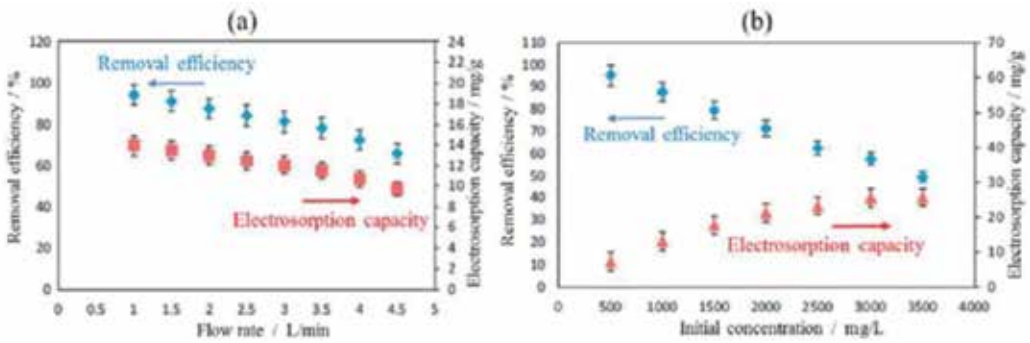


Figure 5. Removal efficiency and electroadsorption capacity as a function of (a) flow rate and of (b) initial concentration of NaCl solution [51].

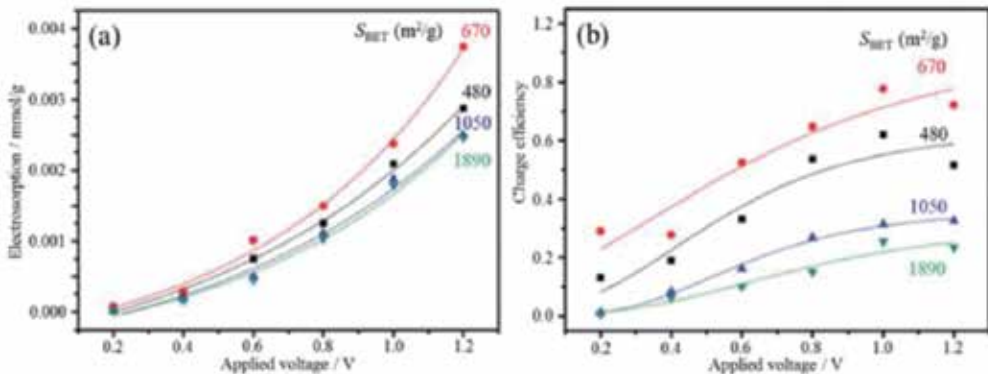


Figure 6. Activated carbon fibers (ACFs) with different S_{BET} (BET surface area): (a) amount of electroadsorption and (b) charge efficiency against applied voltage [52].

be difficult to drop a high salinity level by utilizing small electrode mass and dimensions (e.g., $3 \times 3 \text{ cm}^2$ and 0.6 g) which is the case of any CDI designed for lab-scale analysis [51, 52].

Figure 6 shows the effect of applied potential on SAC and charge efficiency at different activated carbon fibers (ACFs) electrodes with various BET surface area (S_{BET}). It was observed that there will be improvements in both SAC and charge efficiency if higher voltages are applied and higher electrode S_{BET} is achieved. The effect of ACC treatment (with KOH or HNO_3 for different treatment times) on the removal efficiency has been studied and shown that lower treatment (3 h) is favored to achieve a high CDI performance; see **Figure 7**. Conversely, longer CDI desalination times (4 min) are preferred and the desalination cycle may be terminated

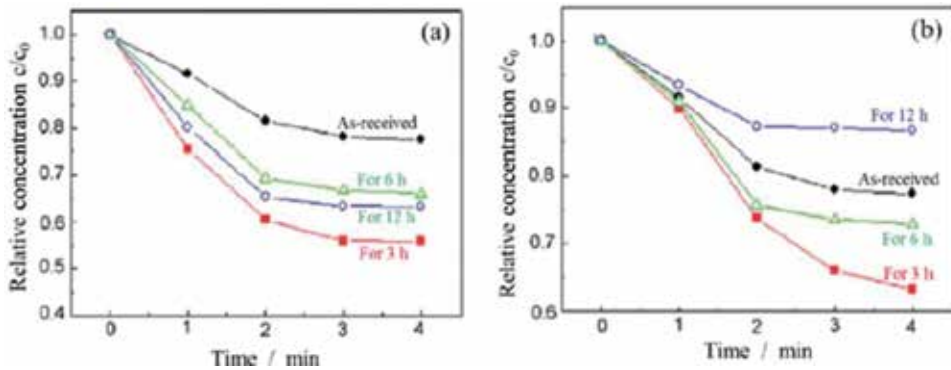


Figure 7. Changes in NaCl concentration (initial conductivity of 2000 mS/cm) with time for ACC. (a) ACC treated in KOH and (b) in HNO_3 [53].

Carbon electrode	Specific surface area (m^2/g)	Initial salt concentration (mg/L)	Applied voltage (V)	Operation time (min)	Salt Rejection (%)	Salt adsorption capacity, SAC, (mg/g)	Ref.
ACC	984	1000	1.6	7	25	5.4	[31]
	1043	100	1.2	12.5	15	—	[32]
	1980	5844	1	300	18	1.75	[54]
	1200	100	1.2	7	15	5.8	[29]
	1980	5844	0 ~ 1.2	1440	12	—	[55]
ACC/ZnO	1300	100	1.2	7	22	8.5	[29]
	637	1000	1.6	7	15	8.1	[31]
	—	100	1.2	12.5	35	—	[32]
ACC/titania	1180	5844	0 ~ 1.2	1440	50	8.1	[55]
	1890	5844	1	300	40	4.3	[54]
	546	500	1.2	200	45	—	[56]

Table 2. Various activated carbon cloth (ACC) electrodes and their CDI treatment performance.

once we reach a stable product concentration; by doing this, one can estimate the highest achievable rejection for a specific CDI cell; see **Figure 7**.

ACC-CDI performance was evaluated to check for the system feasibility for water treatment by comparing the literature results for different studied ACC-CDI systems. Important parameters associated with the used electrode (e.g., specific surface area), electrolyte solution (e.g., initial salt concentration) and experiment operating conditions (e.g., applied voltage and operation time) were gathered and reported in **Table 2**. Observed salt rejections and SACs were gathered for non-composite ACC and composites ACC/ZnO and ACC/titania electrodes to be compared separately. The highest achieved rejections were 25, 35 and 50% for ACC, ACC/ZnO and ACC/titania, respectively, and the maximum observed SACs were 5.8, 8.5 and 8.1 for ACC, ACC/ZnO and ACC/titania, respectively.

6. Conclusion

CDI technology shows a great potential for brackish water desalination due to its simple design, cheap components, low energy-consumption (fairly low potential and recoverable energy), economical feasibility, high efficiency, safety and environmental friendliness. The classical EDL theory explains the concept behind the CDI which is simply associated with electrosorption of ions at the surface of a pair of electrically charged electrodes; counterions will occupy pores inside the carbon particles due to the presence of the Coulomb force. Salt rejection occurs due to both physical adsorption and electrical adsorption contributions. ACC-CDI systems should have feed water salinity between 100 and 1000 ppm (typically between 5 and 50 mM and/or 0.5 and 5 mS/cm) and applied potential must be in the range 0.6–1.6 V DC (typically 1.2 V). Desalination/regeneration time can have any duration/time, from very short ~ 4 min, with little adsorption, to very long > 90 min, depending on when equilibrium concentration becomes stable. ACC-CDI rejections could reach up to 25 and 35% for plain ACC and ACC deposited with ZnO nanorods.

CDI performance metrics and equations, which identify the system feasibility, have been discussed and included the following: desalination efficiency, charge efficiency, SAC, ASAR, specific capacitance and Langmuir isotherm. Selected parameters when choosing an ideal electrode must involve high specific surface area, high electrical conductivity, high stability, high hydrophilicity, low costs and scalability. It was found that traditional CDI design has advantages over newer designs due to its simplicity and lower costs. However, other CDI architectures showed higher system's efficiency (e.g., MCDI), but with a significant added cost. Generally, removal efficiency increases at low salt concentrations and low flow rates. Though high feed concentrations would result in higher SAC, higher applied potentials, higher surface areas and longer CDI desalination times are favored for better CDI performance. Observed salt rejections and SACs of various non-composite ACC and composites ACC/ZnO and ACC/titania showed that the composite electrodes have much higher numbers. The highest achieved rejections were 25, 35 and 50% for ACC, ACC/ZnO and ACC/titania, respectively, and the maximum observed SACs were 5.8, 8.5 and 8.1 for ACC, ACC/ZnO and ACC/titania, respectively.

Author details

Hisham A. Maddah^{1*} and Mohammed A. Shihon²

*Address all correspondence to: hmaddah@kau.edu.sa

1 Department of Chemical Engineering, King Abdulaziz University, Rabigh, Saudi Arabia

2 Department of Chemical Engineering, King Abdulaziz University, Jeddah, Saudi Arabia

References

- [1] Maddah HA, Alzhrani AS. Quality monitoring of various local and imported brands of bottled drinking water in Saudi Arabia. *World Journal of Engineering and Technology*. 2017;**5**(4):551-563
- [2] Maddah HA. Modeling the feasibility of employing solar energy for water distillation. In: *Handbook of Environmental Materials Management*. Springer International Publishing; 2018. pp. 1-25
- [3] Maddah H, Chogle A. Biofouling in reverse osmosis: Phenomena, monitoring, controlling and remediation. *Applied Water Science*. 2016;**7**(6):2637-2651
- [4] Matin A, Khan Z, Zaidi SMJ, Boyce MC. Biofouling in reverse osmosis membranes for seawater desalination: Phenomena and prevention. *Desalination*. 2011;**281**(1):1-16
- [5] Kang G, Cao Y. Development of antifouling reverse osmosis membranes for water treatment: A review. *Water Research*. 2012;**46**(3):584-600
- [6] Maddah HA, Chogle AM. Applicability of low pressure membranes for wastewater treatment with cost study analyses. *Membrane Water Treatment*. 2015;**6**(6):477-488
- [7] Fane AG. Membranes for water production and wastewater reuse. *Desalination*. 1996;**106**(1-3):1-9
- [8] Maddah HA et al. Determination of the treatment efficiency of different commercial membrane modules for the treatment of groundwater. *Journal of Materials and Environmental Science*. 2017;**8**(6):2006-2012
- [9] Jia B, Zhang W. Preparation and application of electrodes in capacitive deionization (CDI): A state-of-art review. *Nanoscale Research Letters*. 2016;**11**(1):1-25
- [10] Oren Y. Capacitive deionization (CDI) for desalination and water treatment - past, present and future (a review). *Desalination*. 2008;**228**(1-3):10-29
- [11] Blair John W, Murphy George W. Electrochemical demineralization of water with porous electrodes of large surface area. *Saline Water Conversion*. 1960;**27**(27):206-223
- [12] Murphy GW, Caudle DD. Mathematical theory of electrochemical demineralization in flowing systems. *Electrochimica Acta*. 1967;**12**(12):1655-1664

- [13] Porada S, Zhao R, Van Der Wal A, Presser V, Biesheuvel PM. Review on the science and technology of water desalination by capacitive deionization. *Progress in Materials Science*. 2013;**58**(8):1388-1442
- [14] Evans S, Hamilton WS. The mechanism of demineralization at carbon electrodes. *Journal of the Electrochemical Society*. 1966;**113**(12):1314-1319
- [15] Johnson AM, Venolia AW, Wilbourn RG, Newman J, Wong CM, Gilliam WS. The electrosorb process for desalting water. Washington: U.S. Dept. Interior pub. no. 516; 1970
- [16] Johnson AM, Newman J. Desalting by means of porous carbon electrodes. *Journal of the Electrochemical Society*. 1971;**118**(3):510
- [17] Suss ME, Porada S, Sun X, Biesheuvel PM, Yoon J, Presser V. Water desalination via capacitive deionization: What is it and what can we expect from it? *Energy and Environmental Science*. 2015;**8**(8):2296-2319
- [18] Biesheuvel PM, Fu Y, Bazant MZ. Electrochemistry and capacitive charging of porous electrodes in asymmetric multicomponent electrolytes. *Russian Journal of Electrochemistry*. 2012;**48**(6):580-592
- [19] Helmholtz H. Ueber einige Gesetze der Vertheilung elektrischer Ströme in körperlichen Leitern mit Anwendung auf die thierisch-elektrischen Versuche. *Annals of Physics*. 1853;**165**(6):211-233
- [20] Gouy G. Sur la Constitution de la Charge Electrique a la Surface d'un Electrolyte. *Comptes rendus de*. 1910;**149**:654
- [21] Chapman DL. A contribution to the theory of electrocapillarity. *Philosophical Magazine, Series 6*. 1913;**25**(148):475-481
- [22] Stern O. Zur Theorie der Elektrolytischen Doppelschicht. *Zeitschrift fur Elektrochemie*. 1924;**30**:508-516
- [23] Duan H, Yan T, An Z, Zhang J, Shi L, Zhang D. Rapid construction of 3D foam-like carbon nanoarchitectures via a simple photochemical strategy for capacitive deionization. *RSC Advances*. 2017;**7**(62):39372-39382
- [24] Kim C, Srimuk P, Lee J, Fleischmann S, Aslan M, Presser V. Influence of pore structure and cell voltage of activated carbon cloth as a versatile electrode material for capacitive deionization. *Carbon N. Y.* 2017;**122**:329-335
- [25] Zhao S, Yan T, Wang Z, Zhang J, Shi L, Zhang D. Removal of NaCl from saltwater solutions using micro/mesoporous carbon sheets derived from watermelon peel via deionization capacitors. *RSC Advances*. 2017;**7**(8):4297-4305
- [26] Huang Z-H, Yang Z, Kang F, Inagaki M. Carbon electrodes for capacitive deionization. *Journal of Materials Chemistry A*. 2017;**5**(2):470-496
- [27] Quan X et al. Capacitive deionization of NaCl solutions with ambient pressure dried carbon aerogel microsphere electrodes. *RSC Advances*. 2017;**7**(57):35875-35882

- [28] Anderson MA, Cudero AL, Palma J. Capacitive deionization as an electrochemical means of saving energy and delivering clean water. Comparison to present desalination practices: Will it compete? *Electrochimica Acta*. 2010;**55**(12):3845-3856
- [29] Myint MTZ, Al-Harathi SH, Dutta J. Brackish water desalination by capacitive deionization using zinc oxide micro/nanostructures grafted on activated carbon cloth electrodes. *Desalination*. 2014;**344**:236-242
- [30] Wang L et al. Capacitive deionization of NaCl solutions using carbon nanotube sponge electrodes. *Journal of Materials Chemistry*. 2011;**21**(45):18295
- [31] Laxman K, Myint MTZ, Khan R, Pervez T, Dutta J. Effect of a semiconductor dielectric coating on the salt adsorption capacity of a porous electrode in a capacitive deionization cell. *Electrochimica Acta*. 2015;**166**:329-337
- [32] Myint MTZ, Dutta J. Fabrication of zinc oxide nanorods modified activated carbon cloth electrode for desalination of brackish water using capacitive deionization approach. *Desalination*. 2012;**305**:24-30
- [33] Hou CH, Huang CY. A comparative study of electrosorption selectivity of ions by activated carbon electrodes in capacitive deionization. *Desalination*. 2013;**314**:124-129
- [34] Chen Z, Zhang H, Wu C, Wang Y, Li W. A study of electrosorption selectivity of anions by activated carbon electrodes in capacitive deionization. *Desalination*. 2015;**369**:46-50
- [35] Kim T, Dykstra JE, Porada S, van der Wal A, Yoon J, Biesheuvel PM. Enhanced charge efficiency and reduced energy use in capacitive deionization by increasing the discharge voltage. *Journal of Colloid and Interface Science*. 2015;**446**:317-326
- [36] Zhao R, Satpradit O, Rijnaarts HHM, Biesheuvel PM, A. van der Wal. Optimization of salt adsorption rate in membrane capacitive deionization. *Water Research*. 2013;**47**(5): 1941-1952
- [37] Villar I et al. Capacitive deionization of NaCl solutions with modified activated carbon electrodes. *Energy and Fuels*. 2010;**24**(6):3329-3333
- [38] Suss ME et al. Capacitive desalination with flow-through electrodes. *Energy and Environmental Science*. 2012;**5**(11):9511
- [39] Porada S et al. Water desalination using capacitive deionization with microporous carbon electrodes. *ACS Applied Materials and Interfaces*. 2012;**4**(3):1194-1199
- [40] Xu P, Drewes JE, Heil D, Wang G. Treatment of brackish produced water using carbon aerogel-based capacitive deionization technology. *Water Research*. 2008;**42**(10-11):2605-2617
- [41] Zhao R, van Soestbergen M, Rijnaarts HHM, van der Wal A, Bazant MZ, Biesheuvel PM. Time-dependent ion selectivity in capacitive charging of porous electrodes. *Journal of Colloid and Interface Science*. 2012;**384**(1):38-44
- [42] Avraham E, Bouhadana Y, Soffer A, Aurbach D. Limitation of charge efficiency in capacitive deionization I. On the behavior of single activated carbon. *Journal of the Electrochemical Society*. 2009;**156**(6):P95

- [43] Suss ME, Biesheuvel PM, Baumann TF, Stadermann M, Santiago JG. In situ spatially and temporally resolved measurements of salt concentration between charging porous electrodes for desalination by capacitive deionization. *Environmental Science and Technology*. 2014;**48**(3):2008-2015
- [44] Lee JB, Park KK, Eum HM, Lee CW. Desalination of a thermal power plant wastewater by membrane capacitive deionization. *Desalination*. 2006;**196**(1-3):125-134
- [45] Zhao R, Biesheuvel PM, van der Wal A. Energy consumption and constant current operation in membrane capacitive deionization. *Energy and Environmental Science*. 2012;**5**(11):9520
- [46] Gao X, Omosibi A, Landon J, Liu K. Surface charge enhanced carbon electrodes for stable and efficient capacitive deionization using inverted adsorption-desorption behavior. *Energy and Environmental Science*. 2015;**8**(3):897-909
- [47] Pasta M, Wessells CD, Cui Y, La Mantia F. A desalination battery. *Nano Letters*. 2012;**12**(2):839-843
- [48] Porada S, Biesheuvel PM, Presser V. Comment on sponge-templated preparation of high surface area graphene with ultrahigh capacitive deionization performance. *Advanced Functional Materials*. 2015;**25**(2):179-181
- [49] Lee J, Kim S, Kim C, Yoon J. Hybrid capacitive deionization to enhance the desalination performance of capacitive techniques. *Energy and Environmental Science*. 2014;**7**(11):3683-3689
- [50] Jeon S et al. Desalination via a new membrane capacitive deionization process utilizing flow-electrodes. *Energy and Environmental Science*. 2013;**6**(5):1471
- [51] Mossad M, Zou L. A study of the capacitive deionisation performance under various operational conditions. *Journal of Hazardous Materials*. 2012;**213-214**:491-497
- [52] Huang ZH, Wang M, Wang L, Kang F. Relation between the charge efficiency of activated carbon fiber and its desalination performance. *Langmuir*. 2012;**28**(11):5079-5084
- [53] Ahn HJ, Lee JH, Jeong Y, Lee JH, Chi CS, Oh HJ. Nanostructured carbon cloth electrode for desalination from aqueous solutions. *Materials Science and Engineering A*. 2007;**448-451**:841-845
- [54] Ryoo MW, Seo G. Improvement in capacitive deionization function of activated carbon cloth by titania modification. *Water Research*. 2003;**37**(7):1527-1534
- [55] Ryoo MW, Kim JH, Seo G. Role of titania incorporated on activated carbon cloth for capacitive deionization of NaCl solution. *Journal of Colloid and Interface Science*. 2003;**264**(2):414-419
- [56] Chang LM, Duan XY, Liu W. Preparation and electrosorption desalination performance of activated carbon electrode with titania. *Desalination*. 2011;**270**(1-3):285-290

Energy Recovery in Capacitive Deionization Technology

Alberto M. Pernía, Miguel J. Prieto,
Juan A. Martín-Ramos, Pedro J. Villegas and
Francisco J. Álvarez-González

Additional information is available at the end of the chapter

<http://dx.doi.org/10.5772/intechopen.75537>

Abstract

Capacitive deionization technique (CDI) represents an interesting alternative to compete with reverse osmosis by reducing energy consumption. It is based on creating an electric field between two electrodes to retain the salt ions on the electrode surface by electrostatic attraction; thus the CDI cell operates as a supercapacitor storing energy during the desalination process. Most of the CDI research is oriented to improving the electrode materials in order to increase the effective surface and ionic retention. However, if the CDI overall efficiency is to be improved, it is necessary to optimize the CDI cell geometry and the charge/discharge current used during the deionization process. A DC/DC converter is required to transfer the stored energy from one cell to another with the maximum possible efficiency during energy recovery, thus allowing the desalination process to continue. A detailed description of energy losses and the DC/DC converter used to recover part of the energy involved in the CDI process will provide the hints to optimize the efficiency of the CDI technique for water desalination. The proposed chapter presents an electric model to characterize the power losses in CDI cells and the power converter required for the energy recovery process.

Keywords: capacitive deionization, energy recovery, up-down DC/DC converter, desalination, carbon electrodes, supercapacitors

1. Introduction

Nowadays it is evident that fresh water, suitable for different types of consumption, is a resource of paramount importance and growing scarcity, although throughout modern history the fact that it is a limited resource has been overlooked. Several factors, such as

overpopulation, global warming, the increase of polluting emissions and the growing energy demand of the world productive model are at the base of numerous studies that indicate an alarming water scarcity in the medium term. Thus, some sources [1] estimate a 40% increase in water demand with respect to its availability within a period of 20 years, which makes it possible to calculate that one-third of the world's population will have access to only 50% of the amount of water necessary to cover their basic needs.

With this forecast and the potential increase of the world population, it is estimated that by 2050 a global water crisis without precedents could be established that would create very high levels of scarcity in large regions of the planet. This necessarily implies investments in the improvement of water saving and the optimization of current methods of water regeneration/purification.

Over the past decades, processes such as reverse osmosis (RO), electrodialysis and various forms of distillation, such as multi-effect distillation and multi-stage flash distillation, have reached a high level of technological and industrial maturity [2, 3], and are currently the reference processes and mostly used for the regeneration/production of drinking water on a large scale. These methods have the main drawback of high energy consumption (e.g. 4–7kWh/m³ for RO) so that new strategies for purification are being investigated in order to reduce their consumption.

CDI technology is presented as an efficient alternative to the previously mentioned technologies, as it allows an important recovery of the energy involved in the process.

2. Capacitive deionization (CDI)

CDI technology uses an electric field created by a pair of electrodes to induce the mobility and separation of the dissolved salts in the water towards the corresponding electrodes (**Figure 1**). The salts (their ionic components) are retained at the interface between the electrode and the aqueous medium, in an electrochemical structure called double-layer. Therefore, CDI is a low-pressure desalination process where an energy recovery process can be used to minimize the energy consumption.

2.1. Operating principle

As it was mentioned, CDI technology uses the electric field created between the electrodes to retain the ions on the electrode surface by means of electrostatic attraction [4]. This accumulation of ions on the electrodes is a thermodynamically reversible process and can be eliminated in a later step, during which the electrodes are depolarized. The behavior of the structure is similar to a supercapacitor that can be charged or discharged. In order to increase the effective surface of the electrode, nanoporous carbon materials are used to cover the surface of the electrode [5–7].

The first phase of operation is called deionization or desalination phase, and more technically, the ionic adsorption phase. This phase lasts as long as it takes the equivalent capacitor to

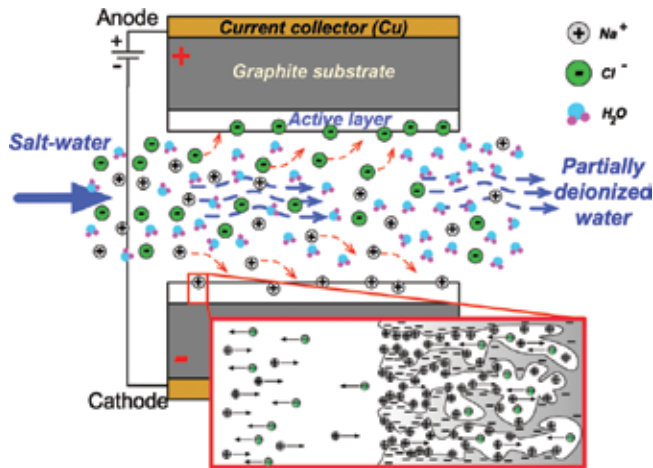


Figure 1. Schematic of ion adsorption during the polarization of electrode plates.

charge to the desired potential, always lower than 1.2 V to avoid water dissociation. The water between the electrodes will be partially deionized during this stage. During the second phase, the electrodes are depolarized or discharged while circulating a flow of water that is used to facilitate the removal of the ions adsorbed by the electrode plates, which will be evacuated in the form of a concentrate or brine. This second phase is called the regeneration or cleaning phase since it makes the electrodes be ready for a new cycle again.

This principle and mode of operation, based on alternating charge-discharge of the equivalent capacitor, suggests the use of the energy accumulated in the electrodes during the regeneration phase (once the electrodes are saturated of salt ions) to supply another deionization module that starts the desalination phase. This principle of energy reuse (transferring energy between deionization modules) implies the possibility of significantly reducing the energy consumption of the system.

The primary energy source will only have to provide the necessary amount of energy to compensate the losses that occur during the energy transfer between the CDI cells.

2.2. Membrane capacitive deionization (MCDI)

In this variant of capacitive deionization, ion-selective membranes are interposed between the electrodes and the solution. In this way, it is possible to use the polarity reversal in the electrodes periodically, drastically improving the efficiency in the cleaning phase [8, 9].

In addition, the use of membranes improves the performance of the process, since it increases the electronic efficiency, which is the ratio between the amount of salt eliminated and the amount of electric current supplied to the CDI cell to achieve that goal.

Figure 2 shows a diagram of the MCDI operation composed of two capacitive units or cells. Each of the cathodes has a cation-selective membrane interposed, and each anode has an anion-selective membrane so that the ions charged with a sign opposite to that of the electrode

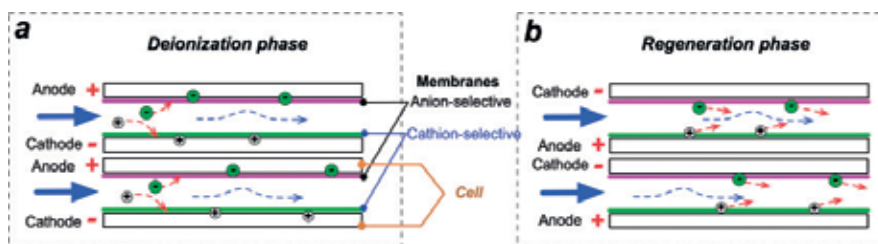


Figure 2. Schematic of a membrane capacitive deionization cell.

(or counter-ions) can move freely through the membrane, while the movement of ions with a charge of the same sign is blocked.

During the purification phase, the electrodes invert the polarity to facilitate the desorption of the adsorbed ions in the previous desalination phase. The re-adsorption of ions is avoided thanks to the barrier posed by the membranes.

In both cases, CDI or MCDI, another important parameter, is the effective electrode surface. This parameter is related to the equivalent capacitance that represents the deionization cell and, therefore, to the quantity of salt that can be adsorbed.

3. CDI module characterization

The interface between an electrically charged electrode and an electrolytic solution is a problem widely studied as part of the so-called surface phenomena. In this interface, a region of ionic accumulation is formed, commonly called electric double-layer, in which the ionic species present in the electrolytic medium are spatially distributed in a characteristic manner responding to the electronic charge present in the electrode. In this type of interfaces, it is known that the accumulated charge density depends on the voltage level of the electrode, the concentration of the solution and its chemical composition.

The double-layer name comes from the first theoretical model formulated to explain the accumulation of charge in these interfaces. In 1883, Helmholtz assumes that the electric charges in the electrode form a layer that induces another layer in the solution, of ionic character and polarity opposite to that of the electrode. In the Helmholtz model, the layer present in the solution is formed by ions intimately in contact with the outer surface of the electrode (the surface in contact with the solution) and it is assumed that there are no further interactions within the solution due to the influence of the electrode beyond this layer adjacent to the surface.

Assuming a flat electrode, the Helmholtz model is equivalent to the classical model of a flat-parallel capacitor (Figure 3) where A is the effective electrode surface, X_H is the distance between ions and ϵ_r is the permittivity.

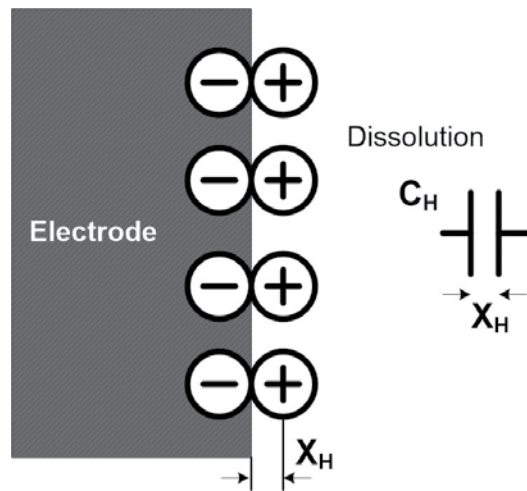


Figure 3. Classical double-layer model of a flat-parallel capacitor.

$$C_H = A \cdot \frac{\epsilon_r \cdot \epsilon_0}{\chi_H} \quad (1)$$

The desalination cell is built by piling several electrodes to increase the capability of water processing. In **Figure 4**, several electrodes are piled controlling the distance between them, “d,” and the number of electrodes placed in series, “n.”

Although there are more complex models of the ion distribution around the electrodes [10–12], the whole desalination cell can be modeled with the traditional circuit used to characterize a capacitor C. In this model two additional resistances are included, a series resistance R_S to model conduction losses, and a parallel resistance R_P that represents the self-discharge of the module.

The proposed electric model of the CDI cell (**Figure 5**) will allow the desalination system to be simulated together with the power topology used for the energy recovery. The electrical parameters defined, R_S , R_P and C, depending on the geometrical characteristics of the CDI cell and on the salt molar concentration (M). In order to obtain their values, a current source is applied to the cell that generates a linear evolution in the voltage across the terminals.

The CDI cell is initially completely discharged. At $t = 0$, a constant current, I_{DC} is applied to initiate the charging process (**Figure 6**). Therefore, since the equivalent capacitor C is initially discharged, the value of the voltage $V_C(t = 0+)$ measured will determine the value of R_S expressed in Ω .

$$R_S = \frac{\Delta V_1}{I_{DC}} \quad (2)$$

The capacitance of the CDI module, C, can be obtained from the linear charging process, during which the parallel resistance, R_P , can be neglected:

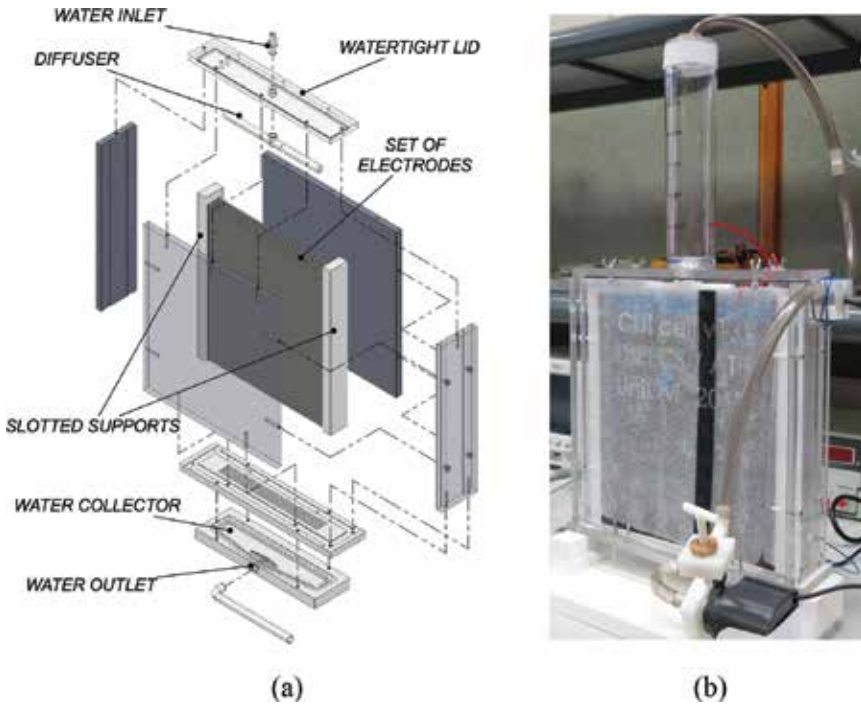


Figure 4. (a) Schematic of a planar desalination module and (b) prototype.

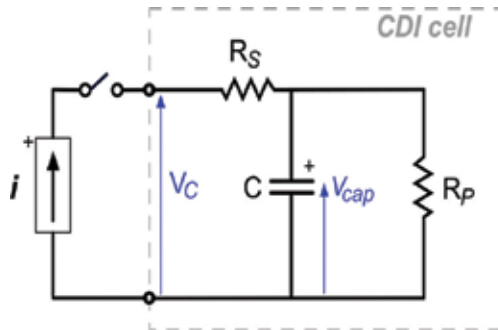


Figure 5. Electric charge/discharge circuit used for the parasitic determination (R_s , R_p , C).

$$C = \frac{I_{DC}}{tg\alpha} \tag{3}$$

Finally, to determine the parallel resistance, R_p , the current source is turned off, and an exponential evolution of the voltage across the CDI cell (V_C) can be approximated by the expression:

$$V_C(t) = V_{Cmax} \cdot e^{-t/R_p C} \tag{4}$$

where V_{Cmax} is the maximum voltage across the CDI module once current I_{DC} turns to 0 A. Several tests were performed, and the absolute error obtained in the adjustment of the R_p calculation was lower than 1%.

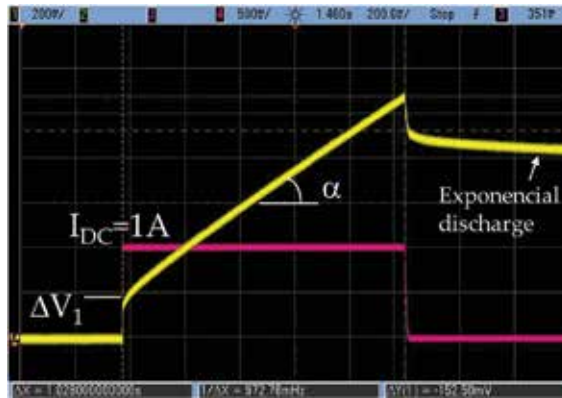


Figure 6. Electric charge/discharge test used for the parasitic determination.

With the proposed method, the values of R_s , R_p , and C can be obtained as a function of geometrical parameters: distance between electrodes “ d ,” number of electrodes “ n ,” the surface of electrodes “ S ” and NaCl molar concentration (M). To determine the tendencies of these values in an actual CDI cell, the prototype shown in Figure 4 was built and tested.

From Figure 7, it can be concluded that capacity C is almost independent of the distance between electrodes.

This fact demonstrates that the capacity is mainly due to the formation of the electric double layer. The addition of several electrodes is equivalent to adding capacitors in series; therefore, the total capacity is reduced although the voltage across the cell can be increased, increasing

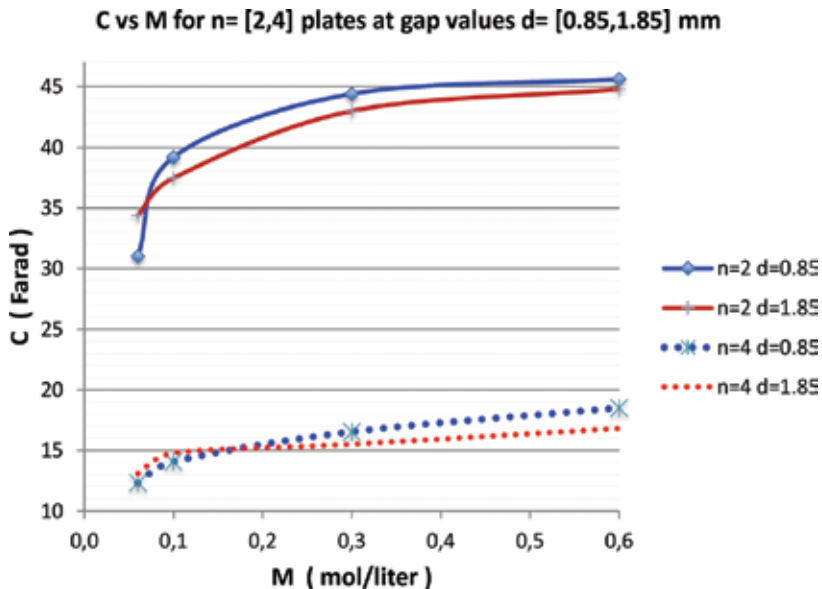


Figure 7. Capacity as a function of M (concentration of NaCl) for different configurations depending on n (number of plates-electrode) and d (distance between electrodes).

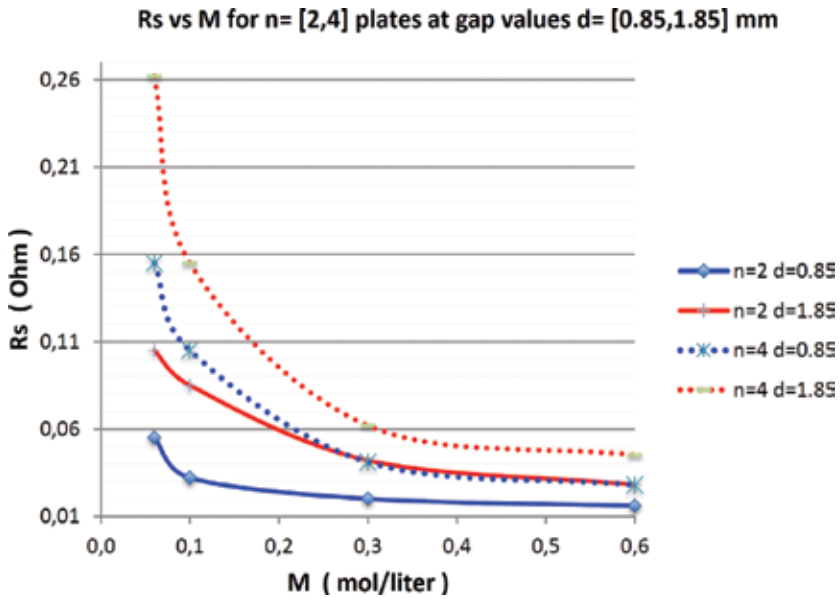


Figure 8. R_s for different configurations.

the total energy stored. For high concentrations (>0.1 to 0.6 M), the change in C is linear with a very little slope (≤ 1 Farad per 0.1 M). This is so because the double electric layer is almost completely formed for concentrations around 0.1 M.

Regarding R_s , the series resistance (Figure 8), it can be seen that it increases a lot for low concentration values, M , and presents a linear trend with small or very small slope from 0.3 M on.

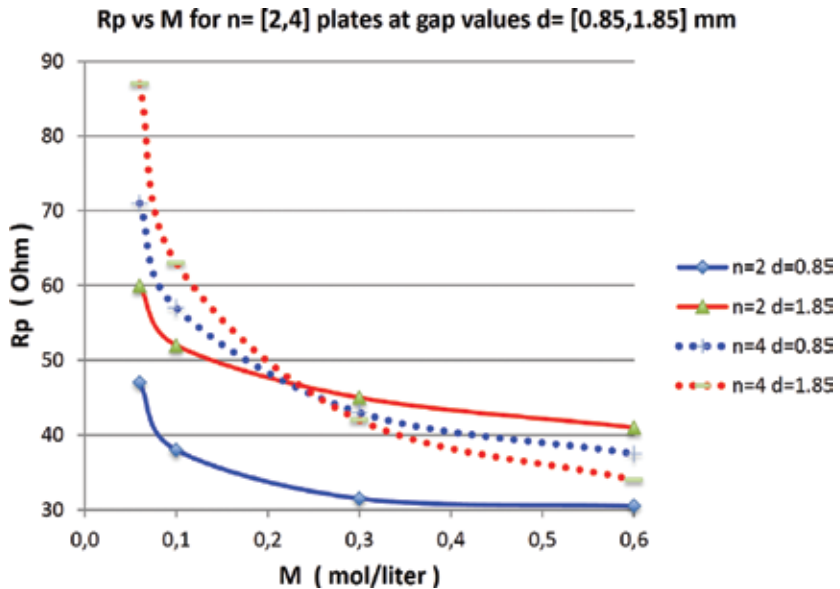


Figure 9. R_p for different configurations.

With reference to the parallel resistance, R_p , (**Figure 9**) the data measured show that it increases at low concentrations and presents a linear trend with a small or very small slope starting at 0.3 M.

4. Estimation of saline retention in electrodes

Tests have been carried out using the CDI cell shown in **Figure 4** to estimate the amount of salt that can be captured by the electrodes of this type of cells when they are completely filled with salt water. The molar salt concentration (M) is one of the parameters used to characterize the cell.

The first tests (performed at zero water flow) consist of series of charge/discharge cycles of the CDI cell using a solution with the maximum concentration considered (0.6 M).

It can be pointed out that, as shown in **Figure 10**, the electrodes present very high retention values taking into account that the initial concentration is 0.6 M. There is a variation throughout the series, tending to stabilize as the number of cycles increase.

In the second set of tests (**Figure 11**), two-electrode cells were used considering different initial concentrations, c_0 , and changing the distance between electrodes (d) to identify the influence of this parameter on the salt retention. The results obtained show that salt retention increases as the distance between electrodes is reduced.

This effect can be justified if we take into account that the series resistance presented in the cell increases with the distance “ d ,” especially at concentrations below 0.3 M, which presumably results in a decrease in the effective voltage in the electric double-layer and, as a result, a lower ionic retention.

Controlling the thickness of the nanoporous carbon layer deposited on the electrode surface, the quantity in grams of activated carbon per electrode can be determined. With the results

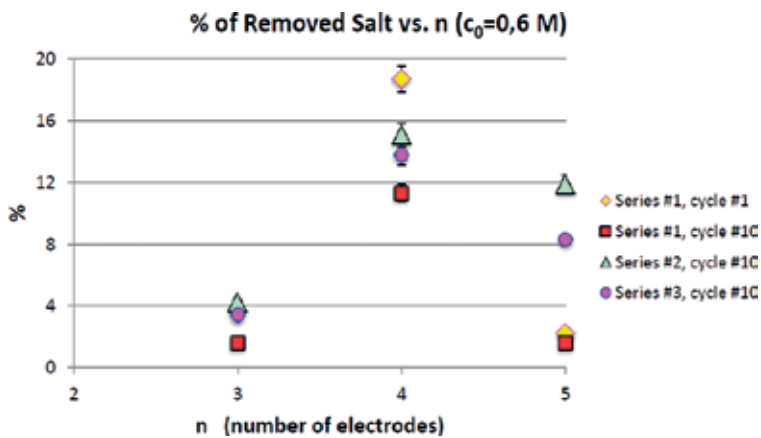


Figure 10. Results obtained by application of several charge-discharge cycles to cell configurations of more than two electrodes.

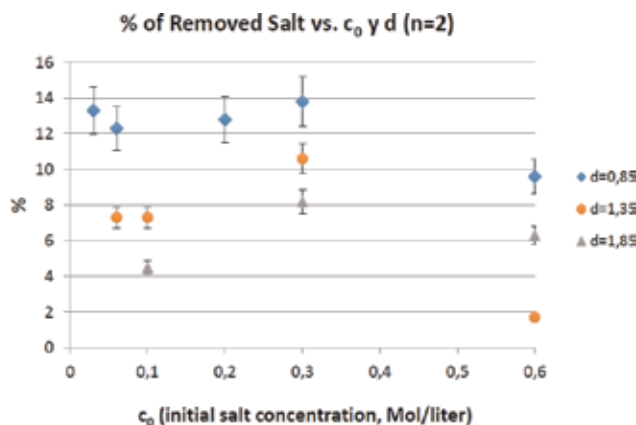


Figure 11. Estimated relative retention for cell configurations of two electrodes at different separations (d) and for different initial concentrations (c_0).

obtained in the previous test, an estimation of milligrams of salt retained per gram of activated carbon was also calculated.

The data plotted in **Figure 12** are susceptible of a logarithmic adjustment in the whole range and a linear adjustment for low concentrations. Both present a good correlation ($R^2 > 0.94$).

One important parameter to be analyzed during the diffusion of ions in the charging/discharging process is the amplitude of the current used.

By reducing the amplitude of the current used during the charging process of the CDI cell, ions have a longer time to move into the carbon porosities, thus increasing the salt retention. This phenomenon seems to reach a limit at which the amount of salt retained remains the same even if the current is doubled (from $i_C = 1$ to 2 A). From this, it can be concluded that the amplitude of the charge/discharge current and the amount of salt retained are two opposed

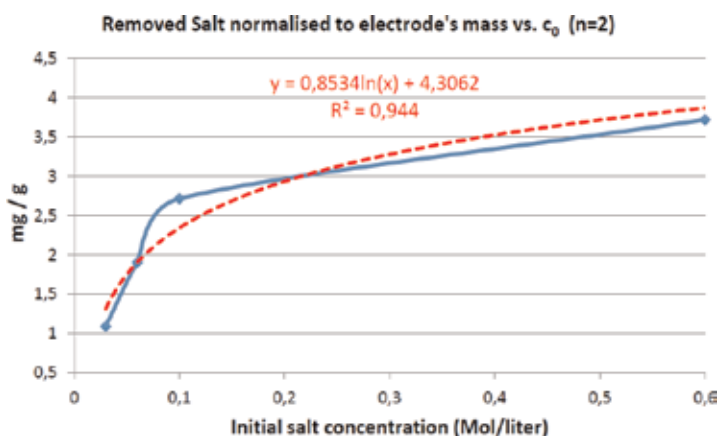


Figure 12. Estimated relative retention for cell configurations of two electrodes and different initial concentrations (c_0).

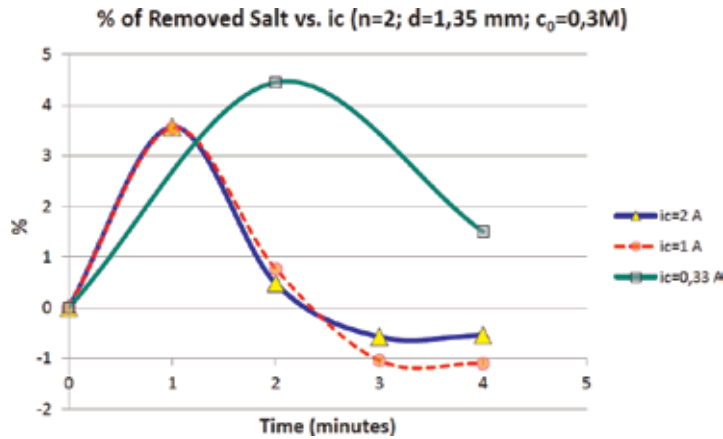


Figure 13. Estimated salt retention at different charging current (i_c).

magnitudes and a trade-off between them will be necessary. Figure 13 also shows the time required by the electrodes to reach saturation, after which the salt retention capability drops.

5. Up/down DC/DC converter for energy recovery

As already mentioned, one of the most interesting aspects of CDI is the possibility of reusing the energy stored in capacitive cells or modules once the deionization phase has finished. The regenerative use of energy in CDI technology consists of using the energy stored in the CDI cell once it is saturated (the deionization process is finished and the cleaning process begins) and transferring it to other modules that begin their deionization phase. This strategy can be applied to several cells that exchange the energy involved in the process, thus defining a cycle to produce clean water.

In order to be able to transfer the energy stored in the CDI cell to another one, it is necessary to include a DC/DC power converter in the system (Figure 14).

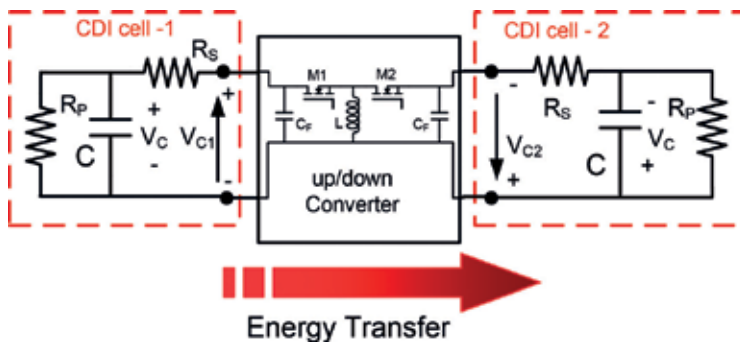


Figure 14. Desalination diagram with an up-down converter for energy transfer from CDI cell-1 to CDI cell-2.

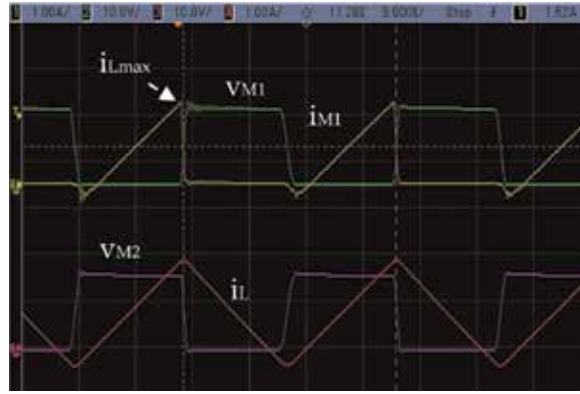


Figure 15. Voltage and current waveforms in the DC/DC converter.

One possible option for the converter topology is a buck-boost that operates at the variable frequency with hysteresis control where the maximum (i_{Lmax}) and minimum (i_{Lmin}) inductor current is fixed (Figure 15).

Limiting the inductor current (i_{Lmin} , i_{Lmax}) conditions the efficiency of the system, since these values are related to conduction and switching losses. The converter operation is based on transferring part of the energy stored at the input cell-1 to the inductor L during the period when transistor $M1$ is closed and $M2$ is open (t_{ON}). This period finishes when the inductor current reaches the maximum value defined by the converter control (i_{Lmax}). After this, transistor $M2$ is closed ($M1$ is opened) during time t_{OFF} and the energy stored in the inductor is discharged on the output cell-2. This stage typically finishes when the inductor current becomes equal to zero ($i_{Lmin} = 0$).

Therefore, i_{Lmax} can be used as the control parameter of the up/down converter during the energy transfer between the input CDI cell, which is completely charged, and the output CDI cell, which is initially completely discharged. By increasing the value of i_{Lmax} , the time involved in the transfer will be reduced.

To optimize the efficiency of the CDI system, it is necessary to define the value of i_{Lmax} during the energy recovery process. High values of this parameter will increase conduction losses, whereas low values of i_{Lmax} will increase the transfer time and the self-discharge through the parallel resistance R_p . On the other hand, the estimation of i_{Lmax} depends on the salt concentration (M) and the geometry of the CDI cells, which define the parameters R_p , R_s and C of the electrical model.

The DC/DC converter can be mathematically modeled assuming linear evolutions of the inductor current in each switching period (i) during the charge and discharge [13]. Therefore, when transistor $M1$ is conducting ($M2$ off), the discharge of the input cell is ideally described by:

$$u_{C1(i)} = u_{C1(i-1)} - \frac{I_{Lmax} + I_{Lmin}}{2 \cdot C} \cdot t_{on(i-1)} \quad (5)$$

Similarly, the output cell increases its voltage when $M2$ is on ($M1$ off). The equation defining such a process in each switching cycle is:

$$uc_{2(i)} = uc_{2(i-1)} + \frac{I_{Lmax} + I_{Lmin}}{2 \cdot C} \cdot t_{off(i-1)} \quad (6)$$

The RMS currents through the cells in each switching period can also be determined by:

$$i_{RMSC1i} = \sqrt{\frac{1}{ton_i + toff_i} \cdot \int_0^{ton_i} \left(\frac{I_{max} - I_{min}}{ton_i} \cdot t + I_{min} \right)^2 \cdot dt} \quad (7)$$

$$i_{RMSC2i} = \sqrt{\frac{1}{ton_i + toff_i} \cdot \int_{ton_i}^{ton_i+toff_i} \left(\frac{I_{min} - I_{max}}{toff_i} \cdot (t - ton_i) + I_{max} \right)^2 \cdot dt} \quad (8)$$

Based on the RMS current values calculated with the equations above, conduction and switching losses can be estimated:

$$P_{cond} = \frac{\sum_i (i_{RMSC1i}^2 + i_{RMSC2i}^2) \cdot (ton_i + toff_i) \cdot R}{T_{total}} \quad (9)$$

$$P_{switch} = \frac{\frac{1}{2} \cdot (tr + tf) \sum_i \left(I_{min} \cdot (uc_{1i} + uc_{2(i+1)}) + I_{max} \cdot (uc_{1(i+1)} + uc_{2i}) \right)}{T_{total}} \quad (10)$$

The parameter R represents the total series resistance along the conduction path.

Voltage losses due to cell self-discharge are also taken into account in the model by incorporating the following expression that represents the energy lost in a cell during the switching period “i” due to self-discharge:

$$E_{C_{Rp}i} = \frac{1}{R_p} \cdot uc_i^2 (t_{ON_i} + t_{OFF_i}) \quad (11)$$

Once the energy dissipated in each cycle ($E_{C_{cond}}$: energy loosed during conduction stage, $E_{C_{switch}}$: energy loosed during switching stage, E_{C_p} : energy loosed in R_p) is known, the real voltages of capacitors C1 and C2 can be recalculated as follows:

$$\Delta E_{C1i} = \frac{1}{2} \cdot C1 \cdot uc_{1(i+1)}^2 - \frac{1}{2} \cdot C1 \cdot uc_{1i}^2 \quad (12)$$

$$\Delta E_{C2i} = \frac{1}{2} \cdot C2 \cdot uc_{2(i+1)}^2 - \frac{1}{2} \cdot C2 \cdot uc_{2i}^2 \quad (13)$$

$$\Delta E_{realC1i} = \Delta E_{C1i} - E_{C1cond_i} - E_{C1switch_i} - E_{C_{Rp}_i} \quad (14)$$

$$\Delta E_{realC2i} = \Delta E_{C2i} - E_{C2cond_i} - E_{C2switch_i} - E_{C_{Rp}_i} \quad (15)$$

From the previous expressions, the real voltage across each capacitor can be derived:

$$u_{C1(i+1)_{real}} = \sqrt{\frac{2 \cdot \left(\Delta E_{realC1i} + \frac{1}{2} \cdot C1 \cdot u_{C1i_{real}}^2 \right)}{C1}} \quad (16)$$

$$u_{C2(i+1)_{real}} = \sqrt{\frac{2 \cdot \left(\Delta E_{realC2i} + \frac{1}{2} \cdot C2 \cdot u_{C2i_{real}}^2 \right)}{C2}} \quad (17)$$

The model described allows users to obtain a large amount of information related to the behavior of the converter: currents, voltages, transfer times, performance. But it can also provide insight into the influence that the desalination cells will have on these parameters. In order for this to be possible, the previous expressions must include the influence of the distance between electrodes “*d*,” the number of electrodes “*n*,” the molarity “*M*,” and the *S* surface.

$$E_{R_{S_{on}(i)}}(d, n, M, S) = R_S(d, n, M, S) \cdot \left(i_{R_{MSC1}(i)} \right)^2 \cdot t_{on} \quad (18)$$

$$E_{R_{S_{off}(i)}}(d, n, M, S) = R_S(d, n, M, S) \cdot \left(i_{R_{MSC2}(i)} \right)^2 \cdot t_{off} \quad (19)$$

$$E_{R_S(i)}(d, n, M, S) = E_{R_{S_{on}(i)}}(d, n, M, S) + E_{R_{S_{off}(i)}}(d, n, M, S) \quad (20)$$

$$E_{R_{P(i)}}(d, n, M) = \int_0^{T(i)} \frac{[u_{C(i)}(t)]^2}{R_P(d, n, M)} \cdot dt \quad (21)$$

$$E_{T(i)}(d, n, M, S) = E_{R_{S(i)}}(d, n, M, S) + E_{R_{P(i)}}(d, n, M, S) + P_{cond(i)}(d, n, M, S) \cdot T + P_{switch(i)}(d, n, M, S) \cdot T \quad (22)$$

From the equation system described above, it is possible to determine the overall efficiency of the DC/DC converter together with the desalination cells [14].

Once the equations to calculate losses have been established, it is possible to determine the optimum $i_{L_{max}}$ current in each switching period by implementing an iterative process according to the flow chart of **Figure 16**. The procedure consists in increasing the value of $i_{L_{max}}$ in each switching period until the maximum efficiency is obtained for that switching period. After that, a new switching period is considered and a new iteration with $i_{L_{max}}$ is carried out in order to derive the optimum $i_{L_{max}}$ value for the new switching period. The process is repeated until the input CDI cell is completely discharged.

The process mentioned was applied to several cell configurations consisting of four electrodes of $250 \times 250 \times 5$ mm placed at different distances from one another, in which the salt concentration was also a parameter under control [14]. As an example, **Figure 17** shows the optimal current when the cell parameters associated with this configuration are: $C = 0.1$ F, $R_s = 25$ m Ω , and $R_p = 40$ Ω . Taking these parameters into account, the calculation of the optimum current as indicated above gives rise to the evolution shown in **Figure 17**.

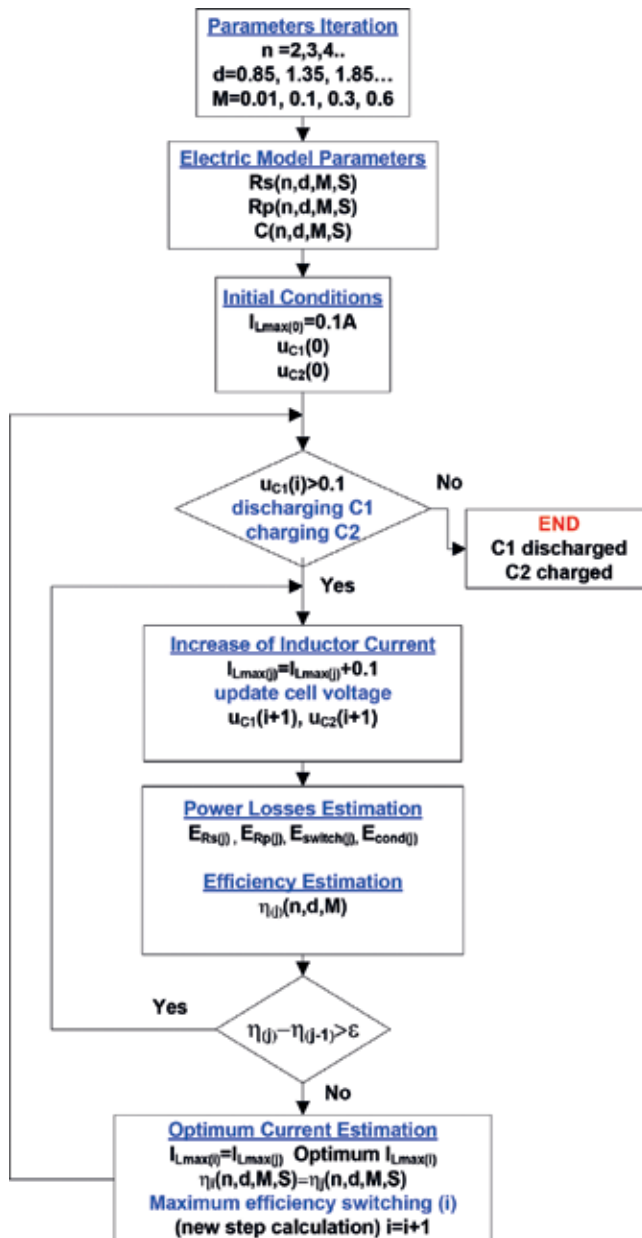


Figure 16. Optimum current i_{Lmax} estimation flow chart per switching period.

By controlling the switching times of the semiconductors it is possible to control that the maximum current through the inductor follows the profile defined by the optimum current for each specific cell. Figure 18 shows the efficiency obtained in several cases when the optimal current is used and the maximum voltage is 1.5 V. It is important to point out the necessity of reducing the series resistance because it limits the maximum efficiency that can be obtained.

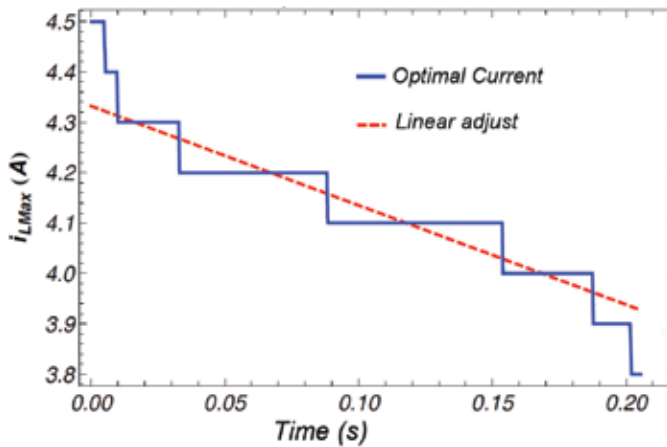


Figure 17. Optimum current i_{Lmax} estimated.

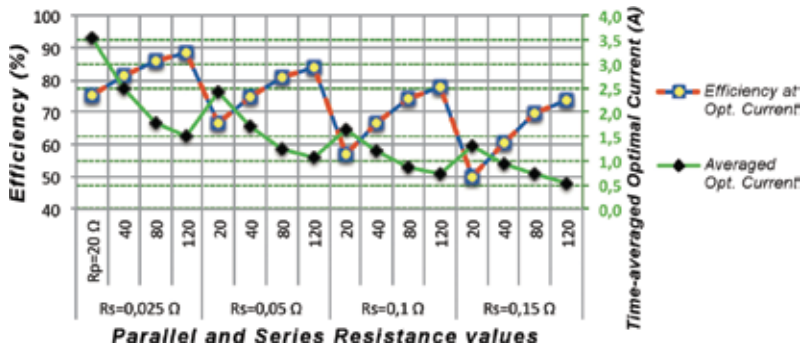


Figure 18. System efficiency operating at optimum current (red) and average optimum current during the energy transference (green).

The green plot determines the average of the optimum current during the whole energy transference process (right-hand scale).

The efficiency improvement depends on the CDI cell geometry and the salt concentration (M) because these magnitudes condition the values of the parameters that define the electrical model of the cell. Actual measurements confirmed that, by applying this control strategy, the efficiency was improved by 10% in most of the cases as compared to that obtained when using a constant current value during the charge/discharge process.

6. Conclusions

The method presented allows the electrical characterization of the CDI cell in terms of salt concentration in the water and cell geometry. A model proposed is based only on three parameters R_p , R_s , C , which simplifies mathematical calculations. Using this electrical model

and the mathematical characterization of the DC/DC converter, it is possible to identify energy losses in the cell either by self-discharge or due to the current handled during the energy recovery processes, together with the power losses in the converter.

As a result, a clear identification of the power losses in all the system components is obtained. This makes it possible to identify the optimum current to minimize losses and optimize process efficiency for any salt concentration once the cell geometry is defined.

The feedback parameter used by the converter control strategy described is the maximum current through the inductor, i_{Lmax} . This parameter is calculated at each switching period so as to obtain the optimum value that maximizes the efficiency of the energy transfer between CDI cells.

Author details

Alberto M. Pernía*, Miguel J. Prieto, Juan A. Martín-Ramos, Pedro J. Villegas and Francisco J. Álvarez-González

*Address all correspondence to: amartinp@uniovi.es

University of Oviedo, Gijón, Spain

References

- [1] UN-Water. Water in a Changing World. The United Nations World Water Development Report 3. UNESCO Publishing; Mar 2009. <http://publishing.unesco.org/>
- [2] Younos T, Tulou KE. Overview of desalination techniques. *Journal of Contemporary Water Research and Education*. 2009;**132**:3-10
- [3] Fraidenraich N, Vilela OC, Lima GA, Gordon JM. Reverse osmosis desalination: Modeling and experiment. *Applied Physics Letters*. 2009;**94**:124102-124103
- [4] Oren Y. Capacitive deionization (CDI) for desalination and water treatment-past, present and future (a review). *Desalination*. 2008;**228**:10-29
- [5] Gao Y, Li HB, Cheng ZJ, Zhang MC, Zhang YP, Zhang ZJ, Cheng YW, Pan LK, Sun Z. Electrosorption of cupric ions from solutions by carbon nanotubes and nanofibres film electrodes grown on graphite substrates. In: *Proceedings of the IEEE Nanoelectronics Conference INEC 2008*; Shanghai, China; 24–27 March 2008. pp. 242-247
- [6] Hwang S, Hyun S. Capacitance control of carbon aerogel electrodes. *Journal of Non-Crystalline Solids*. 2004;**347**:238-245
- [7] Xu P, Drewes JE, Heil D, Wang G. Treatment of brackish produced water using carbon aerogel-based capacitive deionization technology. *Water Research*. 2008;**42**:2605-2617

- [8] Li H, Zou L. Ion-exchange membrane capacitive deionization: A new strategy for brackish water desalination. *Desalination*. 2011;**275**(1-3):62-66
- [9] Hassanvanda A, Chenb GQ, Webleya PA, Sandra E. Kentish improvement of MCDI operation and design through experiment and modelling: Regeneration with brine and optimum residence time. *Desalination*. September 2017;**417**(1):36-51
- [10] Niu R, Yang H. Modeling and identification of electric double-layer supercapacitors. *ICRA Communications*. Feb. 2011:1-4
- [11] Spyker RL, Nelms RM. Classical equivalent circuit parameters for a double-layer capacitor. *IEEE Transactions on Aerospace and Electronic Systems*. Jul. 2000;**36**(3):829-836
- [12] Hemmatifar A, Stadermann M, Santiago JG. Two-dimensional porous electrode model for capacitive deionization. *The Journal of Physical Chemistry C*. 2015;**119**(44):24681-24694
- [13] Pernia AM, Norniella JG, Martín-Ramos JA, Díaz J, Martínez JA. Up-down converter for energy recovery in a CDI desalination system. *IEEE Transactions on Power Electronics*. July 2012;**27**(7):3257-3265
- [14] Álvarez-González FJ, Martín-Ramos JA, Díaz J, Martínez JA, Pernía AM. Energy-recovery optimization of an experimental CDI desalination system. *IEEE Transactions on Industrial Electronics*. March 2016;**63**(3):1586-1597

Computational Study of Liquid Film Condensation with the Presence of Non-Condensable Gas in a Vertical Tube

Adil Charef, M'barek Feddaoui,
Abderrahman Nait Alla and Monssif Najim

Additional information is available at the end of the chapter

<http://dx.doi.org/10.5772/intechopen.76753>

Abstract

The main objective of this chapter is to study the liquid film condensation in a thermal desalination process, which is based on the phase change phenomenon. The external tube wall is subjected to a constant temperature. The set of the non-linear and coupled equations expressing the conservation of mass, momentum and energy in the liquid and gas mixtures is solved numerically. An implicit finite difference method is employed to solve the coupled governing equations for liquid film and gas flow together with the interfacial matching conditions. Results include radial direction profiles of axial velocity, temperature and vapour mass fraction, as well as axial variation of the liquid film thickness. Additionally, the effects of varying the inlet conditions on the phase change phenomena are examined. It was found that increasing the inlet-to-wall temperature difference improves the condensate film thickness. Decreasing the radius of the tube increased the condensation process. Additionally, non-condensable gas is a decisive factor in reducing the efficiency of the heat and mass exchanges. Overall, these parameters are relevant factors to improve the effectiveness of the thermal desalination units.

Keywords: thermal process, vapour-gas mixtures, condensation, heat and mass transfer, phase change

1. Introduction

The demand of fresh water supply is increasing due to the economic development and the fast population growth. With limited resources of fresh water, desalination of seawater and brackish water offers the potential to encounter the increasing water demands around the world. Generally, the reverse osmosis has about the great part of the market share in the world

compared to thermal desalination technologies. Consequently, the necessity to improve the thermal processes, which are based on the phase change phenomenon of evaporation and condensation, continues to receive a high interest. Condensation on the cooling surfaces is a phenomenon of major significance in the chemical industries, refrigeration, heat exchangers and desalination units, including thermal desalination.

The mechanism of condensation can be classified by various ways: geometric configurations like tube, channel, internal, external, horizontal or vertical; species of fluid such as steam, refrigerant or mixture with the presence of non-condensable gas; condensing phenomena as filmwise, dropwise or fog; and flow regime like laminar and turbulent. Since the first analysis of Nusselt [1] for film condensation on a vertical plate, a numerous number of studies have been done on improving film condensation modelling and to contribute to the comprehension of this complex phenomenon. Lebedev et al. [2] performed experimentally a combined study of heat and mass transfer from water vapour on a flat plate. They observed an enhancement of the condensation heat transfer with the increase of the inlet relative humidity. Dobran and Thorsen [3] studied the laminar filmwise condensation of a saturated vapour inside a vertical tube. They found that the mechanism of condensation is governed by ratio of vapour to liquid viscosity, Froude number to Reynolds number ratio, subcooling number and Prandtl number of liquid. Siow et al. [4, 5] presented a numerical study of the laminar film condensation with the presence of non-condensable gas in horizontal and then in vertical channels. They analysed the effect of the inlet Reynolds number, the inlet pressure and the inlet-to-wall temperature difference on the condensation mechanism. They studied also the liquid film condensation from steam-air mixtures inside a vertical channel. Results indicate that a higher concentration of non-condensable gas caused substantial reduces in the local Nusselt number, the pressure gradient and the film thickness. Belhadj et al. [6] conducted a numerical analysis to improve the condensation process of water vapour inside a vertical channel. Their results show that the phenomenon of phase change is sensitive to the inlet temperature of liquid film. For different values of the system parameters at the inlet of the tube, Dharma et al. [7] estimated from a numerical study the local and average values of Nusselt number, the pressure drop, the condensate Reynolds number and the gas-liquid interface temperature. Lee and Kim [8] carried out experimental and analytical studies to analyse the effect of the non-condensable gas (nitrogen) on the condensation of water vapour along a vertical tube with a small diameter. The experimental results demonstrate that the heat transfer coefficients become important with a high inlet vapour flow and the reduction of mass fraction of nitrogen. In addition, the authors developed a new correlation to evaluate the heat transfer coefficient regardless the diameter of the condenser tube. Nebuloni and Thome [9] developed a numerical and theoretical model to predict the laminar film condensation inside various channel shapes. They showed that the channel shape strongly affects the overall thermal performance. Chantana and Kumar [10] investigated experimentally and theoretically the heat transfer characteristics of steam-air during condensation inside a vertical tube. They observed that a higher Reynolds number and mass fraction of vapour improve the process of condensation. Dahikar et al. [11] conducted an experimental and CFD studies in the case of the film condensation with downward steam inside a vertical pipe. They found that a larger interfacial shear affects the momentum transfer because of the great velocity gradient especially at the gas-liquid interface.

Merouani et al. [12] presented a numerical analysis during the condensation of steam-gas mixtures between two coaxial cylinders. They observed that a higher vapour concentration at the inlet and molar mass of the non-condensable gas increases the heat flux at the inner wall. Qiujie et al. [13] presented a numerical study in the case of steam-air condensation on isothermal vertical plate by using volume of fluid (VOF) method. Their results indicate that the mass fraction variation of the non-condensable gas directly affects the liquid film condensation and then influences the heat transfer.

In the thermal desalination unit, the condenser is used for producing freshwater from the saline water sources. In fact, in order to enhance the condensation process with the presence of non-condensable gas in thermal seawater desalination processes, many studies have been conducted. Semiat and Galperin [14] found from steam condensation that even a small air mass fraction decreases the heat transfer coefficient in seawater desalination plant. Al-Shammari et al. [15] have shown from an experimental study that non-condensable gas has a negative effect on the heat transfer. An experimental study on the role of non-condensable gases in the condensation of steam inside slightly inclined tubes was presented by Caruso et al. [16]. The experiments were carried out under the following conditions: inner diameter of the tube 12.6 and 26.8 mm, inclination of the tube 7° , mass fraction of the non-condensable gas between 5 and 42%, and vapour saturated at atmospheric pressure. Due to the gravity, the condensate is collected mainly in the lower part of the tube. They also developed a correlation to calculate the local condensation heat transfer coefficient. Hassaninejadfarahani et al. [17] investigated numerically a liquid film condensation with high amount of non-condensable gas inside vertical tube. They examined the effects of varying the inlet air mass fraction, the inlet relative humidity, the inlet Reynolds number and the radius of the tube on the simultaneous heat and mass transfer during condensation. Recently, Charef et al. [18] investigated the condensation process of water vapour-air into liquid film inside a vertical tube under two different boundary conditions: imposed temperature and imposed heat flux. The results indicated a better condensation process under imposed heat flux. It was found that the presence of non-condensable gas affects negatively the system efficiency.

The purpose of this study is to numerically develop and investigate the problem of water vapour condensation in the presence of non-condensable gas in a vertical tube. In order to improve the effectiveness of the steam condensation in desalination process, special attention is addressed to examine the effects of the tube geometry and the inlet conditions on the condensation process. In the following, we present the studied problem, the numerical method and the main results.

2. Mathematical model

2.1. Physical model and assumptions

The geometry under consideration is a vertical tube with length L and radius R (**Figure 1**). The tube wall is subjected to a constant temperature. A mixture of water vapour and non-

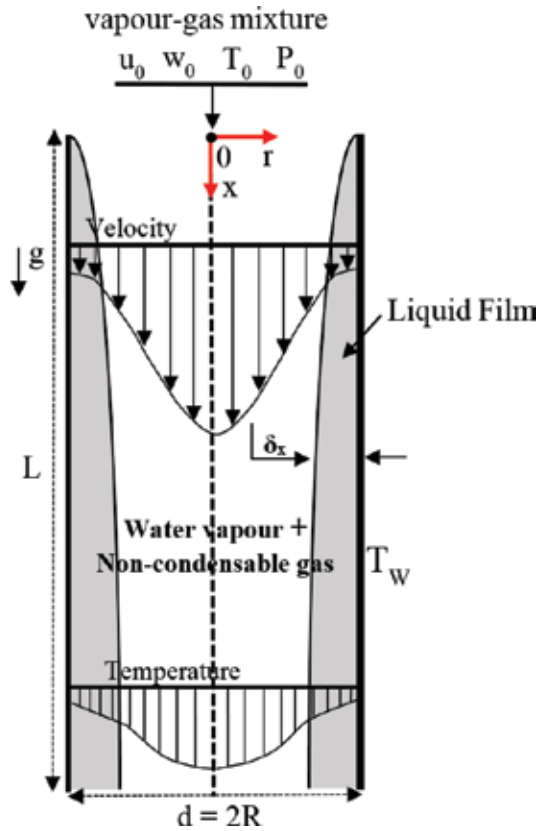


Figure 1. Geometry of the problem.

condensable gas enters the tube with a uniform velocity u_0 , vapour mass fraction w_0 , temperature T_0 and pressure P_0 . The vapour condenses and forms a liquid film thickness as the mixture flowing downwards.

For the mathematical formulation of the problem, it has been assumed that the gas flow is laminar, incompressible and two-dimensional. The vapour and liquid phases are in thermodynamic equilibrium at the interface. In addition, viscous dissipation and other secondary effects are negligible, and the humid air is assumed to be a perfect gas.

2.2. Mathematical formulation

With respect to the mentioned assumptions, the governing equations for the conservation of mass, momentum and energy, respectively, in the liquid region are written as

- Conservation of mass:

$$\frac{\partial}{\partial x}(\rho_L u_L) + \frac{1}{r} \frac{\partial}{\partial r}(r \rho_L v_L) = 0 \tag{1}$$

- Conservation of momentum:

$$\frac{\partial}{\partial x}(\rho_L u_L u_L) + \frac{1}{r} \frac{\partial}{\partial r}(r \rho_L v_L u_L) = -\frac{dp}{dx} + \frac{1}{r} \frac{\partial}{\partial r} \left(r \mu_L \frac{\partial u_L}{\partial r} \right) + \rho_L g \quad (2)$$

- Conservation of energy:

$$\frac{\partial}{\partial x}(\rho_L u_L C_{p,L} T_L) + \frac{1}{r} \frac{\partial}{\partial r}(r \rho_L v_L C_{p,L} T_L) = \frac{1}{r} \frac{\partial}{\partial r} \left(r \lambda_L \frac{\partial T_L}{\partial r} \right) \quad (3)$$

Similarly, the mass conservation, momentum, energy and diffusion equations for the gas phase are written as follows:

- Conservation of mass:

$$\frac{\partial}{\partial x}(\rho_G u_G) + \frac{1}{r} \frac{\partial}{\partial r}(r \rho_G v_G) = 0 \quad (4)$$

- Conservation of momentum:

$$\frac{\partial}{\partial x}(\rho_G u_G u_G) + \frac{1}{r} \frac{\partial}{\partial r}(r \rho_G v_G u_G) = -\frac{dp}{dx} + \frac{1}{r} \frac{\partial}{\partial r} \left(r \mu_G \frac{\partial u_G}{\partial r} \right) + \rho_G g \quad (5)$$

- Conservation of energy:

$$\frac{\partial}{\partial x}(\rho_G u_G C_{p,G} T_G) + \frac{1}{r} \frac{\partial}{\partial r}(r \rho_G v_G C_{p,G} T_G) = \frac{1}{r} \frac{\partial}{\partial r} \left(r \lambda_G \frac{\partial T_G}{\partial r} \right) \quad (6)$$

- Species diffusion equation:

$$\frac{\partial}{\partial x}(\rho_G u_G w) + \frac{1}{r} \frac{\partial}{\partial r}(r \rho_G v_G w) = \frac{1}{r} \frac{\partial}{\partial r} \left(r \rho_G D \frac{\partial w}{\partial r} \right) \quad (7)$$

2.3. Boundary and interfacial conditions

The governing equations are subjected to the following boundary conditions:

- At the tube inlet ($x = 0$)

$$u_G = u_0; \quad T_G = T_0; \quad P_G = P_0; \quad w_G = w_0 \quad (8)$$

- At the centre line of the tube ($r = 0$)

$$v_G = 0; \quad \frac{\partial u_G}{\partial r} = \frac{\partial T_G}{\partial r} = \frac{\partial w}{\partial r} = 0 \quad (9)$$

- At the wall of the tube ($r = R$)

$$u_L = v_L = 0; T_L = T_W \quad (10)$$

- At the interface vapour-liquid ($r = R - \delta_x$)

Continuities of velocity and temperature:

$$u_I(x) = u_{G,I} = u_{L,I}; T_I(x) = T_{G,I} = T_{L,I} \quad (11)$$

Continuity of shear stress:

$$\tau_I = \left[\mu \frac{\partial u}{\partial r} \right]_{L,I} = \left[\mu \frac{\partial u}{\partial r} \right]_{G,I} \quad (12)$$

Heat balance at the interface:

$$\lambda_L \frac{\partial T_L}{\partial r} = \lambda_G \frac{\partial T_G}{\partial r} - J'' h_{fg} \quad (13)$$

where h_{fg} is the latent heat of condensation and J'' is the mass flux at the interface ($J'' = \rho_G v_I$).

The radial velocity of water vapour-air mixture is calculated by considering that the interface is semipermeable [19] and that the solubility of air in the liquid film is negligibly small, which implies that the air velocity in the radial direction is zero at the interface. The velocity of the steam-air mixture at the interface can be written as

$$v_I = - \frac{\sum_{i=1}^2 D_{G,im} \frac{\partial w_{Gi}}{\partial r}}{\left(1 - \sum_{i=1}^2 w_{Gi} \right)} \quad (14)$$

The governing Eqs. (1)–(7) with interfacial conditions (8)–(13) are used to determine the field of variables $u_L, v_L, T_L, u_G, v_G, T_G, w$. To complete the mathematical model, two equations are used. At every axial location, the overall mass balance in the liquid phase and the gas flow should be satisfied:

$$\frac{m_{0L}}{2\pi} = \int_{R-\delta_x}^R (r\rho u dr)_L - \int_0^x \rho_G v_I (R - \delta_x) dx \quad (15)$$

$$\frac{(R - \delta_0)^2}{2} \rho_0 u_0 = \int_0^{R-\delta_x} (r\rho u dr)_G + \int_0^x \rho_G v_I (R - \delta_x) dx \quad (16)$$

A dimensionless accumulated condensation is introduced to estimate the mass transfer along the tube:

$$m_{cd} = 2\pi \int_0^x \rho_G v_l (R - \delta_x) dx \quad (17)$$

A transformation of coordinates was performed to ensure that the computational grid would clearly define the gas-liquid interface at each station along the tube. The r, x coordinates are transformed into η, X as follows:

$$\eta = \frac{(R - \delta_x) - r}{(R - \delta_x)} \quad 0 \leq r \leq (R - \delta_x) \quad (18)$$

$$\eta = \frac{(R - \delta_x) - r}{\delta_x} \quad (R - \delta_x) \leq r \leq R \quad (19)$$

$$X = \frac{x}{L} \quad (20)$$

The pure component data (in previous formulations) is approached by polynomials in terms of mass fraction and temperature. For more information, the thermo-physical properties are available in [20, 21].

3. Numerical solution method

The set of non-linear governing equations are discretized using a finite difference numerical scheme. The radial diffusion and the axial convection terms are approximated by the central and the backward differences, respectively. Hence, we arrange the system of discretized algebraic equations coupled with the boundary conditions into a matrix. Finally, the matrix resolution is carried out using the tri-diagonal matrix algorithm (TDMA) [22]. Besides that, a special care was made to ensure accuracy of the numerical computation, by generating a non-uniform grid in both directions. Accordingly, the grid is refined at the interface. In fact, it is important to note that as the liquid goes to the outlet, the film thickness varies along the tube. For that reason, during the downstream marching at each iteration, our finite difference computational grid deals with the variation of the liquid and gas computational domain.

3.1. Marching procedure

A set of non-linear algebraic equations is realized for $u_L, v_L, T_L, u_G, v_G, T_G, w$ and the two scalars dp/dx and δ_x . The computational solution is advanced as follows:

1. For any axial position x , guess an arbitrary values of dp/dx and δ_x .
2. Solve the finite difference forms of Eqs. (2)–(3) and (5)–(7) simultaneously for u_L, T_L, u_G, T_G, w .
3. Numerically, integrate the continuities of Eqs. (1) and (5) to find v_L and v_G .

4. The interfacial conditions of velocity, temperature, shear stress and heat balance are obtained from Eqs. (11)–(13).
5. Calculate the error of the liquid film mass balance E_L^{itt} using Eq. (15).
6. The best approximation to the thickness of the liquid film is then obtained using the secant method [23]. Thus

$$\delta_x^{itt+1} = \delta_x^{itt} - \frac{\delta_x^{itt} + \delta_x^{itt-1}}{E_L^{itt} - E_L^{itt-1}} E_L^{itt} \quad (21)$$

The convergence criteria used is $E_L^{itt} = 10^{-5}$. Usually, six to seven iterations suffice to get converged solution.

7. Calculate the error in the gas flow balance E_G^{itt} using Eq. (16).
8. Check the satisfaction of the convergence of velocity, temperature and species concentrations. If the relative error between two consecutive iterations is small enough, that is

$$E_{rr} = \frac{\max |\Upsilon_{i,j}^n - \Upsilon_{i,j}^{n-1}|}{\max |\Upsilon_{i,j}^n|} < 10^{-5} \quad (22)$$

The solution for the actual axial position is complete. If not, repeat procedures (1) to (7), where Υ represents the variables u_L, T_L, u_G, T_G, w .

3.2. Velocity and pressure coupling

Owing to satisfy the global mass flow constraint, the pressure correction gradient and axial velocity profile are performed applying a method proposed by Raithby and Schneider [24], described by Anderson et al. [25]. To fully explain, we let $H = dp/dx$. Due to an initial guesses for $(-dp/dx) = (-dp/dx)^*$, we calculate provisional velocities $(u_j^{n+1})^*$ and a mass flow rate of gas $(\dot{M}_j^{n+1})^*$. Because of the linearity of the equation of momentum with frozen coefficients, the correct velocity at each point from an application of Newton's method is as follow:

$$u_j^{n+1} = (u_j^{n+1})^* + \frac{\partial u_j^{n+1}}{\partial H} \Delta H \quad (23)$$

ΔH is the change in the gradient of the pressure required to satisfy the global mass flow constraint. In addition, we specify $u_{p,j}^{n+1} = \frac{\partial u_j^{n+1}}{\partial H}$. The difference equations are indeed differentiated with respect to the pressure gradient (H) to have difference equations for $u_{p,j}^{n+1}$, which have a tridiagonal form. The coefficients for the unknowns in these equations will be the same as for the original implicit difference equations. The system of algebraic equations for $u_{p,j}^{n+1}$ is

resolved by Thomas algorithm. Furthermore, the boundary conditions on $u_{p,j}^{n+1}$ must be coherent with the boundary conditions of the velocity. At boundaries, where the velocity is specified, $u_{p,j}^{n+1} = 0$. The solution of $u_{p,j}^{n+1}$ is used to calculate ΔH , noting that to satisfy the constraint of the global mass flow, $u_{p,j}^{n+1} \Delta H$ is the correction in velocity at each point. So, we can write

$$\dot{M}_i^{n+1} - \dot{M}_i^n = 2\pi\Delta H \int_0^{R-\delta_x} r\rho u_{p,j}^{n+1} dr \quad (24)$$

where the integral is estimated using numerical means. The \dot{M}_i^{n+1} in Eq. (24) is the known value specified in the initial conditions. The required value of ΔH is given by Eq. (24), whereas the correct values of the velocity u_j^{n+1} may be determined from Eq. (23). Besides, the continuity equation then allows to calculate v_j^{n+1} .

3.3. Mesh stability and validation of the numerical model

To validate the grid independency of results and to avoid convergence problems due to the use of thin grids, it is helpful to choose an optimum solution between computational time and result precision. Several grid sizes have been examined to ensure that the results are grid independent. **Figure 2** shows that in all grid arrangements, the difference in local Nusselt number of sensible heat is always less than 3%. The grid with $NI \times (NJ + NL) = 131 \times (81 + 31)$ is chosen because it gives results close enough to those of the thin grid and sufficiently accurate

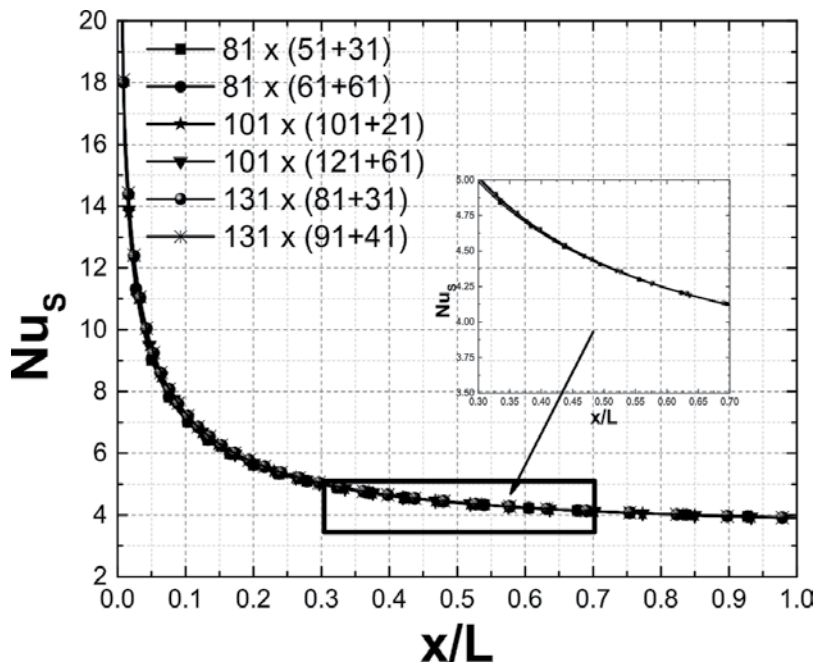


Figure 2. Comparison of sensible heat Nusselt number.

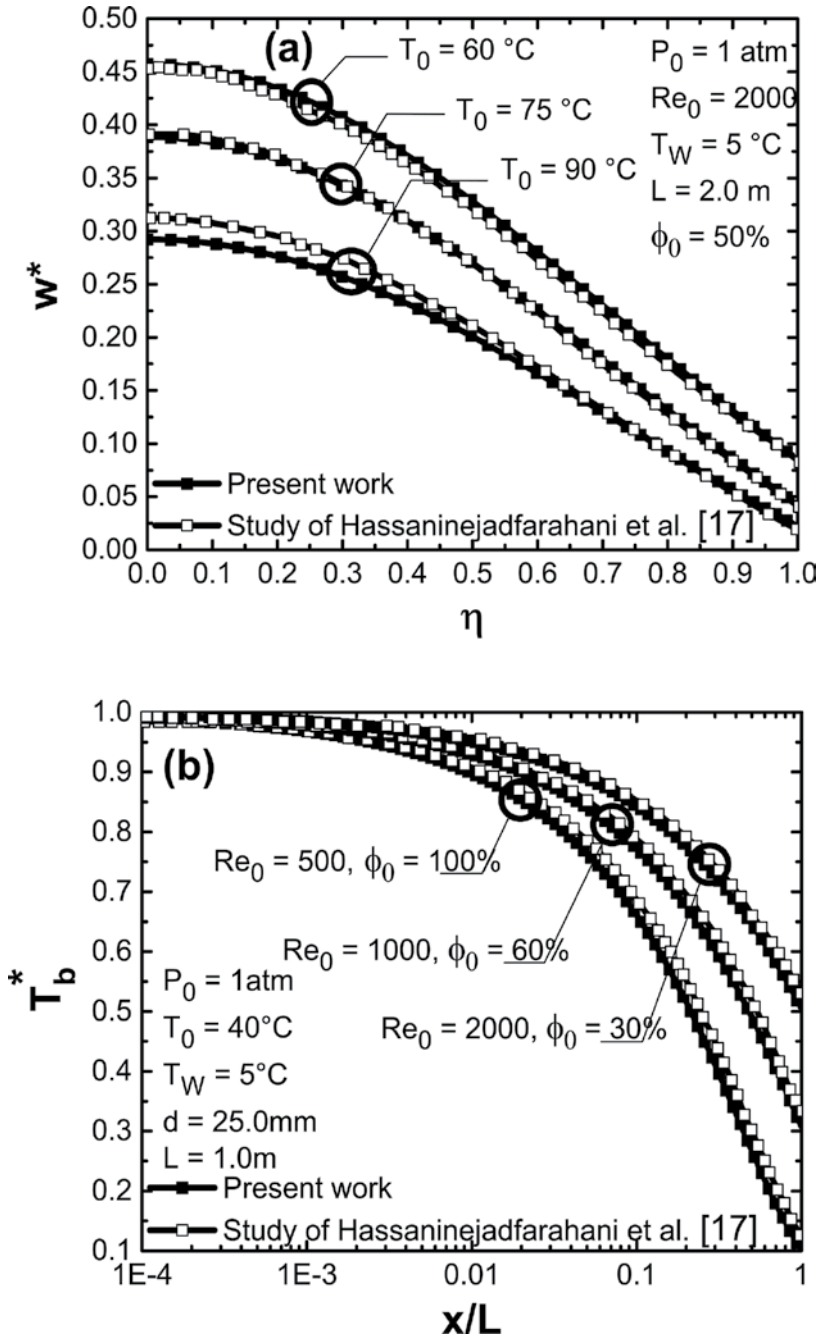


Figure 3. Comparison with numerical study of Hassaninejadfarahani et al. [17] for (a) dimensionless mass fraction at the tube exit, and (b) dimensionless mixture temperature.

to describe the heat and mass transfer. Note that NI is the total grid points in the axial direction, NJ is the total grid points in the radial direction at the gas region, and NL is the total grid points in the radial direction at the liquid region.

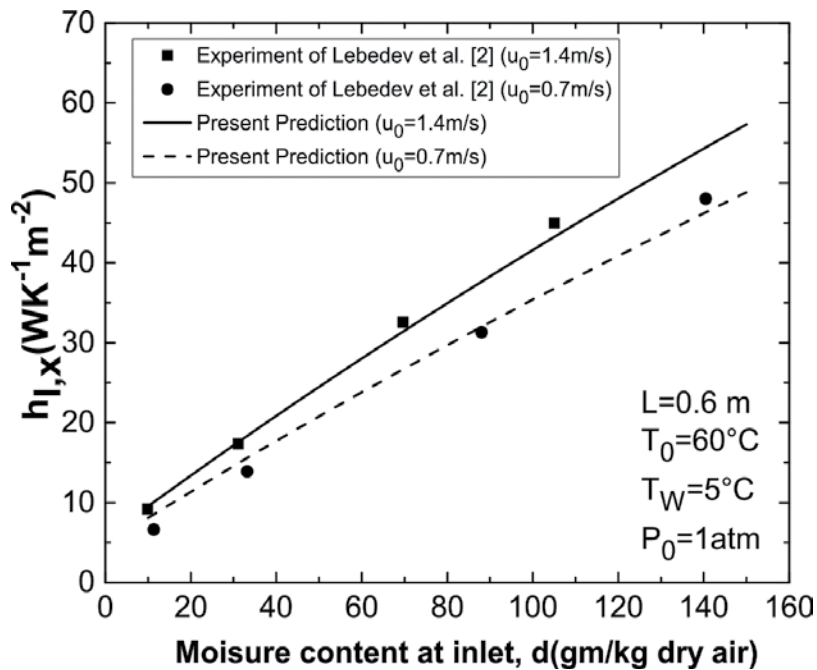


Figure 4. Comparison with experimental data of Lebedev et al. [2] for local condensate heat transfer coefficient.

In order to check the accuracy and validity of the numerical method, the obtained results were first compared to those reported by Hassaninejadfarahani et al. [17] in the case of laminar condensation of a steam and non-condensable gas in a vertical tube, in which the tube wall is maintained at a constant temperature. A good agreement was found between the current computational study and the results provided by Hassaninejadfarahani et al. [17] as shown in **Figure 3a, b**, which illustrates the vapour mass fraction evolution and mixture temperature, respectively.

The computations have been also compared with experimental results of Lebedev et al. [2]. It is important to indicate that Lebedev et al. [2] examined the simultaneous heat and mass transfer during humid air condensation in a vertical duct. So, to obtain the case of Lebedev et al. [2], equivalent hydraulic diameter de is chosen [7, 26]. **Figure 4** is a plot of local condensate heat transfer coefficient compared with the study of Lebedev et al. [2] for $T_0 = 60^\circ\text{C}$, $P_0 = 1 \text{ atm}$, $L = 0.6 \text{ m}$, $T_W = 5^\circ\text{C}$ and $de = 0.02 \text{ m}$. A good agreement between our computations and the experiment curves is found with a maximum relative error of 4.7% for both curves ($u_0 = 1.4 \text{ m/s}$ and $u_0 = 0.7 \text{ m/s}$).

4. Distribution of axial velocity, temperature and mass fraction profiles along the vertical tube

This chapter investigates the process of the liquid film condensation from the water vapour and non-condensable gas mixtures inside a vertical tube. The results of this study have been

obtained for the case of inlet gas temperature $T_0=70^\circ\text{C}$, inlet pressure $P_0=1$ atm and inlet Reynolds number is fixed at $Re_0 = 2000$. The range of each parameter for this study is listed in **Table 1**. At first, the air is used as non-condensable gas.

Figures 5–7 Illustrate the profiles of velocity, temperature and the mass fraction of water vapour at different axial locations of the tube. From the distribution of velocity in **Figure 5**, it is observed that the variation of the velocity in the gas mixture is higher than that in the liquid region. Moreover, as the gas flow progresses along the tube, the velocity in the mixture decreases, while the velocity in the liquid film slightly rises. This behaviour is due to the mass transfer from the mixture to the liquid film. In fact, when the gas mixture loses the mass, it loses velocity too, however, the liquid film gaining mass as well as acceleration. **Figure 6** Presents the evolution of the temperature profiles in both mixture and liquid phases at different tube sections. It can be seen that in the liquid phase, the temperature profiles are close to the temperature of the wall and nearly linear. This indicates that the interface temperature

Tube length (L (m))	3.0, 4.5, 6.0
Tube radius (R (m))	0.008, 0.01, 0.012
Inlet vapour mass fraction (w_0)	0.05, 0.125, 0.2
wall temperature ($T_w(^\circ\text{C})$)	5, 20, 35
Non-condensable gas	Oxygen, air, nitrogen

Table 1. The ranges of the physical parameters.

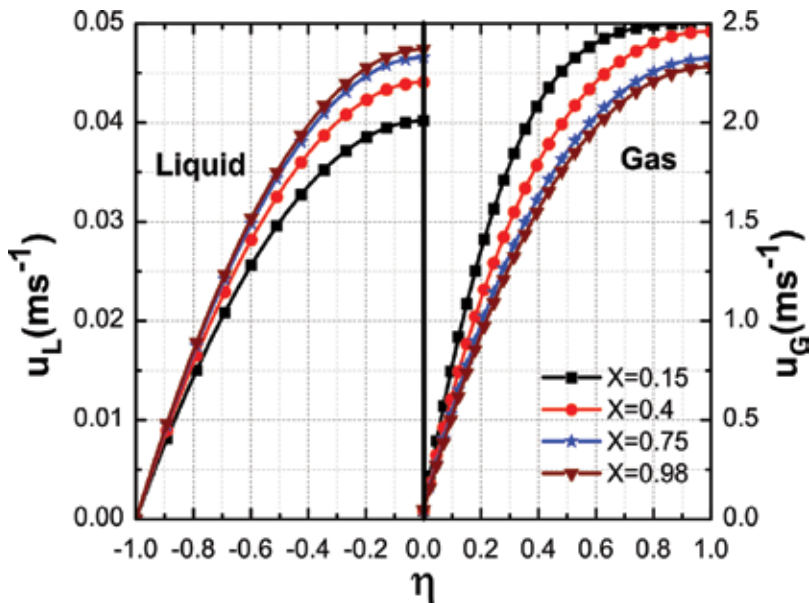


Figure 5. Distributions of axial velocity profile in both the liquid and vapour phases at different tube sections.

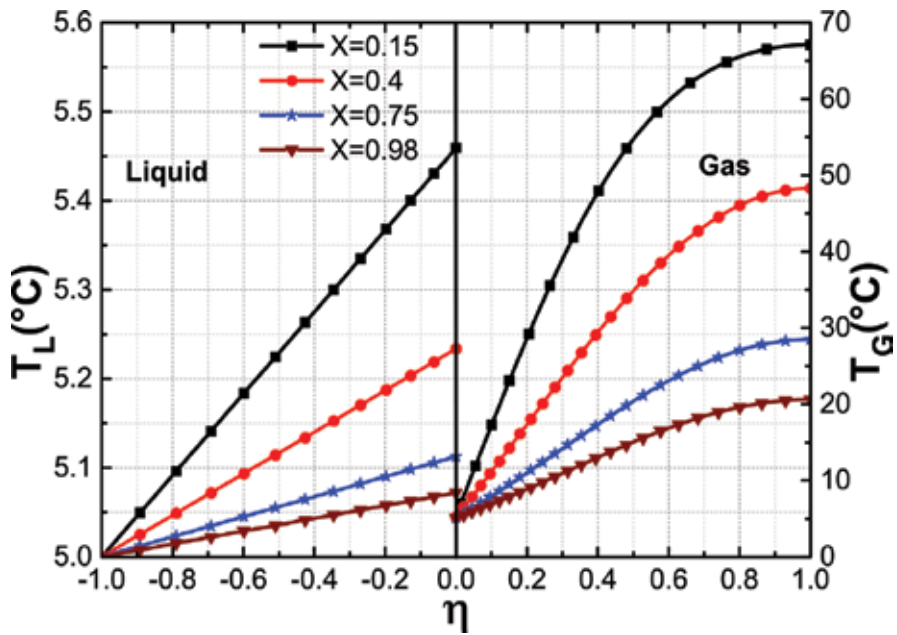


Figure 6. Distributions of axial temperature profile in both the liquid and vapour phases at different tube sections.

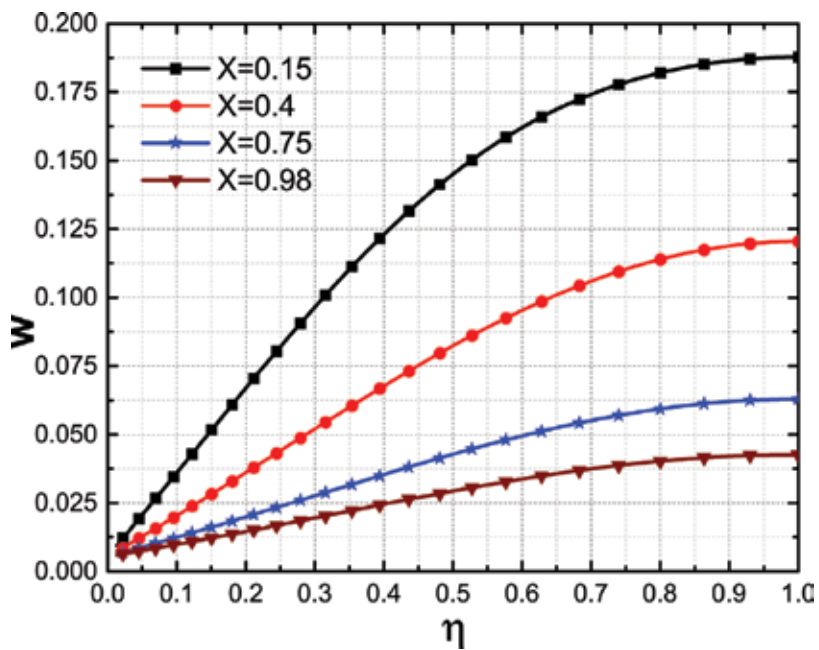


Figure 7. Distributions of axial vapour mass fraction profile in gas phases at different tube sections.

decreases from the inlet to the tube exit, resulting in the reduction of the heat transfer across the condensate film. Also, the slopes of the temperature of the mixture are decreasing along the tube owing to the absorbed energy transferred from the gas flow to the liquid film. The distributions of the mass fraction of water vapour in the gas region are illustrated in **Figure 7**. It is interesting to observe that the vapour mass fraction w_0 decreases from the entrance to the tube exit, which implies that the condensation rate is decreasing along the tube. Consequently, w_0 is reduced from the Centre line ($\eta = 1$) to the liquid-vapour interface ($\eta = 0$).

5. Effect of the tube geometry (length L and radius R)

In the desalination units, the tube geometry of which the water vapour condenses (whether it is the length or the radius) contributes positively to the improvement of the condensation process if they are well dimensioned.

To reveal their impacts, we first examined the impact of the length of the tube on the liquid film thickness and the condensing mass flux at the interface along the tube. **Figure 8** shows the influence of the tube length on the thickness of the film and condensing mass flux at the interface. It is noted that δ_x increases with increasing the tube length L . The results also indicate that, for a high tube length, the mechanism of the condensation is important when the distance is less than ($X = 0.8$), especially for $L = 4.5$ m and 6.0 m, because for a fixed Reynolds gas number (the inlet velocity is fixed too), the condensed vapour decreases with the increase of tube length. This means that near to the tube exit, the condensation process becomes almost unimportant. It is

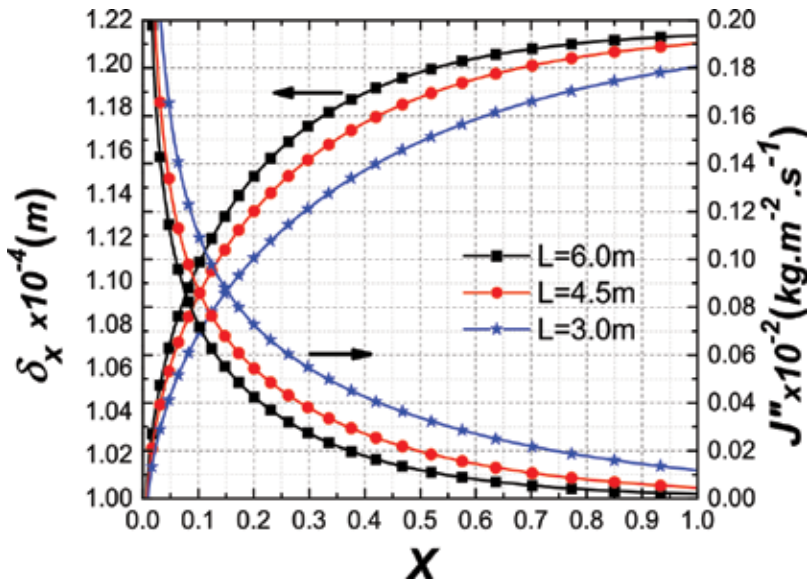


Figure 8. Effect of the tube length on the variation of the liquid film thickness and the condensing mass flux at the interface along the tube.

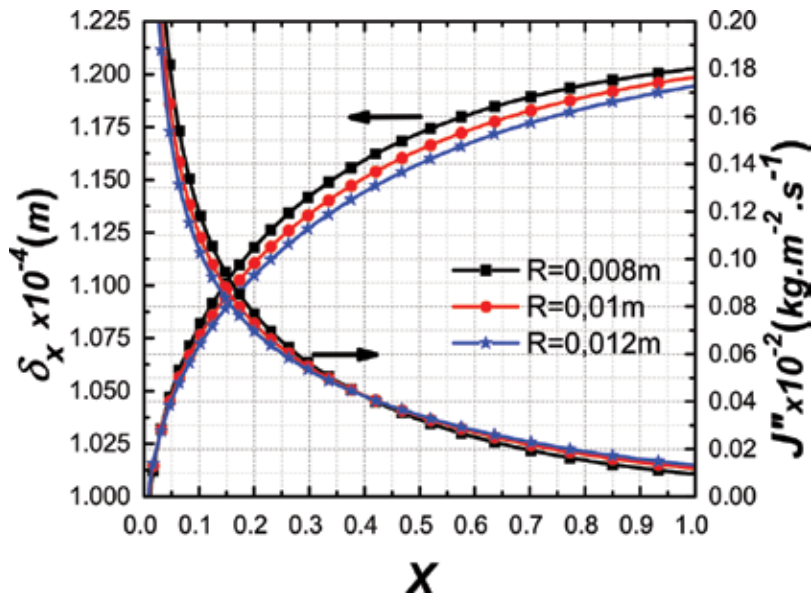


Figure 9. Effect of the tube radius on the variation of the liquid film thickness and the condensing mass flux at the interface.

also observed that the condensing mass flux reduces from the inlet to the outlet, particularly for the two large values of L approaching zero, because the total amount of the water vapour is transferred to liquid film and remains only the air at the vapour-liquid interface.

The effect of changing the tube radius R is shown in **Figure 9**. From the curves in this figure, it is interesting to observe that for a fixed value of T_0 , w_0 and Re_0 , a smaller tube radius corresponds to a thicker liquid film thickness. This trend is true for every position X from the inlet to the outlet of the tube. These results are directly related to the velocity of the gas mixture at the inlet. Obviously, for a fixed Reynolds number, δ_x increases according to the velocity increases with a weak tube radius. This implies that a higher inlet velocity tends to move the air away from the interface and thus maintains its lower fraction, leading to the increase of the heat transfer coefficient, which improves the condensation process. It is also found that the condensing mass flux increases with the tube radius only near the inlet when $X < 4$ due to a high interfacial shear stress. This tendency is reversed as the gas mixture progresses along the tube.

6. Effect of water vapour mass fraction w_0

In the majority of thermal desalination units, the water vapour that does not condense at the first effect, with all the non-condensable gases content, is transferred to the second effect, and this produces gas accumulation up to inadmissible concentrations. These gases cause a reduction in the performance of the system.

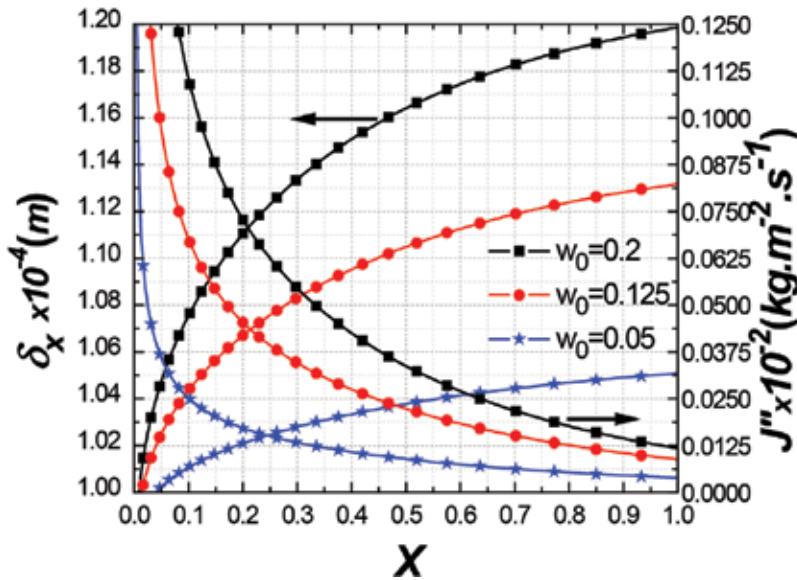


Figure 10. Effect of the inlet vapour mass fraction on the variation of the liquid film thickness and the condensing mass flux at the interface.

This result is confirmed in **Figure 10**, which shows that the thickness of the film increases considerably from the inlet to the exit of the tube. It is also observed that the increase in the mass fraction of water vapour w_0 considerably improves the condensation mechanism along the tube. Indeed, for a constant T_0 , an increase of w_0 affects the thermo-physical properties of the gas mixture at the inlet, which leads to an augmentation of the vapour partial pressure and the temperature at the vapour-liquid interface. Consequently, the condensing mass flux at the interface J'' increases significantly with w_0 leading to an increase in the rate of condensation, which improves the thickness of the liquid film. On the other hand, a small amount of w_0 (inversely proportional to the mass fraction of the non-condensable gas) causes a remarkable reduction of the condensed mass flux rate and the axial variation of the thickness of the film along the tube. This is due to the presence of air, which plays the role of thermal and mass transfer resistance at the vapour-liquid interface.

7. Effect of the wall temperature T_W

The effect of the wall temperature T_W on the liquid film thickness and the condensing mass flux is presented in **Figure 11**. It is noted that the thickness of the liquid film varies inversely with the imposed temperature of the wall. Clearly, there is a significant growth of the liquid film thickness when T_W reduces from 35°C to 5°C because the amount of the condensed vapour is enhanced along the tube by the increase of the heat transfer and hence the thickness of the

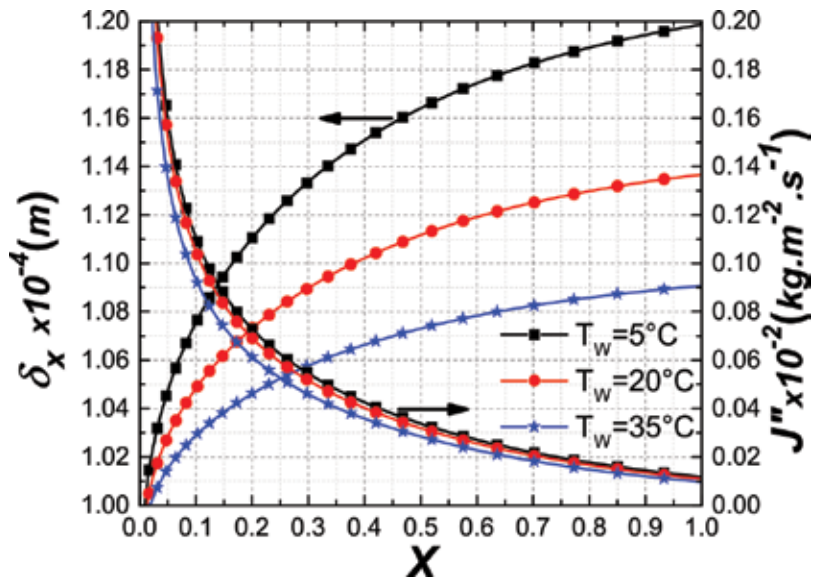


Figure 11. Effect of T_w on the evolution of the liquid film thickness and the condensing mass flux at the interface.

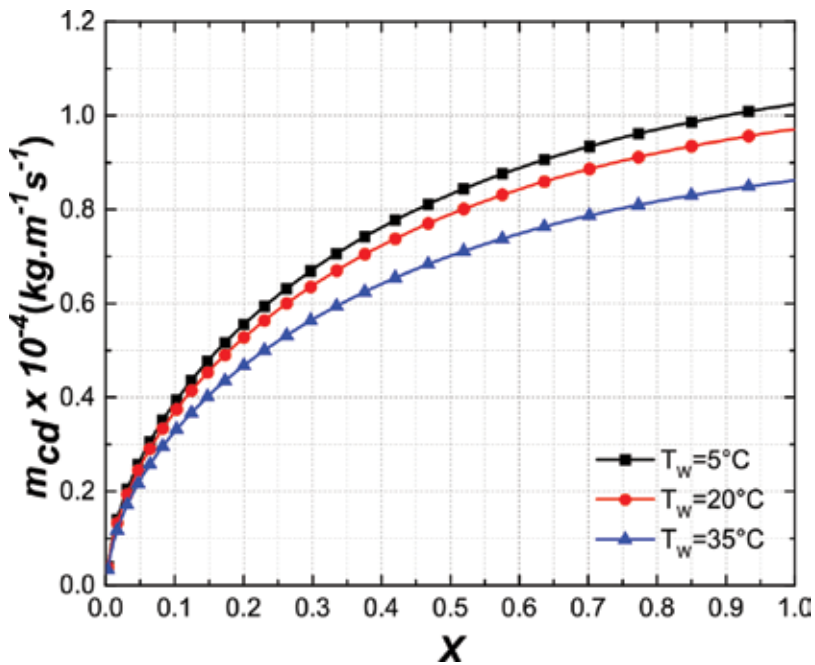


Figure 12. Effect of T_w on the accumulated condensation along the tube.

liquid film becomes thicker. From this figure, it is also observed that the condensing mass flux is important for a large value of the inlet-to-wall temperature difference and then decreases along the tube. The results indicate that J'' decreases as the gas flow progresses along the tube because the condensation is accompanied by a diminution in the temperature of the vapour phase and the heat transferred by the latent mode during the condensation to the liquid film. The effect of wall temperature on the accumulated condensation m_{cd} is illustrated in **Figure 12**. It can be seen that m_{cd} becomes important for low temperatures. When the temperature difference ($T_0 - T_W$) increases, the heat transfer increases, and consequently the density of the condensed flux increases. This explains why the condensation process is favoured for a higher-temperature difference.

8. Effect of the non-condensable gas type

In thermal desalination units, when the water vapour condenses, the presence of a non-condensable gas hinders this phenomenon. The accumulation of non-condensable components at the vapour-liquid interface plays the role of an obstacle for heat and mass transfer. This causes a reduction in the efficiency of the system and therefore an increase in costs in most desalination units using phase change.

In this section, we analyse the influence of the non-condensable gas type during water vapour condensation. We considered mixed mixtures of water-oxygen, water-air and water-nitrogen. The molar mass of oxygen, air and nitrogen are equal to 31.99, 28.95 and 28.01 g/mol, respectively. Since the liquid film thickness δ and the condensing mass flux at the interface J'' determine the condensation efficiency, **Figure 13** illustrates the variation of δ and J'' along the

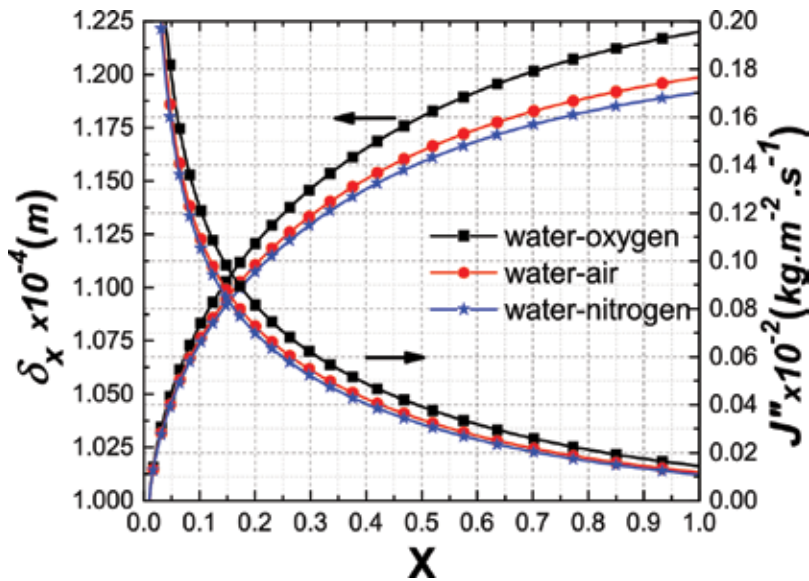


Figure 13. Effect of the type of non-condensable gas on the evolution of the liquid film thickness and the condensing mass flux at the interface along the tube.

tube. For a fixed w_0 , P_0 and Re_0 , an increase in the molar mass of the gas leads to a growth in the density of the gas mixture, the temperature of the gas mixture, as well as a decrease in the saturation concentration especially for water-oxygen mixture. This causes a strong vapour concentration gradient and condensing mass flux at the vapour-liquid interface. The results obtained show that the evolution of the film thickness and condensing mass flux in the water-oxygen mixture are significantly greater than those of the other mixtures. In addition, the condensing mass flux decreases along the tube and tends to a lower value especially near to the tube exit, which means the end of the condensation process.

9. Conclusion

A numerical analysis has been carried out to investigate the liquid film condensation of the water vapour with the presence of non-condensable gas inside a vertical tube. The main conclusions drawn from this study are as follows:

1. The efficiency of the system is enhanced by increasing the tube length and decreasing the radius, which allows condensing the maximum of the water vapour.
2. A small amount of non-condensable gas improves the heat and mass exchanges.
3. Decreasing the wall temperature enhances the liquid film thickness and the accumulated condensation.
4. The non-condensable gas type has a great effect on the condensation process.

Nomenclature

C_p	specific heat ($J \cdot kg^{-1} \cdot K^{-1}$)
D	diffusion coefficient ($m^2 \cdot s^{-1}$)
d	diameter of the tube (m)
R	radius of the tube ($d/2$) (m)
L	tube length (m)
g	gravitational acceleration ($m \cdot s^{-2}$)
Nus	sensible Nusselt number
m_{cd}	accumulated condensation
P	atmospheric pressure (Pa)
T	temperature ($^{\circ}C$)
u	axial velocity ($m \cdot s^{-1}$)

- v radial velocity (m. s^{-1})
 w mass fraction of vapour
 J'' mass flux at the interface ($\text{kg.m}^{-2}.\text{s}^{-1}$)
 h_{fg} latent heat of condensation (J. kg^{-1})
 r radial coordinate (m)

Greek symbols

- δ liquid film thickness (m)
 λ thermal conductivity ($\text{w.k}^{-1}.\text{m}^{-1}$)
 μ dynamic viscosity ($\text{kg. m}^{-1}.\text{s}^{-1}$)
 ρ density (kg. m^{-3})
 τ shear stress
 ϕ relative humidity (%)

Subscripts

- L referring to the liquid
G referring to the gas mixture
I interface
0 condition at inlet of the tube
W condition at wall of the tube
a referring to the air
x axial

Author details

Adil Charef*, M'barek Feddaoui, Abderrahman Nait Alla and Monssif Najim

*Address all correspondence to: adil.charef@edu.uiz.ac.ma

Laboratory of Energy, Materials and Systems Engineering, Ibn Zohr University, Agadir, Morocco

References

- [1] Nusselt W. Die Oberflächenkondensation des Wasserdampfes the surface condensation of water. Zetschr. Ver. Deutch. Ing. 1916:541-546

- [2] Lebedev PD, Baklastov AM, Sergazin ZF. Aerodynamics, heat and mass transfer in vapour condensation from humid air on a flat plate in a longitudinal flow in asymmetrically cooled slot. *International Journal of Heat and Mass Transfer*. 1916;**12**:833-841. DOI: 10.1016/0017-9310(69)90150-1
- [3] Dobran F, Thorsen RS. Forced flow laminar filmwise condensation of a pure saturated vapor in a vertical tube. *International Journal of Heat and Mass Transfer*. 1980;**23**:161-177. DOI: 10.1016/0017-9310(80)90194-5
- [4] Siow E, Ormiston S, Soliman H. Fully coupled solution of a two-phase model for laminar film condensation of vapor-gas mixtures in horizontal channels. *International Journal of Heat and Mass Transfer*. 2002;**45**(18):3689-3702
- [5] Siow E, Ormiston S, Soliman H. A two-phase model for laminar film condensation from steam air mixtures in vertical parallel-plate channels. *Heat and Mass Transfer*. 2004;**40**(5): 365-375
- [6] Belhadj Mohamed A, Orfi J, Debissi C, Ben Nasrallah S. Condensation of water vapor in a vertical channel by mixed convection of humid air in the presence of a liquid film flowing down. *Desalination*. 2007;**204**:471-481
- [7] Dharma Rao V, Murali Krishna V, Sharma K, Rao PM. Convective condensation of vapor in the presence of a non-condensable gas of high concentration in laminar flow in a vertical pipe. *International Journal of Heat and Mass Transfer*. 2008;**51**:6090-6101
- [8] Lee KY, Kim MH. Experimental and empirical study of steam condensation heat transfer with a noncondensable gas in a small-diameter vertical tube. *Nuclear Engineering and Design*. 2008;**238**:207-216. DOI: 10.1016/j.nucengdes.2007.07.001
- [9] Nebuloni S, Thome JR. Numerical modeling of laminar annular film condensation for different channel shapes. *International Journal of Heat and Mass Transfer*. 2010;**53**:2615-2627. DOI: 10.1016/j.ijheatmasstransfer.2010.02.054
- [10] Chantana C, Kumar S. Experimental and theoretical investigation of air-steam condensation in a vertical tube at low inlet steam fractions. *Applied Thermal Engineering*. 2013;**54**: 399-412. DOI: 10.1016/j.applthermaleng.2013.02.024
- [11] Dahikar SK, Ganguli AA, Gandhi MS, Joshi JB, Vijayan PK. Heat transfer and flow pattern in co-current downward steam condensation in vertical pipes-I: CFD simulation and experimental measurements. *The Canadian Journal of Chemical Engineering*. 2012:1-15
- [12] Merouani L, Zeghamati B, Belhamri A. Numerical modelling of convective vapour condensation with non-condensable gases between two coaxial vertical cylinders. *The Canadian Journal of Chemical Engineering*. 2013;**91**:1597-1607
- [13] Qiujie Y, Tian M, Fang D. CFD simulation of air-steam condensation on an isothermal vertical plate. *International Journal of Heat and Technology*. 2015;**33**:25-32. DOI: 10.18280/ijht.330104
- [14] Semiat R, Galperin Y. Effect of non-condensable gases on heat transfer in the tower MED seawater desalination plant. *Desalination*. 2001;**140**(1):27-46

- [15] Al-Shammari S, Webb D, Heggs P. Condensation of steam with and without the presence of non-condensable gases in a vertical tube. *Desalination*. 2004;**169**(2):151-160 <http://dx.doi.org/10.1016/j.desal.2003.11.006>
- [16] Caruso G, Di Maio DV, Naviglio A. Condensation heat transfer coefficient with non-condensable gases inside near horizontal tubes, *Desalination*, vol. 309, (2013) pp. 247-253. DOI: 10.1016/j.ijheatmasstransfer.2013.09.049
- [17] Hassaninejadfarahani F, Guyot MK, Ormiston S. Numerical analysis of mixed-convection laminar film condensation from high air mass fraction steam-air mixtures in vertical tubes. *International Journal of Heat and Mass Transfer*. 2014;**78**:170-180. DOI: 10.1016/j.ijheatmasstransfer.2014.06.047
- [18] Charef A, Feddaoui M, Najim M, Meftah H. Liquid film condensation from water vapour flowing downward along a vertical tube. *Desalination*. 2017;**409**:21-31. DOI: 10.1016/j.desal.2017.01.018
- [19] Eckert E, Drake Jr. *Analysis of Heat and Mass Transfer*. New York: Hemisphere Publishing; 1987
- [20] Poling BE, Prausnitz JM, John Paul O, Reid RC. *The Properties of Gases and Liquids*, 5. New York: McGraw-Hill; 2001
- [21] Perry R, Green D. *Perry's Chemical Engineers Handbook*. New York: McGraw-Hill; 1997
- [22] Patankar S. *Numerical Heat Transfer and Fluid Flow*. New York: Hemisphere/McGraw-Hill; 1980
- [23] Nougier JP. *Méthodes de calcul numérique*. 3rd ed. Paris: Masson; 1991
- [24] Raithby GD, Schneider GE. Numerical solution of problems in incompressible fluid flow: Treatment of the velocity pressure coupling. *Numerical Heat Transfer*. 1979;**2**(4):417-440
- [25] Anderson DA, Tannehill JC, Pletcher RH. *Computational Fluid Mechanics and Heat Transfer*. New York: Hemisphere/McGraw-Hill; 1984
- [26] Charef A, Feddaoui M, Najim M, Meftah H. Comparative study during condensation of R152a and R134a with presence of non-condensable gas inside a vertical tube. *Heat and Mass Transfer*. 2018;**54**:1085-1099. DOI: 10.1007/s00231-017-2205-2

Distilled Water Production by Vacuum Heat Pump

Liu Bin, Cai Ling, Li Tianyin and Sajid Muhammad

Additional information is available at the end of the chapter

<http://dx.doi.org/10.5772/intechopen.76839>

Abstract

A new machine to produce distilled water was provided, which includes a heat pump system and a vacuum system. And in the vacuum system of this new machine, the ejector is the key component. Three kinds of ejectors were studied by using FLUENT software to simulate their parameters. The simulation results showed that a vacuum is formed in the ejector throat, where the speed also reached its maximum value. The optimized ratio between the area of the throat and that of the mixing section can be obtained according to theoretical calculations. The ejector with the ratio 0.0156 can be used to prepare distilled water, and the experimental results show that the energy consumption of 1 kilogram distilled water is lower than 0.3 kWh. In the heat pump system, the capillary is the key component. Five kinds of capillaries were studied by using CFD software to simulate their parameters. The simulation results showed that the larger the degree of supercooling of the refrigerant in the capillary, the larger the liquid volume fraction of the outlet refrigerant. The experimental results show that suitable capillary can greatly improve the efficiency of the system.

Keywords: ejector, simulate, the ratio of ejector, distilled water, capillary tube, condensate depression, energy conservation optimization

1. Introduction

With the development of economy, the problems of water resource shortage and energy shortages appeared in more and more countries and regions. At the same time, people also have increasing demands on the quality and quantity of water, so the research of water treatment and purification has never been stopped.

Although 70% of the earth is covered by water, the freshwater that people depend on is only 2.5–3% of the total water, and the entire world is facing a serious shortage of fresh water resources. In China [1], for example, China's total water resources for 2.81×10^4 one hundred

million tons, accounting for sixth place in the world. However, per capita water resources in the global rankings are 108 in China, and China is one of the most water-short countries in 21 poor countries in the world, and water per capita fresh water is only $\frac{1}{4}$ times the world average per capita. And in 2010, the total water demand was 730 billion tons in China, but the water supply was only 6200~6300 billion tons. By 2030, the water deficit will be higher than 100 billion cubic meters in 2010, and the amount of water per capita will fall to $1760 m^3$. The most severe water shortage is in the coastal industrial cities, where the per capita water resource is much lower than $500 m^3$, which belongs to the severe water shortage area.

Scholars have done a lot of the work on water purification and other aspects, but the principle of the method is not the same, and new methods and new technologies continue to emerge. For example, Sevda et al. [2] use microbial respiration to purify the water, and they have made the single seawater desalination room volume increased from 3 ml to 15 L. There are also a lot of traditional researches on the distilled water by evaporation pipe, for example, Hegazy [3] collected the water through a vacuum evaporator to collect steam condensation, and the energy consumption is about 1.8 Kw/hr/kg; Mahkamov [4] studied a new type of small and dynamic solar desalination device, where the piston converter was driven by solar energy and with periodic changes in volume and pressure, in which the purified water can be collected in evaporation tube. There are also many scholars who used membrane technology to produce distilled water. For example, Deshmukh et al. [5] studied the desalination by forward osmosis, and they summed up quantitative results between the structure parameters of the support layer with reduced film area in a certain range, thereby saving cost. In the direct contact membrane distillation process, Duong [6] optimized the thermal efficiency of the brine, so that the water recycling rate ranges from 20 to 60% and the energy consumption can be reduced by more than half. Khalifa [7] and other studies have used air gap membrane distillation to produce distilled water, and the influence of feed temperature and air gap width on the system performance was obtained. In addition, solar energy as a clean energy was also widely used to produce distilled water, for example, Reif et al. [8] used solar energy to desalination. Comparing with the conversion of solar energy into electricity, they pointed out that it was more effective and attractive for the system to be converted into heat energy. Sahoo et al. [9] used solar energy for desalination of sea water and polygeneration, reducing the cost and greenhouse gas emissions. Combination of distilled water and refrigeration system has been researched in depth by scholars. For example, Wang [10] studied a high-efficiency combined desalination and refrigeration system based on the LiBr-H₂O absorption cycle, getting more high energy utilization rate and lower operating costs. Nada [11] et al. studied the water production rate of distilled water in the process of desiccant air conditioning. Houa et al. [12] used simulation method to verify the feasibility of marine cooling system with seawater cooling and seawater desalination. Chiranjeevi [13] studied the combination of the two-stage seawater desalination and refrigeration system to improve the energy utilization coefficient. Scholars have studied other methods for producing distilled water, for example, Rommerskirchen [14] produced distilled water by using the single module electrode capacitor. Compared to the traditional capacitive deionized, it can produce distilled water continuously. Zhang [15] studied the influence of salt, anionic polyacrylamide, and crude oil on the membrane fouling in the process of polymer flooding. Comparing with the effect of silica gel

and AQSOA-Z02 on distilled water, Youssef [16] summed up the effect of different cooling water temperatures on the two kinds of materials. Ebrahimi [17] studied the use of low-grade heat source for seawater desalination.

Although the principle of the method for producing distilled water is various, the study on the distilled water by vacuum heat pump is relatively rare. In this paper, the effect of the pressure of the ejector pressure on the production of distilled water is studied.

2. System structure

The vacuum heat pump system is shown in **Figure 1**.

The structure of system is divided into two parts: the refrigeration cycle system and the water cycle system.

The principle of refrigeration cycle system is that the high-temperature and high-pressure gas from compressor releases heat when it enters into the vapor generator and auxiliary con-

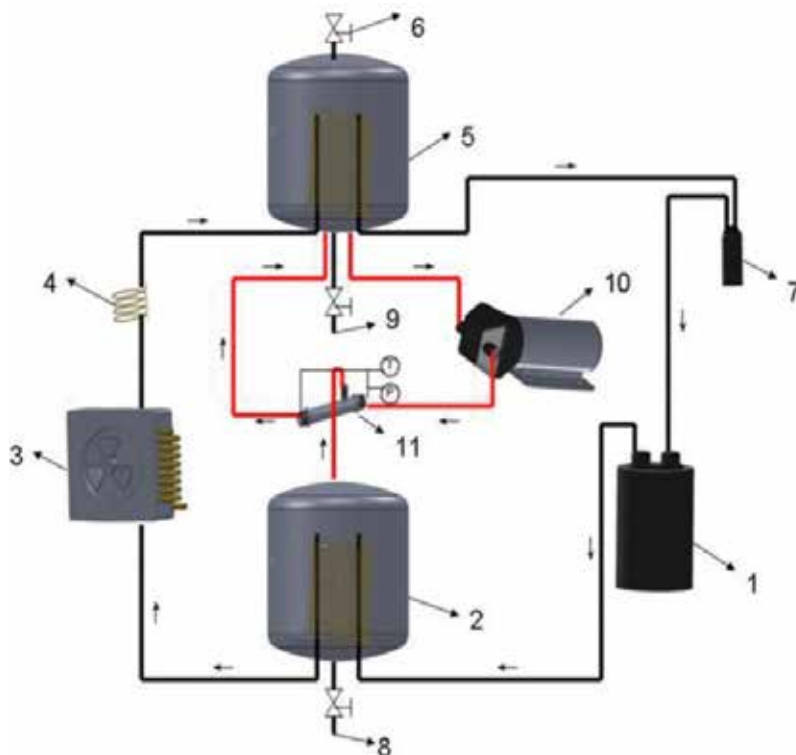


Figure 1. System structure of distilled water. 1, compressor; 2, vapor generator; 3, auxiliary condenser; 4, capillary; 5, condensate absorber; 6, vent valve; 7, gas-liquid separator; 8, water intake; 9, water outlet; 10, high-pressure diaphragm pump; 11, ejector.

denser, and then the gas turns into low-temperature and low-pressure liquid when it flows through the capillary. The liquid will get in the condensate absorber to transfer heat with water vapor. At the end, the low-pressure gas will be back to the compressor after the liquid passing through the gas-liquid separator. In this cycle, the condensing heat of refrigerant is used to produce water vapor by vapor generator, and the evaporative cooling is used to capture water vapor and produce distilled water in condensate absorber.

The work principle of water cycle system is that the water from condensate absorber is sucked by high-pressure diaphragm pump into the ejector, and then the water will be mixed with the vapor sucked by ejector entrainment from vapor generator. After ejector diffuser, the mixture of the vapor and the water returns to the condensate absorber, where the vapor is cooled into distilled water.

2.1. Application of ejector in system

From the working principle of the vacuum heat pump to produce the distilled water, we can find that the function of ejector is of vital importance in this system. The pressure of vapor generator is determined by the sucking pressure resulted from the injecting pressure and velocity of the water. When the injecting pressure is lower, the temperature of the vapor generator is low, so the condensation temperature of the refrigeration system will be reduced and the system efficiency is improved. While the temperature of the condensate absorber is higher, which means a higher temperature of the evaporation temperature of the refrigeration system, it also provides a higher performance of the refrigeration system. **Figure 2** shows the relationship between the water boiling temperature in vapor generator and induced pressure.

It can be seen from **Figure 2**, if a lower water vapor temperature is needed, the lower the induced pressure. When the temperature of water vapor is 30°C, the pressure is 4.25 kPa, and the induced pressure is 7.38kPa at 40°C, which means a very low pressure in vapor generator, so a very good ejector is necessary to obtain an excellent performance of the vacuum heat pump.

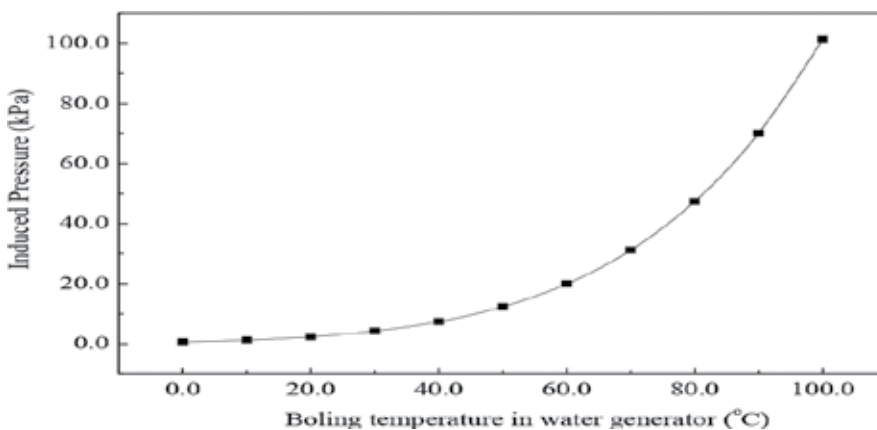


Figure 2. Induced pressure vs. boiling temperature in vapor generator.

2.2. Application of capillary in system

The selection of capillary tubes plays an important role in the system's energy-saving optimization, it is the component for throttling in the system. The refrigerant is pressurized by a compressor and congealed by a condenser. And it becomes a highpressure liquid and then flows into the capillary tube. Because the inner diameter of the capillary tube is very small, the flow of the refrigerant causes great resistance, and the pressure of the refrigerant is gradually reduced. When the pressure is reduced to the gasification pressure at the temperature of the refrigerant throttling, after the metastable process, the refrigerant is gasification.

In this chapter, CFD simulation and experimental test are performed on the matching of capillary tubes.

3. Design and simulation

3.1. Design and simulation of the ejector

For the ejector, in order to get a low suck pressure for the vapor generator, the spreading ratio (SR) defined as the ratio of the throat area to the tube area should be very small, and the velocity should be very high according to energy conservation. So selecting one optimized ejector to obtain a good performance of the vacuum heat pump system is very important; we designed three ejectors with different spreading ratios, of which the ratios were 0.0156, 0.0532, and 0.0946, respectively, and the throat diameters were 1.5, 3, and 4 mm, respectively, shown in **Table 1**.

(A) SR = 0.0156 and $D_t = 1.5$ mm; (B), SR = 0.0532 and $D_t = 3$ mm; and (C), SR = 0.0946 and $D_t = 4$ mm.

The performance of the above three ejectors were analyzed by FLUENT software. The fluid was the water, the inlet pressure was 0.6 MPa, and the inlet velocity is 1.6 m/s. The simulated results were shown in **Figure 3**.

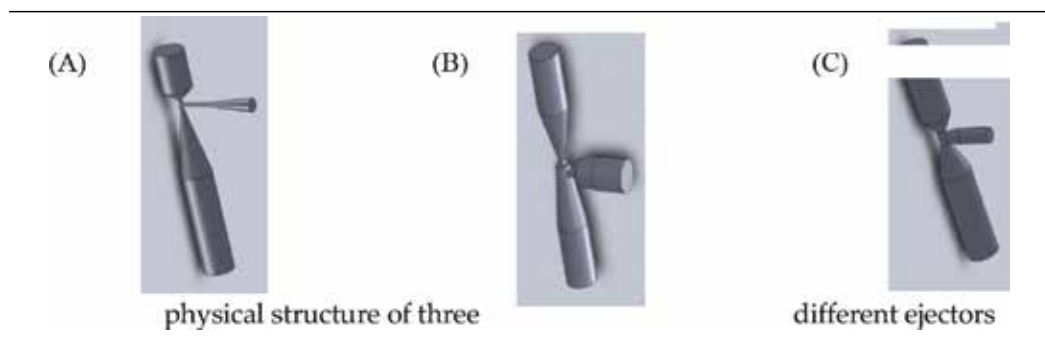


Table 1. Physical structure of three different ejectors 3-a:SR=0.0156,Dt=1.5mm, 3-b:SR=0.0532,Dt=3mm, 3-c:SR=0.0946,Dt=4mm.

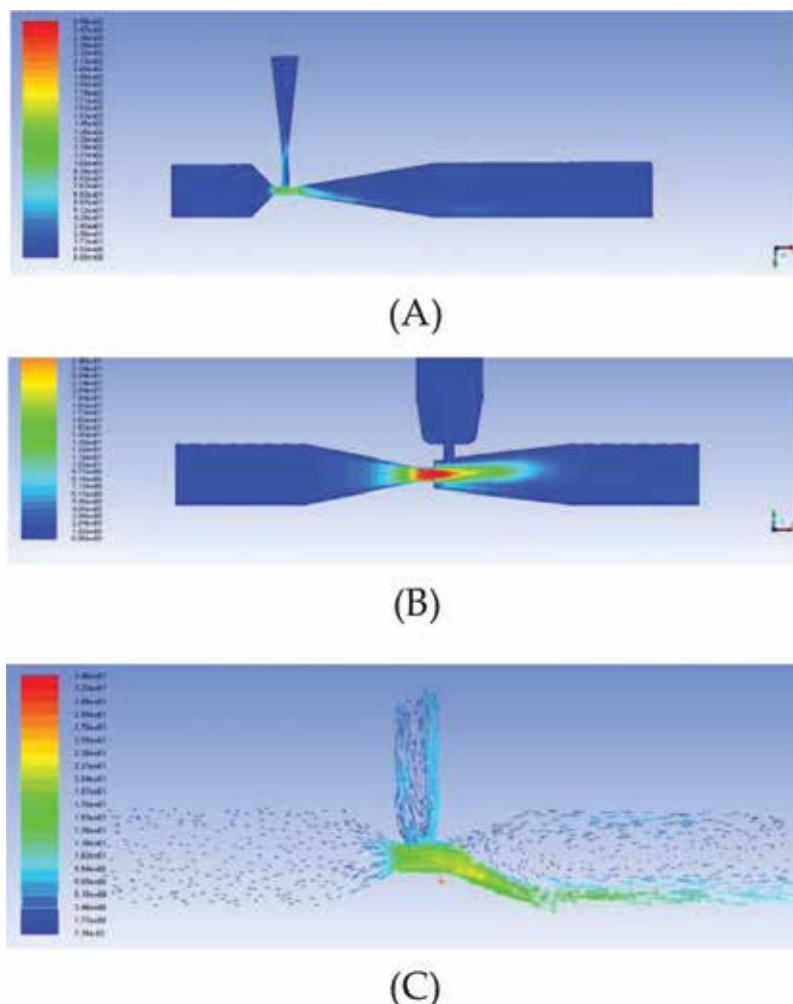


Figure 3. Internal velocity distribution of ejector.

From **Figure 3**, it can be seen that the maximum speed of the ejector (A) throat is 110 m/s and the velocity of the water vapor injection is more than 50 m/s. Compared with the ejector (B), the maximum speed of the throat is 30 m/s, and the velocity of the steam injection is about 4 m/s. While as the ejector (C), there was a reverse flow in the suck line, which implied that the water vapor from the vapor generator cannot be sucked into the condensate absorber. This can be analyzed from the perspective of conservation of energy.

3.2. Design and simulation of the capillary

The capillary tube is a small tube with small inner diameter. Due to the small inner diameter, when the fluid flows through the capillary tube, it will be greatly frictional resistance

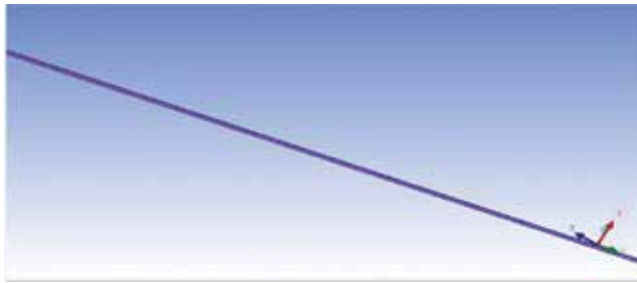


Figure 4. Capillary grid division.

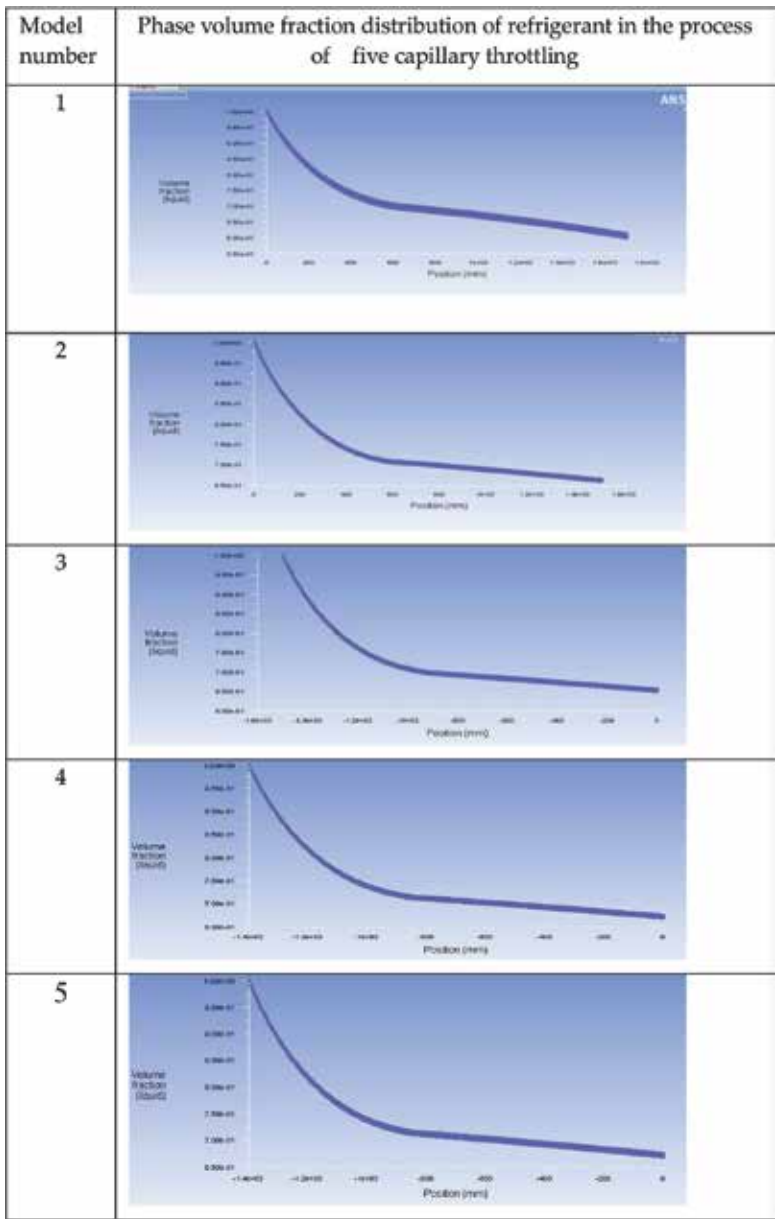
of the inner wall, and the pressure of the fluid will gradually decrease. And the flow of refrigerant in capillary tube can be divided into four stages: overcooling phase, single-phase metastable phase, gas–liquid two-phase metastable phase, and gas–liquid phase in thermal equilibrium phase. Therefore, we should choose different sizes of capillary tubes to measure the influence of different types of capillary tubes on the inlet overcooling and refrigerant liquid phase exit volume fraction. It is very important to select an optimized capillary tube to obtain a great system performance of heat pump distilled water, so we designed five capillary tubes with different sizes (inner diameter \times length, unit mm), of which the sizes were 1.7×1700 , 1.7×1500 , 1.4×1500 , 1.4×1400 , and 1.4×1300 . The inner diameter of the capillary tube used in the system is 0.5–2 mm, and the length is 1–4 m. The inner diameter and length of each capillary tube are different, but their materials are all copper tubes. After selecting the inner diameter and the length, the flow rate of the capillary tube depends on the difference between the cooling degree, the return air pressure, the suction pressure, and so on.

The VOF multiphase flow model is used in the five capillary flow simulations, and the performance is simulated and analyzed by FLUENT software. The fluid is the refrigerant R22, the inlet pressure is 1.8 Mpa, the outlet pressure is 0.6 Mpa, the inlet refrigerant temperature is 314.15 K, and the outlet temperature is 279.16 K.

Capillary tube is a slender structure; the length is greater than the diameter, if only using unstructured grid and drawing the number of grid will be too much; it is easy to exceed the limits of computer processing, so here structured grids are used, internal for hexahedral grid and external for tetrahedron, mesh model as shown in **Figure 4**.

At the inlet pressure which is 1.8 Mpa, the saturation temperature of the refrigerant R22 is 47°C; before entering capillary refrigerant is supercooled. Of five kinds of capillary tube in experimental conditions, the coolant temperature in the entrance of the capillary tube is 41°C, namely, supercooling degree is 6°C; the five models of capillary throttling effect comparing simulation diagram are:

1. Inlet coolant temperature is 41°C, liquid phase distribution of refrigerant in different types of capillary tubes is as follows:



As you can see from the figure above, the shape of the liquid phase change of the five types of capillary tube is similar; the refrigerant gasification rate is faster in the first half of the tube, with the gradual reduction of the refrigerant in the liquid phase; the amount of heat added to refrigerant gasification is also decreasing; this leads to a gradual decrease in the gasification rate of the refrigerant. Obviously, the volume fractions of the liquid phase of the refrigerant after the throttling are, respectively, 5, 4, 2, 3, and 1. The larger the volume fraction of the liquid in the capillary tube, the less the flash gas caused by throttling, the better the system.

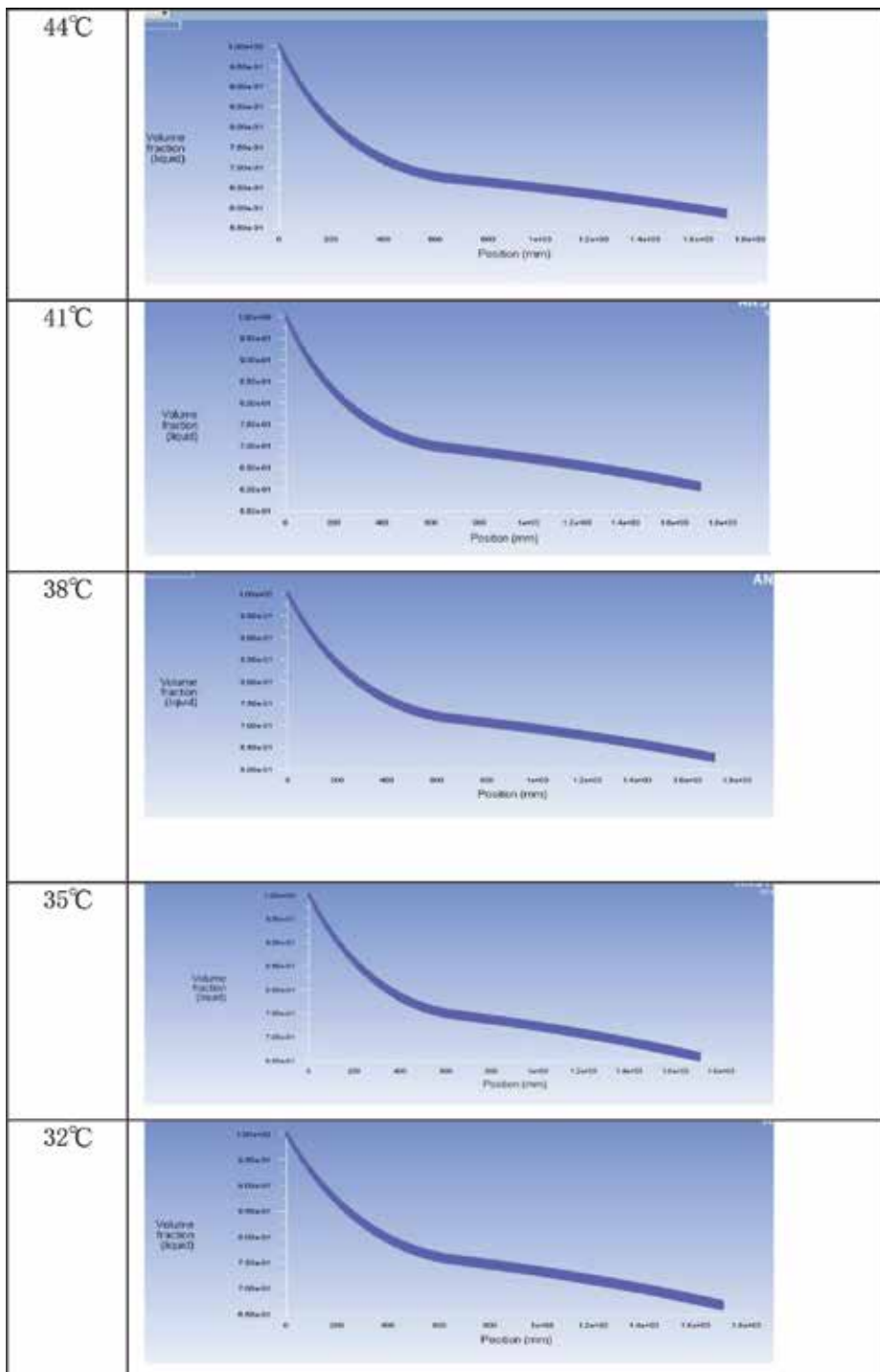


Figure 5. The liquid phase distribution of the refrigerant in capillary tube No. 1 was different.

1. The volume distribution of refrigerant liquid phase in the same type of capillary tube:

In order to study the effect of the cooling degree on the volume fraction of the liquid phase of the capillary export refrigerant, this simulation simulated the distribution of the liquid phase of the refrigerant under five degrees of supercooling for each type of capillary. In this system, before throttling the refrigerant saturation temperature is 47°C. And every 3°C, select a temperature value for degree of supercooling and the selected temperatures are respectively 44, 41, 38, 35, 32, as shown in **Figures 5**. And we only focus on the experiment diagram of capillary No. 1, and the phase volume fraction distribution of refrigerant in the process of capillary throttling of the other four capillary tubes is uniformly expressed in **Table 2**.

According to the results of comprehensive simulation analysis, the volume fraction of the liquid phase of the liquid phase of the five types of capillary tubes shows the trend

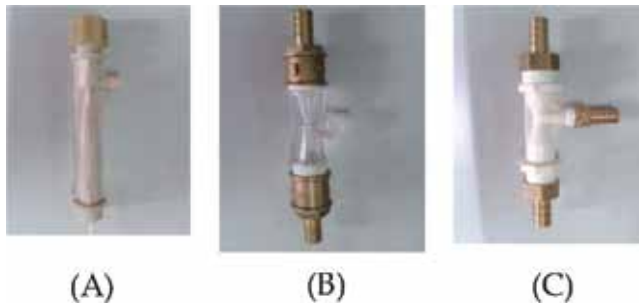
Number of capillaries	Temperature (°C)	Max position (mm)	Max position with its volume fraction (liquid)	Min position (mm)	Min position with its volume fraction (liquid)
2	44	0	1	1500	0.64
	41	0	1	1500	0.646
	38	0	1	1500	0.659
	35	0	1	1500	0.706
	32	0	1	1500	0.732
3	44	-1500	1	0	0.634
	41	-1500	1	0	0.649
	38	-1500	1	0	0.627
	35	-1500	1	0	0.695
	32	-1500	1	0	0.722
4	44	-1400	1	0	0.654
	41	-1400	1	0	0.669
	38	-1400	1	0	0.696
	35	-1400	1	0	0.72
	32	-1400	1	0	0.745
5	44	-1300	1	0	0.68
	41	-1300	1	0	0.695
	38	-1300	1	0	0.723
	35	-1300	1	0	0.739
	32	-1300	1	0	0.769

Table 2. The maximum and minimum position with their volume fractions of other capillaries at different temperatures.

of increasing with the increase of the supercooling degree. Therefore, under certain conditions, the higher the degree of supercooling, the less flash gas produced by throttling, the higher the volume fraction of the liquid component of refrigerant. Combined with the experiment, the entry refrigerants 41°C under 1, 2, 3, 4, and 5 capillary outlet refrigerant liquid volume fractions are, respectively, 0.599, 0.646, 0.649, 0.646, and 0.649; it has already satisfied the requirements of heat pump system. Comprehensive to the practical situation and design experience of heat pump system, this system selects the supercooling degree at 6°C, and the temperature of the refrigerant before the throttling is 41°C as the temperature of the capillary inlet refrigerant.

4. Results and discussion of the experiment

4.1. Experimental results and discussion of ejector



A set of experimental transposition was designed to verify the possibility of producing distilled water by the ejector. The main equipment include compressor (2R11B225A), pump (DP-35), condensation absorber (diameter 100 mm and height 300 mm), water generator (diameter 100 mm and height 300 mm), and capillary (length of 400 mm and diameter 2 mm). The above three kinds of forms of ejector were tested. Ejector C failed to form steam ejector function, so **Figure 6** shows throat pressure of the ejectors (A) and (B) versus time.

From **Figure 6**, it can be seen that the minimum pressure of ejector A can reach -0.085 Pa, the corresponding water vapor generator temperature at 50°C, and it can produce very good water vapor ejector effect, meeting the temperature requirements of the condenser of the refrigeration system. The lowest pressure can reach -0.034 Pa, the corresponding water vapor generator temperature at 73°C, but at this temperature, the efficiency of the refrigeration system will be very low. **Figure 8** is the fluid state of the ejector in the experiments.

From **Figure 7**, it can be seen that there is a mixed fluid of water and vapor in the ejectors A and B, while the ejector C produces the backflow, which cannot form an effective water vapor ejector effect. The ejector A is selected as a system unit, and the three different powers of the compressor were used in the production of distilled water. **Table 3** is the amount of distilled water produced by three experiments.

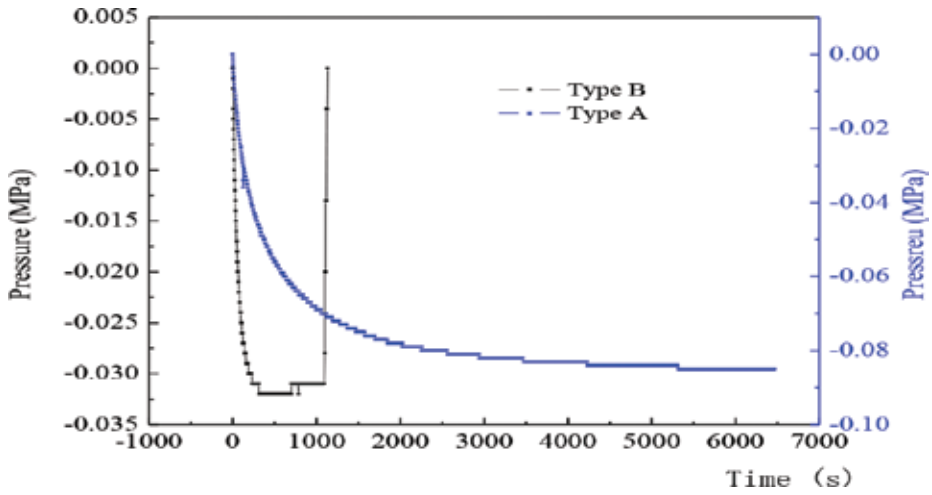


Figure 6. Throat pressure of ejector (a) and ejector (B) vs. time.



Figure 7. The flow state of the water vapor in the ejector.

From **Table 3**, it can be seen that the whole distillation water device runs stably under ejector A, and the water output per unit of electricity is more than 4.7 kg, the energy efficiency of which can be calculated by the following equation:

$$\varphi = \frac{Q}{P} \tag{1}$$

where Q is the heat produced by distilled water (kJ) and P is the power consumed (kJ). Therefore, the energy efficiency of this device is $\varphi = \frac{4.7 \times 2400}{3600} = 3.13$



Figure 8. Five different types of the capillary.

Experiment number	Compressor type	Effluent (kg)	Energy consumption (kWhr)	Unit energy consumption (kg/(kWhr))
1	TH31	9.8	2	4.90
2	PG108X1	4.8	0.98	4.90
3	KH145	5.2	1.1	4.73

Table 3. Quantity of distilled water produced.

4.2. Experimental results and discussion of capillary

A set of experimental equipment was designed to study the problem of capillary matching for a heat pump distiller. The main equipment include compressor (Panasonic centrifugal compressor, 220 V, 50 Hz, 1700 w), swap body (diameter 15 mm and height 27 cm), frozen water tank (length 30 cm, width 30 cm, and height 40 cm), ejector (inlet diameter 6.5 cm, nozzle diameter 1.2 mm, and speed of evacuation 15 L/s), valve (DC2 4 V), and five different types of capillary tubes, as shown in **Figure 8**.

The simulation test of these five capillary tubes found that the capillary tubes No. 1 and No. 2 were most suitable for this system, where No. 2 was slightly worse than No. 1, and the other three kinds of capillaries were not suitable for the system. And then we are just going to think about the simulation results for the No. 1 and No. 2. **Table 4** shows the voltage, current, and temperature of capillary tube No. 1 and No. 2. **Table 5** shows the electric energy per hour of the system under the capillary No. 1 and No. 2. **Table 6** shows the yield and energy efficiency of the distilled water under No. 1 and No. 2.

Number of capillaries	Sizes (inner diameter × length, unit mm)	Voltage (V)	Electricity (A)	Compressor power (W)	Compressor average power (W)
1	1.7 × 1700	220	2.7	594	608.7
		220	2.8	616	
		220	2.8	616	
2	1.7 × 1500	220	2.8	616	616
		220	2.8	616	
		220	2.8	616	

Table 4. The voltage, current, and temperature distribution of the compressor for two most suitable capillaries.

Number of capillaries	Sizes (inner diameter × length, unit mm)	Compressor average power (W)	System power (W)	Consumption of electricity per hour (degree)
1	1.7 × 1700	608.7	716.7	0.7167
2	1.7 × 1500	616	724	0.724

Table 5. Electric energy consumption per hour for two most suitable capillaries.

Number of capillaries	sizes (inner diameter × length, unit mm)	Distilled water production (L/h)	Average production (L/h)	Energy efficiency (L/degree)
1	1.7 × 1700	2.1	2.05	2.86
		2.08		
		1.97		
2	1.7 × 1500	1.69	1.76	2.43
		1.88		
		1.72		

Table 6. Production and energy efficiency of distilled water of two most suitable capillaries.

Heat pump water distiller is a device that uses electric energy to produce distilled water, and in this article the energy efficiency is defined as the ratio of water production to electricity consumption. And the higher the energy efficiency is, the more distilled water is produced per kWh, and the more energy-efficient the system. The energy consumed by the system is compressor, pump, fan, and circuit board. As the power of the fan is negligible, the total power is combined with the power of the compressor and the pump. Energy efficiency is the key factor to consider the performance of the system. The purpose of energy-saving optimization is to improve the energy efficiency of the system under the condition of ensuring stable operation. Considering the selection of capillary tubes, in terms of energy consumption or energy efficiency, capillary tube No. 1 is superior to capillary tube No. 2. It is the most suitable system for smooth operation and energy saving.

5. Conclusion

Utilizing the production of distilled water by heat pump system is a very effective and comprehensive application of energy transposition. The condenser heat is used to generate steam, and then water vapor is caught by the evaporator to produce distilled water. Through the simulation and experimental study of the ejector and capillary, the following conclusions can be drawn:

1. Through theoretical and experimental research, the use of heat pump system to produce distilled water is feasible.
2. The negative pressure produced by the ejector is increasing with the decreasing of the spreading ratio. In this study, the pressure of the ejector can reach the following pressure of -0.85 MPa at the spreading ratio of 0.0156.
3. In this experiment, the amount of distilled water per kilowatt is above 4.7 kg, and the energy efficiency is 3.13.
4. Through theoretical and experimental studies, capillary tube selection plays an important role energy-saving optimization of the system. Suitable capillary can greatly improve the efficiency of the system.
5. Through CFD simulation, it is verified that the greater the degree of supercooling of the refrigerant in the capillary, the larger the liquid volume fraction of the refrigerant at the outlet of the capillary is.

Author details

Liu Bin^{1*}, Cai Ling¹, Li Tianyin¹ and Sajid Muhammad²

*Address all correspondence to: lbtjcu@tjcu.edu.cn

1 Tianjin Key Lab of Refrigeration Technology, Tianjin University of Commerce, Tianjin, People's Republic of China

2 School of Mechanical and Manufacturing Engineering (SMME), National University of Sciences and Technology (NUST), Islamabad, Pakistan

References

- [1] Academy, Chinese. "Strategic Research on Sustainable Development of Water Resource in China". *Engineering* (2000). *Engineering Science*. 2008;2(8) phase8
- [2] Sevda S, Yuan H, He Z, Abu-Reesh IM. Microbial desalination cells as a versatile technology: Functions, optimization and prospective. *Desalination*. 2015;371:9-17. DOI: 10.1016/j.desal.2015.05.021
- [3] Hegazy A, Hegazy M, Engeda A. A novel desalination system for utilizing waste heat contained in cooling salt water of a steam plant condenser. *Desalination*. 2015;371:58-66. DOI: 10.1016/j.desal.2015.05.023
- [4] Mahkamov K, Orda E, Belgasim B, Makhkamova I. A novel small dynamic solar thermal desalination plant with a fluid piston converter. *Applied Energy*. 2015;156:715-726. DOI: 10.1016/j.apenergy.2015.07.016
- [5] Deshmukh A, Yip NY, Lin S, Elimelech M. Desalination by forward osmosis: Identifying performance limiting parameters through module-scale modeling. *Journal of Membrane Science*. 2015;491:159-167. DOI: 10.1016/j.memsci.2015.03.080
- [6] Duong HC, Cooper P, Nelemans B, Cath TY, Nghiem LD. Optimising thermal efficiency of direct contact membrane distillation by brine recycling for small-scale seawater desalination. *Desalination*. 2015;374:1-9. DOI: 10.1016/j.desal.2015.07.009
- [7] Khalifa A, Lawal D, Antar M, Khayet M. Experimental and theoretical investigation on water desalination using air gap membrane distillation. *Desalination*. 2015;376:94-108. DOI: 10.1016/j.desal.2015.08.016
- [8] Reif JH, Alhalabi W. Solar-thermal powered desalination: Its significant challenges and potential. *Renewable and Sustainable Energy Reviews*. 2015;48:152-165. DOI: 10.1016/j.rser.2015.03.065
- [9] Sahoo U, Kumar R, Pant PC, Chaudhury R. Scope and sustainability of hybrid solar-biomass power plant with cooling, desalination in polygeneration process in India. *Renewable and Sustainable Energy Reviews*. 2015;51:304-316. DOI: 10.1016/j.rser.2015.06.004

- [10] Wang Y, Lior N. Proposal and analysis of a high-efficiency combined desalination and refrigeration system based on the LiBr–H₂O absorption cycle—Part 2: Thermal performance analysis and discussions. *Energy Conversion and Management*. 2011;**52**:228-235. DOI: 10.1016/j.enconman.2010.06.064
- [11] Nada SA, Elattar HF, Fouda A. Experimental study for hybrid humidification–dehumidification water desalination and air conditioning system. *Desalination*. 2015;**363**:112-125. DOI: 10.1016/j.desal.2015.01.032
- [12] Houa S, Lia H, Zhang H. An open air–vapor compression refrigeration system for air-conditioning and desalination on ship. *Desalination*. 2008;**222**:646-655. DOI: 10.1016/j.desal.2007.01.190
- [13] Chiranjeevi C, Srinivas T. Combined two stage desalination and cooling plant. *Desalination*. 2014;**345**:56-63. DOI: 10.1016/j.desal.2014.04.023
- [14] Rommerskirchen A, Gendel Y, Wessling M. Single module flow-electrode capacitive deionization for continuous water desalination. *Electrochemistry Communications*. 2015;**60**:34-37. DOI: 10.1016/j.elecom.2015.07.018
- [15] Zhang R, Shi W, Yu S, Wang W, Zhang Z, Zhang B, Li L, Bao X. Influence of salts, anion polyacrylamide and crude oil on nanofiltration membrane fouling during desalination process of polymer flooding produced water. *Desalination*. 2015;**373**:27-37. DOI: 10.1016/j.desal.2015.07.006
- [16] Youssef PG, Mahmoud SM, AL-Dadah RK. Performance analysis of four bed adsorption water desalination/refrigeration system, comparison of AQSOA-Z02 to silica-gel. *Desalination*. 2015;**375**:100-107. DOI: 10.1016/j.desal.2015.08.002
- [17] Ebrahimi K, Jones GF, Fleischer AS. A review of data center cooling technology, operating conditions and the corresponding low-grade waste heat recovery opportunities. *Renewable and Sustainable Energy Reviews*. 2014;**31**:622-638. DOI: 10.1016/j.rser.2013.12.007

Renewable Energy in Desalination

Renewable Energy-Driven Desalination Hybrids for Sustainability

Muhammad Wakil Shahzad, Doskhan Ybyraiymkul,
Muhammad Burhan and Kim Choon Ng

Additional information is available at the end of the chapter

<http://dx.doi.org/10.5772/intechopen.77019>

Abstract

The expansion trend of current desalination processes is expected to boost brine rejection to 240 km³ and CO₂ emission to 400 million tons per year by 2050. This high brine rejection and CO₂ emission rates are copping COP21 goal, maintaining temperature rise below 2°C. An innovative and energy-efficient process/material is required to achieve Paris Agreement targets. Highly efficient adsorbent cycle integration is proposed with well-proven conventional desalination processes to improve energy efficiency and to reduce environmental and marine pollution. The adsorbent cycle is operated with solar or low-grade industrial waste heat, available in abundance in water stress regions. The proposed integration with membrane processes will save 99% energy and over 150% chemical rejection to sea. In case of thermally driven cycles, the proposed hybridization will improve energy efficiency to 39% and will reduce over 80% chemical rejection. This can be one solution to achieve Paris Agreement (COP21) targets for climate control that can be implemented in near future.

Keywords: desalination, hybridization, sustainability, economics, environmental impact

1. Introduction

The inevitable escalation in economic development has serious implications for environment as energy generation and food-processing processes are vicious to the ecosystem. Energy is extremely important for any economy to generate wealth and the key component for GDP growth. A quadruple growth in energy demand is predicted by The International Energy Outlook 2016 (IEO2016) from 2012 to 2040. It is estimated to grow from 549 quadrillion

British thermal units (Btu) in 2012 to 815 quadrillion Btu in 2040, 48% increase in 28 years. The energy demand could have more than doubled without efficiency gain and suitable energy mix. The non-Organization for Economic Cooperation and Development (non-OECD) countries are the major contributor in this drastic energy demand. In these countries, energy demand rises by 71% from 2012 to 2040 in contrast with only 18% in developed countries in same time span as shown in **Figure 1**. An average GDP growth of 4.2% per year is estimated between 2012 and 2014 in non-OECD countries as compared to 2.0% per year in OECD countries as estimated by IEO2016. In terms of energy consumption by sectors, industry is leading followed by residential and transport. This trend persists from 1971 to 2014, but overall consumption doubled during this period. Power plant sectors consume 35% of global energy, and it is estimated to grow due to urbanization in developing countries. Global electricity demand is expected to increase over 65% from 2014 to 2040, 2.5 times faster than overall energy demand [1–7].

Even though there is a competition between countries for development, but it has severe impact on environment in terms of CO₂ emission. Every drop of fuel pollutes environment and intensity depends on process efficiency. Global CO₂ emission measured as 40 gigaton (Gt) per year in 2016 is almost double as compared to 1980 emission level. Energy sector are the major contributor, 68%, in CO₂ emission and power generation sector sharing 42% in energy sector emission followed by transport 23% and industry 19%. A systematic diversification of the global energy mix and technology improvement driven by economics and climate policies almost flattens the CO₂ emission rate in 2014, only 0.8% increase, as compared to 1.7% in 2013 and 3.5% in 2000. In the past 3 years, 2012–2014, the moderate increase in CO₂ emission, 0.8–1.7%, is

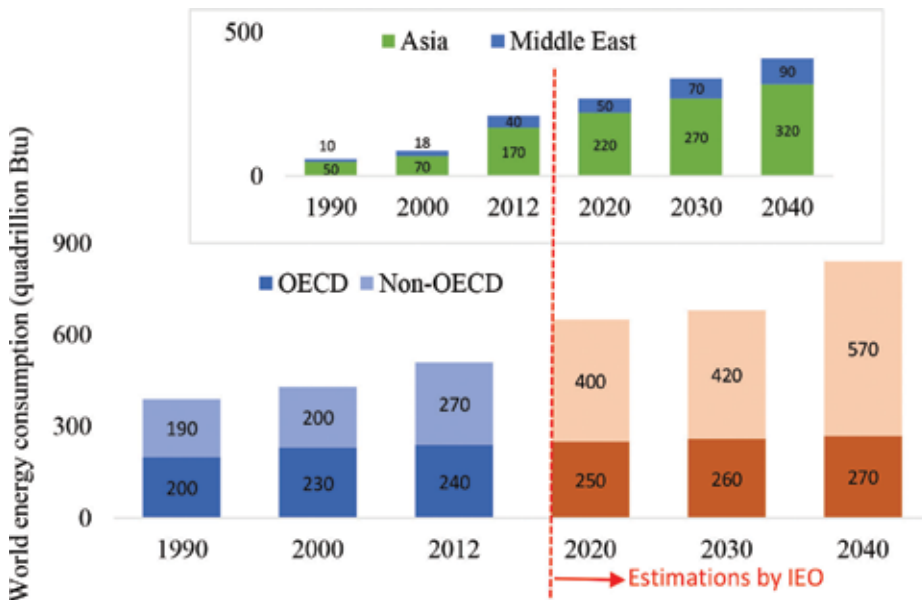


Figure 1. Organization for Economic Cooperation and Development (OECD) and non-OECD countries’ energy consumption from 1990 to 2040. Asia and Middle East region show major share in the world energy consumption. IEO2016 estimated the trend from 2017 to 2040 with BAU process [1].

remarkable when global economic growth rate was 3% as compared to 4% emission annually with GDP growth rate of 4.5% in last decade. In other words, partial decoupling of economic growth and CO₂ emission has been observed in last 3 years due to shift in energy production and consumption, power generation, technological improvements and policy implementation. In 2015, the milestone year, 170 countries signed an agreement at the 21st Conference of the Parties (COP21) in Paris for climate action. The Paris Agreement is the first international climate agreement extending mitigation obligations to all developed and developing countries representing over 90% of energy-related CO₂ emissions and approximately 7 billion people. The agreement aim to achieve CO₂ emission peak as soon as possible to cap the increase in the global average temperature to below 2°C. In addition, it also aims to pursue extra efforts to limit the temperature increase to 1.5°C. Business as usual (BAU) scenario, as most of the countries followed, can lead to over 5°C temperature increase as shown in **Figure 2** [8–25].

In Middle East, fast economic growth along with structural changes is expected to increase energy consumption to over 90% (30 quadrillion Btu) from 2012 to 2040. In GCC countries, the electricity demand has been increased at thrice the global average over the last few years due to many factors such as (i) high economic growth rate, (ii) huge development projects encouraging policies, (iii) government subsidies and (iv) higher cooling and water demand. The United Nations Environment Program identified the GCC countries as the highest per capita energy consumption in the world and they contribute 45–50% cumulative Arab countries’ CO₂ emissions. Saudi Arabia is leading in power generation as well as in CO₂ emission in GCC countries followed by UAE, Kuwait, Qatar, Oman and Bahrain as shown in **Figure 3**. Increasing energy demand and CO₂ emission inspired the regional government to improve energy efficiency, diversifying energy mix and to devise strategies for alternative renewable energy sources to conserve natural resources and environment [26–37].

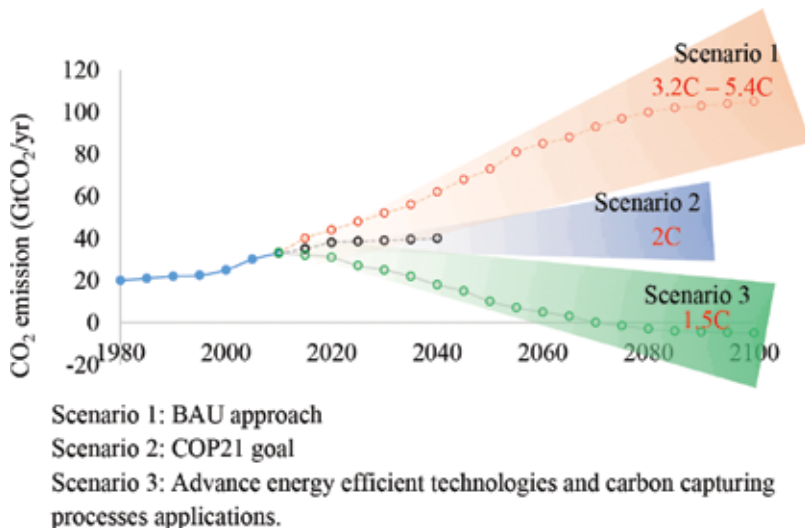


Figure 2. CO₂ emission trends impact on environmental at three different scenarios: (i) business as usual approach will lead to 3–6°C ambient temperature increase, (ii) COP21 goal targets to control emission to maintain temperature increase below 2°C and (iii) advance processes/technologies to lower temperature increase to 1.5°C [8, 9].

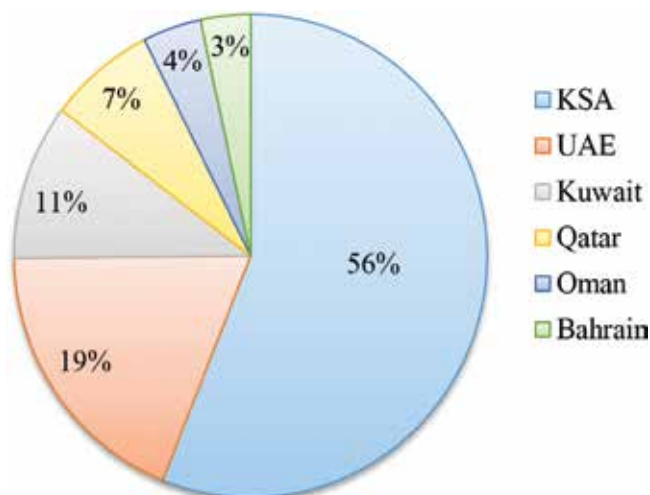


Figure 3. CO₂ emissions trends in Gulf Cooperation Council (GCC) countries. Saudi Arabia is leading with 56% emission due to high electricity and water demand and poor energy-efficient process applications [5].

1.1. Energy efficiency and renewable energy targets for electricity generation

GCC countries already planned energy efficiency and renewable energy targets for 2030 as shown in **Figure 4**. As a global sunbelt region, solar energy has received particular attention due to abundance availability in the region and falling cost of technology, particularly photovoltaic (PV). Renewable energy plans of GCC will result in cumulative 2.5 Billion barrels of oil equivalent saving from 2015 to 2030 equivalent to USD 55–87 billion savings. Implementation of renewable energy sources and decrease of fossil fuel consumption will reduce a cumulative total of 1 gigaton (Gt) of CO₂ emission by 2030. This will result in 8% reduction in the region's per capita carbon footprint, in line with the countries' Intended Nationally Determined Contributions (INDC) submissions to the Paris climate conference (COP21). In addition to CO₂ savings, energy efficiency and renewable energy application will reduce 16% of water consumption in power generation sector. This will save 11 trillion liters of water per year that will not only have ecological benefits but will also reduce energy consumption for water desalination [38–47].

In GCC region, energy intensive desalination processes are the major contributor to satisfy the increasing water demand with the development of infrastructure. The regional water demand is expected to increase to fivefold by 2050. The water is utilized during fossil fuel extraction, industrial processing, domestic purposes, cooling and power generation. The analyst predicted that the scale of water utilized for energy production only will increase from 583 billion cubic meters (bcm) in 2010 to 790 bcm of water in 2013, resulting in even higher demand for desalination in the region [47]. Desalination technologies development and alternate energy mix are required urgently to coup the BAU trend.

1.2. Energy efficiency and renewable application for desalination

Currently, GCC countries' cumulative desalination capacity is 26 million cubic meter (mcm) per day, equivalent to 36% of total global capacity. GCC countries are set to ramp up their desalination infrastructure 6–10% annually till 2040, extending total capacity to almost twofold. These

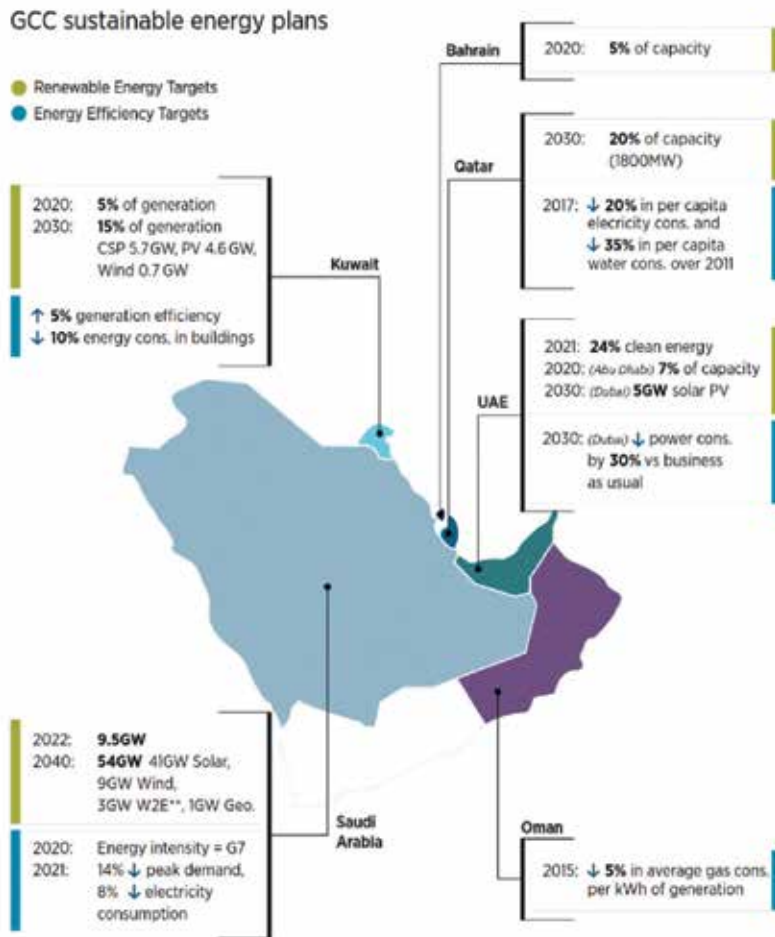


Figure 4. Gulf Cooperation Council (GCC) countries' targets for renewable energy applications and processes energy efficiency. Saudi Arabia planned to inject 54 GW electricity from renewable sources by 2040 [6].

beyond limit extensions of fossil fuel operated desalination capacities will have significant impact on regional economy. For example, Saudi Arabia consuming nearly 300,000 barrels of oil for thermal desalination to fulfill daily water demand and similar challenges are faced by other GCC countries. Traditionally, in GCC region, thermal desalination processes (MSF & MED) are preferred over membrane-based (SWRO) processes due to two main reasons: (i) extensive pre-treatment requirement for SWRO processes due to high salinity in Arabian Gulf and (ii) energy efficiency of thermally driven processes by utilizing residual low grade heat due to integrated water-and-power projects.

Thermal desalination processes gained confidence by operating for over 30 years in GCC region, and they are well integrated into power generation infrastructure. In terms of sea areas, Arabian Gulf is the largest intake facility for desalination capacities and producing 12.1 mcm per day. United Arab Emirates is dominating with 23% desalination capacity in Gulf followed by Saudi Arabia 11% and Kuwait 6%. In the Red Sea area, desalination plants have a total production capacity of 3.6 mcm per day, dominating by co-generation plants (72%).

Saudi Arabia accounts for 92% of the desalinated capacities in the Red Sea region, thermal desalination dominating by 78% installations (2.6 mcm per day). Major desalination installations in Red Sea, their size and technology type are presented in **Figure 5** [48–56].

In addition to less energy efficient, conventional desalination processes have enormous impact on marine line and environmental in terms of volume of brine rejection and CO₂ emissions. It is estimated that the brine rejection will increase to 240 km³ and emission will be approximately

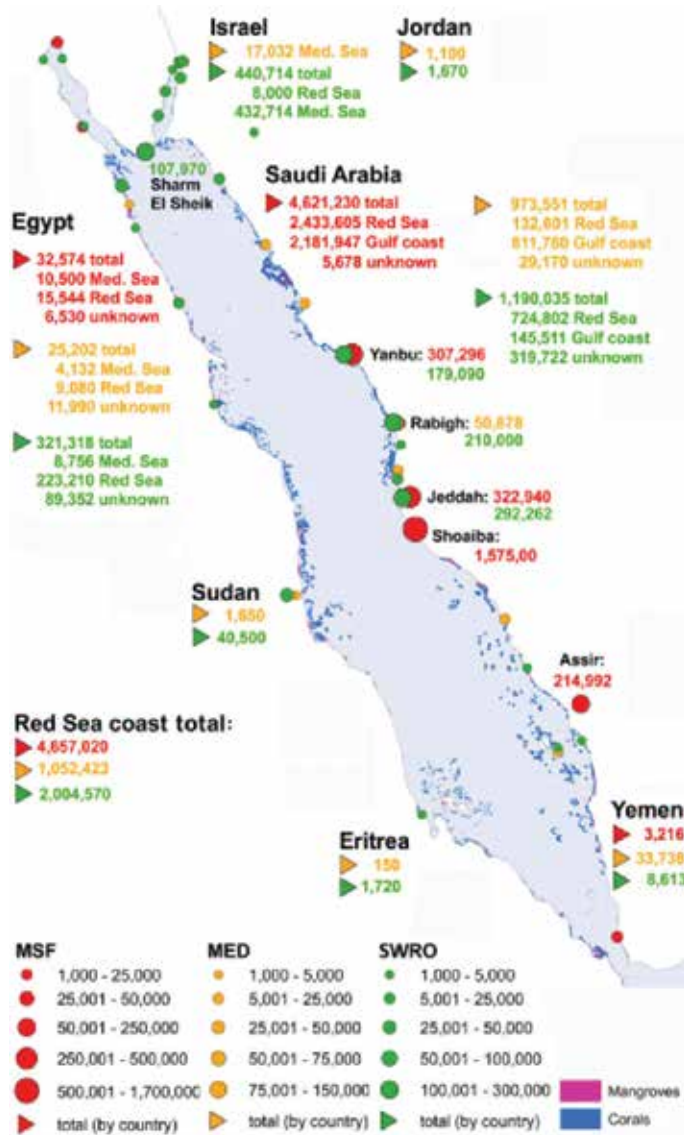


Figure 5. Location and size of major thermal- and membrane-based desalination installations along Red Sea, Gulf Coast and Mediterranean Sea. Thermal desalination processes are dominating due to severe feedwater conditions in GCC countries [56].

		Impact		
Probability		1	2	3
	1			
	2			
	3			
			SWRO (I × P)	Thermal (I × P)
Energy			3 × 3	3 × 3
CO ₂ emission			3 × 3	3 × 2
Chemical rejection			3 × 3	3 × 2
Brine concentration			3 × 2	3 × 1
Brine temperature			1 × 1	1 × 1
Pumps noise			3 × 2	2 × 1
			Low impact	
			Moderate	
			High impact	
			Severe impact	

Table 1. The impact matrix of conventional desalination processes. Both processes showed severe impact in terms of energy consumption, chemical rejection and CO₂ emission. Impact of SWRO processes is worse than thermal processes.

400 million tons of carbon equivalents per year by 2050. In the Gulf, 23.7 metric tons (mt) of chlorine, 64.9 mt of antiscalants and 296 kg of copper rejection are estimated from desalination installations, and in Red Sea, these rejections are 5.6 mt of chlorine, 20.7 mt of antiscalants and 74 kg of copper [57–61]. The impact of conventional desalination processes on energy and environment can be judged by the developed risk matrix as shown in **Table 1**. It can be seen that SWRO processes are operating in severe impact zone (half elements are in the red zone) while thermal desalination processes are higher than moderate zone (two elements are in the red zone).

Therefore, energy-efficient desalination processes (innovative hybrid cycles) and transitioning towards alternate renewable energies are two key innovation pillars needed to address future sustainable desalination water supplies in the region.

Hybrid desalination projects (SWRO/MSF, MSF/MED), for energy efficiency, were proposed and implemented to few facilities such as Jeddah-II, Fujairah II and Ras AL-Khair in the past [62–88]. Unfortunately, hybrid concept was unable to get much industrial implementation due to operational limitations. Today, industrial scale desalination processes pairing with innovative cycles are well needed to pave the way for future desalination in GCC under COP21 goal. We proposed an innovative adsorption (AD) cycle hybridization with SWRO and MED to meet COP21 accord. The proposed AD cycle utilized low-grade waste heat or renewable energy such as solar or geothermal to produce fresh water. The integration of AD

cycle with conventional desalination processes will help to overcome their operational limitations. For example, in first case, RO + AD integration can boost overall recovery to over 80% as compared to 35–40% of RO alone. This will help to protect marine pollution by reducing pretreatment chemical rejection into the sea. In second case, its hybridization with thermal processes such as MED + AD will help to overcome last stage operational temperature limitations of conventional MED system by extending to as low as 7°C as compared to 40°C in conventional processes. It will help to boost water production to almost twofold with same energy input. In both cases, CO₂ emission will reduce as AD cycle utilized only low-grade industrial waste heat or renewable energy. We presented detailed experimentation of both mentioned cases and their economic analysis to show the superiority of hybrid cycles over conventional processes in terms of energy efficiency, marine and environmental impact.

2. The basic adsorbent cycle

The basic adsorbent cycle consists of four major components, namely (i) evaporator, (ii) adsorbent beds, (iii) condenser and (iv) circulation pumps as shown in **Figure 6**. The feedwater is supplied to evaporator and saturation pressure is maintained by the adsorbent uptake capacity to achieve evaporation conditions below ambient level. Once the adsorbent bed is near saturation, adsorption process switched to second bed and regeneration heat is supplied to desorb vapor and prepare adsorbent for next cycle adsorption. The desorbed vapor is condensed in the condenser by circulating the chilled water from evaporator. It can be noticed that electricity

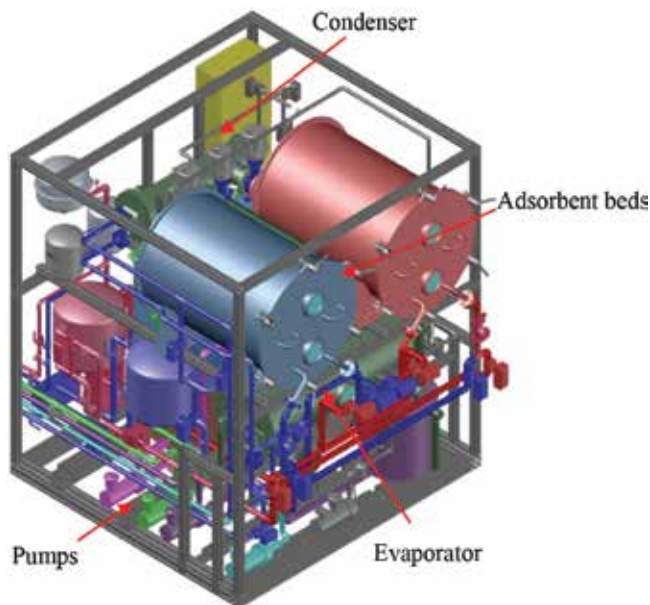


Figure 6. Adsorbent cycle 3D model can operate with solar or industrial waste heat from 55 to 85°C. The adsorbent is packed in the beds.

Adsorbent	Cost	Application status
Silica gel	Low	Industrial scale
Metal organic framework (MOF)	High	Research based only
Zeolite	High	Medium pilot

Table 2. Summary of major adsorbent, their cost and technological application status. Silica gel is most applied adsorbent because of its stability and reliability [110].

is only supplied for pumping of liquid and major thermal energy is supplied from renewable solar or industrial process waste heat from 55–85°C. The detail of adsorption cycle can be found in published literature [89–105]. The adsorbent selection depends on application temperature. The list of most common adsorbent and their application status are provided in **Table 2**. We developed an advance silica gel with improved uptake by pore opening. We also developed silica gel-coated heat exchanger AD cycle that can achieve heat transfer coefficient twofold higher as compared to conventional packed bed AD cycle [106, 107]. Silica gel has many advantages such as (i) easily available, (ii) lower cost as compared to all available adsorbent, (iii) more stable and reliable and (iv) easy to modify for required application [108–111].

The proposed adsorbent cycle has capability to integrate with conventional desalination process to improve their performance. The detail of integration with SWRO and thermal processes and their advantages are discussed in the following sections.

3. Membrane process and their integration: energy and environmental impact

In GCC countries, 42% desalinated water is produced by membrane processes. Conventional SWRO processes consume 7–17 kWh_{pe}/m³ primary energy (equivalent to 3–8 kWh_{elec}/m³) for seawater desalination and they emit 3.0 kg/m³ CO₂ to the environment [112]. Currently, major online SWRO plants in Saudi Arabia and future proposed projects is presented in **Table 3**.

Most of the SWRO plants are operated under saline water conversion cooperation (SWCC), and their overall recovery varies from 17 to 40% depending upon feedwater quality. Four major plants, namely (i) Jeddah, (ii) Rbigh, (iii) Jubail and (iv) Shuqaiq operational data were collected, and analysis results are presented.

3.1. SWRO and hybrid cycle results and discussion

Figure 7(a–c) shows the seawater, retentate and distillate concentration for four mentioned plants. It can be seen that Red seawater feed concentration varies from 37,000 ppm in Jeddah to 40,000 ppm in Jubail. The retentate maximum concentration was observed at Jeddah, 60000 ppm due to better recovery. The distillate concentration met the WHO standard, <500 ppm, except at Rbigh where it can reach to 800 pm and it mixed with thermal-driven processes distillate before distribution to end users.

Plant name	Capacity (m ³ /day)	Overall recovery (%)	Commissioning	Operator	Ref
Jeddah phase-II	48,848	35	1994	SWCC	[113]
Rabigh	168,000	40	2009	RAWEC	[114]
Shuqaiq-II	212,000	40	2010	NOMAC	[115]
Ras Azzour	307,000	40	2014	SWCC	[116]
Shuaiba I & II	76,800	40	2003	SEPCO	[117]
Shuaiba III Extension,	150,000	40	2009	SEPCO	[118]
Medina-Yanbu Phase II	127,825	35	1995	SWCC	[119]
North Obhor, Jeddah	12,500	35	2006	SAWACO	[120]
Jeddah-1	56,800	35	1989	SWCC	[121]
Umm Lujj	4400	24	1986	SWCC	
Haql	4400	30	1989	SWCC	
Duba	4400	31	1989	SWCC	
Al-Barik	2275	17	1983	SWCC	
Barge Raka,	24,981			SWCC	[118]
Future projects					
Jeddah phase (4)	400,000		2019	SWCC	[122]
Rabigh phase (3)	600,000		2019		
Alugair	10,000		2019		
Omluj	18,000		2020		
Yanbu-4	450,000		2020		
Jubail phase (3)	330,000		2021		

Table 3. Major SWRO plants in operation and future proposed projects in Saudi Arabia. They need extensive pretreatment and still recovery is only up to 40% maximum.

At these four locations, we also analyzed the CO₂ emission and chemical rejection in the brine and applied to overall capacity in GCC according to SWRO market share. **Table 4** shows the CO₂ emission and chemical rejection per day in the GCC region by SWRO processes only.

The alarming situation, huge amount of CO₂ emission to environment and chemical rejection to sea on daily basis can be clearly observed by conventional SWRO process operation. These processes cannot be terminated due to water requirement, but they can be improved.

Impact of SWRO processes can be minimized either by material development or process improvements. The variety of efficient materials have been proposed such as (i) catalytic nanoparticle-coated ceramic membranes, (ii) zeolitic, (iii) inorganic-organic hybrid nanocomposite membranes and (iv) bio-inspired membranes that includes protein-polymer hybrid

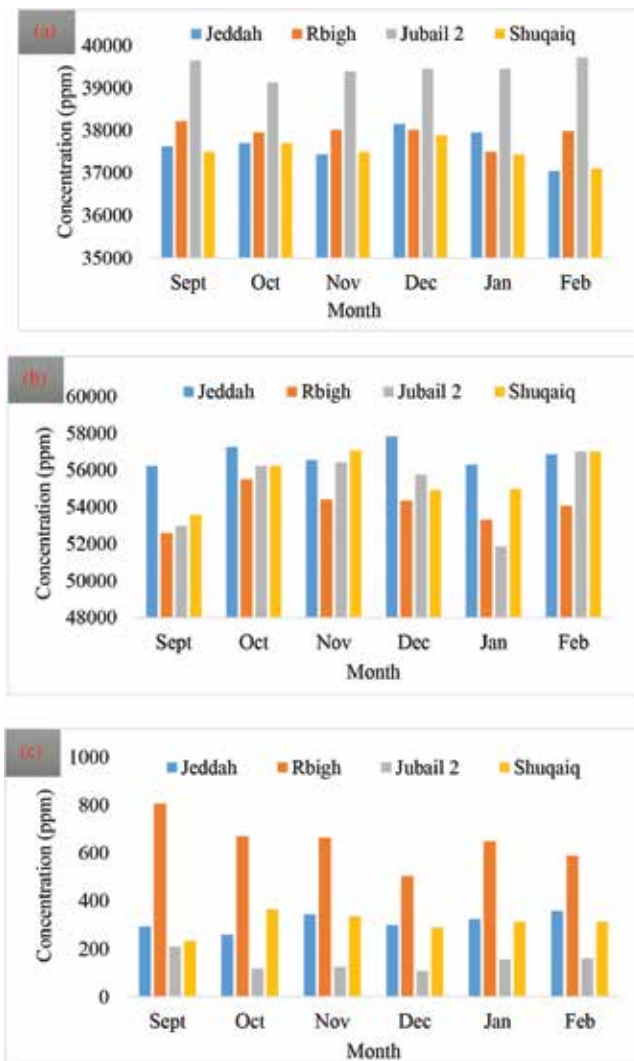


Figure 7. Six-month results of four major SWRO plants in Saudi Arabia. (a) Seawater feed concentration, (b) SWRO retentate concentration and (c) distillate concentration.

biomimetic membranes, isoporous block copolymer membranes and aligned nanotube membranes for energy efficiency [128–135]. In terms of commercialization, most of the proposed materials are farthest (5–10 years) from commercial reality. On the other hand, SWRO processes [136, 137] can be integrated with proposed AD cycle to improve process performance. Both technologies are readily available and can be implemented in near future.

3.2. Membrane process integration with AD cycle

Membrane process can be integrated with AD cycle for energy efficiency and to reduce environmental impact. AD cycle can operate at high concentration, almost near crystallization

Parameters	Quantity	Units
Total GCC capacity	26	Mm ³ /day
SWRO share (42%)	10.92	Mm ³ /day
Total primary energy (PE) consumption*	81.3	GWh/day
CO ₂ emission**	42,855.2	ton/day
Pre-treatment***		
Total feed (30% recovery)	36.4	mm ³ /day
Disinfection, NaOCl or free chlorine (1 ppm)	36.4	ton/day
Acid for pH adjustment, H ₂ SO ₄ (30–100 ppm)	3636.4	ton/day
Coagulation, FeCl ₃ or AlCl ₃ (1–35 ppm)	1272.7	ton/day
Flocculation, polyelectrolyte (0.2–4 ppm)	145.6	ton/day
Antiscaling, polycarbonic acid (2 ppm)	72.8	ton/day
Dechlorination, NaHSO ₃ (3 ppm)	109.2	ton/day

*SWRO electricity consumption = 3.5 kWh_{dec}/m³, Power plant conversion efficiency = 47%.
**CO₂ emission rate = 0.527 kg/kWh_{pe}.
***Pretreatment chemical values are taken from four plants and published literature [123–127].

Table 4. Energy consumption, CO₂ emission and chemical rejection by all SWRO plants in GCC. The severe impact on environment and marine life can be observed clearly.

zone, without fouling and corrosion chances due to low temperature operation. In addition to zero chemical injection, it also has minimal impact on environment as it operated with renewable energy. In this way, this hybridization will not only help to reduce CO₂ emission but also chemical rejection to the sea.

In proposed integration, the SWRO retentate, at 50,000 to 60,000 ppm, is supplied to AD cycle operating at evaporator temperature of 5–30°C. Both heat inputs, silica gel regeneration and evaporator, are supplied from renewable solar energy. This low evaporator temperature

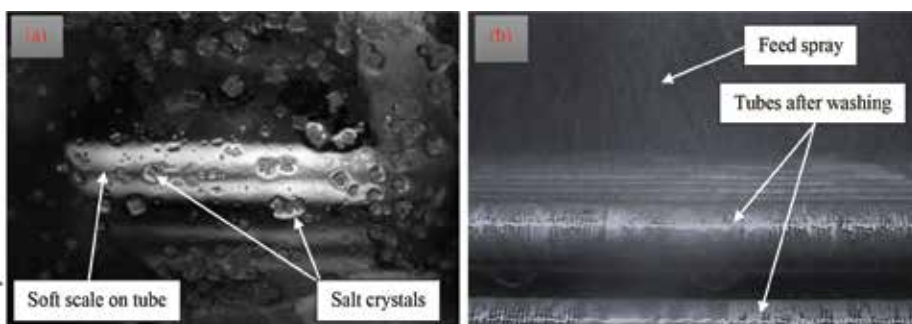


Figure 8. AD cycle evaporator inside view during operation. (a) Salt crystallization at 250,000 ppm at 10°C evaporator temperature and (b) white salt deposition cleared by feed spray jet impingement. It shows AD cycle successful operation at near crystallization zone, over 80% recovery: One of the highest recovery reported up till now.

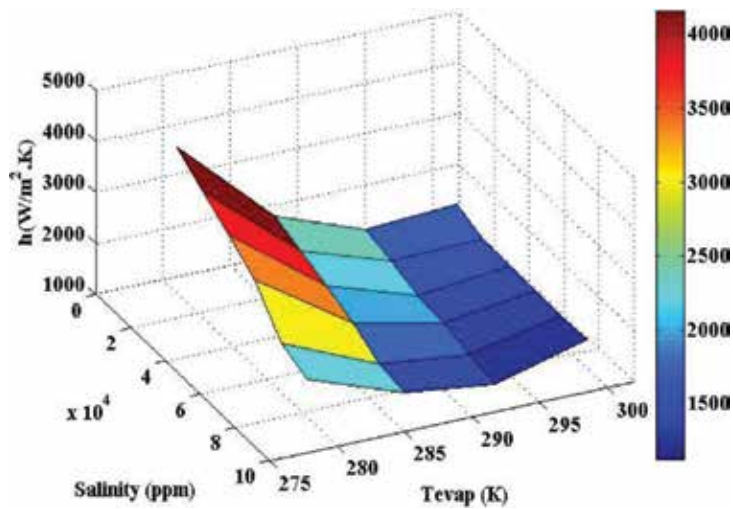


Figure 9. Effect of salt concentration and evaporator temperature on heat transfer coefficient of AD evaporator. The AD cycle evaporator can operate as low as 7°C.

enable AD cycle to operate more than 80% recovery, over 250,000 ppm. Experiments were conducted up to 250,000 ppm concentration to investigate salt concentration effect on heat transfer. **Figure 8(a)** shows salt crystallization in evaporator at 250,000 ppm. Soft scale deposition, in the form of white powder, was observed at high concentration that can be easily washed out by spraying as shown in **Figure 8(b)**. **Figure 9** shows concentration effect on heat transfer at different evaporator temperatures. It can be seen that even at high concentration the heat transfer coefficient has reasonable value that shows successful operation of AD cycle at highest concentration without fouling and scaling chances.

Parameters	SWRO	Hybrid cycle	% Saving by hybridization (%)
Total PE consumption (GWh _{pe} /day)*	81.3	40.9	98.9
CO ₂ emission (ton/day)	42,855.2	21,550.1	98.9
Pretreatment chemicals (ton/day)			
Disinfection, NaOCl	36.4	13.4	170
Acid for pH adjustment, H ₂ SO ₄	3636.4	1348.1	170
Coagulation, FeCl ₃ or AlCl ₃	1272.7	471.8	170
Flocculation, Polyelectrolyte	145.6	53.9	170
Antiscaling, polycarbonic acid	72.8	26.9	170
Dechlorination, NaHSO ₃	109.2	40.4	170

*AD electricity consumption = 1.38kWh_{elec}/m³ [137].

Table 5. Comparison of SWRO and its hybrid with AD cycle. The superiority of hybrid cycle can be seen clearly from summary table.

		Impact		
Probability		1	2	3
	1			
	2			
	3			
			SWRO (I × P)	Hybrid cycle (I × P)
Energy			3 × 3	3 × 1
CO ₂ emission			3 × 3	3 × 1
Chemical rejection			3 × 3	3 × 1
Brine concentration			3 × 2	
Brine temperature			1 × 1	
Pumps noise			3 × 2	

Table 6. The comparison of impact of conventional SWRO and proposed hybrid cycle. The hybrid cycle reduced all parameters impact to medium and low.

The proposed AD cycle recovering 51% more from SWRO retentate booting overall recover to 81%. The final reject concentration was observed as 185,000 ppm from AD cycle. This integration will not only help to save overall energy but also environmental pollution. The summary of savings is presented in **Table 5**. It can be noticed that proposed integration can save up to 100% energy and CO₂ emission. In addition, it will also help to reduce chemical rejection to sea.

The impact matrix as presented in **Table 1** for conventional SWRO processes can be modified for hybrid cycle as presented in **Table 6**. It can be observed clearly that most of the parameters impact is reduced to medium and low from initial high value. This shows that hybridization will not help to produce more water but also with minimum impact on environment and marine life along with energy efficiency.

4. Thermal process and their integration: energy and environmental impact

The present share of thermally driven desalination processes is about 58% within the GCC countries. Typically, the energy requirements for such processes are reported as 2.0 kWh_{elec}/m³ electricity and 60–70 kWh_{th}/m³ of thermal energy. For energy efficiency, the thermally driven desalination processes are designed as an integral part of a cogeneration plant, producing both electricity and water from the temperature cascaded processes. The thermal energy is low-grade bleed steam extracted from the last stages of steam turbines. Based on the exergy destruction analysis of the primary energy input, the gas turbines consumed 75 ± 2% and steam turbines (via the heat recovery from turbine exhaust) extracted 21 ± 2% of input primary energy, leaving a mere 3 ± 1.5% of the total exergy input to the thermally driven desalination processes. Consequently,

Plant name	Capacity (m ³ /day)	Overall recovery (%)	Commissioning	Operator	Ref.
Ras Al Khair	728,000	40	2014	SWCC	[141–147]
Yanbu Phase-II	68,190	40	2012	SWCC	
Yanbu 1	100,800		1981	SWCC	
Yanbu 2	144,000		1999	SWCC	
Yanbu 2 expansion	68, 190		2007	SWCC	
Yanbu 3	550,000	40	2016	SWCC	
Jubail 1	137,729	40	1982	SWCC	
Jubail 2	947,890	40	1983	SWCC	
Khobar 2	223,000	40	1982	SWCC	
Khobar 3	280,000	40	2002	SWCC	
Khafji	22,886	40	1986	SWCC	
Jeddah 4	221,575	40	1981	SWCC	
Shuaiba 1	223,000		1989	IWPP	
Shuaiba 2	454,545		2002	IWPP	
Shuqaiq	97,014		1989	SWCC	
Rabigh 2	18,000		2009	SWCC	
AlWajh 3	9000		1979	SWCC	
Umluj 3	9000		2009	SWCC	
Farasan 2	9000			SWCC	
AlQunfutha	9000			SWCC	
AlLith	9000			SWCC	
Alazizia	4500		1987	SWCC	
Rabigh 1	1204		1982	SWCC	
Future projects					
Jubail phase (3)	15,00,000	40	2021	SWCC	[148, 149]
Khobar 4	250,000		2020		
Khobar 5	220,000		2020		
Yanbu 5	100,000		2020		
Jubail 3	150,000		2021		

Table 7. Major thermal desalination plants in operation and future proposed projects in Saudi Arabia. They need only light pretreatment and can achieve 40% recovery.

the overall primary energy required by thermal desalination processes is merely 6.58 kWh_{pe}/m³ (equivalent of 4.25 kWh_{pe}/m³ from electricity +2.33 kWh_{pe}/m³ from the thermal input) [138–140]. We examine the major online thermal desalination plants in Saudi Arabia as well as the future proposed projects, and a summary of the analysis is outlined in **Table 7**.

Parameters	Quantity	Units
Total GCC capacity	26	mm ³ /day
Thermal share (68%)	17.7	mm ³ /day
Total primary energy (PE) consumption*	116.5	GWh/day
CO ₂ emission**	61,388.8	ton/day
Pretreatment		
Total feed	53.0	mm ³ /day
Scale inhibitor, polyphosphate (1–8 ppm)	424.3	ton/day
Acid, sulfuric acid (100 ppm)	5304.0	ton/day
Antifoam, poly othelyne ethylene oxide (0.1 ppm)	5.3	ton/day
Oxidizing agent, foam of chlorine (1 ppm)	53.0	ton/day
*Electricity consumption = 2.0 kWh _{elec} /m ³ , thermal energy consumption = 70kWh _{th} /m ³ , power plant conversion efficiency = 47%.		
**CO ₂ emission rate = 0.527 kg/kWh _{pe} .		
***Pretreatment chemical values are taken from operational plants and published literature [150–154].		

Table 8. Energy consumption, CO₂ emission and chemical rejection by all thermal desalination plants in GCC. Their impact is less severe as compared to SWRO.

All major integrated thermal desalination plants in Saudi Arabia are under SWCC and their recovery is about 40%. Since thermal desalination processes are robust, they need less chemicals as compared to SWRO processes. We analyzed the energy requirement, CO₂ emission and chemical rejection based on total capacity of GCC.

4.1. Thermal systems and hybrid cycle results and discussion

We analyzed the operational conditions of all major MED/MSF plants in the World and in Saudi Arabia. All mentioned MED plants are operating between top brine temperature (TBT) 60°C to bottom brine temperature (LBT) 40°C. The MSF operational range is slightly wider, between 120 and 40°C. The high temperature of MED/MSF is controlled by scaling and fouling chances and lower brine temperature is by ambient conditions. Limited range of operation put the cap on the performance of thermally driven desalination systems even they are dominating in GCC region. The detailed analysis of all thermal desalination plants in GCC and their impact are presented in **Table 8**.

It can be noticed that impact of thermal desalination processes is less severe than SWRO, but still same trend will have high impact in long-term operation. To maintain secure water supply in GCC, thermal desalination processes need to improve.

The two ways for thermal process improvements are material development for high heat transfer and process improvement to overcome thermodynamic limits of conventional processes.

The material development already reached to asymptotic limit, but processes improvement still have gap and need immediate research data for industrial application. We presented detailed experimentation on thermal system hybridization for industrial reference for future design.

4.2. Thermal process integration with AD cycle

Thermal desalination processes, MED/MSF, can be integrated with AD cycle to enhance their performance by extending their operational range. In these cycles, low temperature heat is supplied to first steam generator only and their performance depends on number of recoveries. The AD cycle hybridization can extend the last stage operational range to as low as 7°C as compared to conventional operational range of 40°C. This extension of LBT helps to insert more number of recoveries and hence boosts the performance.

To investigate hybrid MED performance, a four-stage MED was designed, fabricated and installed in KAUST. This MED is a miniature form of Yanbu MED plant installed by Doosan, Korea. The last stage of MED was integrated with solar thermal-driven AD cycle to extend last stage temperature to below ambient condition. **Figure 10** shows AD and MED pilots installed in KAUST, Saudi Arabia.

The AD regeneration heat, 65°C hot water, is supplied from evacuated tube solar thermal collectors installed on one of the rooftop building. Experiments were conducted with straight MED as well as the hybridized MED + AD cycle to compare the performance. **Figure 11(a)** shows the control of MED pilot. For MED heat source, a small boiler is installed to inject steam into hot water circuit to maintain any set temperature. Feed is supplied parallel to all four stages after extracting condensation heat from last condenser. Distillate and brine are collected in separate tanks via u-tube to maintain the inter-stage pressure difference. Straight MED experiment was conducted for 72 hours continuously to validate the stability of operation. The temporal profile of all components showed stable operation of MED as presented in **Figure 11(b)**. After successful MED testing, it was hybridized with AD cycle to operate as a hybrid cycle. Integration

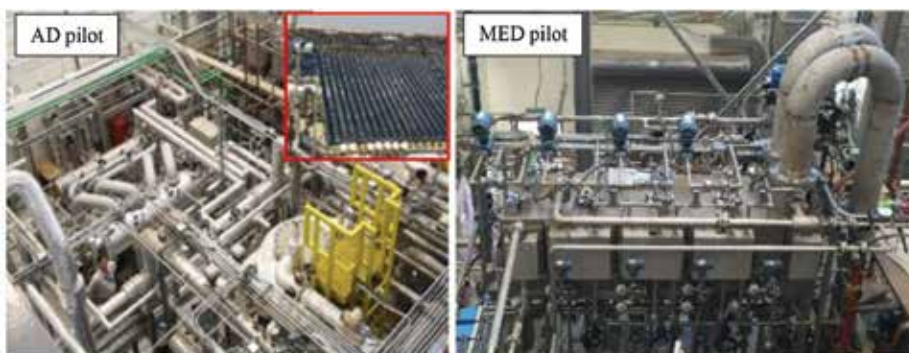


Figure 10. Solar-driven AD pilot and four-stage MED plant to investigate as a hybrid cycle. The pilot plant was designed for overall capacity of 10 m³/day.

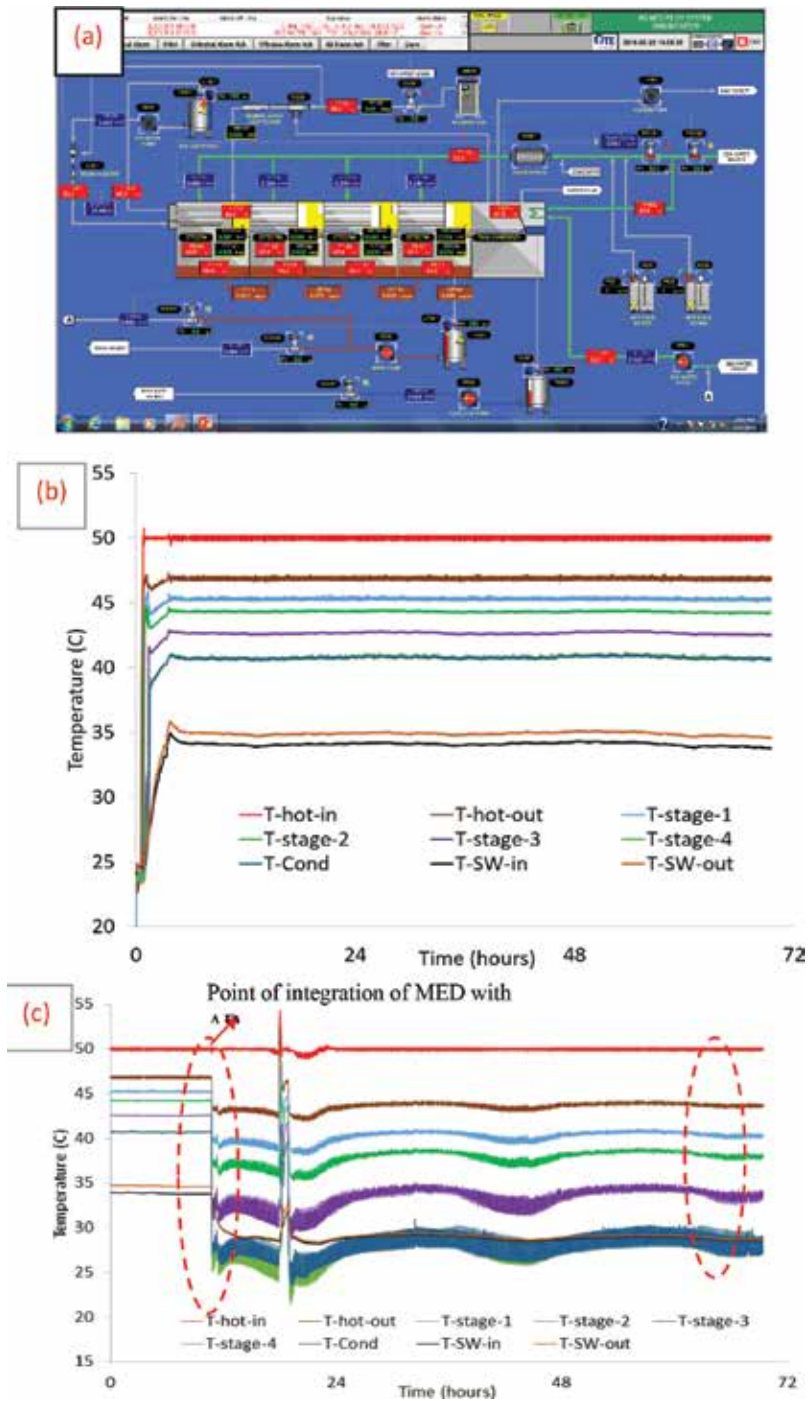


Figure 11. MED and AD pilot results installed in KAUST. (a) Control of MED pilot and (b) straight MED components temperature profiles. Inter-stage temperature varies 2–3°C for 72-hour experiment, (c) MED hybrid cycle components temperature profiles. Inter-stage temperature increased to almost double as compared to straight MED. Also, hybrid cycle can operate below ambient temperature as can be seen last stage temperature.

of AD cycle to the last stage of MED bring down the last stage temperature to below ambient and also inter-stage temperature was observed as 5–6°C as compared to 2–3°C in case of straight MED as shown in **Figure 11(c)**. The excellent thermodynamic synergy of hybridization of two thermally driven cycles boosted water production to more than twofold as compared to straight MED at same top brine temperature. **Figure 12** shows the water production comparison of straight MED and hybrid MEDAD. It can be clearly seen that water production improvement is more than two times by AD cycle integration with last stage of MED.

Based on thermal cycle hybrid results, the impact matrix has been revised and presented in **Table 10**. The hybridization greatly improved the energy efficiency and reduced the environmental impact as compared to conventional processes. In GCC, to maintain the confidence on thermally driven desalination processes, their hybridization is very important. It will help to achieve future water targets to maintain the GDP growth but following the COP21 goals for environmental emission.

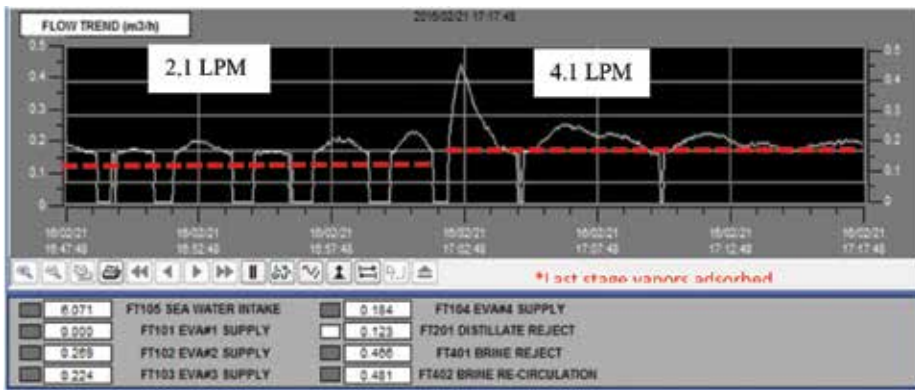


Figure 12. MED and hybrid MEDAD cycle water production comparison. Integration of AD to the last stage of MED can boost water production to twofold by extending inter-stage temperature (**Table 9**).

Parameters	Thermal system	Hybrid cycle	% Saving by hybridization (%)
Total PE consumption (GWh _{pe} /day)*	116.5	84.2	38.3
CO ₂ emission (ton/day)	61,388.8	22,373.1	38.3
Pretreatment chemicals (ton/day)			
Scale inhibitor, polyphosphate	424.3	235.7	80
Acid, sulfuric acid	5304.0	2946.7	80
Antifoam, poly othelyne ethylene oxide	5.3	2.95	80
Oxidizing agent, foam of chlorine	53.0	29.47	80

*AD electricity consumption = 1.38 kWh_{elec}/m³.

MEDAD hybrid cycle improvement factor = 2.0 [155–173].

Table 9. Comparison of thermal desalination and its hybrid with AD cycle. The superiority of hybrid cycle can be seen clearly from summary table.

		Impact		
Probability		1	2	3
	1			
	2			
	3			
			Thermal (I × P)	Hybrid cycle (I × P)
Energy			3 × 3	3 × 2
CO ₂ emission			3 × 3	3 × 1
Chemical rejection			3 × 2	2 × 1
Brine concentration			3 × 1	3 × 2
Brine temperature			1 × 1	1 × 1
Pumps noise			2 × 1	2 × 1

Table 10. The comparison of impact of conventional thermal desalination system and proposed hybrid cycle. The hybrid cycle reduced all parameters impact to medium and low.

5. Conclusions

An efficient and environment-friendly hybrid desalination process has been demonstrated for the first time with different energy mix for future water supplies. The following advantages can be observed clearly by implementation of desalination hybridizations:

- I. Energy consumption and chemical discharge saving up to 99% and 150%, respectively, by the SWRO hybridization with AD cycle.
- II. Thermal process integration with AD cycle will save up to 38% energy and up to 80% chemical rejection to sea.
- III. CO₂ emission saving by SWRO+AD up to 99% and by MEDAD up to 30%.
- IV. Overall recovery up to 80% can be achieved without scaling and fouling chances due to low temperature operation.
- V. Integration will help to reduce overall impact to low or moderate level, acceptable level under COP21 goal.
- VI. Integration will help to secure future water demand for expected GDP growth rate with minimal impact on environment and by implementing different energy mix for higher energy efficiency.

We opine that the higher energy efficiency of hybridized seawater desalination cycles can contribute to meeting the goals of sustainable seawater desalination as outlined under a sub-section of the COP21.

Acknowledgements

The author would like to thank to King Abdullah University of Science and Technology (KAUST) for financial support for MED and AD pilots.

Abbreviations

COP	Conference of parties
IEO	International Energy Outlook
OECD	Organization for Economic Cooperation and Development
Btu	British thermal unit
BAU	Business as usual
GCC	Gulf Cooperation Council
SWRO	Seawater Reverse Osmosis
MED	Multieffect desalination
MSF	Multistage flash
AD	Adsorption cycle

Author details

Muhammad Wakil Shahzad*, Doskhan Ybyraiymkul, Muhammad Burhan and Kim Choon Ng

*Address all correspondence to: muhammad.shahzad@kaust.edu.sa

Water Desalination and Reuse Center, King Abdullah University of Science and Technology, Saudi Arabia

References

- [1] International Energy Outlook 2016 with Projections to 2040. A report by U.S. Energy Information Administration (EIA), 2016. [https://www.eia.gov/outlooks/ieo/pdf/0484\(2016\).pdf](https://www.eia.gov/outlooks/ieo/pdf/0484(2016).pdf) [Accessed: Dec 15, 2017]
- [2] International Energy Outlook 2017 with Projections to 2040. A report by U.S. Energy Information Administration (EIA), 2017. [https://www.eia.gov/outlooks/ieo/pdf/0484\(2017\).pdf](https://www.eia.gov/outlooks/ieo/pdf/0484(2017).pdf) [Accessed: Feb 05, 2018]

- [3] Key World Energy Trends, Excerpt from World Energy Balance (2016), A Report by International Energy Agency (IEA); 2016
- [4] Key world energy statistics, A report by International Energy Agency (IEA). 2017. <https://www.iea.org/publications/freepublications/publication/KeyWorld2017.pdf> [Accessed: Jan 05, 2017]
- [5] BP Statistical Review of World Energy June 2017. <https://www.bp.com/content/dam/bp/en/corporate/pdf/energy-economics/statistical-review-2017/bp-statistical-review-of-world-energy-2017-full-report.pdf> [Accessed: Feb 15, 2018]
- [6] World Energy Resources, A report by World energy council (WEC). 2016. <https://www.worldenergy.org/wp-content/uploads/2016/10/World-Energy-Resources-Full-report-2016.10.03.pdf> [Accessed: Nov 15, 2017]
- [7] Chien T, Hu J-L. Renewable energy and macroeconomic efficiency of OECD and non-OECD economies. *Energy Policy*. 2007;**35**-7:3606-3615
- [8] Key CO₂ Emission Trends, Excerpt from CO₂ Emissions from Fuel Combustion (2016), A report by International Energy Agency (IEA). 2017. <https://www.iea.org/publications/freepublications/publication/CO2EmissionsfromFuelCombustionHighlights2017.pdf> [accessed: Dec 24, 2017]
- [9] Olivier JGJ, Janssens-Maenhout G, Muntean M and Peters JAHW. Trends in Global CO₂ emissions, PBL Netherlands Environmental Assessment Agency Report 2016. http://edgar.jrc.ec.europa.eu/news_docs/jrc-2016-trends-in-global-co2-emissions-2016-report-103425.pdf [accessed: Feb 10, 2018]
- [10] Concept Chapter, Global Clean Water Desalination Alliance “H₂O minus CO₂”. http://www.diplomatie.gouv.fr/fr/IMG/pdf/global_water_desalination_alliance_1dec2015_cle8d61cb.pdf [accessed: Sep 10, 2017]
- [11] Redrawing the Energy-Climate map, World Energy Outlook Special Report, International Energy Agency (IEA). 2013. www.worldenergyoutlook.org/aboutweo/workshops [accessed: Oct 11, 2017]
- [12] Friedlingstein P et al. Persistent growth of CO₂ emissions and implications for reaching climate targets. *Nature Geoscience*. 2014;**7**:709-715
- [13] COP 21: UN Climate Change Conference, Paris 2015. <http://www.cop21.gouv.fr/en/why-2c/> and <http://www.c2es.org/facts-figures/international-emissions/historical> [Accessed: July 12, 2017]
- [14] Francey RJ et al. Atmospheric verification of anthropogenic CO₂ emission trends. *Nature Climate Change*. 2013;**3**:520-524
- [15] Raupach MR, Le Quééré C, Peters GP, Canadell JG. Anthropogenic CO₂ emissions. *Nature Climate Change*. 2013;**3**:603-604
- [16] Carbon Dioxide Information Analysis Center, Oak Ridge National Laboratory, Center for climate and Energy Solutions. 2016

- [17] Francey RJ et al. Reply to anthropogenic CO₂ emissions. *Nature Climate Change*. 2013;**3**: 604-604
- [18] Raupach MR et al. Global and regional drivers of accelerating CO₂ emissions. *Proceedings of the National Academy of Sciences USA*. 2007;**104**:10288-10293
- [19] Pielke R. *The Climate Fix: What Scientists and Politicians Won't Tell You About Global Warming*; New York. 2011; ISBN 978-0-455-02519-0
- [20] Le Quéré C et al. Trends in the sources and sinks of carbon dioxide. *Nature Geoscience*. 2009;**2**:831-836
- [21] Friedlingstein P et al. Update on CO₂ emissions. *Nature Geoscience*. 2010;**3**:811-812
- [22] Peters GP et al. Rapid growth in CO₂ emissions after the 2008-2009 global financial crisis. *Nature Climate Change*. 2012;**2**:2-4
- [23] Peters GP et al. The challenge to keep global warming below 2°C. *Nature Climate Change*. 2013;**3**:4-6
- [24] Desalination for Water Supply (FR/R003), Foundation for Water Research Report. 2015. <http://www.fwr.org/desal.pdf> [Accessed: Oct 12, 2017]
- [25] Aquilina L et al. Impact of climate changes during the last 5 million years on groundwater in basement aquifers. *Nature Scientific Reports*. 2015;**5**, Article number: 14132
- [26] Qader MR. Electricity consumption and GHG emissions in GCC countries. *Energies*. 2009;**2**:1201-1213
- [27] Magazzino C. The relationship between real GDP, CO₂ emissions, and energy use in the GCC countries: A time series approach. *Cogent Economics & Finance*. 2016;**4**:1152729
- [28] Reiche D. Renewable energy policies in the Gulf countries: A case study of the carbon-neutral "Masdar City" in Abu Dhabi. *Energy Policy*. 2010;**38**:378-382
- [29] Hammamet. Overview of CO₂ emissions in the Arab Region: National versus Sectoral Emissions, Economic Development and Globalisation Division 2013. (<https://www.unece.org/fileadmin/DAM/trans/doc/themes/ForFITS/ESCWA%20-%20Overview%20of%20CO2%20emissions%20in%20the%20Arab%20Region.pdf>) [Accessed: Feb 25, 2018]
- [30] Farhani S, Shahbaz M. What role of renewable and non-renewable electricity consumption and output is needed to initially mitigate {CO₂} emissions in {MENA} region? *Renewable and Sustainable Energy Reviews*. 2014;**40**:80-90
- [31] Alshehry AS, Belloumi M. Energy consumption, carbon dioxide emissions and economic growth: The case of Saudi Arabia. *Renewable and Sustainable Energy Reviews*. 2015;**41**:237-247
- [32] Jammazi R, Aloui C. On the interplay between energy consumption, economic growth and {CO₂} emission nexus in the {GCC} countries: A comparative analysis through wavelet approaches. *Renewable and Sustainable Energy Reviews*. 2015;**51**:1737-1751

- [33] Saidi K, Hammami S. The impact of energy consumption and {CO₂} emissions on economic growth: Fresh evidence from dynamic simultaneous-equations models. *Sustainable Cities and Society*. 2015;**14**:178-186
- [34] Salahuddin M, Gow J. Economic growth, energy consumption and {CO₂} emissions in gulf cooperation council countries. *Energy*. 2014;**73**:44-58
- [35] Salahuddin M, Gow J. Economic growth, energy consumption and CO₂ emissions in gulf cooperation council countries. *Energy*. 2014;**73**:44-58
- [36] Meltzer J, Hultman N, Langley C. Low carbon energy transition in Qatar and the GULF cooperation council region, 2014. <https://www.brookings.edu/wp-content/uploads/2016/07/low-carbon-energy-transitions-qatar-meltzer-hultman-full.pdf/>. [Accessed: on Feb 15, 2018]
- [37] CO₂ emission data, World bank data. <https://data.worldbank.org/indicator/EN.ATM.CO2E.KT>. [Accessed: Feb 05, 2018]
- [38] Griffiths S. Renewable energy policy trends and recommendations for GCC countries. *Energy Transitions*. 2017;**1**(3):1-15
- [39] Eckart W. GRC Report: Alternative Energy Trends and Implications for GCC Countries. 2008. https://www.files.ethz.ch/isn/111315/Alternative_Energies_GRC_report_1902.pdf [Accessed: Aug 2017]
- [40] Kazim A, Veziroglu TN. Utilization of solar-hydrogen energy in the UAE to maintain its share in the world energy market of the 21st century. *Renewable Energy*. 2001;**24**:259-274
- [41] Wogan D, Pradhan S, Albardi S. GCC Energy System Overview–2017, A report by King Abdullah Petroleum Studies and Research Center (KAPSARC). (<https://www.kapsarc.org/wp-content/uploads/2017/11/KS-2017-MP04-GCC-Energy-Overview-2017.pdf>) [accessed: Feb 25, 2018]
- [42] Al-Enezi FQ, Sykulski JK, Ahmed NA. Visibility and potential of solar energy on horizontal surface at Kuwait area. *Energy Procedia*. 2011;**12**:862-872
- [43] Al-Nassar W, Alhajraf S, Al-Enizi A, Al-Awadhi L. Potential wind power generation in the State of Kuwait. *Renewable Energy*. 2005;**30**:2149-2161
- [44] El-Katiri L, Husain M. Prospects for Renewable Energy in GCC States: Opportunities and the Need for Reform, Oxford Institute for Energy Studies; 2014, ISBN 978-1-78467-009-2
- [45] Alnaser WE, Alnaser NW. Solar and wind energy potential in GCC countries and some related projects. *Journal of Renewable and Sustainable Energy*. 2009;**1**:022301
- [46] Ahmad A, Babar M. Effect of energy market globalization over power sector of GCC region: A short review. *Smart Grid and Renewable Energy*. 2013;**4**:265-271
- [47] Renewable Energy Market Analysis. The GCC Region, The International Renewable Energy Agency (IRENA) Report 2016. ISBN: 978-92-95111-81-3
- [48] Renewable Energy Desalination: An Emerging Solution to Close the Water Gap in the Middle East and North Africa. International Bank for Reconstruction and Development/ The World Bank; 2012. ISBN (electronic): 978-0-8213-7980-6

- [49] Howells M et al. Integrated analysis of climate change, land-use, energy and water strategies. *Nature Climate Change*. 2013;**3**:621-626
- [50] Rothausen SGSA, Conway D. Greenhouse-gas emissions from energy use in the water sector. *Nature Climate Change*. 2011;**1**:210-219
- [51] Renewable Energy Powered Desalination Systems: Technologies and Market Analysis. Mestrado Integrado em Engenharia da Energia e do Ambiente; 2014
- [52] Shatat M, Worall M, Riffat S. Opportunities for solar water desalination worldwide: Review. *Sustainable Cities and Society*. 2013;**9**:67-80
- [53] Papapetrou M et al. Roadmap for the development of desalination powered by renewable energy. Promotion of Renewable Energy for Water Production through Desalination, Fraunhofer Information-Centre for Regional Planning and Building Construction IRB; 2010. ISBN 978-3-8396-0147-1
- [54] Moser M, Trieb F, Fichter T, Kern J. Renewable desalination: A methodology for cost comparison. *Desalination and Water Treatment*. 2013;**51**:1171-1189
- [55] Abusharkh AG, Giwa A, Hasan SW. Wind and geothermal energy in desalination: A short review on progress and sustainable commercial processes. *Industrial Engineering & Management*. 2015;**4**:1-5; ISSN: 2169-0316
- [56] Lattemann S. Development of an environmental impact assesment and decision support system for seawater desalination plants. Doctoral thesis, Delft University of Technology and UNESCO-IHE Institute for Water Education. 2010
- [57] El-Naas MH, Al-Marzouqi AH, Chaalal O. A combined approach for the management of desalination reject brine and capture of CO₂. *Desalination*. 2010;**251**:70-74
- [58] Lattemann S, Höpner T. Environmental impact and impact assesment of seawater desalination. *Desalination*. 2008;**220**:1-15
- [59] Rao NS, Venkateswara RTN, Rao GB, Rao KVG. Impact of reject water from the desalination plants on ground water quality. *Desalination*. 1990;**78**:429-437
- [60] Sadhwani JJ, Veza JM, Santana C. Case studies on environmental impact of seawater desalination. *Desalination*. 2005;**185**:1-8
- [61] Dawoud MA, Al Mulla MM. Environmental impacts of seawater desalination: Arabian gulf case study. *International Journal of Environment and Sustainability*. 2012;**3**:22-37
- [62] Kuentle K, Brunner G. An integrated self-sufficient multipurpose plan for seawater desalination. *Desalination*. 1981;**39**:459-474
- [63] El-Banna Saad Fath H. Combined multi stage flash-multi effect distillation system with brine reheat, Patent No. 2,190,299; 1998
- [64] Awerbuch L, Sommariva C. MSF distillate driven desalination process and apparatus, Patent No. PCT/GB2005/003329
- [65] Helal AM, Al-Jafri A, Al-Yafeai A. Enhancement of existing MSF plant productivity through design modification and change of operating conditions. *Desalination*. 2012;**307**:76-86

- [66] Nafeya AS, Fathb HES, Mabrouk AA. Thermo-economic investigation of multi effect evaporation (MEE) and hybrid multi effect evaporation-multi stage flash (MEEMSF) systems. *Desalination*. 2006;**201**:241-254
- [67] Junjie Y, Shufeng S, Jinhua W, Jiping L. Improvement of a multi-stage flash seawater desalination system for cogeneration power plants. *Desalination*. 2007;**217**:191-202
- [68] Nasser GED. Apparatus for the distillation of fresh water from seawater, Patent No. 4,636,283; 1987
- [69] Mabrouk ANA. Techno-economic analysis of once through long tube MSF process for high capacity desalination plants. *Desalination*. 2013;**317**:84-94
- [70] Mabrouk A-NA. Techno-economic analysis of tube bundle orientation for high capacity brine recycle MSF desalination plants. *Desalination*. 2013;**320**:24-32
- [71] Al-Rawajfeh AE, Ihm S, Varshney H, Mabrouk AN. Scale formation model for high top brine temperature multi stage flash (MSF) desalination plants. *Desalination*. 2014;**350**:53-60
- [72] Borsani R, Sommariva C, Superina R, Wangnick K, Germana A. MSF desalination: the myth of the largest unit-some technical and economical evaluations. *Proceedings, International Desalination Association Conference; 1995*. pp. 293-325
- [73] Tusel GF, Rautenbach R, Widua J. Sea water desalination plant "Sirte" — An example for an advanced MSF design. *Desalination*. 1994;**96**:379-396
- [74] Helal AM. Once-through and brine recirculation MSF designs, a comparative study. *Desalination*. 2004;**171**:33-60
- [75] Mabrouk ANA. Technoeconomic analysis of once through long tube MSF process for high capacity desalination plants. *Desalination*. 2013;**317**:84-94
- [76] Helal AM, El-Nashar AM, Al-Katheeri E, Al-Malek S. Optimal design of hybrid RO/MSF desalination plants part I: Modeling and algorithms. *Desalination*. 2003;**154**:43-66
- [77] Hamed OA, Hassan AM, Al-Shail K, Farooque MA. Performance analysis of a trihybrid NF/RO/MSF desalination plant. *Desalination and Water Treatment*. 2009;**1**:215-222
- [78] Hamed OA. Overview of hybrid Desalination systems-current status and future prospects. *Desalination*. 2005;**186**:207-214
- [79] Helal AM, El-Nashar AM, Al-Katheeri ES, Al-Malek SA. Optimal design of hybrid RO/MSF desalination plants part III: Sensitivity analysis. *Desalination*. 2004;**169**:43-60
- [80] Al-Mutaz IS. Hybrid RO MSF: A practical option for nuclear desalination. *International Journal of Nuclear Desalination*. 2003;**1**:47-57
- [81] Cali G, Fois E, Lallai A, Mura G. Optimal design of a hybrid RO/MSF desalination system in a non-OPEC country. *Desalination*. 2008;**228**:114-127
- [82] Cardona E, Culotta S, Piacentino A. Energy saving with MSF-RO series desalination plants. *Desalination*. 2002;**153**:167-171

- [83] Hassan MA et al. A new approach to membrane and thermal seawater desalination process using Nanofiltration membranes, part 1. *Desalination*. 1998;**118**:35-51
- [84] Al-Mutaz IS. Coupling of a nuclear reactor to hybrid RO/MSF desalination plants. *Desalination*. 2003;**175**:259-268
- [85] Hamad A, Almulla A, Gadalla M. Integrating hybrid systems with thermal desalination plants. *Desalination*. 2005;**174**:171-192
- [86] Al-Mutaz IS, Soliman MA, Daghtem AM. Optimum Design for a Hybrid Desalting Plant. *Desalination*. 1989;**76**:177-189
- [87] Alardin F, Andrienne J. Thermal and membrane process economics: Optimized selection for seawater desalination. *Desalination*. 2002;**153**:305-311
- [88] El-Sayed E et al. Pilot study of MSF/RO hybrid systems. *Desalination*. 1998;**120**:121-128
- [89] Saha BB, El-Sharkawy II, Shahzad MW, Thu K, Ang L, Ng KC. Fundamental and application aspects of adsorption cooling and desalination. *Applied Thermal Engineering*. 2016;**97**:68-76
- [90] Thu K, Yanagi H, Saha BB, Ng KC. Performance investigation on a 4-bed adsorption desalination cycle with internal heat recovery scheme. *Desalination*. 2017;**402**:88-96
- [91] Thu K, Saha BB, Chua KJ, Ng KC. Performance investigation of a waste heat-driven 3-bed 2-evaporator adsorption cycle for cooling and desalination. *International Journal of Heat and Mass Transfer*. 2016;**101**:1111-1122
- [92] Saha BB, El-Sharkawy II, Shahzad MW, Thu K, Ang L, Ng KC. Fundamental and application aspects of adsorption cooling and desalination. *Applied Thermal Engineering*. 2016;**97**:68-76
- [93] Jun WW, Eric JH, Mark JB. Thermodynamic cycles of adsorption desalination system. *Applied Energy*. 2012;**90**:316-322
- [94] Zejli D, Benchrifa R, Bennouna A, Bouhelal OK. A solar adsorption desalination device: First simulation results. *Desalination*. 2004;**168**:127-135
- [95] Mosry H, Larger D, Genter K. Anew multiple-effect distiller system with compact heat exchanger. *Desalination*. 1994;**96**:59-70
- [96] Wang XL, Ng KC. Experimental investigation of an adsorption desalination plant using low-temperature wasted heat. *Applied Thermal Engineering*. 2005;**25**:2780-2789
- [97] Wang XL, Chakraborty A, Ng KC, Saha BB. How heat and mass recovery strategies impact the performance of adsorption desalination plant: Theory and experiments. *Heat Transfer Engineering*. 2007;**28**:147-153
- [98] Ng KC, Chua HT, Chung CY, Loke CH, Kashiwagi T, Akisawa A, Saha BB. Experimental investigation of the silica gel-water adsorption isotherm characteristics. *Applied Thermal Engineering*. 2001;**21**:1631-1642

- [99] Ng KC, Saha BB, Chakraborty A, Koyama S. Adsorption desalination quenches global thirst. *Heat Transfer Engineering*. 2008;**29**:845-848
- [100] Thu K, Ng KC, Saha BB, Chakraborty A, Koyama S. Operational strategy of adsorption desalination systems. *International Journal of Heat and Mass Transfer*. 2009;**29**:1811-1816
- [101] Ng KC, Thu K, Chakraborty A, Saha BB, Chun WG. Solar-assisted dual-effect adsorption cycle for the production of cooling effect and potable water. *International Journal of Low-Carbon Technology*. 2009;**4**:61-67
- [102] Chua HT, Ng KC, Wang W, Yap C, Wang XL. Transient modelling of a two-bed silica gel-water adsorption chiller. *International Journal of Heat and Mass Transfer*. 2004;**47**:659-669
- [103] Wang XL, Chua HT. Two bed silica gel-water adsorption chillers: An effectual lumped parameter model. *International Journal of Refrigeration*. 2007;**30**:1417-1426
- [104] Chua HT, Ng KC, Malek A, Kashiwagi T, Akisawa A, Saha BB. Multi-bed regenerative adsorption chiller-improving the utilization of waste heat and reducing the chilled water outlet temperature fluctuation. *International Journal of Refrigeration*. 2001;**24**:124-136
- [105] Ng KC, Saha BB, Chakraborty A, Koyama S. Adsorption desalination quenches global thirst. *Heat Transfer Engineering*. 2008;**29**:845-848
- [106] Li A, Thu K, Ismail AB, Shahzad MW, Ng KC. Performance of adsorbent-embedded heat exchangers using binder-coating method. *International Journal of Heat and Mass Transfer*. 2016;**92**:149-157
- [107] Li A, Thu K, Ismail AB, Ng KC. A heat transfer correlation for transient vapor uptake of powdered adsorbent embedded onto the fins of heat exchangers. *Applied Thermal Engineering*. 2016;**93**:668-677
- [108] Cevallos ORF. Adsorption Characteristics of Water and Silica Gel System for Desalination Cycle, Master of Science Thesis. King Abdullah University of Science and Technology; 2012
- [109] Sharma RK, Gaba G, Kumar A, Puri A. Chapter 6, Functionalized Silica Gel as Green Material for Metal Remediation. UK: RSC Publishing; 2013. pp. 105-134; ISBN 978-1-84973-621-3
- [110] Yang RT, John A. *Adsorbents: Fundamentals and Applications*. USA: Willey & Sons, Inc., Publications; ISBN 0-471-29741-0
- [111] Wang LW, Wang RZ, Oliveira RG. A review on adsorption working pairs for refrigeration. *Renewable and Sustainable Energy Reviews*. 2009;**13**(3):518-534
- [112] Shahzad MW, Burhan M, Li A, Ng KC. Energy-water-environment nexus underpinning future desalination sustainability. *Desalination*. 2017;**413**:52-64
- [113] Jeddah Reverse Osmosis Desalination Phase 2, A Project Report by ABB, 2009. <http://new.abb.com/water/references/jeddah-reverse-osmosis-desalination-plant-phase-2> [Accessed: Jan 05, 2018]

- [114] Tanaka K, Matsui K, Hori T, Iwahashi H, Takeuchi K, Ito Y. Mitsubishi heavy industries technical review. 2009;**46**:12-14. <http://www.mhi.co.jp/technology/review/pdf/e461/e461012.pdf> [Accessed: Dec 15, 2017]
- [115] Mantilla D. Feasibility for Use of a Seabed Gallery Intake for the Shuqaiq-II SWRO Facility. Saudi Arabia, Master of Science thesis: King Abdullah University of Science and Technology; 2013
- [116] Fried A, Serio B. Water Industry Segment Report for Desalination, A report by World Trade Center San Diego (WTCSD); 2012
- [117] Shuaibah Independent Water & Power Project (IWPP), Saudi Arabia. <http://www.shuaibahiwpp.com/> [Accessed: July 20, 2017]
- [118] Water Desalination Report, Mott MacDonald. <https://www.desalination.com/desalination-suppliers/mott-macdonald>. [Accessed: July 21, 2017]
- [119] Kishi M, Kawada I, Ohta K, Furuichi M, Tamura M, Fussaoka Y, Nakanishi Y. Practical aspects of large-scale reverse osmosis applications. Encyclopedia of Desalination and Water Resources (DESWARE). <http://www.desware.net/sample-chapters/d05/d09-901a.pdf>
- [120] Kammourie N, Dajani TFF, Cioffi S, Rybar S. SAWACO north Obhor SWRO plant operational experienced. Desalination. 2008;**221**:101-106
- [121] Hassan AM, Abanmy AM, Al-Thobiety M, Mani T. Performance evaluation of SWCC SWRO plants part II, IDA World Conference on Desalination and Water Reuse; August 25-29, 1991
- [122] Al-Breakeit A. Investment Opportunities for New Projects in KSA, A Saline Water Conversion Corporation's report, Singapore International Water Week; 2016
- [123] Tularam GA, Ilahee M. Environmental concerns of desalinating seawater using reverse osmosis. Journal of Environmental Monitoring. 2013;**8**:805-813
- [124] Darwish M, Hassabou AH, Shomar B. Using seawater reverse osmosis (SWRO) desalting system for less environmental impacts in Qatar. Desalination. 2013;**309**:113-124
- [125] Khan MT. Fouling of Seawater Reverse Osmosis (SWRO) Membrane: Chemical and Microbiological Characterization ; Doctoral thesis. King Abdullah University of Science and Technology; 2013
- [126] Münk WF. Ecological and Economic Analysis of Seawater Desalination Plants, ; Diploma thesis. Germany: University of Karlsruhe; 2008
- [127] Desalination for Safe Water Supply. Guidance for the Health and Environmental Aspects Applicable to Desalination, Public Health and the Environment World Health Organization Geneva; 2007
- [128] Hummer G, Rasaiah JC, Noworyta JP. Water conduction through the hydrophobic channel of a carbon nanotube. Nature. 2001;**414**:188-190

- [129] Holt JK et al. Fast mass transport through sub-2-nanometer carbon nanotubes. *Science*. 2006;**312**:1034-1037
- [130] Pendergast MTM, Hoek EMV. A review of water treatment membrane nanotechnologies. *Energy & Environmental Science*. 2011;**4**:1946-1971
- [131] Agre P, Sasaki S, Chrispeels MJ. Aquaporins: A family of water channel proteins. *American Journal of Physiology - Renal Physiology*. 1993;**265**:265-270
- [132] Kaufman Y, Berman A, Freger V. Supported lipid bilayer membranes for water purification by reverse osmosis. *Langmuir*. 2010;**26**:7388-7395
- [133] Fane T. Overview and roadmap for membrane process development in desalination. DesalTech 2015, San Diego, USA Aug 28-29 2015
- [134] Wei QJ, McGovern RK, Lienhard V JH. Saving energy with an optimized two-stage reverse osmosis system, *Environmental Science: Water Research & Technology* 3-4 (2017) 659-670
- [135] Warsinger DEM, Lienhard V John H, Tow EW, McGovern RK, Thiel GP, Batch Pressure-Driven Membrane Separation with Closed-Flow Loop and Reservoir, US patent # 15350064; 2017
- [136] Ali ES, Alsaman AS, Harby K, Askalany AA, Diab MR, Ebrahim Yakoot SM. Recycling brine water of reverse osmosis desalination employing adsorption desalination: A theoretical simulation. *Desalination*. 2017;**408**:13-24
- [137] Shahzad MW, Burhan M, Ng KC. Pushing desalination recovery to the maximum limit: Membrane and thermal processes integration. *Desalination*. 2017;**416**:54-64
- [138] Shahzad MW, Burhan M, Son HS, Seung Jin O, Ng KC. Desalination processes evaluation at common platform: A universal performance ratio (UPR) method. *Applied Thermal Engineering*. 2018;**134**:62-67
- [139] Ng KC, Shahzad MW, Son HS, Hamed OA. An exergy approach to efficiency evaluation of desalination. *Applied Physics Letters*. 2017;**110**:184101
- [140] Lienhard JH, Mistry KH, Sharqawy MH, Thiel GP. Thermodynamics, Exergy, and Energy Efficiency in Desalination Systems, Chapter 4, *Desalination Sustainability*. Elsevier, ISBN: 9780128098967; 2017
- [141] Ras Al Khair Desalination Plant, Saudi Arabia. <http://www.water-technology.net/projects/-ras-al-khair-desalination-plant/> [Accessed: July 25, 2017]
- [142] Yanbu Phase 2 MED Seawater Desalination Plant Expansion, Saudi Arabia. (<http://www.water-technology.net/projects/-yanbu-phase-med-seawater-desalination-plant/> [Accessed: July 25, 2017])
- [143] Yanbu 3 MSF plant in Saudi Arabia. <https://www.desalination.biz/news/0/Doosan-takes-Yanbu-3-MSF-plant-in-Saudi/6838/> [Accessed: July 26, 2017]
- [144] Hamed OA, Sofi MAKKA, Imam M, Mustafa GM, Mardouf KB, Washmi HA. Thermal performance of multi-stage flash distillation plants in Saudi Arabia. *Desalination*. 2000;**128**:281-292

- [145] Desalination in the GCC: The History, the Present & the Future, A Report by Desalination Experts Group, Originating from the Water Resources Committee; 2014
- [146] Doosan Water Plants. A Doosan Heavy Industries & Construction Report 2013. http://www.doosanenpure.com/content/downloads/doosan_water_bg_brochure.pdf [Accessed: July 05, 2017]
- [147] Taher N, Hajjar BA. Energy and Environment in Saudi Arabia: Concerns & Opportunities. USA: Springer Publisher; 2014. ISBN: 978-3-319-02981-5
- [148] Gashlan A. The Saudi Water Sector: Upcoming Projects and Investment Opportunities. <http://worldwatertechinnovation.com/wp-content/uploads/2017/02/DIT-Pre-Summit-Seminar-Ahmed-Gashlan-Alkawther-Industries.pdf> [Accessed: June 15, 2017]
- [149] Alarifi A. Desalination in the Kingdom of Saudi Arabia: Current Practice and Future Trends; 2013. auptde.org/Article_Files/PPTX3~1.PPT
- [150] Budhiraja P, Fares AA. Studies of scale formation and optimization of antiscalant dosing in multi-effect thermal desalination units. *Desalination*. 2008;**220**:313-325
- [151] Warsinger DM, Swaminathan J, Guillen-Burrieza E, Arafat HA, Lienhard JH. Scaling and fouling in membrane distillation for desalination applications: A review. *Desalination*. 2015;**356**:294-313
- [152] Tijjng LD, Woo YC, Choi J-S, Lee S, Kim S-H, Shon HK. Fouling and its control in membrane distillation—A review. *Journal of Membrane Science*. 2015;**475**:215-244
- [153] Budhiraja P, Fares AA. Studies of scale formation and optimization of antiscalant dosing in multi-effect thermal desalination units. *Desalination*. 2008;**220**:313-325
- [154] Mi B, Elimelech M. Gypsum scaling and cleaning in forward osmosis: Measurements and mechanisms. *Environmental Science & Technology*. 2010;**44**:2022-2028
- [155] Ng KC, Shahzad MW. Sustainable desalination using ocean thermocline energy. *Renewable and Sustainable Energy Reviews*. 2018;**82** (240-246)
- [156] Shahzad MW, Burhan M, Ghaffour N, Ng KC. A multi evaporator desalination system operated with thermocline energy for future sustainability. *Desalination*. 2018;**435**: 268-277. DOI: 10.1016/j.desal.2017.04.013
- [157] Shahzad MW, Ng KC. An improved multi-evaporator adsorption desalination cycle for GCC countries. *Energy Technology*. 2017;**5**:1663-1669. DOI: 10.1002/ente.201700061
- [158] Shahzad MW, Ng KC. On the road to water sustainability in the Gulf. *Nature Middle East*. 2016. DOI: 10.1038/nmiddleeast.2016.50
- [159] Shahzad MW, Ng KC, Thu K. Future sustainable desalination using waste heat: Kudos to thermodynamic synergy. *Environmental Science: Water Research & Technology*. 2016;**2**:206-212
- [160] Missimer TM, Ng KC, Thuw K, Shahzad MW. Geothermal electricity generation and desalination: An integrated process design to conserve latent heat with operational improvements. *Desalination and Water Treatment*. 2016;**57**(48-49):23110-23118

- [161] Shahzad MW, Thu K, Ng KC, WonGee C. Recent development in thermally activated desalination methods: Achieving an energy efficiency less than 2.5 kWhelec/m³. *Desalination and Water Treatment*. 2016;**57**:7396-7405
- [162] Saha BB, El-Sharkawy II, Shahzad MW, Thu K, Li A, Ng KC. Fundamental and application aspects of adsorption cooling and desalination. *Applied Thermal Engineering*. 2016;**97**:68-76
- [163] Shahzad MW, Ng KC, Thu K. Future energy benchmark for desalination: Is it better to have a power (electricity) plant with RO or MED/MSF? *International Journal of Modern Physics*. 2016;**42**:166-172
- [164] Shahzad MW, Ng KC, Thu K. An improved cost apportionment for desalination combined with power plant: An Exergetic analyses. *Applied Mechanics and Materials*. 2016;**819**:530-535
- [165] Thu K, Kim Y-D, Shahzad MW, Saththasivam J, Ng KC. Performance investigation of an advanced multi-effect adsorption desalination (MEAD) cycle. *Applied Energy*. 2015;**159**:469-477
- [166] Shahzad MW, Thu K, Kim Y-d, Ng KC. An experimental investigation on MEDAD hybrid desalination cycle. *Applied Energy*. 2015;**148**:273-281
- [167] Ng KC, Thu K, Seung Jin O, Li A, Shahzad MW, Ismail AB. Recent developments in thermally-driven seawater desalination: Energy efficiency improvement by hybridization of the MED and AD cycles. *Desalination*. 2015;**356**:255-270
- [168] Shahzad MW, Ng KC, Thu K, Saha BB, Chun WG. Multi effect desalination and adsorption desalination (MEDAD): A hybrid desalination method. *Applied Thermal Engineering*. 2014;**72**:289-297
- [169] Ng KC, Thu K, Shahzad MW, Gee CW. Progress of adsorption cycle and its hybrids with conventional multi-effect desalination processes. *IDA Journal of Desalination and Water Reuse*. 2016;**6**(1):44-56
- [170] Shahzad MW, Thu K, Saha BB, Ng KC. An Emergin hybrid multi-effect adsorption desalination system. *EVERGREEN Joint Journal of Novel Carbon Resource Sciences & Green Asia Strategy*. 2014;**1**(2):30-36
- [171] Shahzad MW, Myat A, Gee CW, Ng KC. Bubble-assisted film evaporation correlation for saline water at sub-atmospheric pressures in horizontal-tube evaporator. *Applied Thermal Engineering*. 2013;**50**:670-676
- [172] Shahzad MW. The Hybrid Multi-Effect Desalination (MED) and the Adsorption (AD) Cycle for Desalination, Doctoral Thesis. National University of Singapore; 2013
- [173] Thu K, Kim YD, Shahzad MW, Saththasivam J, Ng KC. Performance investigation of an advanced multi-effect adsorption desalination (MEAD) cycle. *Applied Energy*. 2015;**159**:469-477

Solar Desalination

Fadi Alnaimat, James Klausner and Bobby Mathew

Additional information is available at the end of the chapter

<http://dx.doi.org/10.5772/intechopen.76981>

Abstract

There is an increasing demand for advancing conventional desalination technologies and developing novel solar powered desalination processes. In this chapter, the use of solar powered thermal desalination will be discussed comprehensively. The different existing methods of solar energy utilization for seawater desalination will be discussed, which includes solar stills, solar powered humidification-dehumidification (HDH) desalination, solar diffusion driven desalination, solar membrane distillation, concentrated solar power (CSP) based desalination, and solar pond distillation. The advantages and limitations of these thermal desalination technology will be discussed. In addition, the environmental impacts of solar desalination will be discussed due to its importance for adoption.

Keywords: desalination, solar energy, thermal processes

1. Introduction

For many years, efforts have been made to use solar energy for obtaining potable water from saline water. Some of the earliest solar powered desalination technologies were developed centuries ago, such as solar stills. There is an increasing demand for advancing conventional desalination technologies and developing novel solar powered desalination processes. The increasing demand for solar powered desalination systems is driven by the increasing cost of fossil fuels for thermal and electrical energy generation, falling cost of renewable energy technologies, need for small scale decentralized desalination systems to operate in remote areas that lack access to the electrical grid, and the concern over climate change. Solar powered desalination is especially important in remote and rural areas with low infrastructure and without connection to a grid. Small-scale stand-alone solar powered desalination systems are desirable to provide a reliable source of potable water.

The best combination of renewable energy and desalination technology achieves high fresh water production at low cost with efficient energy utilization. An excellent example is the integration of thermal desalination technologies with renewable thermal energy, such as solar and geothermal energy. Solar energy is the most promising energy for seawater desalination. Solar energy utilization systems such as flat plate solar collectors, evacuated tubes, and solar ponds absorb the solar energy and convert it to thermal energy that drives thermal desalination processes. The use of solar energy for desalination can be categorized into direct, where the solar energy is absorbed directly by the saline water (solar pond and solar still), or indirect where the solar energy is absorbed by a solar collector and then transferred to the saline water. Solar energy is well suited for arid regions and rural areas where the solar intensity is high [44].

Desalination of seawater or brackish water is generally accomplished using water evaporation (phase change), or by using a semi-permeable membrane to separate fresh water from concentrated saline water, or by a combination of the two as in membrane distillation. Most conventional desalination plants are large scale centralized units that typically serve urban populations. In recent years, there is considerable interest in developing decentralized desalination technologies. An environmental advantage of decentralized desalination is that the brine discharge is spread out over a large area, and thus the environmental impact is considerably less than that associated with large scale centralized desalination plants. In rural arid regions, populations are distributed over a large land surface area. For such cases, it is more economical to install and operate decentralized water production units that serve the local population in lieu of large centralized water production where water must be transported long distances. The rural arid regions typically have excellent solar resources, and thus solar driven desalination is appealing.

Solar energy, harvested in electrical or thermal form can be used to distill water. Solar thermal energy systems, such as flat plate solar collectors, evacuated tubes, concentrating solar troughs, and solar ponds absorb the solar energy and convert it to thermal energy that drive thermal desalination processes. Solar thermal energy utilization for desalination can be categorized into direct, where the solar thermal energy is collected directly by the saline water, such as in solar stills and solar ponds, or indirect where the solar thermal energy is absorbed by a solar collector and then transferred to the saline water, such as in solar powered humidification-dehumidification (HDH) and diffusion driven desalination. Technical simplicity, low maintenance requirements, and ease of operation are very important to enable successful application of distributed solar powered desalination systems.

The distillation performance can be examined in terms of characteristic parameters which are related to the method of distillations, which include:

1. Specific daily water production which is defined as the amount of water produced using 1 m^2 of solar collector area per day. This parameter describes daily water production normalized by the solar collector area. This parameter is important for all solar powered desalination systems since solar collector area is indicative of the amount of energy that is flowing into the system and is also a proxy for cost. The solar collector cost typically accounts for about 40–45% of the capital cost of air-heated HDH systems and 20–35% of the capital cost of water-heated HDH systems.

2. Gained output ratio (GOR) which is defined as the ratio of the latent heat of evaporation of the distillate produced to the total heat input to the distillation process. It is a measure of how efficiently thermal energy is used in a desalination process. In the case of solar powered desalination systems, GOR is equal to the ratio of latent heat of evaporation of the distillate produced to the heat absorbed by the solar collectors.
3. Recovery ratio (RR) is defined as the ratio of the total fresh water produced to the saline feed water input. RR for small scale solar powered HDH desalination systems is much smaller than RR for conventional desalination processes, such as MSF, MED, VC and RO due to the low production efficiency of small scale systems.

2. Solar thermal energy desalination

2.1. Solar stills

The solar still is one of the oldest and by far the simplest water desalination method. A solar still consists of a structural element called a basin covered with a transparent material to allow the incident solar radiation to pass through to the basin saline water for thermal absorption and evaporation. Solar energy absorption, saline water evaporation, and fresh water condensation occur within a single enclosure for a solar still. Solar stills are inherently direct collection systems. Solar distillation using solar stills is considered to be a mature technology. Because it has a low maintenance requirement, it is used worldwide to produce fresh water. Typically, the basin is colored in dark or black to enhance solar flux absorption. The water is heated by the solar rays absorbed by the basin, which increases the water vapor pressure until some portion of the saline water evaporates as shown in **Figure 1**. The water vapor moves upward and typically condenses on the cool glass cover and run downs through a guiding channel to the collection reservoir.

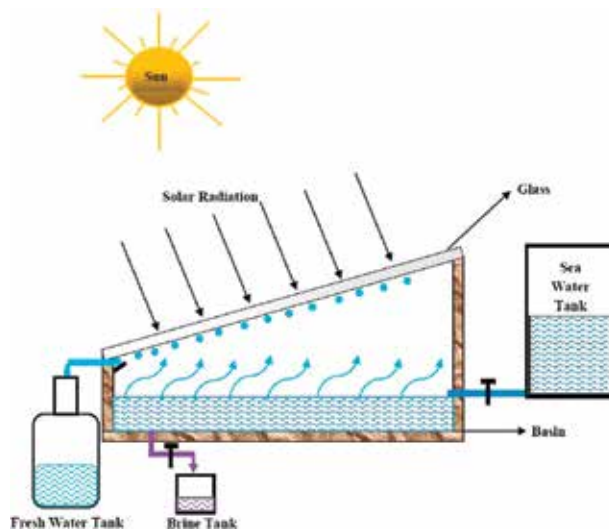


Figure 1. Solar still [47].

There exist many types of solar stills, including single slope, double slope, single and double basin, inverted, tubular, spherical, double effect multi wick, and greenhouse integrated solar stills as shown in **Figure 2**. Solar stills can be passive or active, depending on whether water circulation is needed. The main advantages of passive solar stills are that they do not require electrical energy for pumping (passive solar collector), it is simple, and it is easy to operate. However, the main drawback of the solar still is that it typically has low water production due to the loss of latent heat of condensation through the solar still transparent cover.

The gap distance between the solar still basin and the transparent cover surface has a considerable influence on its performance; the performance increases with decreasing gap distance. As a result, several design improvements have been considered, such as the development of a cascaded type solar still [1]. In this design, the basin is inclined and consists of many small cavities to store water; it is arranged in cascaded manner, as shown in **Figure 3**. The basin is typically made of a metallic corrugated sheet such as flat black coated aluminum.

The performance of a conventional solar distillation system can be predicted by various methods [3–12]. In general, the distillate hourly production rate per square meter of solar still (\dot{m}_w) is given by

$$\dot{m}_w = \frac{3600 \dot{q}_{ev}}{h_{fg}} \quad (1)$$

where \dot{q}_{ev} is the evaporation rate per square meter of solar still cross section, h_{fg} is the latent heat of vaporization. The solar still performance is influenced by several parameters such as wind velocity, sky and ambient temperature, solar radiation, and salt concentration. Various researchers have proposed several modifications to enhance the performance of a conventional solar still. Some study has proposed to reduce the bottom heat loss coefficient [13]. Another study has proposed to reduce water depth in a solar still basin [5, 14, 15] which results in increased temperature and evaporation. It is also suggested to cover the back wall with cotton cloth in the solar still [16]. This is to reduce heat losses from the back of the solar still and enhance the evaporation rate. It has also been proposed to use coloring dye [17–20]

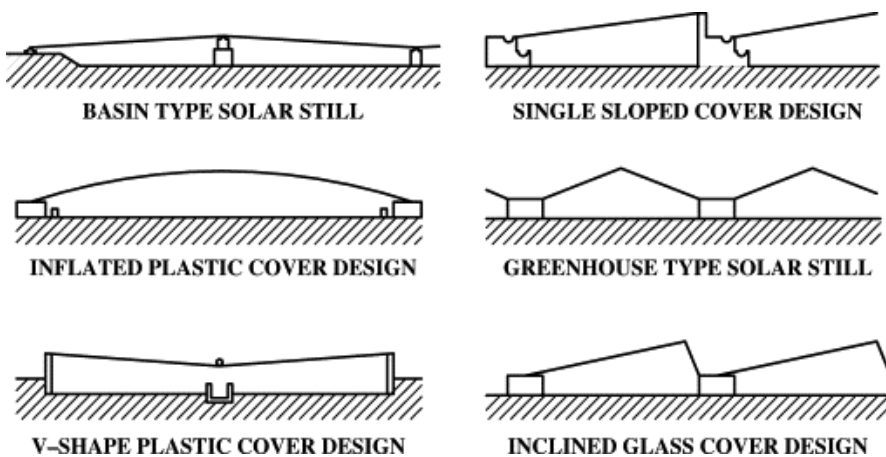


Figure 2. Common designs of solar stills [2].

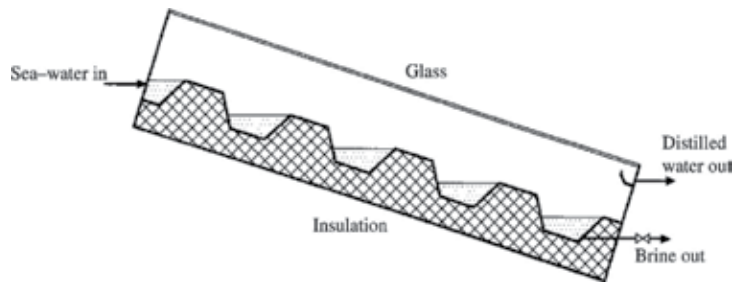


Figure 3. Schematic of a cascaded solar still [2].

and to use charcoal [21–23] to enhance solar energy absorption in the basin. Other studies have suggested to use energy storage to improve water yield [22, 23]. The use of multi-wick solar stills has been suggested to enhance water production performance [1]. Other studies have proposed cooling of the condensing glass cover [24–28] to enhance fresh water yield.

2.2. Solar powered humidification-dehumidification (HDH) desalination

Solar powered humidification-dehumidification (HDH) desalination has gained recent traction because it is viewed as a reliable desalination method for small scale decentralized applications. The humidification/dehumidification (HDH) process is a thermal desalination process that mimics the natural water purification cycle. Solar HDH systems have been investigated extensively and used widely for many decades as an alternative to common desalination systems for decentralized water production, and hence extensive knowledge exists on the design of these systems. HDH is based on water evaporation of heated saline water into an air stream and its subsequent condensation. Water vapor is carried by a circulating air stream from the saline water side, usually called evaporator or humidifier, to the condenser side where vapor is condensed as potable water as shown in **Figure 4**. Solar energy can be used to heat saline water via flat plate or evacuated tube solar collectors and successively directed to the evaporator. In term of solar energy utilization, the water or the circulated air is heated to run the solar HDH process. There are different operating modes of humidification-dehumidification desalination process. These operating mode types include: (1) closed air-closed water cycle, (2) closed air-open water cycle (3) open air-closed water cycle, (4) open air-open water cycle. Fresh water yields depend on the HDH design, operating mode, and operating conditions. In general, the distillation yield in HDH desalination process is calculated as

$$\dot{m}_w = \dot{m}_{air}(\omega_{in} - \omega_{out}) \tag{2}$$

where \dot{m}_{air} is mass flow rate of dry air (kg/s), ω_{in} and ω_{out} are the humidity ratio ($\text{kg}_{\text{H}_2\text{O}}/\text{kg}_{\text{dry air}}$) of inlet and outlet air stream to the condenser, respectively. An important parameter that is used to examine the performance of HDH desalination process is the Gained Output Ratio (GOR) which is defined as the ratio of latent heat of evaporation of the distillate to the thermal energy input by the heated saline water. GOR is defined as,

$$\text{GOR} = \frac{\dot{m}_w h_{fg}}{\dot{m}_{saline} C_p (T_{in} - T_{out})} \tag{3}$$

where \dot{m}_{saline} is mass flow rate of heated saline water (kg/s), c_p is the specific heat of the saline water, T_{in} and T_{out} are the of inlet and outlet saline water temperature to the evaporator, respectively. HDH desalination process is best suited to utilize solar energy to heat saline water to a sufficiently high temperature such that water is evaporated. The temperature of the saline water is usually raised to 60°C; this is a relatively a low water temperature, which gives the HDH process an advantage over other traditional thermal desalination processes such as MSF or VC in that inexpensive materials of construction can be used. The downside of the HDH process is that the conversion rate is low; thus it is best suited for small-scale applications.

A significant advantage of the HDH process is that it typically operates in a low temperature range, which enables it to be driven by solar energy or a low-grade heat source. HDH systems are simple in design and operation; however, their low thermal energy efficiency is a significant drawback. The low thermal efficiency associated with HDH systems is typically due to the low thermodynamic availability of low grade heat. In addition, HDH systems are commonly based on natural draft to circulate the air in the system, which is associated with low heat and mass transfer coefficients compared to forced draft air flow. Film condensation over metallic tubes is usually used to condense the water vapor in the air stream and recover the latent of condensation. Due to the low rate of heat transfer, large metallic surface area is usually required which increases the system cost. Solar HDH technologies have great promise for decentralized small-scale water production applications, although additional improvements in system efficiency are needed to reduce the capital cost.

Humidification and dehumidification method for saline water desalination has been examined by many researchers. Farid et al. proposed a design for a solar energy based HDH desalination unit [29]. The performance factor of the desalination unit for different air and water flow rates have be examined by measuring water temperature. The study observed a variation in daily performance factor between 0.95 and 1.35. It was concluded that decreasing the water mass flow rate to 70 kg/h increases water temperature which increases the performance factor. Nawayseh et al. [30] carried out a simulation study for a closed cycle HDH process to optimize its operating condition. It was concluded that the performance of HDH process is significantly influenced by both water flow rate and to the surface area of humidifier and condenser. In addition, it was found that air flow rate has a small effect on the fresh water production of the unit. The maximum fresh water production for the system less than 0.7 kg/m²h and the average daily production is 3.5 kg/m² day for about 10-h operation. Al-Hallaj et al. [31] investigated a similar process configuration to that of Nawayseh et al. [30] and noticed that fresh water production performance is not affected by air flow rate. On the other hand, when operating at low temperature (50°C), water yields improves with increasing air flow rate. In their experimental study, they reported a maximum fresh water production of 0.65 kg/h, and a total daily production of 5 L/(m².day). Their investigation concluded that fresh water production increases significantly with increasing water mass flow rate to an optimum point. Beyond the optimum point, increasing the mass flow rate decreases fresh water production. They also suggested it is best to operate the unit with forced air circulation while operating at low temperature, and operate with natural air draft circulation the water temperatures is high.

Muller [32] analyzed a small-scale thermal seawater desalination system with a thermal storage tank to enable the system to run 24 h/d of operation. They carried out the analysis using a simulation program to optimize the performance. They proposed to use a highly efficient solar collectors to heat the water to 85°C. Dai et al. [33] have examined an open loop humidification

and dehumidification system that uses a forced convection to circulate the air. A boiler is used to represent the solar collector to heat the saline water. In their system, they reported a thermal efficiency of 80% which is defined as the ratio of the minimum energy to obtain a fixed amount of water to the total heat input. Also, in the study it was reported that the performance is significantly dependent on the inlet saline water temperature, mass flow rate of the saline water and air.

Orfi et al. [34] examined the efficiency of a desalination process with a solar air heater to improve the performance. An electric heater was used to replace the solar water heater. A constant solar irradiation flux of 800 W/m^2 was used, and the maximum fresh water production was $5.2 \text{ kg/m}^2\text{d}$. The experimental results indicate that the performance of the system improves with increasing the ambient air temperature. It was also reported that increasing the cooling water flow rate increases the production to up to an optimum value.

A comprehensive technical review that compares between different thermal desalination techniques is presented by Parekh et al. [35]. The main limitation of the HDH process is that the heat and mass transfer coefficients in the process are low because HDH process typically operate based on a natural draft to drive the airflow in the system. Numerous simulations are required to understand the air and mass flow rate influence on the performance of the HDH desalination process. It is reported that further simulations with a thermal storage module and 24 h operation are recommended to improve the process of the HDH. Condensation over tubes is usually used to condense the water vapor in the air stream. Because of the condenser low efficiency, HDH process require a large surface area condenser which increases the cost of the system.

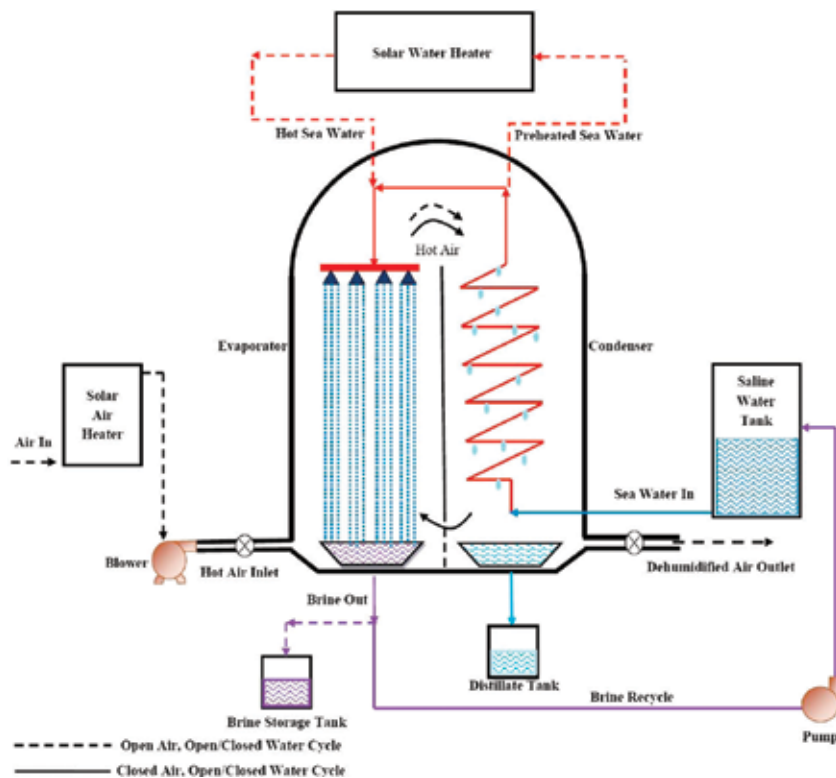


Figure 4. Schematic diagram of the solar HDH [47].

2.3. Solar diffusion driven desalination process

Solar diffusion driven desalination (DDD) is a thermal distillation process similar to the HDH where a solar collector is used to deliver the thermal energy. A simplified schematic diagram of the Solar DDD process is shown in **Figure 5**. The Solar DDD facility consists of two main components: evaporator and condenser. The evaporator and the condenser allows direct contact between air and water and they are mainly composed of a packing material. The packing material is characterized by a high surface area to volume ratio which improve the water and air contact area. A single nozzle is mounted at the top of the packing in the evaporator and the condenser to spray saline water over the packing material in the evaporator, and to spray the cooling water in condenser. A basin at the bottom of the evaporator is installed and used to collect the saline water and another one is installed at the bottom of the condenser to collect the freshwater [44].

The DDD process operates on the principle of humidification and dehumidification of an air stream. The first process is called air humidification and occurs in the evaporator. Heated saline water enters the evaporator, as low as 45°C, and gets sprayed at the top of the packing via the evaporator nozzle. Low humidity air is forced via a fan at the bottom of the evaporator to circulate the air through the system. With this arrangement, the drawn air is flowing counter-currently to the falling water which increase direct heat and mass transfer between air and water. This leads to humidification of the air and increases the air temperature exiting the evaporator. The humidified air leaves the evaporator at the top as fully saturated and then enters the direct contact condenser. In the direct contact condenser, cold fresh water is sprayed on the top of packed bed. As the humidified air is flowing upward, it gets in direct contact with the sprayed cold fresh water which leads to the dehumidification of the air and reduction in its temperature. In dehumidification process, heat will be transferred from air-vapor to the cold freshwater resulting in water vapor condensation which leads to fresh water production. The fresh water is collected at the basin of the condenser and sent to a fresh water production tank or to a heat exchanger to be cooled and recycled again [44].

The performance of the solar DDD have been investigated by various research groups [36–44]. A theoretical model has been developed to describe the heat and mass transfer in the process and the performance has been studied for different operating conditions. A steady state theoretical model for the evaluation of heat and mass transfer in the evaporator for the DDD process is developed by Klausner et al. and Li et al. [36–39], and it is given in Eqs. 4–6. The formulation is based on a two-fluid film model for a packed bed in which conservation equations for mass and energy are applied to a differential control volume. Eqs. 4–6 comprise a set of coupled ordinary differential equations that are used to solve for the humidity ratio, water temperature, and air/vapor mixture temperature distributions along the height of the evaporator,

$$\frac{dT_L}{dz} = \frac{G}{L} \frac{d\omega}{dz} \frac{(h_{fs} - h_L)}{C_{p_L}} + \frac{Ua(T_L - T_a)}{C_{p_L} L}, \quad (4)$$

$$\frac{dT_a}{dz} = -\frac{1}{1 + \omega} \frac{d\omega}{dz} \frac{h_L(T_a)}{C_{p_G}} + \frac{Ua(T_L - T_a)}{C_{p_G} G(1 + \omega)} \quad (5)$$

$$\frac{d\omega}{dz} = \frac{k_c a_w M_v}{G R} \left(\frac{P_{sat}(T_i)}{T_i} - \frac{\omega}{0.622 + \omega} \frac{P}{T_a} \right), \quad (6)$$

where L and G is the water and air mass fluxes, respectively, ω is the humidity ratio k_c is the mass transfer coefficient on gas side, a is the specific area of packing, which is defined as the total surface area of the packing per unit volume of space occupied, a_w is the wetted specific area, M_v is the vapor molecular weight, R is the universal gas constant, and T_i is the liquid/vapor interfacial temperature which is defined as,

$$T_i = \frac{T_L + (U_G/U_L) T_a}{1 + (U_G/U_L)} \quad (7)$$

Similarly, a steady state theoretical model for the evaluation of heat and mass transfer in the condenser for the DDD process is given [36–39],

$$\frac{dT_L}{dz} = \frac{G}{L} \frac{d\omega}{dz} \frac{(h_{fg} - h_L)}{C_{p_L}} + \frac{Ua(T_L - T_a)}{C_{p_L} L}, \quad (8)$$

$$\frac{dT_a}{dz} = -\frac{1}{1 + \omega} \frac{d\omega}{dz} \frac{h_L(T_a)}{C_{p_G}} + \frac{Ua(T_L - T_a)}{C_{p_G} G(1 + \omega)}. \quad (9)$$

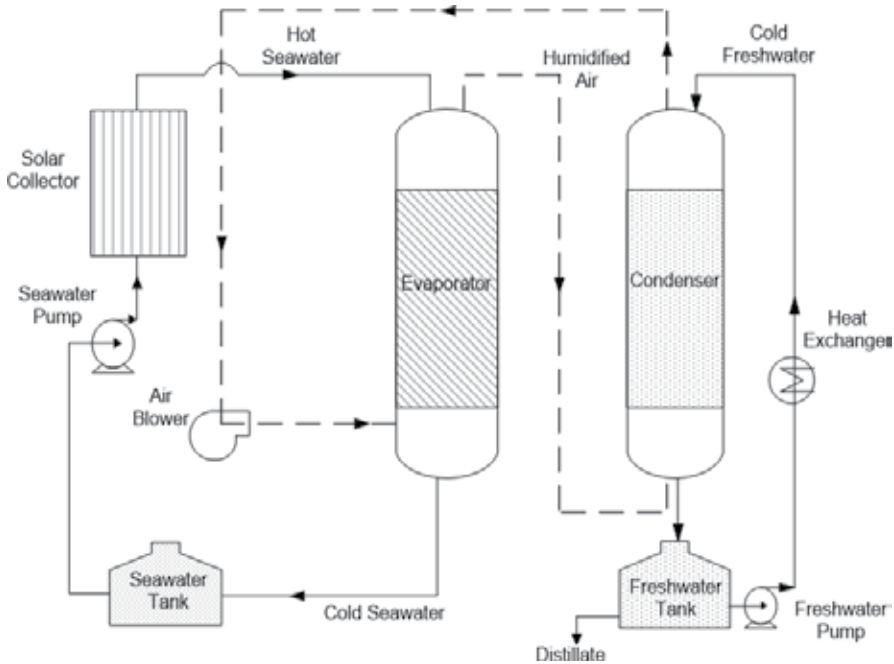


Figure 5. Schematic diagram for the solar diffusion driven desalination process [42].

$$\frac{d\omega}{dz} = \frac{dT_a}{dz} \frac{P}{P - P_{sat}(T_a)} \omega_m (b - 2cT_a + 3dT_a^2). \quad (10)$$

where b , c and d are empirical constants that are given as $a = 0.611379$, $b = 0.0723669$, $c = 2.78793 \times 10^{-4}$, $d = 6.76138 \times 10^{-7}$, and T_a ($^{\circ}\text{C}$) is the air temperature [36–39].

A more recent formulation has been developed for transient solar DDD [40–44]. Alnaimat et al. developed a transient one-dimensional theoretical model for the evaluation of heat and mass transfer within direct-contact evaporators and condensers. Eqs. 11–14 comprise a set of coupled partial differential equations that are used to solve for the humidity ratio, water temperature, air/vapor mixture, and packed bed temperature distributions along the height of the evaporator.

$$\frac{\partial T_L}{\partial t} = \frac{L}{\rho_L \alpha_L} \frac{\partial T_L}{\partial z} - \frac{\partial \omega}{\partial z} \frac{G(h_g - h_L)}{\rho_L \alpha_L C p_L} - \frac{U_L a_w (T_L - T_{pack})}{\rho_L \alpha_L C p_L} - \frac{U a_w (T_L - T_a)}{\rho_L \alpha_L C p_L} \quad (11)$$

$$\frac{\partial T_a}{\partial t} = \frac{-G}{\rho_a \alpha_a} \frac{\partial T_a}{\partial z} - \frac{(h_g(T_L) - h_v(T_a))G}{\rho_a \alpha_a (1 + \omega) C p_{mix}} \frac{\partial \omega}{\partial z} + \frac{U_G (a - a_w)}{\rho_a \alpha_a (1 + \omega) C p_{mix}} (T_{pack} - T_a) + \frac{U a_w}{\rho_a \alpha_a (1 + \omega) C p_{mix}} (T_L - T_a). \quad (12)$$

$$\frac{\partial T_{pack}}{\partial t} = \frac{1}{\rho_{pack} \alpha_{pack} C p_{pack}} (U_L a_w (T_L - T_{pack}) - U_G (a - a_w) (T_{pack} - T_a)) \quad (13)$$

$$\frac{\partial \omega}{\partial z} = \frac{k_G a_w M_v}{G} \left(\frac{P_{sat}(T_i)}{T_i} - \frac{\omega}{0.622 + \omega} \frac{P}{T_a} \right), \quad (14)$$

where α_L and α_a is the liquid and air volume fraction, ρ_L and ρ_a the air and vapor density, respectively, U_L and U_G are the respective liquid and gas heat transfer coefficients. Similarly, Eqs. 15–18 comprise a set of coupled partial differential equations that are used to solve for the humidity ratio, water temperature, air/vapor mixture, and packed bed temperature distributions along the height of the condenser.

$$\frac{\partial T_L}{\partial t} = \frac{L}{\rho_L \alpha_L} \frac{\partial T_L}{\partial z} - \frac{\partial \omega}{\partial z} \frac{G(h_g - h_L)}{\rho_L \alpha_L C p_L} + \frac{U a_w (T_a - T_L)}{\rho_L \alpha_L C p_L} + \frac{U_L a_w (T_{pack} - T_L)}{\rho_L \alpha_L C p_L} \quad (15)$$

$$\frac{\partial T_a}{\partial t} = \frac{-G}{\rho_a \alpha_a} \frac{\partial T_a}{\partial z} - \frac{(h_g(T_L) - h_v(T_a))G}{\rho_a \alpha_a (1 + \omega) C p_G} \frac{\partial \omega}{\partial z} - \frac{U_G (a - a_w)}{\rho_a \alpha_a (1 + \omega) C p_G} (T_a - T_{pack}) - \frac{U a_w}{\rho_a \alpha_a (1 + \omega) C p_G} (T_a - T_L) \quad (16)$$

$$\frac{\partial T_{pack}}{\partial t} = \frac{1}{\rho_{pack} \alpha_{pack} C p_{pack}} (U_G (a - a_w) (T_a - T_{pack}) - U_L a_w (T_{pack} - T_L)) \quad (17)$$

$$\frac{\partial \omega}{\partial z} = \frac{\partial T_a}{\partial z} \frac{P}{P - P_{sat}(T_a)} \omega_m (b - 2cT_a + 3dT_a^2) \quad (18)$$

The given Eqs. 11–18 can be solved numerically simultaneously to predict water, air/vapor mixture and packed bed temperatures and humidity ratio within the evaporator and the condenser. These equations represent the heat and mass transport models in evaporator and condenser and they account for the transient variations within the packed-bed due to time varying inlet air and water temperatures and humidity. **Figure 6** shows the fresh water production rate for the given solar heat input where the condenser is operating with continuous cooling to maintain condenser inlet water temperature at 25°C. It is clear that as the solar heat input increases the evaporator inlet water temperature increases, which improve the water production. **Figure 7** shows the increase in the total fresh water produced and the decline of the saline water volume in the storage tank with time. With its low energy consumption and low fabrication cost, solar DDD is expected to be competitive with other small scale desalination units for decentralized water production. The diffusion driven desalination process is considered promising for water desalination when driven by solar energy or waste heat.

2.4. Solar membrane distillation

In principles, membrane distillation (MD) is a hybrid of thermal distillation and membrane processes. MD has an important feature is that it operates at a low temperature range compared to conventional thermal distillation processes and at a low pressure compared to reverse osmosis desalination. Due to this low temperature operating range, it is well suited to be heated by solar energy. The membranes used are non-wetting (hydrophobic) and typically are made from polypropylene (PP), polyvinylidene fluoride (PVDF), polyethylene (PE), or polytetrafluoroethylene (PTFE). Different membrane module configurations exist such as plate and frame, hollow fiber, tubular, and spiral wound membrane module. Hydrophobic microporous membranes act as a physical support that separates a warm saline water chamber from a cold permeate chamber [45].

In solar membrane desalination, salty water or brackish water is heated using solar energy and then directed to a warm saline chamber. The driving force in solar MD process is vapor pressure difference across the membrane. There are different methods to create a vapor pressure difference across the membrane; thus MD can be categorized in terms of pressure difference creation into the following: direct contact membrane distillation (DCMD); air gap membrane distillation (AGMD); sweeping gas membrane distillation (SGMD); and vacuum membrane distillation (VMD). Water vapor transports through membrane pores from the high vapor pressure feed side to the low vapor pressure permeate side. The most commonly MD types used for desalination are DCMD, AGMD, and VMD as shown in **Figure 8**. **Figure 8a** depicts the direct contact membrane distillation (DCMD) process. In DCMD a pressure difference is created by a temperature difference between the feed water side and permeate side. The hot feed water is in direct contact with the membrane. As the water evaporates in the feed water side, it moves through the membranes and condenses on the lower temperature permeate side. The salty liquid feed water cannot pass through the hydrophobic membrane to the permeate side. DCMD is commonly used for saline water desalination. The main disadvantage of DCMD is the heat loss by conduction from the hot side to the cold side.

In DCMD, the mass flux is typically, assumed to be proportional to the vapor pressure difference across the membrane, and is given by:

$$J = C_m (P_f - P_p) \quad (19)$$

where C_m is the membrane coefficient, P_f and P_p are the vapor pressure at the membrane feed and permeate surfaces. Since the pressure also depends on the feed and permeate temperature, the above equation can be rewritten in terms of temperature difference across the membrane surfaces as:

$$J = C_m \frac{dP}{dT} (T_{f,m} - T_{p,m}) \quad (20)$$

where $T_{f,m}$ and $T_{p,m}$ is the feed and permeate temperatures at the membrane surface respectively. Here dP/dT is the variation in pressure and temperature which is given by the Clausius-Clapeyron equation, as follows:

$$\frac{dP}{dT} = \frac{h_{fg}}{RT^2} P_0(T) \quad (21)$$

where R and h_{fg} represent the universal gas constant and the latent heat of vaporization respectively. Eq. 20 is valid when the separation process is for pure water or very diluted solution, and the temperature difference across the membrane surfaces is less than or equal to 10°C [45].

And for more concentrated solutions, another relation developed by Schofield et al. [46] for the mass flux which is given by:

$$J = C_m \frac{dP}{dT} [(T_{f,m} - T_{p,m}) - \Delta T_{th}] (1 - x_m) \quad (22)$$

where ΔT_{th} is the threshold temperature, which is given by:

$$\Delta T_{th} = \frac{RT^2}{M_w h_{fg}} \frac{x_{f,m} - x_{p,m}}{1 - x_m} \quad (23)$$

Here $x_{f,m}$, $x_{p,m}$, x_m represent the mole fraction of dissolved species at the hot membrane surface side, from the permeate membrane surface side and inside the membrane.

In the Air gap membrane distillation (AGMD) process, depicted in **Figure 8b**, the hot feed water is in direct contact with the membrane while the cold permeate is not in direct contact with the membrane. A stagnant air gap separates the cold water. The water evaporates in the feed water side and it moves across the membranes to condense on the lower temperature surface plate after passing the air gap. AGMD is commonly used for saline water desalination. The advantage of AGMD is that the reduction in the heat loss by from the hot side to the cold side. **Figure 8c** depicts the sweeping gas membrane distillation (SGMD) process. Carrier gas as flows in the permeate side to remove the vapor to a separate component to be condensed. SGMD is more typically used for removing volatile vapors and is less used in desalination. The main drawback of this process is the fact that it requires very large condenser to condense the vapor. In VMD process, vacuum is created in the permeate side via a pump. Water vapor passes

through the membrane due to the pressure difference between the feed water side and the permeate side as depicted in **Figure 8d**. The VMD is also achieved in a condenser outside the membrane which considered an advantageous to reduce the heat lost via across the membrane [45].

The MD process poses some advantages over RO process since it does not require high pressure feed water, and it can process very high salinity brines. The MD process can tolerate complete dry out of the membrane. In comparison with other large thermal distillation processes MD is not limited to large scale applications; it is highly scalable. In addition, MD processes include the rejection of ions, macromolecules, colloids, and other non-volatiles, lower operating temperatures compared to conventional distillation, and lower operating pressures compared to other pressure driven membrane separation processes. A disadvantage of MD process is the high cost of the membranes and the membrane susceptibility to get fouled which diminishes their durability.

2.5. Concentrating solar energy for desalination

Solar energy collectors can be classified in terms of the measured temperature range in the collector. Collectors are classified as low temperature when the measured collector temperature is <100°C, medium temperature collector when temperature is in the range of 100–150°C, and high temperature collector when collector temperature is >150°C. Solar energy plays an important role as a source of energy for low temperature desalination systems. For low temperature collectors, HDH desalination or diffusion driven desalination is very suitable. For medium and high temperature collectors such as concentrated solar trough, conventional thermal desalination such as multi-effect desalination (MED), multistage flash distillation (MSF) and vapor compression distillation (VC) is more suitable to be integrated with these

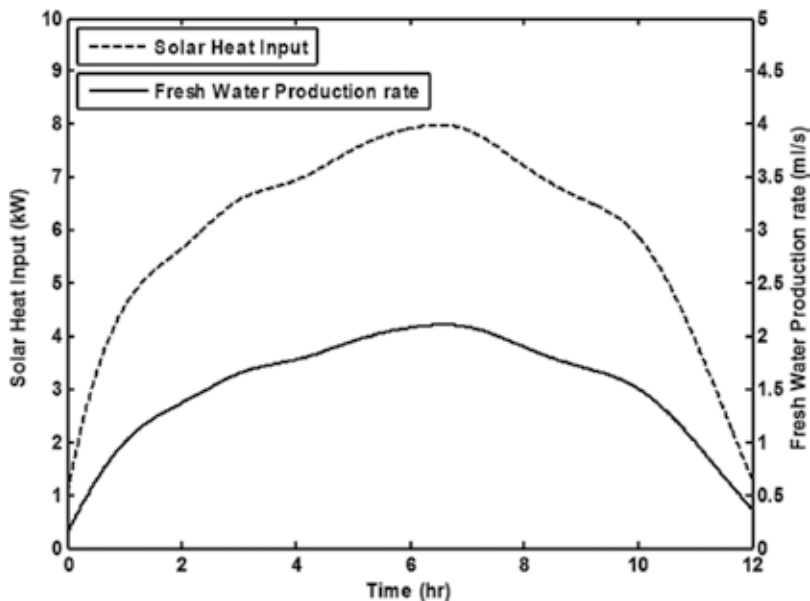


Figure 6. Solar heat input and fresh water production rate of the solar DDD [44].

collectors. MSF, MED, and VC systems can be powered by the thermal energy captured by a concentrated solar energy to distill salty water.

The principle of using concentrated solar energy to power MSF processes is based on generating water vapor by heating seawater using concentrated solar energy. After being heated, water is introduced to a low pressure chamber, where sudden pressure drop occurs and water flashes to vapor. This process is repeated successively in a series of chambers in which the pressure is reduced at different stages. Water vapor is condensed on a heat exchanger bundle (condenser) and collected to produce freshwater. **Figure 9** shows a combined concentrated solar energy system and MSF distillation process. The distillate production rate from MSF desalination process depends primarily on the brine temperature, number of stages, feed water salinity and fouling resistance of the brine heater. The plant distillate production can be increased by increasing the temperature difference between discharged hot brine and inlet seawater temperature [48]. Distillate production in solar multi stage flash desalination could be increased by using water as the heat transfer fluid in solar collectors and also by increasing the size of thermal storage tanks [49].

For MED processes integrated with concentrated solar energy, the distillation process takes place in a series of vessels collectively referred to as effects. **Figure 10** shows a MED distillation process powered by concentrated solar energy. The thermic fluid is heated in the concentrated solar collector field, and thereafter is passed to the effect vessels to heat the sprayed saline water. As shown in **Figure 10**, a pre-heated seawater is introduced at the top of the effects, which is usually sprayed on bundle of tubes in which the thermic fluid is flowing, to create a falling film. The thermic fluid is at higher temperature than saturated temperature of the saline water. Water vapor is generated at the falling film and thereafter directed to the next effect where it releases its latent heat of condensation to the incoming saline water to produce distilled water.

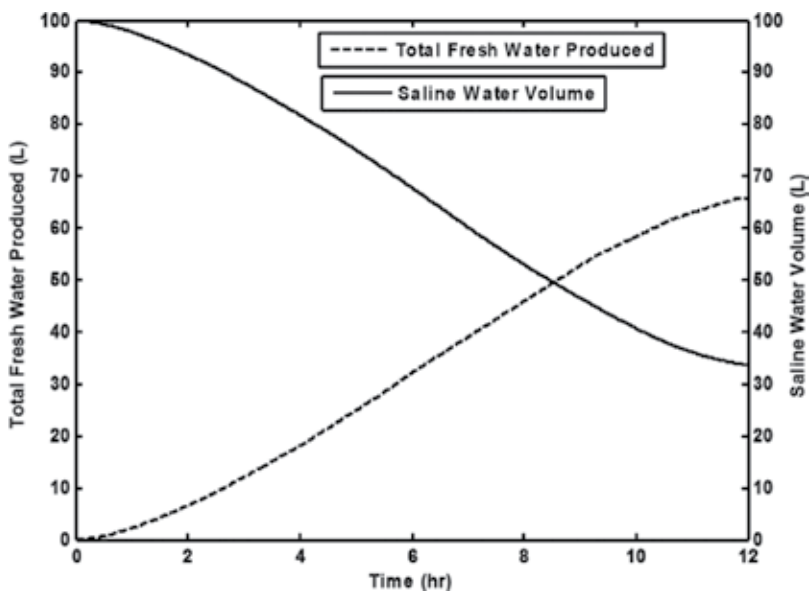


Figure 7. Total fresh water produced and saline water volume in storage tank of the solar DDD [44].

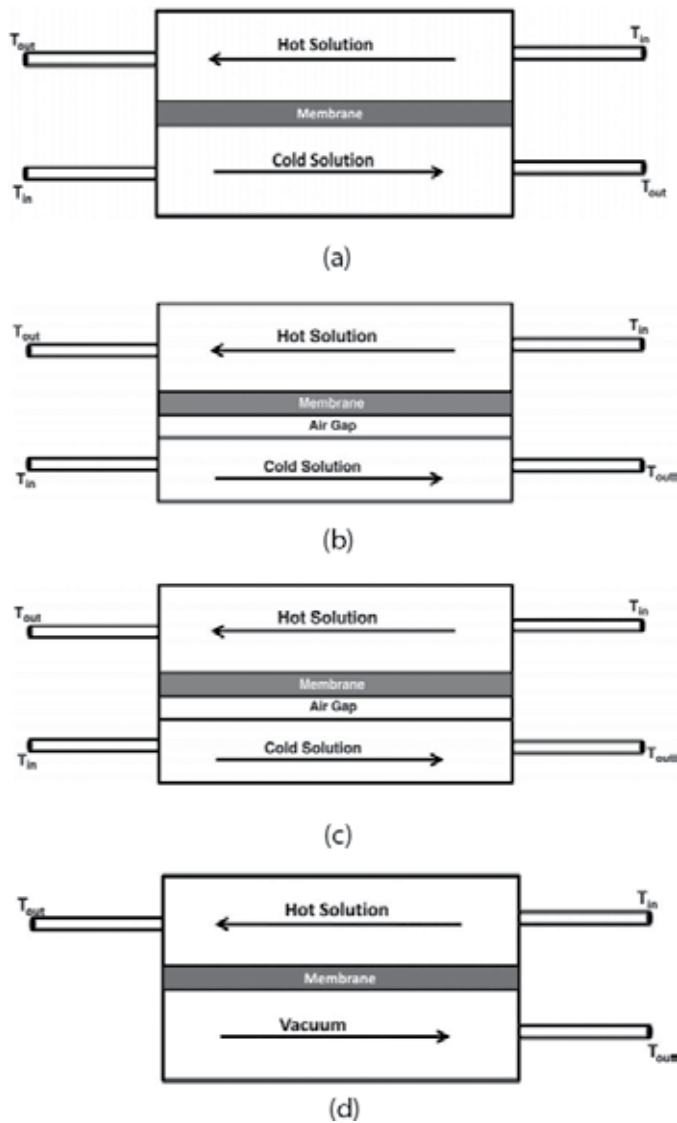


Figure 8. Different types of membrane distillation process: (a) direct contact membrane distillation (DCMD), (b) air gap membrane distillation (AGMD), (c) sweeping gas membrane distillation (SGMD), (d) vacuum membrane distillation (VMD) process, adapted from [45].

For solar powered vapor compression desalination, saline water is heated by a solar collector and directed to a vessel where it flashes to vapor. **Figure 11** shows a VC distillation process powered by concentrated solar energy. The produced vapors are compressed using mechanical vapor compressor (MVC) or thermo vapor compressor (TVC) to raise the condensation pressure and temperature of the vapor. The vapor compression raises the steam pressure and its saturation temperature. The compressed vapor is then used to heat the remaining saline water in the vessel in the first step. Then vapor exits the vessel and thereafter enters the condenser to release its latent heat to the saline feed water as shown in **Figure 11**. The condensed vapor is then collected in the distilled storage tank.

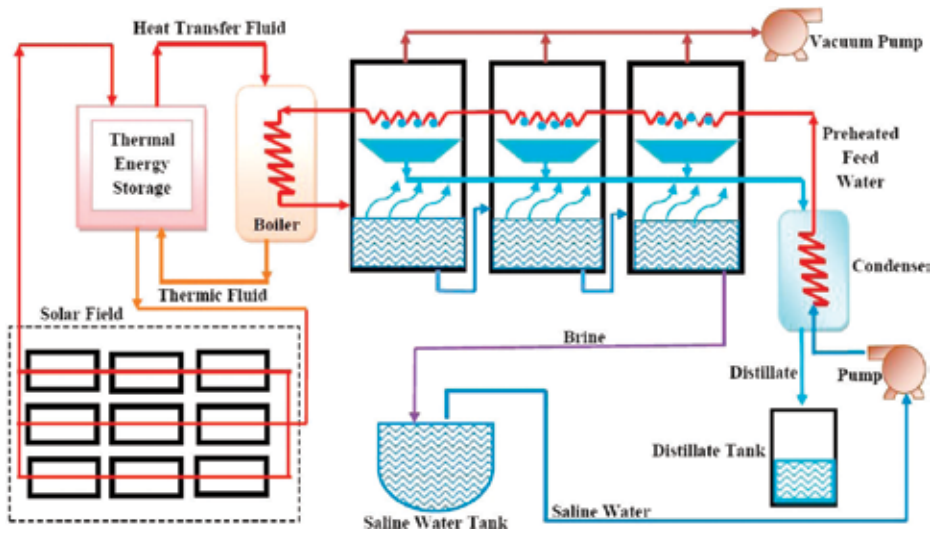


Figure 9. MSF distillation process powered by concentrated solar energy [47].

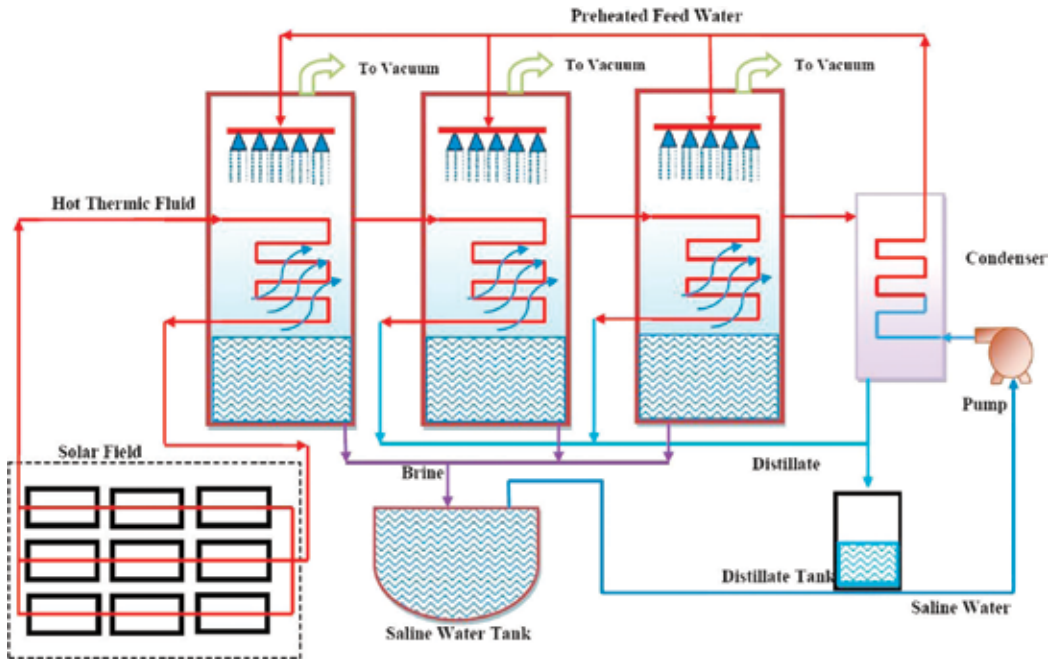


Figure 10. MED distillation process powered by concentrated solar energy [47].

In mechanical vapor compression desalination, a mechanical compressor is used to compress water vapor. The compressed vapor flows inside a bundle of tubes, which leads to condensation at a relatively high temperature. A saline water is sprayed on the outside surface of the bundle of tubes to recuperate the vapor latent heat of condensation. The saline water gets evaporated due to the heated tube bundle. The water vapor is then passed to the condenser to produce a fresh water. **Figure 12a** shows a schematic diagram of a mechanical

vapor compression distillation system coupled with MED powered by concentrated solar energy. Thermal vapor compression is usually coupled with multiple-effect distillation, which utilizes water vapor produced in each effect. Thermal vapor compression desalination process utilizes a steam jet compressor to compress the vapor. A steam jet is used to extract the low-pressure steam from the vessels by creating a vacuum and then after mixing it with high-pressure steam that is supplied to the system. The pressure of the resulting steam mixture is then raised in the diffuser to the pressure required for heating steam in the first effect. **Figure 12b** shows a schematic diagram of thermo vapor compression distillation coupled with MED powered by concentrated solar energy.

Concentrating solar power generation (CSP) for large scale seawater desalination applications is promising as it can achieve very high capacity desalination plants, which can be a primary water source for large centralized communities. It is predicted that energy from CSP plants will become a more cost effective option for electricity generation and water desalination in several decades due to the development of the technology and to more implementation of solar renewable energy projects. Additional research is required to demonstrate long-term reliability of solar powered thermal desalination technologies and to improve the thermal efficiency.

2.6. Solar pond distillation

Thermal desalination by salinity-gradient solar ponds is a promising desalination technology as it is less costly compared to other solar driven desalination options. Solar ponds provide the least expensive option for heat storage with solar powered desalination systems, which is an important economic aspect for desalination processes. Ideally, thermal energy obtained from a salinity-gradient solar pond can be used to power conventional thermal desalination

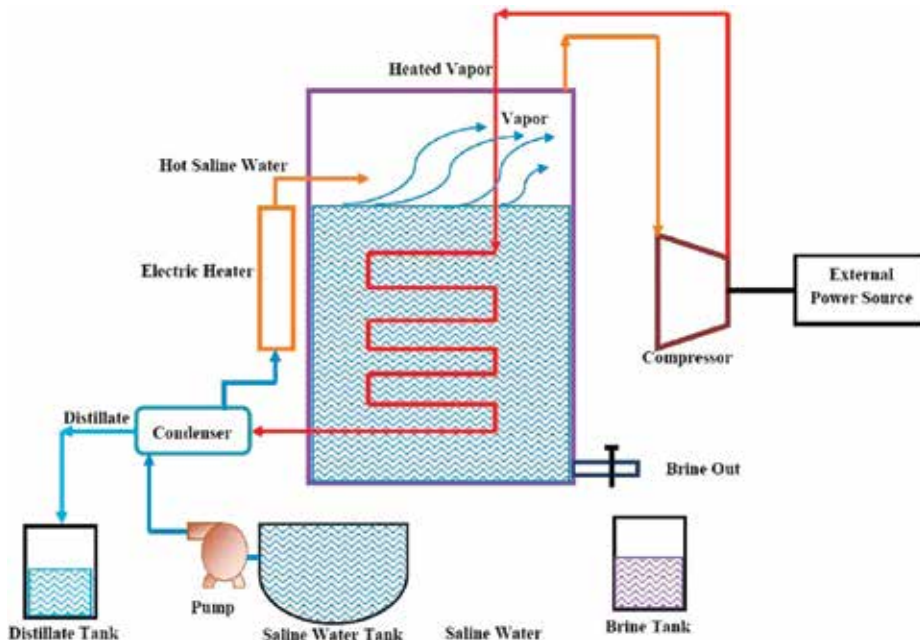


Figure 11. Concentrated solar energy powered MED distillation process [47].

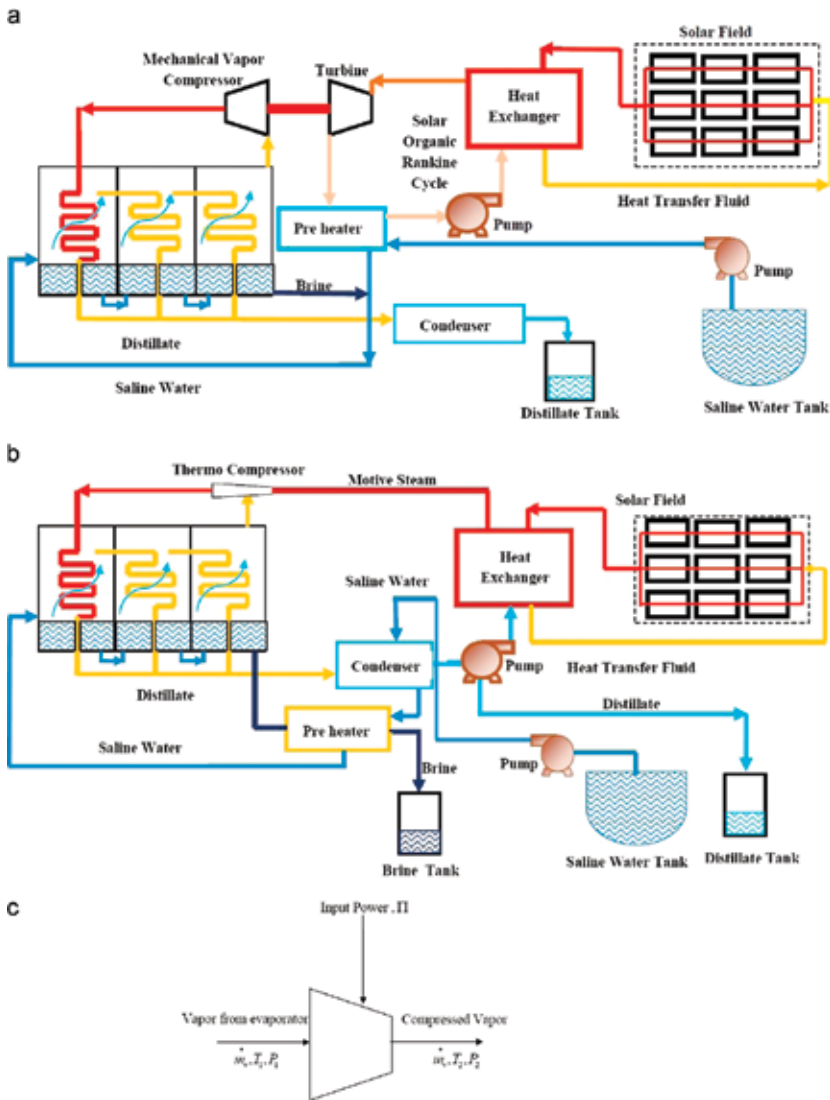


Figure 12. (a) Concentrated solar powered mechanical vapor compression unit coupled with MED, (b) concentrated solar powered thermo vapor compression unit coupled with MED [47].

technologies such as MSF, MED, and VC distillation. Although, this technology is still in the development stage, as demonstration plants have experienced operational difficulties. A lab-scale experimental investigation of an integrated solar pond of 70°C with 10 flash desalination units operating at 0.9 bar has been confirmed to produce approximately 15 m³/d of distilled water [50]. Solar pond technology integrated with MSF desalination plant has potential to be more cost effective than any other solar powered desalination technology [51]. At present, additional research is required to demonstrate long-term reliability of solar pond powered thermal desalination technologies.

3. Environmental impact of desalination

Fresh water shortage and demand are expected to increase in the coming few decades. The development and utilization of alternative water resources such as seawater desalination are becoming inevitable. On the other hand, desalination is very energy intensive process and has negative impact on the environment. The discharge of concentrated brine, hamper the life of marine eco systems. Waste discharge from desalination processes is considered to be a significant challenge that is becoming increasingly important. High energy consumption is considered the most influencing factor that inhibits growth of seawater desalination. Currently, most desalination processes are driven by energy obtained from fossil fuel. With such dependence on fossil fuel based energy sources, the increase in seawater desalination results in gas emissions that pollute the environment. Solar energy based desalination process is considered to be a promising method to alleviate the environmental impact of water desalination and also provide a sustainable source of potable water. This approach significantly mitigates the dependence on fossil fuel.

Large amount of concentrated brine discharge from saline water desalination plants is considered to be unpleasant waste. Marine life is strongly affected by the discharge of the concentrated brine. Concentrated brine is not only salt concentrated, but also contains chemicals such as anti-scaling agents from pre- and post-treatment. This results in high salt concentration in the area near brine discharge point. Brine disposal is a problem that challenges all desalination technologies. Brine discharged from membrane based desalination such as reversed osmosis is more concentrated than the brine discharged from thermal distillation plants. However, brine discharged from thermal distillation plants exits at a relatively high temperature compared with membrane based distillation. This influences the marine life such that only some plants or marine animal can withstand the high temperature near the outlet of thermal distillation plants. Marine life is also influenced by the intake of the seawater for the desalination plant. When a large amount of seawater is drawn from the sea, marine organisms and algae are sucked into the intake which cause a disturbance to the eco-system.

Many methods are currently used for brine disposal from desalination plants. Brine can be discharged to sea or river, discharged to solar ponds, or injected to deep saline aquifers. The discharge of brine to the sea or ocean is the least expensive method compared to other method. When brine is discharged to the sea, it tends to sink at the bottom of the sea because it has higher density than the seawater. A typical standard used in brine discharge is to diluted the brine with seawater to reduce its salinity before being discharged to sea. Furthermore, operating at lower recovery rates reduces the salinity of the brine. Brine is discharged at high depth of seawater which typically have a strong current. This reduces the detrimental effects of brine on the marine life. Brine discharges to a solar pond or the injection to a deep saline aquifer is more expensive method than sea discharge. These solar ponds and saline aquifers are typically located away from the desalination plant which require a long pipeline for transportation. This method has drawbacks because it may increase the salt in the soil and also increases the salinity of the ground water if linear is not used under the solar pond. The utilization of solar pond for brine disposal require a very large surface area, and it carries the risk of contaminating ground water.

4. Conclusions

Potable water is considered to be a scarce commodity especially in arid and remote regions. While conventional desalination technologies offer an excellent solution to meet water demand, they are considered to be energy intensive processes. Conventional desalination technologies are well suited for large scale applications but they are not-efficient and not suited for small scale water demand. Conventional desalination processes are expensive to operate and require continues maintenance which prevent their utilization in remote areas.

With the ever increasing energy cost and unavailability in the future, there is a need for cost effective desalination system that is well suited for small scale application. Solar desalination is expected to be a promising method to alleviate water shortage. The interests in solar desalination technologies have increased significantly in the last few decades. In order to maximize the utilization of solar desalination, the desalination efficacy needed to improved further and its cost must be reduced. Solar energy powered by desalination process can have a positive impact on reducing gas emissions and can considered to be a reliable source for potable water. Solar desalination processes can provide fresh water for remote areas in a sustainable way. Currently, more research is needed for improving solar based desalination and the treatment of waste water using these units.

Acknowledgements

The authors acknowledge the funding for this work from the National Water Center-UAE University through the research grant (G00002607).

Author details

Fadi Alnaimat^{1,3*}, James Klausner² and Bobby Mathew^{1,3}

*Address all correspondence to: falnaimat@ufl.edu

1 Mechanical Engineering Department, UAE University, Al Ain, UAE

2 Mechanical Engineering Department, Michigan State University, East Lansing, Michigan, USA

3 National Water Center, UAE University, Al Ain, UAE

References

- [1] Satcunanathan S, Hanses HP. An investigation of some of the parameters involved in solar distillation. *Solar Energy*. 1973;**14**:353-363. DOI: 10.1016/0038-092X(73)90102-3

- [2] Soteris A. Kalogirou, Seawater desalination using renewable energy sources. *Progress in Energy and Combustion Science*. 2005;**31**(3):242-281. DOI: 10.1016/j.pecs.2005.03.001
- [3] Nayak JK, Tiwari GN, Sodha MS. Periodic theory of solar still. *International Journal of Energy Research*. 1980;**4**:41. DOI: 10.1002/er.4440040106
- [4] Sodha MS, Kumar A, Tiwari GN, Pandey GC. Effect of dye on thermal performance of solar still. *Applied Energy*. 1980;**7**(1-3):147-162. DOI: 10.1016/0306-2619(80)90055-0
- [5] Yadav YP, Yadav BP. Transient analytical solution of a solar still integrated with a tubular solar energy collector. *Energy Conversion and Management*. 1998;**39**(9):927-930. DOI: 10.1016/S0196-8904(97)10025-5
- [6] El-Sayed MM. Comparison of transient performance predictions of a solar operated diffusion type still with a roof type still. *Journal of Solar Energy Engineering, Transactions of the ASME*. 1983;**105**:23. DOI: 10.1115/1.3266341
- [7] Tiwari GN, Madhuri. Effect of water depth on daily yield of still. *Desalination*. 1987;**61**(1):67-75. DOI: 10.1016/0011-9164(87)80007-3
- [8] Toure S, Meukam P. A numerical model and experimental investigation for a solar still in climatic conditions in Abidjan (Cote D'Ivoire). *Renewable Energy*. 1997;**11**(3):319-330. DOI: 10.1016/S0960-1481(96)00131-0
- [9] Lof GOG, Eibling JA, Bloemer JW. Energy balances in solar distillation. *AIChE*. 1961;**7**(4):641. DOI: 10.1002/aic.690070422
- [10] Sartori E. On the nocturnal production of a conventional solar still using solar pre-heated water. In: *Advances in Solar Energy Technology*. Vol. 2. New York: Pergamon Press; 1987. p. 1427. DOI: 10.1016/B978-0-08-034315-0.50277-9
- [11] Sharma VB, Mullick SC. Estimation of heat transfer coefficients, the upward heat flow and evaporation in a solar still. *Journal of Solar Energy Engineering, Transactions of the ASME*. 1991;**113**:36. DOI: 10.1115/1.2929949
- [12] Dunkle RV. Solar water distillation: The roof type still and a multiple effect diffusion still. In: *Proceedings of International Heat Transfer part V International Developments in Heat Transfer ASME*. University of Colorado; 1961. p. 895
- [13] Cooper PI. The maximum efficiency of single-effect solar, stills. *Solar Energy* 1973;**15**: 205-17. DOI: [https://doi.org/10.1016/0038-092X\(73\)90085-6](https://doi.org/10.1016/0038-092X(73)90085-6)
- [14] Yadav YP, Tiwari GN. Demonstration plant of fibre reinforced plastic multiwick solar still: An experimental study. *Solar Wind Technology*. 1989;**6**(6):653-666. DOI: 10.1016/0741-983X(89)90002-7
- [15] Lawrence SA, Gupta SP, Tiwari GN. Effect of heat capacity on the performance of solar still with water flow over the glass cover. *Energy Conversion and Management*. 1990;**30**(3):277-285. DOI: 10.1016/0196-8904(90)90010-V

- [16] Wibulswas P, Tadtium S. Improvement of a basin type solar still by means of a vertical back wall. In: International Symposium Workshop on Renewable Energy Sources, Lahore. Amsterdam: Elsevier; 1984
- [17] Rajvanshi AK. Effects of various dyes on solar distillation. *Solar Energy*. 1981;**27**:51-65. DOI: 10.1016/0038-092X(81)90020-7
- [18] Sodha MS, Kumar A, Tiwari GN, Pandey GC. Effect of dye on thermal performance of solar still. *Applied Energy*. 1980;**7**(1-3):147-162. DOI: 10.1016/0306-2619(80)90055-0
- [19] Rajvanshi AK, Hsieh CK. Effect of dye on solar distillation: Analysis and experimental evaluation. In: Proceedings of International Congress of ISES; Georgia. vol. 20, 1979. p. 327
- [20] Lawrence S, Gupta S, Tiwari GN. Experimental validation of thermal analysis of solar still with dye. *International Journal of Solar Energy*. 1988;**6**:291. DOI: 10.1080/01425918808914235
- [21] Akinsete VA, Duru CU. A cheap method of improving the performance of roof type solar stills. *Solar Energy*. 1979;**23**(3):271-272. DOI: 10.3968/j.est.1923847920140701.3915
- [22] Naim MM, Kawi MA. Non-conventional solar stills with charcoal particles as absorber medium. *Desalination*. 2002;**153**(1-3):55-64. DOI: 10.1016/S0011-9164(02)01093-7
- [23] Naim MM, Kawi MA. Non-conventional solar stills with energy storage element. *Desalination*. 2002;**153**(1-3):71-80. DOI: 10.1016/S0011-9164(02)01095-0
- [24] Bapeshwar V, Tiwari GN. Effect of water flow over the glass on the performance of a solar still coupled with a flat plate collector. *International Journal of Solar Energy*. 1984;**2**:277. DOI: 10.1080/01425918408909932
- [25] Tiwari GN, Prasad B. Thermal modelling of concentrator assisted solar distillation with water flow over the glass cover. *International Journal of Solar Energy*. 1996;**18**(3):173. DOI: 10.1080/01425919608914314
- [26] Bassam A, Hijleh KA, Mousa HA. Water film cooling over the glass cover of a solar still including evaporation effects. *Energy*. 1997;**22**(1):43-48. DOI: 10.1016/S0360-5442(96)00088-6
- [27] Kwatra HS. Performance of a solar still: Predicted effect of enhanced evaporation area in yield and evaporation temperature. *Solar Energy*. 1996;**56**(3):261-266. DOI: 10.1016/0038-092X(95)00101-V
- [28] Garg SK, Gomkale SD, Datta RL, Datar DS. Development of humidification-dehumidification technique for water desalination in arid zones of India. *Desalination*. 1968;**5**:55. DOI: 10.1016/S0011-9164(00)80192-7
- [29] Farid M, Al-Hajaj A. Solar desalination with a humidification-dehumidification cycle. *Desalination*. 1995;**106**:427-429. DOI: 10.1016/S0011-9164(96)00141-5

- [30] Nawayseh N, Farid M, Omar A, Al-Hallaj S, Tamimi A. A simulation study to improve the performance of a solar humidification-dehumidification desalination unit constructed in Jordan. *Desalination*. 1997;**109**:277-284. DOI: 10.1016/S0011-9164(97)00074-X
- [31] Al-Hallaj S, Farid MM, Tamimi AR. Solar desalination with a humidification-dehumidification cycle: Performance of the unit. *Desalination*. 1998;**120-3**:273-280
- [32] Muller-Holst H, Engelhardt M, Scholkopf W. Small-scale thermal seawater desalination simulation and optimization of system design. *Desalination*. 1999;**122-3**:255-262. DOI: 10.1016/S0011-9164(99)00046-6
- [33] Dai YJ, Zhang HF. Experimental investigation of a solar desalination unit with humidification and dehumidification. *Desalination*. 2000;**130**:169-175. DOI: 10.1016/S0011-9164(00)00084-9
- [34] Orfi J, Laplante M, Marmouch H, Galanis N, Benhamou B, Ben Nasrallah S, Nguyen CT. Experimental and theoretical study of a humidification-dehumidification water desalination system using solar energy. *Desalination*. 2004;**168**:151-159. DOI: 10.1016/j.desal.2004.06.181
- [35] Sandeep Parekh MM, Farid JR, Selman SA-H. Solar desalination with a humidification-dehumidification technique—A comprehensive technical review. *Desalination*. 2004;**160**:167-186. DOI: 10.1016/S0011-9164(04)90007-0
- [36] Klausner JF, Li Y, Darwish M, Mei R. Innovative diffusion driven desalination process. *Journal of Energy Resources Technology*. 2004;**126-3**:219-225. DOI: 10.1115/1.1786927
- [37] Klausner JF, Li Y, Mei R. Evaporative heat and mass transfer for the diffusion driven desalination process. *Journal of Heat and Mass Transfer*. 2006;**42**:528-536. DOI: 10.1007/s00231-005-0649-2
- [38] Li Y, Klausner JF, Mei R, Knight J. Direct condensation in packed beds. *International Journal of Heat and Mass Transfer*. 2006;**49**:4751-4761. DOI: 10.1016/j.ijheatmasstransfer.2006.06.013
- [39] Li Y, Klausner JF, Mei R. Performance characteristics of the diffusion driven desalination process. *Desalination*. 2006;**196**:188-209. DOI: 10.1016/j.desal.2006.01.013
- [40] Alnaimat F, Klausner JF. Enhanced performance of solar diffusion driven desalination. *Journal of Thermal Science and Engineering Applications*. 2013;**5**(4):041001-041001-9. DOI: 10.1115/1.4024020
- [41] Alnaimat F, Klausner JF. Transient dynamic response of solar diffusion driven desalination. *Applied Thermal Engineering*. 2013;**51**(1-2):520-528. DOI: 10.1016/j.applthermaleng.2012.09.038
- [42] Alnaimat F, Klausner JF. Solar diffusion driven desalination for decentralized water production. *Desalination*. 2012;**289**:35-34. DOI: 10.1016/j.desal.2011.12.028

- [43] Alnaimat F, Klausner JF, Mei R. Transient analysis of direct contact evaporation and condensation within packed beds. *International Journal of Heat and Mass Transfer*. 2011;**54**:3381-3393. DOI: 10.1016/j.ijheatmasstransfer.2011.03.048
- [44] Alnaimat F. Transient analysis of solar diffusion driven desalination [Thesis]. Gainesville: University of Florida; 2011
- [45] Alkhudhiri A, Darwish N, Hilal N. Membrane distillation: A comprehensive review. *Desalination*. 2012;**287**:2-18. DOI: 10.1016/j.desal.2011.08.027
- [46] Schofield RW, Fane AG, Fell CJD. Heat and mass transfer in membrane distillation. *Journal of Membrane Science*. 1987;**33**(3):299-313. DOI: 10.1016/S0376-7388(00)80287-2
- [47] Sharon H, Reddy KS. A review of solar energy driven desalination technologies. *Renewable and Sustainable Energy Reviews*. 2015;**41**:1080-1118. DOI: 10.1016/j.rser.2014.09.002
- [48] Moustafa SMA, Jarrar DI, El-Mansy HI. Performance of a self-regulating solar multi-stage flash desalination system. *Solar Energy*. 1985;**35**(4):333-340. DOI: 10.1016/0038-092X(85)90141-0
- [49] Hanafi A. Design and performance of solar MSF desalination systems. *Desalination*. 1991;**82**:175-185. DOI: 10.1016/0011-9164(91)85180-3
- [50] Safi MJ. Performance of a flash desalination unit intended to be coupled to a solar pond. *Renewable Energy*. 1998;**14**:339-343. DOI: 10.1016/S0960-1481(98)00087-1
- [51] Suri RK, Al-Marafie AMR, Al-Homoud AA, Maheshwari GP. Cost-effectiveness of solar water production. *Desalination*. 1989;**71**:165-175. DOI: 10.1016/0011-9164(89)80007-4

Factors Affecting the Yield of Solar Distillation Systems and Measures to Improve Productivities

Bao The Nguyen

Additional information is available at the end of the chapter

<http://dx.doi.org/10.5772/intechopen.75593>

Abstract

This chapter presents a numerical model to estimate the performance of solar basin-type distillation systems, both for conventional passive solar stills and active (forced circulation) stills with enhanced heat recovery. It also analyzes the factors affecting the distillate outputs of the still, including environmental factors (external factors or natural), elements of the design and operation (subjective factors). The subjective elements as well as the measures taken to optimize these factors are thoroughly analyzed. With these measures, the distillate yields of solar stills are increased from 30 to 68% compared with traditional distillation systems. This has scientific significance and practicality enabling the application of this technology to solar water distillation using a source of clean and renewable energy. It provides a viable way to alleviating the problem of the availability of clean water, especially in those areas and communities in countries where water resources are increasingly polluted and salty.

Keywords: solar basin-type still, passive solar still, active solar still

1. Introduction

The demand for clean water for domestic use has increased rapidly, especially in certain water-scarce areas located in rural, remote and border areas, islands, arid areas or places with polluted and saline water sources. Therefore, the development and the production of devices to distil water from alkaline, brackish or saline water sources and thus supply fresh water to people in affected areas are a critical issue for many countries whether clean water shortages are periodic or permanent.

There are many research and review papers that focus on solar stills and the factors that affect the output of solar distillation. Manchanda and Kumar [1] comprehensively reviewed and analyzed the designs and performance parameters of passive solar stills, while Sampathkumar et al. [2] reviewed in detail different types of active distillation systems. Velmurugan and Srithar [3] appraised certain modifications to solar still systems and their resulting respective performance enhancement. Focusing on the single-basin passive solar still, Murugavel et al. [4] evaluated the progress in improving the effectiveness of this type of still. Similarly, Kabeel and El-Agouz [5] examined single-type passive solar stills, with emphasis on performance enhancing modifications. Badran [6] studied another aspect experimentally—the performance of a single-slope solar still using different operational parameters. Other researches by Kaushal and Varun [7] evaluated the effect of different designs and methods on solar still output. Muftah et al. [8] comprehensively reviewed the performance of existing active and passive basin-type solar stills and investigated the effects of climatic, operational and design parameters on the output of these stills. Recently, Sharshir et al. [9] reviewed in details factors affecting solar still productivity and improvement techniques, while Kabeel et al. [10] introduced, explained and discussed the effectiveness of different solar stills into which different condenser arrangements were integrated.

All the above-mentioned papers, although comprehensive and thorough, have the same drawbacks that all previous researches and papers reviewed had, namely, they were from countries with different climatic conditions and different levels of technology and manufacturing expertise. This would lead to inconsistencies and differences in improvements to the named stills' output and performance as compared to those outputs and performances claimed or reported. Furthermore, there has been very little information relating to factors affecting forced circulation solar stills with enhanced water recovery.

Therefore this chapter will present the results of the numerical and experimental research carried out in one location so that there is consistency in the factors affecting solar stills' production as well as the gains of the stills' outputs due to the measures taken to optimize these factors. In addition, there will be a focus on the factors affecting the performance of forced circulation solar stills with enhanced water recovery improvement techniques.

2. The numerical modeling of a conventional basin-type solar still

Dunkle [11] was the first to investigate the heat and mass transfer relationships in a solar still under steady-state conditions. Based on the widely used relations from Dunkle, this study has analyzed the transient performance of the solar still in which all coefficients and still parameters are calculated using equations within the model. The weather data used for simulation will be either from actual measured data or data generated from the computer program developed by Nguyen [12].

The heat and mass transfer processes in the still are shown in **Figure 1**. The following assumptions are made in order to develop the equations for the energy balances in the still:

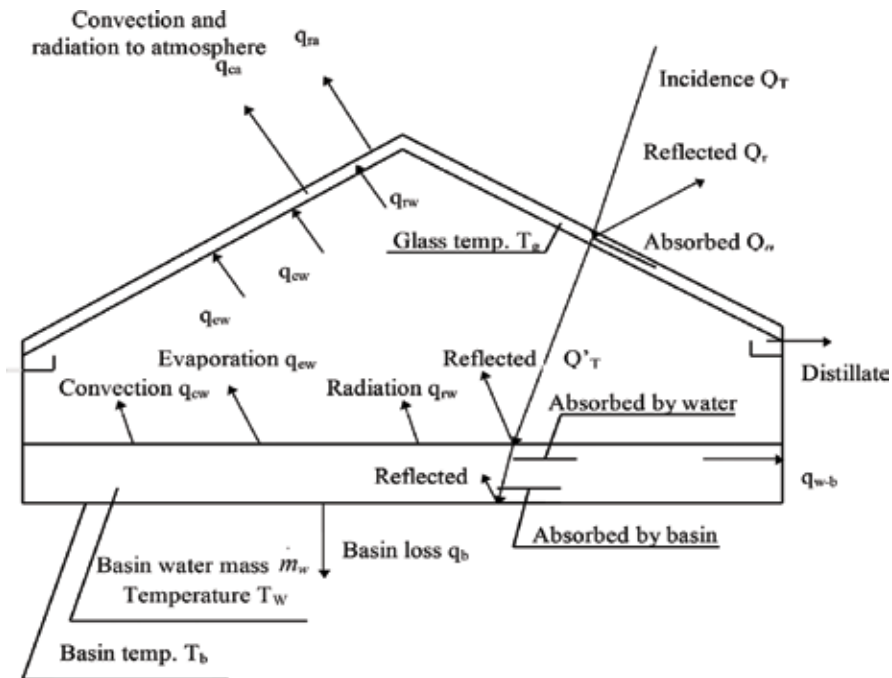


Figure 1. The heat and mass transfer processes in a conventional solar still.

1. The amount of water lost through evaporation is small compared to the amount of saline water in the basin.
2. The heat required to heat the water from the ambient (before adding to the basin) temperature to the temperature of water in the basin is negligible as compared to that required to evaporate the same quantity of water that means $C_{pw}(T_w - T_a) \ll h_w$.
3. There is no vapor leakage in the still, assuming a well-designed still.
4. The areas of the cover, the water surface and the basin are considered to be equal.
5. The temperature gradients along the cover thickness and the water depth are absent.

Based on these assumptions and from **Figure 1**, the energy balances for the glass, for the basin water, and for the basin are:

$$q_{cw} + q_{ew} + q_{rw} + \alpha_g Q_T = (q_{ra} + q_{ca}) + M_g \frac{dT_g}{dt} \quad (1a)$$

$$\alpha_w Q'_T = q_{cw} + q_{ew} + q_{rw} + q_{w-b} + M_w \frac{dT_w}{dt} \quad (2a)$$

$$\alpha_b Q''_T + q_{w-b} = q_b + M_b \frac{dT_b}{dt} \quad (3a)$$

where

- q_{cw} is the convective heat transfer rate between the basin water and the cover (in W/m^2) and can be calculated by using Dunkle's equation:

$$q_{cw} = 0.884 \left[(T_w - T_g) + \frac{(p_w - p_g)(T_w + 273.15)}{(268.9 \times 10^3 - p_w)} \right]^{1/3} (T_w - T_g). \quad (4)$$

with p_w and p_g being the partial pressure of water vapor at the temperatures of the basin water and the cover, respectively (in Pa).

- q_{ew} is the evaporative heat transfer rate between the basin water and the cover (in W/m^2):

$$q_{ew} = 16.276 \times 10^{-3} q_{cw} \frac{(p_w - p_g)}{(T_w - T_g)}. \quad (5)$$

- q_{rw} is the radiative heat transfer rate between the basin water and the cover (in W/m^2), expressed as:

$$q_{rw} = \varepsilon_w \sigma \left[(T_w + 273.15)^4 - (T_g + 273.15)^4 \right]. \quad (6)$$

with ε_w being the emissivity of water surface and σ the Stefan-Boltzmann constant, $5.67 \times 10^{-8} W/m^2.K^4$.

- q_{ca} is the convective heat transfer rate between the cover and the ambient surroundings (in W/m^2), computed from [13]

$$q_{ca} = (5.7w + 3.8)(T_g - T_a). \quad (7)$$

where w is the wind speed (m/s) and T_a is the ambient temperature ($^{\circ}C$).

- q_{ra} is the radiative heat transfer rate between the cover and the ambient surroundings (in W/m^2):

$$q_{ra} = \varepsilon_g \sigma \left[(T_g + 273.15)^4 - (T_a + 261.15)^4 \right]. \quad (8)$$

where ε_g is the emissivity of the cover

- q_{w-b} is the heat transfer rate between the water and the basin (in W/m^2):

$$q_{w-b} = h_{w-b}(T_w - T_b). \quad (9)$$

where h_{w-b} is the heat transfer coefficient between the water and the basin absorbing surface (in $W/m^2.^{\circ}C$).

- q_b is the heat transfer rate between the basin and the ambient surroundings (in W/m^2):

$$q_b = h_b(T_b - T_a). \quad (10a)$$

where h_b is the heat transfer coefficient between the basin and the ambient surroundings (in $W/m^2 \cdot ^\circ C$):

$$\frac{1}{h_b} = \frac{\delta_{insul}}{k_{insul}} + \frac{1}{h_i}. \quad (10b)$$

- δ_{insul} (m) and k_{insul} ($W/m \cdot ^\circ C$) are the thickness and thermal conductivity of the basin insulation, respectively.
- h_i is the combined convective and radiative heat transfer coefficient between the insulation and ambient and can be computed by the derivation of Eqs. (6) and (7).
- Q_T is the total solar radiation incidence on the cover, in W/m^2 .
- Q'_T is the total solar radiation incidence on the water surface, after transmittance through the cover, in W/m^2 .
- Q''_T is the total solar radiation incidence on the basin, after transmittance through the basin water, in W/m^2 .
- α_g , α_w and α_b are the absorptance of the cover, of the water and of the basin for solar radiation, respectively.
- M_g , M_w and M_b are the heat capacities per unit area of the cover, of the water and of the basin for solar radiation, in $J/m^2 \cdot ^\circ C$.
- T_g , T_w and T_b are, respectively, the transient temperatures of the cover, of the water and of the basin for solar radiation, in $^\circ C$.

Equations (1a), (2a) and (3a) can be rewritten as:

$$M_g \frac{dT_g}{dt} = \alpha_g Q_T + q_{cw} + q_{ew} + q_{rw} - (q_{ra} + q_{ca}). \quad (1b)$$

$$M_w \frac{dT_w}{dt} = \alpha_w Q'_T - (q_{cw} + q_{ew} + q_{rw} + q_{w-b}). \quad (2b)$$

$$M_b \frac{dT_b}{dt} = \alpha_b Q''_T + q_{w-b} - q_b. \quad (3b)$$

It is convenient to present all solar components Q_T , Q'_T and Q''_T in the above equations by the common total solar incidence of the sloped cover, Q_T , which is readily calculated [3]. If τ_g , τ_w and τ_b are defined as the fractions of solar insolation incident absorbed by the cover, basin water and basin liner, respectively, Eqs. (1b), (2b) and (3b) may be written as:

$$M_g \frac{dT_g}{dt} = \tau_b Q_T + q_{cw} + q_{ew} + q_{rw} - (q_{ra} + q_{ca}). \quad (1c)$$

$$M_w \frac{dT_w}{dt} = \tau_w Q_T - (q_{cw} + q_{ew} + q_{rw} + q_{w-b}). \quad (2c)$$

$$M_b \frac{dT_b}{dt} = \tau_b Q_T + q_{w-b} - q_b. \quad (3c)$$

3. The numerical modelling of a basin-type forced circulation solar still with enhanced water recovery

In this study, the heat and mass transfer relationships in the forced circulation solar still with enhanced water recovery will be developed. Then, this numerical modeling will be validated by comparing its results with those from the experimental model.

The forced circulation solar still has been chosen in this study for several reasons. Compared with other types of solar powered distillation systems such as the solar multistage flash distillation, solar vapor compression, solar powered reverse osmosis, solar powered electrolysis and solar membrane distillation systems, solar stills represent simple, yet mature technology.

The low efficiencies of a conventional solar still may be overcome by changing the principle of operation as follows:

- Using air as an intermediate medium and substituting forced convection for natural convection to increase the heat coefficients in the still, resulting in increased evaporation of water
- Replacing saturated air in the standard still by “drier” air to increase the potential for mass transfer in the still, leading to higher outputs
- Circulating the air-vapor mixture from the standard still to external water-cooled condensers to gain efficiency from a lower condensing temperature. The cooler the cooling water available, the more effective this condensing process will be
- Recovering some of the heat extracted in the condensing process and using it to preheat the air-vapor mixture entering the still
- Substituting the condensing area of the flat sheet covers in the standard still by the external condenser with much larger heat exchange areas to increase condensation efficiencies

3.1. The development of the heat and mass transfer relationships in a forced circulation solar still

Figure 2 shows a schematic diagram of the forced circulation solar still with enhanced water recovery. The air flow having a temperature of T_{in} and moisture content w_{in} enters the still and is heated up. It absorbs the vapor from the basin water and exits the still at a temperature of

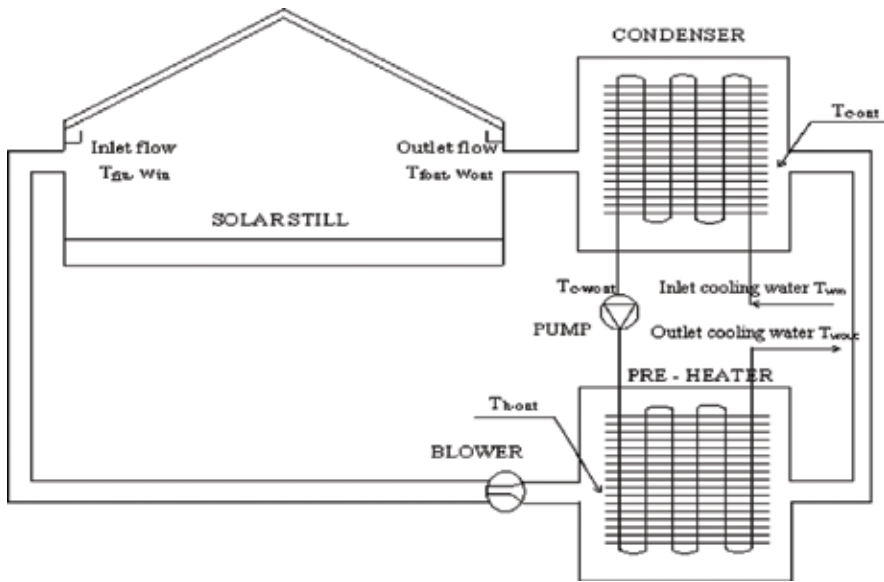


Figure 2. Schematic diagram of a forced circulation solar still with enhanced water recovery.

T_{fout} and moisture content w_{out} . This air flow goes through the dehumidifying coil, which acts a condenser. The hot air-vapor mixture from the still is passed over the coil and attached fins, while the cooling water runs inside the coil.

The hot air-vapor mixture losses heat to the cooling water and subsequently cools down. When the temperature of the mixture falls below its dew point temperature, the condensation process starts. The air exits the condenser at a temperature of T_{c-out} and a moisture content of w_{c-out} . Some of the heat extracted from the air flow will be recovered in the preheater, since the air flow goes through it before going back to the still.

The heat and mass transfer relationships in this still can be seen from **Figure 3**. From this figure, the energy and mass balances for the glass, for the flow in the still, for the basin water and for the basin are

$$q_{cfg} + q_{rw} + \alpha_g Q_T = (q_{ra} + q_{ca}) + M_g \frac{dT_g}{dt} \quad (11)$$

$$q_{ew} + q_{cwf} = q_{cfg} + m_f(h_{out} - h_{in}) + M_f \frac{dT_f}{dt} \quad (12)$$

$$m_{ew} = \frac{q_{ew}}{h_{fg}} = m_f(w_{out} - w_{in}) + m_{ew-g} \quad (13)$$

$$\alpha_w Q'_T = q_{cwf} + q_{ew} + q_{rw} + q_{w-b} + M_w \frac{dT_w}{dt} \quad (14)$$

$$\alpha_b Q''_T + q_{w-b} = q_b + M_b \frac{dT_b}{dt} \quad (15)$$

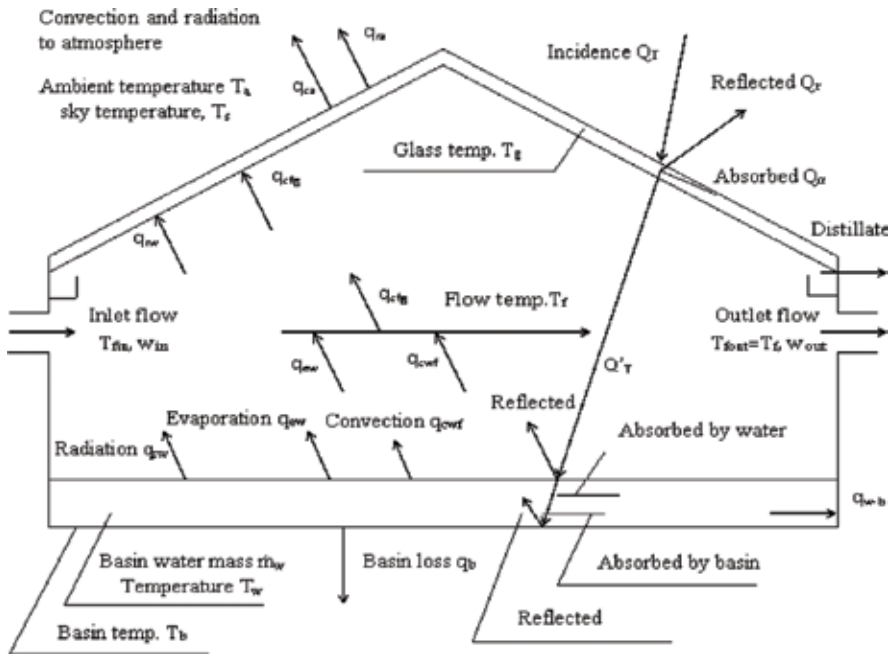


Figure 3. The heat and mass transfer process in a forced circulation solar still.

q_{cwf} is the convective heat transfer rate between the basin water and the flow (in W/m^2). In principle, the blower used to transport the air should have the lowest possible energy consumption. The heat transfer process in the still may be natural convection or combined natural and forced convection. In this model, the heat coefficient in the still is calculated by using the forced and natural convection relations separately, and the larger one is chosen. The Grashof and the Reynolds number are first calculated [13]:

$$Gr = \frac{g' \Delta T L^3}{\nu^2} \tag{16}$$

$$Re = \frac{V D_h}{\nu} \tag{17}$$

where:

L = average spacing between the water surface and the cover, in m.

g = gravitational constant, 9.81 m/s^2 .

β' = volumetric coefficient of expansion, in K^{-1} ; for air $\beta' = 1/T$.

ΔT = temperature difference between the water and the cover, in K.

ν = kinematic viscosity, in m^2/s .

V = air flow velocity, in m/s.

D_h = the hydraulic diameter of the still, defined as $D_h = \frac{4 \times (\text{flow area})}{\text{wetted perimeter}}$.

Then, if the natural convection dominates, the convective heat transfer rate between the basin water and the flow can be derived from

$$Nu = \frac{h_{cwf} L}{k} = 0.075 (Gr.Pr)^{1/3} \quad (18)$$

where Pr = is the Prandtl number,

to achieve a similar equation to Dunkle's expression [2] with T_g replaced by T_f :

$$q_{cwf} = 0.884 \left[(T_w - T_f) + \frac{(T_w - T_f)(T_w + 273.15)}{(268 \times 10^3 - p_w)} \right]^{1/3} (T_w - T_f) \quad (19)$$

where p_w and p_f are partial pressures (in Pa) of water vapor at the temperatures of the basin water and the flow, respectively.

If the forced convection dominates, the relation between Nu and Re is given by [4]

$$Nu = \frac{h_{cwf} D_h}{k} = 0.664 \times Re^{1/2} \times Pr^{1/3} \quad (20a)$$

Considering $T_w = 50^\circ\text{C}$ and $T_f = 40^\circ\text{C}$ and introducing the corresponding air properties into (20a), the convective heat transfer rate between the basin water and the flow can be computed by

$$q_{cwf} = 3.908 \left(\frac{V}{D_h} \right)^{1/2} (T_w - T_f) \quad (20b)$$

q_{ew} is the evaporative heat transfer and the radiative heat transfer rates (in W/m^2) between the basin water and the air flow and can be approximated by (5) with T_g and p_g replaced by T_f and p_r .

q_{rw} is the radiative heat transfer rates (in W/m^2) between the basin water and the cover and can be calculated by (6).

q_{cfg} is the convective heat transfer rate (W/m^2) between the flow and the cover given by

$$q_{cfg} = 2.785 \left(\frac{V^{0.8}}{L_s^{0.2}} \right) (T_f - T_g) \quad (21)$$

where V is the air flow velocity (m/sec) and L_s is the still length (m).

q_{ca} and q_{ra} are the convective and radiative heat transfer rates (in W/m^2) between the cover and the ambient surroundings, computed from by using Eqs. (7) and (8), respectively.

q_{w-b} and q_b are the heat transfer rates (in W/m^2) between the water and the basin and between the basin and the ambient surroundings and can be calculated from Eqs. (9) and (10), respectively.

Q_T is the total horizontal solar radiation incident on the still, in W/m^2 .

Q'_T is the total solar radiation incident on the water surface, after transmittance through the cover, in W/m^2 .

Q''_T is the total solar radiation incident on the basin, after transmittance through the basin water, in W/m^2 .

m_f is the mass rate of the air flow, in kg/s .

m_{ew} is the mass rate of the evaporation from the basin water to the air flow, in kg/s .

g , w and b are the solar absorptance values of the cover, of the water and of the basin, respectively.

M_g , M_w , M_f and M_b are the heat capacities of the unit area of the cover, of the water, of the air in the still and of the basin, in $J/m^2 \text{ } ^\circ C$.

T_g , T_w , T_f and T_b are, respectively, the temperatures of the cover, water, air in the still and the basin, in $^\circ C$.

H_{fg} is the latent heat of vaporization of water at the temperature T_f , in J/kg .

w_{in} and w_{out} are the moisture contents of the air-vapor mixture at the inlet and outlet of the still, in kg/kg .

h_{in} and h_{out} are the enthalpies of the still inlet and outlet air, in J/kg . Assuming that the air in the still is reasonably well mixed, the enthalpy of the still outlet h_{out} can be calculated as a function of the temperature T_f as follows:

$$h_{out} = (T_f + w_{out} \times (2501 + 1.805T_f)) \times 103 \quad (J/kg) \quad (22)$$

The amount of the distillate water collected inside the still will depend on the temperatures of the air and the cover. Water will condense on the cover surface only when the dew point temperature of the air flow, T_{fd} , is higher than the cover temperature, T_g . In this case, the amount of the distillate water collected from the cover, m_{ew-g} (in $kg/s.m^2$), can be calculated from

$$\dot{m}_{ew-g} = \frac{q_{con-g}}{h_{fg}} \quad (kg/s.m^2) \quad (23)$$

h_{fg} is the latent heat of vaporization of water at the temperature, T_f , in J/kg .

$q_{con-g} = h_{con-g}(T_f - T_g)$ is the condensate heat transfer rate between the flow and the cover (in W/m^2). Using the Nusselt number in condensing:

$$Nu = \frac{h_{con-g} L_c}{k} = 0.943 \left(\frac{g^2 \sin \beta h_{fg} L_c^3}{\mu k \Delta T} \right)^{1/4} \quad (24)$$

where:

L_c = the length of the cover, in m; $L_c = L_s$

k = thermal conductivity, in W/m K

g = gravitational constant, 9.81 m/s²

β = the slope of the cover, in degree

ρ = the air density, in kg/m³

ΔT = the difference between the dew point temperature of the flow and the cover temperature, in °K

μ = absolute viscosity, in Pa.s

Using the properties of the air at $T_f = 40^\circ\text{C}$, one can achieve

$$q_{con-g} = 70.93 \left(\frac{\sin \beta}{\Delta T L_c} \right)^{0.25} \quad (25)$$

Therefore, using the five equations from Eqs. (11) and (12), the five unknown parameters, T_g , T_w , T_f , w_{out} and T_b , can be solved.

3.2. The performance of the condenser and preheater

The theory of the performance of dehumidifying and of heating coils has been developed and is presented in [14, 15]. However, an explicit procedure for calculating the performance of dehumidifying coils was not available in these references. Therefore, the modeling of the performance of the condenser and the preheater in this simulation program was derived from the handbook and the standard. The calculation procedures for the psychrometric properties of humid air were given in [14]. A detailed description of the procedures for modeling the performance of the preheater and dehumidifying coils in solar still is described in [15].

The procedure for modeling the performance of the preheating coil involves (i) calculating the overall coefficient of heat transfer for the coil, (ii) calculating the effectiveness of the coil and then (iii) computing the temperatures of the air and cooling water leaving the coil.

The procedure for modeling the performance of the dehumidifying coil involves using an iterative process to find a consistent set of temperature and humidity values, subject to the constraints imposed by the performance characteristics of the dehumidifying coil.

4. Analysis of factors affecting the production of solar stills

The important factors affecting the output of a solar still can be summarized in **Figure 4**.

4.1. Effects of weather conditions

4.1.1. Impact of solar radiation

Solar radiation is the main and the most important factor to yield distilled water. The greater the radiation received, the greater the volume of distilled water produced and vice versa. However, the greater the radiation, the greater the heat loss of the still. Therefore, the insulation of the still needs to be carefully considered.

4.1.2. Effect of wind speed

Wind speed values were varied from 0 to 6 m/s when inputted into SOLSTILL [12]. Hourly solar radiation data and ambient temperature data are included in the software.

The results showed that as the wind speed increased from 0 to 3 m/s, the higher wind speeds gave greater water output. This can be explained by noting that high wind speeds will cool the glass cover faster, leading to an increased temperature difference between the water and the

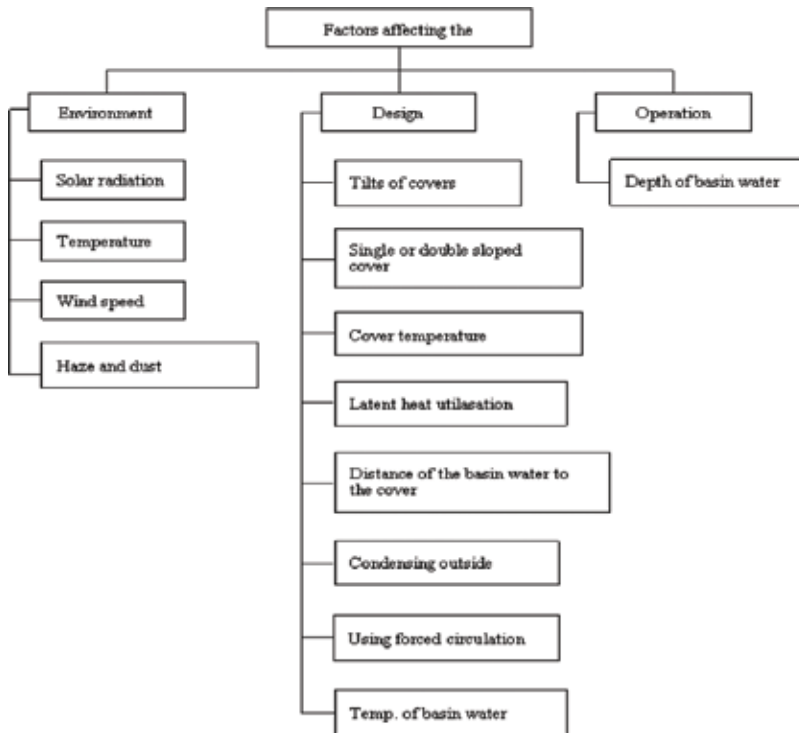


Figure 4. Factors affecting the outputs of solar distillation systems.

cover layer. However, when the wind speed increased from 3 to 6 m/s, the distilled water output increased only 1.6%. As noted above, the wind speed is too high and leads to heat loss, so that the gain in water output is almost negligible. This result is consistent with Cooper's survey [16]. In his research, as Cooper increased wind speeds from 0 to 2.15 m/s, the output of the still rose by 11.5%; when wind speed was increased from 2.15 to 8.81 m/s, the output of distilled water increased by only 1.5%.

4.1.3. Effect of ambient temperature

The influence of ambient temperature on (i) insulated distillation devices and (ii) uninsulated distilling equipment was studied, and the results are shown in **Figure 5**. In case (i), the decrease in ambient temperature leads to a higher distilled water output, while in the case of (ii), the opposite is observed. This can be explained as follows: for the distillation equipment with good insulation, lower temperature will help cool the glass cover faster, thereby increasing the temperature difference between the water layer and cover sheet. However, when the distillation equipment is not insulated, low ambient temperature increases heat loss of the device, leading to a reduction in water temperature in the equipment. Low-temperature still cools the glass cover, but the results in **Figure 5** show that the impact of increased heat loss is more important than the impact of lower glass temperature.

The change of $\pm 5^\circ\text{C}$ in well-insulated distillation systems will make the average distilled water output change $\pm 4.5\%$. This result is consistent with the results of the Khalifa and Hamood [17]. Their research has shown that when the ambient temperature rose from 26.7 to 37.8°C, the outputs may rise 11% and when temperatures are reduced from 26.7 to 15.6°C, the outputs fall 14%.

The change of $\pm 5^\circ\text{C}$ ambient temperature for insulated distillation devices make the distilled water output $\pm 2.5\%$ change, as a result of SOLSTILL [12].

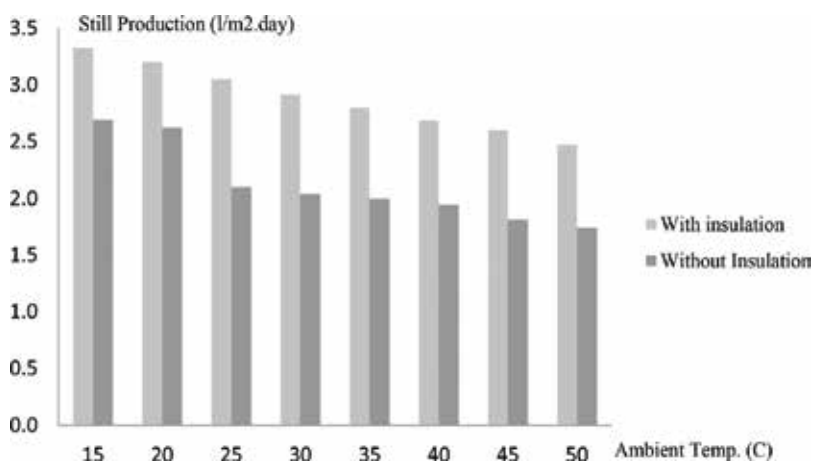


Figure 5. Effect of temperature on the output of solar stills [12].

4.1.4. Effect of the haze and dust

Solar stills, being placed outdoors to receive direct solar radiation, cannot avoid dust on the surface of coated glass. This reduces the coefficient of radiation incidents, thus reducing the efficiency of the distillation equipment. Additionally, if dust enters the inside surface of the glass, it can affect the condensation flow down to the collecting gutters with the distilled water dripping halfway down the glass. So, it is necessary to regularly check and clean the inside and outside of the cover to achieve the highest efficiency.

The simulation results of SOLSTILL show very clearly the dependence of distilled water output to the intensity of solar radiation that the distillation equipment receives [12].

4.2. Effects of cover properties

4.2.1. Effect of glass cover's tilt

Distilled water output depends very much on the elements of the cover's angle and tilt direction. To ensure the distilled water will not drip while halfway down to the collecting gutters, the tilt of the covers must be more than 15° . On the other hand, it is necessary to reduce the average distance between the water surface and the tilted covers; the tilt of the covers must be not more than 20° [17]. The SOLSTILL program also produces similar results, with the still output dropping rapidly when the cover slope angles are greater than 30° [12].

4.2.2. The effects of single-sloped and two-sloped (roof type) covers

SOLSTILL can also be used to simulate the distillation equipment using one cover (single sloped) and two covers (double sloped, also known as roof type); the tilt is 15° in both cases. This assumes that the coverings the two types of devices have are the same and their axes lie along the east-west direction. The yields of the two distillation devices are shown in **Figure 6**.

The results show that the distillation device with double-sloped cover works better in late spring and summer while the distilling equipment with single-sloped cover works better in

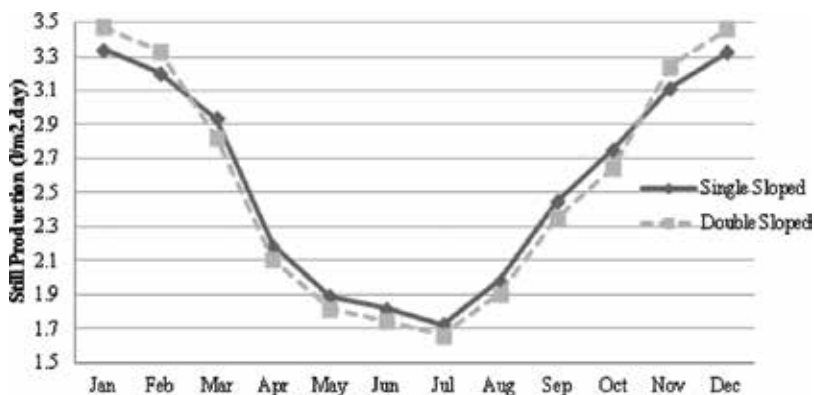


Figure 6. The output of distilled water per month single roof and roof-type double.

other seasons. This can be explained by the fact that in the late spring and summer, sunrise and sunset are to the south of the east-west axis. Therefore the kind of roof-type cover will benefit from having the second roof (that means a south heading) in the early morning and late afternoon. At other times of the year, the still with single-sloped cover will get all the available solar radiation and over a year; this still performs a little better. This is consistent with the experimental results of Garg and Mann [18].

Therefore, theoretically, one sloped cover should give a little more output than those having two slopes. In practice, however, the use of single slope introduces additional difficulties during system construction, requiring additional materials, and has more problems in terms of structural stability in high winds than the roof-type still. This may be the reason why the roof-type stills are still more favored.

4.2.3. Effect of the temperatures of the covers

Cooper, Khalifa and Hamood, Garg and Mann [16–18] showed that the glass covers can absorb approximately 4.75% of solar radiation energy, leading to an increase of the cover's temperature. On the other hand, the condensation of water below the glass surface creates a condensation water film, leading to a partially opaque glass surface and an increase in the glass' temperature. As a result, the temperature difference between the surface of the water and condensation glass cover will be reduced. Therefore, seeking to reduce the surface temperature of the glass is important in order to improve the water productivity (output) of the device [17].

To reduce the temperature of the glass cover, one can speed up the wind outside as mentioned in Section 4.1.2. However the wind is also a natural factor, and it is difficult to control this. So Husham [19] proposed a different approach—use a water cooling membrane on a piece of glass using tap sprays on the glass surface every 30 s with the time interval for the spray test of 10 and 20 min, respectively. Results of regular sprinkling helped increase productivity to 31.8 and 15.7%, respectively.

In the next section, the measures taken to reduce the temperature of covers and results achieved by this will be presented.

4.2.4. Utilizing the latent heat of evaporation

To take advantage of the latent heat of water vapor in the condensation, numerous studies have used distillation device models with two flat tanks (double basin) and three flat tanks (triple basin) [20]. This is a useful way to increase production of distilled water. However this device is complicated and costly. In Section 5 of this chapter, the results of experiments to take advantage of the latent heat of evaporation will also be shown.

4.2.5. Effect of the distance between the water level and covered glass

The distance between the water surface coverings can affect the effectiveness of the solar distillation systems. As discussed in Section 4.2.1, if the distance between the water surface and coverings is small, the convective resistance of wet air flow inside the device is smaller, so that efficiency will be improved. But this gap is influenced by the inclination of coated glass. If

the tilt of the cover is increased, then the average distance between the water surface and coverings is widened, so the output of the still will decrease. In the latter part of this paper, the measures on a stepped solar still to achieve the smallest distance between the water level and the glass in order to achieve highest distilled water output will be presented.

4.3. Effects of water properties

4.3.1. The effect of water temperature in the still

The water temperatures in the equipment greatly affect the output of distilled water. As mentioned in Section 4.2.3, water on the cover as a thin film cools down the glass before running into the still. By using the latent heat of steam in the steam condensation under the glass covers, water can be heated and fed into the device. This approach can be applied to both passive and active solar stills.

In Section 5 of this chapter, the use of glass vacuum tubes to heat up the water in the basin of the still will be presented.

4.3.2. The effects of water depth in the still

The depth of water in the device greatly affects the yield of distilled water. Due to thermal inertia, the deep water layers will make the absorption process of solar energy take longer, thus slowing the increase of water temperature and affecting the amount of distilled water. The experimental results of a single-basin solar still coupled with evacuated glass tubes [21] show that a test with a 1 cm depth of water in the basin produces 5.265 l/m², which is 13.4% higher than a test using a 2 cm depth of water which produces only 4.555 l/m², as shown in **Figure 7**. This agrees with the theoretical and experimental results in other researches [17, 22, 23].

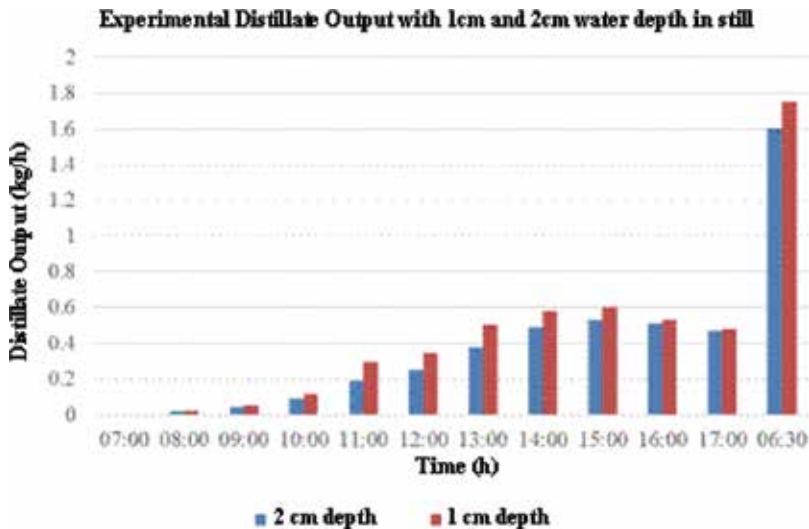


Figure 7. Experimental distillate output with 1 and 2 cm water depth in the single-basin solar still coupled with evacuated glass tubes [21].

4.4. Effects of other factors

4.4.1. Using the external condensing device

In traditional solar basin distillation systems, the glass covers are used to condense distilled water. This method enables the device to have a simple structure, but it also has two disadvantages:

- Latent heat of vaporization released during condensation makes the temperature of the coated glass increase, resulting in increasing water vapor pressure near the coverings. This reduces the pressure difference between the water evaporative layer and the condensation surface.
- The condensation of distilled water under the glass surface creates a film or droplet layer, reducing the ability of solar radiation penetrating the glass cover and reaching the bottom of the absorbing surface.

The use of an external condenser and a recovery heat exchanger to take advantage of moist air stream with high temperature and humidity returned to the distillation system was also proposed and tested [12]. The results showed that the use of an external condenser could increase output by 25% (average daily output of 3.87 l/m² compared to 3.10 l/m²) and the use of a recovery heat exchanger to circulate the moist air can increase by nearly 54% the output of distilled water (average daily output of 4.76 l/m² compared to 3.10 l/m²).

In Section 5 of this chapter, the results of theoretical and empirical research on the use of an external condenser for a solar passive (or natural convective) still will be presented.

4.4.2. The effect of the generation of forced convection inside the still

The process of heat and mass transfer inside a conventional solar still is a natural convective process. The low efficiencies of a conventional solar still may be overcome by changing the operation principles as follows:

- Using air as an intermediate medium and substituting forced convection for natural convection to increase the heat coefficients in the still, resulting in increased evaporation of water
- Replacing saturated air in the standard still by “drier” air to increase the potential for mass transfer in the still, leading to higher outputs
- Circulating the air-vapor mixture from the standard still to external water-cooled condensers to gain efficiency from a lower condensing temperature. The cooler the cooling water available, the more effective this condensing process will be
- Recovering some of the heat extracted in the condensing process and using it to preheat the air-vapor mixture entering the still
- Substituting the condensing area of the flat sheet covers in the standard still by the external condenser with much larger heat exchange areas to increase condensation efficiencies

In Section 5 of the chapter, this issue will be presented in greater detail.

5. Measures to improve the productivity of solar stills

As analyzed above, the elements of the environment are the objective factors and cannot change. In this section we focus on the main measures taken in the design of the still.

5.1. Reducing the cover's temperature

In the experiments on a stepped solar still [22], a cooling water flow is sprayed with 5 l/min for 30 s on the cover with the time between two injections being 10 and 20 min. The schematic diagram of the experimental stepped solar still is shown in **Figure 8**. Experimental results show that, for a day with average solar radiation of 600 W/m^2 , the distilled water obtained is 4.45 and 4.35 l/m^2 corresponding to a period of 10 and 20 min between two injections, compared with 4.08 l/m^2 in the case with no cooling water spray to the coverings, which rises to 9 and 6.6%, respectively, as can be seen in **Figure 9**.

Similarly, in the active (forced circulated) solar still [12], the forced convection also helps to cool the covering surface, increasing the production of distilled water. When the speed of air flow in the distillation system reached 0.005 m/s , the output of distilled water was 3.53 l/m^2 compared to 3.05 l/m^2 in the case of traditional devices, with an increase of 15.7%. This result is consistent with results of Husham [19], as stated in Section 4.2.3.

5.2. Taking advantage of the latent heat of evaporation

In this study, a double-basin solar still (DBSS) combined with evacuated glass tubes has been fabricated and tested to compare it with a single-basin solar still (SBSS) with evacuated glass tubes. **Figures 10** and **11**, respectively, show the schematic diagrams of these two types of stills. Experimental results are shown in **Figure 12**. The outputs of distilled water of the two types

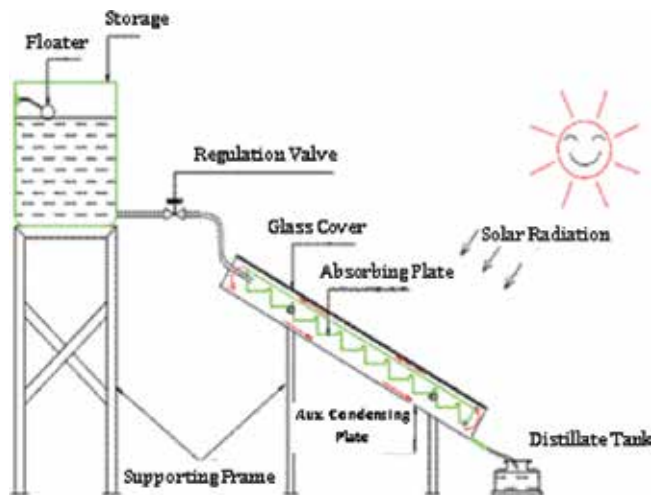


Figure 8. The schematic diagram of the experimented stepped solar still [19].

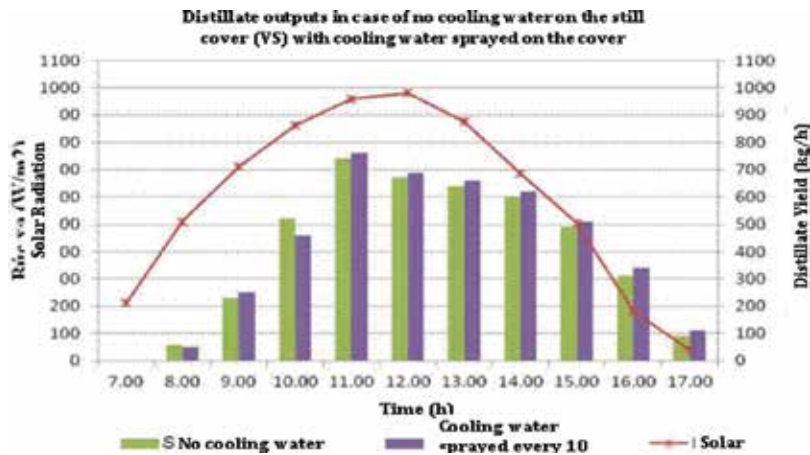


Figure 9. Distillate outputs in the case of no cooling water on the still cover (VS) with cooling water sprayed on the cover.

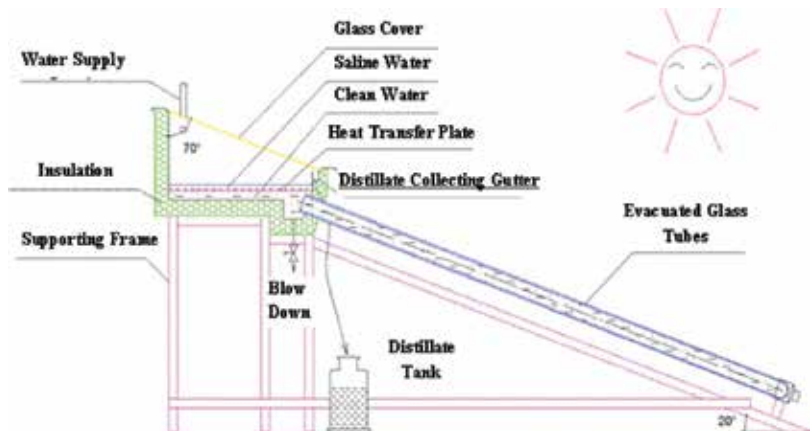


Figure 10. Single-basin solar still coupled with evacuated glass tubes.

are 6.49 and 4.99 l/m², respectively, on a day with 529 W/m² of radiation. Thus by utilizing the latent heat of evaporation, the yield of the solar double basin still was increased by 30%.

In a study on improvement of the Carocell solar distillation equipment [23], a heat exchanger with a coil size of 760 × 220 × 13 (mm) and a total length of pipe Φ8 of 6.5 m was fabricated and mounted just below the distillation equipment to utilize the heat of evaporation. On a good sunny day (700 W/m²), the amount of water collected using this heat exchanger was 6.8 compared to 5 l/m² in the case of the original Carocell still where an increase of 36% can be seen in **Figure 13**.

In the solar active still [12], taking advantage of latent heat of steam is achieved by circulating air flow through the recovery heat exchanger back to the distillation system. When the speed

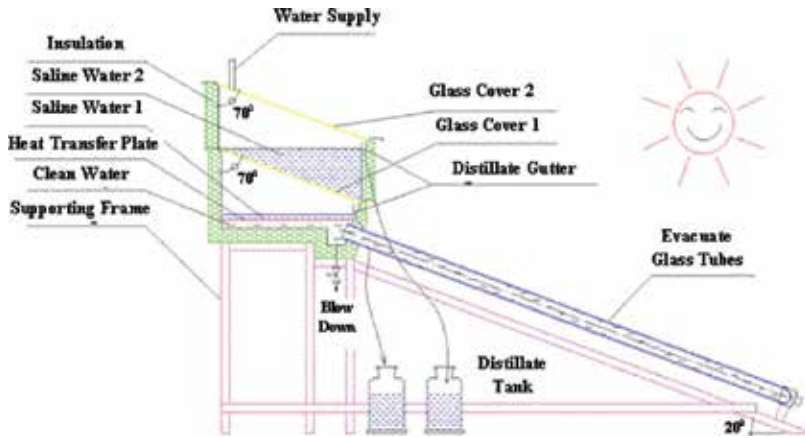


Figure 11. Double-basin solar still coupled with evacuated glass tubes.

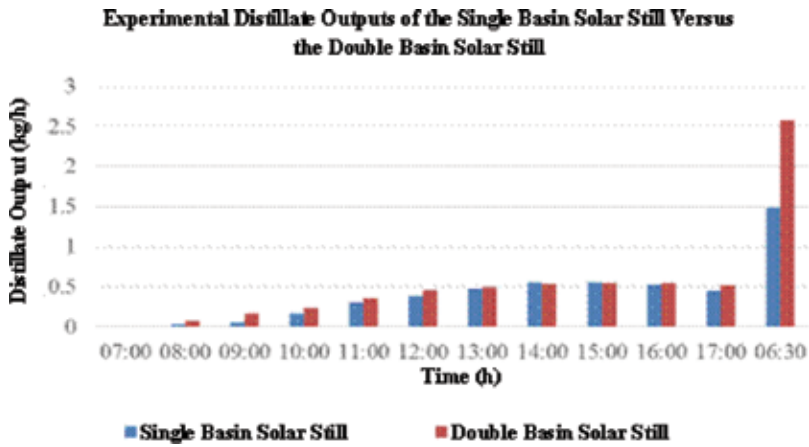


Figure 12. Experimental distillate outputs of the single-basin solar still versus the double-basin solar still.

of air flow in the distillation equipment reached 0.005 m/s, the output of distilled water obtained was 5.94 compared to 3.53 l/m² in the case of no circulation, which rose to 68%.

5.3. Reducing the gap between the glass cover and the water level

In order to reduce the gap between the glass and the water level in the still, a stepped solar distillation equipment was designed, fabricated and tested, as shown in Figure 8 [22]. Some advantages of this device:

- Over a full year, the total energy radiation projected onto the tilted surface was larger than the horizontal surface.

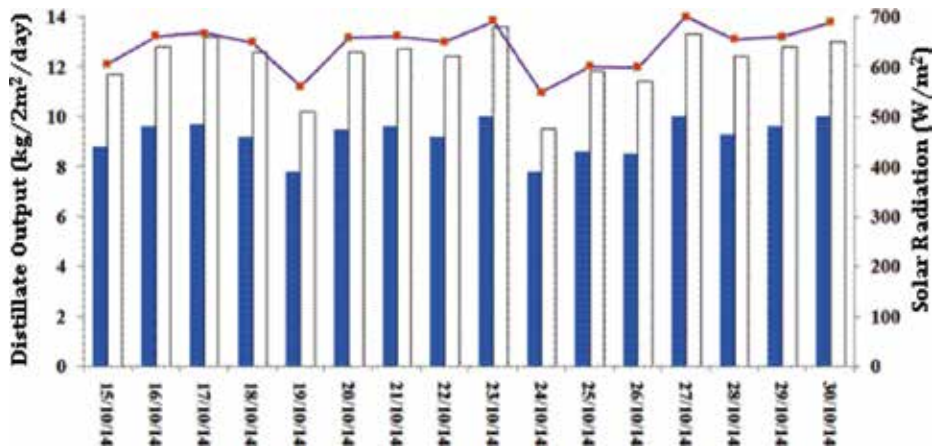


Figure 13. Distillate outputs of 2 m² Carocell solar still, with versus without a heat exchanger.

- The stepped still maintains the distance between the water and the cover at only 1 cm, reducing natural convective obstacles.
- Creating good conditions for condensation to flow into the gutters as well as reducing thermal condensation resistance of the water condensing on coverings.

The experimental results for distilled water output reached 4.9 l/m² with average radiation 635 W/m² compared to 3.05 l/m² in the case of traditional equipment, which rose about 60%, as shown in Figure 14.

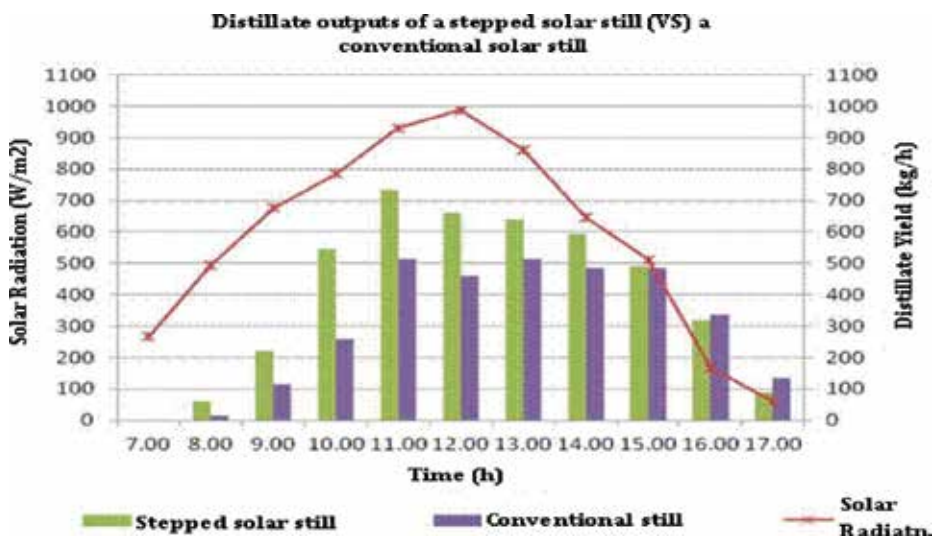


Figure 14. Distillate outputs of a stepped solar still versus a conventional solar still.

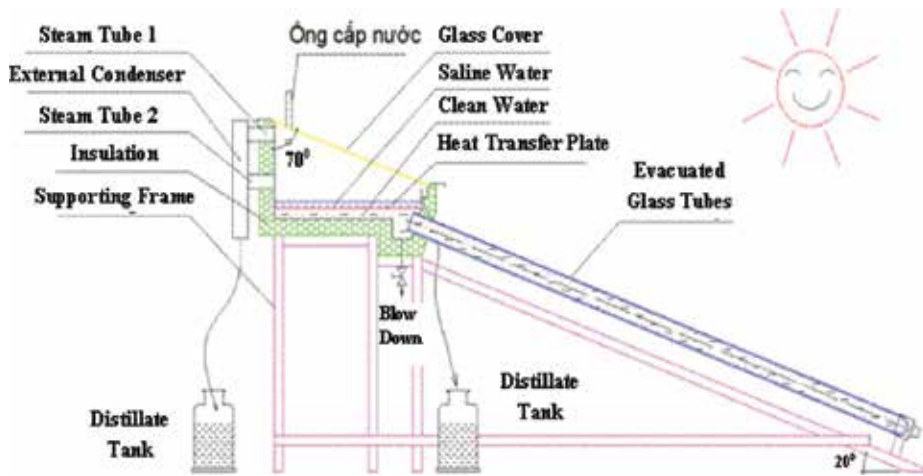


Figure 15. Single-basin solar still coupled with evacuated glass tubes and external condenser.

5.4. Separating the processes of evaporation and condensation in the device

Section 4.4.1 presented the use of an external condenser and a heat recovery to take advantage of moist air stream at high temperature and humidity returning to the still (forced convection).

For a traditional (natural convective) still, the research group manufactured and tested a still with additional external condenser [21]. The schematic diagram of the experiment is shown in **Figure 15**, and the experimental results of the solar still with external condenser in comparison with the still without the external condenser are shown in **Figure 16**. The use of the external

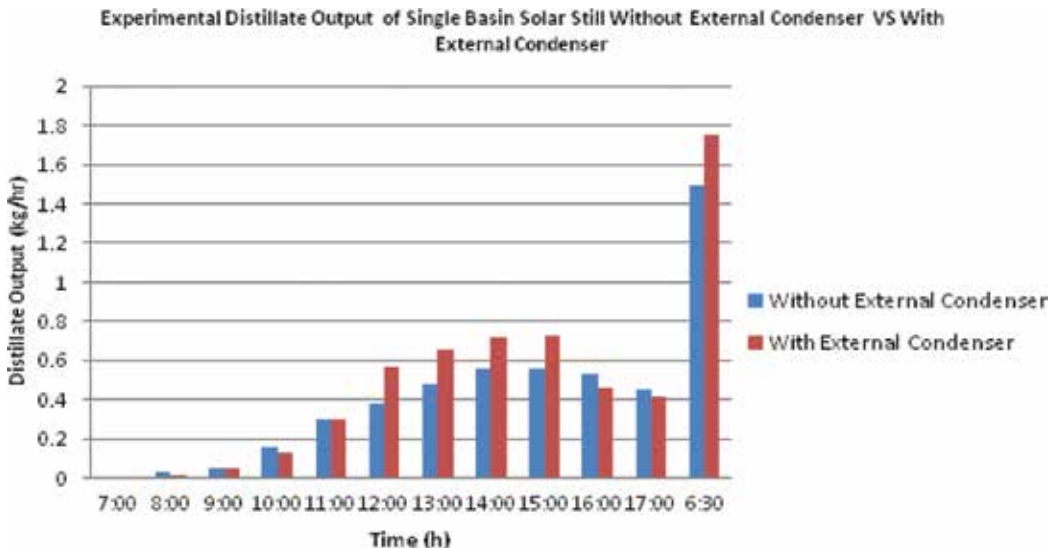


Figure 16. Experimental distillate output of single-basin solar still without external condenser versus with external condenser.

condenser resulted in the distilled water output reaching 6 l/day, almost 15% higher than the output of a still without external condenser, which achieved 5.23 l/day on a day with an average radiation intensity of 517.54 W/m².

5.5. Creating forced convection in the device

Theoretical and empirical research was conducted to assess the impact of forced convection on the solar distillation equipment [12]. The schematic diagram of the experiment is shown in **Figure 2**. A conventional solar still with a collecting area of 2,67m² (2,44 m × 1095 m), with an inside fan to change the speed of air flow, was made to measure parameters and process experimental data. Results for a typical day is shown in **Figure 17** where the water output increased 30–100% compared to a conventional solar still.

The simulation results of SOLSTILL for the production of distilled water for a whole year and the device performance in three cases—(i) forced convection with external condenser and no moist air circulated back to the still, (ii) forced convection with external condenser and moist air circulated back to the still, and (iii) traditional distillation equipment (natural convection)—show that the outputs and still efficiencies in the three cases are, respectively, 3.87, 4.76 and 3.10 l/m² and 42.9, 53.9 and 34.1% [12].

5.6. Increasing the working temperature of water in the still

To increase the working temperature of the water in the equipment in order to increase the production of distilled water, the research group used vacuum tubes to heat the water in the basin [21]. Experimental results corresponding to the day with solar radiation of 514 W/m² for

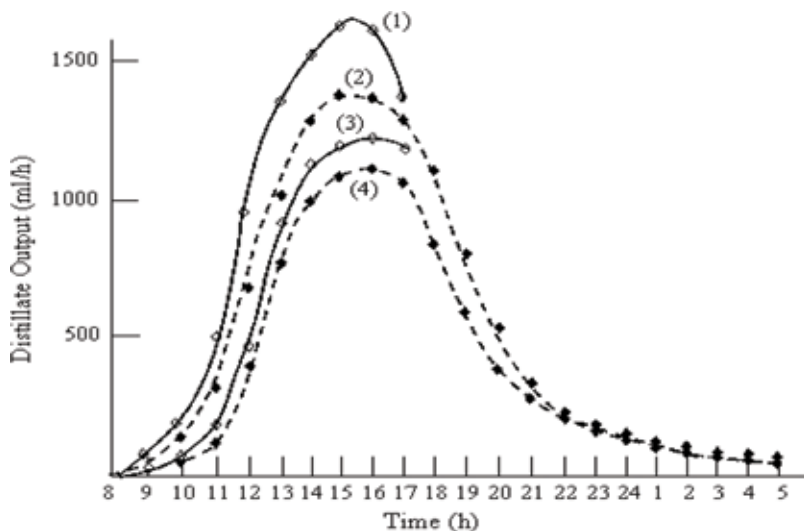


Figure 17. The effect of forced convection in the device to produce distilled water. (1) Data empirical forced convection. (2) The data forced convection theory. (3) Data empirical natural convection. (4) Data natural convection theory.

the production and performance of the device were, respectively, 5.86 l/m² and 50.3%, compared with production of 3.10 l/m² and efficiency of 34.1% of a conventional solar still.

6. Conclusion

This chapter presented a numerical model to estimate the performance of solar basin-type distillation systems, both for conventional passive solar stills and active (forced circulation) stills with enhanced heat recovery. It also analyzed the factors affecting the distillate outputs of the still, including environmental factors (external factors or natural) and elements of the design and operation (subjective factors). The subjective elements as well as the measures taken to optimize these factors were thoroughly analyzed. With these measures, the distillate yield of solar stills was increased from 30 to 68% compared with traditional distillation systems. This has scientific significance and practicality enabling the application of this technology to solar water distillation using a source of clean and renewable energy. It provides a viable way to alleviating the problem of the availability of clean water, especially in those areas and communities in countries where water resources are increasingly polluted and salty.

Author details

Bao The Nguyen^{1,2*}

*Address all correspondence to: drthebao@gmail.com

1 Institute of Sustainable Energy Development (ISED), Ho Chi Minh City, Vietnam

2 University of Technology, Vietnam National University - Ho Chi Minh City, Vietnam

References

- [1] Manchanda H, Kumar M. A comprehensive decade review and analysis on designs and performance parameters of passive solar still. *Renewables: Wind, Water and Solar, Springer Open Journal*. 2015;**2**:1-24
- [2] Sampathkumar K, Arjunan TV, Pitchandi P, Senthilkumar P. Active solar distillation—A detailed review. *Renewable and Sustainable Energy Reviews*. 2010;**14**:1503-1526
- [3] Velmurugan V, Srithar K. Performance analysis of solar stills based on various factors affecting the productivity—A review. *Renewable and Sustainable Energy Reviews*. 2011; **15**:1294-1304
- [4] Murugavel KK, Chockalingam KKSK, Srithar K. Progress in improving the effectiveness of the single basin passive solar still. *Desalination*. 2008;**220**:677-686

- [5] Kabeel AE, El-Agouz SA. Review of researches and developments on solar stills. *Desalination*. 2011;**276**:1-12
- [6] Badran OO. Experimental study of the enhancement parameters on a single slope solar still productivity. *Desalination*. 2007;**209**:136-143
- [7] Kaushal A, Varun. Solar stills: A review. *Renewable and Sustainable Energy Reviews*. 2010;**14**:446-453
- [8] Muftah AF, Alghoul MA, Fudhodi A, Abdul-Majeed MM, Sopian K. Factors affecting basin type solar still productivity: A detailed review. *Renewable and Sustainable Energy Reviews*. 2014;**32**:430-447
- [9] Sharshir SW, Yang N, Peng G, Kabeel AE. Factors affecting solar stills productivity and improving techniques: A detailed review. *Applied Thermal Engineering*. 2016. 10.1016/j.applthermaleng.2015.11.041
- [10] Kabeel AA, Omara ZM, Essa FA, Abdullah AS. Solar still with condenser—A detailed review. *Renewable and Sustainable Energy Reviews*. 2016;**59**:839-857
- [11] Dunkle RV. Solar water distillation: The roof type still and a multiple effect diffusion still. In: *International Developments in Heat Transfer*, American Society of Mechanical Engineers, Proceedings of International Heat Transfer; 1961. pp. 895-902
- [12] Nguyen BT. SOLSTILL—A simulation program for solar distillation systems. In: *Proceedings of EUROSUN*; Freiburg; 2004. pp. 96-105
- [13] Duffie JA, Beckman WA. *Solar Engineering of Thermal Processes*. 4th ed. New York: John Wiley and Sons Inc.; 2013
- [14] ASHRAE *Systems and Equipment Handbook*. New York: American Society of Heating, Refrigerating and Air-Conditioning Engineers; 2012
- [15] AHRI. *Forced-Circulation Air-Cooling and Heating Coils. Standard 410*. Arlington, Australia: Air-Conditioning, Heating and Refrigeration Institute; 2014
- [16] Cooper PL. Digital simulation of transient processes solar still. *Solar Energy*. 1969;**12**:333-346
- [17] Khalifa AJN, Hamood AM. Effect of insulation thickness on the productivity of basin type solar stills: An experimental verification under local climate. *Energy Conversion and Management*. 2009;**34**:2457-2461
- [18] Garg HP, Mann HS. Effect of climatic, operational and design parameters on the year round performance of single sloped and double sloped solar still under Indian arid zone conditions. *Solar Energy*. 1976;**18**:159-163
- [19] Husham MA. Seasonal performance evaluation of external passive solar stills connected to condensers. *Journal of Advanced Science and Engineering Research*. 2012;**2**:1-11
- [20] Tiwari GN, Singh SK, Bhatnagar VP. Analytical thermal modelling of multi-basin solar still. *Energy Conversion and Management*. 1993;**34**:1261-1266

- [21] Hoang VV, Nguyen TB. Numerical modelling of a single basin solar still coupled with evacuated glass tubes, Vietnam. *Journal of Mechanical Engineering*. 2015;6:123-129. (in Vietnamese)
- [22] Le XP, Hoang VV, Nguyen TB. Numerical modelling of a stepped solar still with a condensing auxiliary, Vietnam. *Journal of Mechanical Engineering*. 2016;1 & 2:298-214. (in Vietnamese)
- [23] Tran XA, Hoang VV, Nguyen TB. Experimental study of heat exchanger to utilize the latent heat of evaporation in order to enhance performance of Carocell solar still. *Thermal Energy Review Journal*. 2015;5:45-67

The Use of Renewable Energy for the Provision of Power to Operate Reverse Osmosis Desalination Facilities at Massawa

Cliff Dansoh

Additional information is available at the end of the chapter

<http://dx.doi.org/10.5772/intechopen.76837>

Abstract

The following energy sources, in a various combinations were assessed to provide potable water using seawater reverse osmosis (SWRO) for around 50,000 people in Eritrea: wind power and solar power. Various types of SWRO technology were employed and the cost of scenarios that were able to meet the users' water needs was compared with the costs of the equivalent diesel generator powered scenario over 25 years. The most financially-attractive scenario, a hybridised power plant using solar and wind power was compared with the equivalent conventionally (diesel generator) powered scenario using present and net present value (NPV) methodology. The discount rate used for NPV calculations was found to be pivotal for this comparison, so the logic of the appropriate discount rate was investigated and a discount rate of 3.6% was considered the most appropriate. This resulted in the renewable powered solution for this scenario being financially attractive when compared to the diesel generator powered scenario. This conclusion was mainly due to recent changes in the prices of diesel fuel in Eritrea and solar power generally. Research conducted on this scenario previously, and published in 2014 based on 2010 prices, concluded that this scenario was not financially attractive in comparison to diesel power.

Keywords: reverse osmosis desalination, solar power, wind power, renewable energy economics, discount rate

1. Introduction

Renewable energy is currently considered by many to only have viability for a small portion of energy delivery within a larger system due to intermittency.

This intermittency potentially undermines the environmental and energy security advantages on offer from renewable energy and decentralisation of supply.

This chapter:

- Sets out the investigation of the use of renewable energy sources in such a way that they could be justified for use without reliance on conventional energy sources and to stand alone as an independent and viable power source in their own right; and
- Is a continuation of research initially conducted in 2011 and subsequently published in 2014 [1], to reflect the impact of changes to diesel fuel and solar photovoltaic prices since 2011.

The scenario used to investigate the technical and financial viability of renewable energy was its use to power reverse osmosis (RO) desalination plants to provide water for the personal use of 50,000 people.

1.1. The location

Eritrea was selected due to its susceptibility to droughts, and consequential loss of life. The hypothetical pretext for the need for municipal desalination is that Eritrea has a substantial coastline, and the sea level rise expected due to climate change has the potential to hasten the intrusion of saline water into the fresh groundwater aquifers in the coastal zone. The focus of this research will be the island of Massawa, shown below, which is in a particularly dry part of Eritrea with, typically, less than 200 mm of annual rainfall as shown in **Figure 1**. This is in comparison to the UK, where according to the Metrological Office [2], the minimum rainfall between 1981 and 2010 is around 600 mm.

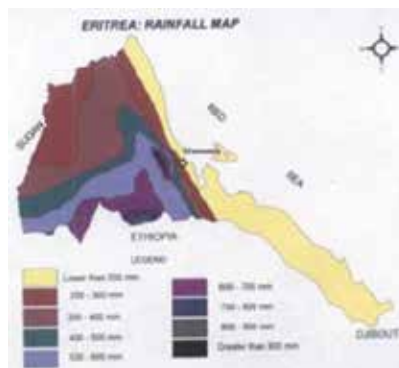


Figure 1. Rainfall map of Eritrea.

2. The modelling exercise

The modelling exercise was conducted in 3 main stages as shown in **Figure 2**.

2.1. Stage 1

Stage 1 employed Solar PV with the No Brine Stream Recovery (BSR) RO plant only as shown in **Figure 3**.

The methodology used to identify the minimum number of membranes that the RO plant would require is shown in **Figure 4**.

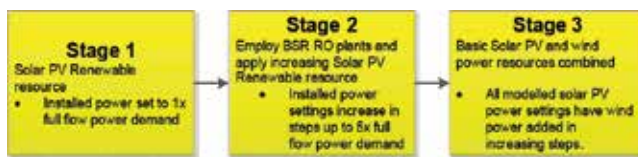


Figure 2. Three stages of modelling exercise.

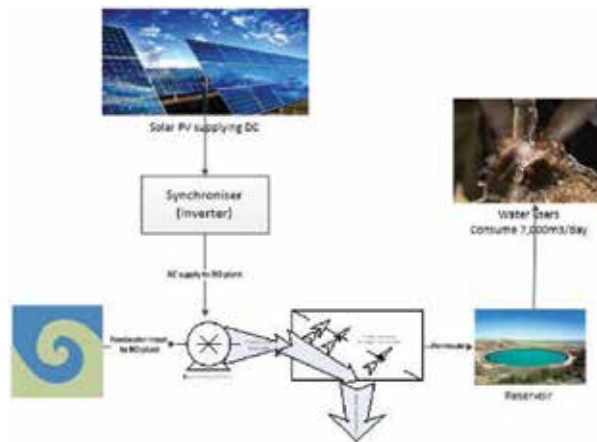


Figure 3. Single source of renewable energy to power RO plant.

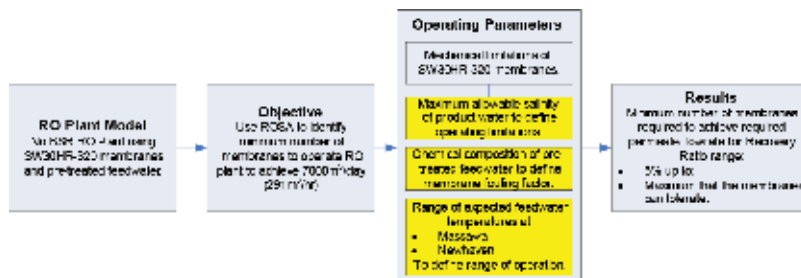


Figure 4. Methodology to identify minimum number of membranes that the no BSR RO plant requires.

2.1.1. Results

The initial results (shown in **Figure 5**) gave the minimum number of membranes required to produce 7000 m³/day, if the plant were run for 24 h continuously at each recovery ratio.

It was decided that the RO plant would operate where the minimum number of membranes required was consistent between 15 and 24% recovery ratios, as shown in **Figure 5**.

A schematic diagram of the No BSR plant employed for the modelling within this research is shown in **Figure 6**.

The resulting No BSR RO plant operating profile, including impacts on efficiency as load changes as expected due to intermittent power as indicated in the US DOE Tip sheet 2 [3], is shown in **Figure 7**.

This surface was mapped mathematically using polynomial equations and the method used to calculate the amount of water produced, was a 'for' loop in Matlab, as shown below:

```

for i = 1:rwr
    newwater1(i) = polyval(ppolycoef(index(i, :)), Pg1(i, :)) ;
end
    
```

(1)

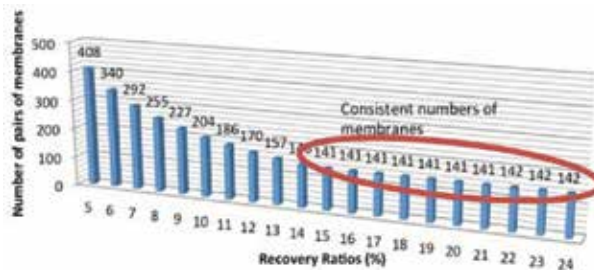


Figure 5. Minimum number of pairs of membranes at each site for maximum temperature at various recovery ratios.

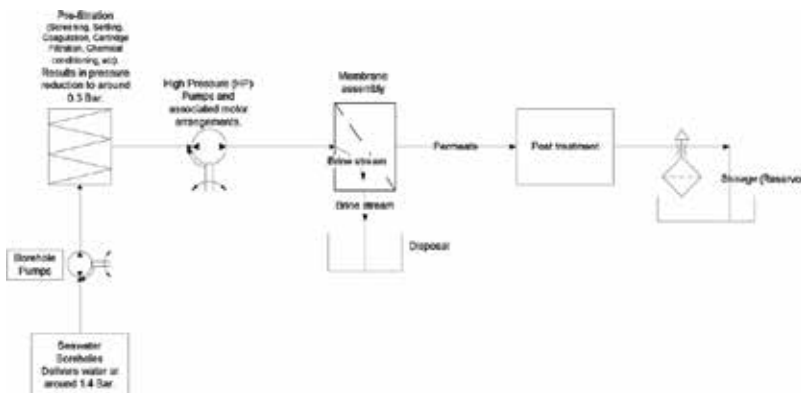


Figure 6. No BSR RO plant.

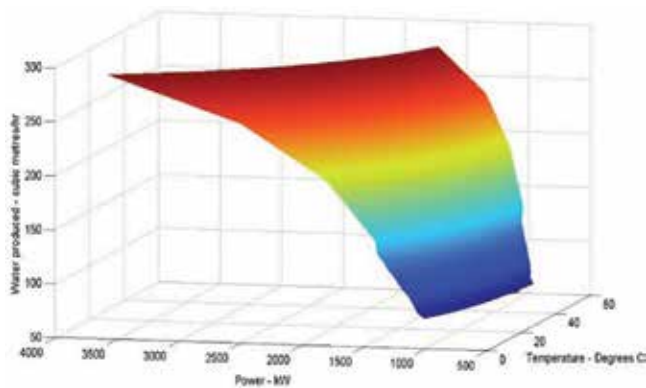


Figure 7. No BSR RO plant water production profile at varying power and feedwater temperature.

where Pg = the power available to operate the RO plant at each hour during the year; $index(i)$ identifies the location of the prevailing seawater temperature for each hour of the year; $ppolycoeff$ is a file that contains all the polynomial equations relating to each 0.01°C step from 3 to 42°C ; $i=1:rwr$ defines the number of times that the calculation should be conducted before stopping; i = the number of the calculation being conducted, in this case, conducted in sequence from $1 - (rwr)$ the max number of which is 8760 (the number of hours in a year); $Polyval$ is the matlab function that then evaluates the polynomial equation identified by $(index(i))$ making the corresponding Pg at (i) the subject.

2.2. Solar power

Massawa is one of the hottest inhabited places in the world, so solar PV was adopted.

HOMER (energy modelling software for renewable energy systems) was employed to derive the solar irradiance on an hour-by-hour basis based on the monthly averages from [4], as shown in **Table 1**.

2.2.1. Renewable energy system employed within model

The solar array for this process assumes that 10% of the available radiation, at any time when the sun is shining, is captured and converted to usable DC electrical power. This DC power is then be converted, by an inverter, to AC power, suitable for use by the RO plant. The efficiency of this power conversion was taken as between 90 and 95%.

Sufficient solar photovoltaic power was installed so that the maximum power output during the year from the solar PV would achieve the maximum flowrate of the RO plant. Additional power was then added in discrete levels, up to (and including), the power required to achieve five times maximum flowrate of the RO plant.

2.3. Stage 2

Stage 2 employed the same methodology as Stage 1 (application of solar PV only), but for the BSR RO plants (Pelton wheel and Pressure exchanger).

Month	Original monthly average (W/m ² /day during that day)	Conversion to kW/h	Clearness index* applied by HOMER
Jan	303	7.272	0.895
Feb	357	8.568	0.954
Mar	366	8.784	0.884
Apr	376	9.024	0.855
May	337	8.088	0.754
Jun	306	7.344	0.686
Jul	300	7.2	0.674
Aug	301	7.224	0.684
Sep	330	7.92	0.784
Oct	319	7.656	0.830
Nov	308	7.392	0.891
Dec	295	7.08	0.905

*The 'clearness index' is a dimensionless number between 0 and 1 indicating the fraction of the solar radiation at the top of the atmosphere that is able to pass through the atmosphere to the Earth's surface.

Table 1. Average monthly irradiance.

2.3.1. Pelton wheel

The Pelton wheel RO plant system modelled is shown in **Figure 8**.

As shown in **Figure 8**, the Pelton wheel BSR RO plant design utilises the brine/concentrate stream to power a Pelton wheel turbine, which is mechanically linked to a high pressure pump arrangement and partially pressurises the incoming feedwater. This reduces the external power required to raise the feedwater pressure. The resulting Pelton wheel BSR RO plant water production profile, at varying input power and feedwater temperatures, is shown in **Figure 9**.

2.3.2. Pressure exchanger

The pressure exchanger RO plant system modelled is shown in **Figure 10**.

As shown in **Figure 10**, the pressure exchanger BSR RO plant uses the brine/concentrate stream to pressurise a hydraulic chamber. This hydraulic chamber acts on a piston arrangement, which in turn is used to partially pressurise the incoming feedwater. A booster pump then raises the now partially pressurised feedwater to the correct pressure to combine with the feedwater pressurised by the high pressure pump for desalination by the RO plant membranes.

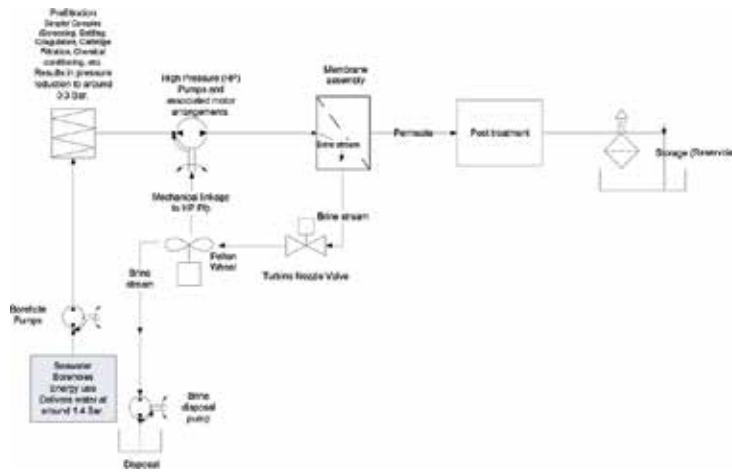


Figure 8. Pelton wheel BSR RO plant.

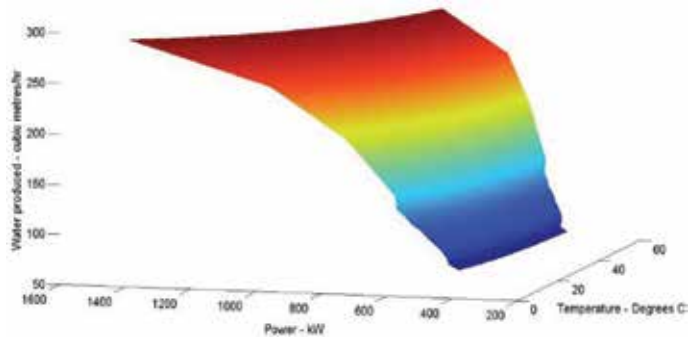


Figure 9. Pelton wheel BSR RO plant water production profile at varying power and feedwater temperatures.

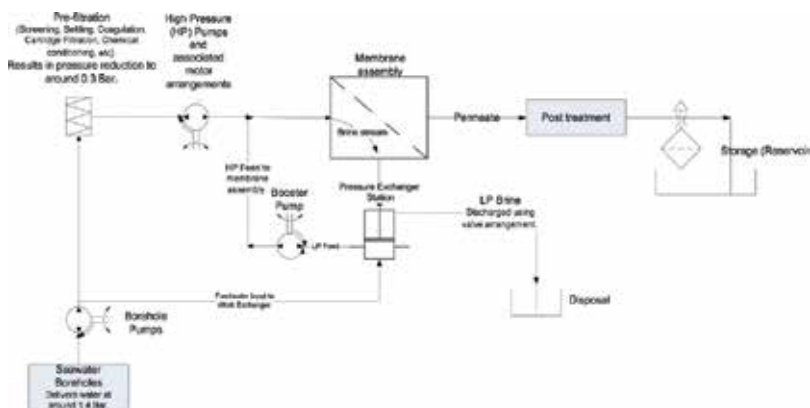


Figure 10. Pressure exchanger BSR RO plant.

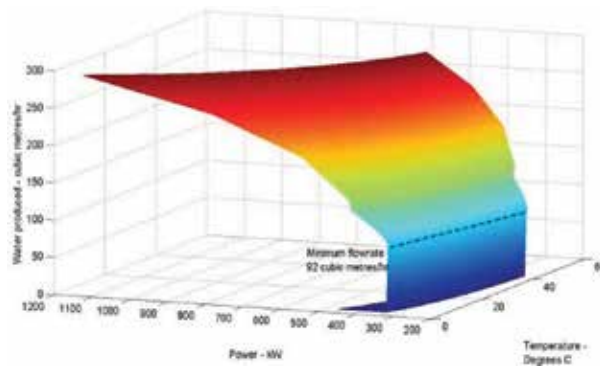


Figure 11. Pressure exchanger BSR RO plant water production profile at varying power and feedwater temperatures.

The resulting pressure exchanger BSR RO plant water production profile, at varying input power and feedwater temperatures, is shown in **Figure 11**.

As was the case in Stage 1, additional solar PV power was added in discrete levels up to (and including) the power required to achieve five times maximum flowrate of each of the RO plants.

2.4. Stage 3

Stage 3 modelled the addition of wind power in an attempt to make the renewable powered scenario competent to produce the correct amount of potable water for the Massawa residents.

2.4.1. Wind resource available Massawa

The monthly average wind speed data at Massawa was taken from monthly average data over 4 years based on local weather reports [5] and applied to HOMER to derive the wind speed for each hour of the year, shown in **Figure 12**.

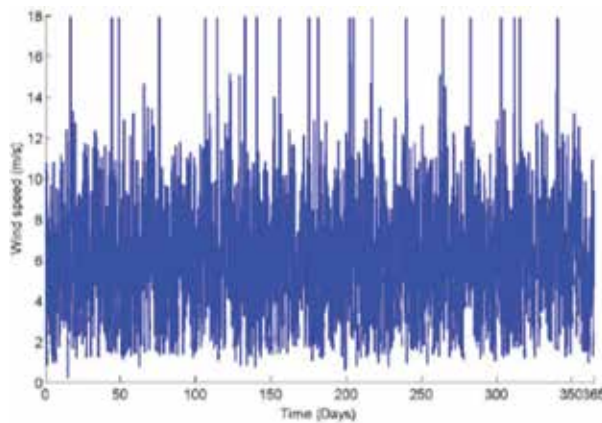


Figure 12. Wind speeds at Massawa over 1 year.

As was the case in the previous Stages, additional wind power was added in discrete levels up to (and including) the power required to achieve five times maximum flowrate of each of the RO plants.

2.5. Scenarios modelled and scaling of renewable energy scenarios

Sixty scenarios were modelled with BSR and No BSR RO plants limited to 7000 m³/day output capacity with varying installed solar PV and wind capacity.

There was limited success in identifying scenarios that were able to meet the water demands of the local population without increasing the capacity of the RO plant to compensate for intermittency.

So, each of the RO and Power plant scenarios were scaled up by the ratio of water shortfall, i.e. if the combined RO plant and Power scenario made 50% of required water, both the RO plant and installed power are doubled in size to fully meet the water demand requirements.

3. Costs

Prices are based on exchange rate of \$1–£0.636 as was the case in 2011, when much of the original research was conducted.

3.1. RO plant and reservoir costs

Table 2 shows the CAPEX and OPEX costs associated with the unscaled RO plants employed based on [6–10].

Reservoir costing was taken as £82,115,200 based on extrapolation of various reservoir costs from [11] to meet the required holding capacity.

3.1.1. Impacts of intermittency

Intermittent operation of desalination plants is possible and has already been realised in smaller systems as shown in [12, 13]. According to Rizzuti [14], however, it is understood that for large-scale seawater desalination plants, the plant’s lifetime could be reduced by increased scaling, fouling and corrosion.

This said, there is potential for the mechanical wear aspects on the plant to be reduced due to the increased size of the scaled up renewable RO plant, as the components will not experience

(£x10 ⁶)	No BSR	Pelton wheel	Pressure exchanger
Capital costs	9.27	10.38	11.12
Total costs over 25 years	48.8	79.1	56.0

Table 2. Capital, O&M and total costs over 25 years for RO plants.

the stress of operating at full load for as much of the time. It was considered reasonable to conclude that the impact on RO plant operation and costs will vary based on the power supply intermittency. The degree of this impact is not well understood and is worthy of further investigation, but based on the research conducted, it is considered appropriate to increase O&M costs to acknowledge the impact of intermittency. Therefore, in the light of the lack of information to support accurate estimates, a pessimistic assumption was employed for intermittent operation that annual O&M costs increase by 100% over those of a continuously operated plant on a per m³ of water produced basis increasing the costs as shown in **Table 3**.

3.2. Renewables

Table 4 shows the CAPEX and OPEX costs associated with the renewable energy sources employed including the reduction in the price of solar PV between 2010 and 2016.

3.2.1. Reduction in solar PV price in 2016

Figure 13, taken from the National Renewable Energy Laboratory (NREL) report on solar costs [17], shows how costs for solar PV has reduced significantly since 2009.

The costs employed for 2017 were based on the ‘utility scale PV, fixed tilt (100 MW) as shown on the right hand side of **Figure 13**. \$1.42/W = £903/kW.

This was considered to be an optimistic price due to Massawa’s relatively remote location and limited market potential and so the supply chain cannot be relied upon to be developed to a stage where it provides competitive pricing. The NREL webpage [18] shows deviation of +/- \$694/kW about a mean cost of \$2025/kW, which would make the worst case cost \$2719/kW (£1729/kW).

So for the purpose of this report the CAPEX for the plant was taken as £1700/kW, which assumes that the PV costs are at the higher end of the range.

Operating cost for	No BSR (£)	Pelton wheel BSR (£)	Pressure exchanger BSR (£)
Continuous operation (£/m ³)	0.62	1.08	0.70
Intermittent operation (£/m ³)	1.24	2.16	1.40
Intermittent operation/ year (£x10 ⁶)	3.16	5.52	3.58
Intermittent operation over project life (£x10 ⁶)	79	138	90

Table 3. Continuous and Intermittent O&M costs for the BSR and no BSR RO plants.

	Solar (2010) [15]	Solar (2016)	Wind [16]
Capital costs (£/kW installed)	3000	1700	1200
O&M costs (£/kW/annum)	15	16	37

Table 4. Capital and O&M costs of renewable energy sources.



Figure 13. Residential, commercial and utility scale PV system cost reduction since 2009 [17].

3.2.2. Operations and maintenance costs

The NREL webpage [18] indicates the O&M costs for a PV system between 1 and 10 MW are \$16 +/- \$9/kW, which equates to a high end cost of \$25/kW (£15.90/kW).

The Operation and Maintenance (O&M) costs for the plant were taken as £16/kW, which assumes that these costs are, once again, at the higher end of the range, due to the expected lack of a competitive local market.

3.3. Conventional power costs

Table 5 shows the CAPEX and OPEX costs associated with the diesel generator power plant modelled at Massawa, which is based on various sources.

3.3.1. Increase in diesel fuel prices in Massawa

The history of the diesel fuel price is shown in **Table 6** based the following internet sources [21–23].

	Diesel generator costs for 25 years based on 2010 fuel price				Diesel generator costs for 25 years based on 2016 fuel price	
	Installed power costs (£) [19]	Fixed O&M costs (£) [19]	2010 fuel costs (£×10 ⁶) based on £0.71/l [20]	Total scenario costs (including RO plant and reservoir) (£×10 ⁶)	2016 fuel costs (£×10 ⁶) based on £1.75/l	Total scenario costs (including RO plant and reservoir) (£×10 ⁶)
No BSR	380,000	40,000	100.2	232	260.1	392
Pelton wheel	160,000	27,500	43.4	205	114.8	276
Pressure exchanger	125,000	22,500	32.8	171	87.5	226

Table 5. Capital and O&M conventional power plant scenario costs.

Date	Price (\$)	Price (£)
2017 (estimated)	2.75	1.749
2014	3.00	1.908
2012	1.71	1.08756
2010	1.07	0.68052
2008	1.07	0.68052
2006	0.81	0.51516
2004	0.40	0.2544
2002	0.25	0.159
2000	0.33	0.20988
1998	0.23	0.14628
1995	0.19	0.12084
1992	0.29	0.18444

Table 6. Historic and estimated diesel fuel cost in Eritrea.

As can be seen from **Table 6** the price of diesel fuel in Eritrea has increased 10 fold between 1992 and 2014, the latest date that price information is available from the sources used. 2014 was a relatively high price point when in the UK diesel fuel was around £1.29/l, but by June 2017 the price of diesel fuel in the UK had fallen to £1.18/l, a reduction of 8.5% due, in part, to the fall in crude oil prices. Although the influences in the price of retail diesel fuel are affected by different variables in the UK and Eritrean economies, for the purposes of this research a reduction of 8.5% of the 2014 price has been adopted for the price of diesel in Eritrea to account of the fall in crude oil price. This results in an estimated price for 2017 of \$2.75/l (1.75/l) as shown in **Table 6**.

4. Results

Shown in **Table 7** are the results for the costs of the most financially attractive scenarios for each stage of modelling power source and RO plant type in comparison with the diesel generator powered plant.

Scenarios that have become financially viable (are cheaper than the diesel generator powered equivalent), due to the application of latest diesel fuel and solar PV prices are highlighted in yellow and the most financially attractive is in 'bold' font.

The changes in solar PV and diesel fuel prices have made the renewable powered scenario much more financially attractive than in 2010, but only the renewable powered No-BSR RO plant scenarios have actually become financially attractive in comparison to the diesel generator powered scenario (**Table 7**). The most financially attractive scenario is estimated to cost 77% (around $\frac{3}{4}$) of the cost of the conventionally powered plant over the project's 25-year life.

Stage	Type of RO plant	Solar Power (MW)	Wind Power (MW)	Ratio of renewable scenario cost against Conventional based on 2010 fuel and solar PV prices	Ratio of renewable scenario cost against Conventional based on 2017 fuel and solar PV prices	Percentage difference (%)
1	No BSR	26.34	0	1.72	0.93	46.01
2	No BSR	37.2	0	1.63	0.84	48.39
	Pelton Wheel	21.3	0	2.02	1.40	30.69
	Pressure Exchanger	17.4	0	1.90	1.34	16.43
3	No BSR	17.37	9.93	1.39	0.77	45.02
	Pelton Wheel	10.24	10.54	1.69	1.21	28.6
	Pressure Exchanger	3.76	9.67	1.46	1.09	25.8

Table 7. Technically competent and most financially viable scenarios at Massawa when latest diesel and solar PV prices are applied.

5. NPV

The net present value (NPV) is a central tool in discounted cash flow (DCF) analysis, where each cash inflow/outflow is discounted back to its present value (PV). Then they are added together. So, NPV is the sum of all the terms:

$$R_t / (1 + i)^t \quad (2)$$

where t - the time of the cash flow; i – the discount rate (the return that could be earned on an investment in the financial markets with similar risk.); the opportunity cost of capital; R_t - the net cash flow (the amount of cash, inflow (value of water sold) minus outflow (the cost to maintain the power source and RO plant) at time t).

The next two sections will derive the following to allow the NPV to be calculated.

- Price of water
- Discount rate

5.1. Price of water

As part of an informal telephone conversation, Tesfai [24] stated that municipal water in Eritrea costs less than 5p/l, and bottled drinking water costs less than 10p/l.

The Munich Re Foundation [25] also states that:

'Water from tank trucks costs 15 Nakfa or about €0.90 per 20-litre canister'.

This equates to 3.8p/l or £38/m³, which is in keeping with Tesfai's estimate of less than 5p/l or £50/m³.

The situation described above is borne out by Awate [26], which reports rationed water being delivered by bowser in Asmara, the capital of Eritrea in 2017, and the quality of the water provided being saline/brackish and requiring disinfection before consumption, which in turn, due to incorrect disinfection dosing, could have longer term health effects.

For the purposes of this research, the cost of water to the end user at Massawa will be taken as £38/m³ based on the estimate from the Munich Re Foundation [25], but as the RO plant will, in effect, only be a different water supply point for the tankers to collect their water from, cannot be given credit for the full £38/m³ that the end user pays.

The overall cost for the most financially viable renewable powered scenario in 2010 based on comparison to the equivalent diesel powered scenario is around £325 million over 25 years, and to break even each cubic metre of water delivered by the RO plant would need to be priced at £5.05, which incidentally is more than 3 times the cost of water in the UK [27].

For the purposes of this research, the cost of the water delivered at Massawa will be £5.05/m³.

5.2. Discount rate

The normal method for calculating the discount rate for UK government financed infrastructure projects, according to the UK Treasury [28], is 3.5% above the inflation rate.

The inflation rate has varied considerably in the UK over the last 10 years as indicated by the graph on the 'Inflation EU' Website [29] which shows an average high of 4.8% in 2011 and a low of 0.05% in 2015. This gives an average of 2.375% average inflation over the last 10 years. The inflation rate adopted for this calculation is 3.5% to include a margin for the inflation risk over the 25-year term of this project. This figure is in keeping with the long-term rate described in the UK Treasury's 'Green Book' [28] on p. 26.

For the purposes of this research, the discount rate was taken as the sum of these two parts (7%).

5.3. NPV results

Shown in **Figure 14** are the accumulated costs for the most financially attractive renewable powered scenario at Massawa (Solar plus Wind power), and the equivalent No BSR RO plant Diesel Generator-powered scenario.

Having set the price of the water revenue at the cost for the break even of the renewable powered scenario, it is shown to break even at the 25 year point, and the diesel generator powered scenario makes a profit of over £50 million over the life of the project.

When the scenario is updated to reflect diesel fuel and solar PV prices in 2016/7 the scenario changes significantly as shown in **Figure 15**.

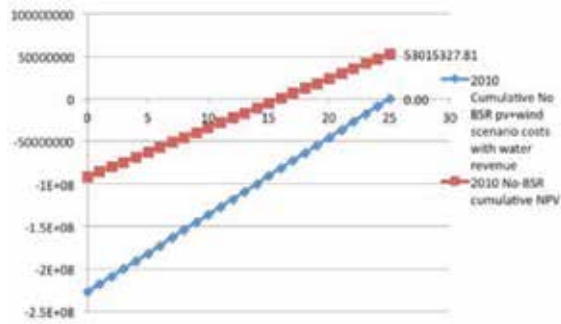


Figure 14. Comparison of cumulative cost for most financially viable renewable and diesel generator-powered scenario in 2010.

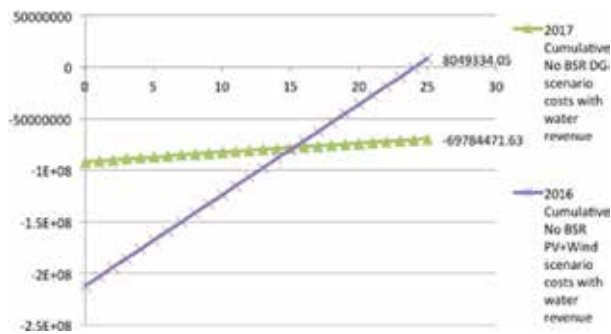


Figure 15. Comparison of cumulative cost of the solar and wind scenario with diesel generator with 2016 prices for diesel fuel and solar PV applied.

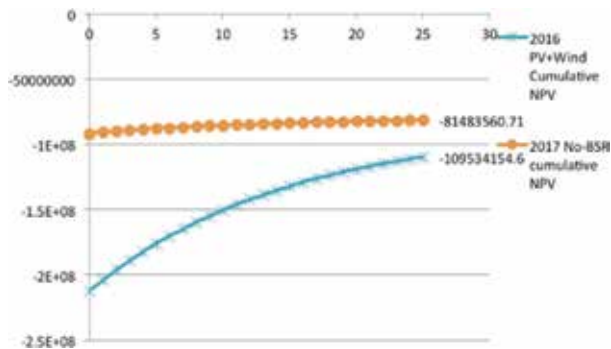


Figure 16. Comparison of the NPV cumulative cost using discount rate of 7% of the solar and wind scenario with diesel generator with 2016 prices for diesel fuel and solar PV applied.

As can be seen from **Figure 15**, the updating of diesel and solar PV prices alters every aspect of the financial viability of the most financially attractive renewable powered scenario, in that:

- It now breaks into profitability;
- It is significantly more financially viable than the diesel generator scenario; and

- The end of life profit for the diesel generator scenario of more than £53 million has now turned into a loss of almost £70 million.

Figure 16 shows the difference that applying the 7% discount rate makes to the financial attractiveness of the scenarios.

As can be seen from **Figure 16**, the application of the 7% discount rate means that neither scenario is now profitable, and further that the renewable powered scenario (PV + Wind) is now more than £28 million less financially attractive than the diesel generator powered scenario.

In selecting the appropriate discount rate for long-term public policy decisions, economic theory tends to distinguish between two components.

- The rate of pure time preference is the discount rate that would apply if all present and future generations had equal resources and opportunities.
- In addition, there is a wealth-based component of the discount rate, reflecting the assumption that if future generations will be richer than we are, then there is less need for us to invest today in order to minimise the financial burden on those that follow.

In the notation of 'The Stern Review' [29], the discount rate, r , is the sum of these two parts:

$$r = \delta + \eta g \quad (3)$$

where δ (delta) is the rate of pure time preference; g is the growth rate of per capita consumption. If per capita consumption is constant, implying that $g = 0$, then the discount rate $r = \delta$; η (eta), determines how strongly economic growth affects the discount rate. A larger value of η implies a larger discount rate, and hence less need to provide today for future generations (as long as per capita consumption is growing).

Stern takes the position that all future generations should be treated equally, except that there is a small probability that future generations will not exist – for example, if a natural or man-made disaster destroys most of, or the entire human race. The probability of destruction of humanity is taken by Stern as 0.1% per year; pure time preference (δ) is therefore set equal to 0.1%. That is, we are only 99.9% sure that humanity will still be here next year, so we should consider the well-being of people next year to be, on average, 99.9% as important as people today. Stated simply, the only reason that the current generation should not consider the needs of those in the future is due to the small possibility that the future generation will not exist, not because the future generation will be rich enough to manage the previous generation's impact on the environment.

To calculate the discount rate, Stern estimates that the growth of per capita income will average 1.3% per year, and sets $\eta = 1$ to indicate that future generations are not richer than the current generation. Therefore, the Stern Report discount rate is:

$$r = \delta + \eta g = 0.1\% + (1 \times 1.3\%) = 1.4\% \quad (4)$$

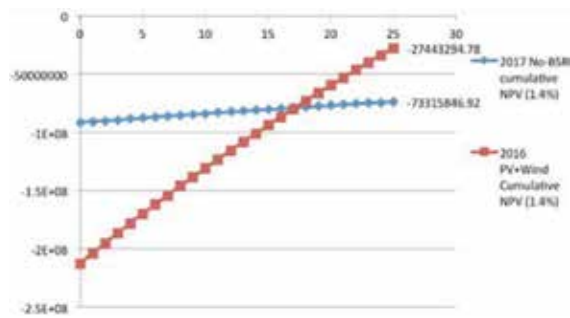


Figure 17. Comparison of the solar and wind with diesel generator no BSR scenario with discount rate of 1.4%.

This makes a marked difference to the viability of the renewable powered scenario, as shown in Figure 17.

As can be seen from Figure 17, the reduction of the discount rate means that, although neither scenario is financially viable, the renewable powered scenario is now more than £45 million more financially attractive than the diesel generator powered scenario.

5.4. An alternative point of view

Taking the Stern position that this generation can only apply 0.1% to the discount rate, it does not seem entirely unreasonable to suggest a discount rate of 3.6% based on:

Long-term view of inflation (3.5% as derived previously) + 0.1% based on probability that next generation will not be here

This would give appropriate recognition to the fact that this project represents a significant CAPEX investment to:

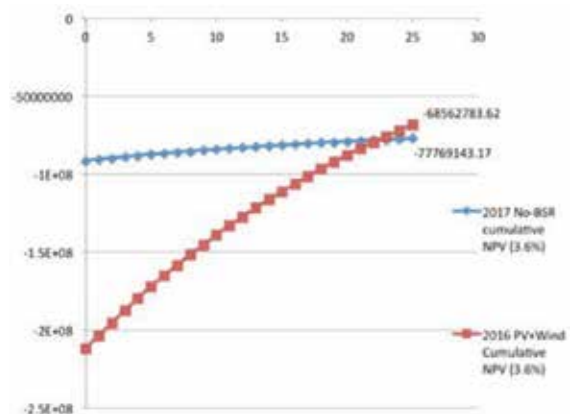


Figure 18. Comparison of the solar and wind with diesel generator powered no BSR RO plant scenario with discount rate of 3.6%.

- Improve the quality of the lives of users, and in so doing;
- Minimises the impacts of climate change and the associated potential costs for future generations, whilst;
- Acknowledging a realistic view of inflation over the longer term of project's of this type for the current generation.

Figure 18 shows the comparison of the renewable and diesel generator powered scenarios.

As can be seen from **Figure 18**, the 3.6% discount rate does not make either option financially viable, but does make the renewable powered scenario around £9.2Million more financially attractive than the diesel powered scenario.

6. Conclusion

Overall conclusions are that:

- It is technically possible to desalinate water for human consumption at Massawa using renewable energy.
- This is financially viable in comparison to the use of diesel generators, but only recently due to the changes in solar PV and diesel fuel prices; but
- The NPV methodology for evaluation of renewable energy projects has a significant impact on the financial viability of such projects; and
- The operational impacts of using intermittent power sources on municipal RO plants needs to be better understood.

Author details

Cliff Dansoh

Address all correspondence to: c.dansoh@kingston.ac.uk

Kingston University, London, UK

References

- [1] Dansoh C. The viability of renewable energy and energy storage as the power source for municipal-scale reverse osmosis desalination. *Desalination and Water Treatment*. 2014;55(11):3064-3090. DOI: 10.1080/19443994.2014.940209
- [2] Meteorological Office. 2018. Available at <https://www.metoffice.gov.uk/learning/rain/how-much-does-it-rain-in-the-uk>. [Last viewed on 30 January 2018]

- [3] US Department of Energy. 'Tip sheet (DOE/GO-102007-2230, pumping systems tip sheet 2 'control strategies for centrifugal pumps with variable flowrate requirements'). 2007 Available at https://energy.gov/sites/prod/files/2014/05/f16/centrifug_pumps_control.pdf [Last viewed on 30 January 2018]
- [4] Thomson AM. Reverse-osmosis desalination of seawater powered by photovoltaics without batteries [doctoral thesis]. Loughborough University. 2003. Available at <https://dspace.lboro.ac.uk/dspace-jspui/bitstream/2134/10701/4/Thesis-2003-Thomson.pdf> [Last viewed on 30 January September 2018]
- [5] Weather reports. Coordinates for Massawa are 15 36' 35' lat: 39 27' 00' long. 2011. Available at <http://www.weatherreports.com/Eritrea/Massawa/averages.html>. [Last viewed on 7 August 2011]
- [6] Affordable Desalination (ADC). see http://www.affordabledesal.com/home/test_data.html on 14 January 2011 for an RO plant using the Filmtec SW30HR-380 membrane. 2011
- [7] Shackleton D. Face to face meeting with Daniel Shackleton-Director of Salt Separation Limited, on 9 November 2009. See website at <http://www.saltsep.co.uk/> for greater details of Salt Separation Limited
- [8] Conlon WJ. E-mail exchange with William J Conlon PE, BCEE F. ASCE technical manager, principal professional associate. Water Technical Excellence Center, Parsons Brinkerhoff Americas, Inc. 2010
- [9] Accepta E-mail exchange with Philip Boswell (International Technical Consultant) Accepta. See website at <http://www.accepta.com/> for details of Accepta. 2010
- [10] Florida. Desalination in Florida: Technology, implementation, and environmental issues. Division of Water Resource Management, Florida Department of Environmental Protection, April, 2010. Available at <http://ufdcimages.uflib.ufl.edu/UF/00/10/03/82/00001/desalination-in-florida-report.pdf>. [Last viewed on 30 January 2018]
- [11] Boyle JW. Design, construction and repair of potable water reservoirs. Proceedings of the British Columbia Water & Waste Association Annual Conference; Whistler; April 2008
- [12] Louw GJ. Development of a solar powered reverse osmosis plant for the treatment of borehole water. WRC Report No 1042/1/01 2001. Available at <http://www.wrc.org.za/Knowledge%20Hub%20Documents/Research%20Reports/1042-1-01.pdf> [Last viewed on 30 January 2018]
- [13] Park GL, Schaefer AI, Richards BS. The effect of intermittent operation on a wind-powered membrane system for brackish water desalination. *Water Science and Technology*. 2012;65(5):867-874. DOI: 10.2166/wst.2012.912 <http://wst.iwaponline.com/content/65/5/867> [Last viewed on 30 January 2018]
- [14] Rizzuti L, Ettourney HM, Cipollina A. Solar desalination for the 21st century. *Autonomous Desalination Units Based on Renewable Energy Systems—A Review of Representative Installations Worldwide*. 2007. ISBN: 13978-1-4020508-9 (e-book). Available at: <http://books.google.co.uk/books?id=iA75bZKcilYC&pg=PA348&lpg=PA348&dq=intermittent>

- t+operation+of+ro+plant&source=bl&ots=CK_s-CRvyO&sig=gDp5Pilzgr8CXXNUVBu0ClbPJ2o&hl=en&sa=X&ei=wRCLT-DBKTC0QWzxcW5CQ&ved=0CFgQ6AEwBA#v=onepage&q=intermittent%20operation%20of%20ro%20plant&f=false [Last viewed on 18 January 2018]
- [15] PwC. 100% renewable electricity. A roadmap for Europe and North Africa. A study by consultants Price Waterhouse Coopers, in collaboration with researchers from the Potsdam Institute for Climate Impact Research (PIK), the International Institute for Applied Systems Analysis (IIASA) and the European Climate Forum (ECF). 2010. Available at https://www.pik-potsdam.de/news/aktuelles/pressemitteilungen/dateien/100_percent_renewable_electricity.pdf [Last viewed on 30 January 2018]
- [16] PwC. Powering the future, full report–Mapping our low-carbon path to 2050. December 2009 by Parsons Brinkerhoff. 2009. Available at <https://hub.globalccsinstitute.com/sites/default/files/publications/138013/powering-future-mapping-low-carbon-path-2050.pdf> [Last viewed on 30 January 2018]
- [17] Fu R, Chung D, Lowder T, Feldman D, Ardani K, Margolis R. National Renewable Energy Laboratory (NREL) U.S. solar photovoltaic system cost benchmark: Q1 2016. (2016) Available at: http://www.nrel.gov/docs/fy16osti/66532.pdf?utm_source=NREL%20Report%20Shows%20U%2ES%2E%20Solar%20Photovoltaic%20Costs%20Continuing%20to%20Fall%20in%202016&utm_medium=email&utm_content=nrel&utm_campaign=NewsRelease [Last viewed on 30 January 2018]
- [18] NREL Webpage. Energy analysis–Distributed generation renewable energy estimate of costs. National Renewable Energy Laboratory (NREL); 2016. Available at http://www.nrel.gov/analysis/tech_lcoe_re_cost_est.html. [Last viewed on 30 January 2018]
- [19] Power Electrics. E-mail exchange with Mie Gabriel–Sales manager power electrics (Bristol). 2011. Ltd see <http://www.power-electrics.co.uk/> for greater detail of power electrics organisation
- [20] GIZ. International Fuel Prices 2010/2011' by The Deutsche Gesellschaft für Internationale Zusammenarbeit (GIZ) GmbH. 2010. Available at <https://www.giz.de/expertise/downloads/giz2012-en-ifp2010.pdf> [Last viewed on 30 January 2018]
- [21] Trading Economics. 2018. See website <https://tradingeconomics.com/eritrea/pump-price-for-diesel-fuel-us-dollar-per-liter-wb-data.html>. [Last viewed on 30 January 2018]
- [22] Energypedia. 2018. See website https://energypedia.info/wiki/Fuel_Price_Data_Eritrea [Last viewed on 30 January September 2018]
- [23] Knoema. 2018. See website <https://knoema.com/atlas/Eritrea/topics/Transportation/Road-transport/Diesel-fuel-prices> [Last viewed on 30 January 2018]
- [24] Tesfai M. Telephone conversation with Michael Tesfai (a member of staff at the Eritrean embassy in London) on the morning of 15 September 2011. 2011
- [25] Munich Re Foundation. Second phase of the project. 2007. Available at http://www.munichre-foundation.org/home/Water/Fognets/Eritrea_ProjectVisit/Eritrea_ProjectVisit_Phase2.html [Last viewed on 30 January 2018]

- [26] Awate.com. Eritrea suffering from persistent water shortage. 8 May 2017. 2017. Available at <http://awate.com/eritrea-suffering-from-persistent-water-shortage/> [Last viewed on 30 January 2018]
- [27] Southern Water. 2018. Available at <https://www.southernwater.co.uk/our-charges> [Last viewed on 30 January 2018]
- [28] Treasury. The Green Book. Appraisal and Evaluation in Central Government. ISBN 978-1-912225-57-6. 2011. Available at https://www.gov.uk/government/uploads/system/uploads/attachment_data/file/220541/green_book_complete.pdf [Last viewed on 30 January 2018]
- [29] Stern N. The Economics of Climate Change. The Stern Review. ISBN: 9780521700801. 04 January 2007. 2006. Available at <http://www.webcitation.org/5nCeyEYJr> [Last viewed on 30 January 2018]

Membrane Applications

Research Trend of Membranes for Water Treatment by Analysis of Patents and Papers' Publications

Chang Hwa Woo

Additional information is available at the end of the chapter

<http://dx.doi.org/10.5772/intechopen.76694>

Abstract

Since the beginning of water shortage by disasters such as global warming, environmental pollution, and drought, development of original technology and studies have been undertaken to increase the availability of water resources. Among the technologies, water treatment technology using membranes has a better water quality improvement than existing physicochemical and biological processes. Moreover, it is environmental-friendly technology that does not use chemicals. Water treatment membranes are applied to various fields such as wastewater treatment, water purification, seawater desalination, ion exchange process, ultra-pure water production, and separation of organic solvents. Furthermore, water treatment technologies using membranes will increasingly expand. The core technology of the water treatment membrane is to control the size of pores for membrane performance and is being researched to improve performance. In this chapter, the frequencies of presentation are filed by country, institution, and company through technology competitiveness and evaluation of patents and papers. In addition, evaluation of technologies for wastewater treatment, water purification, seawater desalination, and ion exchange process was carried out in the same way as before. Finally, future research directions were suggested by using evaluation results.

Keywords: patents, water treatment, desalination, ion exchange, membrane

1. Introduction

The world is now expected to become water scarce as a result of global warming, and by 2025, it is estimated that water-scarce countries will increase by more than 30% compared to 1995 [1]. The twentieth century was the era of black gold, represented by oil, but the age of water, or blue gold, is expected to emerge in the twenty-first century. Due to the global problems

faced by the world, such as population growth, industrialization, and climate change, a steady increase in water demand and a disparity in regional water supply are urgently needed to be resolved. Population Action International (PAI) currently has 550 million people living in water-pressure or water-starved countries, and from 2.4 billion to 3.4 billion people will live in water-starved or water-deprived countries by 2025. According to the World Meteorological Organization (WMO) report, 653 million people in 2025 and 2.43 billion in 2050 will suffer direct water shortages.

Various water treatment techniques have been studied to secure water resources in order to solve the water shortage phenomenon. In the water treatment field, there are water treatment processes such as wastewater and wastewater treatment to remove pollutants, water treatment for drinking water, and seawater desalination for seawater reuse (**Figure 1**).

There are also a number of related technologies, among which water treatment technologies using membranes have shown very high growth rates of 10–20% per year [2, 3]. Frost and Sullivan estimate that the world's membrane-based water treatment market will grow from \$ 5.54 billion in 2012 to \$ 1.27 billion by 2020 (CAGR of 10.2%). Major growth factors include increased demand for drinking water, reuse of sewage, increased desalination facilities based on membranes, and strengthening of environmental standards. In particular, it is expected that there will be a significant increase in the market in the Asia-Pacific region based on rapid industrialization, population growth, and demand for advanced technologies [4].

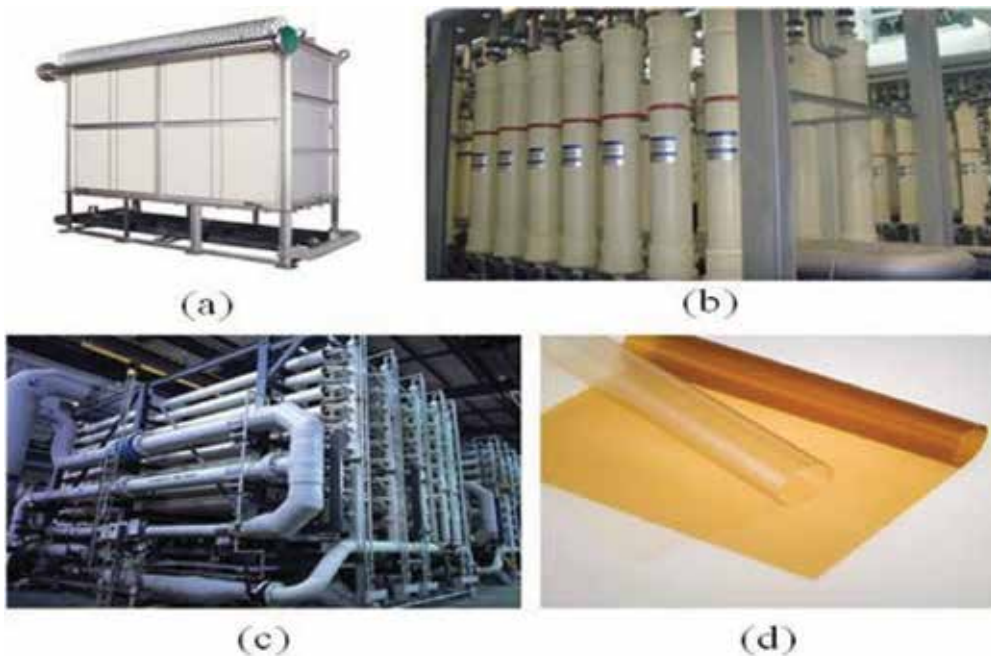


Figure 1. Various applications of water treatment membranes. (a) MBR process (Toray Industries, Inc.), (b) water treatment process (Yeongdeungpo water purification center), (c) desalination process (Doosan heavy industries & construction), (d) ion exchange membrane (Tokuyama America, Inc.).

The separation membrane has a selective filtration function that selectively passes a specific component, as well as selective permeability capable of separating dissolved substances or mixed gases dissolved in a liquid [5–7]. Membrane separation technology comprehensively means various separation processes using such selective permeability of the membrane. As shown in **Figure 2**, the separation membrane used for water treatment produces clean water by allowing the water (B) to pass but not allowing the suspended material (A) to pass through. Membranes can be divided into microfiltration (MF), ultrafiltration (UF), nanofiltration (NF), and reverse osmosis (RO) depending on the pore size [8–10]. **Figure 3** shows the separation performance according to the pore size of the membrane, and **Table 1** shows the membrane characteristics of various process parameters [11].

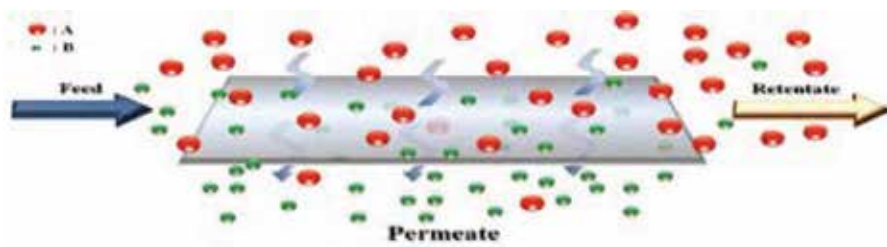


Figure 2. Schematic of membrane filtration process.

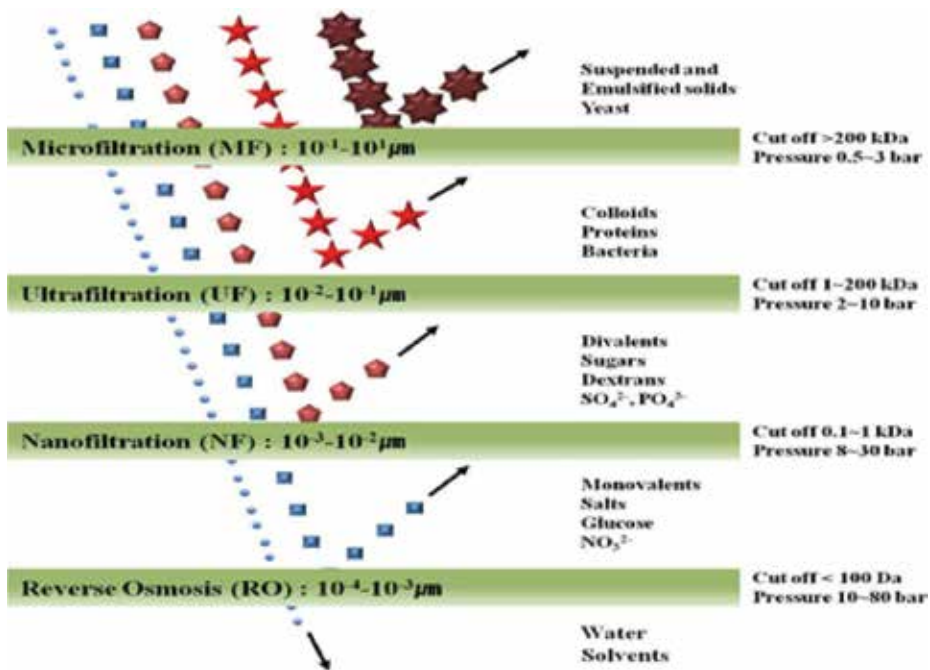


Figure 3. A scheme of the membrane for water purification processes.

	Microfiltration	Ultrafiltration	Nanofiltration	Reverse osmosis
Mechanism or separation	Sieving	Sieving	Sieving + solution/diffusion + exclusion	Solution/diffusion + exclusion
Materials	CA, CE, PAN, PC, PE, POF, PP, PS, PTFE, PVDF	CA, CE, PA, PAN, TFC, PS, PVDF	CA, PA, TFC	CA, PA, PS, TFC
MWCO (Da)	>100,000	>2000–100,000	300–1000	100–200
Structure	Porous isotropic	Porous asymmetric	Finely porous asymmetric/composite	Nonporous asymmetric/composite
Law governing transfer	Darcy's law	Darcy's law	Fick's law	Fick's law
Pore size range (μm)	0.1–10	0.01–0.1	0.001–0.01	<0.001
Rejects	Particulates, clay, bacteria	Macromolecules, proteins, polysaccharides, viruses	HMWC, mono-, di-, and oligosaccharides, polyvalent anions	HMWC, LMWC, sodium chloride, glucose, amino acids, proteins
Operating pressure (psi)	1–30	3–80	70–220	800–1200
Fluxes ($\text{L}/\text{m}^2 \text{ h}$)	500–10,000	100–2000	20–200	10–100

Table 1. Correlation of membrane features with ranges of separation [6].

Microfiltration is a membrane separation process for separating a solute having a solute size of about 0.1–10 μm . It is preferable that the membrane used at this time is about 0.01–10 μm in pore size and the pore accounts for about 80% Do. As for the material of the membrane, cellulose-type, nylon, PVC, polytetrafluoroethylene (PTFE), and various other polymer materials are suitable. In a microfiltration process, propulsion is represented by a pressure difference, where the pressure difference is typically 1–30 psig. The separation effect of this membrane is fundamentally dependent on the pore size of the membrane and the size of the substance to be separated. If the size of the substance to be separated is smaller than the pore size, it does not pass through the entire membrane but the substance to be separated is adsorbed on the membrane or is not transmitted by steric hindrance near the pore. The biggest problem of the microfiltration process is the deposition of colloidal material on the membrane surface, which reduces the flow rate by blocking the pores, which can be replaced or regenerated to restore the original state [12–15].

Ultrafiltration is a membrane separation process that separates macromolecules or colloidal particles with molecular sizes ranging from 10 to 1000 \AA . The pore size ranges from 20 to 500 \AA . This method uses a differential pressure as a thrust for the separation operation similar to the reverse osmosis method. The pressure differential used in ultrafiltration is usually in the range of 10–100 psig because particles with a high molecular weight have relatively low

osmotic pressure and thus do not require high pressure to apply pressure above osmotic pressure. Ultrafiltration is the same as reverse osmosis in mathematical modeling but fundamentally different from reverse osmosis. The reverse osmosis is largely governed by the correlation between the membrane and the dissolved salt, whereas ultrafiltration is dominated by the solute and pore size. In other words, ultrafiltration has a separation effect by the steric hindrance at the micropore inlet and the frictional resistance between the solute and the pore wall in the pore. The molecular weight cut off (MWCO) in the ultrafiltration method is an important item. The closer the slope is to infinity, the narrower the fractional molecular weight distribution which can be regarded as an excellent filter membrane. Ultrafiltration has a wide range of industrial applications in the middle of reverse osmosis and microfiltration in terms of the size of the separation object. The membrane material is the same as the material of the reverse osmosis membrane and has only a large pore size in terms of being hydrophilic [16–18].

Nanofiltration is the process of treating hundreds to thousands of molecules with medium molecular weight, the range of treatment of reverse osmosis membranes and ultrafiltration membranes. Nanofiltration is used for separation of small solvent molecules due to deformation of reverse osmosis membrane, but even large molecules of polysaccharides such as sugar can be separated. Nanofiltration membranes usually have a fractional molecular weight of 20–70% NaCl and organic solvents of 200–500. This fractional range corresponds to a diameter of about 10 Å, or 1 nm, of the molecule. This membrane is used for seawater treatment in the pressure range of 0.4–0.7 MPa which is 1/4–1/2 of the reverse osmosis pressure. The exclusion mechanism is similar to reverse osmosis and is widely applied to the separation of salt and organic matter of appropriate molecular weight. The nanofiltration membranes can be used at a rate of 50–97.5% at the same time and are used to replace the ion exchange method in the water softening process [19–21].

Reverse osmosis is a membrane separation process that separates solutes smaller than 10 Å in size of ions and molecules and was industrialized in seawater desalination and wastewater treatment in the 1970s. The membranes are composed of asymmetric cellulose acetate or aromatic polyamide which is formed as an active layer for a separating effect on the supporting layer. Recently, a composite membrane capable of removing up to 99% of dissolved salts has been developed. The composite membrane is formed of a polymer thin film having a high salt removal effect on the support layer. The support membrane is mainly composed of polysulfone having high mechanical strength and chemical resistance, and cellulose triacetate and cross-linked polyether are mainly used as the separation layer. Since the reverse osmosis membrane has almost no pores, it can be regarded as a nonporous membrane, which is permeated through the gap between micelles forming organic polymers or micelles. In the reverse osmosis method, since the dielectric constant of the organic polymer is low, the dissolved salt is not adsorbed to the membrane. In addition, in high pressure (800–1500 psig), water, which is a solvent, permeates in proportion to the osmotic pressure difference. The separation effect is increased. Since the reverse osmosis is not a separation operation according to the molecular size, deposition of organic substances such as microfiltration and ultrafiltration is less and consequently, the lifetime of the membrane is increased. Reverse osmosis membranes are being used not only for separation and removal of dissolved salts but also for separation of organic and aromatic hydrocarbons with low molecular weight [22–24].

Treatment and the reusing of wastewater are mainly based on the activated sludge process. In the activated sludge process, the amount of generated sludge is large, the treatment cost is high, and it is vulnerable to impacts such as biological oxygen demand (BOD) overload and toxicity, and problems such as sludge bulking occur. However, the membrane bioreactor (MBR) does not need to regulate the amount of microorganisms in the reactor and does not cause the sludge expansion phenomenon. In addition, it has excellent durability against load generated in the operation such as impact, toxicity, and organic load. It is expected that the technology of the MBR process will increase gradually because of the advantages of this separation membrane process [25, 26].

In most of the domestic large and medium-sized water purification facilities, using river water or lake water as a water source, problems occur periodically. However, the conventional water treatment methods such as coagulation, sedimentation, filtration, and disinfection processes are inferior in taste and odor. There is a limit in effectively controlling harmful organic substances and the like. In order to overcome the limitations of this conventional treatment method, microfiltration or ultrafiltration using a membrane has been shown to be a breakthrough technology that can replace the existing rapid sand filtration system because it completely removes turbidity and pathogenic microorganisms. In addition, it can easily combine with the existing unit-altitude water treatment process such as ozone-activated carbon to optimize the process configuration suitable for the characteristics of raw water and water quality, and it is more compact and easier to maintain than the existing water treatment method [27, 28].

Techniques for converting seawater to fresh water include conventional coagulation, coagulation, sedimentation, single- or two-phase granular filtration, dissolved air flotation, and low-pressure membrane filtration techniques using microfiltration or ultrafiltration membranes. Conventional pretreatment processes are generally used in seawater desalination, but it is difficult to completely remove float or colloidal particles, which makes it difficult to supply water in a stable manner. However, when the membrane is pretreated, it has the advantage of reducing the cost required in the desalination process, such as increasing the permeation flow rate, reducing the washing cycle, reducing the use of washing chemicals, reducing energy consumption, and reducing maintenance costs [29, 30].

A membrane electrode assembly (MEA), which is one of the most important components among the separation membranes used in the ion exchange process, includes a proton exchange membrane fuel cell (PEMFC). The membrane consists of two electrodes, cathode and anode, which determine the performance of the fuel cell [31–33]. Currently, the most widely used hydrogen ion exchange membranes are produced by DuPont's nafion® as well as Dow Chemical, 3 M, and others. The perfluorinated proton exchange membrane has been applied to most commercial fuel cell devices due to its high chemical/mechanical stability and excellent hydrogen ion transfer ability. However, since the production process requires high temperature/high pressure conditions, the production cost has increased. The limitation is that it has a pollution problem, and there is a problem that performance is reduced at high temperature due to low glass transition temperature [34, 35]. Therefore, research on the production of a hydrocarbon-based proton exchange membrane having a relatively high manufacturing cost and high thermal stability has been actively pursued as an alternative thereto [36–39].

In this review, the water treatment membranes are divided into wastewater treatment membranes, water treatment membranes, seawater desalination membranes, and ion exchange membrane separators. Through analysis of domestic and foreign patent information and

publication of papers, technical trends and recent technology trends, And to analyze the trend of technology development of water treatment membranes by summarized graphs.

2. Analysis of patents and articles on water treatment membranes

In this chapter, we show all patents and papers for water treatment membranes. In the past 20 years (1995–2014), we have divided membranes for wastewater treatment, separation membranes for water treatment, and seawater desalination membrane trends. In evaluating the competitiveness of patent technology, patents filed after 2015 are analyzed only as valid patents before 2015 except for the fact that they were undisclosed. The patent database of WIPS was used for the analysis of the patent. The patent data were searched through the keyword search and the secondary classification was performed using the library method for noise and pattern removal. Finally, a final classification was carried out by experts in each field. The patent activity index (PAI), the patent intensity index (PII), the patent market-power index (PII), the patent market power index (PMI), and patent citation index (PCI) were the categories. These terms can be defined as follows. Patent activity is defined as the absolute number of patent applications based on the number of public/patent publications issued by the Patent Office. Patent concentration refers to providing information about the technological innovation activities that a country concentrates on relative to other countries. The patent market power refers to the use of patents as an indicator of the patentability of patents when the number of family patents is large, because patents are applied only when they are in commercial profit or for technology competition in the relevant country. Finally, patent impact is the measure of the impact of the patent on future patents, and the US patent with patent information for the patents is targeted [40–43].

The number of patent applications has been evaluated in the 10 countries, including Korea, the USA, Japan, China, and Europe, which are the major developing countries, for patent technology competitiveness. A total of 4629 patent applications were searched. 1144 patents were related to separation membranes for wastewater treatment, 734 patents related to water treatment membranes, 668 patents related to seawater desalination membranes, and 2083 patents related to membranes for ion exchange processes. **Figure 4** shows the patent application trends by technology in the last 20 years.

The thesis has been published in the past 20 years (1997–2016), and it has been evaluated for technical competitiveness. 13,506 papers are related to the separation membrane for wastewater treatment, 7958 papers are related to the separation membrane for water treatment, 9524 papers related to separation membrane for desalination, and 16,254 papers related to separation membrane for an ion exchange process. **Figure 5** shows the trend of publications by technology in the past 20 years. The database used to analyze the technological competitiveness of the paper is the Scopus paper retrieval system, which collects information by category and country and uses the Bibliometric Activity Index (BAI), Bibliometric Citation Index (BCI), and Bibliometric Intensity Index (BII). These terms can be defined as follows. The thesis activity is the number of absolute dissertations, which shows the corresponding country for the technology divided by the total number of countries. The impact of a paper is defined as an index that provides information that can be compared with other countries in terms of the quality of the paper. Finally, the thesis density can be defined as an index that provides information on the

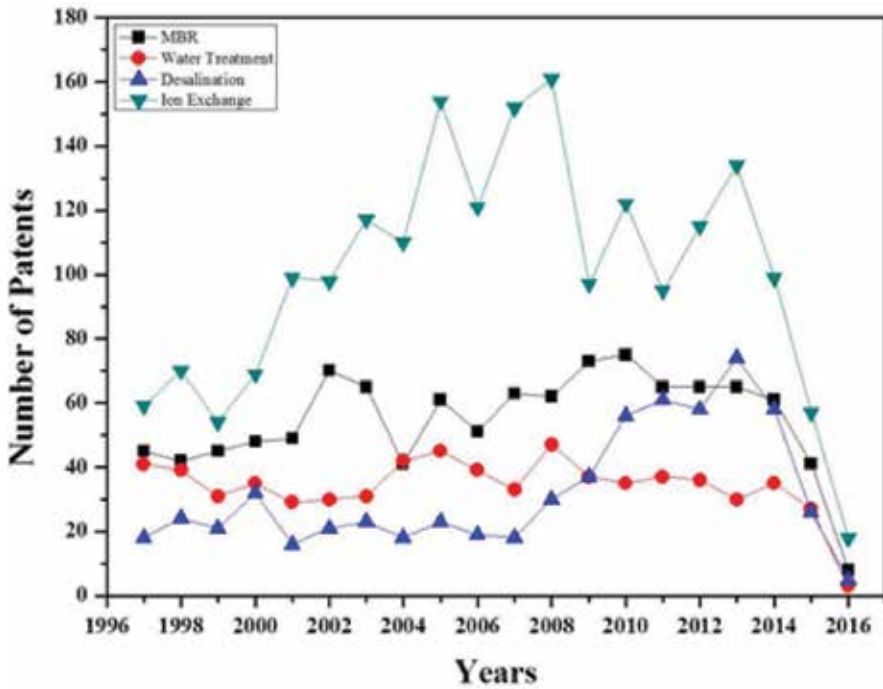


Figure 4. Patent applications 1996–2016 in membrane related technology.

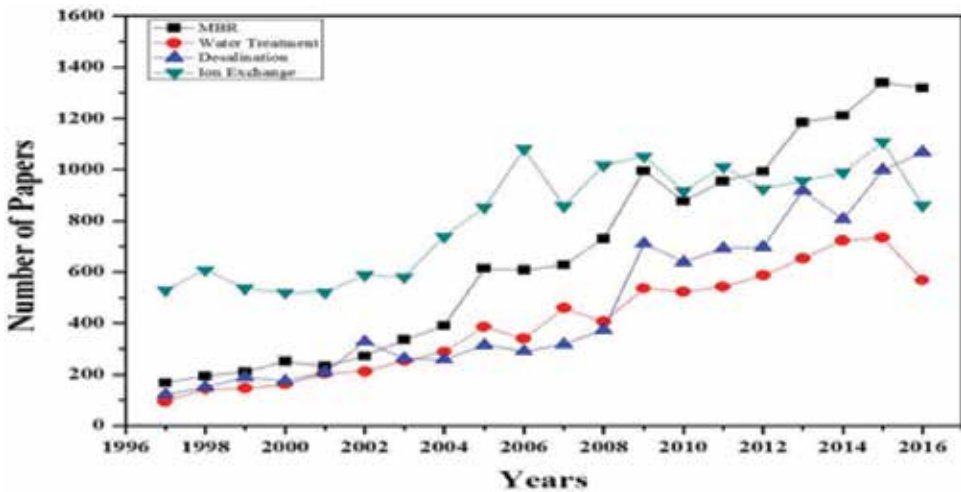


Figure 5. Papers publications 1996–2016 in membrane related technology.

relative concentration of a technological innovation activity in a given technology sector relative to other countries in terms of the number of relative papers published. Major countries participating in the analysis of information are the top 13 countries such as Korea, the USA, Japan, China, and Europe (Figure 6).

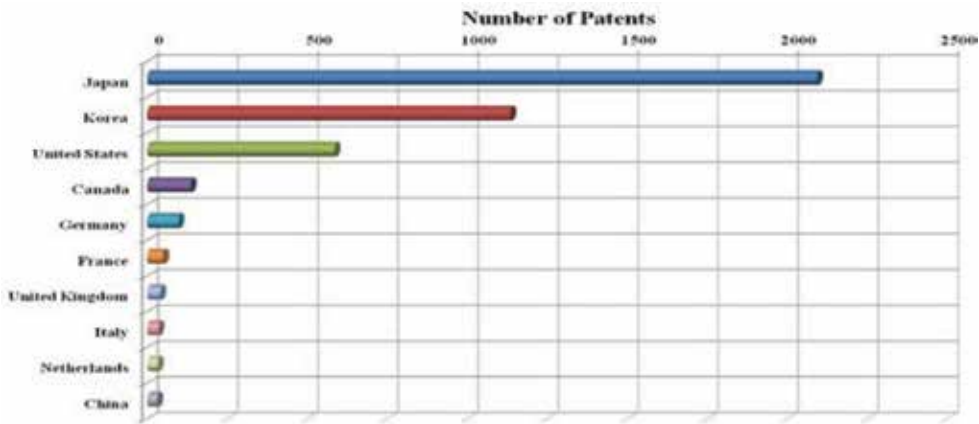


Figure 6. Top countries with the highest number of patent application.

2.1. Evaluation of patent technology competitiveness of water treatment membranes

As a result of analyzing the number of applications for separation membrane-related patents, the following results were obtained: Japan (2093 cases), Korea (1134 cases), the USA (585 cases), Canada (135 cases), Germany (97 cases), France (49 cases), Italy (35 cases), the Netherlands (33 cases), and China (31 cases). As for the patent activities, Japan was overwhelmingly ranked high (0.49), followed by Korea (0.27), the USA (0.14), Canada (0.03), and Germany (0.02). **Table 2** and **Figure 7** show the patents' utilization rate, patent concentration, patent market power, and patent influence by country.

In terms of the degree of patent concentration in each country, Japan tends to concentrate most on water treatment membranes (1.20), Korea on wastewater treatment membranes (1.72), and the USA on ion exchange membranes (1.13)—1.37, 1.39, 1.32, and 1.86 for Canada, Germany, the United Kingdom, and Italy, respectively, for the ion exchange membrane, 1.25 for the wastewater treatment membrane for France and 1.77 and 1.25 for the water treatment membranes.

As a result of analyzing the number of family patents of separation membrane-related patents, the following results were obtained: Japan (5651 cases), the USA (3328 cases), Korea (1743 cases),

Index of evaluation	KR*	JP	US	CA	DE	FR	GB	IT	NL	CN
PAI**	0.27	0.49	0.14	0.03	0.02	0.01	0.01	0.01	0.01	0.01
PII	4.46	3.92	3.76	3.42	3.13	3.59	3.91	2.76	3.85	3.98
PMI	0.46	0.81	1.71	2.02	2.64	2.66	3.12	3.49	2.06	1.23
PCI	0.51	0.50	1.18	1.87	0.67	0.51	1.02	2.40	0.66	0.14

*ISO code: KR, Korea; JP, Japan; US, United States of America; CA, Canada; DE, Germany; FR, France; GB, United Kingdom; IT, Italy; NL, Netherlands; CN, China.

**PAI: Patent Activity Index, PII: Patent Intensity Index, PMI: Patent Market-power Index, PCI: Patent Citation Index.

Table 2. An analysis table about PAI, PII, PMI, and PCI by each country.

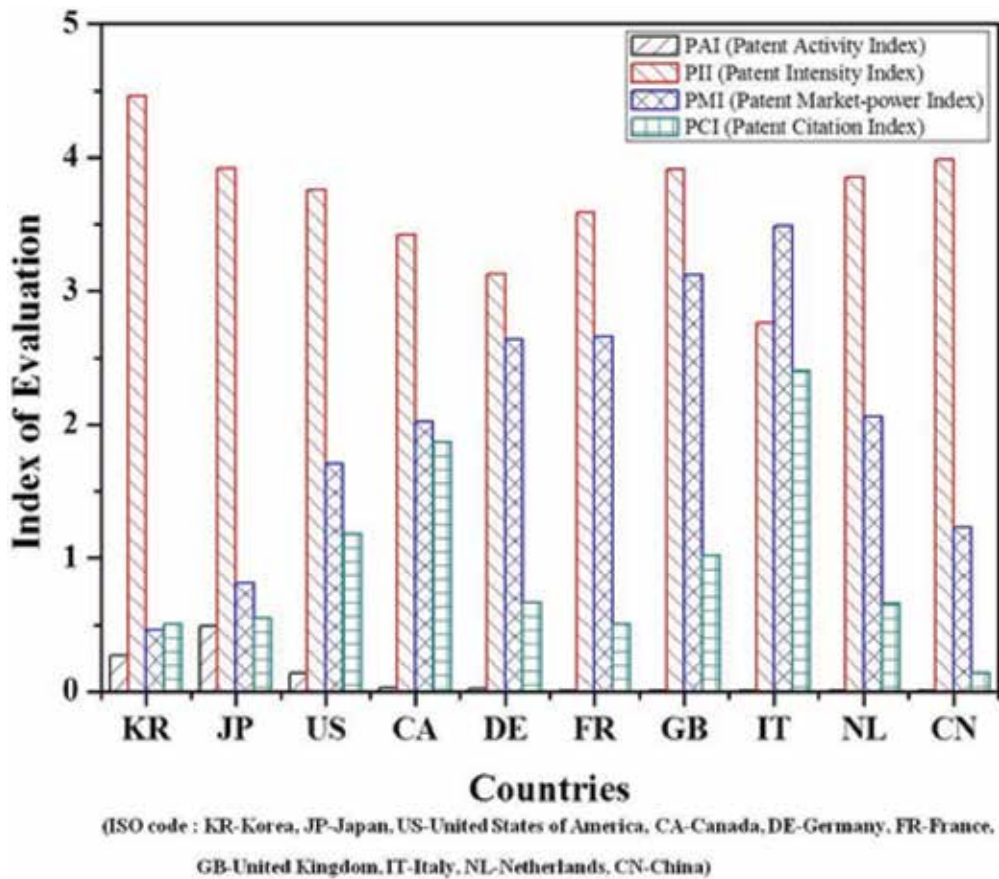


Figure 7. An analysis graph about PAI, PII, PMI, and PCI by each country.

Canada (910 cases), Germany (852 cases), France (426 cases), Italy (407 cases), the Netherlands (226 cases), and China (127 cases). (11.63), Britain (10.39), France (8.86), Germany (8.78), Netherlands (6.85), Canada (6.74), the United States (5.69) and China (4.10), Japan (2.70), and Korea (1.54). The results of this study are as follows: Italy (3.49), Britain (3.12), France (2.66), Germany (2.64), the Netherlands (2.06), Canada (2.02), the USA (1.71) (0.81), followed by Korea (0.46).

As a result, the total number of patents for separator-related patents was derived from the USA (4238 cases), Canada (1537 cases), Japan (979 cases), Germany (267 cases), Italy (163 cases), France (101 cases), the Netherlands (96 cases), and China (11 cases). The number of registered patents related to membranes was 271 in the USA, 147 in Japan, 62 in Canada, 30 in Germany, 26 in Korea, 15 in France, 12 in the UK, (31.86), Canada (24.79), the United States (15.64), and the United States (15.64), followed by the United States), Britain (13.58), Germany (8.90), Netherlands (8.73), Korea and France (6.73), Japan (6.66) and China (1.83). The results of this study are as follows: Italy (2.40), Canada (1.87), the USA (1.18), the UK (1.02), Germany (0.67), the Netherlands (0.66), Korea and France (0.51), and China (0.14). Among them, Korea ranked 2nd place in patent activity, 10th place in patent market power, and 7th place in patent

efficacy, and patent concentration tended to be concentrated on wastewater treatment membrane (1.72) (Figure 8).

2.2. Evaluation of technology competitiveness of water treatment membranes

As a result of analyzing the number of published papers related to membranes, the results obtained were as follows: the USA (11,435), China (9235), Japan (3183), Korea (3013), Germany (3005), Canada (2370), the United Kingdom (2312), Spain (2296), Australia (2260), Italy (1710), and the Netherlands (1422). Therefore, in the activity of the thesis, the USA (0.24) was the highest, followed by China (0.20), Japan (0.07), Korea (0.06), and Germany (0.06). Table 3 and Figure 9 show the activities of each country, the influence of the thesis, and the concentration of the thesis.

As a result, the total number of citations for the membrane-related papers was found to be 351,996 in the US, 125,276 in China, 84,777 in Japan, 69,354 in Japan, 66,727 in the UK, 66,492 in Canada, (66,239), Australia (61,057), Korea (60,156), Netherlands (43,128), Spain (41,663), Italy (41,281) and India (40,121), Followed by the United States (0.31), China (0.11), Germany (0.08), Japan / France / Canada / Britain (0.6).

According to the concentration of each country, the USA tends to concentrate the most in the ion exchange process membrane (1.15), China in the wastewater treatment membrane (1.36), and Korea in the seawater desalination membrane (1.19). China, Spain, and Italy are the most

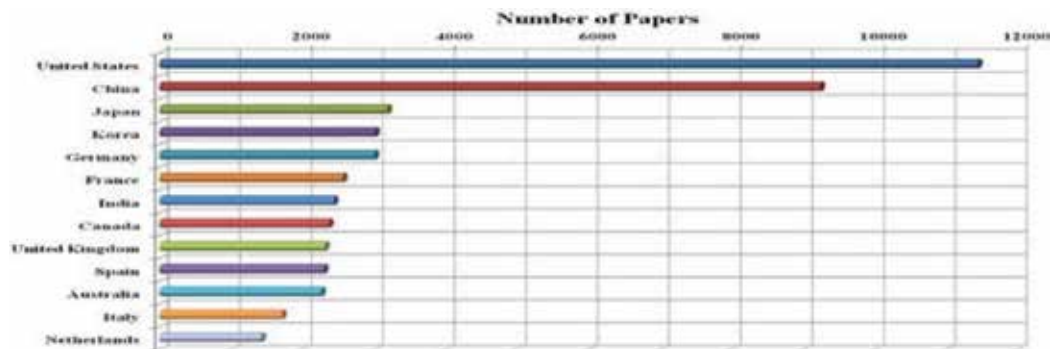


Figure 8. Top countries with the highest number of paper publications.

Index of evaluation	KR*	JP	US	CA	DE	FR	GB	IT	NL	CN	IN	CA	ES
BAI**	0.06	0.07	0.24	0.05	0.06	0.05	0.05	0.04	0.03	0.2	0.05	0.05	0.05
BCI	4.03	3.8	4.02	3.91	4.04	3.99	3.98	3.95	4.21	3.94	4.02	3.91	4.06
BII	0.05	0.06	0.31	0.06	0.08	0.06	0.06	0.04	0.04	0.11	0.04	0.06	0.04

*ISO code: KR, Korea; JP, Japan; US, United States of America; CA, Canada; DE, Germany; FR, France; GB, United Kingdom; IT, Italy; NL, Netherlands; CN, China; IN, India; CA, Canada; ES, Spain.

**BAI: Bibliometric Activity Index, BCI: Bibliometric Citation Index, BII: Bibliometric Intensity Index.

Table 3. An analysis table about BAI, BII, and BCI by each country.

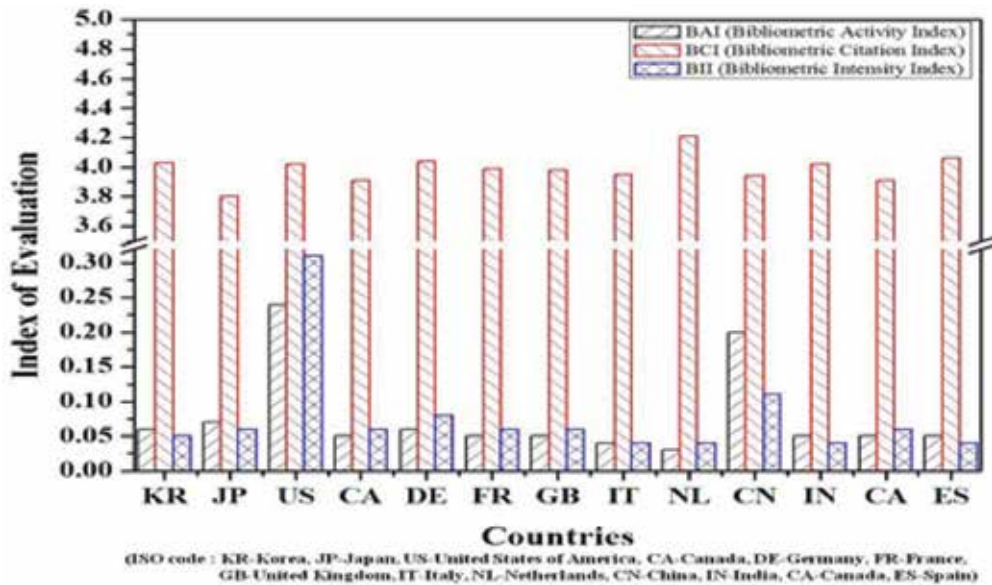


Figure 9. An analysis graph about BAI, BII, and BCI by each country.

important for separating membranes for wastewater treatment, Germany for water treatment membranes, Korea, India, the UK, Australia, and the Netherlands for seawater desalination membranes, USA, Japan, And the researcher.

3. Analysis of patent applicants and papers published by technology

In this chapter, we analyzed the top applicants and papers published by each technology and each classification (separation membranes for wastewater treatment, purification membranes for water treatment, separators for seawater desalination, and separation membranes for ion exchange processes). In the case of patents, applicants from all countries are categorized as applicants according to the section. The applicants are divided into three sections (1995–1999), two sections (2000–2004), three sections (2005–2009) (1997 ~ 2001), two sections (2002 ~ 2006), three sections (2007 ~ 2001), and three sections (2011 ~ 2016), and the changes in the top 13 countries were confirmed.

Looking at the top applicants by overall technology, although the overall strength of Japan can be seen, the number of Korean applicants for technology is gradually increasing (Korea Institute of Energy Research, Woongjin Chemical, LG Chem).

Toray Industries, Japan, ranked second place (31), second place (43), second place (43), and third place (48) (53 cases).

In the case of the thesis, if we look at the top publishing countries by overall technology, the overall strength of the USA is strong, but China and Korea are showing a sharp rise, and Japan is steadily declining. In Korea, it is ranked 13th place (130 cases) in one section, 7th place (538 cases) in two sections, 5th place (890 cases) in three sections, and 3rd place (1455 cases) in four sections.

Figures 10 and 11 and Tables 4 and 5 show the top patent applicants and top papers published by technology in the last 10 years.

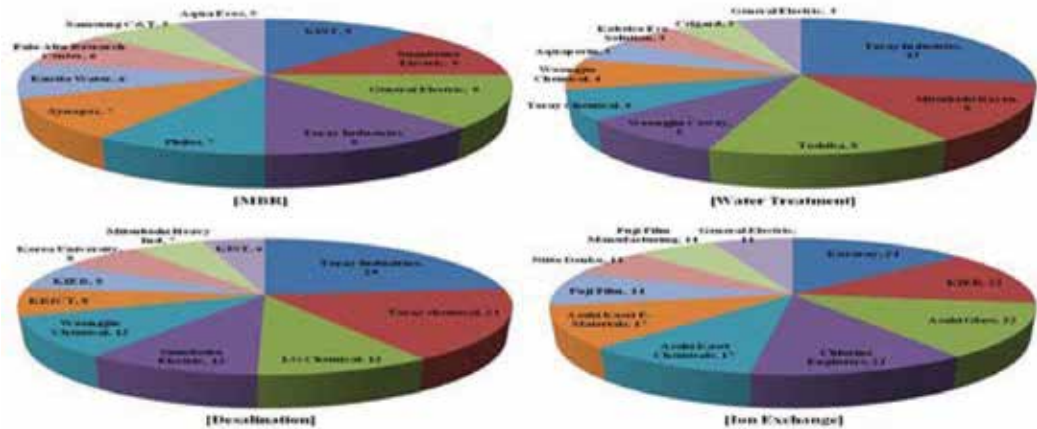


Figure 10. Comparison of total number of patent applications of global company in field of different membrane technology between the periods 2006 and 2016.

3.1. Top applicant and posting office of separation membranes for wastewater treatment

Japan is the main applicant of the separation membranes for wastewater treatment. In Korea, the rankings are gradually increasing over time. (Korea Institute of Science and Technology, Korea Advanced Institute of Science and Technology, Woongjin Chemical), 4 (Korea Institute of Science and Technology), 2 (Korea Institute of Science and Technology, Phylos, Sinopec, and Samsung C & T). Among them, Korea Institute of Science and Technology (KIST) ranked eighth place (4 cases) in two sections, third place (7 cases) in three sections, and first place (9 cases) in four sections.

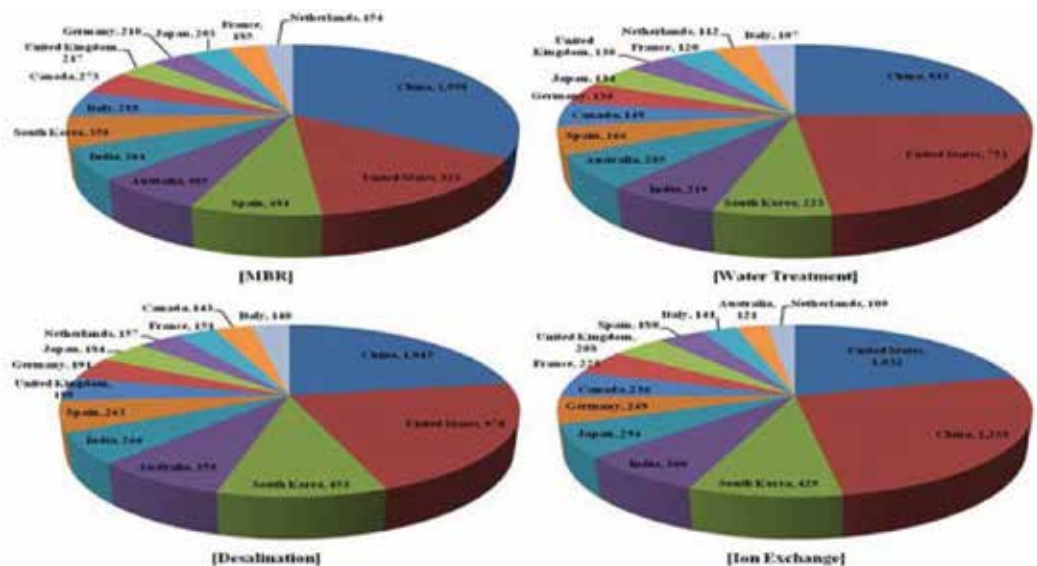


Figure 11. Comparison of total number of papers publications of global company in field of different membrane technology between the periods 2006 and 2016.

In the case of the top publishing countries, the USA is strong overall, but China has steadily climbed to the top of the four sections, and Japan is steadily declining. In Korea, Korea ranked eighth place (46 cases) in the first section, fourth place (179 cases) in the second section, sixth place (236 cases) in the third section, and sixth place (350 cases) in the fourth section.

3.2. Top applicants and posting authorities for separation membrane for water treatment

The top applicants of water treatment membranes are generally Japan, but in Canada and the UK in the second section, in Korea in the third section and in Korea and the United States and Denmark in the fourth section, It can be seen that patent applications are increasingly being made in various countries. Toray Industries in Japan has filed more than 10 patents in all segments and continues to apply for patents related to separation membranes for water treatment. The Korean applicant has applied for Woongjin Coway (fourth place, 6 cases) in three sections, Woongjin Coway (fourth place, 5 cases) and Woongjin Chemical (sixth place, 4 cases) Can be.

In the case of the top publishing countries, the overall strength of the USA is strong, but China and Korea have shown a sharp rise, and Japan is showing a steady decline. In Korea, there are 12 (17 cases), 1 (5 cases), 3 (7 cases), and 3 (223 cases).

3.3. Top applicant and posting office of seawater desalination membrane

The top applicant for seawater desalination membranes is Toray Industries, Japan, which has filed more than 10 applications in all segments, showing continuous applications for membrane-related desalination membranes. There are four applicants from Korea (Saehan), two from two sections (Saehan and KEPCO), four from three sections (Gwangju Institute of Science and Technology, Woongjin Chemical, Siontech and Hyosung) (LG Chem, Woongjin Chemical, Korea Research Institute of Chemical Technology, Korea Institute of Energy Research, Korea University, Korea Institute of Science and Technology).

In the case of the top publishing countries, the overall strength of the USA is strong but China and Korea have shown a sharp rise and Japan is showing a steady decline. Korea ranked 13th place (14 cases) in the first section, 13th place (53 cases) in the second section, 3rd place (203 cases) in the third section, and 3rd place (453 cases) in the fourth section.

3.4. Top applicant and posting office for separation membranes for ion exchange processes

Asahi Glass is ranked first place in the first section (28 cases), first place in the second section (41 cases), first place in the third section (76 cases) (22 cases), showing a slight decline. In addition, Chlorine Engineers ranked sixth (8 cases) in one section, fourth place (19 cases) in two sections, fifth place (19 cases) in three sections, and fourth place (21 cases) in four sections. The application rose steadily. 1 in the three sections (Samsung SDI) and one in four sections (Korea Institute of Energy Research) in the ion exchange process.

In the case of top publishing countries, the USA has shown a decline but China and Korea have shown a sharp rise. Korea ranked 13th place (53 cases) in the first section, 7th place (207

Ranking	MBR	Water treatment			Desalination			Ion exchange				
		Company	Country	Number	Company	Country	Number	Company	Country	Number		
1	KIST	KR	9	Toray Industries	JP	15	Toray Industries	JP	29	Kuraray	JP	24
2	Sumitomo Electric	JP	9	Mitsubishi Rayon	JP	8	Toray chemical	JP	21	KIER	KR	22
3	General Electric	US	9	Toshiba	JP	8	LG Chemical	KR	12	Asahi Glass	JP	22
4	Toray Industries	JP	9	Woongjin Coway	KR	5	Sumitomo Electric	JP	12	Chlorine Engineers	JP	21
5	Philos	KR	7	Toray Chemical	JP	4	Woongjin Chemical	KR	12	Asahi Kasei Chemicals	JP	17
6	Synopex	KR	7	Woongjin Chemical	KR	4	KRICT	KR	8	Asahi Kasei E-Materials	JP	17
7	Kurita Water	JP	6	Aquaporin	DK	3	KIER	KR	8	Fuji Film	JP	14
8	Palo Alto Research	US	6	Kobelco Eco-Solution	JP	3	Korea University	KR	8	Nitto Denko	JP	11
9	Samsung C&T	KR	5	Celgard	US	3	Mitsubishi Heavy Ind	JP	7	Fuji Film Manufacturing	NL	11
10	Aqua Ecos	JP	5	General Electric	US	3	KIST	KR	6	General Electric	US	11

ISO code: KR, Korea; JP, Japan; US, United States of America; DK, Denmark; NL, Netherlands.

Table 4. Patent application company by each technology (past 10 years).

Ranking	MBR		Water treatment		Desalination		Ion exchange	
	Country	Number	Country	Number	Country	Number	Country	Number
1	China	1998	China	812	China	1015	United States	1032
2	United States	921	United States	751	United States	970	China	1255
3	Spain	481	South Korea	223	South Korea	453	South Korea	429
4	Australia	405	India	219	Australia	358	India	360
5	India	364	Australia	205	India	266	Japan	294
6	South Korea	350	Spain	166	Spain	263	Germany	249
7	Italy	288	Canada	149	United Kingdom	199	Canada	236
8	Canada	273	Germany	136	Germany	191	France	225
9	United Kingdom	217	Japan	134	Japan	184	United Kingdom	208
10	Germany	210	United Kingdom	130	Netherlands	157	Spain	180
11	Japan	203	France	120	France	151	Italy	141
12	France	185	Netherlands	112	Canada	143	Australia	121
13	Netherlands	154	Italy	107	Italy	140	Netherlands	109

Table 5. Papers application country by each technology (past 10 years).

cases) in the second section, 4th place (325 cases) in the third section, and 4th place (429 cases) in the fourth section.

4. Conclusion

The purpose of this review is to examine the progress of research on the water treatment membranes of each country by evaluating the technical competitiveness of the patent and thesis of the water treatment membranes. In order to evaluate the competitiveness of patent technology, we analyzed the technology using four evaluation items: patent activity, patent concentration, patent market power, and patent influence. Of the 4433 valid patents searched for in relation to water treatment membrane technology, Korea, which belongs to the top 10 countries, ranked second place in patent activity, 10th place in patent market power, and 7th place in patent efficacy, indicating a concentration tendency. As a result of analyzing the top applicants by technology and section, it is found that Japan is much stronger overall, among which Toray Industries, Nitto Denko, and Asahi Glass are among the top applicants. In recent years, however, applications have been actively being made in Korea, such as Korea Institute of Energy Research, Korea Institute of Science and Technology, and Saehan. In addition, some applications related to the technology have appeared in other

countries such as the USA and Canada. The competitiveness of patent technology in Korea can be relatively low compared to Japan in relation to technology, but if the trend is steadily rising in the recent years, the competitiveness of patent technology in Korea will sufficiently increase in future.

In case of publishing the thesis, we analyzed the technical competitiveness of the thesis on the related technology by using three evaluation items, thesis activity, thesis influence, and thesis concentration. Among the 47,242 validated papers related to water treatment membrane technologies, Korea ranked among the top 13 countries in terms of thesis activities and ninth in terms of thesis influence, and the concentration of thesis was mostly on seawater desalination membranes (1.19). As a result of analyzing the top ranking countries by technology and sector, overall, the USA has shown stronger strength; China and Korea are rising sharply, and Japan has shown a declining trend. The technology competitiveness in Korea can be relatively low compared to the developed countries in the related technology, but if the trend is steadily rising in the recent years, the competitiveness of paper technology in Korea will sufficiently increase in future.

When the patent application and the publication of the papers are comprehensively judged, the activities of patents and theses are actively carried out, but the qualitative level (market power, influence, concentration) is lower than those of the competitors. Among the four water treatment membrane technologies, Ion Exchange Membrane has the highest concentration of patents, of 0.57, the lowest among the top 10 countries, and its market power and influence remain low. The results of the papers showed a similar tendency as the patent applications. Though the activities of the thesis were recorded in the top 13 of the top applications, the influence of the quality of the thesis was recorded at the lowest level (ninth place). Particularly, in the case of the Republic of Korea, the separation membrane for ion exchange process among the four water treatment membrane technologies has the highest activity rate but the least influence. This is considered to be a result of the high price formation, low durability, commercialization technology, and the formation of a supply system in the ion exchange membrane for the ion exchange process in the domestic market. In order to solve this problem (solar, wind, geothermal, etc.), technological internalization through technological advancement, as well as a system that can secure economic efficiency, is important. In addition, it is necessary to develop pro-market-type products suitable for demand sites such as urban areas and industrial complexes that can respond to the increase in social demand for greenhouse gas reduction and stability of the metropolitan area system. It is necessary to utilize it as a strategy to cope with climate change and power plants and to utilize renewable energy in the medium and long term. Will gradually increase..

Acknowledgements

This study was carried out through the analysis of the data of WIPS, a patent analysis agency, and with the help of Kim Se-Jong, Ph.D.

Author details

Chang Hwa Woo

Address all correspondence to: woo@gnu.ac.kr

Gyeongsang National University Academy and Industry Collaboration, Jinjusi,
Republic of Korea

References

- [1] Peter H. Global freshwater resources: Soft-path solutions for the 21st century. *Science*. 2003;**22**:1524-1528
- [2] Hong S, Lee S, Kim J, Kim J, Ju YG. Evolution of RO process for green future. *KIC News*. 2011;**14**:9-20
- [3] Kim S, Lee J, Nam S. Characterization of PVDF-DBP materials for thermally induced phase separation. *Membrane Journal*. 2016;**26**:449-457
- [4] Mallevalle J, Odeldaal PE, Wiesner MR. *Water Treatment Membrane Processes*, 11-11. NY, USA: McGraw-Hill; 1996
- [5] Hwang H, Nam S, Koh H, Ha S, Barbieri G, Drioli E. The effect of operating conditions on the performance of hollow fiber membrane modules for CO₂/N₂ separation. *Journal of Industrial and Engineering Chemistry*. 2012;**18**:205-211
- [6] Park J, Kim D, Nam S. Characterization and preparation of PEG-polyimide copolymer asymmetric flat sheet membranes for carbon dioxide separation. *Membrane Journal*. 2015;**25**:547-557
- [7] Kim D, Nam S. Research and development trends of polyimide based material for gas separation. *Membrane Journal*. 2013;**23**:393-408
- [8] Strathmann H. Membrane separation process. *Journal of Membrane Science*. 1981;**9**: 121-189
- [9] Hong S, Park J. Hybrid water treatment of tubular ceramic MF and photocatalyst loaded polyethersulfone beads: Effect of organic matters, adsorption and photo-oxidation at nitrogen back-flushing. *Membrane Journal*. 2013;**23**:61-69
- [10] Park Y, Nam S. Characterization of water treatment membrane using various hydrophilic coating materials. *Membrane Journal*. 2017;**27**:60-67
- [11] Zhang TC, Surampalli RY, Vigneswaran S, Tyagi RD, Ong SL. *Membrane Technology and Environmental Applications*, 41-74. VA, USA: American Society of Civil Engineers; 2012
- [12] Choi H, Park H. Preparation of higher reinforced PVdF hollow fiber microfiltration. *Membrane Journal*. 2010;**20**:320-325

- [13] Laninovic V. Relationship between type of non solvent additive and properties of polyethersulfone membranes. *Desalination*. 2005;**186**:39-46
- [14] van de Witte P, Dijkstra P, van den Berg JWA, Feijen J. Phase separation processes in polymer solutions relation to membrane formation. *Journal of Membrane Science*. 1996;**117**:1-31
- [15] Shim H, Lee Y, Nam S, Choi Y. Depth cartridge filter for industrial liquid filtration. *Membrane Journal*. 2009;**19**:173-182
- [16] Kim M, Park J. Membrane fouling control effect of periodic water-back-flushing in the tubular carbon ceramic ultrafiltration system for recycling paper wastewater. *Membrane Journal*. 2001;**11**:190-203
- [17] Fiksdal L, Leiknes T. The effect of coagulation with MF/UF membrane filtration for removal of virus in drinking water. *Journal of Membrane Science*. 2006;**279**:364-371
- [18] Jang J, Chung Y, Lee Y, Nam S. Preparation and properties of membranes for the application of desalting, refining and concentrating for dye processing. *Membrane Journal*. 2006;**16**:213-220
- [19] Costa A, Pinho M. Performance and cost estimation of nanofiltration for surface water treatment in drinking water production. *Desalination*. 2006;**196**:55-65
- [20] Hilal N, Al-Zoubi H, Mohammad A, Darwish N. Nanofiltration of highly concentrated salt solutions up to seawater salinity. *Desalination*. 2005;**184**:315-326
- [21] Courfia K, Saidou N, Mouhamadou A, Michel F, André D. Performance of nanofiltration (NF) and low pressure reverse osmosis (LPRO) membranes in the removal of fluorine and salinity from brackish drinking water. *Journal of Water Resource and Protection*. 2011;**3**:912-917
- [22] Dalvi A, Al-Rasheed R, Javeed M. Studies on organic foulants in the seawater feed of reverse osmosis plants of SWCC. *Desalination*. 2000;**132**:217-232
- [23] Kim S, Woo S, Hwang H, Koh H, Ha S, Choi H, Nam S. Preparation and properties of chlorine-resistance loose reverse osmosis hollow-fiber membrane. *Membrane Journal*. 2010;**20**:304-311
- [24] Hwang H, Koh H, Nam S. Preparation and properties of cellulose triacetate membranes for reverse osmosis. *Membrane Journal*. 2007;**17**:277-286
- [25] Won I, Kim D, Chung K. Transmembrane pressure of the sinusoidal flux continuous operation mode for the submerged flat-sheet membrane bioreactor in coagulant dosage. *Membrane Journal*. 2015;**25**:7-14
- [26] Mayhew M, Stephenson T. Low biomass yield activated sludge: A review. *Environmental Technology*. 1997;**18**:883-892
- [27] Marcel M. *Basic Principles of Membrane Technology*. 2nd ed. Dordrecht/Boston/London, USA: Kluwer Academic Publishers; 1996. pp. 157-209

- [28] Watanabe Y, Kimura K, Suzuki T. Membrane application to water purification process in Japan—Development of hybrid membrane system. *Water Science and Technology*. 2000;**41**:9-16
- [29] Knops F, van Hoof S, Futselaar H, Broens L. Economic evaluation of a new ultrafiltration membrane for pretreatment of seawater reverse osmosis. *Desalination*. 2007;**203**, 300-306
- [30] Jang H, Kwon D, Kim J. Seawater desalination pretreatments and future challenges. *Membrane Journal*. 2015;**25**:301-309
- [31] Kim D, Jo M, Nam S. A review of polymer-nanocomposite electrolyte membranes for fuel cell application. *Journal of Industrial and Engineering Chemistry*. 2015;**21**:36-52
- [32] Kim D, Jeong M, Nam S. Research trends in ion exchange membrane processes and practical applications. *Applied Chemical Engineering*. 2015;**26**:1-16
- [33] Hwang H, Kim Y, Nam S, Rhim J. Preparation of PVA/PAM/zirconium phosphate membrane for proton exchange membranes. *Membrane Journal*. 2004;**14**:117-125
- [34] Yu D, Nam S, Yoon S, Kim T, Lee J, Nam S, Hong Y. Edge protection using polyacrylonitrile thin-films for hydrocarbon-based membrane electrode assemblies. *Journal of Industrial and Engineering Chemistry*. 2015;**28**:190-196
- [35] Jeong M, Nam S. Reviews on preparation and membrane applications of polybenzimidazole polymers. *Membrane Journal*. 2016;**26**:253-265
- [36] Kim D, Hwang H, Jung S, Nam S. Sulfonated poly(arylene ether sulfone)/laponite-SO₃H composite membrane for direct methanol fuel cell. *Journal of Industrial and Engineering Chemistry*. 2012;**18**:556-562
- [37] Lee S, Kim H, Nam S, Park C. Synthetic strategies for high performance hydrocarbon polymer electrolyte membranes (PEMs) for fuel cells. *Membrane Journal*. 2016;**26**:1-13
- [38] Lee D, Kim S, Nam S, Kim H. Synthesis and ion conducting properties of anion exchange membranes based on PBI copolymers for alkaline fuel cells. *Membrane Journal*. 2010;**20**:217-221
- [39] Park C, Nam S, Hong Y. Molecular dynamics (MD) study of proton exchange membranes for fuel cells. *Membrane Journal*. 2016;**26**:329-336
- [40] Woo CH. Study on Matrix Module for Predicting of Emerging ICT Technology [master degree dissertation]. Asan, Korea: Hoseo University; 2014
- [41] No SY, Jang GY, Kim MJ, Lee JW. 2009 National R&D Patent Performance Survey, Analysis Report. Korea: KIPO; 2009. pp. 109-110
- [42] Development of Core Components and Element Technology for Wearable Smart Device. Korea: KISPEP; 2016. pp. 232-233
- [43] Analysis of ICT Technology Competitiveness using Quantitative Information for 2015. Korea: IITP; 2015. pp. 11-15

Alumina Membranes for Desalination and Water Treatment

Saad Alami Younssi, Majda Breida and
Brahim Achiou

Additional information is available at the end of the chapter

<http://dx.doi.org/10.5772/intechopen.76782>

Abstract

In recent years, there has been a growing interest in utilizing inorganic membranes, particularly alumina (Al_2O_3) ceramic membranes (CMs), and to address a variety of separation problems in miscellaneous industry. Al_2O_3 membranes are commercially predominant in CMs market. Al_2O_3 material is generally used either as membrane support and/or as membrane layer due to advantages provided by this material and its derivatives such as availability in tonnage quantities, chemical inertness, good hardness, and thermal stability of the porous texture during elaboration steps. In this chapter, we comprehensively look at the recent studies related to desalination and water treatment by ultrafiltration (UF), nanofiltration (NF) Al_2O_3 membrane, and highlight the separation properties of the membrane in specific environmental pollution. The influences of membrane operating conditions and water quality on the rejection of pollutant by Al_2O_3 membrane are reported through a series of bench-level experiments.

Keywords: Al_2O_3 , ceramic membrane, nanofiltration, ultrafiltration, desalination, wastewater treatment

1. Introduction

The rapid increase in urbanization and industrialization has led to the global economic development, which has significantly contributed to the human welfare, but led at the same time to severe environmental degradation that automatically affects sustainable development. Indeed, the uncontrollable rise of waste and wastewater discharges create a series of environmental issues, making difficulty to access to water of adequate quality for human consumption

and for industrial-scale production [1]. This strong dependence of pollution and water deterioration on industrial activities is well witnessed in developing countries, where 90% of raw sewage and 70% of untreated industrial wastewater are released into water sources (surface and groundwater) [2]. Furthermore, the influence of industrial activities along with the variability of effluents quality and the leak of information of the exact amount of the untreated effluents exacerbates the situation [3]. The physicochemical analysis of wastewater demonstrated a wide range of pollutants such as nitrates, nitrites, dyes, organic components, and toxic heavy metals has been reported [4]. In addition, the presence of different pollutants in water has a direct impact in increasing chemical oxygen demand (COD), biological oxygen demand (BOD), total dissolved solids (TDS), and salinity. Furthermore, regulations related to the quality of drinking water and wastewater has increasingly become severe. Therefore, the aim of finding a balanced solution between environmental protection and industrial progress is an overarching objective for all policy-makers and scientific researchers. As a result, industries gained awareness of the importance of treating wastewater (recycle/reuse), and some treatment technologies have already been brought into practice [5]. However, the use of one technology over another depends on several factors. The efficiency of many current treatment technologies still needs significant improvements, from the energy point of view. Membrane technology has become a promising industrial alternative compared with traditional treatment techniques, such as distillation, absorption, adsorption, extraction, activated sludge, trickling filters, stabilization ponds, and constructed wetlands. In fact, membrane processes for water treatment such as microfiltration (MF), ultrafiltration (UF), nanofiltration (NF), and reverse osmosis (RO) have been used in industrial-scale for years now [6, 7]. These membranes are divided (based on material nature) into two categories, organic membranes (or polymeric membrane) and inorganic membranes (also referred to as ceramic or mineral membranes).

Polymeric membranes (PMs) are considered to be the first membrane generation, and they are on the frontline of wastewater treatment [8], recognized as an integral part of treatment processes. However, PMs suffer from several limitations such as low-mechanical strength, low fluxes, restricted chemical and thermal stability, and the trade-off relationship between permeability (P) and selectivity as well as membrane fouling [9]. In contrast, the application of ceramic membranes (CMs) offers the advantage to work in harsh operating conditions due to their superior mechanical, thermal, chemical stability, and prolonged lifetime [10–12]. In addition, CMs are less exposed to the phenomenon of biofouling, caused by the membrane deterioration by bacteria [13]. Depending on the material nature, CMs can be elaborated in many configurations and with different pore size, which facilitates their use. Among the various mineral materials (titania (TiO_2), silica (SiO_2), and zirconia (ZrO_2)...) used in CMs elaboration. Alumina (Al_2O_3) is the most applied material due to economical consideration along with its ability to resist in high transmembrane pressures (TMP) [14]. Usually, Al_2O_3 CMs (Al_2O_3 -CM) are fabricated in a multi-layer structure, in other words, each layer is different than another in pore size and thickness. Furthermore, Al_2O_3 is known by two impressive characteristics, namely by its hydrophilic and covalent bonding characteristics [11, 15].

Al_2O_3 -CMs for UF and NF have shown an interesting efficiency in desalination and water treatment. As known in membrane technology, the efficient membrane should combine high permeability with high rejection. These membranes have found several industrial

applications, which cover sea water desalination, food production, gas and vapor separation, and domestic and oily wastewater treatment. Indeed, UF membranes demonstrate good performance in removing turbidity and pathogens, and they are very effective and reliable in removing microbiological parasites, dyes, and some ions in specific conditions. Mostly, Al_2O_3 -UF has been efficiently applied for the separation of components with a size ranging from 2 to 100 nm (like proteins and colloidal particles). The Al_2O_3 -NF membranes have been operated for separation of components with low-molecular weight (MWCO 200–1000) and electrolyte by optimization of operating conditions.

2. Development of ceramic membranes (CMs)

The word membrane in association with the separation phenomenon, purification or concentration processes is defined as a thin semi-permeable layer, which separates two phases. This semi-permeable layer is able to selectively restrict the transport of one or many components. In other words, a membrane is a thin layer that allows a component to pass more readily than others (**Figure 1**). The components that pass through the membrane are called permeate, whereas the components that are retained are defined as retentate [16]. Also, it should be noted that the first recorded research on membrane phenomenon appears to be done by French Abbe Nollet in 1748, and Fick is the first to synthesize membrane from nitrocellulose (organic). The first membrane filters were commercialized in 1927 by the Sartorius Company [17].

However, the elaboration of inorganic membranes only started around the 1940s, by the development of Vycor glass membranes [18]. The first application of the CM is related to the uranium isotopes separation by gaseous diffusion processes. In 1973, two companies Ceraver and Euroceral started to produce ceramic oxide support for nuclear fission industries, which still are operating in Eurodif plant (France) [19]. The intensive research and the continuous development of CMs have resulted in the elaboration of MF and UF membranes. The concept of liquid filtration was developed by Carre in 1960, and the filtration was done on dynamic zirconium hydroxide. In addition, SFEC is the first company to manufacture cross-flow filtration system equipped with the inorganic membrane (1978s) [18]. Recently, CMs have undergone notable development due to its different advantages and have been widely adopted.

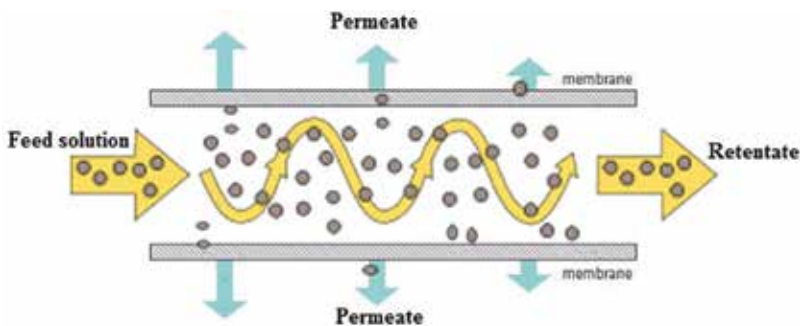


Figure 1. Principe filtration by membranes.

Membrane processes are categorized based on the types of driving force and pore size solution as well as the phases of permeate and feed. The driving force can take different forms; this force can be a concentration gradient, pressure, or voltage difference across the membrane. Depending on the driving force as well as the pore size, membrane processes are classified, therefore, to MF, UF, NF, RO, dialysis, electrodialysis (ED), and gas separation (GS) as in **Table 1**. However, it should be noted that even though dialysis, ED, and GS process are conducted in liquid phase, but CMs have not been yet applied to this kind of separation processes [20]. To overcome the problem of complexity of water pollution, as well as the limitations of individual systems, a combination of membrane techniques can be used.

2.1. Membrane materials

Inorganic membranes are generally classified into porous and amorphous membranes, porous and crystalline membranes, and dense membranes. The materials used in the elaboration of dense CMs are usually metals, such as palladium, nickel, silver, and zirconium, while porous CMs are produced from metallic oxides (Al_2O_3 , ZrO_2 , TiO_2 , and SiO_2), carbon, and zeolites. The use of a material than another depends on the preparation technique and the desired membrane structure. CMs with a large range of pores size can be obtained with different preparation techniques, as an example the slip-casting tape-casting technique, pressing, extrusion, the sol-gel, and dip-coating processes (**Table 2**).

Tighter UF and NF membranes are generally prepared by the sol-gel technique. In addition, alpha alumina ($\alpha\text{-Al}_2\text{O}_3$) and gamma alumina ($\gamma\text{-Al}_2\text{O}_3$) are the most common CMs materials. The attractive use of Al_2O_3 in membrane elaboration is mainly due to its properties, such as high resistance to organic solvent, narrow particle size distribution, high-surface area as well as a high-density. **Table 3** demonstrates the thermal and mechanical properties of Al_2O_3 as CMs material. In addition, the great abundance of this material, as well as its chemical stability and a small amount of shrinkage makes Al_2O_3 the most encouraging option in CMs elaboration [21–23].

Al_2O_3 powder (as a raw material) is principally produced by the Bayer process using the bauxite mineral. While Al_2O_3 porous membrane have been prepared by the holds method in which

Process	Nominal pore size	Driving force	Average permeability $\text{L/m}^2 \text{ h bar}$
Microfiltration	0.05–10 μm	1–3 bar	500
Ultrafiltration	0.001–0.05 μm	2–5 bar	150
Nanofiltration	<2.0 nm	5–15 bar	10–20
Reverse osmosis	<1 nm	15–75 bar	5–10
Gas separation	<0.5–1 nm		
Membrane distillation	0.5–2 nm		
Electrodialysis	MW < 200 Da	Electrical potential, 1–2 V/cell	

Table 1. Classification of membrane processes [8, 20].

Preparation techniques	Metallic oxides
Sol-gel	γ -Al ₂ O ₃ , SiO ₂ , TiO ₂ , ZrO ₂
Chemical vapor deposition	SiO ₂
Pyrolysis	SiC, Si ₃ N ₄
Hydrothermal treatment	Silicalite
Anodic oxidation	Al ₂ O ₃ (Amorphous)
Phase separation/ leaching	SiO ₂
Dynamic membranes	ZrO ₂ (Amorphous)

Table 2. Preparation techniques of CMs [8].

Mechanical properties	
Tensile Strength (MPa)	117–173
Bending Strength (MPa)	307–413
Modulus of Elasticity (E) ×10 ⁸ (MPa)	21.27–26.8
Compressive Strength (MPa)	1600–3733
Modulus of Rigidity (G) × 10 ⁸ (MPa)	8.67–11.3
Hardness on the Mohs scale	9
Thermal properties	
Melting point (°C)	2051 ± 9.7
Thermal coefficient at 200–1000°C	8.80 × 10 ⁻⁶
Boiling point (°C)	3530 ± 200

Table 3. Mechanical and thermal properties of alumina [21, 22].

boehmite sol is made by the hydrolysis of aluminum butoxide or aluminum propoxide in hot water (above 80°C) and peptized by acid (nitric acid) afterward [20]. Al₂O₃ is classified into two major groups depending on the purity of Al₂O₃, the first of high-grade with 99%, and the second grade between 80 and 99% of Al₂O₃. The color of Al₂O₃ changes along with the addition of additives or the presences of impurities, the sintering atmosphere, and by the interaction with ionizing radiation. In general, Al₂O₃ is characterized by a white color. However, in some cases, it can change the coloration to pink (when the purity of Al₂O₃ is equal to 88%) or brown (96% alumina).

Generally, the oxide of stoichiometry Al₂O₃ is well known by a large diversity of phases. The structural diversity of Al₂O₃ is emphasized in a series of transitions (α , γ , χ , κ , δ , θ , and η). Transition means that the crystal structure of Al₂O₃ depends on temperature. It is thermodynamically varied from unstable to stable, and it should be noted that α -Al₂O₃ (Corundum) is the most thermodynamically stable form of alumina (Al₂O₃) (**Figure 2**).

An increase in firing temperature above 1000°C leads to the phase transition of γ -Al₂O₃ to α -Al₂O₃. As a result, a conversion of UF membranes to MF membranes is obtained. Further, **Figure 3**

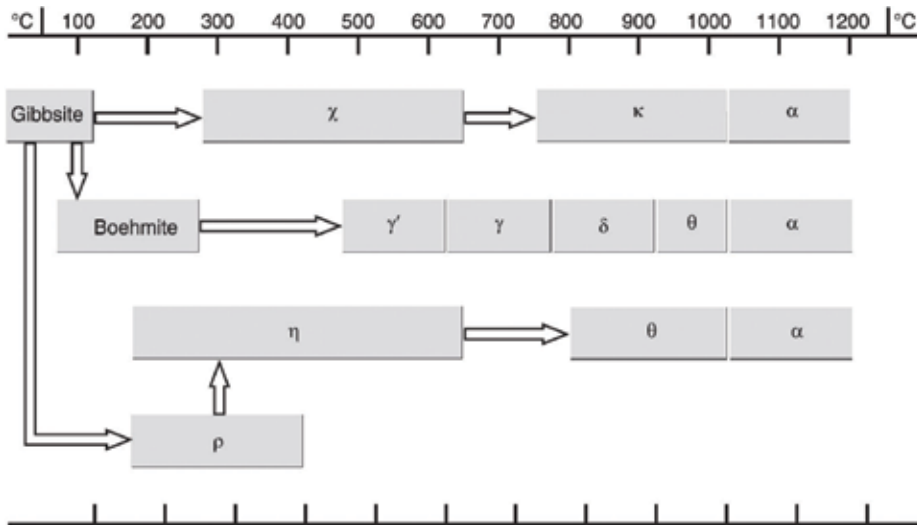


Figure 2. Transitions of alumina (Al_2O_3) [24].

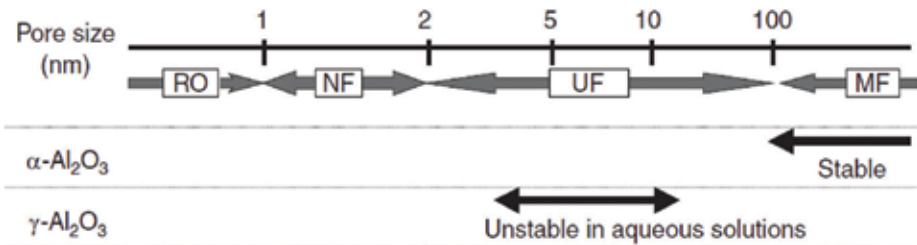
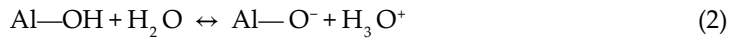
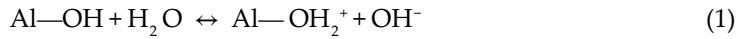


Figure 3. Material and pore sizes for use in liquid separation [20, 25].

shows a schematic diagram of pore sizes obtained with Al_2O_3 materials that have been used for liquid separation. α -Alumina has excellent stability in both acidic and basic pH; however, it has a limitation in pore size, which is in a range of MF (larger than 100 nm). On the other side, γ - Al_2O_3 is not stable as in the case of α - Al_2O_3 , however, it has a pore size as in UF range (4 nm).

When Al_2O_3 surface is hydrated, there is a finite solubility of Al_2O_3 into the water. The limit of solubility as well as the type of species in the solution depends upon the solution pH and temperature. Indeed, the hydrated surface of Al_2O_3 is known by amphoteric behavior, which means that the sign and the charge density of membrane surface can be controlled by controlling pH solution. The point of zero charge (pzc) is the value for which the electric charges of the fixed cations globally neutralize anions, which was found to be around 8 and 9. At pH above the pHpzc, the surface of membrane is negative, which is explained by the acidic dissociation of the surface hydroxyl groups Eq. (1). While the positive charge when the pH is below pHpzc is explained by proton addition to the neutral aquo complex due to the existence of AlOH_2^+ groups Eq. (2), depending on the following reactions (Eqs. (1) and (2)):



Application of Al_2O_3 membrane widely use a porous structure specially in solid–liquid and solid–GS, which is due to Al_2O_3 high structural durability, low-energy, easy cleaning, and mostly controllable microstructure [26]. In general, the elaboration of porous Al_2O_3 membrane implicates several techniques like green compact shaping and sintering, suspension preparation (by slurry or sol–gel processes). The preparation of Al_2O_3 -CMs by extrusion method is commonly applied for membrane with tubular or multi-channel membrane, whereas tape-casting technique is more suitable for Al_2O_3 -CMs with flat sheet structure. Furthermore, pressing and slip-casting methods are usually used for the production of symmetric structure of Al_2O_3 -CMs. The preparation of porous Al_2O_3 -CM of an asymmetric structure is achieved by tape-casting using phase-inversion techniques [27]. Furthermore, multi-layer composite membranes with an asymmetric structure can be processed using coating techniques [28]. It is worth to mention that Al_2O_3 membranes (MF, UF, and NF) have naturally hydrophilic character due to the presence of an oxide material in the hydroxyl group. The hydrophilic character presents extremely polar properties, which causes the absorption of water molecules by forming a hydrogen bond [29]. However, a strong adhesion between Al_2O_3 -CMs surface and foulants can mainly cause membrane fouling. Therefore, a superhydrophilic character of alumina’s membrane surface is more preferable [30].

2.2. Filtration modes

Membrane separation can be mainly operated in two modes (**Figure 4**), dead-end (frontal filtration) and cross-flow (tangential filtration). In dead-end filtration, feed solution flows perpendicularly

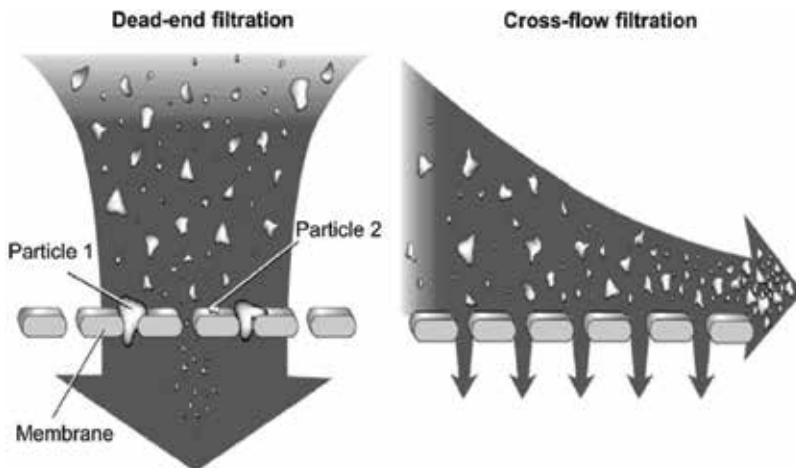


Figure 4. Schematic of dead-end and cross-flow filtrations [8].

on the membrane surface, which leads to the accumulation and disposition of the retained substance on membrane surface. In most filtration applications, the accumulation of particles on the membrane surface causes the formation of cake over the operating time. Consequently, the membrane performance is severely reduced and required a periodic backwash to control the cake formation and fouling phenomenon. Therefore, the dead-end mode is impractical for effluent highly charged with solid particles and it recommended for conventional filtration processes with dilute feed, such as filtration of surface water or secondary industrial effluents [10].

In another hand, in the cross-flow filtration, the feed solution flows tangentially (in a perpendicular direction) across the membrane. The cross-flow mode can result in higher permeation flux compare with the dead-end mode due that the stream continuously removes particles and simultaneously reduces the formation of cake layer as well as polarization layer [31]. Furthermore, the cross-flow filtration is extensively applied in most industrial large scales.

2.3. Membrane configuration

Large range of membrane devices is available for both cross-flow and dead-end modes. The expression "membrane configuration" makes reference to the membrane geometry and shape that depends on the flux of both permeate and feed solution pressure and fouling phenomenon. Generally, for CMs membrane, tree configurations are used in the water purification, namely tubular, flat disk and hollow fiber (as illustrated in **Figure 5**). These configurations are the commonly used the most in cross-flow mode [33].

In principle, the three types can be applied in dead-end configuration, however, there are susceptible to high fouling. For this reason, specific devices have been developed for dead-end

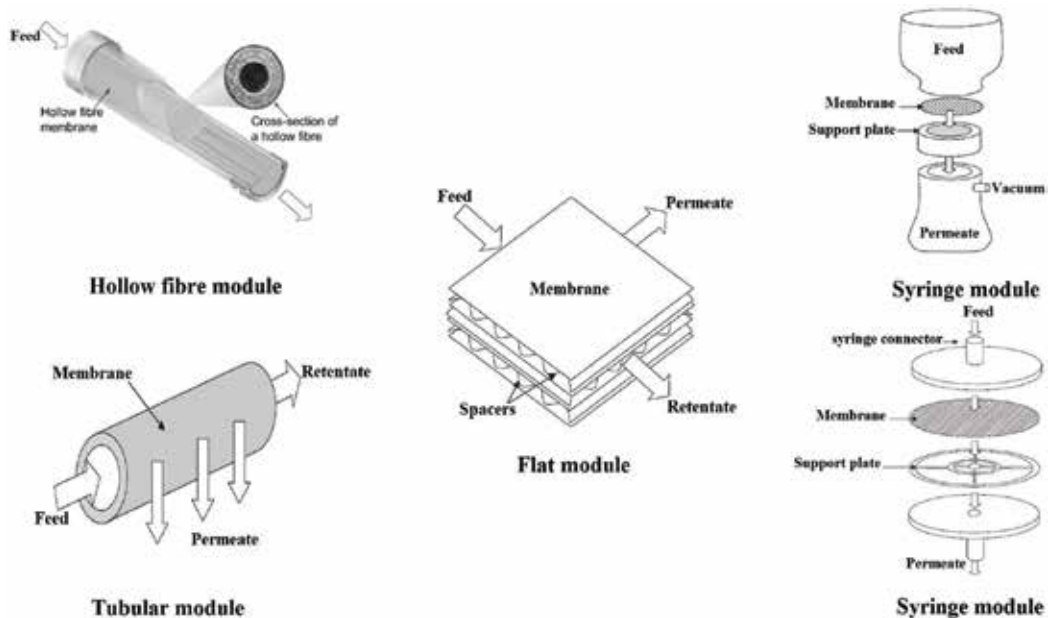


Figure 5. Membrane configurations [8, 32].

applications [34] such as syringe-end filters, centrifugal membrane, and vacuum filtration devices as illustrated in **Figure 5**. The most important properties for perfect membrane modules are high packing density, low-cost (operating and maintenance), good hydrodynamic propriety as well as cost-efficient production [35].

2.4. Membrane performance

For liquid separation, membrane performance is evaluated by simultaneous parameters, which are the permeate flux through the membrane and the rejection of soluble species, suspended or dispersed species. In order to characterize the rejection of membrane R generally, size exclusion technique is used, where R depends on the pore size and the membrane character (hydrophilic/hydrophobic), and the operation conditions (pH, pressure...).

Furthermore, dissimilar types of solute/solvent solutions can be applied. Usually, macrosolute solutions (as PEGs) or dextrans are employed for UF membranes, while for characterization of NF membranes, a mixture of mono- and multivalent salt solutions are used. The apparent rejection (R_a) and the intrinsic rejection (R_i) are defined, respectively, as follows (Eqs. (3) and (4)):

$$R_a = 1 - \frac{C_p}{C_f} \quad (3)$$

$$R_i = 1 - \frac{C_p}{C_w} \quad (4)$$

where C_p , C_f and C_w are, respectively, the species concentration in the permeate (C_p), feed, and at the membrane wall. The R_a is measured by sampling the feed and permeate phase, R_i takes into consideration the solute concentration at the membrane interface. It should be noted that a difference between R_i and R_a is due to the hydrodynamic resistance. To reduce this difference control of concentration and velocity of the feed solution is needed. $R = 0$ indicates no separation acquired, whereas $R = 1$ reveals that solute is retained, and the only solvent passes through the membrane.

In the case of a pressure-driven process, the membrane hydraulic permeability (L_p) (m/s Pa) is an important indicator of the membrane functionality. Darcy's law of flow through porous materials and r laminar flow conditions allows the determination the value of L_p according to Eq. (5). It should be noted that the volumetric permeate flux (J_v) ($m.s^{-1}$) is related to the TMP.

$$L_p = J/\Delta TMP \quad (5)$$

In addition, membranes know by fouling phenomenon. The membrane fouling is defined as the progressive accumulation of particles at the surface or in the pores of the membrane, which cause a decrease of permeates flux. The decrease in membrane capacity is mainly caused by the formation of a boundary layer during the process of filtration (**Figure 6**). Membranes fouling come in two forms: external fouling, which is the accumulation of rejected particles (foulants) on the external surface of the membrane, and an internal membrane fouling that

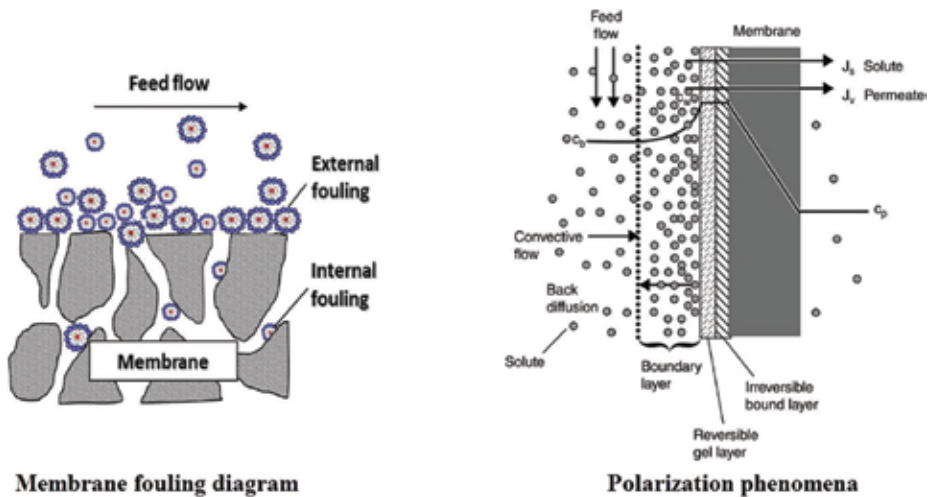


Figure 6. Schematic figure of membrane fouling and polarization phenomena [36].

represents the deposition or adsorption of microminiature particles or macromolecules within the internal pore structure of the membrane. The concentration polarization, during the initial period of filtering operation time, is one of the primary reasons for flux decline.

3. Different applications of Al_2O_3 UF, and NF ceramic membranes (CMs)

3.1. Desalination

Nowadays, desalination has become a very affordable solution to cope with the growing global water gap. However, even though water covers 70% of the earth surface but 97% of it has too high-salt content. The applications of separation techniques for desalination only cover 1% of the world's potable water supply. Desalination by membrane technology is commonly performed by RO membranes. The use of polymeric as material for membrane desalination has demonstrated some limitations such as membrane deterioration. For these reasons, research and development of new membrane materials could allow more opportunities for water desalination. Since the last decade, ceramic materials have known significant progress in desalination, especially using NF and UF membranes. The use of CMs especially $\gamma\text{-Al}_2\text{O}_3$ membranes in water desalination and water softening showed potential application [37, 38].

$\gamma\text{-Al}_2\text{O}_3$ NF membranes were primarily investigated in salt rejection by different authors. Baticle et al. [39] compared the filtering performance of two tubular $\gamma\text{-Al}_2\text{O}_3$ NF membranes, fired at 450–650°C, in terms of ion rejection and flux. The two NF membranes were prepared by a sol–gel process [40] having a pore size near to 1.3 nm for the membrane fired at 450°C (M1), and near to 2 nm for the membrane fired at 650°C (M2). The filtration tests were carried out in a tangential filtration setup. The tests were performed with different salts at a

concentration of 0.01 mol/l for M1 and 0.005 mol/l for M2 at applied pressure of 10 bar and pH (5, 0–5.6). For each salt, volume flux and rejection were measured at the steady state. In addition, an earlier work by Alami Younssi et al. [41] highlighted the rejection of mineral salts by a monotubular γ -Al₂O₃ NF membrane (M3) with a pore size of 0.7 nm obtained by sol-gel [40] and fired at 450°C. The filtration experiments of different salts at concentration of 0.01 mol/l were performed on tangential pilot and fixed pressure of 10 bar. The filtration results of the three membranes (M1, M2, and M3) are grouped in **Table 4**.

From **Table 4**, it can be concluded that the charge and size of different ionic species dramatically influence on the salt rejection. The ion valency has a dramatic effect, which can be manifested by an increase in salt rejection when the valency of the associated cation increase, M²⁺ (divalent cation) > M⁺ (monovalent cation). However, salt rejection decreases when the valency of the anion increases in the following order: NO₃⁻ > Cl⁻ > SO₄²⁻. Furthermore, the difference in rejection obtained for ions having the same charge (rejection of Na⁺ > K⁺) is mainly due to hydration effect. It was also found that the low permeation rates lead to negligence of the concentration polarization phenomenon. The effect of sintering temperature was marked by a small decrease of salt rejection, when the temperature is changed from 450 to 650°C. This decline is in agreement with weak electric interactions caused by larger pores. However, a variation in the density of the charges on the surface of the two membranes cannot be excluded.

In addition, the sintering temperature of the membrane has a profound effect on water permeability rather than salt permeability, which is not radically affected. The main responsible phenomenon for the electrolyte rejection in the different experiments is the electric repulsion or attraction happening between the dissolved ions and the membrane surface charge.

Anions	Cations	pH	R% of M1	R% of M2	R% of M3
NO ₃ ⁻	K ⁺	5.6	55	41	55
NO ₃ ⁻	Na ⁺	5.5	70		70
NO ₃ ⁻	Ca ²⁺	5.6	95		95
NO ₃ ⁻	Cu ²⁺	5.5	97		97
NO ₃ ⁻	Cd ²⁺	5.6	97		97
NO ₃ ⁻	Ni ²⁺	5.6	97		97
Cl ⁻	K ⁺	5.5	36		36
Cl ⁻	Na ⁺	5.6	50		50
Cl ⁻	Ni ²⁺	5.5	97	95	90
SO ₄ ²⁻	K ⁺	5.6	1		1
SO ₄ ²⁻	Na ⁺	5.6	20		20
SO ₄ ²⁻	Ca ²⁺	5.5	40		40
SO ₄ ²⁻	Cu ²⁺	5	45		45
SO ₄ ²⁻	Cd ²⁺	5.6	40		40
SO ₄ ²⁻	Ni ²⁺	5.9	40	20	40

Table 4. Rejection rate of different salts on γ -alumina NF membrane.

The typical behavior of Al_2O_3 NF membranes was also found during the filtration of different salt solutions, such as AlCl_3 , FeCl_3 , CaCl_2 , MgCl_2 , NaCl , NH_4Cl , MgSO_4 , and Na_2SO_4 , by a $\gamma\text{-Al}_2\text{O}_3/\alpha\text{-Al}_2\text{O}_3$ hollow fiber NF composite membranes (HFNF) prepared and characterized by Wang et al. [42]. The elaborated inorganic composite membranes were prepared by dip-coating $\gamma\text{-AlOOH}$ sol on $\alpha\text{-Al}_2\text{O}_3$ hollow fiber and sintered at 750°C . The optimal hollow fiber NF membrane has a mean pore size of 1.61 nm and permeability P equal to $17.4 \text{ L/m}^2 \text{ h bar}$; this permeance was found to be much higher than reported in the literature (**Table 5**) due to the relatively high-porosity (45%). Also, the membrane exhibited great chemical resistance in different solvents and harsh pH. Separation performance of the studied membrane, at applied pressure of 5.0 bar and fixed salt concentration of 2000 ppm, exhibited higher retentions of multivalent ions than monovalent ions, such as Fe^{3+} (97.1%) > Al^{3+} (90.9%) > Mg^{2+} (85.0%) > Ca^{2+} (84.1%) as in **Figure 7**. It could be explained by the dominance of Donnan exclusion mechanism and size exclusion mechanism [43].

Di Yu et al. [37] elaborated a thin homogeneous supported mesoporous $\gamma\text{-Al}_2\text{O}_3$ membrane on top of hybrid $\alpha\text{-Al}_2\text{O}_3$ support with a pore size of 4 nm. The preparation of the $\gamma\text{-Al}_2\text{O}_3$ membranes was obtained by dipping supports in a nanoparticle precursor dispersion and applied for water permeation and purification of salt solutions. The experiments were conducted on a dead-end mode (300 kPa), and the water flux was measured to calculate the permeability of the membrane ($7.7 \text{ L/m}^2 \text{ h bar}$). Aqueous solutions prepared from CaCl_2 and NaCl salts with a concentration of 10^{-3} mol/l along with an artificial sea water sample were used to demonstrate the permselectivity of the NF membrane. The pH of the synthesized salt solutions (except the pH of sea water is natural pH) was adjusted to be 4.6 to the surface of the $\gamma\text{-Al}_2\text{O}_3$ is properly charged with adsorbed positive ions, and not chemically attacked. The results showed a high-rate rejection for Ca^{2+} and Na^+ ions (98.7% for Ca^{2+} , > 79.0% for Na^+) and matched the typical behavior of NF membrane in the manner that retained hydrated ions ($\sim 0.5 \text{ nm}$) are much smaller than the NF membrane pore size ($\sim 4 \text{ nm}$). However, the rejection of sea water is weak and found to be 6.3%. These results were explained either by a surface adsorption chemistry and/or electrokinetic interaction between the ions in the solution and the adsorbed ions.

From the different parameters influencing the selectivity and permeability of NF and UF CMs filled with electrolytes, we found pressure and potential gradients the consequences of these parameters are the results of phenomena like streaming potential, electro-osmosis, and electroviscous retardation, which influences the flow of electrolyte solutions [48]. This was in coincidence with the results as Wang et al. [42] observed. The salts transport mechanism through this membrane, relied on diffusion and convection [49]. The diffusion which resulted from a concentration difference governed at lower pressure. Contrary, the convection which is due to a pressure gradient across the membrane dominates the filtration process at elevated applied pressures [50]. That is the drag forces are less important than the surface forces, when the pressure is low. In contrast, as the pressure increases the surface forces stays constant while increasing velocity in membrane pores leads to an increase of the drag forces toward the permeate.

For a fixed concentration it has demonstrated that the reflection coefficient (σ) and solute permeability (P), which are the phenomenological coefficients, depend on the nature of the cation

Type membrane	Sintering T°	Elaboration technique	Permeability	Experimental set-up	Pore size (nm)	CM Shape	Concentration	Rejection	Article
γ -Al ₂ O ₃ / hybrid α -Al ₂ O ₃ membrane	950°C	Dip-coating	7.7 L/m ² h bar	Dead-end filtration	4	Disk-shape	0.001 mol/l	Ca ²⁺ > 98.7% Na ⁺ > 79.0%	[37]
γ -Al ₂ O ₃ / α -Al ₂ O ₃	450°C	Sol-gel process		Cross-flow filtration	1.3	Tubular	0.01 mol/l	Ca ²⁺ > 95	[39]
γ -Al ₂ O ₃ / α -Al ₂ O ₃	650°C	Sol-gel process		Cross-flow filtration	2	Tubular module	0.005 mol/l		[39]
γ -Al ₂ O ₃ / α -Al ₂ O ₃	450°C	Sol-gel process	12 L/m ² h bar.	Cross-flow filtration	0.7	Tubular		Ca ²⁺ > 95%	[41]
γ -Al ₂ O ₃ / α -Al ₂ O ₃		Dip-coating	17.4 L/m ² h bar	Cross-flow filtration	1.61	Hollow fiber	2000 mol/l	Ca ²⁺ > 84.1%	[42]
A1100/TiO ₂ / γ -Al ₂ O ₃		Dip-coating	4.5 L/m ² h bar	Dead-end	4.4	Flat disk	005–0.1 mol/l	Ca ²⁺ > 80% Mg ²⁺ > 80%	[43]
γ -Al ₂ O ₃ / α -Al ₂ O ₃	600°C	Dip-coating	1.2 L/m ² h bar	Dead-end filtration	4.5–7.5	Flat disk			[44]
γ -alumina NF membrane	500°C	Dip-coating	5.4 L/m ² h bar	Cross-flow filtration	1.9	Flat disk	260–80 mg/kg	TOC (oil hydrocarbons) > 90%	[45]
N-membrane			7.4 L/m ² h bar		2.7	Tubular			
C8/ γ -Al ₂ O ₃ / anatase-TiO ₂	400°C	Sol-gel process	2.8 L/m ² h bar		1.5	Flat disk			[46]
A025/Si	500°C	Sol-gel process	2.2 L/m ² h bar	Dead-end filtration	0.5	Flat disk	50 mol/l	PEG400 > 90%	[47]
γ -Al ₂ O ₃ / α -Al ₂ O ₃	450°C	Sol-gel process	5 L/m ² h bar	Cross-flow filtration	5	Tubular	50 mol/l	Ca ²⁺ > 80% Mg ²⁺ > 87%	[1]
γ -Al ₂ O ₃ -clay composite	600°C	Dip-coating	0.02357 × 10 ⁻⁵ m/s kPa	Bubble point setup	5.4–13.6	Flat disk	3000 mol/l	AlCl ₃ > 88%	[48]

Table 5. Comparison of γ -Al₂O₃ membranes.

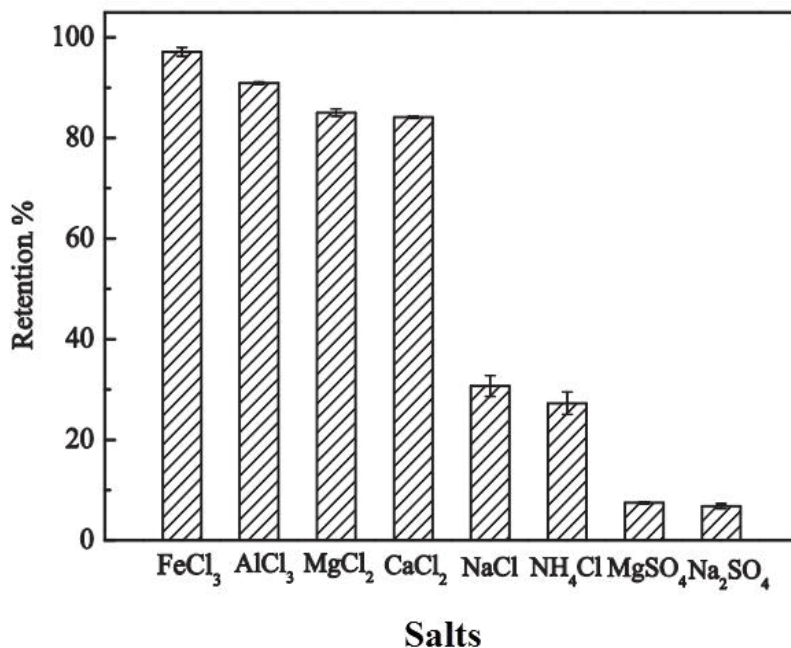


Figure 7. Retentions of various salts for HFNF membrane (at ΔP 5.0 bar and fixed salt concentration of 2000 ppm) [42].

and the anion of the solution [39]. In general, the highest σ along with the weakest permeabilities has been achieved with divalent cation associated to a monovalent anion. Contrary, salt with monovalent cation and divalent anion lead to an increase in salt permeability and a decrease of σ . Similar behavior was observed by Bejaoui et al. [51] with an Osmonics spiral module equipped with a thin film composite HL membrane, characterized by a molecular weight cut-off (MWCO) for the organic compounds of about 150–300 Da. The results of the studies are grouped in **Table 6**. The same founding was also reported for γ -Al₂O₃ UF membrane [52].

One of widespread behavior is the dependence of both flux and salt rejection on salt concentration. The osmotic effect governs the permeate, whereas increasing the feed concentration led to a decrease of the rejection rate caused by shielding of the effective charge of the membrane in the presence of a high electrolyte.

Among the first results appear to be promising in using γ -Al₂O₃ NF in water denitrification, is the study done by Alami Younssi et al. [41]. The removal of nitrate (NO₃⁻) ions in soft drinking water doped with NO₃⁻ was investigated using a NF tangential filtration pilot equipped with a membrane with 0.7 nm pore size and a fixed pressure of 10 bars. The preliminary results demonstrated that it is possible to reduce the concentration of NO₃⁻ from 50 to 31 mg/l, by a single filtration step.

A recent study by Breida et al. [1] was carried out to highlight and understand the transport mechanism that governs the tangential filtration of NO₃⁻ solutions through an UF γ -Al₂O₃

Salts	Membrane $\gamma\text{-Al}_2\text{O}_3$ NF (at 5×10^{-3} mol/l)			HL membrane (at 1×10^{-3} mol/l)		
	pH	σ	P (cm/s)	pH	σ	P (cm/s)
NaCl	5.5	0.65	1.86×10^{-4}	6	0.803	26.02
NaNO ₃	5.5	0.80	1.52×10^{-4}			
NaF	6			6	0.923	15.18
Na ₂ SO ₄	5.5	0.17	2.2×10^{-4}	6	0.947	1.29
NiCl ₂	5.6	0.86	0.13×10^{-4}			
NiSO ₄	5.6	0.37	3.1×10^{-4}			

Table 6. σ and P parameters in the presence of different salts for NF membranes.

membrane with a nominal pore size of 5 nm and water permeability of 5 L/m² h bar. The experimental filtration results were done on a series of various sources of NO₃⁻ solutions and operating conditions (as pH, applied pressure, the initial concentration of NO₃⁻, and cation valency). The effect of applied pressure on NO₃⁻ removal (the concentration of the different solution was equal to 50 mg/l, at natural pH) indicated that the rejection increased with pressure due to twofold force, the convection and friction forces. Furthermore, the rejection varies according to the associated cations and increases in the order of the following sequence Mg²⁺ > Ca²⁺ > Na⁺ > K⁺, with highest NO₃⁻ rejection above 80%, and at 6 bar for Mg (NO₃)₂ salts. Thereby, the hydrated radius and valency of associated cation had a dramatic effect on NO₃⁻ rejection. Further, the results demonstrated that the rejection and permeate fluxes gradually decreased when the initial NO₃⁻ concentration increased. The primary phenomenon that can justify the decrease in flux with concentration is the osmotic pressure difference and the partial plugging at higher concentration. In addition, the best ions rejections was obtained at low concentration (25 mg/l) with rate rejections equal to 87%, 80%, 60%, and 52%, respectively, for Mg(NO₃)₂, Ca(NO₃)₂, NaNO₃, and KNO₃. An increase of the water complexity, especially the presence of divalent anions such as SO₄²⁻, decreased the rejection of NO₃⁻.

The selectivity of the $\gamma\text{-Al}_2\text{O}_3$ UF membrane in NO₃⁻ removal strictly depended upon the pH [53–55]. Strong repulsion happened between the positive charged membrane and the multivalent cations, which lead to a high rejection of ions (Mg²⁺, Ca²⁺...). The rejection of NO₃⁻ was found to grow with an increase of feed pH (range of pH from 3 to 9), due to electro-neutrality consideration. The high rejection of NO₃⁻ was obtained around pH_{pzc} by a rejection rate, which exceeded 80% for divalent cation Mg (NO₃)₂ and 50% for monovalent cation NaNO₃. The charge density and hence the Donnan exclusion changed depending on the pH and governed the NO₃⁻ separation (**Figure 8**. Electroneutrality).

The same UF membrane ($\gamma\text{-Al}_2\text{O}_3$ UF with a nominal pore size of 5 nm and water permeability of 7 L/m² h bar) showed similar behavior in the removal of heavy metals such as Cd(NO₃)₂, CdSO₄, and CdCl₂ [52]. The result obtained during the study of the variation of salt's retention

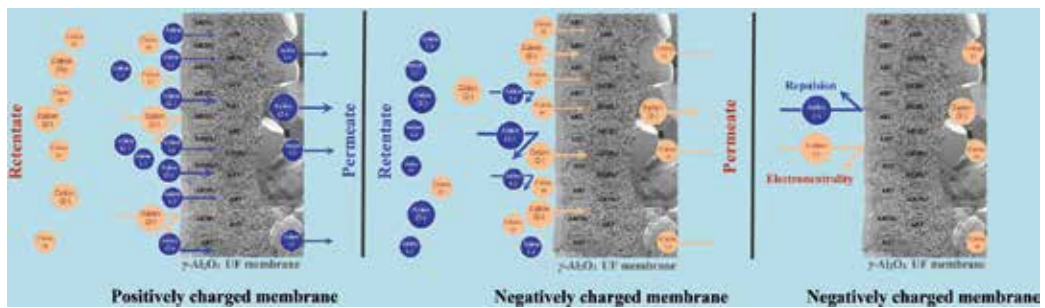


Figure 8. Electroneutrality phenomenon.

when the pH varies between 4 and 7 (concentration of 0.001 mol/l and pressure of 10 bar) demonstrate a greater dependency on pH irrespective of the heavy metals. However, no marked effect was observed with respect to flow variation as a function of pH.

To summarize, Al_2O_3 NF, and UF membranes can be successfully employed in ions separation, this separation is governed by size and charge effect.

In order to enhance the performance of organic membranes, nano Al_2O_3 could be introduced in polymeric membrane to form new generation of membranes (composite membranes) with new performances that combine organic and CM properties. García-Fernández et al. [56] introduced $\gamma\text{-Al}_2\text{O}_3$ nanoparticles to polyethersulfone (PES) membrane and evaluate the effect of nanoparticles in improving the membrane performance for copper ion removal from aqueous solutions. The obtained results showed that $\gamma\text{-Al}_2\text{O}_3$ nano-composite membranes prepared with 1.0 wt% of $\gamma\text{-Al}_2\text{O}_3$ nanoparticles possesses higher swelling and porosity compared to intact PES. In addition, the membrane could remove around 60% of copper.

3.2. Dyes removal

Textile industries are reported to be one of the most polluting industries out of the different industrial sectors, considering both volume and composition of the discharged effluents [57, 58]. The textile wastewater is composed of an elevated variability and complexity of pollutants, caused by the use of dyes, and several reactive agents. They are characterized by high COD, salts concentration, pH, and strong coloration [59]. In addition, recent survey conducted by FICCI [60] reported that the water demand for the textile sector is likely to witness an increase due to the forthcoming industrial growth beside the significant rise in population. In order to overcome the problems generated by these effluents and to reuse it in the processes for industrial production, different chemical, physical, and biological techniques have been devoted to eliminate dyes from wastewaters. However, these methods are reviewed as good solution to meet legislative requirements but not enough to allow water reuse.

The process of separation by membrane techniques are currently viewed as economically, and technologically lucrative options for industrial wastewater treatment and the textile industry is one of the principal beneficiaries of membrane process [26, 59]. UF had been efficiently used for recycling insoluble dyes (such as indigo) and high-molecular weight, auxiliary chemicals,

and water [61, 62]. Al₂O₃ UF, and NF membranes result in reducing the various contaminants present in textile effluents, especially dyes, below permissible levels.

DeFriend et al. [63] investigated the use of Carboxylate-aluminoxane nanoparticles as an alternative to the traditional sol-gel method, for forming UF Al₂O₃ membranes. Al₂O₃ membranes derived from A-alumoxane, prepared by the reaction of boehmite in acetic acid, and disposed on a α -Al₂O₃, were calcinated at 600°C. The average pore size was found to be 11 nm. The performance and rejection characteristic of the new A-alumoxane membranes along with the used support is described in the following **Table 7**.

The results presented in **Table 7**, demonstrate that the deposition of Al₂O₃, which was obtained from A-alumoxane, α -Al₂O₃ support results in a decrease in the permeability. Furthermore, the performance of the elaborated membrane was envisaged in the separation and discrimination of various synthetic dyes (Direct Red 81 (DR 81), Direct Red 75 (DR 75), Direct Blue 71 (DB 71), Direct Yellow 62 (DY 62), and Direct Yellow 50 (DY 50)), the studied dyes have different molecular weights, sizes, and formal charge. The dye solutions were passed through a dead-end filtration system (pressure of 5.5x10⁴ Pa (8 psi)), and the pH of these solutions was between 5.7 and 7.1 for all the dyes. The rate retentions obtained by the support, 40% for DB 71, 39% for DR 75, 38% DY 50, 20% for DY 62, and 0% DR 81, were much weaker than the retentions achieved by the membrane (88% for DB 71, 90% for DR 75, 73% DY 50, 20% for DY 62, and 90% DR 81), and this is for all dyes. The A-alumoxane membrane (7 nm) improves dye's retention of about 40–90% over the support, without a significant increase in the total surface area. The used dyes are poly-sulfate salts characterized by a charge dependence on pH. Furthermore, the Al₂O₃ is well known for its dependency on the pH. On the basis of the amphoteric character of both dyes and membrane material, the authors study the effect of pH (an acidic pH = 1, 5, neutral pH = 6.5, and basic pH = 12, 5) on dyes removal. The results of this study are presented in **Table 8**.

Variations of pH value has no marked effect on the retention of dye by the support, but the alteration of pH has resulted either in increasing or decreasing the retention characteristics of the membranes. Under acidic conditions, there is a meaningful absorption of dyes on the

Performance measurements	α -Al ₂ O ₃ support	New A-alumoxane membranes
Particle size (nm)	100–500	7–25
Surface area (m ² /g)	3.85	111
Average pore size (nm)	50	7
Surface roughness (nm)	67	9
Permeate flux (10 ⁻⁶ m/s)	1.42	0.85
Permeability (nm ²)	36.7	22
MWCO (g/ mol)	>500,000	>1000
MWCO pore size (nm)	31	>4

Table 7. Characteristics of Al₂O₃ and aluminate UF membranes derived from Al₂O₃ nanoparticles [63].

Synthetic dyes	Dye MW (g/mol)	Dye charge	pH	Retention by membrane (%)	Retention by support (%)
DR 81	675	-2	1.87	100	0
			6.05	90	0
			12.52	94	0
DR 75	991	-4	1.63	97	20
			6.45	20	20
			12.56	66	20
DB 71	1030	-4	1.76	100	38
			6.95	90	38
			12.41	95	38
DY 62	771	-2	1.82	99	39
			7.07	73	39
			12.44	44	39
DY 50	957	-4	1.62	100	40
			5.73	88	40
			12.57	93	40

Table 8. Retentions of selected dyes by A-alumoxane-derived Al_2O_3 membranes at a specific pH [63].

Al_2O_3 surface leading to a high rejection. However, in the basic pH range, the retention is mainly due to the charge repulsion between membrane pore surfaces and the dyes.

In the past few years, several major reports highlighted the effect of changing the charge of Al_2O_3 surface on permeate flux [42, 49]. At the pzc, the membrane has a lower net charge, which assumed that the permeate flux is higher as the electroviscous effects should be reduced. In another study (using a single tubular $\alpha\text{-Al}_2\text{O}_3$ CMs) an increase in permeate flux with decreasing pH was either below or above the pzc [64]. Further, the study indicated that during the filtration of solutions containing SiO_2 on Al_2O_3 membrane, the highest permeation occurred at pH values of 2, and pH above 10. However, the lowest flux was obtained near a pH equal to 9.

Most recently, Oun et al. [65] prepared an UF membrane (mean pore diameter of about 50 nm) by simple deposition of TiO_2 nano-powder on the internal surface of the tubular porous clay- Al_2O_3 membrane support. The membrane is the result of a combination of extrusion, sintering, and slip-casting methods. Cross-filtration membrane tests were conducted to estimate the permeability and rate rejection of alizarin red dye. The decolorization efficiency of the membrane was studied as a function of the initial dye concentration, pH of the dye solutions, and the TMP. UF membrane demonstrated a water permeability of 117 L/m^2 h bars. The highest retention of about 99% was observed at TMP of 5 bars, which is due to the dual functionality of the TiO_2 layer, namely adsorption and filtration. Giving that the efficiency of the UF process of dyes removal dramatically depends on the pH of the feed solution, the alizarin dye showed a significant dependence on pH. Indeed, the best rejection (above 98%) was obtained in alkaline solution at pH = 9. However, in acidic feed solution pH = 2 the rejection decreased to a value of 40%.

3.3. Application of Al_2O_3 NF and UF membranes in food applications

The demand for products with higher nutritional value and of processing procedures less harmful to the environment and to human health has recently known a tremendous growth. Furthermore, transferring of membrane processing to food industries has been the objective of many studies [18, 66]. The choice of working with CMs technologies in the food industry is mainly based on the different advantages obtained by these techniques such as ease of cleaning, food safety [67, 68], and the acquisition of newly food fractions that can be used for other food process. CMs allow simplifying the different production stages, by avoiding complex, and chemically stressful steps. This section investigates the application of Al_2O_3 NF and UF CMs in the field of food processing.

3.3.1. Filtration of dietary fats

Authors such as, Alicieo et al. [69] investigated the purification of crude soybean oil from several components (like pigments, sterols, phospholipids, free fatty acids, carbohydrates, proteins...), by use of UF membranes. The applied ceramic UF is a tubular membrane made of $\alpha\text{-Al}_2\text{O}_3/\text{TiO}_2$, with nominal pore size of 10 nm. The filtration tests were performed in cross-flow configuration at 6 bar pressure. The UF membranes provide a high rejection for most of components. The rate rejection for phospholipids is 99.14%, 97.91% for soaps, along with a medium rejection for both free fatty acids, and color (54 and 42%, respectively).

In another work [70], Al_2O_3 multi-channel CMs with an average pore size of 50 nm was used to UF vegetable oil miscella (specifically removal of phospholipids from a mixture of extracted corn oil and solvent). The influence of TMP (0.5 and 1.5 bar) and the composition of miscella (between 25 and 35% w/w of corn oil) on phospholipids and permeates flux were studied. The increase of crude oil percentage into the miscella negatively influenced the flux of permeate. However, it favored the retention of phosphorus (P). In addition, it has been demonstrated that high TMP results in high retentions, however, when it comes to permeate flux, the tangential velocity had a greater influence on flux than TMP. UF of 35% w/w of crude corn oil at 1.5 bar resulted in 93.5% w/w rejection of the phospholipid.

3.3.2. Filtration of proteins

The purpose of protein separation and purification by membrane technologies is to ameliorate the stability and purity by removing pollutants. Furthermore, the membrane allows increasing the range of products that can be offered and reduced waste treatment costs. Some works have been carried out to upgrade liquids effluents by recovering proteins using UF and NF membranes [71].

Fist work on fish proteins recovering from the use of CMs was reported in 2003 [72]. The wastewaters were pretreated by a Al_3O_2 MF and filtered with NF membrane made of TiO_2 and deposited on a $\text{Al}_3\text{O}_2\text{-TiO}_2$ support. The applied pressures in the MF tests were ranging from 3 to 5 bars with a cross-flow velocity (CFV) ranging from 2 to 4 m/s. Permeate and concentrate were recycled to the feed tank, in order to maintain the feed at an approximately constant concentration. The optimal conditions used during the effluent filtration by NF membrane

were obtained from previous microfiltrated fish meal effluent, and the subsequent concentration experiment was carried out at 4 bar, 4 m/s, ambient temperature, and pH = 6.3. Due to the deposition and adsorption of proteins on the surface and pore walls of Al_3O_2 membranes, the flux was found to decrease to 21% of the pure water values.

Recent research highlighted the potential use of ceramic modified nanofiber membrane for protein recovery [73]. The elaboration of the membrane was done through steps. Firstly, the boehmite nanofibres were prepared by a hydrothermal reaction from Al_2O_3 colloidal gels [74, 75] and calcined at 500°C for 5 h to form $\gamma\text{-Al}_2\text{O}_3$. The prepared boehmite nanofibers were coated on the surface of α -alumina supports, calcinated at 500°C. Furthermore, silane groups were introduced to change the surface proprieties of the prepared $\gamma\text{-Al}_2\text{O}_3$ nanofiber membranes. The pore size distribution indicated that the addition of nanofiber had improved remarkably the pore size of the support, from 700 to 11 nm and through reduced the permeability. However, the silane-grafted fiber membrane had no marked effect on pore size, but it changed the membrane surface from hydrophilic to hydrophobic. Both $\gamma\text{-Al}_2\text{O}_3$ fiber membranes and silane-grafted fiber membrane demonstrated good separation efficiency with the MWCO of 70 kDa (90%). The performance of the support and the resultant fiber membranes was investigated by tangential flow filtrations of proteins such as bovine serum albumin (BSA), cellulose, and trypsin. The rejection ability has been improved by 30% when Al_2O_3 nanofibres were coated on the support and this for all protein and concentrations. Furthermore, the silane-grafted Al_2O_3 fiber membrane rejected 100% BSA protein, 92% cellulase protein, and 75% in case of trypsin protein (at a concentration of 400 ppm). Inconstancy, the efficiency of $\gamma\text{-Al}_2\text{O}_3$ fiber membrane in rejecting BSA is between 58 and 36% with various feeding concentrations. The difference in rate rejection of the two membranes can be attributed to the differences of pore size.

Because of ceramic fouling phenomena, more particularly in the case of whey proteins separation, Svetlana Popovi et al. [76] studied the flux recovery procedure for ceramic tubular membrane fouled with whey proteins. The study evaluated the effect of the choice of rinsing, cleaning agents and concentration, and on CM cleaning efficiency. The experiments were done on two membranes of different pore size, an UF membrane made of ZrO_2 filtering layer on an $\alpha\text{-Al}_2\text{O}_3$ support (with a pore size of 50 nm), and a MF membrane of a 200 nm mean pore size made of an $\alpha\text{-Al}_2\text{O}_3$ filtering layer on an $\alpha\text{-Al}_2\text{O}_3$ support. The synthesized effluents were made by dissolving whey powder (the powder composition was 11.8% (w/w) proteins, 75.0% (w/w) lactose, 3.3% (w/w) fat, 9.5% (w/w) ash, and 2.3% (w/w) water) in deionized water with a concentration of 10 g/l. The pH of solutions was kept at a neutral value (pH = 6.0). The retentate and permeates were both recycled to the feed tank. Experiments have been conducted following steps, pure water flux measurement, fouling, rinsing, chemical cleaning, rinsing, and pure water flux measurement. Furthermore, the chemical cleaning and rinsing was carried out for 30 min with full recycle. The sodium hydroxide solution was used as an alkaline cleaning agent, different concentrations of NaOH was studied. In addition, the caustic cleaning was done with commercially available detergents P3-ultrasil 67 and P3-ultrasil 69.

Chemical cleaning (**Figure 9**), by caustic solution (1.0% (w/w)) of the UF membrane gives a flux recovery equal to 97%, in the other hand the cleaning of MF with (0.6% (w/w)) caustic solution achieved a best flux recovery of 78% (regardless of the applied concentration). The

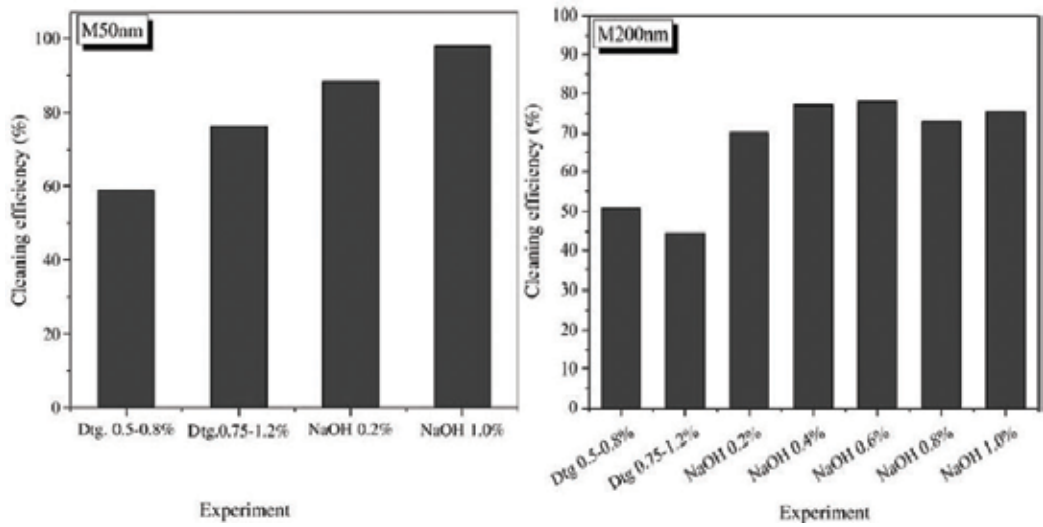


Figure 9. Cleaning efficiency for the 200–50 nm membranes on the pure water flux measurements before fouling and after cleaning at the same conditions 25°C, TMP [76].

application of commercial detergents in the cleaning of both membranes is less efficient than the caustic solution. However, it was noted that the flux recovery risen with increasing of detergent concentration from 60 to 75%.

Beside the different methods used for membrane cleaning and fouling prevention, membrane fouling can be reduced by improving the preparation methods and modifying the membrane in a way to decrease the surface interaction between the membrane material and the proteins [77]. Recently, researchers targeted two potentials in the modification of Al_2O_3 surface, which are the super-hydrophobicity (contact angle $>150^\circ$) and super-hydrophilicity (contact angle $<5^\circ$), that enhance the anti-fouling, and self-cleaning applications. Furthermore, graphene derivatives are viewed as having high-potential to serve as modified materials [30, 78, 79].

3.4. Oily wastewater treatment

Oily industrial wastewaters are highly heterogeneous, due to the different pollutants (hydrocarbons, surfactants, metals, acids, etc.) coming from the diverse stages of oil production. The most challenging in terms of effective treatment is the stable oily effluents consisting of highly chemically and physically emulsified oils. The classical separation processes used for oily effluents does not meet the established standards (The European standard for effluent from onshore petroleum activities is, 5 mg/l total hydrocarbons (HC) and less than 10 mg/l suspended solids). Membrane technology is used in both, industrial processes, and oily effluents treatment [12, 80]. Application of membrane in the petroleum industry is mostly done in hydrogen recovery and olefins such as ethylene and propylene in polyolefin production beside the removal of aromatics from gasoline [81]. Furthermore, major studies on filtration of industrial oily wastewaters were performed in the 1990s and research has continuously increased in recent years.

The research done by Ebrahimi et al. [82] is one of the primary works in oil separation by CM. The application of a combination of commercially ceramic, MF, UF, and NF was evaluated for the removal of oil from used model solutions and oil-field produced water, respectively. The study aimed to investigate the variation of permeates flux and the removal efficiency of total organic carbon (TOC) and oil. The studied UF and NF membranes had TiO_2 as active layer and Al_2O_3 as membrane support. Cross-flow filtration (velocities ranged from 1.3 to 6 m/s) processes were conducted using a continuous stirred tank reactor. The experiment showed that the average percentages of oil removal by UF and NF are 80 to 84%, respectively. However, the TOC removal is relatively low (27% for UF and 13% for NF). Furthermore, the MF, UF, and NF membranes used in combination were able to provide a total oil removal percentage of 82% in terms of initial feed concentration at 1 bar TMP. The same authors [83] reported that TOC removal was modest (27% for UF, and 13% for NF, as pretreatment for wastewater. The efficiency of single application of dissolved air flotation (process in removing oil pollutants was found to be up to 90% in 90 min with airflow rate of 0.8 NI/s. In addition, the combination of the two techniques allowed 99.5% oil removal and 50% TOC elimination. The NF in oil industry has replaced RO in many applications due to higher flux rates and lower energy consumption [84].

Sadeghian et al. [45] prepared supported $\gamma\text{-Al}_2\text{O}_3$ NF membrane from colloidal dispersions of bonhomie, through a sol-gel method. The pore size at the support and $\gamma\text{-Al}_2\text{O}_3$ layer was determined to be 22 and 0.99 nm, respectively. The $\gamma\text{-Al}_2\text{O}_3$ NF was applied for removal of oily hydrocarbon wastewater, via a cross-flow NF pilot. The applied TMP pressure was in the range of 0.7–1.1 MPa and the CFV was between 0.56 and 2.8 m/s. The membrane efficiency was determined based on the measurements of permeate flux and rejection of TOC. The permeation of flux increased with an increase of pressure (from 0.7 to 1.1 MPa), the highest flux was obtained at 1.1 MPa with 46.3 L/m² h. Furthermore, the flux increased when the CFV increases and when the concentration of oily effluent was minimum (260 ppm, concentration of TCO in feed solution). Under the various operation conditions, the TOC rejection efficiencies were higher than 90%.

In another work done by Zhang et al. [85], CMs with different membrane pore sizes and materials were studied in the treatment of oilfield produced water. Membranes of 200–500 nm pore size were made from $\alpha\text{-Al}_2\text{O}_3/\alpha\text{-Al}_2\text{O}_3$, beside two other membranes with a pore size of 20–50 nm made from $\text{ZrO}_2/\alpha\text{-Al}_2\text{O}_3$ materials. The study investigated the effects of NaCl and Polyacrylamide (PAM) on the membrane performance. The effect of pore size was primarily seen during the measure of pure water flux. The permeability of both membrane (M) increased with an increase of the pore size from 200 to 180 L/m² h, respectively, for M 20 nm and M 50 nm (at, PAM 5 mg/l, NaCl 3% (w/w), TMP 0.1 MPa, CFV 2 m/s, T 25°C).

For the $\text{ZrO}_2/\alpha\text{-Al}_2\text{O}_3$ UF membranes, the average MW of PAM in the permeate experienced a little change with the different concentrations of PAM. In addition, it was found that an increase of NaCl concentration led to a decrease of PSF of the membrane because the increased viscosity of the feed water and the change in the PAM morphology causes strong membrane fouling. Moreover, in alkali solutions, the PAM was easily hydrolyzed and degraded, and the membrane fouling can be avoided with a simple cleaning by aqueous NaOH solutions (pH > 12).

Overview of the experimental results indicates that Al_2O_3 UF and NF membranes can be applied to offer high-efficiency in oil HC removal as well as a relatively high-flux. Despite the difference in operational conditions, the flux of permeate was found to rise with increasing TMP, CFV, and low oil concentration in the feed (C_f) solution. Furthermore, TOC rejection was higher than 90% and this for all experiments. It is worth mentioning that the concept of MF of oily wastewater by Al_2O_3 -MF membrane (where cleaned permeate can be obtained and recycled/reused in the oil refining process), showed promising results and possibly large-scale application [86].

Many studies showed the high-efficiency of Al_2O_3 -MF membranes in oil removal. Recently, Zita-Sere et al. [87] demonstrated that a Al_2O_3 ceramic tubular membrane with a pore size of 200 nm is an adequate secondary treatment technique to decontaminate wastewater from an oil refinery. The wastewater was characterized by turbidity in the range of 200–2500 NTU and COD ranging from 5000 to 18,000 mg O_2/l . Batch cross-flow MF runs were performed at TMP in the range of 1–3 bar and a flow rate of 100–300 L/h. The MF of the oily effluents provided satisfactory removal, expressed by the good COD retention (75%), and the significant turbidity removal (99%). The characteristics of the obtained permeate allow the circulation of the water in the process.

Yeom et al. [88] prepared Al_2O_3 -coated clay–diatomite composite membranes using inexpensive raw materials by a simple pressing and dip-coating method. The study of raw material compositions demonstrate that the optimal membrane support was obtained with, 48.6% Diatomite, 18.8% Kaolin, 14.8% bentonite, 14.8% Talc, 2.0% sodium borate, and 1.0% BaCO_3 . Meanwhile, the pore size of the Al_2O_3 -coated clay– diatomite composite membrane (with optimal support) is equal to 120 nm, and the steady state flux was $6.91 \times 10^{-6} \text{ m}^3/\text{m}^2 \text{ s}$, at an applied pressure of 101 kPa. The membrane performance in oily wastewater filtration was excellent with rate rejection of 99.9% with a feed oil concentration of 600 mg/l and an applied pressure of 101 kPa.

Chang et al. [89] studied the hydrophilic modification of a tubular Al_2O_3 -MF membrane (with a19 channels configuration) by nano- TiO_2 coating, using the in situ precipitation method, and evaluated the modified membrane in treating stable oil in water emulsions. The membrane modified with 2 mol/l Ti (SO_4)₂ solutions, was the best for water MF. The results of nano-coating on the membrane surface allowed an increase of the membrane hydrophilic character; however, no marked influence was observed in the layer pore size. The stable flux of the modified membrane was higher by 30–40% compared to the unmodified membrane, and this when the feed temperature was 40°C, a CFV of 5 m/s, and TMP of 0.16 MPa. The increase of flux is mainly due to the presence of hydrophilic nano- TiO_2 . The elimination of oily contamination was demonstrated by a fall in concentration from an initial feed concentration of 4 g/l to a concentration of 10 mg/l in the permeate.

3.5. Domestic wastewater treatment

Domestic or municipal wastewater (MWW) is now considered more as a resource than as a waste. The MWW can be used a resource for energy, for plant fertilizing, and recovery of both

nitrogen (N) and P [90]. Moreover, the reclaimed wastewater of MWW is widely accepted for landscape and crop irrigation thereby preserving the water sources. The anaerobic membrane bioreactor (AnMBR) systems have become an advantageous technique for treating domestic MWW. Giving the advantages of CMs, recent studies targeted the use for fouling control of anaerobic ceramic MBR (AnCMBR) [91, 92].

In this context, Jeong et al. [93] are the first to suggest the application of CMs for the anaerobic treatment of domestic wastewater (AnCMBR). In this study, The membrane bioreactor holds either a flat sheet Al_2O_3 -based anaerobic ceramic membrane (AnCMBR-ACM) or a flat-sheet Pyrophyllite-based anaerobic ceramic membrane (AnCMBR-PCM), the AnCMBR-ACM has a pore size of 100 nm, pure water permeability of $1104.2 \text{ L/m}^2 \text{ h bar}$, and were operated in the inside-out mode. The performance of CMs was principally done by evaluating the filtering efficiency and treatment performances. For AnCMBR-ACM, at longer hydraulic retention time (HRT) condition (44 ± 3.1 for 1–45 days), the efficiencies of COD, DOC (Dissolved Organic Carbon), and methane content removal reached values of $90.5 \pm 6.8\%$, $95.9 \pm 5.3\%$, and $56.2 \pm 5.3\%$, respectively. Furthermore, the reactor performance was not significantly affected by changes in HRT, which is seen by the rate rejection of COD ($96.1 \pm 5.1\%$), DOC ($98.5 \pm 0.5\%$), and methane ($60.2 \pm 4.9\%$) when the HRT was (18 ± 1.3 for 46–80 days). Both CMs were successfully operated and been suggested as a treatment technique for domestic wastewater treatment.

The following study confirms the applicability of ceramic membrane bioreactor (CMBR) for urban wastewater, C.-H. Xing et al. [94] used an UF membrane to address wastewater treatment. The UF membrane is composed of a top layer of ZrO_2 and a support made of $\gamma\text{-Al}_2\text{O}_3$. It had a tubular configuration with seven channels that have a diameter of 4.5 mm. Performance of the UF-CMBR was examined with a HRT of 5 h, membrane flux between 75 and $150 \text{ L/m}^2 \text{ h}$, and a sludge retention time (SRT) of 5. The removal efficiency of COD, $\text{NH}_3\text{-N}$, and suspended solid was on the average as high as 97, 96.2, and 100%, respectively. In addition, the bioreactor was found to be responsible for 85% of COD removal, while 12% was due membrane separation.

The study done by Ali Farsi et al. [95] focuses on the treatment of effluents, from a secondary municipal wastewater treatment plant (MWWTP), by mean of different CMs. The wastewater was characterized by a conductivity of $1120 \mu\text{S/cm}$, 2.8 mg/l organic compounds matters and 5 mg/l inorganic N. The efficiency of MF $\alpha\text{-Al}_2\text{O}_3$, TiO_2 -UF membrane (with MF $\alpha\text{-Al}_2\text{O}_3$ support), $\gamma\text{-Al}_2\text{O}_3$ NF membrane (with $\alpha\text{-Al}_2\text{O}_3$ MF a support), TiO_2 -NF membrane (with TiO_2 -UF interlayer and $\alpha\text{-Al}_2\text{O}_3$ MF support), and hybrid silica membrane (with $\gamma\text{-Al}_2\text{O}_3$ NF on a $\alpha\text{-Al}_2\text{O}_3$ MF support) were investigated to assist the membranes ability to remove toxic compounds. The samples from MWW plant were filtered by cross-flow setup at room temperature. The comparative study shows that the NF $\gamma\text{-Al}_2\text{O}_3$ membrane was the most promising membrane, in terms of its selectivity, and flux for wastewater treatment plants. The permeability of the treated MWW effluent ($6.6 \text{ L/m}^2 \text{ h bar}$) by $\gamma\text{-Al}_2\text{O}_3$ NF was lower than deionized water ($12.8 \text{ L/m}^2 \text{ h bar}$). In addition, the NF $\gamma\text{-Al}_2\text{O}_3$ removed the UV254-absorbing components by 75, and 15% of the total ions. During the cross-filtration of the spiked MWWTP effluent (copper concentration was set at approximately $1 \pm 0.1 \text{ mg/l}$). The membrane was able to reject CuCl and CuSO_4 by 40 and

25%, respectively. The treatment by NF γ -alumina membrane was also efficient in reducing the toxicity present in the WWTP effluent with elevated concentrations of toxic ions.

4. Conclusion

The increase in energy costs and the demands of products with high quality, that answers consumer needs, and which are less toxic to the environment are all reasons to apply membrane process in industrial activities and water treatment. Current applications of membrane technologies have shown their high-potential to answer the industrial needs. CMs materials with good thermal and chemical stability, such as Al_2O_3 , would allow their use in different chemical processes, which are not largely explored with membranes process. Knowledge of the chemistry of Al_2O_3 UF and NF membranes elaboration and performance their characteristics were reported. The choice of Al_2O_3 material is due to the different advantages (chemical, physical characteristics) over other mineral materials and mostly over the organic material. Furthermore, the chapter summarizes studies available in treatment by UF and NF Al_2O_3 membranes of wastewater from different industrial activities such as desalination, dyes effluents, discharges from the food industry (namely dietary fats and proteins), oily wastewater effluents, and domestic wastewater. The results obtained by Al_2O_3 -CMs during desalination and water treatment can be explained by membrane dependency on the complexity of the ionic composition of the solution, and the interaction solute-solute and membrane-solute, and the influence of parameters such as the solute hydration radius and its energy. The UF- Al_2O_3 or NF- Al_2O_3 membranes can successfully eliminate the dyes from industrial waste. It can reach 100% of dye elimination and simultaneously contribute to the progress of the textile industrial activity. The use of CMs in the food industry is gradually increasing, however, particular efforts are needed to understand and reduce membrane fouling, which enables the gains in productivity. The experimental results indicate that the Al_2O_3 ceramic UF and NF membranes can be applied to offer a high relative flux and high-oil HC removal efficiency, especially if they are used as secondary treatment. In the other hands, the use of Al_2O_3 -CMs for AnCMBR was found to be effective in COD and DOC removal with rejection exceeded 90%.

Competing interest statement

The authors declare no conflict of interest.

Funding statement

This work was supported by MESRSFC Ministère de l'Enseignement Supérieur et de la Recherche Scientifique et de la Formation des cadres – Morocco) and CNRST (Centre National pour la Recherche Scientifique et Technique – Morocco) (Project number PPR/2015/72).

Nomenclature

COD	chemical oxygen demand
BOD	biological oxygen demand
TDS	total dissolved solids
MF	microfiltration
UF	ultrafiltration
NF	nanofiltration
RO	reverse osmosis
PM	polymeric membranes
CM	ceramic membrane
TiO ₂	titania
SiO ₂	silica
ZrO ₂	zirconia
Al ₂ O ₃	alumina
Al ₂ O ₃ -CM	Al ₂ O ₃ ceramic membranes
ED	electrodialysis
GS	gas separation
α-Al ₂ O ₃	alpha alumina
γ-Al ₂ O ₃	gamma alumina
pHpzc	the point of zero charge
Lp	the membrane hydraulic permeability
R	the membrane rejection
C _p	concentration in the permeate
C _f	concentration in the feed
C _w	concentration at the membrane wall
Ra	the observed solute rejections
TMP	transmembrane pressure
J _v	the volumetric permeate flux
HFNF	γ-Al ₂ O ₃ /α-Al ₂ O ₃ hollow fiber NF composite membranes

PES	polyethersulfone
PAI	γ -Al ₂ O ₃ nanocomposite membranes
MWCO	molecular weight cut-off
NO ₃ ⁻	nitrate
VRF	volume reduction factor
BSA	proteins as bovine serum albumin
HC	hydrocarbons
CFV	cross-flow velocity
MWW	municipal wastewater
N	nitrogen
P	phosphorus
AnMBR	anaerobic membrane bioreactor
AnCMBR	anaerobic ceramic MBR
AnCMBR-ACM	Al ₂ O ₃ -based anaerobic ceramic membrane
AnCMBR-PCM	pyrophyllite-based anaerobic ceramic membrane
DOC	dissolved organic carbon

Author details

Saad Alami Younssi*, Majda Breida and Brahim Achiou

*Address all correspondence to: alamiyounssisaad@yahoo.fr

Laboratory of Materials, Membranes and Environment, Faculty of Sciences and Technologies of Mohammedia, University Hassan II, Casablanca, Morocco

References

- [1] Breida M, Alami Younssi S, Bouazizi A, Achiou B, Ouammou M, El Rhazi M. Nitrate removal from aqueous solutions by γ -Al₂O₃ ultrafiltration membranes. *Heliyon*. 2018;4 e00498
- [2] Goh PS, Ismail AF. A review on inorganic membranes for desalination and wastewater treatment. *Desalination*. 2017. DOI: 10.1016/j.desal.2017.07.023
- [3] Hader D-P. Ecotoxicological monitoring of wastewater. *Bioassays, Advanced Methods and Applications*. 2018:369-386

- [4] Azizullah A, Richter P, Häder D-P. Ecotoxicological evaluation of wastewater samples from Gadoon Amazai industrial estate (GAIE), Swabi, Pakistan. *International Journal of Environmental Sciences*. 2011;**1**:959
- [5] Lee D-J. *Current Developments in Biotechnology and Bioengineering: Biological Treatment of Industrial Effluents*. New York: Elsevier; 2017
- [6] Tul Muntha S, Kausar A, Siddiq M. Advances in polymeric nanofiltration membrane: A review. *Polymer-Plastics Technology and Engineering*. 2017;**56**:841-856
- [7] Chong TH, Loo S-L, Krantz WB. Energy-efficient reverse osmosis desalination process. *Journal of Membrane Science*. 2015;**473**:177-188. DOI: 10.1016/j.memsci.2014.09.005
- [8] Lee KP. *Fabrication and Applications of Nanoporous Alumina Membranes*, PhD Thesis. University of Bath; 2013
- [9] Ng LY, Mohammad AW, Leo CP, Hilal N. Polymeric membranes incorporated with metal/metal oxide nanoparticles: A comprehensive review. *Desalination*. 2013;**308**:15-33
- [10] Wang LK, Chen JP, Hung Y-T, Shammas NK, editors. *Membrane and Desalination Technologies*. Totowa, NJ: Humana Press; 2011. DOI: 10.1007/978-1-59745-278-6
- [11] Kumar RV, Basumatary AK, Ghoshal AK, Pugazhenti G. Performance assessment of an analcime-C zeolite–ceramic composite membrane by removal of Cr(VI) from aqueous solution. *RSC Advances*. 2015;**5**:6246-6254. DOI: 10.1039/C4RA14527E
- [12] Ebrahimi M, Kerker S, Schmitz O, Schmidt AA, Czermak P. Evaluation of the fouling potential of ceramic membrane configurations designed for the treatment of oilfield produced water. *Separation Science and Technology*. 2018;**53**:349-363. DOI: 10.1080/01496395.2017.1386217
- [13] Shih M-C. An overview of arsenic removal by pressure-driven membrane processes. *Desalination*. 2005;**172**:85-97. DOI: 10.1016/j.desal.2004.07.031
- [14] Elaine Fung Y-L, Wang H. Investigation of reinforcement of porous alumina by nickel aluminate spinel for its use as ceramic membrane. *Journal of Membrane Science*. 2013;**444**:252-258. DOI: 10.1016/j.memsci.2013.05.025
- [15] Rezaei Hosseinabadi S, Wyns K, Meynen V, Carleer R, Adriaensens P, Buekenhoudt A, Van der Bruggen B. Organic solvent nanofiltration with Grignard functionalised ceramic nanofiltration membranes. *Journal of Membrane Science*. 2014;**454**:496-504. DOI: 10.1016/j.memsci.2013.12.032
- [16] Mulder M. *Basic Principles of Membrane Technology*. Dordrecht, Netherlands; Boston: Kluwer Academic; 1991
- [17] Singh R, Hankins NP. Introduction to membrane processes for water treatment. In: *Emerg. Membr. Technol. Sustain. Water Treat.* Elsevier; 2016. pp. 15-52. DOI: 10.1016/B978-0-444-63312-5.00002-4
- [18] Mancinelli D, Hallé C. Nano-filtration and ultra-filtration ceramic membranes for food processing: A mini review. *Journal of Membrane Science and Technology*. 2015;**05**. DOI: 10.4172/2155-9589.1000140

- [19] Crespo JG, Bøddeker KW. *Membrane Processes in Separation and Purification*. Springer; 1994
- [20] Elssner G, editor. *Ceramics and Ceramic Composites: Materialographic Preparation*. Amsterdam; New York: Elsevier Science B.V; 1999
- [21] Vasanth D, Uppaluri R, Pugazhenth G. Influence of sintering temperature on the properties of porous ceramic support prepared by uniaxial dry compaction method using low-cost raw materials for membrane applications. *Separation Science and Technology*. 2011;**46**:1241-1249. DOI: 10.1080/01496395.2011.556097
- [22] Auerkari P. Mechanical and physical properties of engineering alumina ceramics. VTT Manufacturing Technology-Research Notes. 1792
- [23] Lim HB, Cho W-S, Kim CY. Effect of particle size distribution of alumina on strength of glass-infiltrated alumina. *Ceramics International*. 2012;**38**:3069-3074. DOI: 10.1016/j.ceramint.2011.12.005
- [24] Lumley R. *Fundamentals of Aluminium Metallurgy: Production, Processing and Applications*. Elsevier; 2010
- [25] Tsuru T. Inorganic porous membranes for liquid phase separation. *Separation and Purification Methods*. 2001;**30**:191-220. DOI: 10.1081/SPM-100108159
- [26] Koltuniewicz AB, Drioli E. *Membranes in Clean Technologies 2 Volume Set: Theory and Practice*. Weinheim: Wiley-VCH Verlag GmbH & Co.KGaA; 2008
- [27] Fang H, Ren C, Liu Y, Lu D, Winnubst L, Chen C. Phase-inversion tape casting and synchrotron-radiation computed tomography analysis of porous alumina. *Journal of the European Ceramic Society*. 2013;**33**:2049-2051. DOI: 10.1016/j.jeurceramsoc.2013.02.032
- [28] Falamaki C, Naimi M, Aghaie A. Dip-coating technique for the manufacture of alumina microfilters using PVA and Na-CMC as binders: A comparative study. *Journal of the European Ceramic Society*. 2006;**26**:949-956. DOI: 10.1016/j.jeurceramsoc.2004.11.018
- [29] Mendret J, Hatat-Fraile M, Rivallin M, Brosillon S. Hydrophilic composite membranes for simultaneous separation and photocatalytic degradation of organic pollutants. *Separation and Purification Technology*. 2013;**111**:9-19. DOI: 10.1016/j.seppur.2013.03.030
- [30] Ishak NF, Hashim NA, Othman MHD, Monash P, Zuki FM. Recent progress in the hydrophilic modification of alumina membranes for protein separation and purification. *Ceramics International*. 2017;**43**:915-925. DOI: 10.1016/j.ceramint.2016.10.044
- [31] Baker RW. *Membrane technology and applications*. Membrane Technology. 2004
- [32] Charcosset C. Principles on membrane and membrane processes. In: *Membr. Process. Biotechnol. Pharm.* Elsevier; 2012. pp. 1-41. DOI: 10.1016/B978-0-444-56334-7.00001-0
- [33] Mehta A, Zydney AL. Permeability and selectivity analysis for ultrafiltration membranes. *Journal of Membrane Science*. 2005;**249**:245-249. DOI: 10.1016/j.memsci.2004.09.040
- [34] Zeman LJ et al. *Microfiltration and Ultrafiltration Principles and Applications*. New York: Marcel Dekker, Inc.; 1996

- [35] Strathmann H. Membrane separation processes: current relevance and future opportunities. *AICHE Journal*. 2001;**47**:1077-1087
- [36] Goosen MFA, Sablani SS, Al-Hinai H, Al-Obeidani S, Al-Belushi R, Jackson D. Fouling of reverse osmosis and ultrafiltration membranes: A critical review. *Separation Science and Technology*. 2005;**39**:2261-2297. DOI: 10.1081/SS-120039343
- [37] Yu D, Mottern ML, Verweij H, Bukowski J, Lewis JA. Highly Permeable Supported γ -Alumina Membranes for Water Purification, in: *AICHe Annu. Meet. Conf. Proc. Austin TX U. S.*, 2004
- [38] Achiou B, Elomari H, Bouazizi A, Karim A, Ouammou M, Albizane A, Bennazha J, Alami Younssi S, El Amrani IE. Manufacturing of tubular ceramic microfiltration membrane based on natural pozzolan for pretreatment of seawater desalination. *Desalination*. 2017;**419**:181-187. DOI: 10.1016/j.desal.2017.06.014
- [39] Baticle P, Kiefer C, Lakhchaf N, Larbot A, Leclerc O, Persin M, Sarrazin J. Salt filtration on gamma alumina nanofiltration membranes fired at two different temperatures. *Journal of Membrane Science*. 1997;**135**:1-8
- [40] Larbot A, Alami-Younssi S, Persin M, Sarrazin J, Cot L. Preparation of a γ -alumina nanofiltration membrane. *Journal of Membrane Science*. 1994;**97**:167-173
- [41] Alami-Younssi S, Larbot A, Persin M, Sarrazin J, Cot L. Rejection of mineral salts on a gamma alumina nanofiltration membrane application to environmental process. *Journal of Membrane Science*. 1995;**102**:123-129
- [42] Wang Z, Wei Y-M, Xu Z-L, Cao Y, Dong Z-Q, Shi X-L. Preparation, characterization and solvent resistance of γ -Al₂O₃ / α -Al₂O₃ inorganic hollow fiber nanofiltration membrane. *Journal of Membrane Science*. 2016;**503**:69-80. DOI: 10.1016/j.memsci.2015.12.039
- [43] Qi H, Niu S, Jiang X, Xu N. Enhanced performance of a macroporous ceramic support for nanofiltration by using α -Al₂O₃ with narrow size distribution. *Ceramics International*. 2013;**39**:2463-2471. DOI: 10.1016/j.ceramint.2012.09.004
- [44] Chowdhury S. Pore size and surface chemistry effects on the transport of hydrophobic and hydrophilic solvents through mesoporous γ -alumina and silica MCM-48. *Journal of Membrane Science*. 2003;**225**:177-186. DOI: 10.1016/j.memsci.2003.07.018
- [45] Sadeghian Z, Zamani F, Ashrafizadeh SN. Removal of oily hydrocarbon contaminants from wastewater by γ -alumina nanofiltration membranes. *Desalination Water Treatment*. 2010;**20**:80-85. DOI: 10.5004/dwt.2010.1154
- [46] Van Gestel T, Van der Bruggen B, Buekenhoudt A, Dotremont C, Luyten J, Vandecasteele C, Maes G. Surface modification of γ -Al₂O₃/TiO₂ multilayer membranes for applications in non-polar organic solvents. *Journal of Membrane Science*. 2003;**224**:3-10. DOI: 10.1016/S0376-7388(03)00132-7
- [47] Ahmad AL, Leo CP, Shukor SRA. Preparation of γ -alumina thin layer with bimodal pore size distribution for diminution of transport resistance in bi-layered membrane. *Thin Solid Films*. 2008;**516**:4319-4324. DOI: 10.1016/j.tsf.2007.12.078

- [48] Majhi A, Monash P, Pugazhenth G. Fabrication and characterization of γ - Al_2O_3 -clay composite ultrafiltration membrane for the separation of electrolytes from its aqueous solution. *Journal of Membrane Science*. 2009;**340**:181-191. DOI: 10.1016/j.memsci.2009.05.030
- [49] Schaep J, Vandecasteele C, Peeters B, Luyten J, Dotremont C, Roels D. Characteristics and retention properties of a mesoporous γ - Al_2O_3 membrane for nanofiltration. *Journal of Membrane Science*. 1999;**163**:229-237
- [50] Puspasari T, Pradeep N, Peinemann K-V. Crosslinked cellulose thin film composite nanofiltration membranes with zero salt rejection. *Journal of Membrane Science*. 2015;**491**:132-137. DOI: 10.1016/j.memsci.2015.05.002
- [51] Bejaoui I, Mnif A, Hamrouni B. Influence of operating conditions on the retention of fluoride from water by nanofiltration. *Desalination Water Treatment*. 2011;**29**:39-46. DOI: 10.5004/dwt.2011.1836
- [52] Benalla R, Persin M, Toreis N, Sarrazin J, Larbot A, Bouhaouss A. Rétention de sels simples par une membrane chargée d'ultrafiltration à base d'alumine gamma. *Journal de Chimie Physique et de Physico-Chimie Biologique*. 1999;**96**:1387-1399
- [53] Shang R, Verliefe ARD, Hu J, Zeng Z, Lu J, Kemperman AJB, Deng H, Nijmeijer K, Heijman SGJ, Rietveld LC. Tight ceramic UF membrane as RO pre-treatment: The role of electrostatic interactions on phosphate rejection. *Water Research*. 2014;**48**:498-507. DOI: 10.1016/j.watres.2013.10.008
- [54] Shang R, Verliefe ARD, Hu J, Heijman SGJ, Rietveld LC. The impact of EfOM, NOM and cations on phosphate rejection by tight ceramic ultrafiltration. *Separation and Purification Technology*. 2014;**132**:289-294. DOI: 10.1016/j.seppur.2014.05.024
- [55] Narong P, James AE. Sodium chloride rejection by a UF ceramic membrane in relation to its surface electrical properties. *Separation and Purification Technology*. 2006;**49**:122-129. DOI: 10.1016/j.seppur.2005.09.005
- [56] Ghaemi N. A new approach to copper ion removal from water by polymeric nanocomposite membrane embedded with γ -alumina nanoparticles. *Applied Surface Science*. 2016;**364**:221-228. DOI: 10.1016/j.apsusc.2015.12.109
- [57] Dasgupta J, Sikder J, Chakraborty S, Curcio S, Drioli E. Remediation of textile effluents by membrane based treatment techniques: A state of the art review. *Journal of Environmental Management*. 2015;**147**:55-72. DOI: 10.1016/j.jenvman.2014.08.008
- [58] Barredo-Damas S, Alcaina-Miranda MI, Bes-Piá A, Iborra-Clar MI, Iborra-Clar A, Mendoza-Roca JA. Ceramic membrane behavior in textile wastewater ultrafiltration. *Desalination*. 2010;**250**:623-628. DOI: 10.1016/j.desal.2009.09.037
- [59] Fersi C, Gzara L, Dhahbi M. Treatment of textile effluents by membrane technologies. *Desalination*. 2005;**185**:399-409. DOI: 10.1016/j.desal.2005.03.087
- [60] F.W. Mission, *Water Use in Indian Industry Survey*, New Delhi. (2011)
- [61] Liu TH, Simms KM, Zaidi SA. Selection of ultrafiltration nanofiltration membrane for treatment of textile dyeing wastewater. *Water Treatment*. 1994;**9**:189-198

- [62] Bouazizi A, Breida M, Achiou B, Ouammou M, Calvo JI, Aaddane A, Alami Younssi S. Removal of dyes by a new nano-TiO₂ ultrafiltration membrane deposited on low-cost support prepared from natural Moroccan bentonite. *Applied Clay Science*. 2017;**149**:127-135. DOI: 10.1016/j.clay.2017.08.019
- [63] DeFriend KA, Wiesner MR, Barron AR. Alumina and aluminate ultrafiltration membranes derived from alumina nanoparticles. *Journal of Membrane Science*. 2003;**224**:11-28. DOI: 10.1016/S0376-7388(03)00344-2
- [64] Nazzal FF, Wiesner MR. pH and ionic strength effects on the performance of ceramic membranes in water filtration. *Journal of Membrane Science*. 1994;**93**:91-103
- [65] Oun A, Tahri N, Mahouche-Chergui S, Carbonnier B, Majumdar S, Sarkar S, Sahoo GC, Ben Amar R. Tubular ultrafiltration ceramic membrane based on titania nanoparticles immobilized on macroporous clay-alumina support: Elaboration, characterization and application to dye removal. *Separation and Purification Technology*. 2017;**188**:126-133. DOI: 10.1016/j.seppur.2017.07.005
- [66] Salehi F. Current and future applications for nanofiltration technology in the food processing. *Food and Bioproducts Processing*. 2014;**92**:161-177. DOI: 10.1016/j.fbp.2013.09.005
- [67] Maneenpun S, Yunchalad M. Developing processed mango products for international markets. In: VII Int. Mango Symp. 645. 2002. pp. 93-105
- [68] Saja S, Bouazizi A, Achiou B, Ouammou M, Albizane A, Bennazha J, Alami Younssi S. Elaboration and characterization of low-cost ceramic membrane made from natural Moroccan perlite for treatment of industrial wastewater. *Journal of Environmental Chemical Engineering*. 2018;**6**:451-458. DOI: 10.1016/j.jece.2017.12.004
- [69] Alicio TVR, Mendes ES, Pereira NC, Lima OM. Membrane ultrafiltration of crude soybean oil. *Desalination*. 2002;**148**:99-102
- [70] Sousa L d S, Cabral BV, Madrona GS, Cardoso VL, Reis MHM. Purification of polyphenols from green tea leaves by ultrasound assisted ultrafiltration process. *Separation and Purification Technology*. 2016;**168**:188-198. DOI: 10.1016/j.seppur.2016.05.029
- [71] Bourseau P, Vandanjon L, Jaouen P, Chaplain-Derouiniot M, Massé A, Guérard F, Chabeaud A, Fouchereau-Péron M, Le Gal Y, Ravallec-Plé R, Bergé J-P, Picot L, Piot J-M, Batista I, Thorkelsson G, Delannoy C, Jakobsen G, Johansson I. Fractionation of fish protein hydrolysates by ultrafiltration and nanofiltration: Impact on peptidic populations. *Desalination*. 2009;**244**:303-320. DOI: 10.1016/j.desal.2008.05.026
- [72] Afonso MD, Bórquez R. Nanofiltration of wastewaters from the fish meal industry. *Desalination*. 2003;**151**:131-138
- [73] Ke X, Huang Y, Dargaville TR, Fan Y, Cui Z, Zhu H. Modified alumina nanofiber membranes for protein separation. *Separation and Purification Technology*. 2013;**120**:239-244. DOI: 10.1016/j.seppur.2013.10.011
- [74] Shen SC, Chen Q, Chow PS, Tan GH, Zeng XT, Wang Z, Tan RBH. Steam-assisted solid wet-gel synthesis of high-quality nanorods of boehmite and alumina. *Journal of Physical Chemistry C*. 2007;**111**:700-707. DOI: 10.1021/jp065767d

- [75] Alami-Younssi S, Kiefer C, Larbot A, Persin M, Sarrazin J. Grafting alumina microporous membranes by organosilanes: Characterisation by pervaporation characterisation by pervaporation. *Journal of Membrane Science*. 1998;**143**:27-36
- [76] Popović S, Milanović S, Iličić M, Djurić M, Tekić M. Flux recovery of tubular ceramic membranes fouled with whey proteins. *Desalination*. 2009;**249**:293-300. DOI: 10.1016/j.desal.2008.12.060
- [77] Zhou S, Xue A, Zhao Y, Li M, Wang H, Xing W. Grafting polyacrylic acid brushes onto zirconia membranes: Fouling reduction and easy-cleaning properties. *Separation and Purification Technology*. 2013;**114**:53-63. DOI: 10.1016/j.seppur.2013.04.023
- [78] Kang C, Lu H, Yuan S, Hong D, Yan K, Liang B. Superhydrophilicity/superhydrophobicity of nickel micro-arrays fabricated by electroless deposition on an etched porous aluminum template. *Chemical Engineering Journal*. 2012;**203**:1-8. DOI: 10.1016/j.cej.2012.06.128
- [79] Karim A, Achiou B, Bouazizi A, Aaddane A, Ouammou M, Bouziane M, Bennazha J, Alami Younssi S. Development of reduced graphene oxide membrane on flat Moroccan ceramic pozzolan support. Application for soluble dyes removal. *Journal of Environmental Chemical Engineering*. 2018. DOI: 10.1016/j.jece.2018.01.055
- [80] Hua FL, Tsang YF, Wang YJ, Chan SY, Chua H, Sin SN. Performance study of ceramic microfiltration membrane for oily wastewater treatment. *Chemical Engineering Journal*. 2007;**128**:169-175. DOI: 10.1016/j.cej.2006.10.017
- [81] Karhu M, Kuokkanen T, Rämö J, Mikola M, Tanskanen J. Performance of a commercial industrial-scale UF-based process for treatment of oily wastewaters. *Journal of Environmental Management*. 2013;**128**:413-420. DOI: 10.1016/j.jenvman.2013.05.053
- [82] Ebrahimi M, Ashaghi KS, Engel L, Willershausen D, Mund P, Bolduan P, Czermak P. Characterization and application of different ceramic membranes for the oil-field produced water treatment. *Desalination*. 2009;**245**:533-540. DOI: 10.1016/j.desal.2009.02.017
- [83] Ebrahimi M, Willershausen D, Ashaghi KS, Engel L, Placido L, Mund P, Bolduan P, Czermak P. Investigations on the use of different ceramic membranes for efficient oil-field produced water treatment. *Desalination*. 2010;**250**:991-996. DOI: 10.1016/j.desal.2009.09.088
- [84] Shon HK, Phuntsho S, Chaudhary DS, Vigneswaran S, Cho J. Nanofiltration for water and wastewater treatment – A mini review. *Drinking Water Engineering and Science*. 2013;**6**:47-53. DOI: 10.5194/dwes-6-47-2013
- [85] Zhang H, Zhong Z, Xing W. Application of ceramic membranes in the treatment of oilfield-produced water: Effects of polyacrylamide and inorganic salts. *Desalination*. 2013;**309**:84-90. DOI: 10.1016/j.desal.2012.09.012
- [86] Buecker B. Microfiltration for industrial water treatment in power generation, *Ind. WaterWorld*. 2007:20e23
- [87] Šereš Z, Maravić N, Takači A, Nikolić I, Šoronja-Simović D, Jokić A, Hodur C. Treatment of vegetable oil refinery wastewater using alumina ceramic membrane: Optimization

- using response surface methodology. *Journal of Cleaner Production*. 2016;**112** (3132-3137). DOI: 10.1016/j.jclepro.2015.10.070
- [88] Yeom H-J, Kim SC, Kim Y-W, Song I-H. Processing of alumina-coated clay–diatomite composite membranes for oily wastewater treatment. *Ceramics International*. 2016;**42**:5024-5035. DOI: 10.1016/j.ceramint.2015.11.177
- [89] Chang Q, Zhou J, Wang Y, Liang J, Zhang X, Cerneaux S, Wang X, Zhu Z, Dong Y. Application of ceramic microfiltration membrane modified by nano-TiO₂ coating in separation of a stable oil-in-water emulsion. *Journal of Membrane Science*. 2014;**456**:128-133. DOI: 10.1016/j.memsci.2014.01.029
- [90] Leila S, Mhamed M, Hermann H, Mykola K, Oliver W, Christin M, Elena O, Nadia B. Fertilization value of municipal sewage sludge for *Eucalyptus camaldulensis* plants. *Biotechnology Reports*. 2017;**13**:8-12. DOI: 10.1016/j.btre.2016.12.001
- [91] Mei X, Quek PJ, Wang Z, Ng HY. Alkali-assisted membrane cleaning for fouling control of anaerobic ceramic membrane bioreactor. *Bioresource Technology*. 2017;**240**:25-32. DOI: 10.1016/j.biortech.2017.02.052
- [92] Düppenbecker B, Engelhart M, Cornel P. Fouling mitigation in anaerobic membrane bioreactor using fluidized glass beads: Evaluation fitness for purpose of ceramic membranes. *Journal of Membrane Science*. 2017;**537**:69-82. DOI: 10.1016/j.memsci.2017.05.018
- [93] Jeong Y, Cho K, Kwon EE, Tsang YF, Rinklebe J, Park C. Evaluating the feasibility of pyrophyllite-based ceramic membranes for treating domestic wastewater in anaerobic ceramic membrane bioreactors. *Chemical Engineering Journal*. 2017;**328**:567-573. DOI: 10.1016/j.cej.2017.07.080
- [94] Xing C-H, Tardieu E, Qian Y, Wen X-H. Ultrafiltration membrane bioreactor for urban wastewater reclamation. *Journal of Membrane Science*. 2000;**177**:73-82
- [95] Farsi A, Jensen SH, Roslev P, Boffa V, Christensen ML. Inorganic membranes for the recovery of effluent from municipal wastewater treatment plants. *Industrial and Engineering Chemistry Research*. 2015;**54**:3462-3472. DOI: 10.1021/acs.iecr.5b00064

Development, Characterization, and Applications of Capsaicin Composite Nanofiltration Membranes

Jesús Álvarez-Sánchez,
Griselda Evelia Romero-López, Sergio Pérez-Sicairos,
German Eduardo Devora-Isiordia,
Reyna Guadalupe Sánchez-Duarte and
Gustavo Adolfo Fimbres-Weihs

Additional information is available at the end of the chapter

<http://dx.doi.org/10.5772/intechopen.76846>

Abstract

Biofouling in reverse osmosis (RO) membranes is a severe problem, causing a decrease in both permeate flux and salt rejection and increasing transmembrane pressure. Capsaicin extract inhibits bacterial growth and is therefore used in this study to prepare a thin-film composite membrane and membrane support. Four types of nanofiltration (NF) membranes were prepared by interfacial polymerization onto a porous support prepared by the phase inversion method. Membrane A was the control membrane with no capsaicin extract, membrane B contains capsaicin in the polyamide thin film, membrane C contains capsaicin in the porous support, and membrane D contains capsaicin in both the thin film and support layers. Three different salts (Na_2SO_4 , MgSO_4 , and NaCl) were used at different concentrations (1000, 3000, and 5000 ppm) to test the performance of the membranes in terms of salt rejection and permeate flux. Membrane B showed the highest rejection for all the salts and concentrations tested. For 5000 ppm NaCl , the permeate flux for membrane B was 14.81% higher, and salt rejection was 19.6% higher than membrane A. Future work will evaluate the anti-biofouling properties of the membranes prepared with capsaicin, when exposed to seawater microorganisms.

Keywords: nanofiltration membrane, capsaicin, characterization, atomic force microscopy, contact angle, reverse osmosis

1. Introduction

The capability of several human activities, like industry and mining, has expanded throughout the last decades [1], which has led to a similar pace of improvements in membrane technology for separation. Drinking water treatment processes have developed to the point of requiring more advanced pretreatment processes [2]. Nanofiltration (NF) might function as a pretreatment for reverse osmosis desalination [3], as it can remove hardness, specific heavy metals, and reduce the salt content of feed water [4].

In addition, one of the main problems faced by desalination processes is the inevitable appearance of biofouling on its membranes [5, 6]. This causes problems such as decreases in permeate flux and salt rejection, as well as an increase in transmembrane pressure [7]. In an effort to reduce the most damaging effects of biofouling, there have been many studies for testing numerous anti-fouling agents and solutions added during membrane fabrication. However, not all these attempts include organic-based preparation, suggesting that there may be possible hazards for human health, after consumption [8, 9]. Pepper extract, the source of the capsaicin molecule, has proven to limit bacterial growth [10]; therefore, its addition during the membrane fabrication process may help control biofilm formation on the membrane surface.

In this study, nanofiltration membranes were prepared (**Figure 1**) for brackish water treatment. It is desirable for the desalination membranes to have hydrophilic properties, as this usually correlates with the tendency of a membrane for allowing water to permeate instead of rejecting it (hydrophobic) [11]. Contact angle measurements are usually carried out to determine the degree of hydrophilicity or hydrophobicity of a surface [12]. This study includes an analysis of the fabrication, as well as the characterization of four nanofiltration membranes, before and after their performance testing on a cross-flow module, operated with an aqueous salt solution to determine salt rejection. Membrane characterization is also performed through atomic force microscopy (AFM) and attenuated total reflectance infrared spectroscopy (ATR-IR) [13]. Membranes prepared with capsaicin will later be assessed for their anti-biofouling properties, to evaluate whether they are resistant to biofouling by seawater microorganisms.

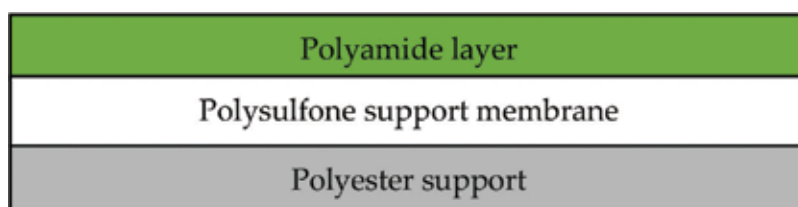


Figure 1. Scheme of composite membrane.

2. Methodology

2.1. Polymers and monomers

Polysulfone (PS purity > 99%), polyether sulfonyle (PES; purity > 99%), piperazine (PP; purity > 99%), and 1,3,5-Benzenetricarbonyl chloride (TMC; purity > 98%) were obtained from Sigma-Aldrich. Chiltepin pepper extract [9] (capsaicin extract) was obtained in the laboratory as a source of the capsaicin molecule (**Figure 2**). This extract was used to prepare nanofiltration membranes.

To corroborate the extraction of capsaicin, infrared spectroscopy was performed, showing the following signals:

- tension vibration for N-H present on the amide group, shown at 3381.8 cm^{-1} ; this signal hides within the O-H functional group, which has a range from 3400 to 3200 cm^{-1} ;
- vibration departing from tension on C-H at alkene located at 3010.36 cm^{-1} ;
- C-H vibration corresponds to methylene alkanes, at 2924.8 cm^{-1} ;
- methylene symmetrical tension for C-H present at 2853.77 cm^{-1} ;
- vibration through tension for C = O for the amide group at 1744.74 cm^{-1} ;
- vibration through stretching on C = O of the amide group at 1652.78 cm^{-1} ;
- vibration through the asymmetrical bending of CH_2 at 1464.28 cm^{-1} ;
- the signal at 1374.7 cm^{-1} , corresponding to a CH_3 bending; and
- an asymmetrical deformation of CH_2 at 721.66 cm^{-1} .

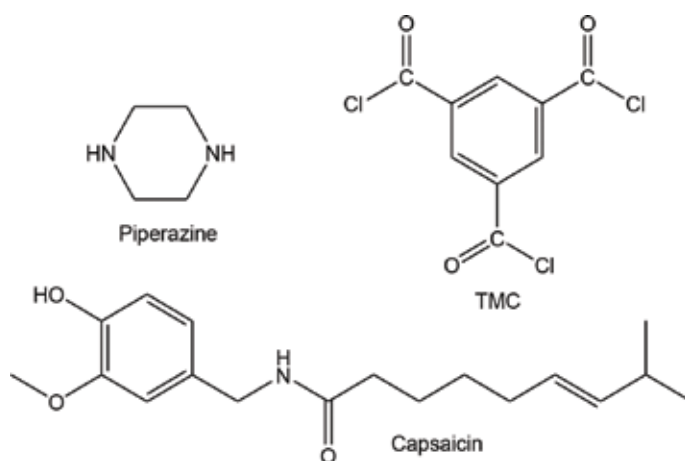


Figure 2. Chemical structure of the monomers for preparation nanofiltration composite membranes: piperazine, capsaicin and 1,3,5-benzenetricarbonyl chloride (TMC).

2.2. Preparation of the microporous polysulfone membrane

Sheets of microporous polysulfone membrane supports were prepared, following the methodology by Perez-Sicairos et al. [14] and Lin et al. [15]. Four sheets were prepared through a phase inversion process; a polymer solution including 18% w/w of dried polysulfone (12 g) was dissolved in a mixed solvent of n-methyl-pyrrolidone (NMP, 82 g) and an independent addition of sulfonated polysulfone (6 g), inside a clear jar and sealed with a Teflon cap. This glass bottle was subjected to a rotator device, spinning at 52 rpm under a heating light, to achieve a homogeneous polymer solution. A 71 × 28 cm Holytek paper piece (0.12 mm thick) was cut and held onto the membrane casting machine, where the polymeric solution was spread through the casting blade, allowing a solution spreading to a depth of 0.004 mm. Submersion speed was set at full capacity (11 m/min). The tank was filled with distilled water, providing a bath to induce phase inversion and a resting pace for 6 min. Finally, the membranes proceeded to a rinsing stage with distilled water for 2 min, in order to eliminate the excess of floating polymer.

2.3. Preparation of nanofiltration membranes with capsaicin

Nanofiltration membrane production started with the preparation of porous polysulfone membrane via the phase inversion method, as reported by [14, 15]. The NF membrane was prepared by interfacial polymerization, over the porous polysulfone membrane. Two chemical solutions were prepared, an aqueous solution containing piperazine (solution A) and an organic solution containing 1, 3, 5 benzene-tricarbonyl trichloride (TMC). The composition of each of these solutions was as follows. The composition of the aqueous solution (A) was piperazine (0.25% w/w), polyvinyl alcohol (0.25% w/w), and sodium hydroxide (0.5% w/w). This solution was prepared as follows: for each 250 g of solution A, 1.25 g of sodium hydroxide were weighed and placed inside a 250 mL flask, with 100 mL of distilled water. The preparation was stirred. Moreover, 0.63 g of polyvinyl alcohol was added until full dilution. Then, 0.63 g of piperazine was added to the flask and filled to 250 mL. The composition of the organic solution (solution B) was TMC (1.0% w/w) and hexane. To prepare it, the procedure was as follows: for each 250 mL of solution B, 1 g of capsaicin extract and 1.5 g of TMC were weighed and the solution was filled to 250 mL with hexane. The first of the membranes, labeled control, was prepared from solution A and solution B.

In order to prepare the experimental membranes with distinctive characteristics, capsaicin extract was added during the preparation process, using four different concentrations, as shown in **Table 1**.

Membrane	Support layer	Composite layer	Capsaicin (g)
A	Polysulfone	Polyamide	0
B	Polysulfone	Polyamide + capsaicin	1
C	Polysulfone + capsaicin	Polyamide	1
D	Polysulfone + capsaicin	Polyamide + capsaicin	2

Table 1. Composition for nanofiltration membrane preparation.

Once the porous support for the membranes was prepared, two of the pieces were designated as composite membranes. These membranes received the concentrations shown in **Table 2**.

2.4. Characterization of nanofiltration membranes

2.4.1. Atomic force microscopy

Atomic force microscopy (AFM) was performed with a PS 50–50-15 (50 μm) scanning probe microscope instrument (AFM workshop) to determine the surface morphology of the nanofiltration membrane. The software Gwyddion 2.4 was used to obtain 3D images and roughness measurements (root mean square, RMS). A sample size of 0.5 × 0.5 cm was used to analyze the nanofiltration membranes.

2.4.2. Attenuated total reflectance infrared spectroscopy

Attenuated total reflectance infrared (ATR-IR) characterization of the nanofiltration membrane surface was carried out with a Nicolet iS5 Fourier transform infrared spectrometer and the accessory iD3 ATR (thermo Fisher scientific). For ATR-IR analysis of the nanofiltration membranes samples, a germanium crystal was employed. A sample size of 0.5 × 0.5 cm was used to analyze the nanofiltration membranes.

2.4.3. Contact angle

Contact angle measurements were performed with a dataphysics contact angle system (OCA15SEC), camera iDs and injection system ES. A sample size of 3 × 2 cm was used to analyze the nanofiltration membranes. The water used was previously distilled and filtered (0.2 μm). The water drop was placed on different locations on the membrane surface, at a temperature of 22°C.

2.4.4. Cross-flow equipment

The operation of the cross-flow cell unit (**Figure 3**) was as follows. Starting from a 20 L feed tank, the feed solution (NaCl, MgSO₄ and Na₂SO₄ at the different concentrations) is conducted

Membrane	Polysulfone support			Polyamide layer		
	Polysulfone (g)	Sulfonated polysulfone (g)	Capsaicin (g)	Trimesoyl chloride (mL)	Piperazine (mL)	Capsaicin (g)
A	12.0	6.0	NA	100	0.25	NA
B	12.0	6.0	NA	100	0.25	1
C	11.5	5.5	1	100	0.25	NA
D	11.5	5.5	1	100	0.25	1

Table 2. Polysulfone and polyamide composition.

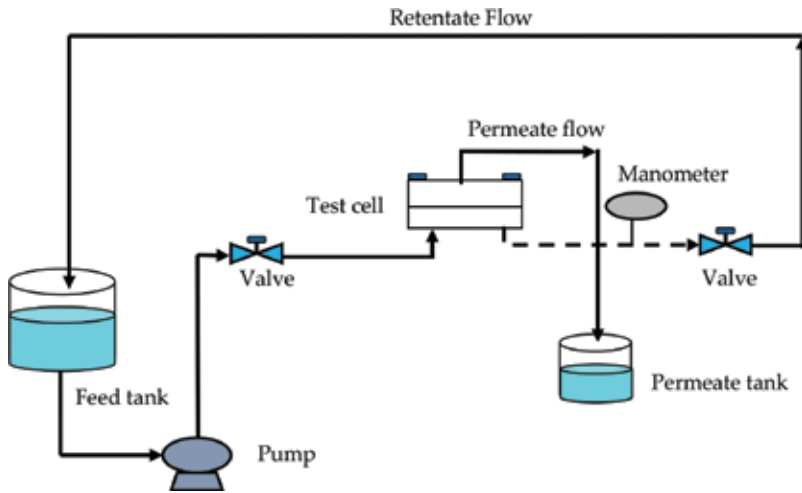


Figure 3. Cross-flow equipment for membrane testing.

to the cross-flow cell, with an applied and stable pressure (80 psi). A 3.5×2 membrane piece is placed in the interior of the cell. Once feed water reaches the membrane cell, two outcomes occur: some water permeates through the membrane, leaving impurities behind and producing purified water, and the rest of the water that does not cross the membrane flows to a retentate tank. This latter effluent will have a distinctive characteristic of higher salinity than the feed flow.

The thickness of the membranes was measured using a micrometer (Holytex paper 0.12 mm). This information can be related to the uniformity of the membrane surface. Finally, the salt rejection by the membrane is calculated considering the conductivity in the feed flow and in the permeate flow (after 60 min). For concentrations in the range of different salts used, the conductivity is proportional to solution concentration, so salt rejection can be determined using the following equation:

$$\% \text{Conductivity rejection} = \frac{\Omega_0 - \Omega_{60}}{\Omega_0} \times 100\% \quad (1)$$

where Ω_0 represents the conductivity of the feed and Ω_{60} represents conductivity of the permeate after 60 min of permeation. In terms of concentration, the rejection percentage is given by:

$$\%R = \frac{C_f - C_p}{C_f} \times 100\% \quad (2)$$

where %R is salt rejection, C_f is the concentration of salt in the feed, and C_p is the concentration of salt in the permeate.

3. Results and discussion

3.1. Test on cross-flow equipment

The data in **Figure 4** point to a decrease in permeate flux as the salt concentration increases. This can be appreciated for the three salts tested (Na_2SO_4 , MgSO_4 , and NaCl) under constant pressure (80 psi). Comparing the control membrane A with the rest of the membranes that include capsaicin in their formulation, it is observed that capsaicin addition tends to increase permeate flux.

For the NaCl solution at 1000 ppm, membrane B presented a permeate flux increase of 9.1% compared to membrane A, whereas at 5000 ppm, the increase was 14.81%. Membrane B presented the highest permeate flux increment, with membranes C and D also having permeate flux increases compared to membrane A but not as high as those of membrane B.

Due to the hydrophilic properties of capsaicin, the flux increments observed can be attributed to the capsaicin present in the membrane elaboration process for membranes B, C, and D. The capsaicin molecule has two main functional groups: hydroxyl, a polar group which presents affinity to water, and amide, which has nitrogen and a couple of free electrons generating polarity, also resulting in affinity to water. Hence, both characteristics result in hydrophilic properties on the membrane surface.

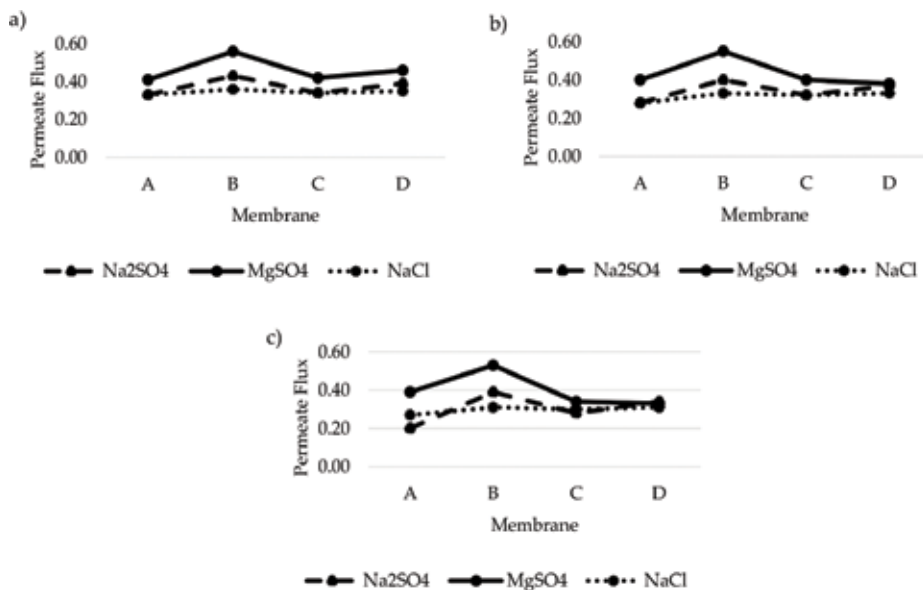


Figure 4. Permeate flux results for the membranes, with Na_2SO_4 , MgSO_4 and NaCl solutions at (a) 1000, (b) 3000 and (c) 5000 ppm respectively.

Even more important than its ability to permeate the main function of a membrane is to separate undesired impurities from water, that is, their salt rejection. All the membranes were tested using an NaCl solution at different concentrations (1000, 3000, and 5000 ppm) with the results shown in **Figure 5**. For each of these concentrations, the membranes show a very similar trend: membrane A (blank) has less salt removal in relation to membrane D. Membrane C shows less rejection than every other membrane (**Table 3**).

The membranes that include capsaicin extract also present a higher salt rejection than the control membrane. Membrane D presented the highest salt rejection. A possible reason of this greater NaCl rejection is the content of capsaicin placed on the support layer (polysulfone) or on the active layer (polyamide). The capsaicin functional groups having free electrons provoke major NaCl rejections. Membrane B also presented a significant increase in salt rejection compared to the control membrane A.

3.2. Characterization by atomic force microscopy

Atomic force microscopy allows us to zoom into a small area of the membrane surface. Using this technique, the roughness of the membrane can be visualized, providing measurement data in the scale of microns. Membrane roughness affects both the permeate flux and the salt rejection. Furthermore, roughness provides spaces for marine bacteria to settle, initiating biofilm formation, which later leads to membrane biofouling. For these reasons, smooth surfaces are most desirable on membranes.

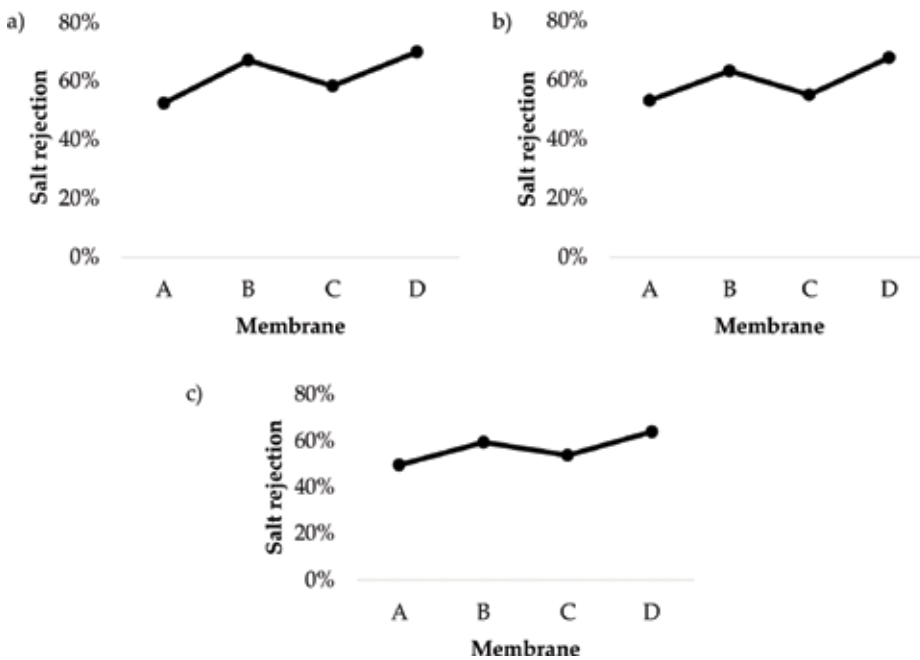


Figure 5. Salt rejection results for the membranes, with NaCl solutions at (a) 1000, (b) 3000 and (c) 5000 ppm respectively.

NaCl (ppm)	A (%)	B (%)	C (%)	D (%)
1000	52.5	67.22	58.41	70.06
3000	53.05	63.09	55.00	67.62
5000	49.59	59.30	50.98	63.92

Table 3. NaCl rejection percentage for membranes A, B, C, and D.

Atomic force microscopy was performed (**Figure 6**) in order to characterize the surface of the membranes. A scale of 50 μm was used, such that the scanned area was 2500 μm^2 for each membrane. Each membrane was measured at five different points. The RMS roughness measurements for each membrane, as well as the average measurements, are presented in **Table 4**.

From **Table 4**, it is evident that adding capsaicin extract to the active layer reduces the average roughness from 334.08 (membrane A) to 129.4 nm (membrane B). Similarly, when capsaicin was added to both the active layer and the porous support, the average roughness decreased from 334.08 (membrane A) to 221.26 nm (membrane D). On the other hand, the membrane with capsaicin only in the porous support (membrane C) presented the smallest reduction in average roughness, from 334.08 (membrane A) to 276.66 nm (membrane C). This suggests that including capsaicin on the polyamide active layer reduces the surface roughness the membranes.

3.3. Characterization by contact angle measurement

The contact angle measurement calculates the angle formed between the surface of a water droplet and a solid surface (see **Figure 7**). This measurement is related to the wettability. In

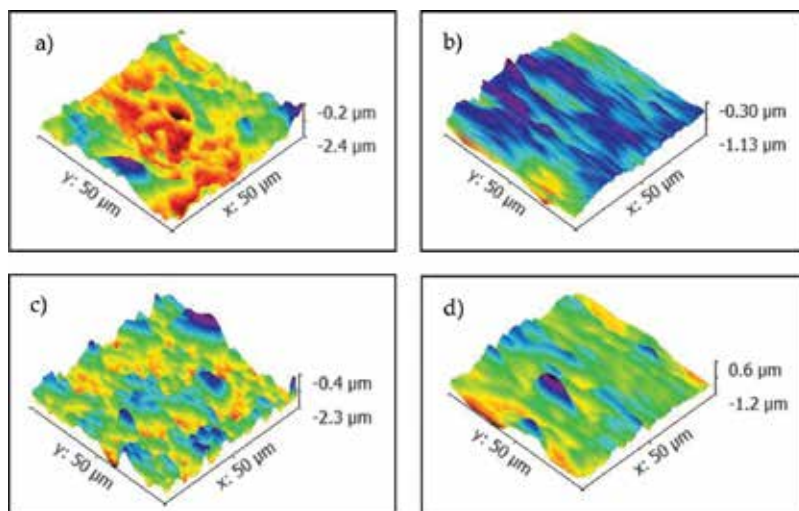


Figure 6. Atomic force microscope images and measurements for membranes A, B, C and D.

Membrane	AFM Measurement of RMS roughness (nm)					Average RMS roughness (nm)
A	306.2	325.5	357.8	318.8	362.1	334.08
B	97.4	108.8	176.6	100.0	164.2	129.39
C	294.2	305.1	264.9	245.7	273.4	276.66
D	266.2	203.7	185.5	199.1	251.8	221.26

Table 4. Membrane roughness values from AFM measurements.

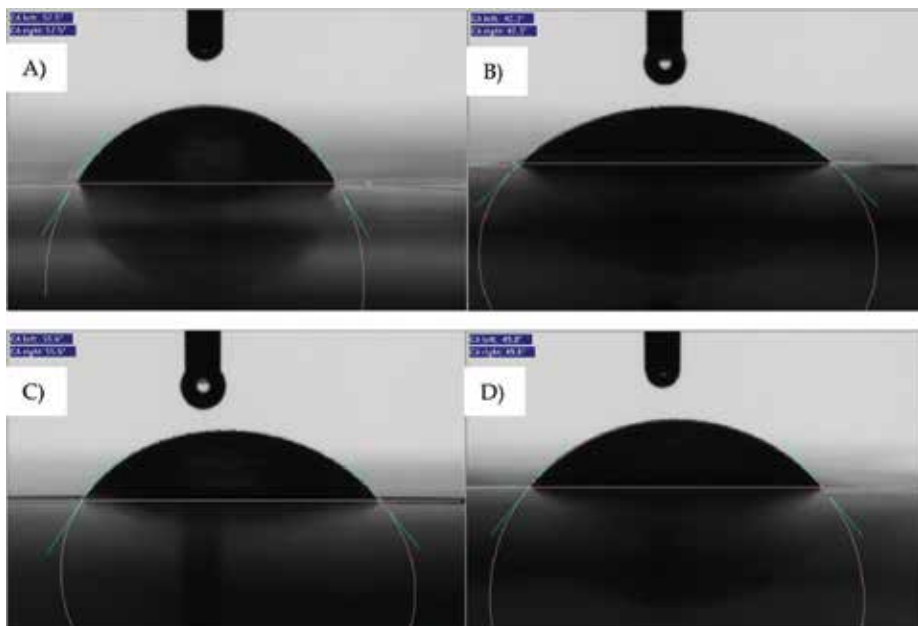


Figure 7. Contact angle measurements for membranes A, B, C and D.

the case of membranes, it can also be related to the permeability of the membrane, as a smaller angle means that water can dissolve more readily in the membrane matrix. Every liquid, at a given temperature, will show a unique equilibrium contact angle.

Table 5 shows contact angle measurements for the membranes tested, at an ambient temperature of 22°C. The control membrane A had the largest contact angle and membrane B presented the smallest. The lower contact angles exhibited by membranes B and D may be attributed to the presence of capsaicin on the surface of those membranes. This is also supported by the permeate flux results, as membranes B and D resulted in the highest values for flux. Moreover, it was also found that the inclusion of capsaicin in the porous support layer of the membrane (membrane C) also leads to a smaller contact angle than the control membrane A, albeit to a lesser degree than when capsaicin is included in the active layer.

Membrane	Description	Measurement					Average
		1	2	3	4	5	
A	PS-TMC	56.8	57.5	59.5	58.6	57.0	57.88
B	PS-TMCCAP	34.9	42.3	40.7	38.1	34.4	38.08
C	PSCAP-TMC	55.0	55.6	52.1	53.5	54.9	54.22
D	PSCAP-TMCCAP	48.1	47.3	49.8	47.2	49.1	48.30

Table 5. Contact angle measurements for membranes.

3.4. Characterization by ATR-IR

The infrared spectra for the four membranes are shown in **Figure 8**. The spectra for membranes A and C do not show vibration through stretching on C=O of the amide group at 1652.78 cm⁻¹. This is due to the absence of capsaicin in membrane A, while membrane C only included capsaicin in the porous support layer and, therefore, the infrared spectrum is not able to detect it. On membrane B, the signal is found at 1605.97 cm⁻¹ and for membrane D at 1619.90 cm⁻¹.

It is possible that the signal at 1652.78 cm⁻¹ was not seen due to a new link formed between capsaicin and the acyl on TMC, developing a new covalent link between a carbonyl group and

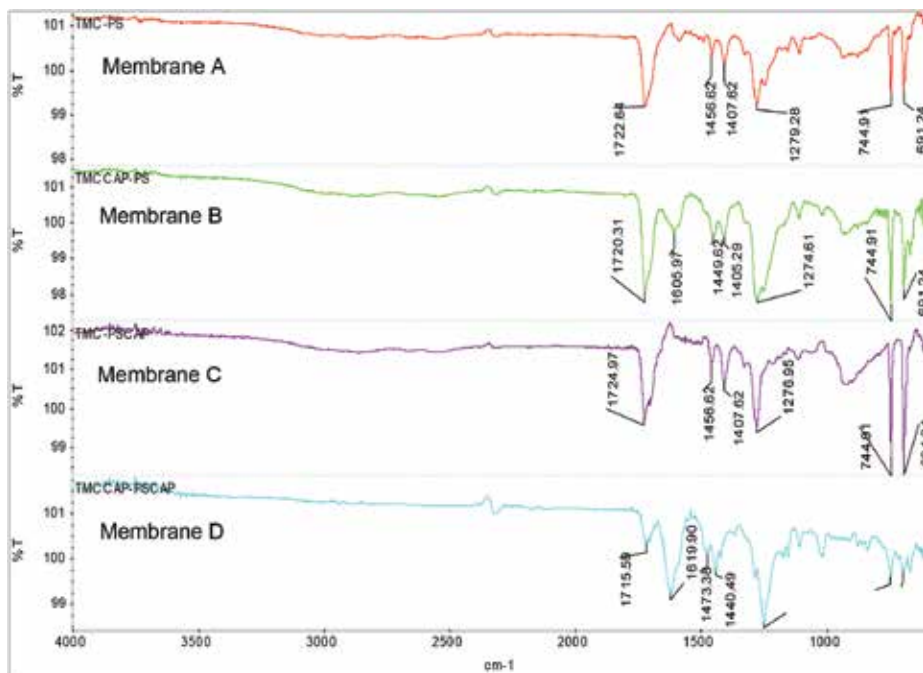


Figure 8. Infrared spectra for membranes A, B, C and D.

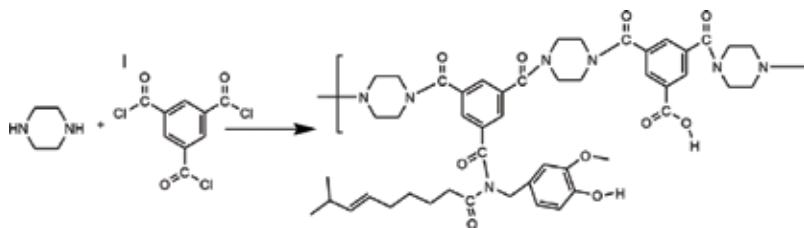


Figure 9. Piperazine – 1,3,5 Benzenetricarbonyl trichloride – capsaicin reaction.

nitrogen on the amide of capsaicin. Then, a new functional group is formed: $\text{Ar}-\text{C}=\text{O}-\text{N}-\text{C}=\text{O}$ (**Figure 9**). The wavelength for this new link would be lower, because of the resonance effect of the free electrons of nitrogen, generating a simple C-O link, as Pavian et al. [16] had expressed.

4. Conclusions

Nanofiltration membranes including capsaicin were prepared and characterized through contact angle measurements, AFM, ATR infrared spectroscopy and cross-flow tests. The ATR infrared spectroscopy showed that capsaicin reacted with the TMC, forming a new covalent link, which did not exist in the control membrane without capsaicin. In addition, AFM imaging showed that the surface of membranes with capsaicin in the active layer presented reduced roughness compared to the control membrane.

The results presented in this chapter show that capsaicin-based composite membranes present higher hydrophilic characteristics than traditional composite membranes. These properties of the capsaicin molecule can be attributed to its hydroxyl and amide groups, resulting in affinity to water. The hydrophilic character of the membranes with capsaicin was also reflected higher water permeability by the membranes.

It was also found that higher hydrophilicity and permeability could mostly be attributed to capsaicin present on the active layer of the membranes. This is because the presence of capsaicin in the porous membrane support layer did not show significant flux increases. Although capsaicin in the porous support increased salt rejection, we concluded that the application of capsaicin on the support layer of the membrane is not necessary. It is expected that nanofiltration membranes with capsaicin will result in better anti-biofouling properties than typical commercial membranes and, therefore, their service life would be longer. Future work will test this hypothesis.

Acknowledgements

The authors acknowledge project funding provided by PROMEP, CONACYT and the Instituto Tecnológico de Sonora.

Author details

Jesús Álvarez-Sánchez¹, Griselda Evelia Romero-López¹, Sergio Pérez-Sicairos², German Eduardo Devora-Isiordia¹, Reyna Guadalupe Sánchez-Duarte¹ and Gustavo Adolfo Fimbres-Weihs^{3*}

*Address all correspondence to: gustavo.fimbres@itson.edu.mx

1 Departamento de Ciencias del Agua y Medio Ambiente, Instituto Tecnológico de Sonora, Cd. Obregón, Sonora, México

2 Instituto Tecnológico de Tijuana, Tijuana B.C., Mexico

3 CONACYT-ITSON, Departamento de Ciencias del Agua y Medio Ambiente, Instituto Tecnológico de Sonora, Cd. Obregón, Sonora, México

References

- [1] Le NL, Nunes SP. Materials and membrane technologies for water and energy sustainability. *Sustainable Materials and Technologies*. 2016;7:1-28. <http://dx.doi.org/10.1016/j.susmat.2016.02.001>
- [2] Ray C, Jain R. *Drinking Water Treatment Technology—Comparative Analysis*. Dordrecht: Springer ; 2011. DOI: 10.1007/978-94-007-1104-4_2. ISBN: 978-94-007-1103-7
- [3] Llenas L, Martinez-Llado X, Yaroshchuk A, Rovira M, de Pablo J. Nanofiltration as pretreatment for scale prevention in seawater reverse osmosis desalination. *Desalination and Water Treatment*. 2012;36:310-318. DOI: <https://doi.org/10.5004/dwt.2011.2767>
- [4] Carrero-Parreño A, Onishi VC, Salcedo-Díaz R, Ruiz-Femenia R, Fraga RE, Caballero JA, Reyes-Labarta JA. Optimal pretreatment system of flowback water from shale gas production. *Industrial and Engineering Chemistry Research*. 2017;56:4386-4398. DOI: 10.1021/acs.iecr.6b04016
- [5] Nguyen T, Roddick FA, Fan L. Biofouling of water treatment membranes: A review of the underlying causes. *Monitoring Techniques and Control Measures. Membranes*. 2012;2:804-840. DOI: 10.3390/membranes2040804
- [6] Suwarno SR, Hanada S, Chong TH, Goto S, Henmi M, Fane AG. The effect of different surface conditioning layers on bacterial adhesion on reverse osmosis membranes. *Desalination*. 2016;387:1-13. <http://dx.doi.org/10.1016/j.desal.2016.02.029>
- [7] Al Ashhab A, Sweity A, Bayramoglu B, Herzberg M, Gillor O. Biofouling of reverse osmosis membranes: Effects of cleaning on biofilm microbial communities, membrane performance, and adherence of extracellular polymeric substances. *Biofouling*. 2017;33(5):397-409. DOI: 10.1080/08927014.2017.1318382

- [8] Food and Drug Administration. Code of Federal Regulations. Title 21, Volume 2. Revised as of April 1, 2017. United States of America. ISBN: 978-1-68388-080-6
- [9] Rodríguez-Maturino A, Troncoso-Rojas R, Sánchez-Estrada A, Daniel González-Mendoza D, Ruiz-Sánchez E, Zamora-Bustillos R, Ceceña-Duran C, Grimaldo-Juarez O, Aviles-Marina M. Efecto antifúngico de extractos fenólicos y de carotenoides de chiltepín (*Capsicum annum* var. *glabriusculum*) en *Alternaria alternata* y *Fusarium oxysporum*. *Revista Argentina de Microbiología*. 2015;47(1):72-77. <http://dx.doi.org/10.1016/j.ram.2014.12.005>
- [10] Omolo MA, Wong ZZ, Mergen AK, Hastings JC, Le NC, Reiland HA, Case KA, Baumler DJ. Antimicrobial properties of chili peppers. *Department of Food Science and Nutrition*. 2014;2:145-152. DOI: 10.4172/2332-0877.1000145
- [11] Omidvar M, Soltanie M, Mousavi SM, Saljoughi E, Moarefian A, Saffaran H. Preparation of hydrophilic nanofiltration membranes for removal of pharmaceuticals from water. *Journal of Environmental Health Science & Engineering*. 2015;13(42):1-9. DOI: 10.1186/s40201-015-0201-3
- [12] Mitrouli ST, Karabelas AJ, Isaias NP, Rammah AS. Application of hydrophilic macromolecules on thin film composite polyamide membranes for performance restoration. *Desalination*. 2011;278:105-116. DOI: 10.1016/j.desal.2011.05.014
- [13] Wu D, Liu X, Yu S, Liu M, Gao C. Modification of aromatic polyamide thin-film composite reverse osmosis membranes by surface coating of thermo responsive copolymers P(NIPAM-co-Am). I: Preparation and characterization. *Journal of Membrane Science*. 2010;352:76-85. DOI: 10.1016/j.memsci.2010.01.061
- [14] Pérez-Sicairos S, Miranda-Ibarra SA, Lin-Ho SW, Álvarez-Sánchez J, Pérez-Reyes JC, Corrales-López KA, Morales-Cuevas JB. Nanofiltration membranes, prepared via interfacial polymerization, doped with ZnO nanoparticles: Effect on performance. *Revista Mexicana de Ingeniería Química*. 2016;15(3):961-975. <http://rmiq.org/iqfvp/Pdfs/Vol.%2015,%20No.%203/Poli1/RMIQTemplate.pdf>
- [15] Lin SW, Pérez-Sicairos S, Félix-Navarro RM. Preparation, characterization and salt rejection of negatively charged polyamide nanofiltration membranes. *Journal of the Mexican Chemical Society*. 2007;51(3):129-135 <http://www.scielo.org.mx/pdf/jmcs/v51n3/v51n3a1.pdf>
- [16] Pavia DP, Lampman GM, Kriz GS, Vyvyan JR. *Introduction the Spectroscopy*. 4th ed. USA: Cengage Learning; 978-0-495-11478-9

Water Treatment Applications

Automatic Control Technologies to Enhance Water

Magdi Osman Ali Hamed

Additional information is available at the end of the chapter

<http://dx.doi.org/10.5772/intechopen.76841>

Abstract

Due to the explosive population growth, the demand of adequate hygiene drinkable water has been increased. Therefore, it has become more necessary to apply the automatic control system for water treatment production, in order to attain the health required outcomes. According to complexities of the process and the intersection of the treatment states, the suggested methodology in this chapter anticipates for the development of an automatic control based on wireless sensing networks (WSNs) to be applied in water treatment process. The wireless automatic systems are deployed in order to manage the processes of the production and increase the efficiency to the maximum level, along with the minimum cost. It is, therefore, important that the automated system works professionally, in order to get the utmost profit from the processes of the production. Practically, an effective control models have been designed and implemented using simulation software. Therefore, the research successfully managed to automatically control in the working pumps operation. The addition of purification and disinfection chemicals doses successfully calculated and added to the water in a real-time operation mode. In filtration phase, the process of filters backwashing has been completely automated. The obtained results were essential, beneficial and prove the system's applicability with minimum cost.

Keywords: water treatment, WSN, automatic control, pumps, filter backwashing, chemicals addition, sensors and valves

1. Introduction

One of the significant applications of the wireless automation system is to ensure the safe operation of the plant and to avert fatal possible accidents, which can also be catastrophic disaster and can have an adverse effect on the environment [1]. The undesirable incidents at the site of the plants can be condensed with the installation of the well-designed safe WSN

automatic system [2]. It can also reduce the overall cost and possible systematic error to a remarkable extent. Consequently, high reliability of the automation system is mandatory for the safety and economic reasons [3]. **Figure 1** shows examples of wireless application with different wireless devices connected to central automation control systems [4].

WSNs represent one of the most interesting research areas, with profound impact on technological development [6]. WSNs are regarded as a revolutionary technological that builds the information gathering method of the system. The information and communication built will greatly improve the reliability and efficiency of infrastructure systems. Compared with the wired solution, WSNs feature easier deployment and better flexibility of devices. With the rapid technological development of sensors, WSNs will become the key technology for Industries [7]. Several applications are being proposed, such as detected physical phenomena (e.g. light, heat, pressure, and flow), environmental monitoring (e.g. detection of fires in forests), structural monitoring of civil engineering structures, and industries monitoring and control [6]. Whereas the replacement of the wired technology with that of the wireless is illustrated in the below mention **Figure 2**.

The main purposes of this chapter are: to establish a WSNs as the key ingredient in the course of the applications of the process control. To inculcate the wireless systems in industries and environment process control in order to replace old traditional systems especially those related to human beings health and safety such as a water treatment plant.

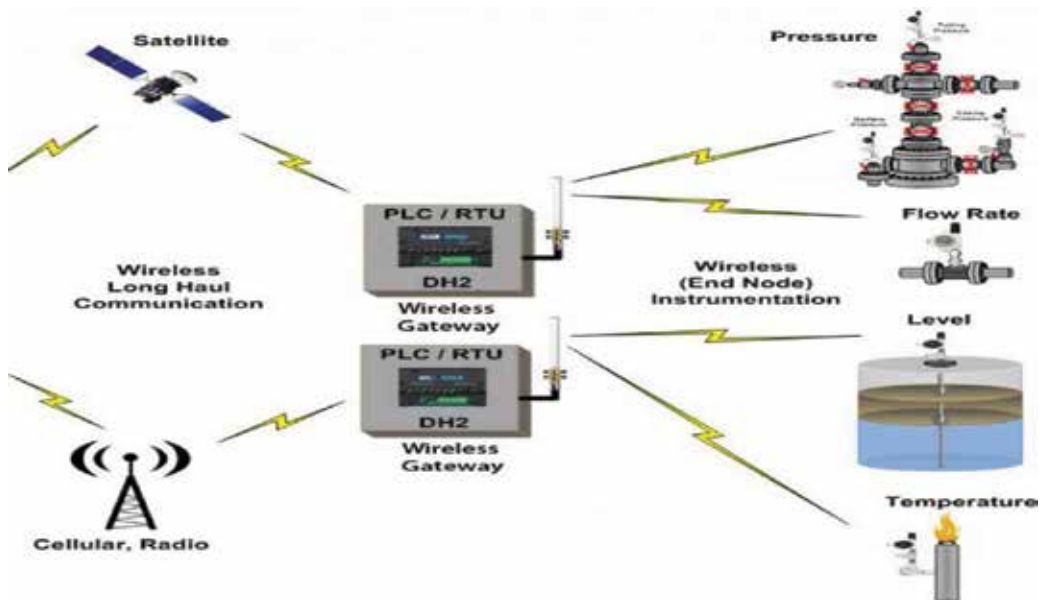


Figure 1. Applications of wireless sensor network [5].

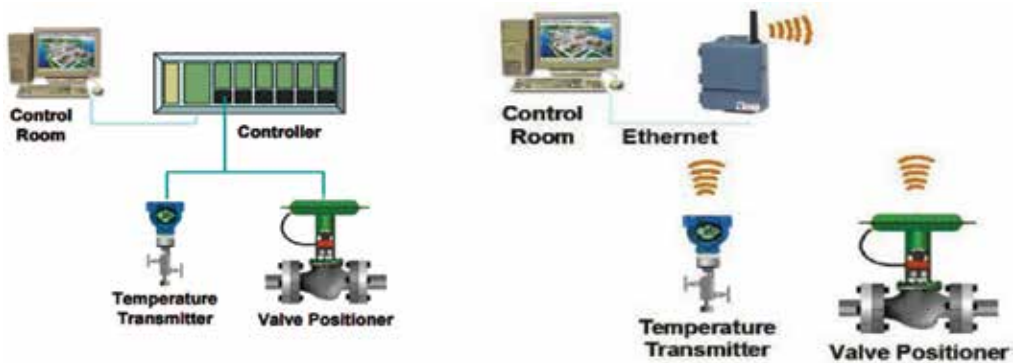


Figure 2. Replacement of the wired technology with that of the wireless [8].

2. Wireless sensing networks in industrial applications

According to [9], WSNs are being widely deployed in process industries, in order to ensure reliable and integrated control and monitoring of the processes. In this regard, [10] has stated that process control and monitoring is the combination of algorithms, mechanisms, and architectures, which ensures the reliability of different industrial processes. According to [11], several applications of process control are critical mission and possess stringent requirements. In such circumstances, flawed control loop may result in unpredictable and unwanted shut-down of the plant. It has been recognized from the study of [7] that such failures may also result in fatal accidents in process controlled plants. Thereby, it can be asserted that wireless networks also comprise wide range of challenges and issues, which are needed to be considered to ensure the integrity of industrial operations.

It has been claimed by [12] that main stream process control devices, like motors, valves, temperature sensors that are ready-equipped with wireless transmitters, foolproof wireless process control systems and network standards are not yet accessible.

It has been stated by [13] that WSN systems are widely being used in different applications of industrial automation. In this regard [14] has claimed that such applications provide commendable safety, efficiency, conservation, and control to the processes of the industry. On the other hand, it has been asserted by [15] that automated sensing applications play an inevitable role in improving the reliability of process control systems as well as pre-existing manufacturing. However, [16] has stated that sensing applications are found to be highly effective, in terms of improving and enhancing management of industry's assets. It is due to the fact that such systems foster continual monitoring of critical equipment, which may create different issues in industrial processes. It has been documented in the research, which was conducted by [17] that sensing applications play a major role in reducing and minimizing excessive cost, which is required for optimized processes of manufacturing.

In addition to this, sensing applications also assist in identifying and recognizing inefficient operations or malfunctioned equipment. According to [15], sensing applications enable the process industry in automating the process of data acquisition, from remote sensors, in order to minimize user intervention. It has been affirmed by [18] that application of automated sensing, within process industry, assists in implementing certain networks, in order to improve and increase public and employee safety. It has been stated by [16] that automated and wireless sensing applications also enable process industry to streamline the process of data collection for more integrated and valuable compliance of reporting.

2.1. Monitoring and controlling

It has been documented in the research, which was conducted by [10] that one of the major industrial applications of WSN includes monitoring and controlling of industrial processes. In this account, [9] have claimed that WSN assists the plant operators to evaluate and ensure the performance and health of machine and products. According to [18], WSN systems were developed, in order to support machinery CBM (machinery condition based maintenance). It is due to the fact that process industries have to face various issues, in terms of enabling new functionality and higher costs of maintenance and implementation. In such circumstances, wireless sensors can be located in the problematic and vulnerable areas, where wired systems cannot be reached easily. These areas may include un-tethered vehicles and rotating machineries.

Data logging can also be considered as one of the greatest industrial applications of wireless sensors. It is due to the fact that wireless sensor networks facilitate the practices of data collection, in order to monitor environmental conditions of the plant. These may include temperature, pressure, density, flow rate, overflow tanks, volume, etc. In addition to this, WSN systems also assist in gathering statistical information, which enables the machine operators to examine and evaluate potential malfunctioning of the machines. Waste water monitoring and water consumption monitoring can also be performed by the help of WSN systems. All of these features eventually results in the reduction of water wastage. It has been recognized from the assessment of studies carried out by [17] that WSN systems can also be adopted in order to evaluate the integrity of physical infrastructure as well as geo-physical processes, which are closed to real time and over long periods, through the process of data logging, by the help of interfaced sensors.

3. Wireless sensing networks in water treatment applications

The standards of water quality and quantity are necessary for survival and reduce the risk of disease. The main health problems associated with drinking water contamination are caused by insufficient water for hygiene purposes and consumption of that contaminated water [19]. There are two standards defined for water supply standards. The first standard involves the quantity of water, while the second standard regulates water quality [20]. The minimum amount of water for safe and healthy consumption is summarized by around 7.5–15 l of water per person per day. Water quality is a secondary standard, according to [20], therefore, once water quantity has been assured, water quality should be improved to reduce the risk of dysentery and other diseases.

The quality parameters such as turbidity, coliforms, and chlorine residual are specified as the minimum standards that must be met by water treatment technologies.

This work intends to enhance the production of water treatment plant by controlling the treatment processes and their affecting parameters by using controlling and measuring instruments such as what it uses to adjust the clarification and disinfection chemical materials addition. Besides, the instrument's readings are used for further studies concerns.

In the following sections the traditional systems and the proposed techniques that have been developed for water treatment plant will be discussed. The proposed control system design consists of five phases: intake, sedimentation, filtration, disinfection, and distribution as shown in **Figure 3**.

The devices used this design and its abbreviations are shown in **Table 1**. Various types of devices such as sensors, valves, pumps, microcontrollers, communication modules and PLC are communicated wirelessly.

3.1. Sukking/distribution pumps operation

The operation of the intake and distribution pumps is based on the Delta/Star control circuit called (starter). In the traditional plants, the starter and pump are basically located at the main supply bank, therefore, the operation process of these pumps is applied manually using start/stop pushbuttons. The starter circuit as shown in the **Figure 4** consists of three main contactors (K1, K2 and K3) in addition to a timer control to accomplish the pumps' starting conditions. K1 controls the pump's main power supply and protects it from short circuit and current overload circumstances. K2 is adjusted by the timer control circuit to initialize the pump at Star (Y) condition. Finally, K3 operates simultaneously when K2 releases (by means of interlock) to inject full supply voltage to operate the pump at Delta (Δ) condition [21].

3.1.1. The subsystem developed for intake/distribution pumps

The intake/distribution pumps (P1, P2, ..., Pn) work through WSN control circuits (C1, C2, ..., Cn). The circuits operated according to wireless control signals generated by a central control unit and sent wirelessly via communication module to the new installed power switch (on/off) sensor.

The reservoir water level changed regularly during a day time according to the treated and distributed water. Thus, control on reservoir water level can be achieved by regulating the operated and standby pumps. Therefore, reservoir level sensors has been used to continuously collect levels readings and feed the central control module that uses a designed program to specify the number of pumps to be work and which should be in standby state. **Figure 5**, illustrated the developed system in case of intake phase, while distribution phase illustrated in **Figure 6**.

3.2. Chemicals materials used

Physical properties such as suspended mater and turbid caused by these matters, and the living organisms on the other hand threat the health of consumers, thus water treatment plants are designed and established to remove the risk of these problems, and to put the final product within the standard guidelines of potable water.

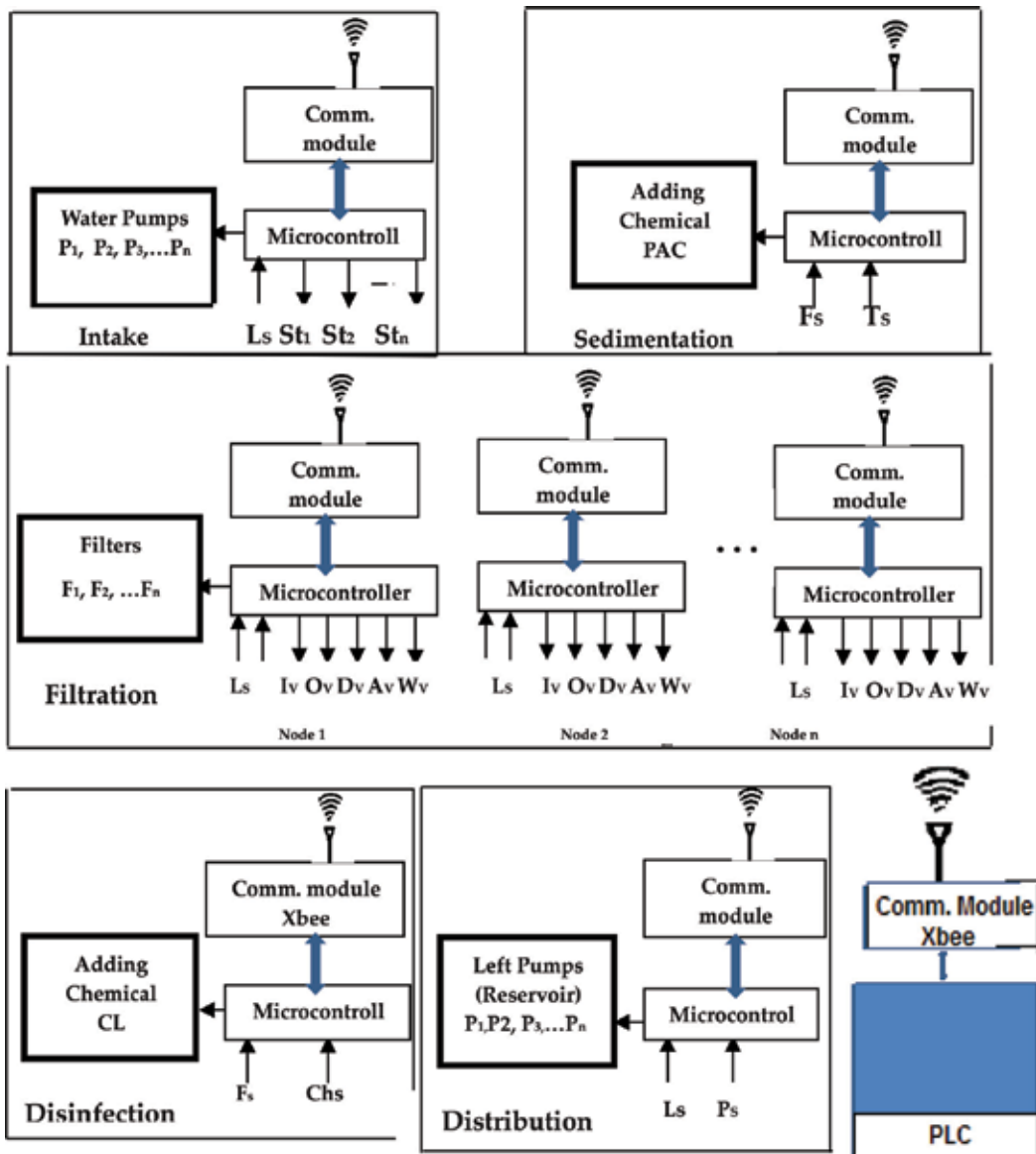


Figure 3. The wireless control system designed for water treatment plant.

Purified water and safety to be drunk depend on added sedimentation and disinfection chemicals materials, which are defined by reading many parameters concerned with quantity and quality of raw water as shown in Figure 7.

In water treatment plants there is a chemical room for preparing chemical materials. This unit includes feeding machines, chemical coagulants daily tanks and other equipment. The popular chemicals added are:

Pump motor	Pm	Level sensor control	Ls	Inlet valve	Iv
Injection motor	Im	Flow sensor control	Fs	Outlet valve	Ov
Power switch	SW	Turbidity sensor control	Ts	Drain valve	Dv
Power supply	P	Chlorine sensor	Chs	Wash valve	Wv
Communication module	Cm	Pressure sensor control	Ps	Air valve	Av
Microcontroller	Mc	Pumps control circuit	St	Backwashing	BW

Table 1. Devices and abbreviation.

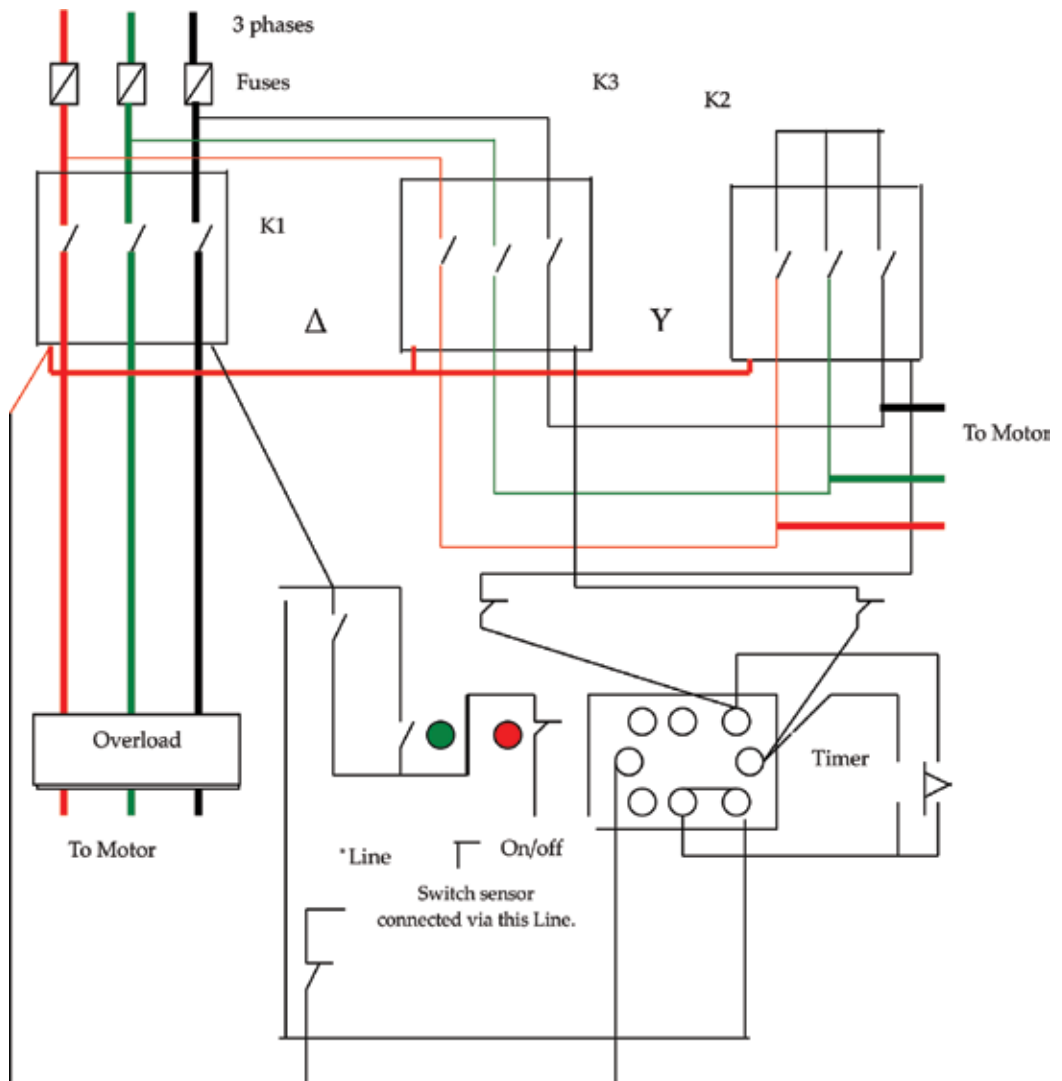


Figure 4. Control circuit of the pump operation.

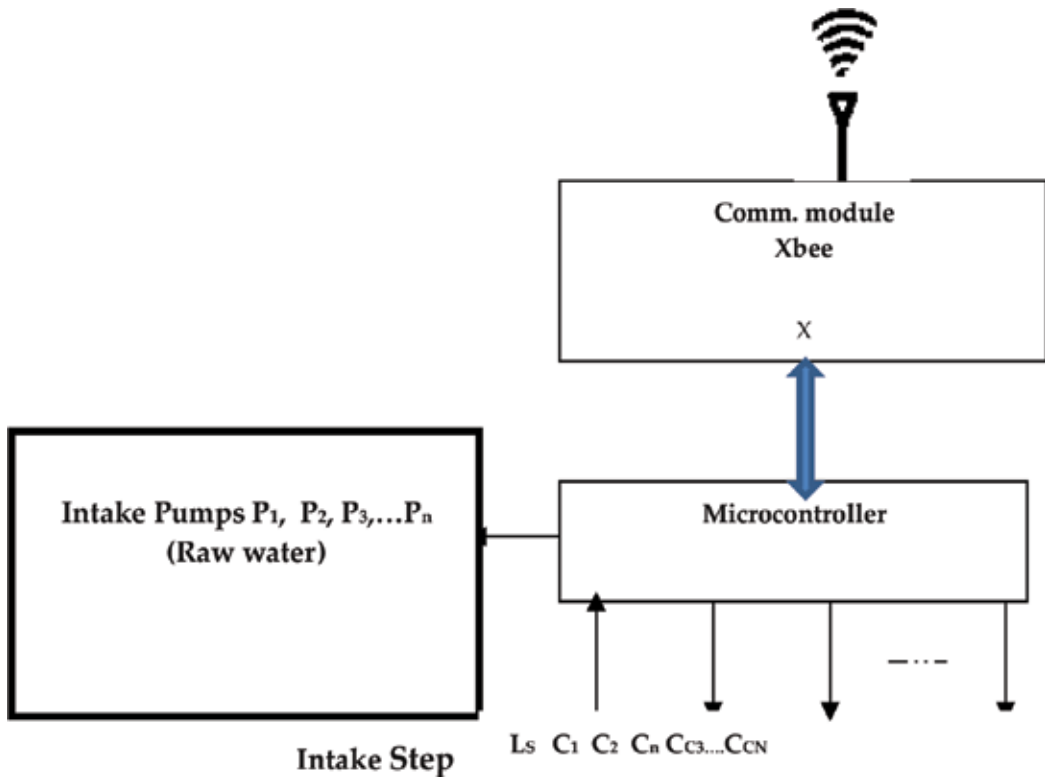


Figure 5. The intake subsystem.

- Poly aluminum chloride

Extra power inorganic aluminum salt used as cationic coagulant, max permissible dose 250 mg/l.

- Chlorine gas

Oxidant uses in trace dosage for the removing bacteria, so the recommended dose is 1 mg/l.

3.2.1. Adding chemical material

In case of turbidity removal a process called a Jar Test was used to identify the estimated dose from purification chemical material. This test conducted every 2 h to check the amount of change in water quality. While in case of disinfection, the current process is to inject the estimated chlorine first then read the residence chlorine in the water every 2 h to decide in increasing or decreasing the injected doses.

3.2.2. Suggested techniques

In any fraction of time the water types and flow rate are subjected to change. Therefore, the suggested developed model intends to enhance the addition of chemicals materials by introducing a real-time application that reads the water parameters and immediately adds the corresponding doses.

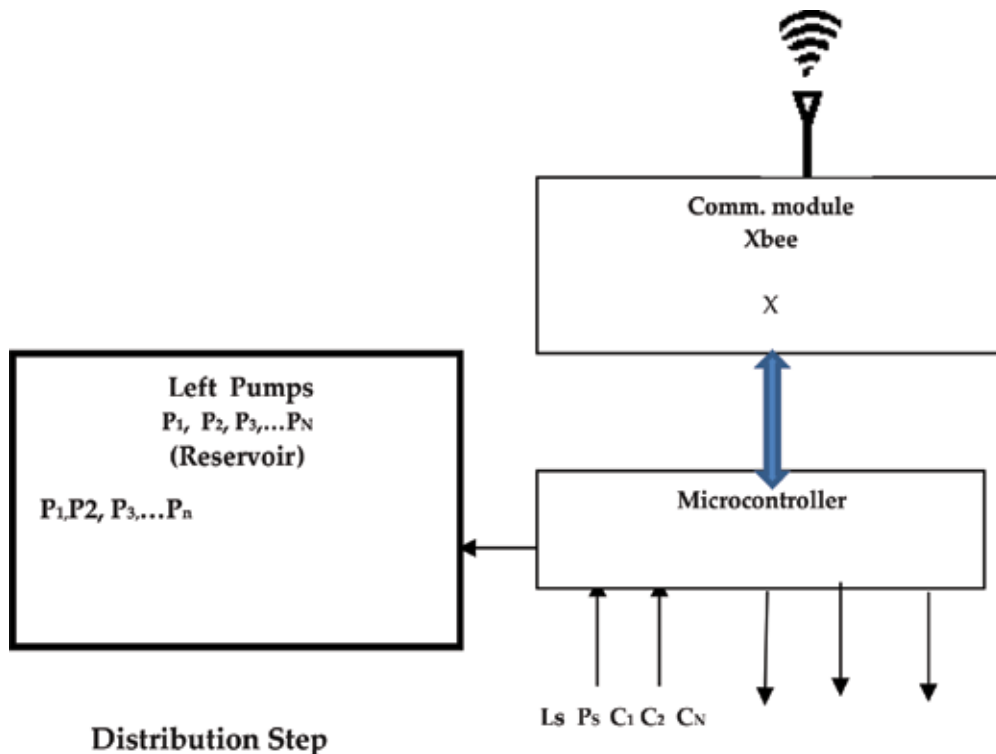


Figure 6. The distribution subsystem.

To implement this system, a control unit using a PLC has been suggested to accomplish the process in order to raise quality to the best possible level without chemical materials misuse. The modification focuses mainly on improving the quality of treated water in plant using instruments to measure parameters that affect the quality. Depending on the reading, the accurate doses from chemical materials which are used for water sedimentation e.g. poly aluminum chloride (PAC) and disinfection e.g. chloride (Cl_2) will be determined [22]. Accordingly, pumps are used to inject the corresponding doses to the water. Therefore, it is important that automated system works efficiently to ensure good quality produced water, prevent possible fatal error or even disasters that might affect people, as well as, to reach the highest level of production [23].

3.2.3. Control system implementation

The proposed control systems to be implemented are demonstrated in **Figure 8**. In these systems sensors with different functions has been used. Therefore, sensors are used to read water turbidity, flow rate, pH, and resident chlorine in the water and connected directly to microcontroller.

The microcontroller used a designed algorithm to calculate the required doses from clarification and disinfection chemical materials to be added to water in real-time application mode,

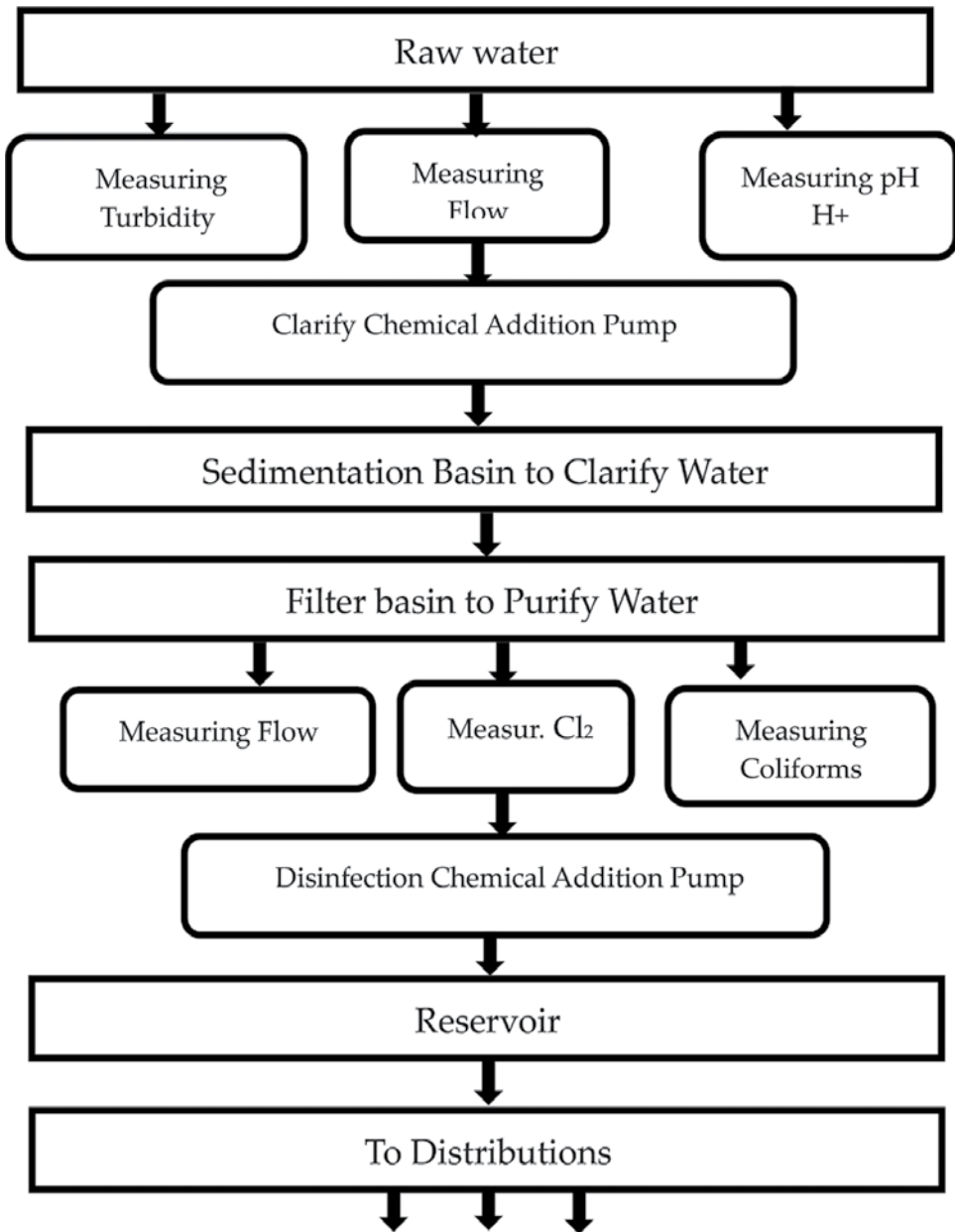


Figure 7. The water treatment proposed control instruments.

and sends appropriate signals to the central PLC via a wireless communication module. The PLC generates the corresponding output pulses and communicates with actuators that govern the working dosing pumps. These dosing pumps have broad range of flow rate in liters per hour (l/h) [24].

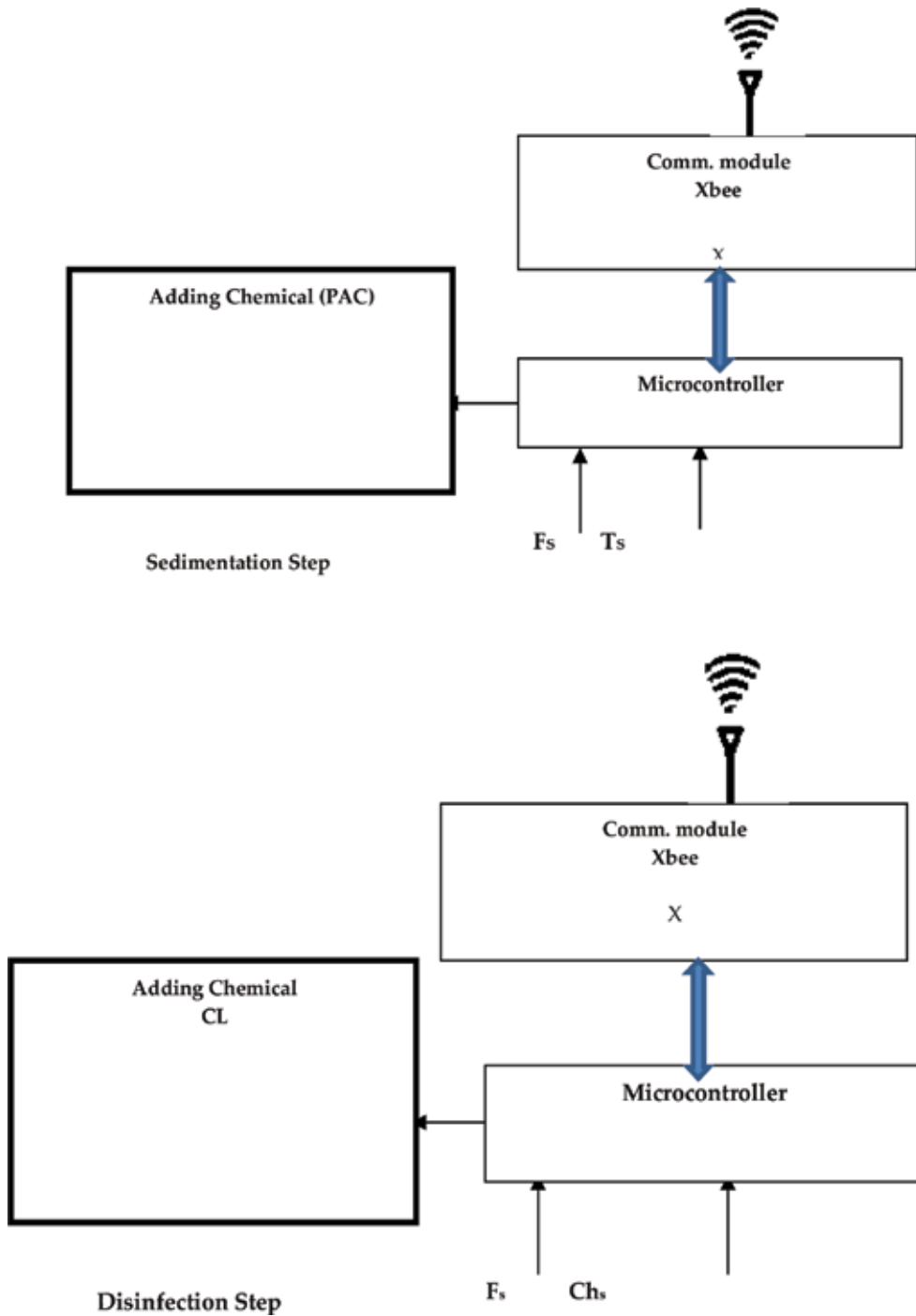


Figure 8. The sedimentation and disinfection systems.

3.2.4. System algorithm

The following algorithm designed to calculates the amount from purification and disinfection chemical materials to be added to water [25].

Algorithms: Calculation of clarification and disinfection chemicals

For $i=0$ to ∞ do

Input: read (T_{S1}, T_{S2}) , read (F_{m1}, F_{m2}) , read ($Ref.Cl2$) , read (F_{m3}) , read ($Ref.Dose$)

Calculate:

T_S Average (T_{S1}, T_{S2}).

F_m Average (F_{m1}, F_{m2})

Convert water rate (W_{rate}) to water volume (W_{volume})

$W_{volume1} = W_{rate1} \cdot t$

$W_{volume2} = W_{rate2} \cdot t$

Clarification (e.g. Ploy Aluminum Chloride) injection

Calculate the dosing $Clar_{dose}$

$Clar_{dose} = Ref.Dose \times T_S \times W_{volume1}$

Set injector control pulse P_{C1}

Calculate injection time T_{i1} :

$T_{i1} = \frac{Clar_{dose}}{Injector_{rate}}$

Output: pulse control P_{C1} (To drive injector)

$P_{C1} =$ pulse modulation (P_{i1}, T_{i1})

Disinfection (Residual chlorine injection)

Calculate the dosing (Di_{dose})

$Di_{dose} = Ref.Cl2 \times W_{volume2}$

Set injector control pulse P_{C2}

Calculate injection time T_{i2} :

$T_{i2} = \frac{Di_{dose}}{Injector_{rate}}$

Output: pulse control P_{C2} (To drive injector)

$P_{C2} =$ pulse modulation (P_{i2}, T_{i2})

End

3.3. Filtration phase

The water from sedimentation basins distributed to the filtration basins by gravity. The filtration process involves passing water through fine granular materials, such as sand [26]. As more and more raw water passed through the filter, suspended particles are accumulating within the filter media, reaching impermissible levels that lead to one of the two destructive events. They can either cause the filter head loss within the filter to reach excessively high levels, or hardly pushed through the media, resulting of bad quality of treated water. Therefore, in order to maximize the use of a given filter within a safe mode, it becomes necessary to remove these entrapped particles from the media itself. Filter backwashing is the process by which this is accomplished. It refers to pumping water and compressed air backwards through the filters media as illustrated in **Figure 9**.

3.3.1. Suggested techniques

In order to be safe and function perfectly with full capacity through a day, the filter efficiency influenced by the effectiveness of the backwashing methods. This efficiency can be controlled by installed water level sensors in the filter basin. When the water level inside the basin exceeds impermissible level, backwashing operation is executed automatically with the PLCs program aid.

To implement the system, the researcher used sensors for measuring the water level, XBee as a wireless communication module, microcontroller as a data acquisition unit, automated water valves for inlet (Iv), outlet (Ov), drain (Dv), washing (Wv), and compressed air valve (Av) to be opened and closed according to the received signals from the PLC control module. The illustration of the system design is shown in **Figure 10**.

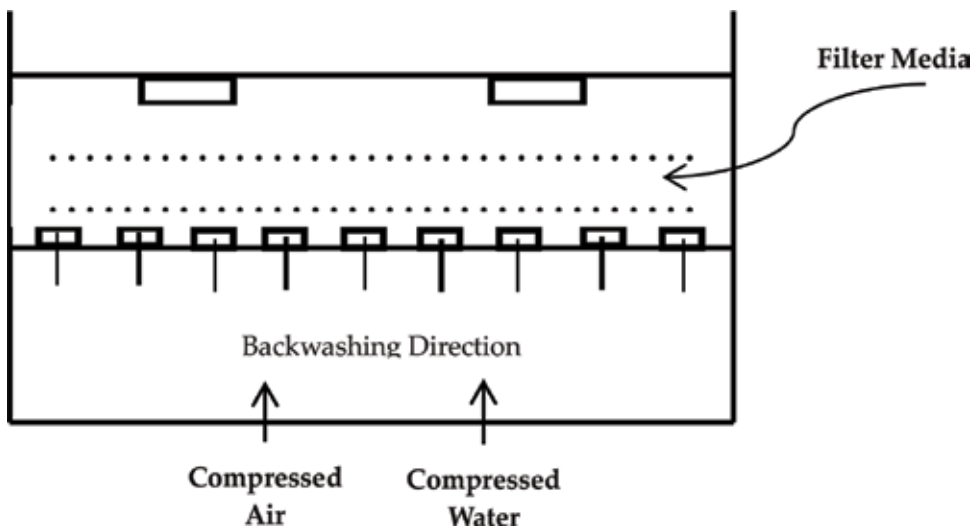


Figure 9. Washing filter.

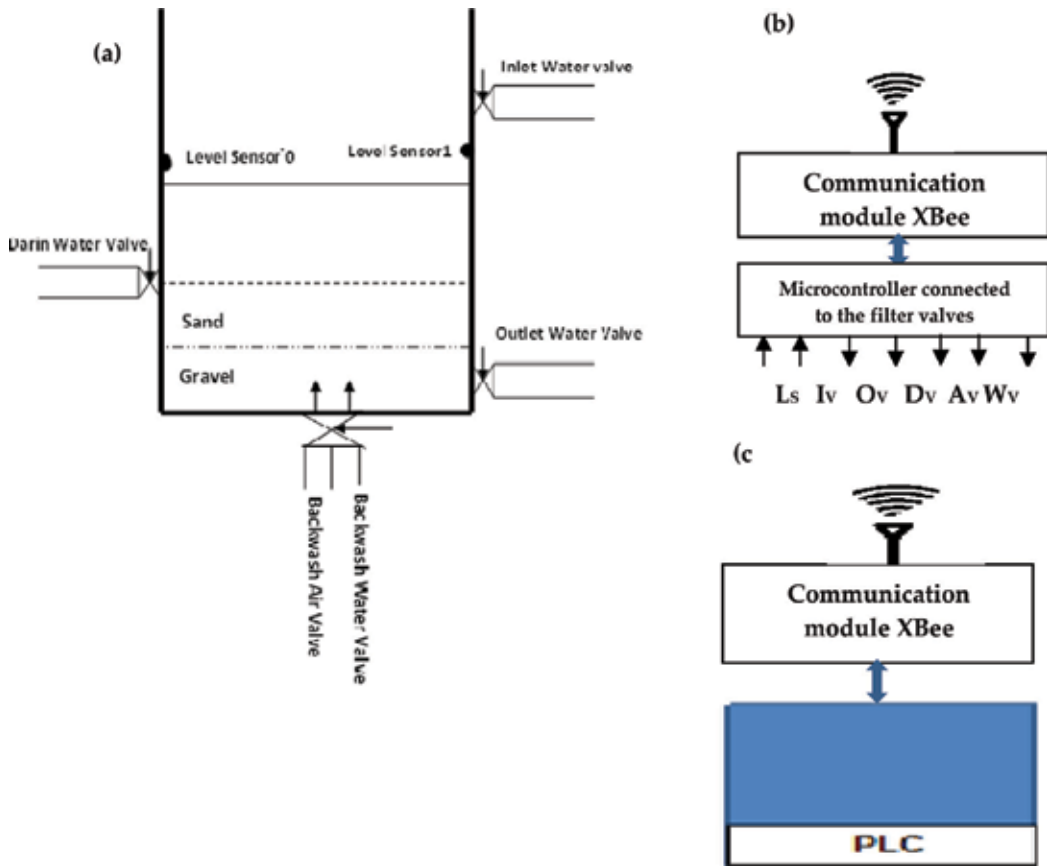


Figure 10. System model. (a) Filter basin components, (b) communication module and actuators, and (c) control module.

4. Results and discussion on implemented systems

The obtained simulation results for the implemented subsystems will be discussed in this section. The PLCs is communicated wirelessly with inputs and outputs through communication modules and microcontrollers as demonstrated in in the previous developed subsystem design. The different water treatment processes consideration has been setup, where the subsystems have been controlled successfully under various operations settings.

4.1. Control on motor operation

The Motor operation is controlled by a motor starter (M) which is connected in series with a normally open (NO) momentary pushbutton (Start), a normally closed (NC) momentary pushbutton (Stop), and the normally closed (NC) overload relay (OL), as shown in Ladder Logic diagram **Figure 11**. The NO start pushbutton is connected to the input I0.0 while the NC stop pushbutton is connected to input I0.1. The NC overload relay contact as part of the motor starter is connected to input I0.2. The input (I0.0–I0.1–I0.2) forms an AND circuit and controls

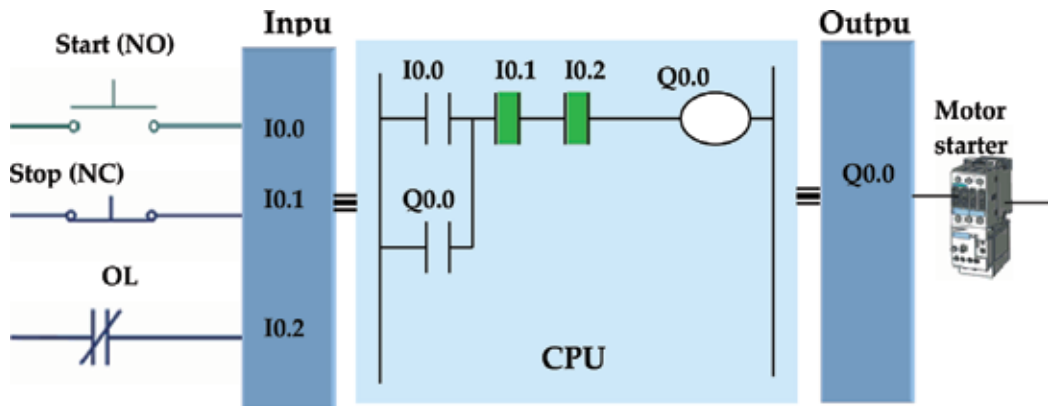


Figure 11. Ladder logic diagram represents the motor's operation.

the operation of output (Q0.0). The logic state of input bit I0.1 is logic 1 because of the NC stop pushbutton. The logic state of input bit I0.2 is logic 1 also because protective overload relay is NC. By A program a NO contact Q0.0 is added to ladder logic, which is in direct relation with output (Q0.0) and forms an OR circuit with input (I0.0). Motor starter is connected to output Q0.0 at output module [27].

When the pushbutton is initialized, unit CPU receives logic 1 signal from input I0.0 at input module. This causes contact I0.0 at ladder logic to close. In this case, all contacts are on ladder logic 1 state, so the logic condition of output Q0.0 on the ladder logic is logic1 [27].

4.2. Control on purification and disinfection addition

In this section the results obtained from the simulations of the model developed using MATLAB will be presented. The modeled system was successfully executed. The simulation program fed with measured data of water quality values, and then generated the required doses in four modes of injection methods at different times.

Figure 12 shows the time relation between the flow rate and the injected doses of materials in mg/l. The system collects the values of turbidity and flow rate intervals of 10, 20, 30, and 40 s. These obtained reading values are feed the modes from one to four consequently. According to the equation used in the model mode 1, the injected purification material was due to the optimal dose, this is presented in Figure 12 with black graph. The system injected doses in the other modes (2, 3, 4) varied from the required value in respect to the time differences specially in mode 4 (green graph). For example, in case of 45 l/s flow rate, mode 4 injects excess material by around 30 mg, mode 3 injects less material by around 20 mg, while at 80 l/s flow rate mode 4 injects less material by around 60 mg from the reference mode (mode 1). Therefore, according to the frequent changes in water turbidity and flow rate, the injection at higher rate (mode 1) is likely to be accurate and close to optimal dose.

Figure 13 illustrates the efficiency of the four modes according to the change in flow rate and random values of turbidity. In mode 1 as nominated to be the optimal reference mode, the

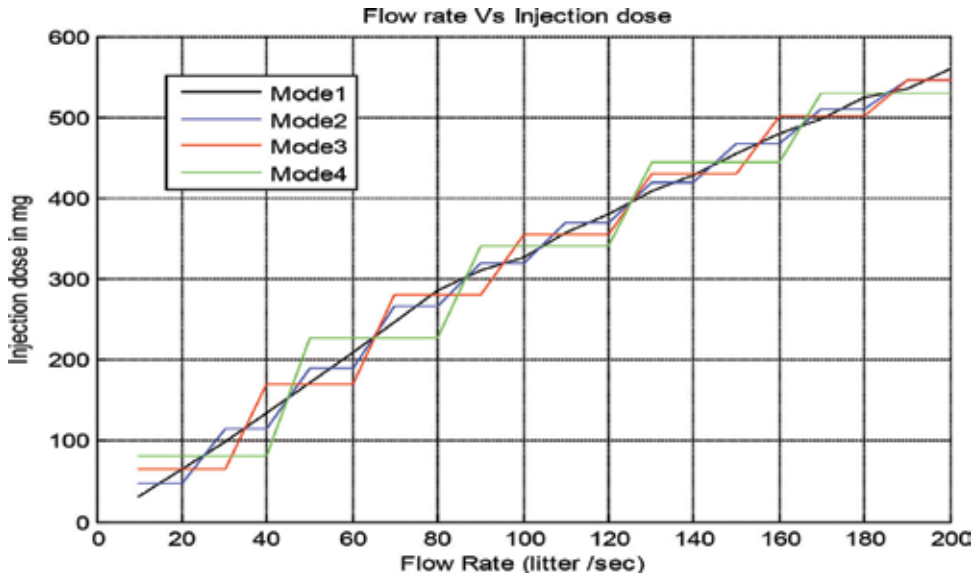


Figure 12. The relation in time between the flow rate and the injected doses.

efficiency represented in **Figure 4** by black graph bounded between 83 to 87%, so that the system in mode 1 is likely to be stable. In mode 2 which is represented by blue graph, the efficiency is bounded between 80 to 90% but there are large fluctuations. The remaining higher modes gave unstable and poor efficiency fluctuated between 0 and 95%.

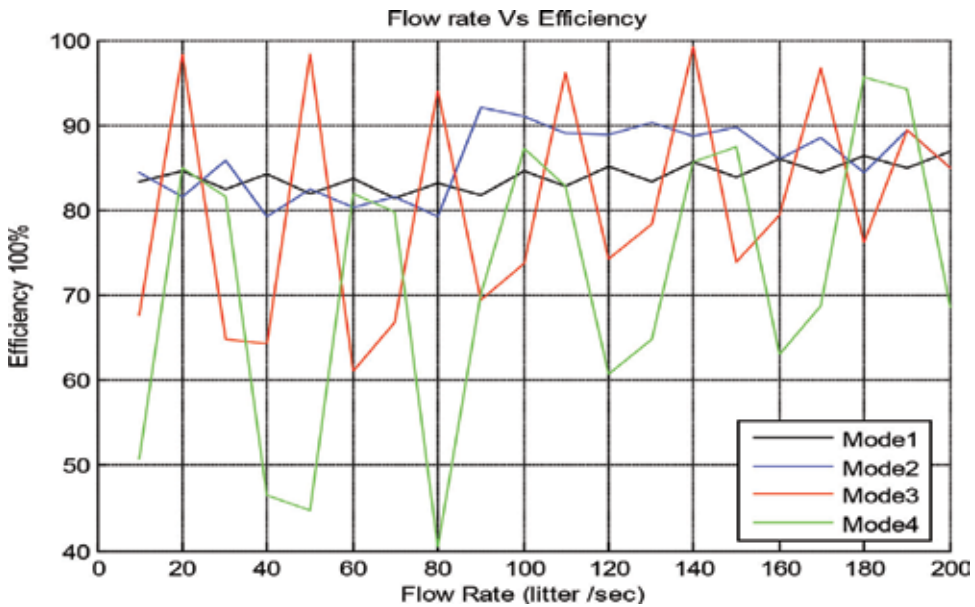


Figure 13. The relation between injection efficiency and the flow rate.

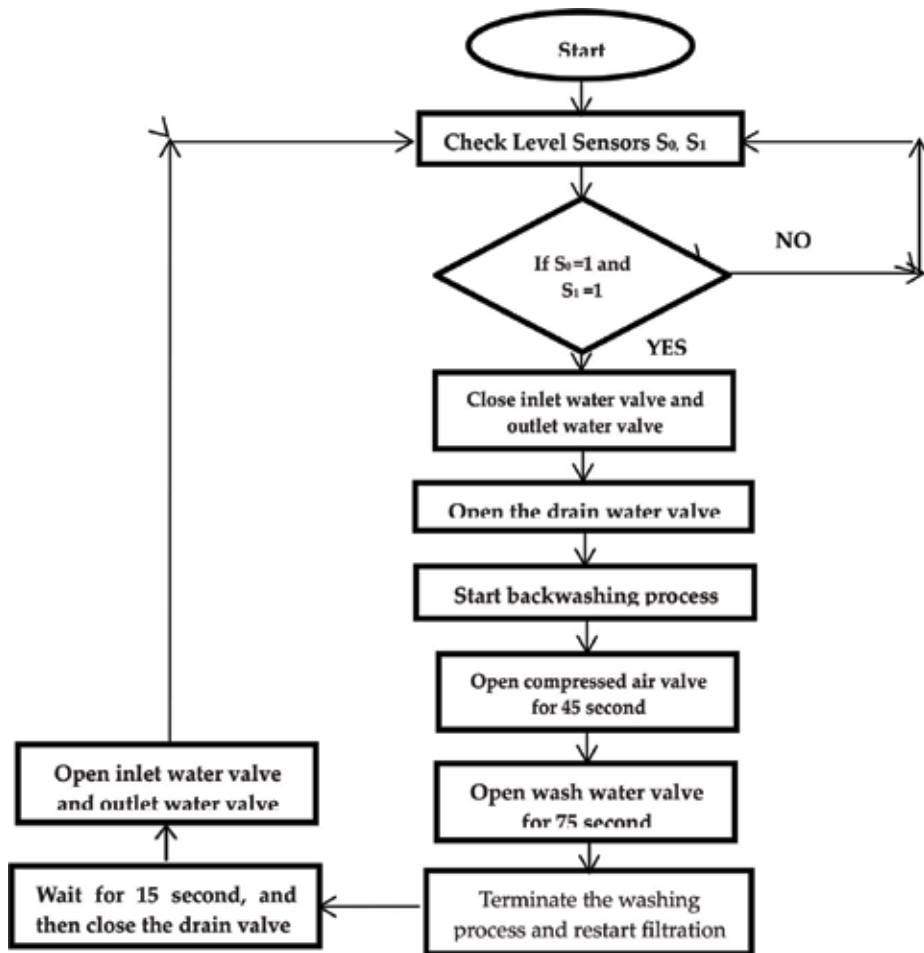


Figure 14. Backwashing control system flowchart.

Step	Valve	PLC timers configuration		Operation
		Timer	Time (s)	
1	I.W. Valve	TT1	15	Closing filter inlet water valve
2	O.W. Valve	TT2	15	Closing of outlet clarified water valve
3	D.W Valve	TT3	15	Opening of drain water valve
4	A. Valve	TT4	45	Opening of air valve
5	C.W Valve	TT5	75	Opening of clean wash water valve
6	Aux Timer	TTC	15	To closing the washing valve
7	Reset Timer	TTG	30	To terminate the washing process

Table 2. A complete time cycle of the filter washing process.

Program diagram

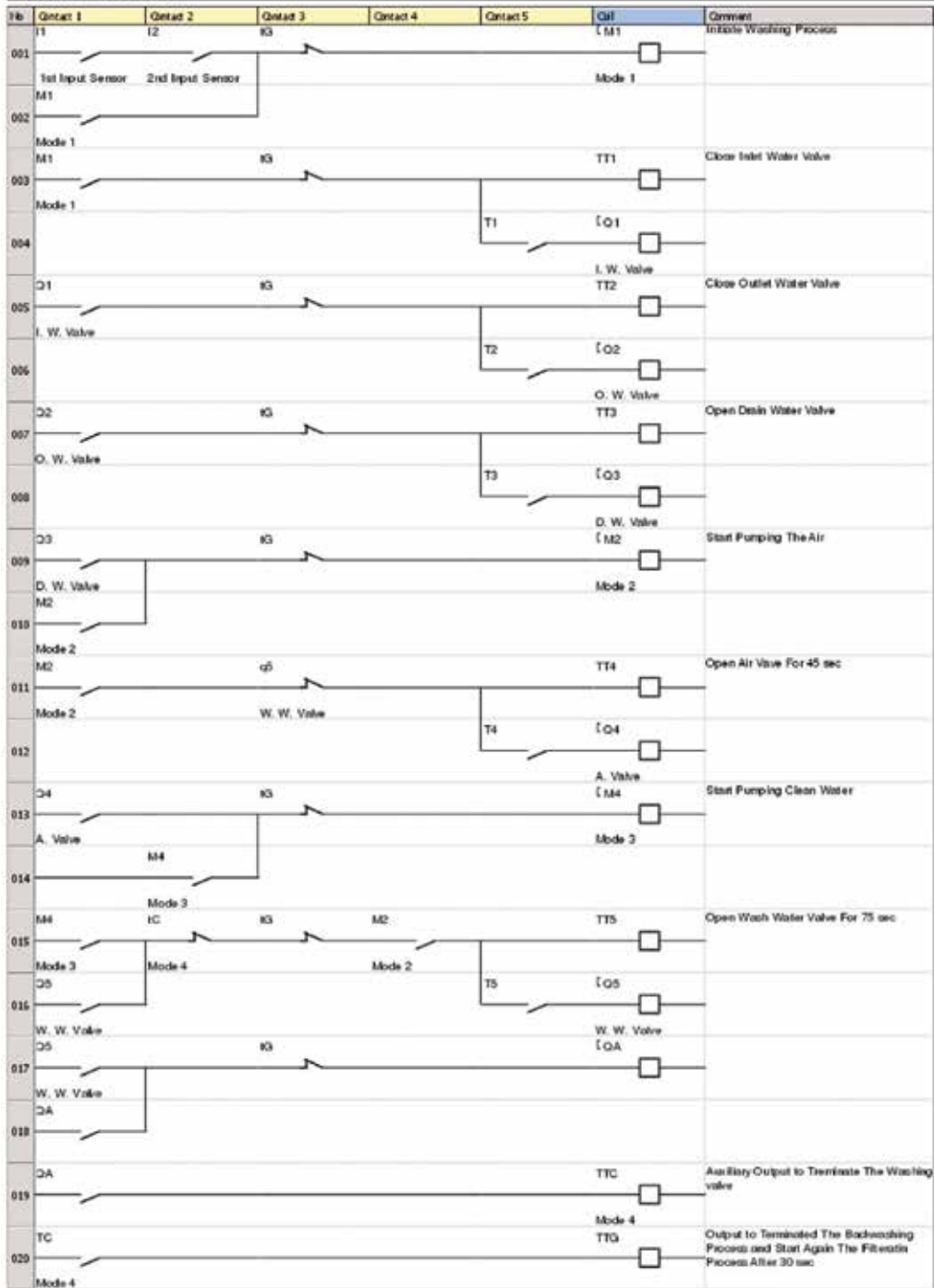


Figure 15. Ladder logic inputs and outputs for filter backwashing process control.

4.3. Control on filter backwashing process

The control runs as it follows: when the PLC receives a signal coming from the sensors, it determines the start of the washing process, then accomplishes the following steps: first, closes the filter inlet and outlet water valves. Second, opens drain valve and then opens the backwash compressed air valve for 30 s. Then closes air valve and opens the backwash clean water valve for 60 s, Third, closes the wash valve and the system waits for 15 s until the dirty water passes before terminates the backwashing process. Finally, reverses the state of inlet, outlet and drain water valves to restart the filtration process again. The operations time of valves collected from plant and it was arranged to be used in the program. The control steps which have been implemented by PLCs is illustrated by the following flowchart, **Figure 14**.

In this simulation seven timers as shown in **Table 2** are set within the PLC program to control the time for each step of the filter washing process. Also, five indicators are connected to the outputs of the PLC to represent the valves which are involved in the filter washing process.

A Ladder Logic has been used for programming backwashing process so as to be functioned in the PLCs. The program output represented these processes shown in **Figure 15** [28].

5. Conclusions

The automatic control system has been proposed and implemented in this chapter regarding water treatment system. The water treatment system was dealt within two ways: the traditional system and the modified system after using WSN components. A controlled pump system has been fully developed on a PLCs system with sensors. An algorithm was designed to calculate the required doses from purification and disinfection chemical materials according to flow rate, pH, turbidity, and resident chlorine sensors reading, then added to water in a real-time application mode. The backwashing process for filters accomplished automatically using level sensors installed inside the filter basin, and automated valves. Therefore, the filter valves are working properly according to PLCs wireless control signals. In conclusion, the proposed control system has been successfully tested and the obtained results were significant. It was clear that the traditional system without WSN devices was poor and sometimes may have high risks especially in such system of drinkable water treatment. In contrast, the modified and improved system using WSN components has shown a high degree of dependability.

Author details

Magdi Osman Ali Hamed

Address all correspondence to: mag.osman2009@gmail.com

College of Engineering and Architecture, Omdurman Ahlia University, Sudan

References

- [1] Anastasi G, Conti M, Di FM. A comprehensive analysis of the MAC unreliability problem in IEEE 802.15.4 wireless sensor networks. *IEEE Transactions on Industrial Informatics [Internet]*. 2011;7(1):52-65. DOI: 10.1109/TII.2010.2085440. Available from: http://ieeexplore.ieee.org/xpls/abs_all.jsp?arnumber=5613224
- [2] Chen R, Speer AP, Eltoweissy M. Adaptive fault-tolerant QoS control algorithms for maximizing system lifetime of query-based wireless sensor networks. *IEEE Transactions on Dependable and Secure Computing*. 2011;8(2):161-176. DOI: 10.1109/TDSC.2009.54
- [3] Ali MO, Ahmed MM. Design of a Dependable Automatic Water Treatment Wireless Sensing Process Control System. Unpublished Ph.D. Thesis, University of AL-Neelain, Sudan; 2017
- [4] Haule J, Michael K. Deployment of wireless sensor networks (WSN) in automated irrigation management and scheduling systems: A review. In: 2014 Pan African Conference on Science, Computing and Telecommunications (PACT); IEEE; July 14, 2014. pp. 86-91
- [5] <https://www.oleumtech.com/what-is-scada/>
- [6] CinqueM, Cotroneo D, DiMC, Russo S, Federico N. Dependability evaluation of wireless sensor networks: A hybrid simulation tool. 2014;2(1):1-2. <http://citeseerx.ist.psu.edu/viewdoc/download?doi=10.1.1.608.5801&rep=rep1&type=pdf>
- [7] Mainetti L, Patrono L, Vilei A. Evolution of wireless sensor networks towards the internet of things: A survey. In: 2011 19th International Conference on Software, Telecommunications and Computer Networks (SoftCOM); IEEE; September 15, 2011. pp. 1-6
- [8] <http://www.ijecct.org/v4n4/694-700CRP0404M14.pdf>
- [9] Puccinelli D, Haenggi M. Wireless sensor networks: Applications and challenges of ubiquitous sensing. *IEEE Circuits and Systems Magazine*. 2005;5:19-29. DOI: 10.1109/MCAS.2005.1507522
- [10] Stankovic JA. Wireless sensor networks. *Computer (Long Beach, California)*. 2008;41(10):92-95. DOI: 10.1016/S1389-1286(01)00302-4
- [11] Yu J, Qi Y, Wang G, Gu X. A cluster-based routing protocol for wireless sensor networks with nonuniform node distribution. *AEU International Journal of Electronics and Communications*. 2012;66(1):54-61. DOI: 10.1016/j.aeue.2011.05.002
- [12] Agrawal DP, Zeng QA. *Introduction to Wireless and Mobile Systems*. CENGAGE Learning Custom Publishing; 2015
- [13] Zhao G. Wireless sensor networks for industrial process monitoring and control: A survey. *Network Protocols and Algorithms*. 2011;3(1):46-63
- [14] Cai S, Becherif M, Wack M. Wireless control of automotive actuator based on PID and fuzzy logic. In: *IFAC Proceedings Volumes (IFAC-Papers Online)*; 2011. pp. 9745-9750. DOI: 10.3182/20110828-6-IT-1002.03067

- [15] Tranquillini S, Spiess P, Daniel F, Karnouskos S, Casati F, Oertel N, et al. Process-based design and integration of wireless sensor network applications. *Business Process Management*. 2012;**7481**:134-149
- [16] Ali MO. Design and implementation of an automation control system for drinkable water plant [Unpublished M.Sc. dissertation]. Sudan: Faculty of Engineering and Technology, University of Gezira; 2007
- [17] Viani F, Rocca P, Oliveri G, Massa A. Pervasive remote sensing through WSNs. In: 6th European Conference on Antennas and Propagation (EUCAP); IEEE; March 26 2012. pp. 49-50. DOI: 10.1109/EuCAP.2012.6206049
- [18] Dorf RC, Bishop RH. *Modern Control Systems*. Pearson; 2011. http://cds.cern.ch/record/1361774/files/9780131383104_TOC.pdf
- [19] World Health Organization. *Guidelines for Drinking-Water Quality*. World Health Organization; 2004. http://www.who.int/water_sanitation_health/dwq/gdwq0506.pdf
- [20] Ray C, Jain R. *Low Cost Emergency Water Purification Technologies: Integrated Water Security Series*. Butterworth-Heinemann; 2014. <https://www.sciencedirect.com/science/book/9780124114654>
- [21] Ali MO, Alzubaidi AJ. The use of technology in a water treatment process. *African Journal of Science, Technology, Innovation and Development*. 2015;**7**(5):336-341. DOI: 10.1080/20421338.2015.1085158
- [22] Okuda T, Nishijima W, Sugimoto M, Saka N, Nakai S, Tanabe K, Ito J, Takenaka K, Okada M. Removal of coagulant aluminum from water treatment residuals by acid. *Water Research*. 2014;**60**:75-81. DOI: 10.1016/j.watres.2014.04.041
- [23] Haight JM, Kecojevic V. Automation vs. human intervention: What is the best fit for the best performance? *Process Safety Progress*. 2005;**24**(1):45-51
- [24] Milton Roy Europe. Dosing Pumps LMI. 2017. Available from: <http://www.miltonroy-europe.com/lmi/product-3.html> [Accessed: June 2017]
- [25] Ali M, Ahmed M, Hussian M. Design and evaluation of control system for water treatment quality based chemical added process. *OIDA International Journal of Sustainable Development*. 2017;**10**(09):39-46. Available at SSRN: <https://ssrn.com/abstract=3066197>
- [26] Xue F. The Effect of Backwashing Procedures on Filter Ripening and General Effluent Quality. 2017. Available from: www.citg.tudelft.nl/fileadmin/Faculteit/.../Thesis_Report_Final_-_Feng_Xue.pdf [Accessed: 2017]
- [27] Abdelrahman AM, Ali MO, Alzubaidi AJ. Development of a programmable logic controller based control system for a water plant. *Gezira Journal of Engineering and Applied Sciences*. 2009;**4**(2):69
- [28] Ali MO, Muawia MA. Design a WSN Control System for Filter Backwashing Process. August 2017;**7**(7):71. www.ijmer.com. <https://www.slideshare.net/IJMERCJOURNAL/design-a-wsn-control-system-for-filter-backwashing-process>

A Survey of Deep Learning Methods for WTP Control and Monitoring

Bouchra Lamrini and El-Khadir Lakhal

Additional information is available at the end of the chapter

<http://dx.doi.org/10.5772/intechopen.77196>

Abstract

Drinking water is vital for everyday life. We are dependent on water for everything from cooking to sanitation. Without water, it is estimated that the average, healthy human won't live more than 3–5 days. The water is therefore essential for the productivity of our community. The water treatment process (WTP) may vary slightly at different locations, depending on the technology of the plant and the water it needs to process, but the basic principles are largely the same. As the WTP is complex, traditional laboratory methods and mathematical models have limitations to optimize this type of operations. These pose challenges for water-sanitation services and research community. To overcome this matter, deep learning is used as an alternative to provide various solutions in WTP optimization. Compared to traditional machine learning methods and because of its practicability, deep learning has a strong learning ability to better use data sets for data mining and knowledge extraction. The aim of this survey is to review the existing advanced approaches of deep learning and their applications in WTP especially in coagulation control and monitoring. Besides, we also discuss the limitations and prospects of deep learning.

Keywords: artificial neural networks, deep learning, machine learning, coagulation process, water treatment

1. Introduction

1.1. Overview of water treatment process

Water is a unique substance known for its ability to dissolve a variety of substances. When water moves through its hydrological cycle, including precipitation, runoff, infiltration, impounding, use, and evaporation, it comes into contact with different substances that may

be more or less dissolved or be suspended in the water. Thus, the type and quantity amount of the dissolved substances, suspended substances, and colloidal substances together determine the overall quality of the water and its fitness for domestic use. Purification and sanitation of water vary as to the source and kinds of water. Municipal waters, for example, consist of surface water and ground water, and their treatment is to be distinguished from that of industrial water supplies. Municipal water supplies are treated by public or private water utilities to make the water potable (safe to drink) and palatable (esthetically pleasing) and to insure an adequate supply of water to meet the needs of the community at a reasonable cost. Except in exceedingly rare instances, the entire supply is treated to drinking water quality for three reasons: it is generally not feasible to supply water of more than one quality; it is difficult to control public access to water not treated to drinking water quality; and a substantial amount of treatment may be required even if the water is not intended for human consumption.

In order to achieve this, a water treatment plant employs many unit treatment processes that are linked in a process train to produce water that is fit for domestic use reliably and consistently from a raw water source at a cost that is reasonable to the consumers. Municipalities are over time facing an increase in population, a decrease in available freshwater supplies, and stricter regulation. The water treatment process may vary slightly at different locations, depending on the technology of the plant and the water it needs to process, but the basic principles are largely the same.

Purification water systems use various methods of water treatment to ensure ongoing water quality, including water quality testing. The testing helps ensure the water treatment process results in a product that meets federal water quality guidelines. Water analysis involves looking for several kinds of contaminants, including unsafe levels of organic, inorganic, microbial, and/or radioactive contaminants. At present, the most common steps in water treatment used by community water systems, mainly surface water treatment [1–3], include:

- Pretreatment: Pumps bring raw (untreated) water, often from lakes or rivers, into the purification plant through screens that exclude fish, weeds, branches, and large pieces of debris. Screening may not be necessary for groundwater. The plant may aerate the water at this point to increase the oxygen content and thus help remove problematic odors and tastes.
- Coagulation and flocculation: Coagulation and flocculation are often the first steps in water treatment. Chemicals with a positive charge are added to the water. The positive charge of these chemicals neutralizes the negative charge of dirt and other dissolved particles in the water. When this occurs, the particles bind with the chemicals and form larger particles called floc.
- Sedimentation: During sedimentation, the heavy floc settles to the bottom of the water supply due to its weight.
- Filtration: Once the floc has settled to the bottom of the water supply, the clear water on top will pass through filters of varying compositions (sand, gravel, and charcoal) and pore sizes, in order to remove dissolved particles, such as dust, parasites, bacteria, viruses, and chemicals.

- Disinfection: After the water has been filtered, a disinfectant (for example, chlorine and chloramine) may be added in order to kill any remaining parasites, bacteria, and viruses and to protect the water from germs when it is piped to homes and businesses.

The main goals of these various operations of water treatment process are to reduce the chemical cost, control the energy consumption required to work the treatment processes, and reduce the water wastes. Many research and studies are performed in order to increase the water treatment plant performances. **Figure 1** presents a schematic overview of these various operations necessary to treat the water. Many measurements of variables recorded by sensors such as turbidity level (TUR), PH, conductivity (COND), dissolved oxygen (DO), and temperature (T) are needed to carry out the jars test in order to determine the optimal dose of the aluminum sulfate.

The modeling of water treatment processes is challenging because of its complexity, nonlinearity, and numerous contributory variables, but it is of particular importance since water of low quality causes health-related and economic problems which have a considerable impact on people's daily lives. In most research works, linear and nonlinear modeling methods are used to model for example residual aluminum, turbidity, and coagulant dose in treated water, using both laboratory and process data as input variables. The approach includes variable selection to find the most important factors affecting the quality parameters.

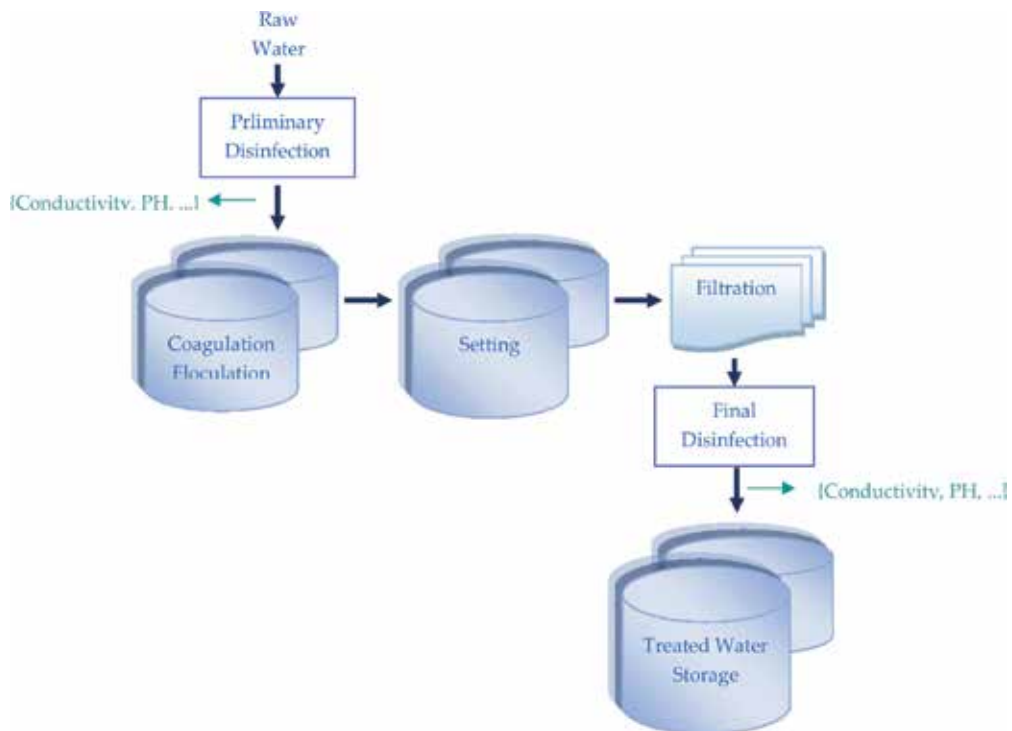


Figure 1. Simplified synopsis of the water treatment plant.

In the following, we review some techniques used for purifying raw water and the control strategies proposed so far trying to supply drinking water in a reliable manner. This control problem is very complex due to the variable quality of raw water, the seasonal changes that temperature and PH have on disinfection capabilities, the transport delays associated with the transport time of water from one point to another, and the multiple-input, multiple-output nature of the issue in question. In this chapter, we focus on one of main aspects related to the optimization of water treatment plants, which is the control and monitoring of coagulant dose, in which we have experience. There are two families of approaches that are described in this chapter: the first one covers the classical applications dedicated to understand and establish relationships between raw water characteristics and the coagulant reagent destabilizing the colloidal matter in suspension. The second family deals the leading applications carried out in machine learning, especially those using deep neural networks for automatic control of coagulation process.

1.2. Coagulant control and monitoring

Purification of drinking of drinking water is a very important problem in environmental engineering. Stricter drinking water quality standards demand improvement of control systems for water treatment. The efficient operation of a water plant depends upon the success of the clarification stage. Generally, the regulation of chlorination in drinking water systems is based on open-loop control. The application of feedback control in drinking water purification systems has been delayed due to the lack of sensors for measuring chlorine concentration in a reliable fashion. Although chlorine concentration sensors have been used in large drinking water systems, these sensors are typically used for monitoring purposes mostly for coagulation control. Various closed-loop controllers have been proposed. In [4], a feedback control scheme is implemented using color and turbidity sensors and variable speed pumps. The sensors are used to determine the current characteristics (i.e., color and turbidity) of the raw water, and the pumps are used to dose a coagulant into the raw water, which achieves clarification of the water. A third measurement, a conductivity sensor, has been considered in to suppress errors obtained from the color sensor (i.e., color sensor measurements are considerable higher than laboratory results), when the turbidity of the water is high.

Coagulation process is one of the critical processes performed in the water treatment of surface waters, involving many biological, physical, and chemical phenomena [1–3]. The control and monitoring of a good coagulation are essential for maintenance of satisfactory treated water quality and economic plant operation. Basically, colloidal particles are separated by means of a chemical coagulation process that consists to destabilize charge of the suspended particles by adding coagulant. The coagulant generally used in the drinking water industry is aluminum sulfate because of its effectiveness, accessibility, and low price. Some studies have been carried out to improve the effectiveness of the aluminum sulfate or to replace this coagulant by another natural, available, and cheaper. Mukheled [5] used Date seeds and Pollen Sheath as coagulant to treat different levels of turbidity (75, 150 and 300 NTU). Ali et al. [6] tried *Moringa oleifera* seed in the coagulation process to treat low turbid water in Malaysia. However, Aho et al. [7] highly recommended the use of this natural coagulant in the domestic turbid water purification in Nigeria. Other natural coagulants are proposed as an important alternative in

the water treatment plant. The coagulants are from plant origin such as nirmali seed and maize [8], *Cassia angustifolia* seed [9], mesquite bean and cactus latifaria [10], chestnut and acorn [11], *Coccinia indica* fruit mucilage [12], and from different leguminous species [13]. Those natural products have coagulating activity in the treatment of turbid water and can be used as coagulant or as coagulant aid with other synthetic and industrial coagulants (aluminum sulfate...) in order to reduce the coagulant consumption in the water treatment plant [14].

Coagulant dosage is chosen empirically by operators based on their past experience, laboratory jar-testing, and various information on water quality parameters. The jar-test apparatus simulates mixing, flocculation, setting, and a single test may take about 1 hour to be performed. Jar-test involves taking a raw water samples and applying different quantities of coagulant to each sample [15]. After a short period of time, each sample is assessed for water quality and the dosage that produces the optimal result used a set point. This operation should be repeated by the operators each time when the quality of raw water changes. The aluminum sulfate is the compound likely to be mathematically modeled, and therefore, its value can be estimated according to the data available in the treatment plant. Disadvantages associated with jar-testing are that regular samples have to be taken requiring manual intervention and operators can make manually in raw water quality. Both manual and automatic methods are used to predict optimum coagulant dose [15, 16]. Automatic method is ensured by streaming current detectors [17–19]. The streaming current detector (SCD) is an instrument used to measure coagulated particle stability for the feedback control of coagulant dosage. Muzi Sibiyi [20] reports the results of the online control of polymeric coagulant dosage at rapid mixing step in water treatment. The results show that the SCD reading increases as the polymeric coagulant dosage increases. The supplier recommended cationic polymer concentration for an SCD calibration standard of 100 mg/l was found suitable for SCD calibration purposes. The streaming current reading of the coagulated water at optimum coagulant dose was not significantly affected by raw water turbidity.

There is no mechanistic model describing the coagulant dosage related to the different variables affecting the process and also by using cheapest products. An interesting alternative to elaborate models is the use of deep neural networks often used in machine learning. Process data can be used directly to represent input-output process relationships. Artificial neural networks (ANN) proved to be extremely flexible in representing complex nonlinear relationships between many different process variables [21]. They do not require any a priori precise knowledge on the relationships of the process variables. Various applications were performed in order to develop a neural model for the online estimation of optimal coagulant dosage from raw water characteristics. Previous researches [22–26] show the efficiency of such approach using neural networks.

2. Deep neural networks for coagulation control and monitoring

2.1. Overview of artificial neural networks and deep learning

Since their origin in 1943 [27], artificial neural networks (ANNs) have been used to provide the best solutions to large various nonlinear problems. The ANNs have generated a lot of

motivation of machine learning research and industry, thanks to many progress results in robotic processing [28], object recognition [29], speech and handwriting recognition [30], and even real time sign-language translation [31]. Overall, an artificial neural network can be described by three main parts: (1) Input nodes that provide information from the external source (signals, features, image, and measurements) to the network. Each input has an associated weight, which is assigned on the basis of its relative importance to other nodes. These input nodes are usually normalized via the activation functions, which perform a certain fixed mathematical operation. (2) Hidden nodes responsible for extracting patterns associated with the process or system are being analyzed. These layers perform most of the internal processing from a network. (3) Output nodes are collectively responsible for computations (processing performed by the neurons in the previous layers) and producing the final network outputs. Depending on the arrangement of neurons and their interconnection via the processing layers, the main architectures of artificial neural networks can be divided as follows: single-layer feedforward network (as example, perceptron and the ADALINE), multilayer feedforward networks (multilayer perceptron (MLP) and the radial basis function (RBF)), recurrent networks, and mesh networks (The Self-Organizing Map the main representative of mesh architectures).

Despite the idea that deeper architectures would provide better results compared that are shallower already used, empirical tests with deep networks had found similar or even worse results when compared to networks with only one or two layers [32, 33]. Training was also found to be difficult and often inefficient [33]. Finally, this concept started to change with the proposal of greedy layer-wise unsupervised learning [34], which allowed for the fast learning of deep belief networks and solving the vanishing gradients problem. Thus, since 2006, deep learning's revolutionary advances in speech recognition, image analysis, and natural language processing have gained significant attention. With the ever-growing volume, complexity, and dynamicity of online information, deep learning approach has been an effective key solution to overcome such information overload. Recent studies also demonstrate its effectiveness in anomaly detection and prediction tasks. Deep learning is a sub research field of machine learning. It learns multiple levels of representations and abstractions from data, which can solve both supervised and unsupervised learning tasks [35]. In this subsection, we briefly review the key array of deep learning concepts using some of the sources included in the annotated section of the bibliography [36–38]:

- Multilayer perceptron (MLP) is a deep artificial neural network with hidden layers (one/or multiple layers) between input layer and output layer that makes a decision or prediction about input. An MLP can be viewed as a logistic regression classifier where input is first transformed using a nonlinear transformation to project the input data into a space linearly separable. A single hidden layer is sufficient to consider MLP a universal approximator. Since 2006, scientific researchers have shown that there are considerable benefits to using many such hidden layers, e.g., the very premise of deep learning.
- Recurrent neural network (RNN) performs the same task for every element of a sequence, with the output being depended on the previous computations. In a traditional neural network (feedforward neural network), all inputs and outputs are independent of each other. The idea behind RNN is to employ sequential information in order to capture information

about what has been calculated so far. We can say that RNNs have a “memory”. Long short term memory (LSTM) and gated recurrent unit (GRU) network are two variants generally chosen to solve the vanishing gradient problem.

- Convolutional neural network (ConvNet) is a special kind of feedforward neural network with convolution layers and pooling operations. Each neuron receives some inputs, performs a dot product, and optionally follows it with a nonlinearity. ConvNet architecture posits an explicit assumption that the inputs are images, which provide (encode) certain properties into the architecture. These then allow to perform two things: easily and efficiently implement the forward function and vastly reduce the amount of parameters in the network.
- Restricted Boltzmann machine (RBM) is a parameterized generative model representing a probability distribution. Boltzmann machine consist of two types of layers, so called visible and hidden neurons. The visible layer corresponds to the components of an observation. The hidden layer models dependencies between the components of observations (for a digital input image, one visible unit for each pixel). Restricted means that there are no intra-layer communications in visible layer or hidden layer.
- Auto-encoder (AE) is an unsupervised model pretraining that has three layers: an input layer, an encoding (hidden) layer, and a decoding layer. The AE model is trained to reconstruct its inputs, which forces the hidden layer to try to learn good representations of the inputs. The learned representation of auto-encoder can be used for dimensionality reduction and can be used as a feature for another task. There are many variants of auto-encoders such as denoising auto-encoder, marginalized denoising auto-encoder, sparse auto-encoder, contractive auto-encoder, and variational auto-encoder (VAE).
- Deep semantic similarity model (DSSM) has developed for representing text strings (sentences, queries, predicates, entity mentions, etc.) in a common low-dimensional semantic space and measuring their semantic similarities. DSSM is frequently used in various applications including information retrieval and Web search ranking, contextual entity search and interestingness, image captioning, etc.
- Neural autoregressive distribution estimation (NADE) is an unsupervised neural network which is inspired by RBM but uses feed-forward neural network and the framework of auto-regression for modeling the probability and density distribution of binary variables in high-dimensional vectors.
- Generative adversarial network (GAN) is a generative neural network comprised of two nets: a discriminator and a generator, pitting one against the other, e.g., the two neural networks are trained simultaneously by competing with each other in a minimax game framework.

In the article, Zhang et al. [38] provide a comprehensive review of recent research efforts on deep learning-based recommender systems toward fostering innovations of recommender system research. A taxonomy of deep learning-based recommendation models is presented and used to categorize the surveyed articles. Wide and deep learning (WDL) is one of the models presented in this paper. This model can improve the accuracy, as well as the diversity of recommendation. The WDL (shown in **Figure 2**) can solve both problems, regression and

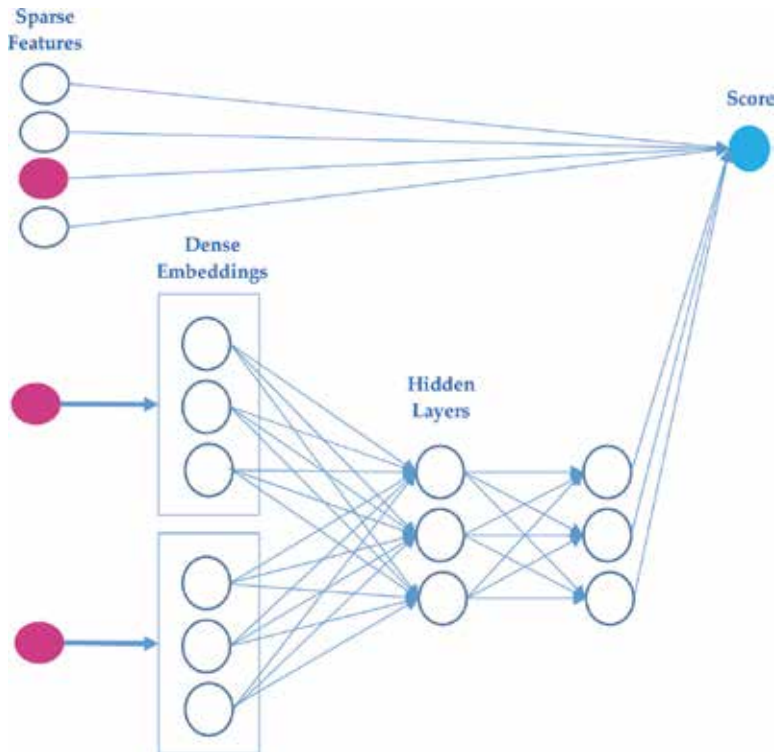


Figure 2. Illustration of a wide and deep learning.

classification, by combining two learning techniques: the wide learning component (single-layer perceptron) and deep learning (multilayer perceptron). The aim searched from combining these two learning techniques is that it enables the recommender system to capture both tasks: (1) memorization, which is the capability of catching the direct features from historical data, and (2) generalization by producing more general and abstract representations.

For different fields, suitable applications vary depending on the nature, type, and purpose of the data. While scientific researchers can be interested in searching for anomalies in the sleep patterns of a patient, economists and industrials may be more interested in forecasting the next prices some stocks of interest will assume. These kinds of problems are addressed in the literature by a range of different approaches used to perform tasks such as classification, segmentation, anomaly detection, and prediction. Applying deep neural network techniques also into treatment water process [25, 39–46] has been gaining momentum due to its state-of-the-art performances and high-quality recommendations. In contrast to traditional recommendation models, deep learning provides a better understanding of user's demands, item's characteristics, and historical interactions between them.

2.2. Neural software sensors for coagulation automatic control

Several works [25, 39–42] have already shown the potential of these techniques for modeling the coagulation process. All these studies propose to relate the coagulant dose to different

descriptors parameters of the quality of raw water, such as turbidity, pH, conductivity, etc., using a neural network. The learning base is constructed using a jar-test test history to model the optimal coagulant dose. Agdar et al. [39] propose to use the color, conductivity, and turbidity of raw water to predict the dose of coagulant. The results obtained on a pilot site [39] seem encouraging. However, the lack of input descriptor parameters does not allow to take into account all variations in the quality of the raw water. Another study [40] proposes to use many more input parameters of the RNA model. Mirsepassi et al. [41] also propose to use a history of these different parameters, that is, to consider the value of the parameters at times $\{t - 1, t - 2, \dots, t - 6\}$ (t represents the current day). Gagnon et al. [25] show the interest of building seasonal models. They use four descriptors parameters of the raw water quality: pH, turbidity, conductivity, and temperature. This study compares the accuracy of an annual year-round model with four seasonal patterns. Nevertheless, the determination of the four periods of application of each model seems difficult. Valentin et al. [42] have developed an alternative to the jar-test and SCD methods allowing for the automatic determination of optimal coagulant dose from raw water characteristics, using a self-organizing map and MLP approaches to validate the sensor measurements before coagulant dose estimation.

Given the strong evolution of the raw water characteristics, an important property for such system is indeed the robustness with regard to the sensors failings or to the unexpected raw water characteristics, owing to accidental pollution for example. Coagulation process is one of the critical processes performed in the drinking water treatment, involving many biological, physical, and chemical phenomena. As we have already mentioned, the control of a good coagulation is essential for maintenance of satisfactory treated water quality and economic plant operation. Thus, an over-dosage can lead both to an increase in the operating costs and to public health concerns. While an underdosage can cause failure to meet the water quality targets, the coagulation has a strong impact on the clarification step. In addition to these developments on the coagulation automatic control, we have developed a software sensor based on a hybrid system [44–47], including a Self-Organizing Map (SOM) for measurements validation and missing data reconstruction [45], a multilayer perceptron (MLP) for coagulant dose prediction [47], and a neuro-fuzzy method to identify functional states of treatment plant [44, 45]. The main objective of our works conducted was to validate and rebuild the measurements of characteristics raw water so as to provide reliable inputs to the automatic coagulation control system.

In many anomaly detection applications, abnormal (negative) samples are not available at the training stage. For instance, in a computer security application, it is difficult to have information about all possible attacks. In the machine learning approaches, the lack of samples from the abnormal class causes difficulty in the application of supervised techniques. Therefore, the obvious machine-learning solution is to use an unsupervised algorithm. For this, we adopted an unsupervised learning approach based on the self-organizing map algorithm introduced by Kohonen [48]. Self-organizing map is one of the most popular neural network models. It belongs to the category of competitive learning networks. The SOM method is based on unsupervised learning, which means that no human intervention is needed during the learning and that little needs to be known about the characteristics of the input data. We could, for example, use the SOM for clustering data without knowing the class memberships of the input data. The SOM can be used to detect features inherent to the problem and thus has also been called SOFM (self-organizing feature map).

For coagulant dosage prediction, the MLP architecture (inputs, number of hidden layers, and number of neurons) has been fixed a priori. To define relevant descriptors of raw water quality affecting the coagulant dosage, a principal components analysis (PCA) is used within this framework. The number of neurons in the hidden layer has been optimized with a pruning method “weight-decay” [49, 50] in combination with the “Levenberg–Marquardt” algorithm [51], allowing the weak weights to be penalized (the connections with weak weight are eliminated). In this framework, the weights and biases of the network are assumed to be random variables with specified distributions. The regularization parameters are related to the unknown variances associated with these distributions. To take into account the uncertainty bound to the size limited of the learning set, the “Bootstrap” sampling [52] has been used to generate confidence interval for the model outputs. The results confrontation with test data of treatment plant located in Morocco [45, 46] shows that it is possible to determine online and in a very satisfactory way the optimal coagulant dose and this in various phases of functioning.

To assure a good monitoring and contribute to a good operation of this process, it would be necessary to exploit all process information, such as the measurements of raw water characteristics and their evolutions resulting for example from unforeseen abnormalities, as well as the expert knowledge. For these reasons, we chose to carry the behavior monitoring of this process by using a neuro-fuzzy method, called “LAMDA” (Learning Algorithm for Multivariate Data Analysis) classification technique [53, 54], which allows aggregating this information for informing the operator by specific situations. The classification idea is the evaluation of the significant system signals (raw water quality measurements + neural coagulant dose) to recognize the factors related to such or such other situation and to help the operator to make a decision during the failure appearance. This approach was a first application that shows the utility of classification techniques in the monitoring and the surveillance of this process type. It is clear that the final objective was to spread this monitoring to other treatment processes in order to detect at the earliest a drift functioning or to identify a failure on an upstream unit (Figure 3).

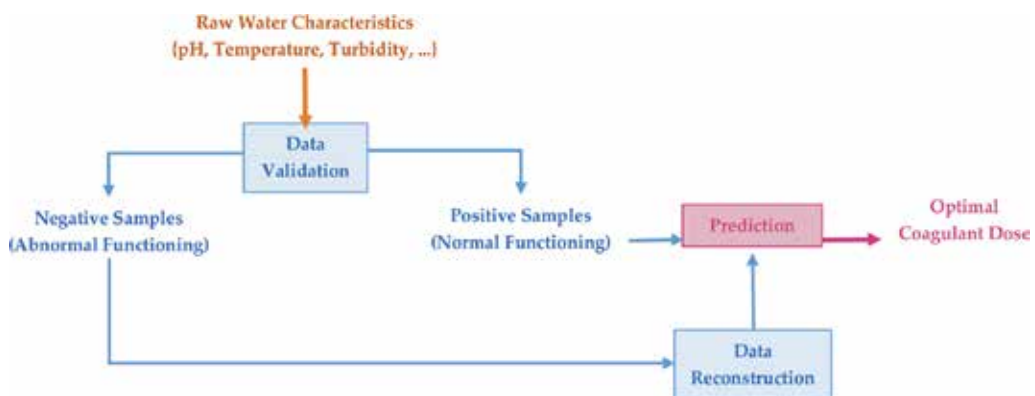


Figure 3. Hybrid system proposed for coagulation control and monitoring.

3. Other propositions to purification water processes control

An expert system for a water purification system that performs supervisory control of water quantity, and automatic filter basin control, is developed in [55]. The sand bed filters can be in four possible states: waiting for filtering, filtering, waiting for scouring, and scouring. The filter basins in a water purification system are usually divided into groups connected in parallel. Online data are gathered from distributed control systems throughout the water purification system. In [56], filter basin control is based on control of filter scouring basin and control of the number of filter basins in operation. Filter scouring occurs when the water flow falls below a preset minimum value. The number of filters in operation is controlled to match the plant processing flow to total filtering flow. A different approach is presented in [56], where the proposed chlorination control system for water treatment is a double cascade PI loop for controlling the hypochlorite dosed in the system by means of free chlorine measurements taken at two sample points of the disinfection system. Denitrification of drinking water has been also proposed in several studies. In [57], SISO and MIMO robust variable structure controls for fixed bed bioreactors are developed. A SISO variable structure control is used to control the total concentration of nitrates and nitrites by changing either the inlet flow rate or the ethanol concentration. A MIMO variable structure control is needed to optimally regulate the ethanol concentration of drinking water. In [58], drinkable water is also treated by a fixed bed bioreactor. A multiinput and multioutput sliding control law of a distributed parameter bio-filter is designed to improve the quality of the water in order to control the harmful component concentration at the outlet of the bioreactor and to optimize the addition of carbon source. However, to our knowledge, it is certainly regrettable that no specific model based on deep neural networks is performed on this type of process.

4. Conclusions

Water resources systems management practice, include drinking water treatment process, around the world is challenged by serious problems. Climate change and land use change are increasingly recognized as having the major impact on hydrologic variables and therefore on management of water resources. Certainly, the profession has been slow to acknowledge these changes, and that fundamentally new approaches will be required to address them. Evolutionary algorithms are becoming more prominent in the water treatment processes field. Significant advantages of evolutionary algorithms include: (1) no need for an initial solution; (2) ease of application to nonlinear problems and to complex systems; (3) production of acceptable results over longer time horizons; and (4) generation of several solutions that are very close to the optimum (and that give added flexibility to a water manager). Special attention is given to evolutionary optimization by deep neural networks to predict and capture anomalies in coagulation process, regarded as a complex and critical process. The use of deep neural networks for process modeling and control in the drinking water treatment is currently on the rise and is considered to be a key area of research. With regard

to previous works, the neural approach offers the advantage of very short computational times and to be able intrinsically to describe some nonlinear relations between inputs and outputs system. In this chapter, we provided an extensive review of the most notable works to date on coagulation control and monitoring. Both classical methods and deep neural networks are ongoing hot research topics in the recent decades. There are a large number of new developing techniques and emerging models each year; here, we provide an inclusive framework for comprehensive understanding toward the key aspects of this field, clarify the most notable advancements and shed some light on future studies to promote lines of action for the work on this issue: developing intelligent systems for water process managing and optimization.

When applying deep learning, one seeks to stack several independent neural network layers that, working together, produce better results than the already existing shallow structures. In this paper, we have reviewed some of these modules, as well the recent work that has been done by using them, found in the literature. Employing deep learning to data analysis and forecasting has yielded results in these cases that are better than the previously existing techniques, which is an evidence that this is a promising field for improvement in order to propose and develop online reliable systems to WTP monitoring and automatic control.

Author details

Bouchra Lamrini^{1*} and El-Khadir Lakhel²

*Address all correspondence to: lamrini.bouchra@gmail.com

1 Senior Research and Development Engineer, Toulouse, France

2 AEPT Laboratory, FSSM, Cadi Ayyad University, Marrakech, Morocco

References

- [1] Degrément, editor. *Mémento technique de l'eau – Tome 1*. 10th ed. Tec & Doc Lavoisier; 2005. 1718 p. ISBN: 9782743007171
- [2] Pizzi NG, Lauer WC, editors. *Water Treatment Operator Training Handbook*. 3th ed. American Water Works Association (AWWA); 2013. 306 p. ISBN: 9781583218617
- [3] Howe KJ, Hand DW, Crittenden JC, Rhodes Trussel R, Tchobanoglous G, editors. *Principles of Water Treatment*. 1st ed. Wiley; 2012. 672 p. ISBN: 9780470405383
- [4] Cox C, Graham J. Steps towards automatic clarification control (water supply). In: *IEEE Colloquium on Advances in Control in the Process Industries: An Exercise in Technology Transfer*; 30 March 1994; London; UK; p. 6/1-6/4

- [5] Mukheled A. A novel water pretreatment approach for turbidity removal using date seeds and pollen sheath. *Journal of Water Resource and Protection*. 2012;**4**(2):79-92. DOI: 10.4236/jwarp.2012.42010
- [6] Ali EN, Muyibi SA, Salleh HM, Alam MZ, Salleh MRM. Production of natural coagulant from moringa oleifera seed for application in treatment of low turbidity water. *Journal of Water Resource and Protection*. 2010;**2**(3):259-266. DOI: 10.4236/jwarp.2010.23030
- [7] Aho IM, Lagasi JE. A new water treatment system using moringa oleifera seed. *American Journal of Scientific and Industrial Research*. 2012;**3**(6):487-492. DOI: 10.5251/ajsir.2012.3.6.487.492
- [8] Raghuwanshi PK, Mandloi M, Sharma AJ, Malviya HS, Chaudhari S. Improving filtrate quality using agrobased materials as coagulant aid. *Water Quality Research Journal of Canada*. 2002;**37**(4):745-756. Available from: <https://www.cawq.ca/journal/temp/article/112.pdf>
- [9] Sanghi R, Bhattacharya B, Singh V. Cassia angustifolia seed gum as an effective natural coagulant for decolourisation of dye solutions. *Green Chemistry*. 2002;**4**:252-254. DOI: 10.1039/B200067A
- [10] Diaz A, Rincon N, Escorihuela A, Fernandez N, Chacin E, Forster CF. A preliminary evaluation of turbidity removal by natural coagulants indigenous to Venezuela. *Process Biochemistry*. 1999;**35**(3-4):391-395. DOI: 10.1016/S0032-9592(99)00085-0
- [11] Šciban M, Klačnja M, Antov M, Škrbic B. Removal of water turbidity by natural coagulants obtained from chestnut and acorn. *Bioresource Technology*. 2009;**100**(24):6639-6643. DOI: 10.1016/j.biortech.2009.06.047
- [12] Patale V, Pandya J. Mucilage extract of coccinia indica fruit as coagulant-flocculent for turbid water treatment. *Asian Journal of Plant Science and Research*. 2012;**2**(4):442-445. Available from: www.pelagiarsearchlibrary.com
- [13] Šciban M, Klačnja M, Stojimirovic J. Investigation of coagulation activity of natural coagulants from seeds of different leguminose species. *Acta Periodica Technologica*. 2005;**(36)**:81-87. DOI: 10.2298/APT0536081S
- [14] Farhaoui M, Derraz M. Optimizing coagulation process by using sludge produced in the water treatment plant. *Journal of Chemical and Pharmaceutical Research*. 2016;**8**(4):749-756. Available from: www.jocpr.com
- [15] Lind C. Coagulation control and optimization: Part one. *Public Works for October*. 1994:56-57
- [16] Lind C. Coagulation control and optimization: Part two. *Public Works for October*. 1994;**125**(12):32-33
- [17] Dentel SK. Use of the streaming current detector in coagulation monitoring control. *Journal of Water Sciences Research and Technologies-Aqua*. 1995;**44**(2):70-79

- [18] Walker CA, Kirby JT, Dentel SK. The streaming current detector: A quantitative model. *Journal of Colloid and Interface Science*. 1996;**182**(1):71-81. Available from: <https://pdfs.semanticscholar.org/93da/5cf52027691c7822a4f59d58161b5b3ae19b.pdf>
- [19] Liu H, Rong Q, Xu L, Zhang Y. Application of automatic control system in water plant in China. *Journal of Convergence Information Technology*. 2013;**8**(5):243-250. DOI: 10.4156/jcit.vol8.issue5.29
- [20] Muzi Sibiya S. Evaluation of the Streaming current detector (SCD) for coagulation control. *Procedia Engineering*. 2014;**70**:1211-1220. DOI: 10.1016/j.proeng.2014.02.134
- [21] Cybenko G. Approximation by superposition of a sigmoid function. *Mathematics of Control and Systems*. 1989;**2**(4):303-314. DOI: 10.1007/BF02551274
- [22] Canu S, Sobral R, Lengellé R. Formel neural network as an adaptative model for water demand. In: *Proceedings of INNOC'90*. Vol. 1. Kluwer Academic Publishers; 1990. pp. 131-136
- [23] Thiria S, Lechevallier Y, Gascul O, Canu S. *Statistiques et Méthodes Neuronales (Chapitre 7)*. Dunod. 1997. 311 p. DOI: 9782100035441
- [24] Adgar A, Cox CS, Daniel PR, Lowdon A. Chemical dosing philosophies for a water treatment plant: results of some pilot plant experimentation. *Proceeding of the IEE Conference Publication*. 1996;**427**(2):1052-1057. DOI: 10.1049/cp:19960698
- [25] Gagnon C, Grandjean B, Thibault J. Modelling of coagulant dosage in a water treatment plant. *Artificial Intelligence in Engineering*. 1997;**11**:401-404. DOI: 10.1016/S0954-1810(97)00010-1
- [26] Evans J, Enoch C, Johnson M, Williams P. Intelligent based auto-coagulation control applied to a water treatment works. In: *Proceedings of International Conference on Control (Control '98)*; 1998. p. 141-145. DOI: 10.1049/cp:19980216
- [27] McCulloch WS, Pitts W. A logical calculus of the ideas immanent in nervous activity. *The Bulletin of Mathematical Biophysics*. 1943;**5**(4):115-133. Available from: <https://link.springer.com/article/10.1007/BF02478259>
- [28] King SY, Hwang JN. Neural network architectures for robotic applications. *Robotics and Automation, IEEE Transactions*. 1989;**5**(5):641-657. DOI: 10.1109/70.88082
- [29] Szegedy C, Toshev A, Erhan D. Deep neural networks for object detection. In: Burges CJC, Bottou L, Welling M, Ghahramani Z, Weinberger KQ, editors. *Advances in Neural Information Processing Systems*; 2013. pp. 2553-2561. Available from: <http://papers.nips.cc/paper/5207-deep-neural-networks-for-object-detection.pdf>
- [30] Graves A. Supervised Sequence Labelling with Recurrent Neural Networks. Vol. 385; 2012. Berlin Heidelberg: Springer-Verlag. 146 p. DOI: 10.1007/978-3-642-24797-2
- [31] Akmeliawati R, Ooi MPL, Kuang YC. Real-time malaysian sign language translation using colour segmentation and neural network. In: *Instrumentation and Measurement Technology Conference Proceedings*; 2007. pp. 1-6. DOI: 10.1109/IMTC.2007.379311

- [32] Tesauro G. Practical issues in temporal difference learning. In: *Machine Learning*. Vol. 8. Springer; 1992. pp. 257-277. DOI: 10.1007/BF00992697
- [33] Bengio Y, Lamblin P, Popovici D, Larochelle H. Greedy layer-wise training of deep networks. *Advances in Neural Information Processing Systems*. 2007;**19**:153-160. Available from: <http://papers.nips.cc/paper/3048-greedy-layer-wise-training-of-deep-networks.pdf>
- [34] Hinton GE, Osindero S, The YW. A fast learning algorithm for deep belief nets. *Neural Computation*. 2006;**18**(7):1527-1554. DOI: 10.1162/neco.2006.18.7.1527
- [35] Deng L, Yu D. Deep learning: Methods and applications. *Foundations and Trends® in Signal Processing*. 2014;**7**(3-4):197-387. DOI: 10.1561/20000000039
- [36] Goodfellow I, Bengio Y, Courville A. *Deep Learning*. Cambridge: MIT Press; 2016. Available from: <http://www.deeplearningbook.org>
- [37] Cheng HT, Koc L, Harmsen J, Shaked T, Chandra T, Aradhye H, Anderson G, Corrado G, Chai W, Ispir M, Anil R, Haque Z, Hong L, Jain V, Liu X, Shah H. Wide & deep learning for recommender systems. In: *Proceedings of the 1st Workshop on Deep Learning for Recommender Systems (DLRS)*. ACM, New York, NY, USA; 2016. pp. 7-10. DOI: 10.1145/2988450.2988454
- [38] Zhang S, Yao L, Sun A. Deep learning based recommender system: A survey and new perspectives. *ACM Journal on Computing and Cultural Heritage*. 2017;**1**(1):35(1)-35(35). Available from: <https://arxiv.org/pdf/1707.07435.pdf>
- [39] Adgar A, Cox CS, Daniel PR, Billington AJ, Lowdon A, Experiences in the application of the artificial neural networks to water treatment plant management. In: *Proceedings of the International COMDEM'95*; June 1995; Canada; 1:33-38
- [40] Nahm E, Lee S, Woo K, Lee B, Shin S. Development of an optimum control software package for coagulant dosing process in water purification system. *Proceedings of the Society of Instrument and Control Engineers Annual Conference*; Tottori: Japan. 1996;**35**:157-1161. DOI: 10.1109/SICE.1996.865428
- [41] Mirsepassi A, Cathers B, Dharmappa HB. Application of Artificial Neural Networks to the Real Time Operation of Water Treatment Plants. In: *Proceeding of the International Conference on Neural Networks*. Perth, Australia; 1995;**1**:516-521. DOI: 10.1109/ICNN.1995.488231
- [42] Valentin N, Denoeux T. Prediction of Optimum Coagulant Dosage in a Water Treatment Plant Using Neural Networks. In: *Proceedings of Water Quality Technology Conference*; 31 October-3 Novembre. Tampa, Floride; 1999
- [43] Baxter CW, Stanley SJ, Zhang Q, Smith DW. Developing artificial neural network models of water treatment processes: A guide for utilities. *Journal of Environmental Engineering and Science*. 2000;**1**(3):201-211. DOI: 10.1139/s02-014
- [44] Lamrini B, Benhammou A, Le Lann MV, Lakhel EK. Detection of functional states by "LAMDA" classification technique: Application to a coagulation process in drinking water treatment. *Journal of Comptes Rendus Physique*. 2005;**6**:1161-1168. DOI: 10.1016/j.crhy.2005.11.017

- [45] Lamrini B, Lakhal E-K, Le Lann M-V, Wehenkel L. Data validation and missing data reconstruction using self organizing map for water treatment. *Journal of Neural Computing and Applications*. 2011;**20**(4):575-588. DOI: 10.1007/s00521-011-0526-5
- [46] Lamrini B, Lakhal EK, Le Lann MV. A decision support tool for technical processes optimization in drinking water treatment. *Desalination and Water Treatment Science and Engineering Journal*. 2014;**52**(22-24):4079-4088. DOI: 10.1080/19443994.2013.803327
- [47] Lamrini B, Benhammou A, Le Lann MV, Karama A. A neural software sensor for on-line prediction of coagulant dosage: Application to a drinking water treatment plant. *Journal of Transactions of the Institute of Measurement and Control*. 2005;**27**(3):195-213. DOI: 10.1191/0142331205tm141oa
- [48] Kohonen T, Oja E, Simula O, Visa A, Kangas J. Engineering applications of the self-organizing map. *Proc IEEE*. 1996;**84**(10e):1358-1384. DOI: 10.1109/5.537105
- [49] Mackay DJC. Bayesian interpolation. *Neural Computation*. 1992;**4**(3):415-447. DOI: 10.1162/neco.1992.4.3.415
- [50] Mackay DJC. A particle Bayesian framework for Backpropagation networks. *Neural Computation*. 1992;**4**(3):448-472. DOI: 10.1162/neco.1992.4.3.448
- [51] Dan Foresee F, Hagan MT. Gauss-Newton Approximation to Bayesian Regularisation. In: *Proceedings of the 1997 International Joint Conference on Neural Networks*; 1997. p. 1930-1935. DOI: 10.1109/ICNN.1997.614194
- [52] Efron B, Tibshirani R J. *An Introduction to the Bootstrap*. New York: Chapman & Hall; 1993. 456 p. ISBN-13: 978-0412042317
- [53] Aguilar-Martin J, Balssa M, Lopez De Mantras R. Recursive estimation of partitions: Examples of learning and self-teaching in RN and IN. *Questiio: Quaderns d'Etadistica, Siestems, Informatica i Investigacio Operativa*. 1981;**5**(3):150-172. ISSN: 0210-8054. Available from: <http://eudml.org/doc/39988>
- [54] Kempowsky T. *Surveillance des procedés à base de méthodes de classification: conception d'un outil d'aide pour la detection et le diagnostic des défaillances [Thesis]*. Toulouse : LAAS-CNRS/Institut National des Sciences Appliquées (INSA); 2004. Available from: <https://tel.archives-ouvertes.fr/tel-00010247/file/tel-00010247.pdf>
- [55] Miyajima Y, Katou T, Inaba R, Kobayashi S, Ezure H. A knowledge-based water purification control system. In: *Proceedings of IEEE International Workshop on Artificial Intelligence for Industrial Applications*; May 1988; p. 455-460. DOI: 10.1109/AIIA.1988.13331
- [56] Kingham T, Hoggart T. Chlorination control in a large water treatment works. In: *IEEE Colloquium on Application of Advanced PLC (Programmable Logic Controller) Systems with Specific Experiences from Water Treatment*. June 1995. p. 2/1-2/16. DOI: 10.1049/ic:19950738

- [57] Boubaker O, M'Hiri R, Ksouri MM, Babary J. SISO and MIMO variable structure control of fixed bed bioreactors. In: Control '98 UKACC International Conference on Control; 1-4 September 1998. p. 1/229-1/234. DOI: 10.1049/cp:19980232
- [58] Boubaker O, Babary JP. On SISO and MIMO sliding control of a distributed parameter biological process. In: 1999 IEEE International Conference on Systems, Man and Cybernetics (SMC'99), October 1999, Tokyo, Japan; 1999. p. 1/50-1/55. DOI: 10.1109/ICSMC.1999.814045

Fluorescent Markers in Water Treatment

Maxim Oshchepkov and Konstantin Popov

Additional information is available at the end of the chapter

<http://dx.doi.org/10.5772/intechopen.76218>

Abstract

Both phosphonate- and polymer-based scale inhibitors have a broad spectrum of applications in water treatment technologies. However, the “online” monitoring of antiscalant content in an aqueous phase is still a challenge for researchers. A possible solution is provided by the fluorescent markers added to the feeding water. These can be either an antiscalant tagged or may represent the independent species. The review summarizes both the advantages and the drawbacks of these approaches along with such markers’ classification, with a special emphasis on the novel fluorescent-tagged phosphonates. Besides, some unique opportunities provided by the fluorescent-tagged antiscalants for reverse osmosis membrane mapping, scale inhibition traceability, and a scale inhibitor localization in a circulation water facility are also considered and discussed.

Keywords: scale inhibition, fluorescent markers, water treatment

1. Introduction

Fluorescence is the emission of light by a substance that has absorbed light with a different wavelength or electromagnetic radiation. It has many practical and valuable applications, including in mineralogy, gemology, medicine, chemical sensors (fluorescence spectroscopy), fluorescent labeling, dyes, biological detectors, environmental monitoring, cosmic-ray detection, and, most commonly, fluorescent lamps [1–5]. However, in the field of water treatment, it has gained increasing interest mostly in the last decade [6–8]. The water treatment technologies use fluorescence phenomenon for the oil component control in wastewater [9], gaseous oxygen monitoring in wastewater [10], water leaks in industrial pipelines [11], for the total bacterial count [12], and for online scale inhibitors’ content monitoring [6–8, 13]. Besides, the problem of a scale inhibition mechanism is still actual and requires applications of fluorescent-tagged inhibitors [14]. All these applications are to be considered in a recent review.

2. Fluorescent monitoring of a scale inhibitor content

Scale formation in the upstream oil and gas industry, reverse osmosis desalination processes, steam generators, boilers, cooling water towers, and pipes is a serious problem, causing significant plugging of wells, pipelines, membranes, and increasing the production cost [15]. A widely used technique for controlling scale deposition is an application of chemical inhibitors [16, 17]. Commonly used commercial antiscalants are represented by chemical families: polyphosphates (hexametaphosphate (HMP), tripolyphosphate (TPP), etc.), organophosphonates (aminotris(methylenephosphonic acid), ATMP; 1-hydroxyethane-1,1-bis(phosphonic acid), HEDP; 2-phosphonobutane-1,2,4-tricarboxylic acid (PBTC); ethylenediaminetetra(methylenephosphonic acid), EDTPH, etc), and organic polyelectrolytes (polyacrylates (PA), polycarboxysulfonates, (PCS)). Among these, the organophosphonates are dominating the world market at present. At the same time, phosphorus-based inhibitors are hardly biodegradable and persist for many years after their disposal, which lead to eutrophication problems. Phosphorus discharges are therefore regulated in many countries worldwide, and permissible limits are constantly decreasing [18].

Increasing environmental concerns and discharge limitations have forced the scale-inhibitor chemistry to move toward “green antiscalants,” that are readily biodegradable and have minimal environmental impact [17, 18]. Intensive efforts have been applied recently to develop the “green” alternatives to organophosphonates and nonbiodegradable polyacrylates. Among these novel inhibitors, such chemicals as polymaleates (PMAs), polyaspartates (PASPs), polyepoxysuccinates (PESAs), as well as their various derivatives, including co-polymers with PA, are worth mentioning [19, 20].

The concentration of polymeric antiscalants in the circulating system is usually changed by evaporation of water, reagent sorption on the pipe surfaces, and by a periodical discharge of the circulating water with some deposit. Therefore, an adequate monitoring of the polymer concentration is needed to minimize the consumptions of both scale inhibitor and water. Along with conventional monitoring methods based on UV-vis or potentiometry, the intensity of fluorescence emitted from either indifferent markers or a covalently bound to polymer tracer becomes a matter of choice [6].

The conventional monitoring methods for PA and for other polymeric antiscalants are classified into four groups [21]: (i) monitoring a spectral change caused by the interaction of PA with some metal-reagent complex (e.g., Fe^{3+} - SCN^- [22], Hg^+ -diphenylcarbazide [21]); (ii) monitoring the concentration of an inert tracer added in proportion to PA by potentiometry or spectrophotometry (e.g., Li^+ , K^+ , Br^- , I^- , transition metal ion, dye) [23–25]; (iii) monitoring the intensity of fluorescence emitted from a tag covalently bound to PA [26, 27], and (iv) monitoring a change in spectroscopic characteristic on the interaction of PA with a metachromic or fluorochromic dye or a change in turbidity on the interaction of PA with a cationic surfactant [28–31]. Each of the abovementioned approaches has both advantages and the drawbacks. Indeed, the light absorption of PA complexes can be masked by the corrosion byproducts (formation of iron and copper complexes), by water background cation (iron, calcium, magnesium, copper) complexes formation, as well as by calcium carbonate and calcium sulfate colloid formation. At the same time, the indifferent markers do not guarantee the correct

PA concentration indication. Due to the differences in chemical properties of PA and a marker, the latter could have a different sorption ability relative to PA in a particular system. Therefore, the marker can provide either overestimation or an underestimation of PA content with a sequence of time. The PA-tagged fluorescent markers are treated as more reliable, although the more expensive solution [6]. Besides there is a risk of the PA antiscalant ability change due to the fluorescent fragment implementation. Thus, the chemical behavior of PA and of a corresponding PA-tagged fluorophore would be somehow different.

Recently, all the publications on the covalent binding of a fluorophore fragment to the antiscalant molecule are restricted by either the polyacrylate or polyaspartate moieties [6–8, 13, 32–36]. Any reports on the fluorescent-tagged phosphonate-based antiscalants are missing, although the online phosphonate monitoring is no less actual.

2.1. Inert tracers added to polymeric antiscalants

Irrespective of a broad spectrum of the commercially available fluorescent dyes, the number of reagents that have a high quantum yield in an aqueous medium is relatively small [37]. It should be noted that the fluorescence intensity strongly depends on pH, background cation concentration, and bioimpurities, normally present in the circulating systems. Besides, some dyes may change the color of industrial water. Therefore, it is desirable to use those reagents that have maximal light absorption in the ultraviolet spectral range, while the emission spectrum is likely to correspond to the visible blue light.

Usually the fluorescent marker molecules combine sulfo-1,8-naphthalimide with some carboxylate or sulfo-groups to provide an aqueous solubility (fluorescein, rhodamine, sodium 1,3,6,8-pyrene-tetrasulfate) [38–40]. These reagents have high quantum yield, chemical, and photostability

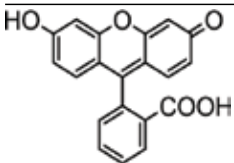
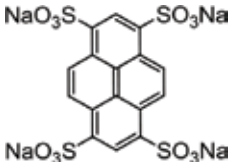
Dye formula	Absorption maximum in H ₂ O, nm	Fluorescence maximum in H ₂ O, nm	Quantum yield, %
 <p>Fluorescein</p>	473 (Buffer pH 5.0); 490 (Buffer pH 9.0)	514 (Buffers pH 5.0, pH 9.0)	92
 <p>1,3,6,8-pyrene tetrasulfonic acid tetrasodium salt</p>	374	403	56

Table 1. The excitation and emission properties of fluorescein and of 1,3,6,8-pyrene tetrasulfonic acid tetrasodium salt [11, 41].

[11, 41] as shown in **Table 1**. Besides, Kurita Water Industries Ltd. offers a 2-phenylbenzimidazole as a marker [42], while Kemira Oyj proposes a lanthanoid-based tracer [43].

2.2. Fluorescent-tagged scale inhibitors

An antiscaling ability of fluorophore-tagged polymers relative to their non-tagged analogues was reported in a very few studies [6, 44–46], as shown in **Table 2**. Usually the implementation of a fluorophore fragment either does not change the inhibitor efficacy or even provides some enhancement.

Fluorescent-tagged scale inhibitors *	Concentration scale inhibitors, mg·dm ⁻³	Inhibitor efficacy, %	Reference
CaCO₃ scale			
PA-F1	10	49 ± 3	[6]
PA-F2	10	51 ± 2	[6]
MA-AA-F1	10	44 ± 2	[6]
MA-AA-F2	10	54 ± 2	[6]
PA	10	70 ± 2	[6]
FPASP	6	90	[44]
PASP	6	70	[44]
CaSO₄ scale			
PA-F1	10	73 ± 3	[6]
PA-F2	10	78 ± 2	[6]
MA-AA-F1	10	61 ± 2	[6]
MA-AA-F2	10	65 ± 2	[6]
PA	10	58 ± 2	[6]
AA-APEM-APTA	9	96	[45]
AA-APEM	9	95	[45]
PAA	9	85	[45]
Ca₃(PO₄)₂ scale			
FPASP	12	95	[46]
PASP	12	30	[46]

PA-F1: co-polymer acrylic acid–N-allyl-4-methoxy-1,8-naphthalimide. **PA-F2:** co-polymer acrylic acid–N-allyl-2-(6-hydroxy-3-oxo-3H-xanthen-9-yl)benzamide (N-allylamidefluorescein). **MA-AA-F1:** co-polymer acrylic acid–fumaric acids–N-allyl-4-methoxy-1,8-naphthalimide. **MA-AA-F2:** co-polymer acrylic acid–fumaric acids–N-allyl-2-(6-hydroxy-3-oxo-3H-xanthen-9-yl)benzamide (N-allylamidefluorescein). **PA:** Na-salt of polyacrylic acid (Shandong TaiHe Water Treatment Co.Ltd.). **FPASP:** fluorescent polyaspartic acid was synthesized with partially ethanolamine-modified polysuccinimide, p-toluenesulfonyl chloride and 3-amino-9-ethyl carbazole. **AA-APEM-APTA:** co-polymer acrylic acid–oxalic acid–allylpolyethoxy carboxylate–8-hydroxy-1,3,6-pyrene trisulfonic acid trisodium salt (pyranine). **AA-APEM:** co-polymer acrylic acid–oxalic acid–allylpolyethoxy carboxylate. **PAA:** poly(acrylic acid), MW 1800 Da.

Table 2. An antiscaling ability of fluorophore-tagged polymers relative to their non-tagged analogues.

Inhibitor, 10 mg·dm ⁻³	Cation									
	Ca ²⁺	Mg ²⁺	Zn ²⁺	Cu ²⁺	Fe ³⁺					
Cation concentration, mg·dm ⁻³										
	20	200	10	100	2	20	0.5	5	0.3	3
Fluorescence intensity change relative to the cation-free solution, %										
PA-F1	100 ± 1	93 ± 1	100 ± 1	100 ± 1	97 ± 1	96 ± 1	91 ± 1	74 ± 1	99 ± 1	94 ± 1
PA-F2	58 ± 1	43 ± 1	66 ± 1	62 ± 1	85 ± 1	42 ± 1	96 ± 1	48 ± 1	108 ± 1	94 ± 1
MA-AA-F1	81 ± 1	71 ± 1	91 ± 1	84 ± 1	93 ± 1	85 ± 1	90 ± 1	74 ± 1	94 ± 1	62 ± 1
MA-AA-F2	87 ± 1	81 ± 1	100 ± 1	138 ± 1	93 ± 1	90 ± 1	88 ± 1	69 ± 1	92 ± 1	60 ± 1

Table 3. The dependence of inhibitor fluorescence intensity on inorganic cation concentration (pH 8.0, 25°C) [6].

However some more experimental work has to be done in this field to make the situation clear.

Only a single paper reports on the influence of the background cations on the quantum yield of an antiscalant [6], as shown in **Table 3**. The corresponding data clearly indicate that cations can either increase or sufficiently diminish the fluorescence intensity of some reagents, while some others stay insensitive to this influence. Anyhow this property has to be taken into account for any particular application of a tracer.

A covalent implementation of the fluorescent fragment into the polymer moiety can be performed in two ways. The first one assumes an attachment along with the polymer formation process. Another one is based on the fluorophore binding to the readymade polymer matrix. The first approach is used for the radical involved synthesis of co-polymers bearing carboxylate, sulfonic, or polyalkylenoxyde groups (acrylic, methacrylic, or maleic acids) and the dyes with an active double bond. The reaction runs in an aqueous solution being initiated by persulfates, by H₂O₂, benzoylperoxide, or by 2,2'-azobisisobutyronitrile (0.1–1.0%, mass). Also, such molecular mass regulators as sulfur compounds [47] or sodium hypophosphite are used [48]. These regulators keep the molecular masses within 2000–200,000 Da. The low molecular mass Mw of a polymer (1000 Da < Mw < 10,000 Da) is known to provide the most effective scale inhibition.

Generally, the fluorescent markers should meet the following requirements: (i) synthetic availability of the dyes capable for polymerization; (ii) a dye chemical stability during polymerization; (iii) a minimal influence of a dye on the polymer structure and on its Mw; (iv) the polymer structure, which should not affect the optical properties of a marker.

Fluorescent monomers used for a scale inhibitor implementation could be classified into three main categories: (i) aromatic hydrocarbons and their derivatives, for example, polyphenilic hydrocarbons, hydrocarbons with arylethylene or arylacetylene groups, and so on; (ii) heterocyclic monomers; and (iii) monomers with a carbonyl group.

Polyphenylhydrocarbons demonstrate an intensive fluorescence within a violet-to-blue visible spectrum region. Among these there are vinylanthracene (Rhodia Operations) [49], potassium

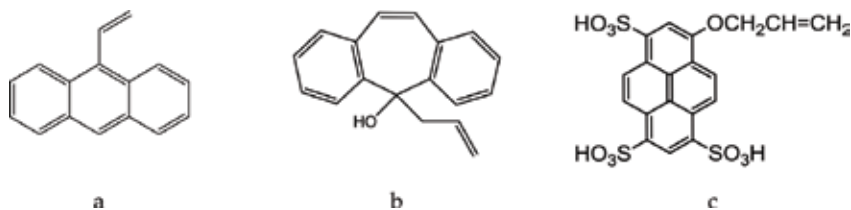
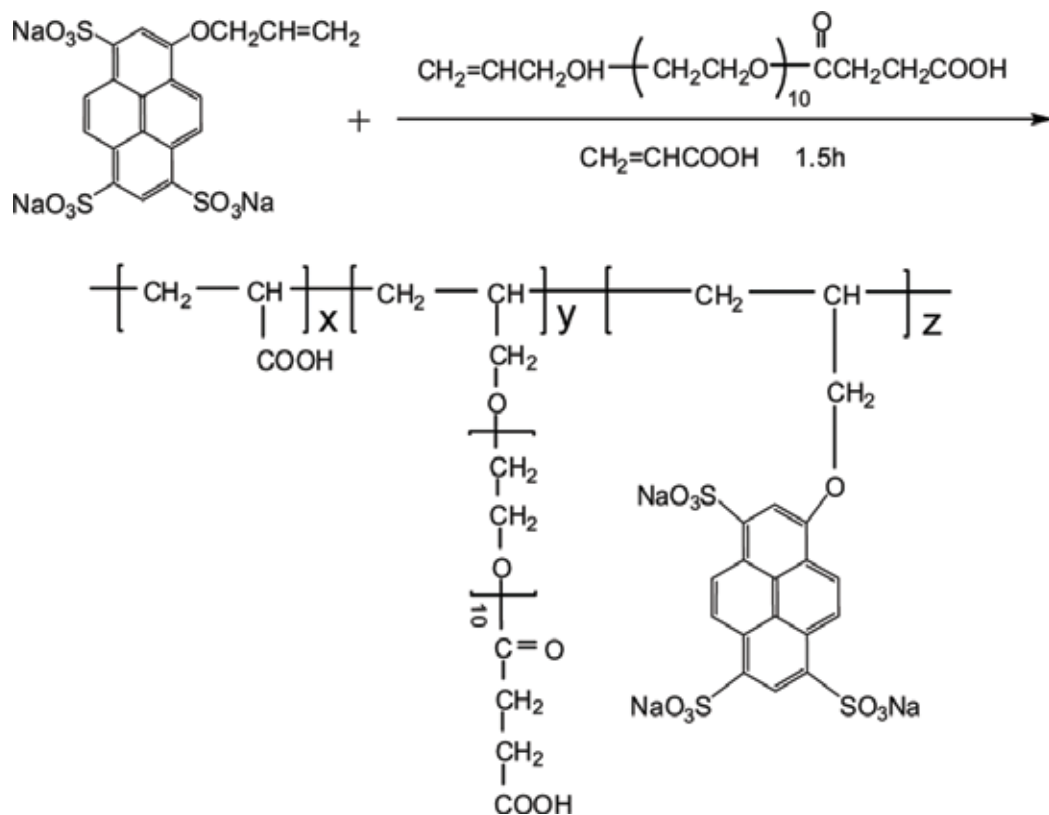


Figure 1. 9-vinyl anthracene (a), 2-allyldibenzosuberanol (b), and 8-(allyloxy)-1,3,6-pyrene trisulfonic acid (c) chemical structures.

2-alkyloxonaphthyl-6,8-disulfonate (China National Offshore Oil Corp.) [50], 2-allyldibenzosuberanol, and 9-allyl-9-hydroxyanthrene (Kurita Water Industries Ltd.) [51], as shown in **Figure 1**.

Numerous research groups synthesize a marker monomer via the 8-hydroxypyrene-1,3,6-trisulfonic acid (pyranine) interaction with allylchloride (**Figure 1c**) [52, 53]. Such a monomer reveals an intensive fluorescence with a maximum at 431 nm. Quantum yield is high. It depends on pH and varies within 80–90%. Then, these fluorescent monomers are co-polymerized (radical polymerization) with an antiscalant-forming monomers, for example, acrylic acid and so on. (**Scheme 1**) [8].



Scheme 1. Preparation of co-polymer acrylic acid-oxalic acid-allylpolyethoxy carboxylate-8-hydroxy-1,3,6-pyrene trisulfonic acid trisodium salt.

A co-polymerization of the pyranine-based monomers with maleic anhydride is also possible [35, 53–56]. The fluorescence intensity of an antiscalant correlates well with the fluorophore content in the scale inhibitor ($R \sim 0.99$), while the detection limit ranges from 1 to 2 $\text{mg} \cdot \text{dm}^{-3}$ [35, 53–56]. Among the numerous water treatment reagents developed by Nalco Chemical Co. there are two fluorescent monomers of the pyranine group [57], as shown in **Figure 2**.

Besides antiscalants, these monomers can also be implemented into some biocides. However, the Nalco Chemical Co. also uses some inert tracers along with the polymer-tagged ones.

Another important group of fluorophore monomers is represented by 5- and 6-member heterocycles [44, 49], particularly by a vinylimidazolic monomer [58], as shown in **Figure 3**.

Among the fluorophores with a carbonyl group, it is reasonable to mention an inhibitor with a fluorescence fragment dimethyl-(4-(7-methoxycoumarin))-methyl-(acryloyloxy)-ethyl-ammonium bromide [59], as shown in **Figure 4**. It reveals the maximal fluorescence intensity at 390 nm.

Several publications report on the naphthalic acid-based markers for biochemical analysis application [60, 61]. An interest in these reagents is associated with both synthetic availability of some valuable 1,8-naphthalimide derivatives and with promising optical properties [62–64]. Ecolab Inc. (USA) has proposed fluorescent monomers derived from 3,4-7H-benzo[d,e]anthracenedicarboxylic acid for the antiscalant labeling [65]. Among these N-(3-N',N'-Dimethylaminopropyl)benzo(k,l)xanthene-3,4-dicarboxylic imide of 2-hydroxy-3-allyloxypropyl quaternary salt seems to be the most interesting, as shown in **Figure 5**.

A considerable attention is paid to the 1,8-naphthalimide derivatives in relevance to the desalination processes (reverse osmosis) [66–68], as shown in **Figures 6 and 7**.

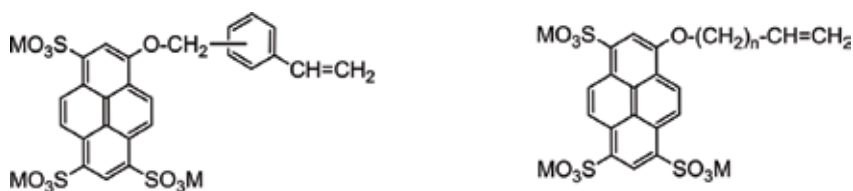


Figure 2. Nalco fluorophores for a covalent attachment to the scale inhibitors [57]; $M = \text{H}^+, \text{NH}_4^+, \text{K}^+, \text{Na}^+, \text{Cs}^+, \text{Rb}^+, \text{Li}^+$; $n = 1, 2, 3, 4, 6$ or 9 .

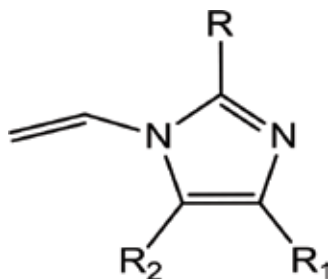


Figure 3. Vinylimidazolic monomer structure; $R, R^1,$ and R^2 are denoted as $\text{H},$ alkyl, aryl, phosphate, nitrate, or sulfate groups.

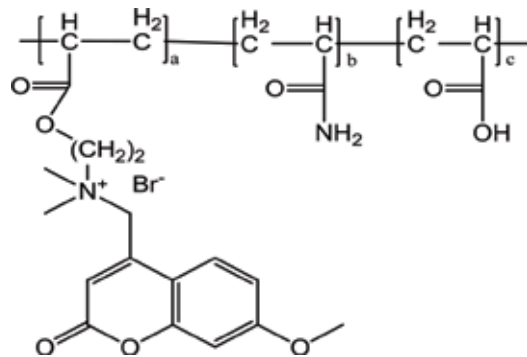


Figure 4. An antiscalant with a dimethyl-(4-(7-methoxycoumarin))-methyl-(acryloyloxy)-ethyl-ammonium bromide fragment [59].

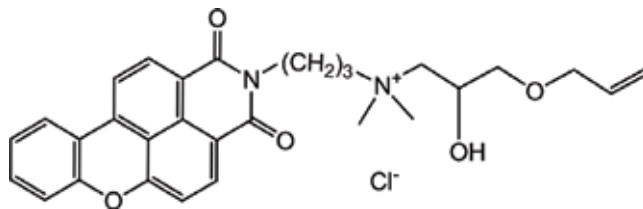


Figure 5. N-(3-N',N'-Dimethylaminopropyl)benzo(k,l)xanthen-3,4-dicarboxylic imide of 2-hydroxy-3-allyloxypropyl quaternary salt [65].

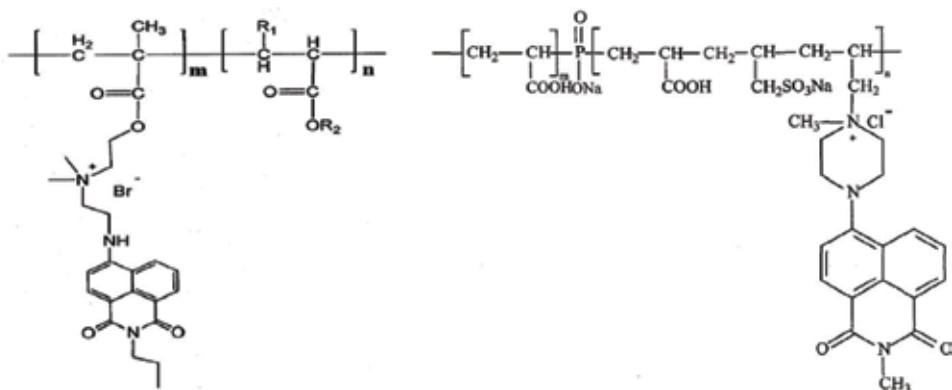


Figure 6. Some 1,8-naphthalimide-tagged antiscalants [66, 67].

An implementation of a fluorophore into a PASP molecule is normally performed not via copolymerization but by its attachment the already formed polymer molecule [46, 69, 70]. Some authors propose 3-amino-9-ethylcarbazole [71] or N-(2,3-epoxypropyl)carbazole [72] for the PASP molecule labeling, as shown in **Figure 8**.

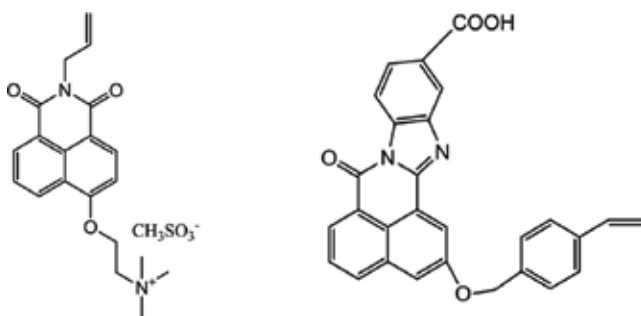


Figure 7. Some 1,8-naphthalimide-based fluorophore monomers developed by Nalco for antiscalant labeling [68].

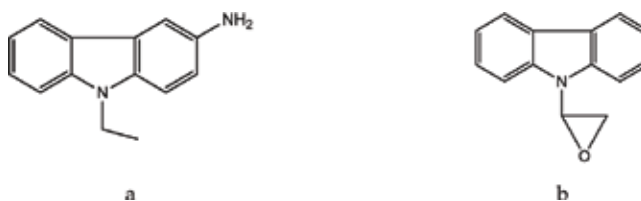
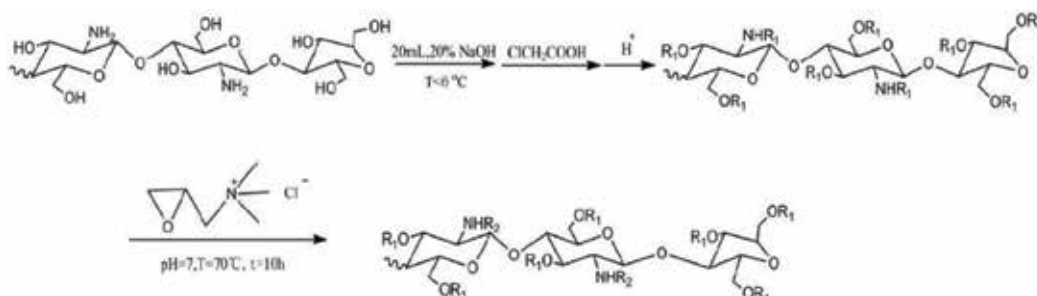


Figure 8. 3-amino-9-ethylcarbazole (a) and N-(2,3-epoxypropyl)carbazole (b) fluorophore structures.

A special attention has to be paid to the communication, where a fluorescence of the inhibitor itself (carboxymethyl ammonium oligochitosan) is reported [73]. This antiscalant does not need any fluorescent marker attachment. The corresponding synthetic method is presented in **Scheme 2**.

It was found that the fluorescence intensity increases under acidic conditions. Thus, the hydrogen bonding and the electrostatic repulsion provide a rigid and densely stabilized structure formation, which is necessary for inducing fluorescence. Hence, the fluorescence of carboxymethyl quaternary ammonium oligochitosan may have been caused by the effect of the $n \rightarrow \pi^*$ transition between $-C=O-$ and $-NH-$ and the special rigid structure formed by hydrogen bonding and a charge-charge repulsion [73]. The fluorescence maximum corresponds to 460 nm, while the detection limit at pH 5–9 is within $0.61 \text{ mg}\cdot\text{dm}^{-3}$.



Scheme 2. Carboxymethyl quaternary ammonium oligochitosan synthesis.

2.3. Visualization of scale inhibition mechanisms

Irrespective of the broad, successful, and long-term antiscalant applications, the mechanisms of scale inhibition still appear in the matter of discussions [14, 74–81]. In this sense, the fluorophore-tagged antiscalants can provide the unique and amazing opportunities to get a deep insight of the scale inhibition mechanisms. As far as we know, recently, such reports on the scale inhibition visualization are missing. However, our research group managed to synthesize a conjugate of 1,8-naphthalimide and HEDP: 1-hydroxy-7-(6-methoxy-1,3-dioxo-1*H*-benzo[de]isoquinolin-2(3*H*)-yl)heptane-1,1-diyl-di(phosphonic acid), (HEDP-F), as shown in **Figure 9a**. This reagent was tested as an antiscalant in gypsum scale formation experiments performed according to NACE protocol [82]. According to this protocol, a calcium-containing brine and a sulfate-containing brine are mixed to form a supersaturated gypsum aqueous solution in the presence of 0.5–15 mg·dm⁻³ of an inhibitor at ambient temperature. Then, this solution is kept for 24 h at 71°C, cooled, and analyzed for residual calcium content by EDTA titration. In a parallel run, the gypsum crystals have been isolated and analyzed with a fluorescence scanning microscope, as shown in **Figure 9b**.

Unlike the scanning electron microscopy, the fluorescence provides a unique possibility to look inside the crystal. Therefore, all the steps of crystal formation become visible. One can see that the bright crystal rod (“lightsaber”), initially formed by nanoparticles, is completely covered with HEDP-F. Then, this rod becomes the center of gypsum layers’ growth without any resistance or involvement of a HEDP-F antiscalant (massive dark layer). Finally, after the gypsum crystal formation is finished, the residual HEDP-F molecules get adsorbed on its surface, particularly at the edges of a crystal lattice, forming the outer layer. This is indicated by green spots and stripes¹. Evidently,

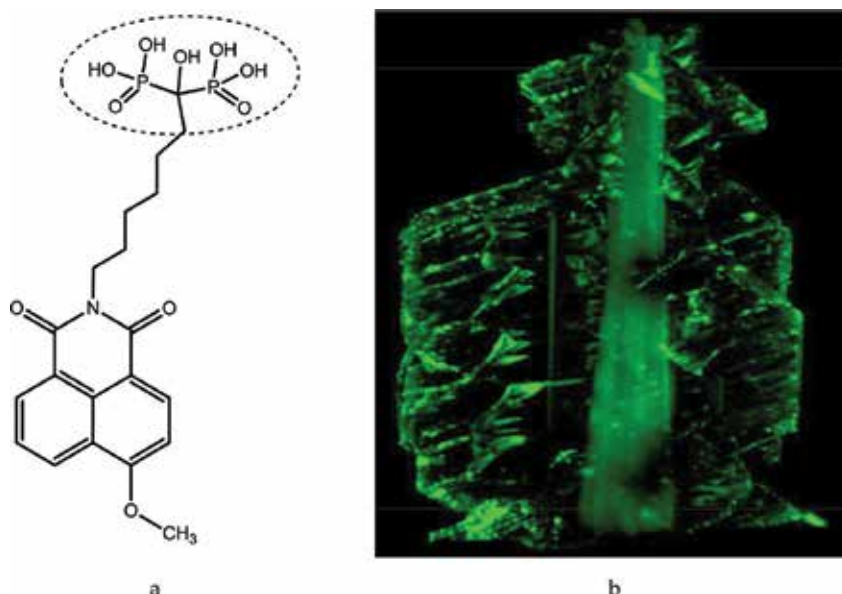


Figure 9. HEDP-F (a) and an image of a Gypsum crystal, isolated in presence of HEDP-F (b); laser scanning microscope LSM-710 Carl Zeiss, lambda mode with 458 nm excitation; 26.10.2017. Data presented by Semen Kamagurov, Sergey Tkachenko and Maxim Oshchepkov.

¹A full-scale publication is under in preparation

these data reveal a mechanism, significantly different from the conventional ones [74–81]. By all means the visualization of scale inhibition mechanisms by fluorescent-tagged antiscalants seems to become a very promising tool of the scale inhibition theory development.

Besides, these reagents can provide some unique opportunities for reverse osmosis membrane mapping, scale inhibition traceability in the pipes, and a scale inhibitor localization in a circulation water facility.

3. Gaseous oxygen monitoring in wastewater

Biological treatment of wastewater includes activated sludge aeration. This in turn raises a problem of the gaseous oxygen content monitoring. One of the most promising solutions here is the fiber-optic oxygen sensor application. This method is based on the ability of oxygen molecules to suppress the luminescence of some luminophores [10, 83]. A fruitful application of some pyrene- or decacylene-based fluorophores along with some ruthenium complex is reported: $(Ru(bpy)_3)_2^+$, $Ru(phen)_3$, $[Ru(dpp)_2Phen]^{2+}$ (dpp = 4, 7-diphenyl-1,10-phenanthroline, Phen = 1,10-phenanthroline) [84], as shown in **Figure 10**. Also some terbium(III) complexes have been immobilized

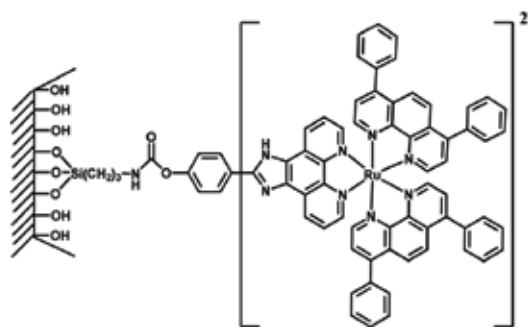


Figure 10. Structure of $[Ru(dpp)_2Phen]^{2+}$.

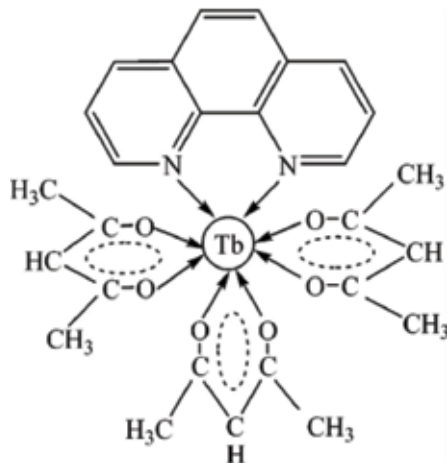


Figure 11. Structure of $Tb(acac)_3phen$.

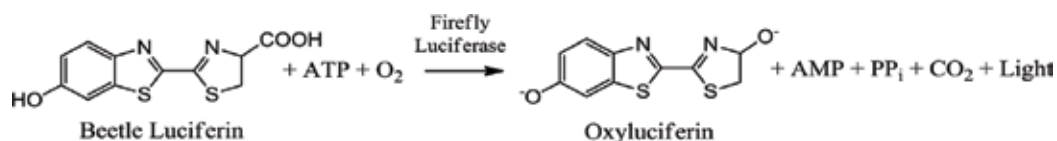
on aluminum oxide ($\text{Tb}(\text{acac})_3\text{phen}$), where acac-acetylacetonate [85], as shown in **Figure 11**, as well as some porphyrin complexes of Pt and Pd [86], is worth mentioning.

The emitted blue light (~ 475 nm) of a photogenerator excites the fluorescence of a specially selected chemical complex, placed at the end of a fiber-optic oxygen sensor (sol-gel matrix). The excited complex generates fluorescence with a wavelength which is around 600 nm. This fluorescence gets suppressed by the oxygen present in a sample [87–89]. This provides an effective oxygen concentration measurement in water within the range from 0 to 40.7 ppm [90].

4. Fluorescent total ATP count in wastewaters

The total bacterial count in wastewater is based on bioluminescence. Normally it is used for the industrial and wastewater quality assessment, while for the drinking water it is not so common. The method is known since 1947, when McElroy has demonstrated that bioluminescence of a glowworm is closely associated with adenosine triphosphate (ATP) content [91]. Thus, the measurement of ATP provides an efficient indication of bacterial pollution of water according to **Scheme 3** [12]:

Analysis involves the firefly luciferase-luciferin system. Its contact with ATP molecules generates the “cold” light, counted by a luminometer within 15–20 s. The sensitivity of analysis is very high. It provides detection of 10^{-17} ATP moles per liter. Recently, there have been some standard solutions for luminometers present at the market: EnSURE™, SystemSURE Plus™ Clean Trace™, NovaLum™, Firefly 2™, Accupoint™, russian-made LYUM-1, Lumitester PD-20™ etc. [92].



Scheme 3. Bioluminescent reaction catalyzed by firefly luciferase.

5. Other applications

Some water treatment facilities require the oil component control in wastewater [9, 93]. Organic pollutants can occur in the cooling water, in the technical-use water, in a boiler-feeding water, and due to the leaks of oils into the steam condensate. For online pollutants' monitoring, the fluorescent sensors are broadly used. The method is highly sensitive. Depending on the type of oil, the detection limits may vary from 1 to 100 ppm. Most of the oils contain some polycyclic aromatic hydrocarbons (PAHs) [94], capable of generating blue or violet fluorescence being exposed to UV irradiation. Usually the excitation light wavelength corresponds to 254 nm, while the detection operates in a 360 nm spectrum range.

Finally, one of the first known applications of fluorophores in water treatment should be mentioned. It is associated with water leaks detection in industrial pipelines. To solve this problem, some fluorescent indicators, for example fluorescein, have been merely added to the circulating water [11].

6. Conclusions

The fluorescent markers added to the circulating water or wastewaters find a broad spectrum of analytical applications for online quality monitoring. The most promising and a fast-developing field is a scale inhibitor concentration detection via antiscalant-tagged reagents. At the same time the visualization of scale inhibition mechanisms by the fluorescent-tagged antiscalants is a very promising tool of the scale inhibition theory development. Besides, these reagents can provide some unique opportunities for reverse osmosis membrane mapping, scale inhibition traceability, and a scale inhibitor localization in a circulation water facility.

Acknowledgements

The authors would like to thank the Russian Foundation for Basic Research (Project No. 17-08-00061).

Conflict of interest

For the present study, no economic interest or any conflict of interest exists.

Author details

Maxim Oshchepkov^{1,2} and Konstantin Popov^{2*}

*Address all correspondence to: ki-popov@mtu-net.ru

1 Mendeleev University of Chemical Technology of Russia, Moscow, Russian Federation

2 PJSC "Fine Chemicals R&D Centre", Moscow, Russian Federation

References

- [1] Duval R, Duplais C. Fluorescent natural products as probes and tracers in biology. *Natural Product Reports*. 2017;**34**:161-193. DOI: 10.1039/C6NP00111D

- [2] Drummen GPC. Fluorescent probes and fluorescence (microscopy) techniques – Illuminating biological and biomedical research. *Molecules*. 2012;**17**:14067-14090. DOI: 10.3390/molecules171214067
- [3] Lange J, Olsson O, Sweeney B, Herbstritt B, Reich M, Alvarez-Zaldivar P, Payraudeau S, Imfeld G. Fluorescent tracers to evaluate pesticide dissipation and transformation in agricultural soils. *Science of the Total Environment*. 2018;**619-620**:1682-1689. DOI: 10.1016/j.scitotenv.2017.10.132
- [4] Arenas-Vivo A, Beltran FR, Alcazar V, de la Orden MU, Martinez UJ. Fluorescence labeling of high density polyethylene for identification and separation of selected containers in plastics waste streams. Comparison of thermal and photochemical stability of different fluorescent tracers. *Materials Today Communications*. 2017;**12**:125-132. DOI: 10.1016/j.mtcomm.2017.07.008
- [5] Jiangli F, Suzhen W, Wen S, Shigang G, Yao K, Jianjun D, Xiaojun P. Anticancer drug delivery systems based on inorganic nanocarriers with fluorescent tracers. *American Institute of Chemical Engineers Journal Ahead of Print*. 2017. DOI: 10.1002/aic.15976
- [6] Popov K, Oshchepkov M, Kamagurov S, Tkachenko S, Dikareva Y, Rudakova G. Synthesis and properties of novel fluorescent-tagged polyacrylate-based scale inhibitors. *Journal of Applied Polymer Science*. 2017;**134**:45017. DOI: 10.1002/APP.45017
- [7] Zhenling S, Xin Z, Puyu Z. Preparation of fluorescent polyaspartic acid and evaluation of its scale inhibition for CaCO_3 and CaSO_4 . *Polymers for Advanced Technologies*. 2017;**28**:367-372. DOI: 10.1002/pat.3897
- [8] Guangqing L, Xue M, Yuming Z. Fluorescent-tagged block copolymer as an effective and green inhibitor for calcium sulfate scales. *Russian Journal of Applied Chemistry*. 2016;**89**:1861-1868. DOI: 10.1134/S1070427216110185
- [9] Ruhala SS, Zarnetske JP. Using in-situ optical sensors to study dissolved organic carbon dynamics of streams and watersheds: A review. *Science of the Total Environment*. 2017;**575**:713-723. DOI: 10.1016/j.scitotenv.2016.09.113
- [10] Allen CB, Schneider BK, White CJ. Limitations to oxygen diffusion in in vitro cell exposure systems in hyperoxia and hypoxia. *American Journal of Physiology-Lung Cellular and Molecular Physiology*. 2001;**281**:L1021-L1027. DOI: 10.1152/ajplung.2001.281.4.L1021
- [11] Sabnis RW. *Handbook of Fluorescent Dyes and Probes*. 1st ed. Hoboken, NJ, USA: John Wiley & Sons, Inc; 2015. DOI: 10.1002/9781119007104
- [12] Guardigli M, Lundin A, Roda A. "Classical" applications of Chemiluminescence and bioluminescence. In: Roda A, editor. *Chemiluminescence and Bioluminescence: Past, Present and Future*. Royal Society of Chemistry; 2010. pp. 143-190. DOI: 10.1039/9781849732024-00141
- [13] Jiao CL, Wu YF, Hou CY, Cheng GC, Wu DX, Xu X, Yin JH. Determine the consumption of fluorescent scale inhibitor SC260 using Dibenzofuran-2-sulfonic acid hydrate. *Advanced Materials Research*. 2014;**997**:247-250. DOI: 10.4028/www.scientific.net/AMR.997.247

- [14] Popov KI, Oshchepkov MS, Shabanova NA, Dikareva YM, Larchenko VE, Koltinova EY. DLS study of a phosphonate induced gypsum scale inhibition mechanism using indifferent nanodispersions as the standards of a light scattering intensity comparison. *International Journal of Corrosion and Scale Inhibition*. 2018;**7**:9-24. DOI: 10.17675/2305-6894-2018-7-1-2
- [15] Amjad Z, editor. *The Science and Technology of Industrial Water Treatment*. Boca Raton Florida: CRS Press; 2010. p. 530
- [16] MacAdam J, Parsons SA. Calcium carbonate scale formation and control. *Reviews in Environmental Science and Biotechnology*. 2004;**3**:159-169. DOI: 10.1007/s11157-004-3849-1
- [17] Popov KI, Kovaleva NE, Rudakova GY, Kombarova SP, Larchenko VE. Recent state-of-the-art of biodegradable scale inhibitors for cooling water treatment applications (review). *Thermal Engineering*. 2016;**63**:122-129. DOI: 10.1134/S0040601516010092
- [18] Hasson D, Shemer H, Sher A. State of the art of friendly “green” scale inhibitors: A review article. *Industrial and Engineering Chemistry Research*. 2011;**50**:7601-7607. DOI: 10.1021/ie200370v
- [19] Popov K, Rudakova G, Larchenko V, Tusheva M, Afanas'eva E, Kombarova S, Kamagurov S, Kovaleva N. A comparative performance ranking of some phosphonates and environmentally friendly polymers on CaCO₃ scaling inhibition by NACE protocol. *Desalination and Water Treatment*. 2017;**69**:163-172. DOI: 10.5004/dwt.2016.0336
- [20] Pervov A, Andrianov A, Rudakova G, Popov K. A comparative study of some novel “green” and traditional antiscalants efficiency for the reverse osmotic Black Sea water desalination. *Desalination and Water Treatment*. 2017;**73**:11-21. DOI: 10.5004/dwt.2017.20363
- [21] Yuchi A, Gotoh Y, Itoh S. Potentiometry of effective concentration of polyacrylate as scale inhibitor. *Analytica Chimica Acta*. 2007;**594**:199-203. DOI: 10.1016/j.aca.2007.05.049
- [22] Glukhova LY, Perov PA. Spectrophotometric method for the determination of an acrylic acid-acrylamide copolymer in highly mineralized waters. *Khimiya i Tekhnologiya Vody. Soviet Journal of Water Chemistry and Technology*. 1981;**3**:236-237. ISSN: 0204-3556
- [23] Hoots JE, Hunt BE. Monitoring chemical treatment with fluorescent tracers. U.S. Patent. US4783314 A 19881108; 1988
- [24] Hoots JE, Banks RH, Johnson DA. Transition metals as chemical tracers in aqueous systems. U.S. Patent. US4966711 A 19890227; 1990
- [25] Yoshimura S, Kuzumaki S, Imahama T. Method for controlling concentration of chemicals added to industrial water. JPN Patent. JP2788354B2; 1991
- [26] Myers RR, Fink JE. Method for the colorimetric determination of polycarboxylates in aqueous systems. U.S. Patent. US4894346A; 1990
- [27] Hoots JE, Pierce CC, Kugel RW. Monitoring and in-system concentration control of poly-electrolytes in waters using fluorochromatic dyes. U.S. Patent. US5389548A; 1995

- [28] Ma J, Sun Y, Yu Z. High-efficiency phosphorus-free corrosion and scale inhibition dispersion agent, preparation method thereof and application thereof. PRC Patent. CN102139967B; 2012
- [29] Tong Z, Chu C, Fan E, Sha Z. High-efficiency low-phosphorus corrosion and scale inhibiting dispersant and its preparation method. PRC Patent. CN102745825A; 2012
- [30] Fong DW, Hoots JE. Fluorescent group-tagged acrylic polymers and their synthesis by post-polymerization (trans)amidation. U.S. Patent. US5128419; 1992
- [31] Kira M, Kobayashi N. Agent for water treatment containing a polymer for water treatment and a process for producing said polymer. U.S. Patent. US5635575; 1997
- [32] Hoots J, Burkart C, Paulson S. Tracing process problems. *Chemical Engineering Progress*. 2002;**98**:66-70
- [33] Zeiner KEH, Ho B, Williams KD. Novel antiscalant dosing control. *Desalination*. 2003;**157**:209-216. DOI: 10.1016/S0011-9164(03)00400-4
- [34] Vazques O, Mackay E, Tjomsland T, Nygard O, Storås E. Use of tracers to evaluate and optimize scale squeeze treatment design in the Norne field. *SPE Production and Operations*. 2014;**29**:5-13. DOI: 10.2118/164114-PA
- [35] Wu K, Chen F, Liu Y, Luo J. Preparation and properties of β -cyclodextrins polymer used as calcium carbonate scale inhibitor containing fluorescent groups. *Research on Chemical Intermediates*. 2014;**41**:7617-7630. DOI: 10.1007/s11164-014-1847-7
- [36] Wang J, Peng Y, Guo W, Ji R, Zhao L, Jia Y, Gao C. Characterization of Tinopal CBS-X as a fluorescent tracer in cooling water. *Instrumentation Science and Technology*. 2016;**45**:301-311. DOI: 10.1080/10739149.2016.1237367
- [37] Lakowitz JR. *Principles of Fluorescence Spectroscopy*. 3rd ed. New York: Springer; 2006
- [38] Feng H, Luo R, Shang W, Zhang L, Zhang W. Phosphorus-free corrosion and scale inhibitor. PRC Patent. CN101767885B; 2011
- [39] Ito M, Ichikawa S, Kashimura H. Method For Stabilizing Fluorescence Intensity Of Rhodamine-Based Fluorescent Material. JPN Patent. JP5297851B2; 2013
- [40] Xu Guangming, Chen Jun, Lv Zhen, Chen Bo, He Gongzhe, Shi Yadong, Zhang Feiyan, Zhu Di, Guan Yuntao, He Kai. Scale and corrosion inhibitor. PRC Patent. CN103319010A; 2013
- [41] Tran-Thi T-H, Prayer C, Millie P, Uznanski P, Hynes JT. Substituent and solvent effects on the nature of the transitions of pyrenol and pyranine. Identification of an intermediate in the excited-state proton-transfer reaction. *The Journal of Physical Chemistry*. 2002;**106**:2244-2255. DOI: 10.1021/jp0125606
- [42] Hajime I, Mayumi K, Kanji N. Concentration control method for water-based additive. Jpn patent. JPH09178662A; 1997

- [43] Nuutinen V, Toivonen S, Johnstone J, Harma H, Lehmusto M, Tiittanen S, Vaisanen P, Siivonen J, Mundill P. Method for analyzing a sample comprising at least a first and a second oil field scale inhibitor. (2015). PCT Int. Appl. WO2015075309A1
- [44] Kamagurov SD, Kovaleva NE, Oshchepkov MS, Popov KI, Tkachenko SV, Starkova ES. Fluorophor and method for obtaining salt inhibitor containing fluorofor as fluorescent mark. Russ. Patent. RU 2640339 C2 20171227; 2017
- [45] Wang H, Zhou Y, Yao Q, Sun W. Calcium sulfate precipitation studies with fluorescent-tagged scale inhibitor for cooling water systems. *Polymer Bulletin*. 2015;**72**:2171-2188. DOI: 10.1007/s00289-015-1396-2
- [46] Feng J, Gao L, Wen R, Deng Y, Wu X, Deng S. Fluorescent polyaspartic acid with an enhanced inhibition performance against calcium phosphate. *Desalination*. 2014;**345**:72-76. DOI: 10.1016/j.desal.2014.04.019
- [47] Detering J, Urtel B, Weber H, Ettl R, Gaedt T, Heintz E, Bastigkeit T, Eiting T, Sendor-Mueller D. Copolymers containing carboxylic acid groups, sulphonic acid groups and polyalkylene oxide groups as anti-scaling additive to washing and cleaning agents. Russ. Patent RU2574395; 2016
- [48] Detering J, Urtel B, Nied S, Heintz E. Low-Molecular, Phosphorus-containing polyacrylic acids and use thereof as scale inhibitors in water supply systems. Russ. Patent. RU2593591C2; 2016
- [49] Hills E, Touzet S, Langlois B. Stimulating Oilfields Using Different Scale-Inhibitors. U.S. Patent. US7703516B2; 2007
- [50] Shuzhong H, Weisheng Z, Yu R, Houkai T, Xiangyan M, Longxin Y, Wu X, Wang J. Preparation method of acrylic polymer with fluorescence characteristic. PRC Patent. CN103242476B; 2015
- [51] Mayumi K, Norimasa K. Agent for water treatment containing a polymer for water treatment and a process for producing said polymer. U.S. Patent (1997). US5635575A
- [52] Liu G, Huang J, Zhou Y, Yao Q, Wang H, Ling L, Zhang P, Ke C, Liu Y, Wendao W, Sun W. Carboxylate-terminated double-hydrophilic block copolymer containing fluorescent groups: An effective and environmentally friendly inhibitor for calcium carbonate scales. *International Journal of Polymeric Materials and Polymeric Biomaterials*. 2013;**62**:678-685. DOI: 10.1080/00914037.2013.769226
- [53] Kun D, Zhou Y, Dai L, Wang Y. Preparation and properties of polyether scale inhibitor containing fluorescent groups. *International Journal of Polymeric Materials and Polymeric Biomaterials*. 2008;**57**:785-796. DOI: 10.1080/00914030801962988
- [54] Kun D, Zhou Y, Wang L, Wang Y. Fluorescent-tagged no phosphate and nitrogen free calcium phosphate scale inhibitor for cooling water systems. *Journal of Applied Polymer Science*. 2009;**113**:1966-1974. DOI: 10.1002/app.30213

- [55] Huang G, Zhou J, Yao Y, Ling Q, Zhang L, Wang P, Cao H, Liu K, Wu Y, Sun W, Hu W, Zhengjun. Fluorescent-tagged double-hydrophilic block copolymer as a green inhibitor for calcium carbonate scales. *Tenside Surfactants Detergents*. 2012;**49**:404-412. DOI: 10.3139/113.110210
- [56] Wang H, Zhou Y, Yao Q, Ma S, Wendao W, Sun W. Synthesis of fluorescent-tagged scale inhibitor and evaluation of its calcium carbonate precipitation performance. *Desalination*. 2014;**340**:1-10. DOI: 10.1016/j.desal.2014.02.015
- [57] Moriarty Barbara E, Wei Mingli, Hoots John E, Workman David P, Rasimas Jeffrey P. Fluorescent monomers and polymers containing same for use in industrial water systems. U.S. Patent (2001). US6312644B1
- [58] Moore L, Clapp L. Tagged scale inhibitor compositions and methods of inhibiting scale. U.S. Patent. US8980123B2;2015
- [59] Ying W, Peng L, Jiajun F, Xiaodong L, Zhuo L, Xuelong L. Fluorescence-trace water processing agent containing coumarins derivative groups and preparation method thereof. PRC Patent. CN103482777B; 2015
- [60] Mittapalli RR, Namashivaya SSR, Oshchepkov AS, Kuczyńska E, Kataev EA. Design of anion-selective PET probes based on azacryptands: The effect of pH on binding and fluorescence properties. *Chemical Communications*. 2017;**53**:4822-4825. DOI: 10.1039/C7CC01255A
- [61] Oshchepkov AS, Mittapalli RR, Fedorova OA, Kataev EA. Naphthalimide-based polyammonium chemosensors for anions: Study of binding properties and sensing mechanisms. *Chemistry - A European Journal*. 2017;**23**:9657-9665. DOI: 10.1002/chem.201701515
- [62] Oshchepkov AS, Oshchepkov MS, Arkhipova AN, Panchenko PA, Fedorova OA. Synthesis of 4-nitro-N-phenyl-1,8-naphthalimide annulated to thia- and azacrown ether moieties. *Synthesis-Stuttgart*. 2017;**49**:2231-2240. DOI: 10.1055/s-0036-1588712
- [63] Oshchepkova MV, Oshchepkov MS, Fedorova OA, Fedorov YV, Lozinskii VI. New copolymer gels based on N,N-dimethylacrylamide and crown-containing allyl derivative of 1,8-naphthalimide as optical sensors for metal cations in an organic medium. *Doklady Physical Chemistry*. 2017;**476**:181-185. DOI: 10.1134/S0012501617100050
- [64] Oshchepkova MV, Oshchepkov AS, Zaborina OE, Fedorova OA, Fedorov YV, Lozinsky VI. Fluorescent cryogels based on copolymers of N,N-dimethylacrylamide and allyl derivatives of 1,8-naphthalimide. *Polymer Science Series B*. 2015;**57**:631-637. DOI: 10.1134/S1560090415060159
- [65] Atkins JM, Moriarty BE, Zinn PJ. Fluorescent monomers and tagged treatment polymers containing same for use in industrial water systems. U.S. Patent. US2014183140A1; 2014
- [66] Zhang Y, Zhang Q, Shi Y, Lei W, Xia M, Wang F. Fluorescence labeling acrylic acid-sodium acrylic sulphonate co-polymer water treatment agent and preparation method thereof. PRC Patent. CN101381168B; 2010

- [67] Lei XM. Methoxy group naphthyl fluorescence marked water treating agent and its preparing method. PRC Patent. CN1781857A; 2006
- [68] Morris JD, Moriarty BE, Wei Mingli, Murray PG, Reddinger JL. Fluorescent Monomers and Tagged Treatment Polymers Containing Same for Use in Industrial Water Systems. 2001. PCT Int. Appl. WO 2001081654 A1 20011101
- [69] Zhang B, Zhou D, Lu X, Xu Y, Ciu Y. Synthesis of polyaspartic acid/3-amino-1H-1,2,4-triazole-5-carboxylic acid graft copolymer and evaluation of its corrosion inhibition and scale inhibition performance. *Desalination*. 2013;**327**:32-38. DOI: 10.1016/j.desal.2013.08.005
- [70] Xu Y, Zhang B, Zhao L, Ciu Y. Synthesis of polyaspartic acid/3-aminoorotic acid graft copolymer and evaluation of its scale inhibition and corrosion inhibition performance. *Desalination*. 2013;**311**:156-161. DOI: 10.1016/j.desal.2012.11.026
- [71] Gao L-J, Feng J-Y, Jin B, Zhang Q-N, Liu T-Q, Lun Y-Q, Wu Z-J. Carbazole and hydroxy groups-tagged poly(aspartic acid) scale inhibitor for cooling water system. *Chemistry Letters*. 2011;**40**:1392-1394. DOI: 10.1246/cl.2011.1392
- [72] Lijun G, Jiuying F. Fluorescent labeling polyaspartic acid scale inhibitor and preparation method thereof. PRC Patent. CN102910746B; 2013
- [73] Huixin Z, Zhiyue C, Xiuhong J, Dongxue S, Dongdong W, Tingru Y, Jie Z, Xu H. Preparation of modified oligochitosan and evaluation of its scale inhibition and fluorescence properties. *Journal of Applied Polymer Science*. 2015;**132**:42518. DOI: 10.1002/app.42518
- [74] Elliott MN. Scale control by threshold treatment. *Desalination*. 1970;**8**:221-236. DOI: 10.1016/S0011-9164(00)80231-3
- [75] Reddy MM, Nancollas GH. Calcite crystal growth inhibition by phosphonates. *Desalination*. 1973;**12**:61-73. DOI: 10.1016/S0011-9164(00)80175-7
- [76] Tomson BM, Fu G, Watson MA, Kan AT. Mechanisms of mineral scale inhibition. *SPE Production & Facilities*. 2003;**18**:192-199. DOI: 10.2118/84958-PA
- [77] GuiCai Z, JiJiang G, MingQin S, BinLin P, Tao M, ZhaoZheng S. Investigation of scale inhibition mechanisms based on the effect of scale inhibitor on calcium carbonate crystal forms. *Science in China, Series B Chemistry*. 2007;**50**:114-120. DOI: 10.1007/s11426-007-0010-3
- [78] Lixiu L, Aijiang H. Research progress of scale inhibition mechanism. *Advanced Materials Research*. 2014;**955-959**:2411-2414. DOI: 10.4028/5j.scientific.net/AMR.955-959.2411
- [79] Al-Roomi YM, Hussain KF. Potential kinetic model for scaling and scale inhibition mechanism. *Desalination*. 2016;**393**:186-195. DOI: 10.1016/j.desal.2015.07.025
- [80] Ji-jiang G, Wang Y, Gui-cai Z, Jiang P, Mingqin S. Investigation of scale inhibition mechanism based on the effect of HEDP on surface charge of calcium carbonate. *Tenside, Surfactants, Detergents*. 2016;**53**:29-36. DOI: 10.3139/113.110407

- [81] Hoang TA. Mechanisms of scale formation and inhibition. In: Amjad Z, Demadis K, editors. *Mineral Scales and Deposits, Scientific and Technological Approaches*. 1st ed. Elsevier; 2015. pp. 47-83
- [82] NACE Standard TM0374-2007 (formerly TM0374-2001) Laboratory Screening Tests to Determine the Ability of Scale Inhibitors to Prevent the Precipitation of Calcium Sulfate and Calcium Carbonate from Solution (for Oil and Gas Production Systems). Item No. 21208. 2007
- [83] Krihak M, Murtaugh MT, Shahriari MR. Fiber Optic Oxygen Sensors Based on the Sol-Gel Coating Technique. *Proc. SPIE-The International Society for Optical Engineering (Chemical, Biochemical and Environmental Fiber Sensors VIII)*. Vol. 28361996. pp. 105-115. DOI: 10.1117/12.260583
- [84] Lei B, Li B, Zhang H, Zhang L, Li W. Synthesis, characterization, and oxygen sensing properties of functionalized Mesoporous SBA-15 and MCM-41 with a covalently linked ruthenium(II) complex. *Journal of Physical Chemistry C*. 2007;**111**:11291-11301. DOI: 10.1021/jp070008w
- [85] Li S, Song H, Li W, Ren X, Lu S, Pan G, Fan L, Yu H, Zhang H, Qin R, Dai QL, Wang T. Improved photoluminescence properties of ternary terbium complexes in Mesoporous molecule sieves. *The Journal of Physical Chemistry. B*. 2006;**110**:23164-23169. DOI: 10.1021/jp064509d
- [86] Papkovskij DB, Ponomarev GV, Kurochkin IN, Chernov SF. Metal complexes of porphyrin-ketones, sensitive member for oxygen optical assay in liquid or gaseous medium and a method of oxygen determination. *Russ. Patent. RU2064948C1*; 1996
- [87] Krihak M, Shahriari MR. A highly sensitive, all solid state Fiber optic oxygen sensor based on the sol-gel coating technique. *Electronic Letters*. 1996;**32**:240-242. DOI: 10.1049/el:19960104
- [88] Shahriari MR, Murtaugh MT, Kwon HC. Ormosil Thin Films for Chemical Sensing Platforms. *Proc. SPIE-The International Society for Optical Engineering (Chemical, Biochemical and Environmental Fiber Sensors IX)*. Vol. 31051997. pp. 40-51. DOI: 10.1117/12.276133
- [89] Wang W, Reimers CE, Wainright SC, Shahriari MR, Morris MJ. Applying Fiber-optic sensors for monitoring dissolved oxygen. *Sea Technology*. 1999;**40**:69-74
- [90] Weiwei F, Na Z, Lingxin C, Bowei L. An optical sensor for monitoring of dissolved oxygen based on phase detection. *Journal of Optics*. 2013;**15**:055502/1-005502/7. DOI: 10.1088/2040-8978/15/5/055502
- [91] McElroy WD. The energy source for bioluminescence in an isolated system. *Proceedings of the National Academy of Sciences of the United States of America*. 1947;**33**:342-345. DOI: 10.1073/pnas.33.11.342

- [92] Björkman KM, Karl DM. A novel method for the measurement of dissolved adenosine and guanosine triphosphate in aquatic habitats: Applications to marine microbial ecology. *Journal of Microbiological Methods*. 2001;**47**:159-167. DOI: 10.1016/S0167-7012(01)00301-3
- [93] Han TN, Hao NH, Taro U, Yew-Hoong GK. A critical review on characterization strategies of organic matter for wastewater and water treatment processes. *Bioresource Technology*. 2015;**193**:523-533. DOI: 10.1016/j.biortech.2015.06.091
- [94] Carstea EM, Bridgeman J, Baker A, Reynolds DM. Fluorescence spectroscopy for wastewater monitoring: A review. *Water Research*. 2016;**95**:205-219. DOI: 10.1016/j.watres.2016.03.021

Desalination of Water

Manish Thimmaraju, Divya Sreepada,
Gummadi Sridhar Babu, Bharath Kumar Dasari,
Sai Kiran Velpula and Nagaraju Vallepu

Additional information is available at the end of the chapter

<http://dx.doi.org/10.5772/intechopen.78659>

Abstract

Water is very essential for all living beings. It covers nearly 70% of earth's surface. Even though the major portion of earth is covered by water, there is severe shortage of drinking water in most of the countries across the world. Safe drinking water is vital for all forms of life though it does not provide any calories. Desalination of sea water appears as a solution for this problem. Advanced desalination technologies that are applied to seawater and brackish water prove to be effective alternatives in a variety of situations. This study mainly focuses on upcoming trends in modern desalination technologies and emphasizing the options offered by them. Desalination is a technique where the excess salts are removed from sea water or brackish water converting it into safe potable or usable water. Desalination methods are categorized into thermal processes and membrane processes. In this chapter we discuss about different thermal processes like multistage flash distillation, multiple effect distillation, vapour compression evaporation, cogeneration and solar water desalination. We also discuss about various categories of membrane processes like reverse osmosis, electro dialysis and membrane distillation methods. This chapter also concentrates on advantages and disadvantages and economical parameters involved in each of these methods.

Keywords: desalination, sea water, potable water, desalination techniques

1. Introduction

Water is very essential for life. It is one of the most abundant resources of the earth, covering about 3/4th of earth's surface. Though it covers earth's major portion yet there is severe shortage of potable water in many countries around the world mainly developing

countries and middle east region countries. The reason for this situation is that nearly 97.5% of earth's water is salt water present in oceans and remaining 2.5% is fresh water which is in the form of ground water, ice-mountains, lakes and rivers, which serves most human and animal needs [1, 2].

According to UNEP (United Nations Environment Programme) 1/3rd of the world's population lives in countries with insufficient freshwater resources [3]. Hence enormous efforts are required to make new water resources available and minimize water deficiency in countries with shortage of fresh water [4]. World Health Organization guidelines state that the permissible limits of salinity in drinking water are 500 ppm and in few cases it may extend up to 1000 ppm [5]. Most of the water on earth has salinity ranging upto 10,000 ppm and for sea water it may be in the range of 35,000–45,000 ppm due to its dissolved salts [6].

For every 20 years, the consumption rate of water is doubling exceeding by two times the rate of population growth. The potable water resources are on the decline and water demand is high. In recent times various industrial and developmental activities have resulted in increasing pollution and deteriorating the quality of water. Thus water shortages and unreliable quality of water are considered to be major hindrances for sustainable development of society.

The existing water resources are decreasing

- Due to unbalanced distribution of rain water and drought
- Extreme exploitation of ground water resources and its un sufficient recharge
- Degradation of water quality due to the discharge of domestic and industrial wastes without sufficient treatment

Since the fresh water resources are very limited to serve the major population needs and salt water is unsuitable for many applications, desalination of salt water (sea water) emerges as a boon to most of the population to serve their needs [6]. This chapter gives detailed information on different desalination techniques used across the world. It also highlights the merits and demerits involved in these processes.

2. Desalination

It can be defined as any process which removes excess salts and minerals from water (or) the chemical process of changing seawater into potable water are called desalination. These processes may be used for municipal, industrial or any commercial uses. In major desalination methods the feed water is treated and two streams of water are obtained

- Treated potable fresh water that has less amounts of salt and minerals (treated water or product water)
- Concentrate or brine that has salt and mineral concentrations higher than that of original feed water or saltwater [7, 8].

Salt water or feed water sources may include sea water, brackish, wells, surface (rivers and streams), wastewater, and industrial feed and process waters. With advancements in technology, desalination processes are becoming cost effective compared to other methods of producing usable water to meet the growing demands. The water that is obtained after desalination should be remineralised to be fit for human consumption. The concentrated brine obtained in desalination process must be disposed of in a proper manner.

3. Desalination technologies

Different desalination processes have been developed, some of them are at present under research and development. The two major technologies that are mainly used for desalination are

- Thermal desalination technology
- Membrane desalination technology

Both the technologies include a number of different processes, a part from these there are alternative technologies like freezing and ion exchange which are not generally used. All these technologies need energy to operate. Conventional energy or renewable energy is generally used in these methods (Figure 1).

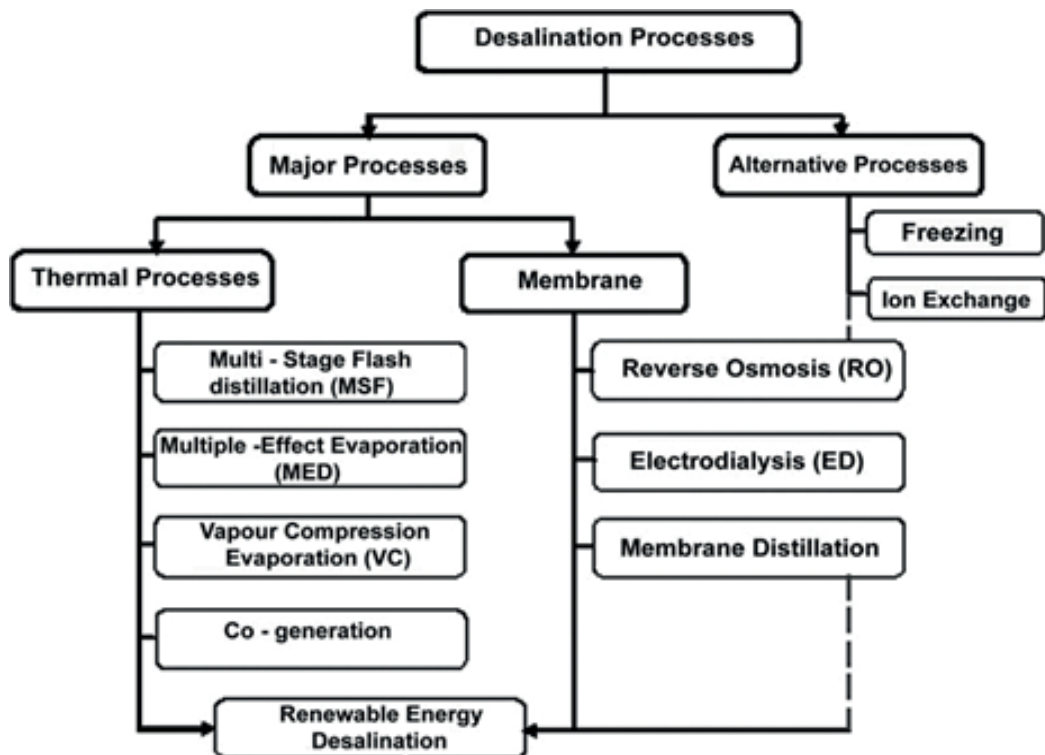


Figure 1. Classification of water desalination processes. Source: [2].

3.1. Thermal desalination processes

It is generally known as distillation. It is one of the most ancient ways of desalinating sea water and converting them to drinking water. This technology is rarely used for desalinating brackish water since it is expensive.

This technology is based on principles of boiling the saline water and evaporating it and then collecting the condensed vapour to obtain pure water. The salt is left behind and the distillate is collected, [9].

The thermal desalination processes are subdivided into the following types

- Multi-stage flash distillation (MSF)
- Multi-effect distillation (MED)
- Vapour compression evaporation (VC)
- Cogeneration
- Solar water desalination

3.1.1. Multi-stage flash distillation (MSF)

Multistage flash distillation process principle involves the distillation through many (multi-stage) chambers (**Figure 2**). Here each successive stage of the plant runs at progressively low pressures. The feed water is initially heated under high pressure and is passed into the first flash chamber. In first flash chamber the pressure is released causing the water to boil rapidly resulting in quick evaporation or flashing. This process continues in each successive stage because the pressure in the next stage is less than the previous stage. The vapour that is

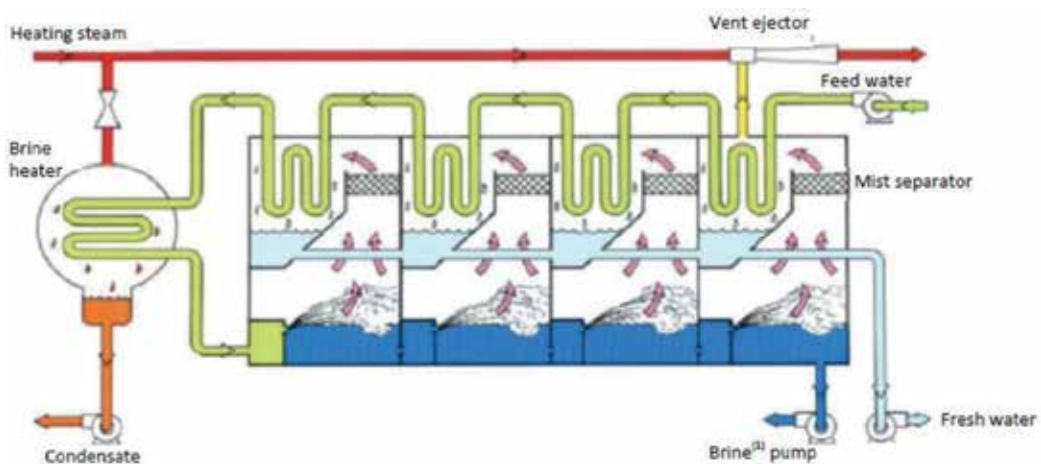


Figure 2. Multi-stage flash distillation. Source: [10].

produced by flashing is converted into fresh water by condensing it on heat exchanger tubing present in each stage. The tubes are then cooled by incoming cooler feed water.

In the MSF process as shown in Figure, the feed water (saline water) is heated in a vessel known as the brine heater until it reaches a temperature below the saturation boiling temperature.

The heated seawater then flows through a series of vessels, in sequence, where the lower atmospheric pressure causes the water to boil quickly and get vaporized. This sudden introduction of hot water into the reduced-pressure chamber is referred to as the 'flashing effect' because the water nearly flashes into steam [11]. A small percentage of this water is converted into water vapour and this percentage is mainly dependent on the pressure inside the stage. The vapour that is generated by flashing is converted to fresh water by getting condensed on the tubes of heat exchangers (condenser) that pass through each stage. The incoming feed water going to the brine heater cools the tubes. This, in return, heats up the feed water and thus increases the thermal efficiency by reducing the amount of thermal energy required by the brine heater to raise the temperature of the seawater.

Building of MSF distillation plants started in late 1950s. Some of these MSF plants can comprise 15–25 stages [12]. These distillation plants can possess either

- Once-through or
- Recycled process
- In once-through design, the feed water or saline water is passed through the heater and flash chambers only once and then it is disposed of
- In recycled design, the feed water used for cooling purpose is also recycled.

All of these processes can be structured as a long tube or cross tube design. In case of long tube design the tubing is parallel to the concentrate flow and in case of cross tube design, the tubing is perpendicular to concentrate flow.

MSF is producing around 64% of the total world desalinated water at present. Though this process is the most reliable source for the production of potable water from seawater, yet it is considered as an energy demanding process that requires both thermal and mechanical energy [12].

MSF plants are prone to corrosion unless stainless steel is used. In addition to corrosion, MSF plants are also subjected to erosion and impingement attack. This erosion is generally caused by the turbulence of the feed water in the flash chamber, when it passes from one stage to another.

3.1.1.1. Advantages and disadvantages of MSF

- MSF plants are relatively simple to construct and easy to operate [11]
- They have no moving parts, other than conventional pumps, and contains only some amount of connection tubing [11]

- The quality of effluent water contains 2–10 ppm of dissolved solids which means a high level of purification. So it is re-mineralized in the post-treatment process to make it palatable and fit for consumption [13].
- Though operating plants at higher temperatures (over 115°C) improves their efficiency but causes scaling problems because the salts such as calcium sulphate precipitate on the tubes surfaces and cause thermal and mechanical problems like tube clogging.
- It is considered as an energy intensive process, which requires both thermal and mechanical energy, but it can be overcome by the cogeneration system.
- Adding more stages in MSF improves its efficiency and increases water production, but it increases the capital cost and causes operational complexity [14] (**Figure 3**).

3.1.2. Multiple effect distillation

The multi-effect distillation process has been used since the late 1950s and early 1960s. Multi-effect distillation employs the same principles of multi-stage flash distillation but contrary to it, it occurs in a series of vessels (effects) and uses the principles of evaporation and condensation at reduced ambient pressure [17].

In Multi- effect distillation process, a series of evaporator effects produce water at progressively lower pressures. As pressure decreases successively water boils at lower temperatures and the water vapour of the first vessel serves as the heating medium for the second, and so on. The more the vessels or effects, the higher the performance ratio. The water vapour which

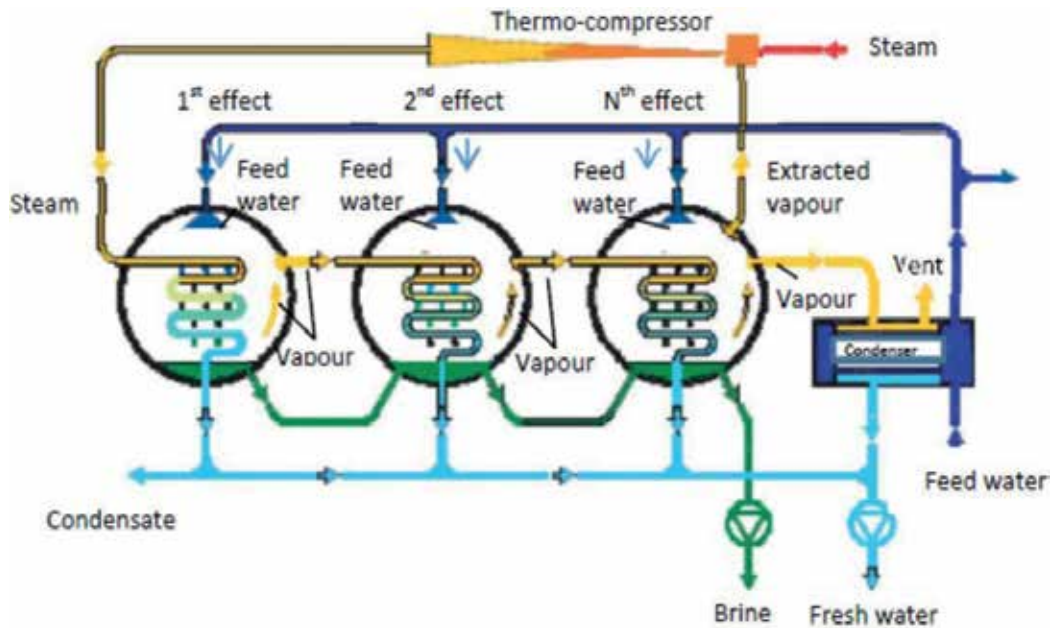


Figure 3. Multiple effect distillation. Sources: [15, 16].

is formed during boiling of water is condensed and collected. The use of multiple effects makes this process more efficient.

Multi-effect distillation is known to be the oldest large scale distillation method for desalinating sea water. Its major characteristics are high quality distilled water, high unit capacity and high heat efficiency.

3.1.2.1. Advantages and disadvantages of multi-effect distillation

- The multi-effect distillation process is designed to operate at lower temperatures of 70°C. This lessens tube corrosion and the scale formation on the tube surfaces.
- The quality of the feed water is not as important as that in Reverse Osmosis system technology. Hence the cost of pre-treatment and operation of this technology is low.
- The power consumption in this technology is lower than that of the MSF and performance is higher than MSF plants. Hence MED technology can be considered to be cost effective and more efficient than MSF technology in terms of potable water production [11] (**Figure 4**).

3.1.3. Vapour compression evaporation

The vapour compression distillation (VCD) or vapour compression evaporation process is operated individually or used along with other processes like MED and single-effect vapour compression. In this method the heat for evaporating the feed water comes from the compression of vapour and not by the direct exchange of heat from steam produced in a boiler [7].

Two devices are generally used in this process to condense the water vapour to generate adequate heat to evaporate the seawater. Among them one is a mechanical compressor (mechanical vapour compression) and the other a steam jet (thermal vapour compression), Vapour compression (VC) units are built in different configurations. Mechanical compressor is

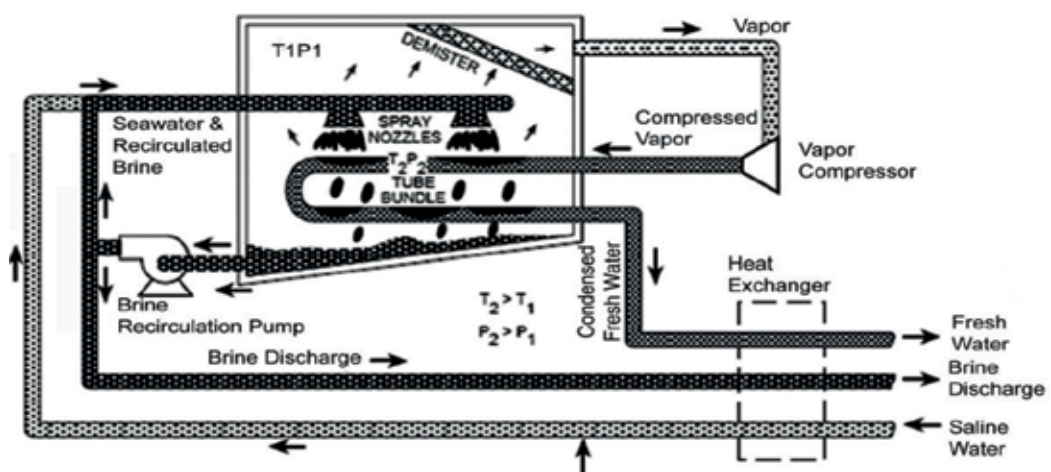


Figure 4. Vapour compression evaporation. Source: [7].

generally used to generate the heat for evaporation and it runs normally by electricity or diesel. This compressor creates vacuum in the evaporator and compresses the vapour obtained from the evaporator, condenses it in a tube bundle.

The feed water is sprayed outside the heated tube bundle. Here the water boils and gets evaporated partially creating more vapour.

In case of steam jet type of vacuum compression distillation, a venture orifice present at the steam jet creates water vapour and extracts it from the water vapour, creating a lower atmospheric temperature. The water vapour that is extracted is compressed by the steam jet and condensed on the tube walls to furnish heat of condensation to evaporate the feed water that is being pumped on the other side in the evaporator.

These units are generally smaller in capacity, and are mostly used at hotels, resorts and in industries.

3.1.3.1. Advantages and disadvantages of vapour compression evaporation

- This method is simple and reliable and hence it can be considered as a better option for small-scale desalination units. They usually have a capacity of 3000 m³/day and are generally used for resorts, industries and drilling sites where fresh water is in shortage.
- The operating temperature of VC distillation or evaporation is low which makes it a simple and efficient process in terms of power consumption.
- Since the operating temperatures are low (below 70°C), the potential for scale formation and tube corrosion is reduced.

3.1.4. Solar desalination

Solar desalination method is generally used for small-scale operations (**Figure 5**). Though the designs of these units are different, but the basic principle is the same. Here the sun provides heat energy to evaporate freshwater from salt water. In solar distillation process, the water vapour generated from the evaporation process condenses on a clear glass or plastic covering and then it is collected as freshwater in a condensate trough. The covering is used for dual purposes one to transmit radiant energy and second to allow water vapour to condense on its interior surface. The salt that is left behind and un-evaporated water present in the still basin must be disposed of appropriately [17].

Solar distillation is mostly used in arid regions where safe freshwater is not available. Solar distillation units produce varying amounts of freshwater, basing on their design and geographic location.

3.1.5. Cogeneration system for power and water desalination

There is a possibility to use energy for dual purpose or cogeneration systems in which the energy sources can perform various different functions such as electric power generation and desalination of water.

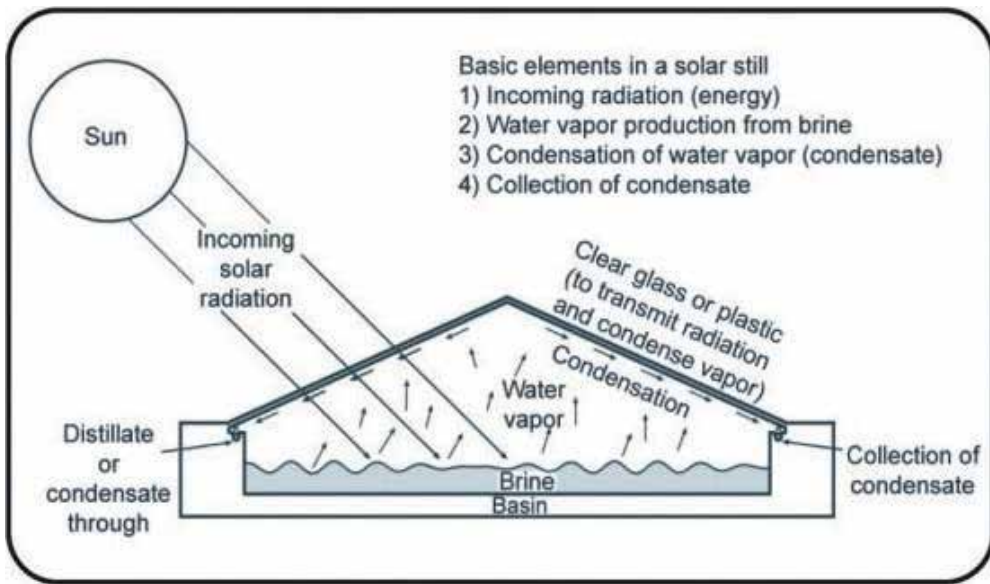


Figure 5. Solar desalination. Source: [17].

In these cogeneration plants, the electricity is generated with high-pressure steam to operate the turbines and the steam is produced by boilers at temperatures up to 5408°C. When this steam expands in turbines, its temperature and energy levels get reduced. As we know that distillation plants need steam with temperatures lower than 1208°C, this can be easily obtained at the end of the turbine after maximum energy has been utilized in electric power generation. The steam is used for the desalination process and the condensate from the steam is then returned to the boiler to get reheated again to be used in the turbine [18].

3.1.5.1. Advantages and disadvantages

- The major advantage of cogeneration system is that it uses very less fuel than other plants operating separately and the energy costs are less for desalination process.
- In contrary, one of the disadvantages is that, problems can occur due to permanent coupling between the desalination plant and the power plant which can create a problem in water production when the need for electricity is reduced or when the turbine or generator has a problem.

3.2. Membrane processes

Initially membrane applications were confined to municipal water treatment such as micro-filtration and desalination but due to advancements in technology and development of new membranes, it is used not only for water purification but also in chemical separations, concentration of enzymes and purification of beverages.

Membrane processes use a relatively permeable membrane to move either water or salt to produce two zones of differing concentrations to produce fresh water. These processes are also useful in municipal water treatment. Reverse osmosis and electro dialysis (ED) are replacing other phase change desalting technologies for supplying water to coastal and island communities all over the world. RO is emerging as an economical alternative to the traditional water softening processes [11].

Membrane technology consists of several processes, but the major difference between them lies in the size of the ions, molecules and suspended particles that are retained or allowed to pass via the membranes. Major separation processes include nano-filtration, ultra-filtration, microfiltration and filtration used in the pre-treatment stages of desalination that are used to remove large particles, bacteria, ions and for water softening.

The membrane processes are further categorized into

- Reverse osmosis
- Electro dialysis
- Membrane distillation

3.2.1. Reverse osmosis (RO) and nanofiltration (NF)

When compared to other processes, Reverse Osmosis (RO) is a relatively a new process used for desalination (**Figure 6**). The principle involved in this RO process is that, it uses pressure as the driving force to push feed water through a semi-permeable membrane into a product water stream and a concentrated brine stream [20].

Nano-filtration (NF) is also a similar membrane process which is used for removal of divalent salt ions such as Calcium, Magnesium, and Sulphate. RO is also used for removal of Sodium and Chloride ions.

Osmosis is a natural phenomenon by which water from a low salt concentration solution flows into a more concentrated solution via semi-permeable membrane. When pressure is applied to the solution of higher salt concentration solution, the water starts flowing in a reverse direction through the semi-permeable membrane, leaving the salt behind. This is known as the reverse osmosis process or RO process. Here the membrane configurations consist of spiral

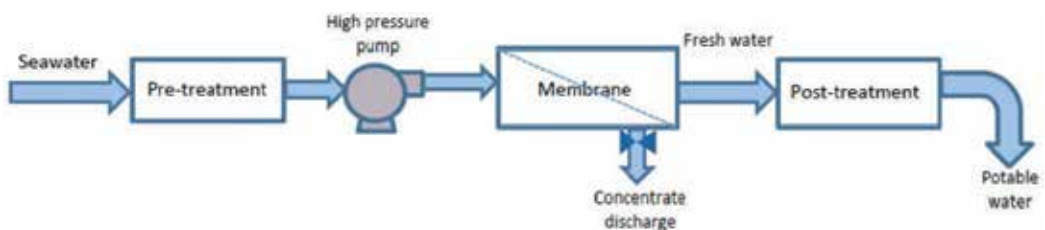


Figure 6. Reverse osmosis (RO). Source: [19].

wound, hollow fibre and sheet with spiral. The operating pressures for reverse osmosis and nano-filtration range in between 50 and 1000psig.

An RO desalination plant mainly comprises of four major systems:

- Pre-treatment system
- High-pressure pumps
- Membrane systems
- Post-treatment

3.2.1.1. Advantages and disadvantages of RO process

- Problems related to corrosion of metals are very less compared to MSF and MED processes due to ambient temperature conditions
- Polymeric materials are preferred to metal alloys [21].
- In seawater desalination, to produce 5 gallons of usable water, 40–90 gallons of water are wasted [1].

3.2.2. Electrodialysis (ED)

Electrodialysis (ED) method is a voltage-driven process. This process uses electrical potential to remove salts using a membrane, leaving fresh water behind. ED was initially used as a seawater desalination process; it is now used for brackish water desalination process also.

Electrodialysis (ED) process is operated using direct current (DC) in which ions (contrary to water in pressure-driven processes) flow via ion selective membranes to oppositely charged electrodes. In these systems, the polarity of the electrodes is reversed repeatedly.

Since water contains dissolved salts in the form of ions and these ions get attracted towards oppositely charged electrodes, electrodialysis can be used to separate salts and fresh water. this method uses suitable membranes to permit passage of selective ions either cations or anions [26].

3.2.3. Membrane distillation

This technology uses the principles of both thermal and membrane technologies, that is, distillation and membrane based desalination processes. In this method temperature difference is created in between the supply solution that is coming in contact with the surface on one side of microporous membrane and the space left on its other side [22]. This temperature difference causes difference in vapour pressure, resulting in the transfer of the produced vapour through the membrane onto the condensation surface. The whole process is based on the use of hydrophobic membranes that are permeable only to the vapour, thus excluding liquid vphase and dissolved particles. The vapour produced then passes through the membrane and gets condensed on the cooling surface producing fresh water.

3.2.3.1. Advantages and disadvantages of MD

- Membrane distillation is simple and operates at low temperature. Hence it utilizes less amount of heat. Coupling MD units with solar energy sources makes it more attractive.
- It operates at a lower pressure than other pressure-driven membrane processes
- Main disadvantage is that MD requires more space compared to other membrane processes [23]
- In this process the feed water should not have any organic pollutants. This fact turns to be a limitation for this process [11].

3.3. Alternative processes

Though a number of other methods have been used in water desalination process, but none of them turned to be commercially as successful as MSF, RO, and ED technologies. Some alternative methods are also used for desalination process. They are

- Freezing and ion exchange processes

3.4. Freezing

The principle involved in freezing desalination is that, in the process of freezing, the dissolved salts present in the feed water are separated during the formation of ice crystals. Seawater can be desalinated by cooling the water to form crystals under controlled conditions. Before the total amount of feed water has been frozen, the mixture is washed and rinsed to remove the salts present in the remaining water or that is sticking to the ice crystals. The ice is then melted to produce fresh water. Since the main heat transfer processes involved are freezing and melting which are regenerative, this method is said to have very high energy efficiency [24].

3.4.1. Advantages and disadvantages

- This process uses theoretically lower energy and has less chance for corrosion and scaling.
- It produces pure drinking water and also water for irrigation
- The disadvantage in this process is handling ice and water mixtures which are mechanically complicated to move and to be processed [25].

3.5. Ion exchange: Solvent process

Ion exchangers are generally organic or inorganic solids which are capable of exchanging one type of cation (or anion) immobilized on the solid surface for another type of cation (or anion) present in solution. For example, Na^+ ions in solution can be replaced with H^+ by a cation exchanger and Cl^- ions can be similarly replaced with OH^- by an anion exchanger, resulting in the complete 'demineralization' of a NaCl solution. This process can be reversed by regenerating the cation exchanger with an acid, and the anion exchanger with a base.

4. Conclusion

The desalination of brackish water and seawater proves to be a reliable source of fresh water and is proves to be a solution for the world's water shortage problem. Desalination processes are normally used to produce drinking water in areas where only seawater or brackish water is the source of water. A number of technologies have been developed and many more methods are under R&D for desalination. They can be used for small scale, that is, supplying water for small communities (e.g. solar distillation) and large scale to supply water to cities, that is, huge plants (e.g. reverse osmosis).

Though desalination costs seem to be progressively decreasing, but they are still costlier than conventional drinking water processes. Coming to environmental aspects each desalination plant has to take proper measures in case of intake of water, pre-treatment of water as well as disposing concentrate reject water that is produced in the process because environmental aspects are equally important as commercial aspects.

Author details

Manish Thimmaraju^{1*}, Divya Sreepada², Gummadi Sridhar Babu³, Bharath Kumar Dasari⁴, Sai Kiran Velpula⁴ and Nagaraju Vallepu⁴

*Address all correspondence to: manishcancer@gmail.com

1 Department of Pharmaceutical Analysis, Balaji Institute of Pharmaceutical Sciences, Warangal, Telangana, India

2 UCPSc, Kakatiya University, Warangal, Telangana, India

3 Sri Shivani College of Pharmacy, Warangal, Telangana, India

4 Department of Pharmacy, Balaji Institute of Pharmaceutical Sciences, Warangal, Telangana, India

References

- [1] Al-Kharabsheh S. Theoretical and experimental analysis of water desalination system using low grade solar heat. PhD dissertation. University of Florida; 2003
- [2] Water desalination technologies utilizing conventional and renewable energy sources. *International Journal of Low-Carbon Technologies*. March 1, 2014;9(1):1-19. DOI: 10.1093/ijlct/cts025
- [3] United Nations Environment Programme. April 10, 2008. Available from: <http://www.unep.org/themes/freshwater.html>

- [4] Colombo D, De Gerloni M, Reali M. An energy-efficient submarine desalination plant. *Desalination*. July 7, 1999;**122**:171-176
- [5] WHO/EU Drinking Water Standards Comparative Table, Water Treatment & Air Purification and Other Supporting Information. October 26, 2007. Available from: <http://www.lenntech.com/WHO-EU-water-standards.html>
- [6] Tiwari GN, Singh HN, Tripathi R. Present status of solar distillation. *Solar Energy*. November 1, 2003;**75**:367-373
- [7] Krishna HJ. Introduction to Desalination Technologies. Austin, Texas, USA: Texas Water Development Board. 2004. Available from: http://www.twdb.texas.gov/innovativewater/desal/doc/VOL1-v7_Final.pdf [Accessed: March 05, 2012]
- [8] Shatat MIM. New and renewable energy and environmental engineering. Durham Theses, Durham University; October 7, 2008
- [9] Winter T, Pannell J, Mc MC. The Economics of Desalination and its Potential Application in Australia. University of Western Australia; 2005
- [10] Lahmeyer International GmbH. Water Desalination. 2003. Available from: <http://www.uwphoto.de/Dateien%20Info%20+%20Kontakt/desalination-brochure.pdf> [Accessed: September 2015]
- [11] Introduction to Desalination Technologies. October 2, 2007. Available from: <http://www.texaswater.tamu.edu/readings/desal/IntrotoDesal.pdf>
- [12] Khawaji AD, Wie J-M. Potabilization of desalinated water at Madinat Yanbu Al-Sinaiyah. Saudi Arabia: *Desalination*. 1994;**98**:135-146. DOI: 10.1016/0011-9164(94)00138-3
- [13] Buros OK. The ABCs of Desalting, 2nd edn. ASIN: B0006S2DHY, International Desalination Association, 2000. Vol 3. October 12, 2013
- [14] Raluy RG, Serra L, Uche J, et al. Life-cycle assessment of desalination technologies integrated with energy production systems. *Desalination*. 2004;**167**:445-458
- [15] Australian Department of the Environment. Introduction to desalination Technologies in Australia. 2002. Available from: <http://www.environment.gov.au/system/files/resources/ef2c1cc7-07d8-4ed8-8f79-816d36fb959e/files/desalination-summary.pdf> [Accessed: September 2015]
- [16] Veolia Water Technologies. Multiple Effect Distillation: Processes for Sea Water Desalination. 2006. Available from: http://technomaps.veoliawatertechnologies.com/processes/lib/pdfs/productbrochures/key_technologies/F733L0vn8nCHqOV2TEb2h77N.pdf [Accessed: September 2015]
- [17] Buros OK. The ABCs of Desalting. International Desalination Association; 1999. p. 31
- [18] Ayyash Y, Imai H, Yamada T, et al. Performance of reverse osmosis membrane in Jeddah phase I plant. *Desalination*. 1994;**96**:215-224

- [19] Banat F. Economic and Technical Assessment of Desalination Technologies. 2007. Available from: <http://www.desline.com/Geneva/Banat.pdf> [Accessed: September 2015]
- [20] Khawaji AD, Kutubkhanah IK, Wie J-M. Advances in seawater desalination technologies. *Desalination*. 1 March 2008;**221**:47-69
- [21] Darwish MA, El-Dessouky H. The heat recovery thermal vapour compression desalting system: A comparison with other thermal desalination processes. *Applied Thermal Engineering*. 1996;**16**:523-537
- [22] Tomaszewska M. Membrane distillation—Examples of applications in technology and environmental protection. *Polish Journal of Environmental Studies*. 2000;**9**:27-36
- [23] Rice W, Chau DSC. Freeze desalination using hydraulic refrigerant compressors. *Desalination*. 1997;**109**:157-164
- [24] Xu T. Ion exchange membranes: State of their development and perspective. *Journal of Membrane Science*. 15 October 2005;**263**:1-29
- [25] El-Dessouky H, Ettouney H. Study on Water Desalination Technologies. Prepared for ESCWA, United Nations; July 27, 2001
- [26] Mathioulakis E, Belessiotis V, Delyannis E. Desalination by using alternative energy: Review and state-of-the-art. *Desalination*. 5 Feb 2007;**203**:346-365

Experimental Study of Standard Aeration Efficiency in a Bubble Column

Florentina Bunea and Gabriel Dan Ciocan

Additional information is available at the end of the chapter

<http://dx.doi.org/10.5772/intechopen.76696>

Abstract

Water aeration is a major feature in many industrial applications, for example, hydraulic turbines, fish farms, water treatment, and so on. A key consideration is the efficiency of the aeration itself, that is, the effectiveness of the transfer of oxygen from air to water in relation to the energy consumed by injection. In this chapter, several configurations of the aerator are analyzed for overall efficiency optimization. Two different parameters are investigated (the arrangement of aeration apertures and aperture diameters between 0.2 and 1.6 mm) using aerators with perforated metal plates and, for comparison, ceramic and fritted (sintered) glass plates. For the arrangement of the apertures on the perforated metal plates, bubble coalescence and contraction coefficients are measured. Each configuration's results (K_L , SOTR, SAE) are compared and analyzed.

Keywords: standard aeration efficiency, oxygen transfer, bubble column, aerator, standard oxygen transfer rate, aeration optimization

1. Introduction

Oxygen transfer in water is a key component in environmental technologies, for example, in wastewater treatment, by virtue of the efficiency of the transfer of oxygen and the total costs of the air injection process, and water treatment itself is common in many industrial applications, for example, in the chemical, hydraulic, and nuclear industries, for which biphasic air-water flow characterization is required for each particular case. For example, for water treatment, energy consumption is the highest for aeration processes, as compressed air is an expensive working medium. The same behavior occurs in aeration for biological purposes, for example in fish farming, or in water aeration downstream of

hydraulic turbines, in which the design of the aeration systems (orifice diameter, configuration, operating conditions, and location) may significantly improve the quality of turbine aeration [1, 2]. The aerator design parameters are used to determine the best balance between oxygen transfer (volume of air injected and size and shape of generated bubbles) and energy consumption.

Aerators (spargers) can be made from porous ceramic or metallic materials, fritted (sintered) glass, or plastic, each having specific features in emitting bubbles to increase the contact surface between the gas and the liquid.

In literature, the volumetric mass transfer coefficient Kla was also obtained in situ, [3–6], for different configurations. As the configuration and operating conditions are far from this experiment, a direct comparison cannot be performed.

The main objective of this study is to optimize an aeration device, that is, to achieve the best dissolved oxygen (DO) transfer versus minimized energy consumption for injection. The classical experiment of an ascending bubble column was used to compare many injection devices. The aeration devices are mainly perforated metallic plates (MPs). Two parameters are studied: orifice size and arrangement. As a control, the active admission area is kept constant for all configurations. The injection air flow rate is controlled and the main aeration parameters (Kla and standard oxygen transfer rates [SOTR]) measured. Comparison of standard aeration efficiency (SAE) is also recorded. The efficiency results are compared with two other aerators, that is, a ceramic plate (CP) and a glass plate (GP). Finally, the optimized configuration in terms of SAE (best compromise between dissolved oxygen transfer and energy consumption for the air injection) is chosen.

2. Experimental setup to study the oxygen transfer of aerators

The setup [7] consists of a rectangular tank (**Figure 1**) with $L = 0.3$ m, $h = 0.88$ m, and hydrostatic load $H = 0.8$ m, filled with 79.2 l of water. In the tank (1) the aerator (2) equipped with interchangeable metallic plates (MPs) is immersed and tested. Upstream of it a flow-meter (3) is connected for measuring the air flow rate through the aerator and a differential manometer (5) for measuring the pressure drop across the aerator. The experimental setup is sized so that the walls of the tank do not affect the mass transfer of the air bubble column to the water ($L = 6 \cdot D$). With the peristaltic pump (6) the water is sampled in the middle of the tank, 2 cm from the wall, avoiding the air bubbles in the DO measuring cell. The water passes through the oximeter (7) and is then reintroduced into the system.

Five interchangeable perforated metallic plates with holes of $d = 0.2, 0.3, 0.5, 0.9, 1.6,$ and 2.4 mm (**Figures 2 and 3**) are tested. To avoid bubble coalescence, the holes are located $10 d$ apart, and to negate any influence of the contraction coefficient of the hole, its length is $5 d$. To increase the active emission area, and implicitly the interface area, the measurements are repeated for a second series of MPs with orifices placed $7 d$ apart. For both series of tests, the diameter of the MP is $D = 44.8$ mm. The aerator intake has a conical shape to ensure uniform air repartition at the intakes of the aeration holes.

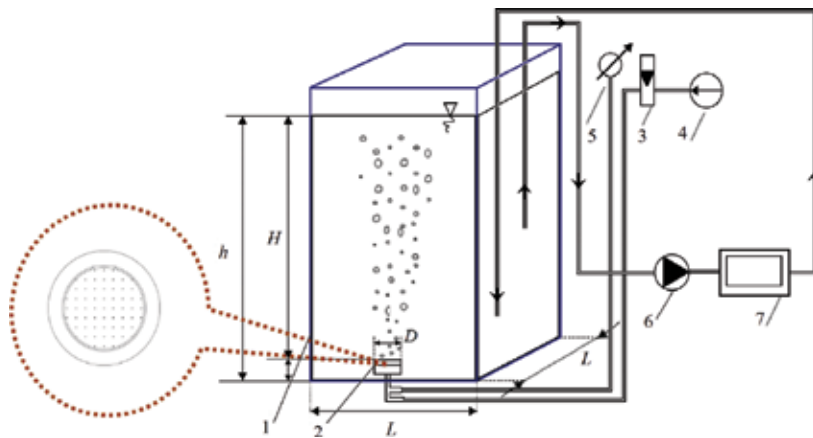


Figure 1. Experimental setup (1–tank, 2–aerator, 3–flow-meter, 4–air compressor, 5–manometer, 6–peristaltic pump, 7–oximeter, MP–interchangeable metallic plate).

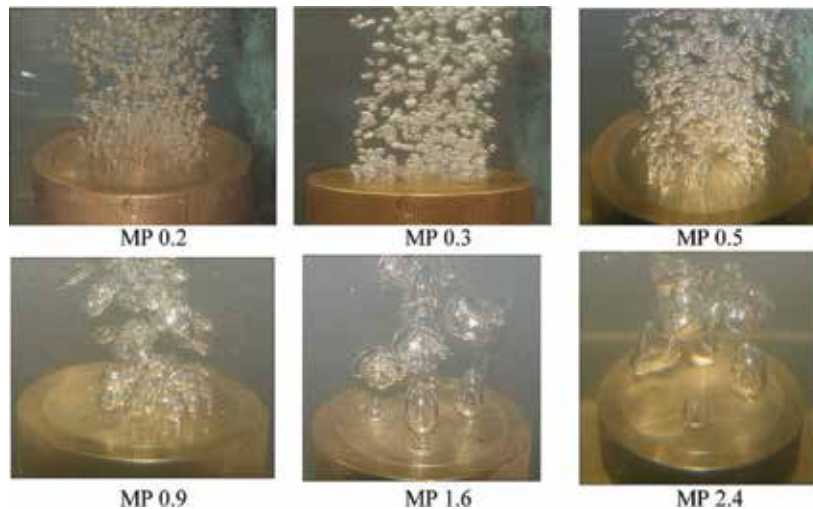


Figure 2. Tested metallic plates in operation.

In **Table 1** the geometric characteristics of MPs, series 1 and 2, are presented. The last column shows, in bold, the theoretical air-water interface area at the outlet of the bubble from the injection aperture. The design of MP in the second series increases the air-water interfacial area (a) at the bubbles outlet by up to 2.5 times (**Table 1**).

The initial radius (R_0) of an air bubble at its detachment from the hole of an aerated system immersed at a depth H is calculated from the balance of the Archimedean and superficial tension forces, neglecting the weight of the air in the bubble [8].

$$R_0 = \left(\frac{3}{4} \cdot \frac{d\sigma}{\rho g} \right)^{1/3} \quad (1)$$

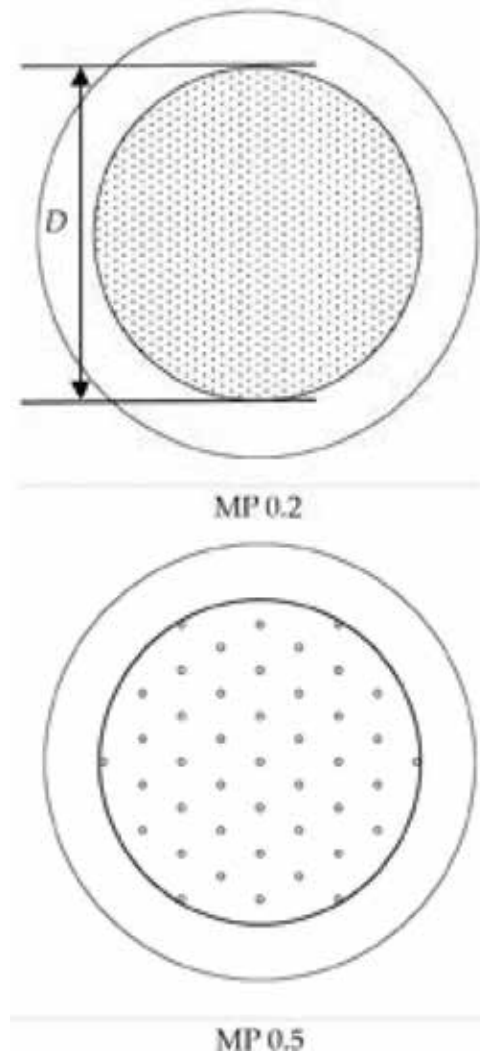


Figure 3. Layout of holes for 7d arrangement for 0.1 and 0.5 mm hole diameter.

The interface area (a) of the first swarm of bubbles is considered spherical at the time of detachment and is calculated with the relationship shown in Eq. (2). The active area of the intake of the air into water is calculated with the relationship (3).

$$a = n \cdot \pi R_0^2 \quad (2)$$

$$s = n \cdot \pi d^2 / 4 \quad (3)$$

The interface area (a) increases in the second series by up to 2.8 times (**Table 2**).

<i>d</i> (mm)		<i>N</i>		<i>R</i> ₀ (mm)		<i>s</i> (mm ²)		<i>s</i> ' (%)		<i>a</i> (mm ²)		$\frac{a_{S2}}{a_{S1}}$
S1	S2	S1	S2	S1	S2	S1	S2	S1	S2	S1	S2	
2.4	—	4	—	2.38	—	18.1	—	1.1	—	285	—	—
1.6	1.6	6	14	2.08	2.08	12.1	28.1	0.8	1.8	326	761	2.33
0.9	0.9	21	43	1.72	1.72	13.4	27.4	0.9	1.7	781	1599	2.05
0.5	0.5	61	151	1.41	1.41	12.0	29.6	0.8	1.9	1524	3772	2.47
0.3	0.3	177	414	1.19	1.19	12.5	29.3	0.8	1.9	3150	7367	2.34
0.2	0.2	385	951	1.04	1.04	12.1	29.9	0.8	1.9	5233	12,926	2.47

Table 1. Emission performance of the two series of metallic plates S1 and S2.

<i>MP</i>	<i>V</i> _{void} (l)	<i>n</i> _b (-)	ϵ (%)
MP 1.6	0.25	2953	0.347
MP 0.9	0.26	4601	0.361
MP 0.5	0.27	8449	0.375
MP 0.3	0.28	15,905	0.389
MP 0.2	0.29	27,403	0.403
MP 0.1	0.3	42,468	0.417

Table 2. Void fraction for the second series of plates at *Q* = 0.1 l/s.

For the theoretical evaluation of the interfacial area (*a*_i) of all the bubbles in the system an air flow rate *Q* = 0.1 l/s is injected in water. By measuring the contact time of air bubbles in water (*T*) and the sudden shutdown of the air supply, the void volume from the system is obtained: *V*_{void} = *T* · *Q*. The interfacial area of the all bubbles in the system is calculated using relationship (4)

$$a_i = n_b \cdot A_b = \frac{3TQ}{R_0} \tag{4}$$

The average global void fraction is calculated using relationship (5)

$$\epsilon = \frac{V_{void}}{V} 100. \tag{5}$$

The experimental results of the mass transfer of the two sets of plates are presented in the next chapter.

3. Volumetric mass transfer coefficient corresponding with energy consumption

To obtain the oxygen transfer the following configurations are tested:

- series 1 of five metallic plates (MP 0.2, MP 0.3, MP 0.5, MP 0.9, and MP 1.6);
- series 2 of two metallic plates (MP 0.2 and MP 0.5);
- a ceramic plate (CP) with volume porosity in the range 45–50%; and
- a fritted (sintered) glass plate (GP) with porosity controlled in the range 0.25–0.315 μm .

For all series of metallic plates, the following injected air flow rates are tested: $Q = 180, 360, 480, 600, 720, 960, 1140$ l/h. The results are then compared with the aeration performance of the CP and GP.

The method of measuring dissolved oxygen (DO) in clean water, according to the standard for measuring oxygen transfer in water [9], requires removing DO from water (using Na_2SO_3) and then reoxygenating up to at least 90% of the saturation concentration value. To obtain standard oxygen transfer rates (SOTR), the water in which testing takes place must be qualitatively equivalent to drinking water. Concentration of dissolved oxygen in time (C) is measured while maintaining constant air flow injected into the system. The measurements are repeated for each of the air flow rates with the abovementioned plates. After each set of measurements, the standard procedure is applied for the removal of DO from water and reoxygenation up to 90% of the saturation concentration value.

3.1. Processing of the experimental data

The following is an example of estimating the $K_L a$ and C_s parameters for the plate MP 1.6 operating at an injection air flow rate of $Q = 360$ l/h. The concentration of DO in time $C = f(t)$ is shown in the figure (Figure 4).

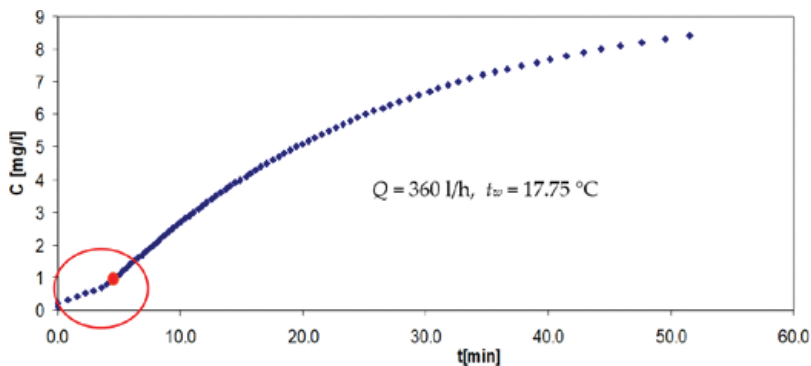


Figure 4. $C = f(t)$ and the inflection point detection.

In the event of an inflection point (marked in red in **Figure 4**), it is allowed to truncate the curve up to the concentration at $C = 1.5 \cdot C_i$, where C_i represents the concentration corresponding to the inflection point. If the curve does not have an inflection point, the data can be truncated to 20% of the C_s .

To obtain time delay, the remaining data are extrapolated through the intersection of the fitted curve at the time axis (**Figure 5**). The primary data are corrected by shifting the curve to the initial moment that the concentration of dissolved oxygen is zero—see **Figures 5** and **6**.

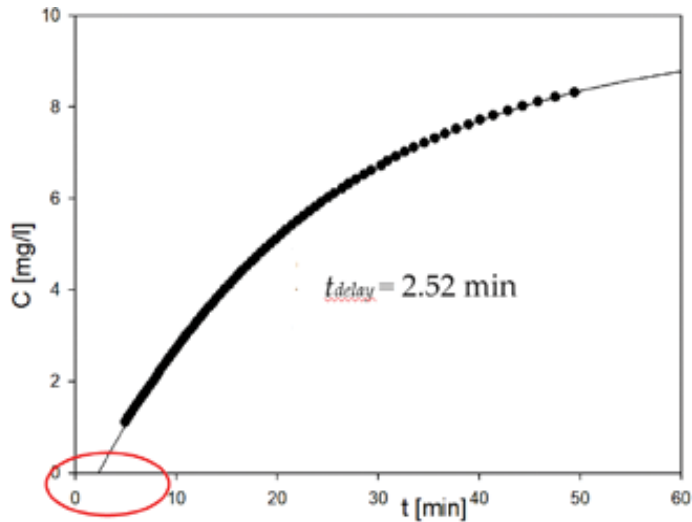


Figure 5. Extrapolation of experimental data to obtain the delay time, for MP 1.6, at $Q = 360$ l/h.

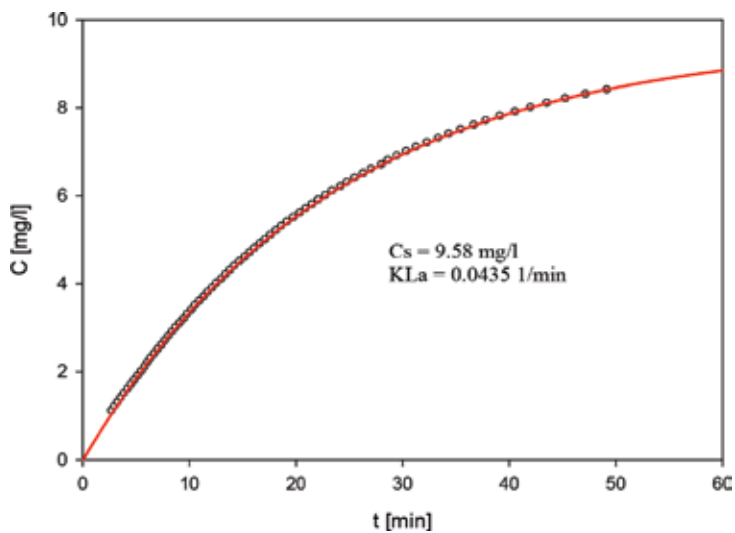


Figure 6. Estimation of KLa and C_s parameters by non-linear regression for MP 1.6, at $Q = 360$ l/h.

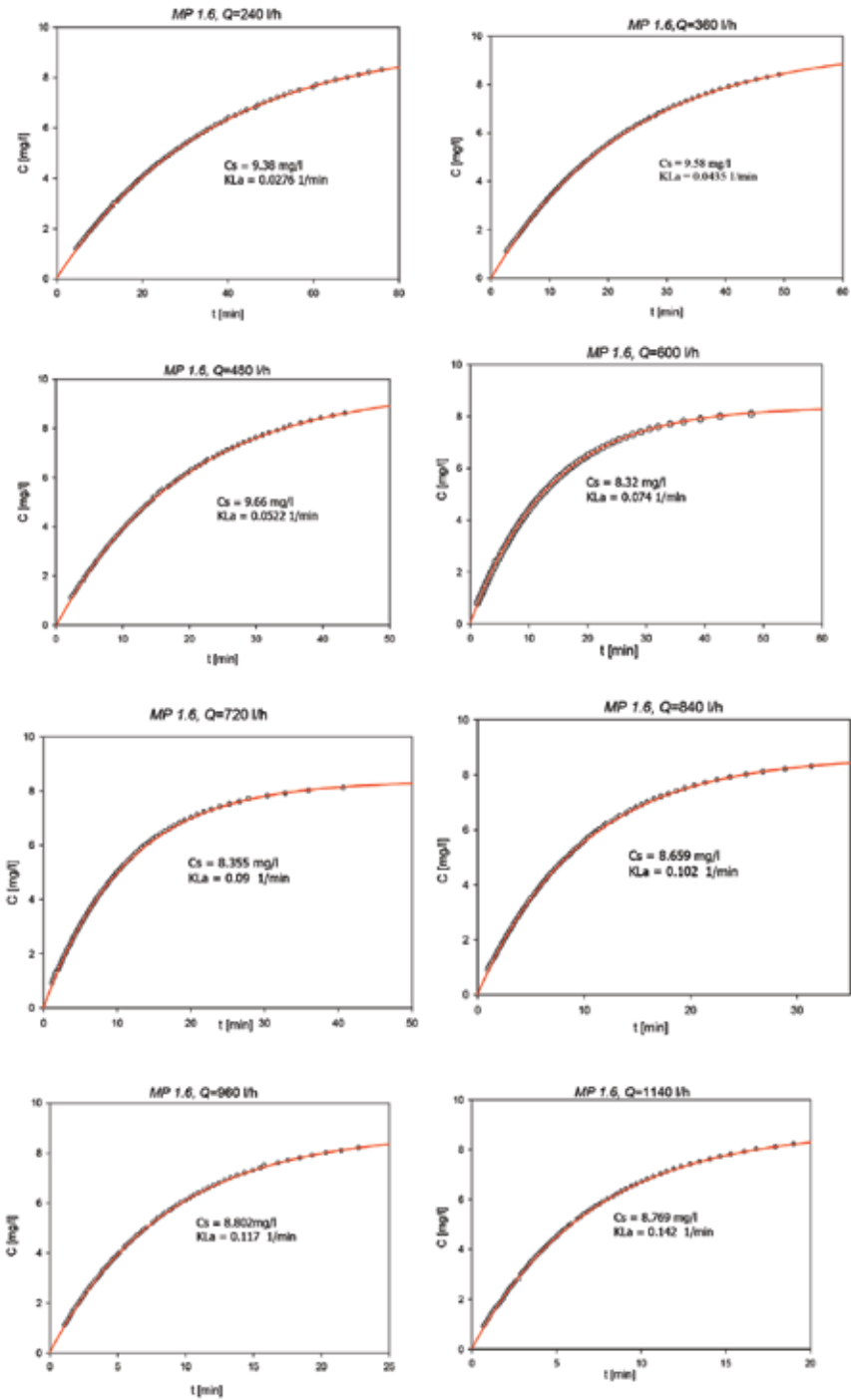


Figure 7. Estimation of KLa and C_s parameters by non-linear regression for MP 1.6.

The chart (Figure 5) is replotted with corrected data using the mathematical model described by Eq. (6):

$$C = C_s - (C_s - C_0) e^{-k_{La}t} \quad (6)$$

The K_{La} and C_s parameters are obtained (Figure 6).

The procedure is repeated for all the test plates for the air flow rate range: $Q = 96\text{--}1140$ l/h.

Figures 7 and 8 show the graphs for K_{La} and C_s estimation of MP 0.5 and MP 1.6 at injected air flow rates, $Q = 240\text{--}1140$ l/h.

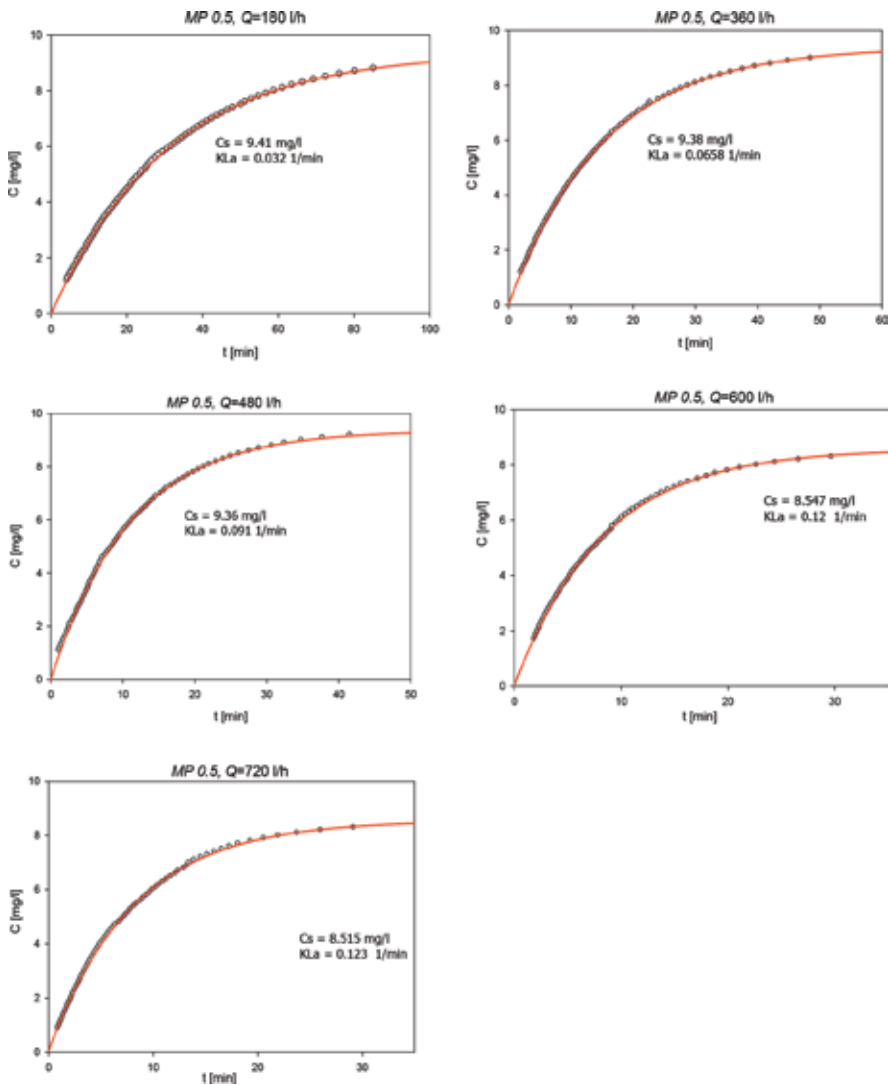


Figure 8. Estimation of K_{La} and C_s parameters by non-linear regression for MP 0.5.

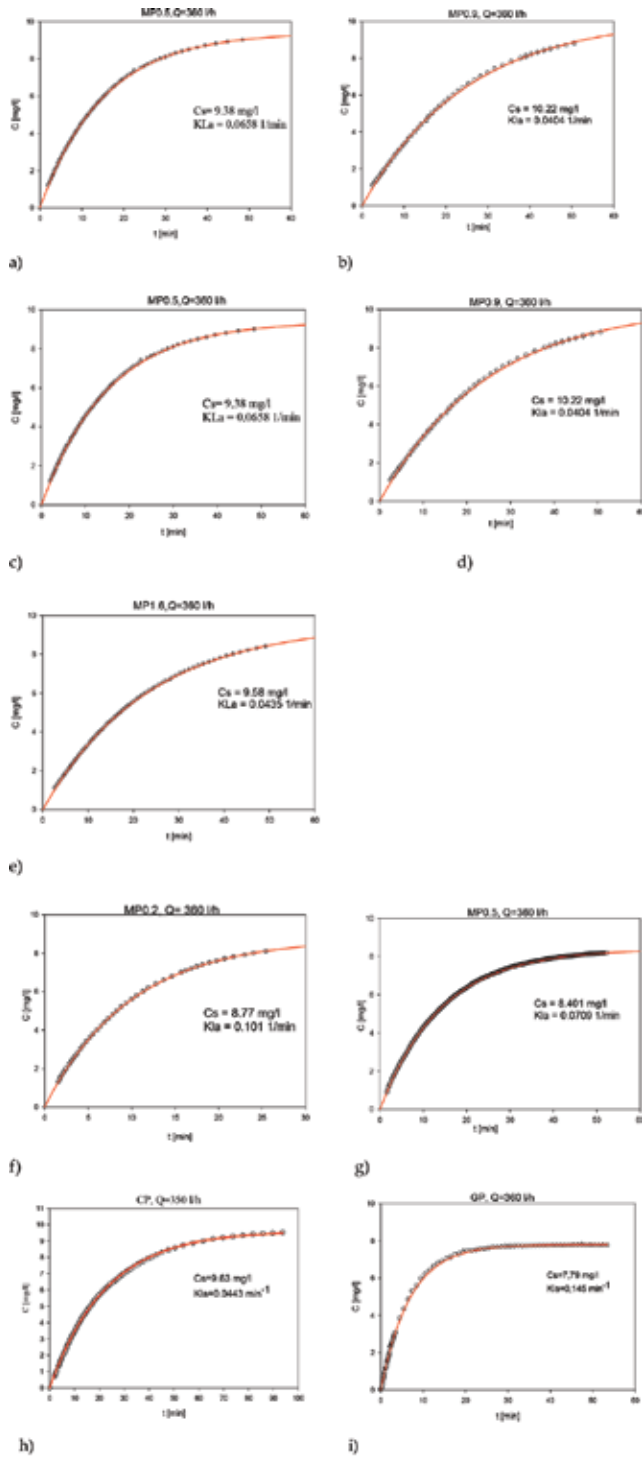


Figure 9. Estimation through nonlinear regression of KLa and C_s parameters for $Q = 360$ l/h. (a) MP 0.2, series 1. (b) MP 0.3, series 1. (c) MP 0.5, series 1. (d) MP 0.9, series 1. (e) MP 1.6, series 1. (f) MP 0.2, series 2. (g) MP 0.5, series 2. (h) Ceramic plates with volume porosity in the range 45÷50%. (i) Glass plates with porosity controlled in the range 0.25÷0.315 μ m.

The regression curves for the estimated parameters K_{La} and C_s for all nine tested plates at the injection flow rate $Q = 360$ l/min are presented for comparison in **Figure 9**.

From the aeration point of view (dissolved oxygen transfer), an improvement is observed between the first and second series of the MP, the second giving a better performance as the interphase area is higher. However, the MP aeration characteristics K_{La} and C_s are lower compared with CP and GP. GP provides the best aeration characteristics.

Krishna and van Baten [10] illustrate the influence of column diameter on K_{La} (**Figure 10**), assuming that a homogeneous flow regime prevails (with dispersion consisting of 5 mm of small-sized bubbles). In this study, the diameter of the aeration device is equal to the diameter of the tank. A strong reduction of aeration characteristics is observed. The bubble column is confined by the walls and the flow velocity induced in the ascending column produces an increased velocity in the air column that tends to accelerate the bubbles in the central core, reducing gas-liquid contact time.

In our study the water column is higher than the bubble column, $L/D = 6.8$, in order not to have the water column constrained by confinement. For this reason, K_{La} is less than in the Krishna experiment, for equivalent bubble diameters (MP 0.5) around 5 mm.

The initial theoretical ascending velocity of the bubbles can be calculated using:

$U = Q/A$, where Q [m^3/s] is the air flow rate through the aerator and A [m^2] is the emission surface of the plate (active area). The hypothesis of the uniform initial ascending velocity is a rough estimation, which is more realistic for MP (because of uniform orifice losses) but less so for GP and CP. Krishna and van Baten [10, 11], obtained from CFD, using the effective area of transfer, with large bubbles corresponding to 20 mm are represented in (**Figure 11**) by filled circles, and the 5 mm sized bubbles, are represented by filled squares. The open circles relate to experimentally determined values and U_{trans} is the transition velocity.

A decrease in the K_{La} coefficient is observed with an increasing bubble diameter, as transfer performance is related to the interfacial area (for the same air flow rate). However, it is observed that K_{La} is comparable for two experiments. The difference is explained by the limitation of the bubble column size and the acceleration of the bubble column in Krishna's experiment.

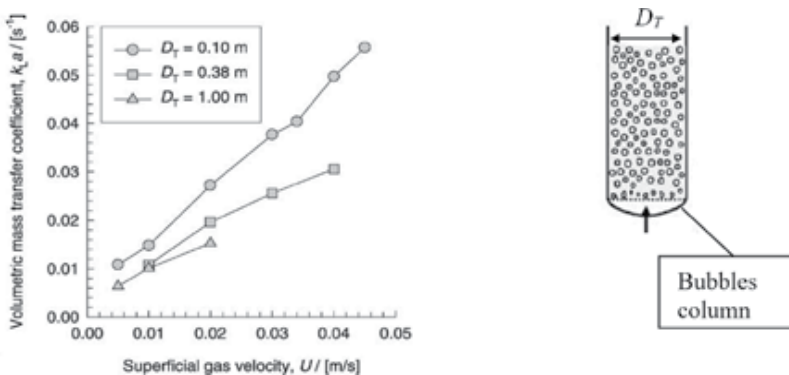


Figure 10. Influence of column diameter D_T (by numerical simulations) on K_{La} coefficient for operation in the homogeneous flow regime [10].

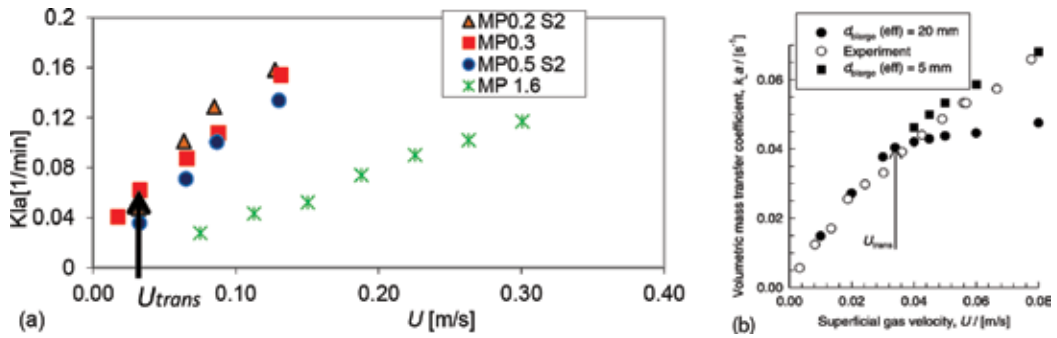


Figure 11. Volumetric mass transfer coefficient as a function of U , from the homogeneous to the heterogeneous flow regime, (a) our experiments, (b) Krishna experiment's [9].

4. Air flow influence on the aeration efficiency

The experimental data were post-processed following standard procedures [9] and reduced to the same temperature and pressure conditions ($t_w = 20^\circ\text{C}$ and $p_{atm} = 1 \text{ atm}$) in order to ascertain the influence of hole size on the aeration efficiency.

As per the standard process the following steps was considered:

- volumetric mass transfer coefficient, estimated by regression and corrected at 20°C

$$Kla_{20} = KLa \cdot \theta^{120-t} [1/\text{min}] \tag{7}$$

- concentration of DO at the measuring point, at saturation, corrected at temperature 20°C , at standard pressure 101 kPa, and relative humidity conditions are 100%

$$C_{s20} = C_s \left(\frac{1}{\tau \Omega} \right) \tag{8}$$

- standard oxygen transfer rate (SOTR)

$$SOTR = kla_{20} \cdot C_{s20} \cdot V [\text{mg}/\text{min}] \tag{9}$$

- standard oxygen transfer efficiency (SOTE)

$$SOTE = \frac{SOTR}{W_{O_2}} [-] \tag{10}$$

- standard aeration efficiency (SAE)

$$SAE = \frac{SOTR}{P} [\text{kg}_{\text{OD}}/\text{kWh}] \tag{11}$$

The power consumed for the injection of air through the aerator

$$P = Q \cdot (dp + \rho gH)/1000 \quad [\text{kW}] \quad (12)$$

Figure 12 shows the pressure losses measured for all MPs, CPs, and GPs. The injection losses on MPs are 10 times inferior to the CPs and GPs. The losses decrease with increasing diameter of the orifice but in a reduced report compared to CPs and GPs. The arrangement of the holes plays a role, too, with the second series of MPs exhibiting smaller losses at the point of air injection.

Aeration parameters compared with CPs and GPs from the two series of MPs are presented in **Figures 13–18**. The ceramic plate has volume porosity in the range 45–50% and the fritted (sintered) glass plate has a porosity which is controlled in the range 0.25–0.315 μm .

These experiments show that increases in the air flow rate lead to increased dissolved oxygen transfer and K_La up to a certain value, after which K_La remains constant. Increasing the air flow rate induces the losses of air admission increases. In such as way the maximum aeration and minimum energy consumption is optimized, reflected by SAE (**Figure 18**).

Following this analysis, the MP gives the best results compared to the equivalent configurations in CP or GP. The pressure losses are 10 times less important compared with the CP and GP. Reducing the distance between the holes from 10 to 7 diameters, increasing the number of holes for the same active surface, and thus reducing the bubble size lead to an increase in the air-water contact surface and the retention time in water and thereby improves the transfer of dissolved oxygen.

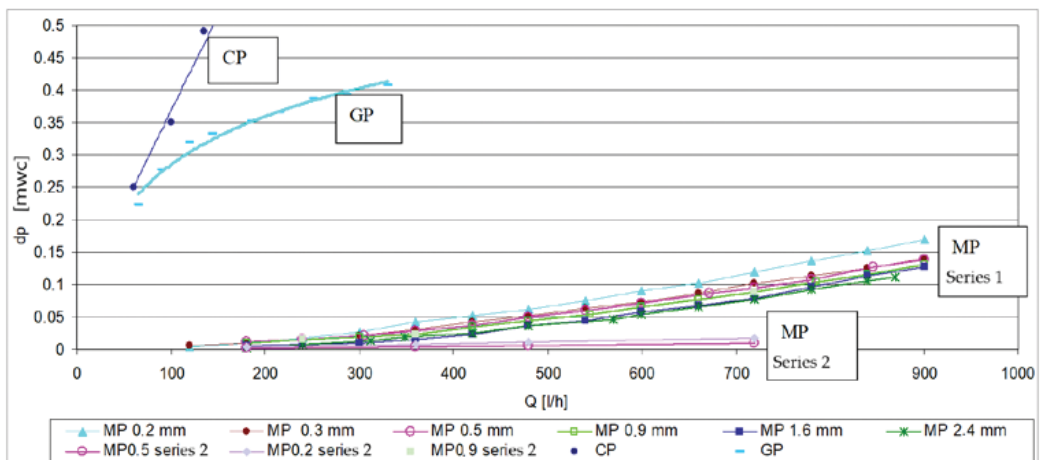


Figure 12. Pressure drop on the aerator variation for different types of plates (MP series 1, MP series 2, ceramic plate CP and glass plate GP).

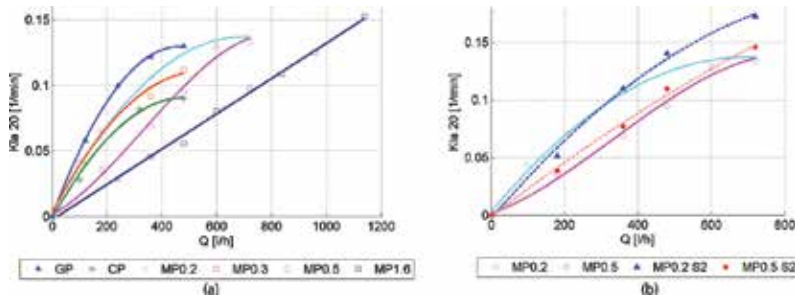


Figure 13. K_{la20} variation function of the air flow rate under standard conditions and comparison between the two MP series (right side).

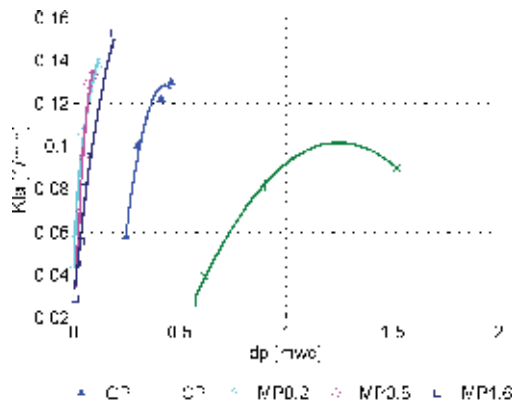


Figure 14. K_{la} variation function of aerator pressure drop for MP and comparison with GP and CP.

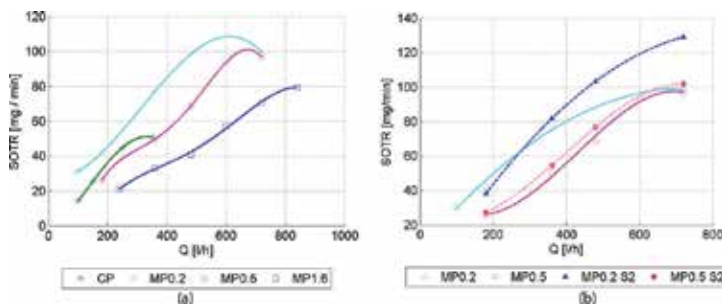


Figure 15. Standard oxygen transfer rate (oxygenation capacity) variation function of injected air flow rate.

Experimental 2D particle image velocimetry (PIV) measurements, with uniform background lighting and laser-induced fluorescence (LIF) of the tracking particles, were performed in order to characterize the air-water biphasic flow and the 2D bubble column rising velocity in static water—see works by Murgan et al. [12]. For complete characterization of the flow, the

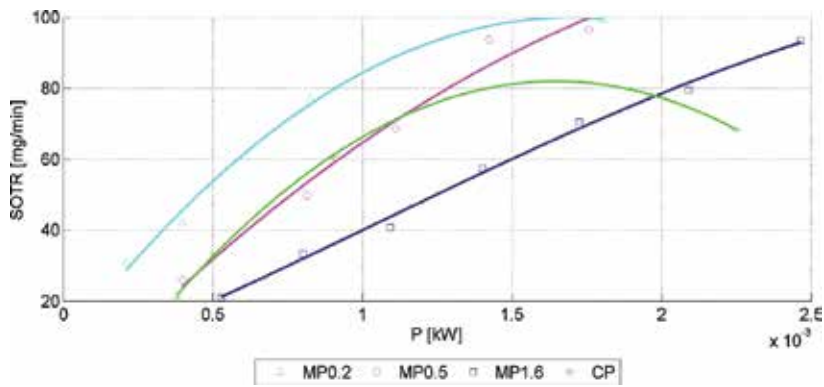


Figure 16. Standard oxygen transfer rate variation function of the power consumed for the air injection through the aerator.

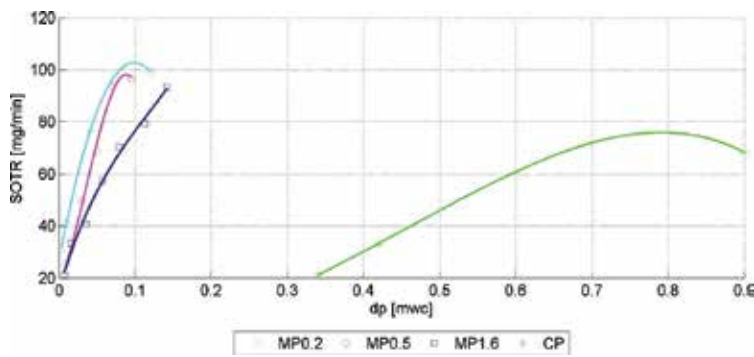


Figure 17. Standard oxygen transfer rate variation function of the aerator pressure drop.

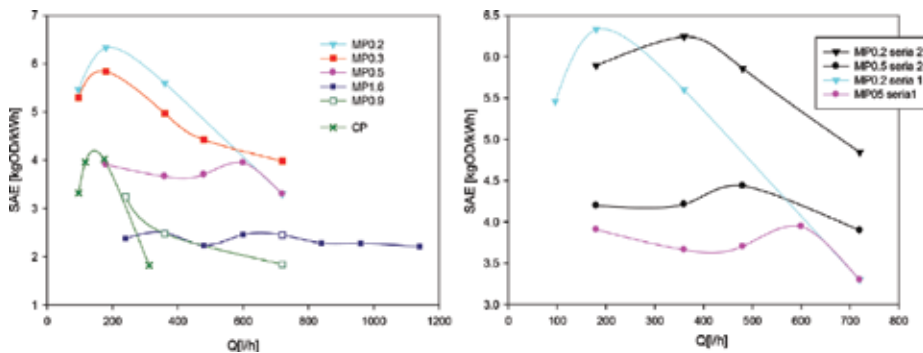


Figure 18. Standard aeration efficiency at different injection air flow rates. Comparison between the two series of MP (right side).

velocity field induced by the column of bubbles and the bubbles features are simultaneously determined using image processing technics. The bubbles features include: ascension velocity, diameter variation, interfacial area and shape factor.

5. Conclusions

This chapter presents an experimental study for the global optimization of aeration in the industrial configuration. For optimization two main parameters were considered: aeration performance (dissolved oxygen transfer) and energy consumption for the air injection.

Was considered many injection devices: two series of metallic plates with different designs (the arrangement of aeration holes, hole shapes, and diameter) and hole diameters between 0.2 and 2.4 mm, ceramic plates, and glass plates in an air bubble column in water. The investigations were performed for the following air flow rates: $Q = 180, 360, 480, 600, 720, 960, 1140$ l/h. The aeration performances were obtained, using the procedure of the standard procedure ASCE 2-91/1993 (K_{La} and SOTR), and compared with other literature results. The results are coherent for the tendencies and the differences were explained.

Based on these results and injection loss measurements, the SAE—standard aeration efficiency—was calculated for all plates and global efficiency curves were plotted.

Taking into account these parameters in an aerator design, and optimizing the total efficiency, allows for an efficient deployment of aeration devices in industrial systems. As variations in efficiencies for dissolved oxygen transfer, or losses, in different aeration devices can be greater than a factor of 10, the findings of this optimization study are significant for achieving the best design of aeration systems for hydraulic turbines and in water treatment and so on in regulation to the specific needs and capacity of each application (available air flow rate, pressure of injection, aeration need, etc.).

This study shows the importance of the optimization of the aerator device in terms of materials, aperture arrangement, aperture shape, aperture dimension for the specific conditions of each application (air flow rate, pressure gradient, emplacement of the aeration device), and for the best global efficiency—best compromise between the energy needed for the injection of the air and the quantity of dissolved oxygen obtained by the aeration process.

In the next step, these results and the detailed bubble flow morphology [12] will be used to validate numerical simulations for dissolved air transfer, to realize the sparger optimization by numerical calculations.

Acknowledgements

This work was performed in the frame of the project NUCLEU PN18240202, ctr. 24N/2018 ElectroEchipaMat, financed by the Ministry of Research and Innovation.

Appendices and nomenclature

A_b [mm ²]	area of an air bubble considered spherical
a [mm ²]	interfacial area of the first swarm of bubbles

a_i [mm ²]	interfacial area of the all bubbles in the system
C [mg/l]	concentration of dissolved oxygen at the moment t
C_0 [mg/l]	concentration of dissolved oxygen at the moment $t = 0$
C_{st} [mg/l]	concentration of dissolved oxygen at saturation, at the surface, at working temperature, at standard pressure of 1 atm, and relative humidity conditions of 100%
C_s [mg/l]	concentration of dissolved oxygen at saturation (estimated by non-linear regression) at working temperatures
C_{s20} [mg/l]	concentration of dissolved oxygen at saturation, corrected at temperature 20°C, at standard pressure of 1 atm, and relative humidity conditions of 100% ($C_{20} = 8.62$ mg/l)
CP	ceramic plate with volume porosity in the range 45–50%
D [mm]	diameter of the plate MP ($D = 44.8$ mm)
DO	dissolved oxygen
d [mm]	diameter of a hole in the plate MP
dp [mwc]	pressure drop on the aerator
GP	fritted (sintered) glass plate with porosity controlled in the range 0.25–0.315 μm
H [m]	hydrostatic head on aerator ($H = 0.8$ m)
g [m/s ²]	gravity
Kla [1/min]	volumetric mass transfer coefficient (estimated by regression)
Kla_{20} [1/min]	Kla , corrected at temperature 20°C
$Klat$ [1/min]	Kla , volumetric mass transfer coefficient at the moment t
Q [m ³ /s]	air flow rate injected through the MP
Q_s [m ³ /s]	air flow rate at standard conditions: $Q_s = \frac{Q \cdot 273.15}{(273.15 + t_0)}$
MP 0.1–2.4	interchangeable perforated metallic plates with circular holes of 0.1–2.4 mm
N	number of holes on an MP
n_b	number of bubbles in the system $n_b = \frac{V_{\text{out}}}{V_b}$
P [W]	the power consumed for the injection of air through the aerator
P_b [Pa]	atmospheric pressure at the time of testing
P_s [Pa]	standard atmospheric pressure (1 atm)
R_0 [m]	the initial air bubble radius
r_0 [m]	radius of the hole

t [s]	time
t_0 [°C]	air temperature at sampling time
t_w [°C]	water temperature at sampling time
T [s]	air-water contact time
s [mm ²]	active area of intake of the air into the water (sum of the areas of all holes from a an MP)
s' [%]	active area of intake of the air into the water from an MP
SAE [kgO ₂ /kWh]	standard aeration efficiency
$SOTE$ [-]	standard oxygen transfer efficiency
$SOTR$ [mg/min]	standard oxygen transfer rate
U [m/s]	theoretical ascending velocity of the bubbles
V [l]	water volume in the tank ($V = 72$ l)
V_b [l]	volume of an air bubble considered spherical
V_{void} [l]	void volume from the system
W_{O_2} [kg/s]	mass flow rate of oxygen from the air stream ($W_{O_2} = 0.2765 Q_s$)
Δp_{tot} [Pa]	total pressure drop (including hydrostatic head), $\Delta p_{tot} = (\Delta p + H)\rho g$
ε [%]	void fraction
$\tau = C_{st}/C_{20}$ [-]	temperature correction factor
σ [N/m ²]	air-water surface tension coefficient
ρ [kg/m ³]	water density
θ [-]	empirical temperature correction factor ($\theta = 1.024$, unless another value is proven experimentally)
Ω [-]	pressure correction factor, $\Omega = \frac{P_b}{P_s}$

Author details

Florentina Bunea^{1*} and Gabriel Dan Ciocan²

*Address all correspondence to: florentina.bunea@icpe-ca.ro

1 National Institute for R&D in Electrical Engineering, ICPE-CA, Romania

2 Laboratoire de Machines Hydrauliques, Laval University, Québec, Canada

References

- [1] Bunea F, Bucur DM, Dumitran GE, Ciocan GD. Water quality in hydroelectric sites. In: Voudouris K, ed. *Ecological Water Quality-Water Treatment and Reuse*. InTech; 2012. pp. 391-408. DOI 10.5772/32078
- [2] Bunea F, Ciocan GD, Nedelcu A, Bucur DM, Dunca G, Chihaiia R. Experimental setup for the study of new aeration devices in hydraulic turbines. *Environmental Engineering and Management Journal*. 2017;**16**(5):1033-1040
- [3] Fayolle Y, Gillot S, Cockx A, Bensimhon L, Michel R, Alain H: In situ characterization of local hydrodynamic parameters in closed-loop aeration tanks. *Chemical Engineering Journal*. 2010;**158**:207-212. DOI: 10.1016/j.cej.2009.12.043
- [4] Gillot S, Capela S, Héduit A. Alpha Factor and In-Process Efficiency in Horizontal-Flow Aeration Basins, Aeration Conference: Aeration in Deep Basins and Sequencing Batch Reactors. Rome: ITA; 4 May 1998. 11 p
- [5] Giovannettone JP, Gulliver JS. Gas transfer and liquid dispersion inside a deep airlift reactor. *AIChE Journal*. 2008;**54**(4):850-861. DOI: 10.1002/aic.11449
- [6] Behin J, Dolati F, Vasseghian Y. Estimation of mass transfer coefficient in different regions of forced circulation airlift loop reactor. In: 7th International Congress on Chemical Engineering; 21-24 November 2011; Kish, Iran
- [7] Bunea F, Oprina G, Baran G. Experimental setup for the study of the bubble diffusers hydrodynamic performance. Patent RO 125997 B1, 28.02.2012
- [8] Băran G, Băran N. Hidrodinamica bulelor generate de difuzori porosi (hydrodynamics of bubbles generated by porous diffusers). *Revista de Chimie*. 2003;**54**(5):436-440
- [9] ASCE (Standard Measurement of Oxygen Transfer in Clean Water). *Measurement of Oxygen Transfer in Clean Water*. 2nd ed. American Society of Civil Engineers. Standard no. ANSI/ASCE 2-91/1993. ISBN 087262885x. 45 p
- [10] Krishna R, van Baten JM. Mass transfer in bubble columns. *Catalysis Today*. 2003;**79-80**: 67-75. DOI: 10.1016/S0920-5861(03)00046-4
- [11] Krishna R, Van Baten JM, Urseanu MI. Three-phase Eulerian simulations of bubble column reactors operating in the churn-turbulent regime: A scale up strategy. *Chemical Engineering Science*. 2000;**55**(16):3275-3286. DOI: 10.1016/S0009-2509(99)00582-5
- [12] Murgan I, Bunea F, Ciocan GD. Experimental PIV and LIF characterization of a bubble column flow. *Flow Measurement and Instrumentation*. 2017;**54**:224-235. DOI: 10.1016/j.flowmeasinst.2017.02.004

Extraction and Use of Plant Biopolymers for Water Treatment

Jesús Epalza, Jhoan Jaramillo and Oscar Guarín

Additional information is available at the end of the chapter

<http://dx.doi.org/10.5772/intechopen.77319>

Abstract

The action of promoting the removal of particles in water requires coagulant substances, which destabilize the equilibrium of the mixture in aqueous solution; this is needed to perform the coagulation and flocculation operations, in the treatment of drinking water and wastewater; especially for the removal of solids with diameters smaller than 0.2 mm; this operation is carried out with chemical compounds capable of breaking the ionic stability of a mixture and segregating the solids that cannot be separated without this operation; The plants tested to be used as coagulants or flocculants have had a traditional use, which indicates their ability to carry out the separation of solids. The plants described in this chapter are *Melocactus* sp., *Opuntia* sp., *Stenocereus griseus*, *Cereus forbesii*, *Aloe arborescens*, *Aloe vera*, and Kabuli chickpea (*Cicer arietinum* L.), of these plants have been used different parts, either their stems, their fruits, or other parts of the plant that have demonstrated a coagulating or flocculating capacity.

Keywords: biopolymer, coagulation, flocculation, turbidity and color

1. Introduction

Conventional water treatment processes include coagulation and flocculation, especially that which is chemically assisted, for both drinking water and wastewater. The removal capacity of these operations is effective and with a speed that could have been used, especially with waters that have high concentrations of organic matter, for this purpose, reagents have been used such as aluminum sulfate, which is usually obtained from the reaction of aluminum hydroxide with sulfuric acid [1]. Another reagent used is ferric chloride, which is obtained by the reaction of

chlorine gas on heated iron [2]; and a reagent used in recent years is the aluminum polychloride obtained by the reaction of aluminum with hydrochloric acid in aqueous solution [1].

The reactions associated with the coagulants are determined by some parameters such as the pH, the temperature of the water, and the concentrations of the solids that are going to be complexed to form flocs that can be separated by density difference inside the mixture. When the flocs are separated from the mixture, sludge is generated that must be thickened and then disposed of, within a waste management plan; these residues will have a high concentration of aluminum and iron, respectively, according to the type of coagulant used, whether it be aluminum sulfate, aluminum polychloride, or ferric chloride. The final disposal of these sludges is usually difficult, because of the load of aluminum or iron as they are considered toxic for the soil in high concentrations[3].

These disposal problems of the sludge, which generally has a high concentration of organic matter, generate environmental impacts when they are discharged into soils or bodies of water, changing the natural microbiota and affecting the species that have contact with high concentrations of aluminum and iron. To overcome this difficulty, different products of vegetable origin have been studied, which have properties similar to those of aluminum or iron compounds, generate coagulation and flocculation, but with organic compounds, are part of the natural components of plants come, as is the case of *Melocactus* sp., *Opuntia dillenii*, *Stenocereus griseus*, *Cereus forbesii*, *Aloe arborescens*, *Aloe vera*, and Kabuli chickpea (*Cicer arietinum* L.). These plants have shown an activity for the flocculation of substances with small particle size, below 0.2 mm, which generally cannot be separated by natural sedimentation [3].

The sludge derived from the coagulation and flocculation processes with plant extracts has a completely organic composition, which means that they can be digested by microorganisms and transformed into carbon, nitrogen, and phosphorus substances that can be incorporated into the corresponding biogeochemical cycles, with absence of toxic metals for the soil [4], or with safe concentrations for this vital resource. This technological alternative transforms water treatment into a less aggressive process with the environment, taking into account that most of the waste generated in drinking water and domestic waste treatment is sludge.

The extraction systems of plant biopolymers have different methodologies, which are easy to apply, proven, and are part of already standardized unit operations. Taking into account that different parts are harvested from each plant, we must understand that for most of the plants, their use is of the majority of the biomass, whereas when we speak of Kabuli chickpea (*Cicer arietinum* L), we are using only their seed, which diminishes its use, taking into account the weight ratio of the plant and the mass used for the preparation of the coagulant.

The operations developed to determine the efficiency of each plant extract in the coagulation and flocculation are defined within the established for jar tests and some of them have Z potential measurements (measure of the magnitude of the repulsion or attraction between the particles).

2. Selection of plants with the potential to produce biopolymers for coagulation and water flocculation

Plants with the capacity to generate biopolymers with coagulant and flocculant uses have been under study during the last decades, especially *Moringa oleifera*, *Opuntia* spp., *Cicer arietinum* [5], and others that have demonstrated coagulant capacity, as part of the traditional empirical knowledge of indigenous communities [6].



Figure 1. *Stenocereus griseus*. Source: <http://cactiguide.com/cactus/?genus=Stenocereus&species=griseus>.



Figure 2. *Cereus forbesii*. Source: http://www.kakteensammlungholzheu.de/en/cereus_forbesii.html.



Figure 3. *Aloe arborescens*.

The selected plants took a part of those referenced and others of those present in semi-arid regions in Colombia, such as La Guajira in northern Colombia and the banks of the Chicamocha River, in the northeastern region. The species not studied are *Stenocereus griseus* (**Figure 1**), *Cereus forbesii* (**Figure 2**), *Aloe arborescens*, and *Aloe vera*; and one already studied is the Kabuli chickpea (*Cicer arietinum* L.) [6].

In the case of *Opuntia* sp., they are used to be present in the Colombian regions already named and sufficiently studied, in the same way *Aloe vera* and *Aloe arborescens* were selected (**Figure 3**). Kabuli chickpea (*Cicer arietinum*) is reviewed with studies already elaborated by other authors [7]. It should be noted that some species of *Opuntia* spp. are used as part of the animal and human diet in communities of northeastern Colombia, in semidesert areas [8].

To have a better selection, we reviewed the massive presence of these plants and that they were not part of the list of plants in danger of extinction, to be able to access their manipulation.

3. Biopolymer extraction methodologies

3.1. Extraction of the plants *Melocactus* sp., *Opuntia dillenii*, *Stenocereus griseus*, *Cereus forbesii*, *Aloe arborescens*, and *Aloe vera*

The extractions of each plant have particularities, taking into account the usable parts in the search of their coagulating capacity. The extractions are segregated into two types: the plants that are used in all their foliage are *Melocactus* sp. (**Figure 4**), *Opuntia dillenii* (**Figure 5**) [9], *Stenocereus griseus*, *Cereus forbesii*, being belonging to the family Cactaceae and the other part corresponds to *Aloe arborescens* and *Aloe vera*, belonging to the Xanthorrhoeaceae family, with superior *Aloe* classification.



Figure 4. *Opuntia* sp. Source: <http://www.fichas.suculentas.es/Almacenfichas/903/903.html>.



Figure 5. *Aloe vera*. Source: <http://www.fichas.suculentas.es/Almacenfichas/903/903.html>.

For the *Cactus* and *Aloe* species, an extraction methodology was used with different operations that are:

- Selection of parts of the plant for cutting: The operation of cutting parts of the plant is done taking into account mature parts, with the presence of thorns in the case of cacti, with a hard external surface, similar to the criteria used for the animal or human consumption of

Opuntia spp. [10]. In the case of *Aloe* species, the maturity of the leaves is considered, with the presence of perimeter spines. This shows the possibility of isolating the crystals of the plant.

Figure 5 shows a part of the penca or cladodes of a cactus *Opuntia* sp., with skin and thorns, but the part to be used is the vascular tissue of the plant, eliminating skin and spines [11].

For the sampling of the species of *Aloe* (**Figure 6**), garden plants were considered, which are cultivated in a homemade way, taking into account the age of the plant, as it must have enough leaves with enough crystals, and it must not present any evidence of contamination or parasites, especially the characteristics of the green color of the leaves, absence of external insects, and total absence of organisms associated with diseases of the plant.

- Cut and transport to the laboratory: The cutting of the parts of the plant takes measurements (**Figure 7**), to then make a transport to the site of obtaining the coagulant. The transport must be carried out in refrigeration, to avoid possible contamination with environmental fungi or other organisms that can significantly change the composition of the parts obtained.
- Weighing of the gross material: The weighing of the material is carried out on a 25-kg scale, to determine the weight of the sample taken and then determine its performance according to its humidity.
- Cutting of thorns and removal of the bark: To perform the extraction of the coagulant, the cut parts are taken and the thorns are removed (**Figure 8**), and the skin of the cacti, also



Figure 6. *Melocactus* sp. Source: <http://www.tephroweb.ch/kuas/melo.htm>.



Figure 7. *Opuntia* sp. and *Cereus forbesii* samples. Source: authors.



Figure 8. Removal of thorns. Source: authors.

called epidermis, which is the external hard part of the pads or cladodes, in the case of cactus and leaves in the case of *Aloe* species.

- Cutting of clean material: In order to follow the extraction process, the tissue of the plants is cut. This is done to improve the moisture loss of the plant, increasing the contact surface with the atmosphere (**Figure 9**).

- **Drying the pieces:** The drying of the material is carried out outdoors (**Figure 10**). It is important to note that the region in which these operations are carried out is of a warm tropical climate with low humidity, in which the temperature ranges between 20 and 35°C with relative humidities between 50 and 70% on average.
- **Weighing of dehydrated material:** The material is kept outdoors, taking care that it is not hydrated by rain, the drying time is between 48 and 96 h depending on the temperature and relative humidity of the place where they are dried.
- **Grinding of the material:** The grinding of the dried material is done with a food processing device and then it is passed through a mill that pulverizes the material.



Figure 9. Cutting of the plants. Source: authors.



Figure 10. Desiccation of the specimens. Source: authors.

The final characteristics of the material are similar to the raw materials used in the coagulation and flocculation process, that is, a presentation similar to the presentation of type A and B aluminum sulfate and aluminum polychloride, in their solid presentations, the liquid presentation is not sought because it is an organic material with nutritional characteristics for filamentous fungi and bacteria, which would require a procedure for its sterilization, and any application of excessive heat, a degradation of the biopolymers will be carried out, condition that impairs its performance in coagulation.

- **Material screening:** The material after being macerated is taken to a 1-mm sieve (**Figure 11**), which separates the thick parts that cannot be diluted efficiently in aqueous solution. This characteristic is based on the solubility of complex organic substances, such as the vascular tissue of these cacti and *Aloe* plants.
- **Weighing of the material of interest:** The material obtained from the plants *Melocactus* sp., *Opuntia dillenii*, *Stenocereus griseus*, *Cereus forbesii*, *Aloe arborescens*, and *Aloe vera* is weighed to have a reference of its performance in relation to weight to weight, with respect to its use.

3.2. Extraction of Kabuli chickpea coagulant (*Cicer arietinum* L.)

The seeds of the anionic coagulant Kabuli Garbanzo (*Cicer arietinum* L.) were selected and then the following procedures were performed.

- **Washed:** The seeds selected without evidence of the presence of fungi or yeasts were washed with large amounts of water to eliminate impurities related to bulk handling and then in their fractionation and packaging that can take other materials such as small sand stones or other grain waste.



Figure 11. Maceration of the material. Source: authors.

- **Drying:** After washing, it was dried for 2 days in the sun, taking into account that they cannot be wetted by rain or other water source.
- **Crushed:** The material was crushed using a mixer (Oster). The resulting powder was sieved with a No. 200 sieve to obtain a very fine powder for storage in plastic containers to avoid hydration and subsequent use in the preparation of the solutions of the coagulant.

4. Tests of the biopolymers obtained

After obtaining the biopolymers, we proceed to prepare solutions of these extracts, to perform jar tests, and thus to determine the coagulant and flocculant capacity of natural biopolymers.

The tests are carried out with water of natural characteristics with different types of solids, which include natural tannins, solids smaller than 0.2 mm, organic matter, and other substances typical of raw or residual waters.

4.1. Preparation of the solutions for coagulation and flocculation of *Melocactus* sp., *Opuntia dillenii*, *Stenocereus griseus*, *Cereus forbesii*, *Aloe arborescens*, and *Aloe vera*

After obtaining the biopolymers of the plants *Melocactus* sp., *Opuntia dillenii*, *Stenocereus griseus*, *Cereus forbesii*, *Aloe arborescens*, and *Aloe vera*, the preparation of the solutions is carried out to realize the tests of jars, which prove the action of coagulant and flocculant.

The flocculant preparation process was weighed 1 g of biopolymer, then 1000 ml of distilled water was added and manual agitation was carried out until completely diluted.

4.2. Preparation of coagulation solutions of Kabuli chickpea (*Cicer arietinum* L.)

About 1% solution was prepared by adding 10 g of the anionic coagulant in 1000 ml with Milli-Q® water, obtaining a solution of 10,000 mg/l, after which stirring was carried out for 1 h to homogenize the mixture. In this solution, the tests were carried out to know the adequate doses to treat the synthetic water prepared in the laboratory.

To prepare the synthetic water, laboratory clay was used for the preparation of samples of turbid water for all the experiments. About 20 g of clay were added to 1 l of distilled water. The suspension was gently stirred for 1 h on a magnetic stirrer in order to achieve a uniform dispersion of the clay particles. The suspension was allowed to stand for 24 h to achieve complete hydration of the clay. This clay suspension served as a stock solution using distilled water to prepare water samples with a turbidity of 200 NTU.

4.3. Control parameters in rockrose tests

To test the coagulating and flocculating effect of the biopolymers of *Melocactus* sp., *Opuntia dillenii*, *Stenocereus griseus*, *Cereus forbesii*, *Aloe arborescens*, *Aloe vera*, and Kabuli chickpea (*Cicer arietinum* L.), jug tests were performed as provided in ASTM D2035: 08 [12].

The control parameters normally used in the efficiency of a coagulant are pH, turbidity, and color, which are governed by standardized methodologies [13], which determine the ability to remove solids from water based on their behavior, pH, and with its spectrophotometric absorbance, turbidity and color at different wavelengths.

In accordance with the regulations in force in Colombia, the tests were carried out taking into account the technical standards adopted by the country for each test [14].

The removal obtained is processed in terms of percentages, to be able to compare. In the case of pH, it is observed that it complies with the provisions of the national standard for this parameter [15]; and in the case of turbidity and color, the percentage of removal is taken into account, which is directly proportional to the decrease in absorbance in each test.

5. Results of jar tests with natural coagulant biopolymers

The results of the tests of the biopolymers, natural coagulants, are collected in four main tests, the first ones refer to the pH, the turbidity, and the color; the last one takes the coagulants with good performance and measures the Z potential.

Turbidity and color in water is related to the presence of substances or microorganisms, which is directly related to its quality to be consumed or used in other ways; the results offer an overview of the potentialities of all the plants for the coagulation and flocculation processes, with different degree of efficiency.

To control the efficiency of coagulation and flocculation as a function of pH, the pH was taken after coagulation, taking into account that the initial pH of the water is 7.2. The pH results are shown in **Graph 1**, showing that the coagulant that most affected the final pH was the biopolymer of *Melocactus* sp., which brought the pH up to 6.2. The data show a standard deviation of 0.3.

Graph 1 shows that the only one that did not affect the pH in the jar test was *Stenocereus* spp.; the others lowered the pH moderately to values of 7 or 6.8.

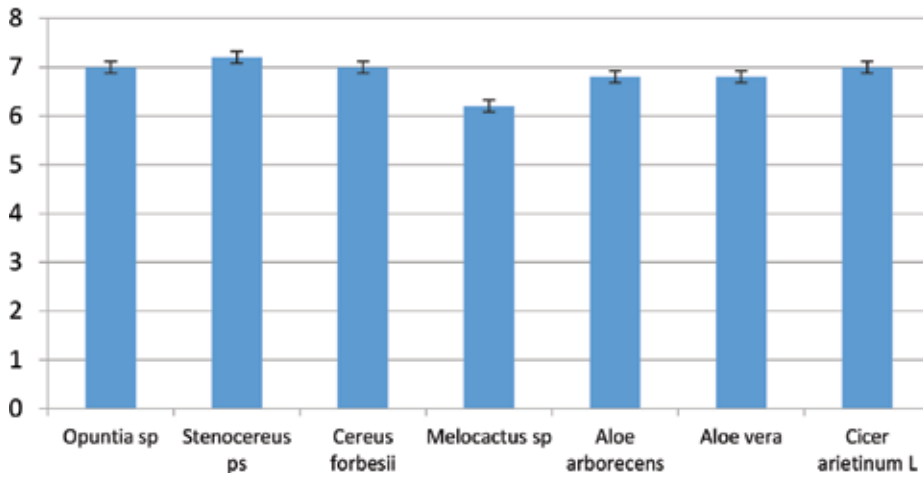
The turbidity results (**Graph 2**) showed that the best biopolymers to remove these solids associated with turbidity were *Melocactus* spp. and Kabuli chickpea (*Cicer arietinum* L.), which showed turbidity removals greater than 95 and 97%, respectively. The data show a standard deviation of 3.1.

The results of the other biopolymers showed a removal capacity greater than 88 and up to 92%, which shows the effectiveness of these biopolymers with water that has a neutral pH.

All the biopolymers tested showed effective action in the removal of turbidity, in a range between 88 and 97%, with some differences and affectations to the pH of the sample at the final moment of the jar test.

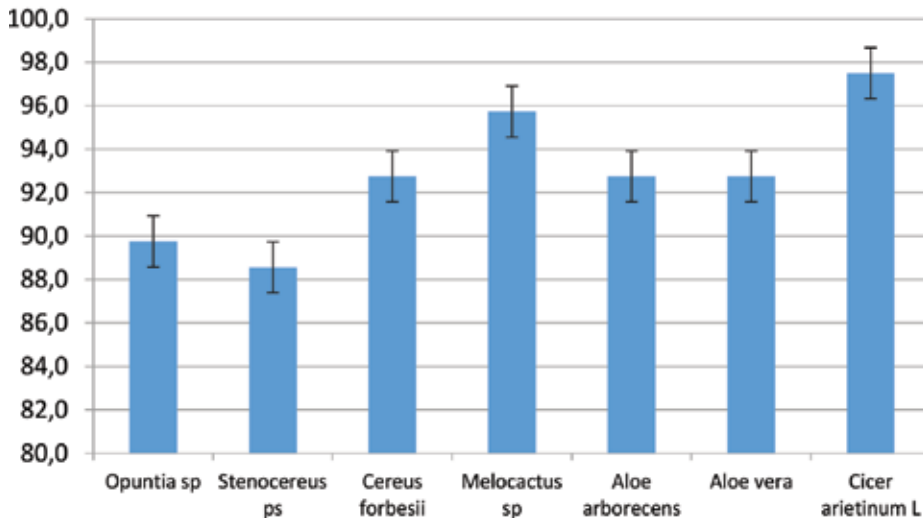
For the case of the color results (**Graph 3**), we can see a good activity of all the biopolymers, taking into account that the one that showed the best performance in the removal of the

Final pH of the tests



Graph 1. Results of the pH test for studied coagulants. Source: authors.

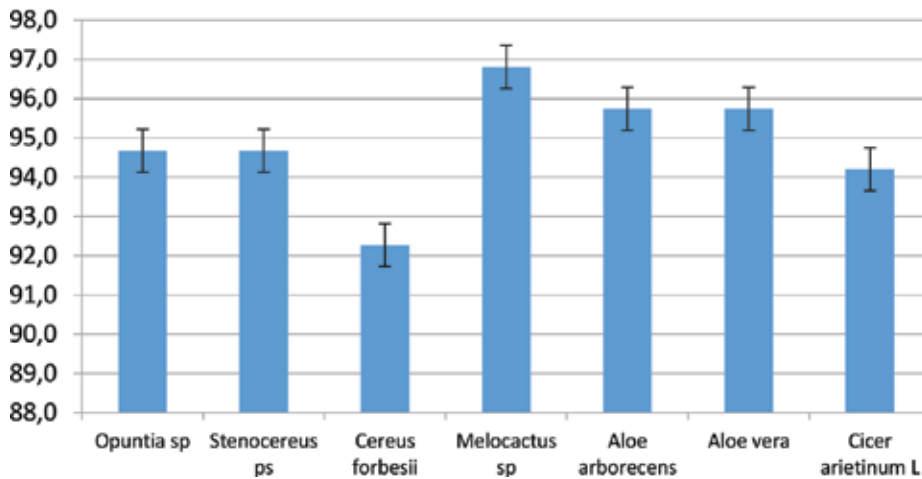
Turbidity removal percentage



Graph 2. Turbidity removal with each coagulant studied. Source: authors.

color was the biopolymer of *Melocactus sp.*, with a performance greater than 96%, and then it was appreciated that the two species of *Aloe sp.* with a removal greater than 95%; then there are *Opuntia sp.*, *Stenocereus sp.*, and Kabuli chickpea (*Cicer arietinum L.*), with performances greater than 94% and the last one was evidenced by *Cereus forbesii* with a performance greater than 92%. The data show a standard deviation of 1.4.

Color removal percentage



Graph 3. Color removal with each coagulant studied. Source: authors.

The results show a greater efficiency in the removal of color. The best performance of these tests lies in the *Melocactus* that was the best removing species in case of both turbidity and color, but with the highest incidence in the pH. The other biopolymer with high performance is the Kabuli chickpea (*Cicer arietinum* L.), which showed a good turbidity and color removal capacity with very little pH affection.

Z potential measurements were made to the biopolymers with better performance, which showed the following results.

Table 1 shows the results of the Z potential of the *Melocactus* sp. and Kabuli chickpea (*Cicer arietinum* L.), with pH between 3 and 10.

pH	Zeta potential (mV) <i>Melocactus</i> sp.	Zeta potential (mV) Kabuli chickpea
3	-1.7	15.1
4	-3.9	-2.5
5	-12.9	-11.8
6	-19.6	-19.8
7	-22.9	-21.9
8	-22.9	-21.9
9	-27.1	-24.5
10	-29.4	-27.1

Source: authors.

Table 1. Z potential of *Melocactus* sp. and Kabuli chickpea (*Cicer arietinum* L.).

The Zeta potential of the biopolymers shows similar values in the range of pH 4 and 10, which may indicate a similar activity with solid particles of small size, such as those that generate turbidity and color in the water.

It is important to note that all plants used have the potential to treat water; and that the efficiency differences can be associated to the affinity for different particles and their extraction form.

6. Conclusions

All the extracts showed turbidity and color removal, with efficiencies higher than 88%, which indicates that the extraction methodologies conserve the coagulant and flocculant capacity of each plant.

The biopolymers of *Melocactus* sp., *Opuntia* sp., *Stenocereus griseus*, *Cereus forbesii*, *Aloe arborescens*, *Aloe vera*, and Kabuli chickpea (*Cicer arietinum* L.) have an activity for coagulation and water flocculation.

The plants with the best performance in the removal of turbidity and color were *Melocactus* sp., and Kabuli chickpea (*Cicer arietinum* L.), with the best percentages of elimination of solids of small size of water.

The Z potential measured to the extracts of *Melocactus* sp. and Kabuli chickpea (*Cicer arietinum* L.) has similar values in the range of pH 4–10, which shows a similar activity for the suspended particles of the water used in the tests.

The biopolymers of the plants *Melocactus* sp., *Opuntia* sp., *Stenocereus griseus*, *Cereus forbesii*, *Aloe arborescens*, *Aloe vera*, and Kabuli chickpea (*Cicer arietinum* L.) can be a viable alternative for the treatment of drinking and residual water, in replacement of sulfate of aluminum, aluminum polychloride, and ferric chloride; decreasing the amounts of dissolved metals in drinking water of humans and animals, especially with the aluminum residues associated with diseases such as autism and Alzheimer [16-23].

Acknowledgements

We are very grateful to the University of Santander in Colombia, which granted a large part of resources to carry out this book chapter; also to the University of Valladolid Spain, for facilitating that one of our authors could be part of this document.

Likewise to all the people of the universities, who personally helped their commitment to this work.

Conflict of interest

The authors declare that there is no conflict of interests regarding the publication of this document.

Author details

Jesús Epalza^{1*}, Jhoan Jaramillo² and Oscar Guarín¹

*Address all correspondence to: manuelepalza@gmail.com

¹ Environmental Engineering, University of Santander (UNDES), Bucaramanga, Colombia

² Environmental Engineering, University of Valladolid (UVA), Valladolid, Spain

References

- [1] C. and. Wilkinson. Advanced Inorganic Chemical. New York: Interscience Publishers; 1998
- [2] L. C. A. J. H. M. Burriel Martí. Qualitative Analytical Chemistry. Madrid: Parainfo; 1992
- [3] V. S. a. B. K. D. G. Jayalakshmi. A review on native plant based coagulants for water purification. International Journal of Applied Environmental Sciences. 2017;**12**(3):469-487
- [4] A. A. O. Casierra PosadaFanor. Stress due to aluminum in plants: Reactions in the soil, symptoms in plants and correction possibilities. A review. Colombian Journal of Horticultural Science. 2007;**1**(2):246-257
- [5] Yin C-Y. Emerging usage of plant-based coagulants for water and wastewater treatment. Process Biochemistry. 2010:1437-1444
- [6] A. B. A. A. B. W. Moa Megersa. The use of indigenous plant species for drinking water treatment in developing countries: A review. Journal of Biodiversity and Environmental Sciences. 2014;**5**(3):269-281
- [7] Hildebrando Ramírez Arcila JJ. Natural agents as an alternative for the treatment of water. Journal of the Faculty of Sciences. 2015;**11**(2):136-153
- [8] Fernández JX. Taxonomic news and synopsis of the genus *Melocactus* Link and Otto (Cactaceae) in Colombia. Journal of the Colombian Academy of Exact Physical and Natural Sciences. 2002:353-365
- [9] Villabona Angel PIM. Characterization of *Opuntia ficus-indica* for use as a natural coagulant. Colombian Journal of Biotechnology. 2013;**XV**(1):137-144
- [10] V. Á. T. C. G. R. Guzman Luis. Reduction of water turbidity using natural coagulants: A review. Revista U.D.C.A Actualidad & Divulgación Científica. 2013:253-262
- [11] C. M. D. A. C. E. Martinez Damarys. Performance of *Cactuslefaritato* use like coagulating in the water clarification. Technical Journal of the Faculty of Engineering. April 30, 2003;**26**(1):76-82
- [12] ASTM. Standard Practice for Coagulation-Flocculation Jar Test Water. New York: ASTM; 2008

- [13] American Public Health Association. Standard Methods. Washington, D.C: American Public Health Association; 1995
- [14] ICONTEC. NTC 3903 Procedure for the Test of Coagulation-Flocculation in A Water-Based Container or Method of Jars. Bogotá: ICONTEC; 2010
- [15] Decree 3930 Republic of Colombia. Decree 3930 of 2010. Bogotá: Official Gazette; 2010
- [16] D. U. A.K.C. E. Matthew Mold. Aluminum in brain tissue in autism. Journal of Trace Elements in Medicine and Biology. 2018;**46**(1):76-82
- [17] S. T., V. K. A. Vijayaraghavan G. Application of plant based coagulants for waste water treatment. International Journal of Advanced Engineering Research and Studies. 2011:88-92
- [18] C.-U. S. C. Torres Bustillos Luis G. Production and characterization of *Opuntia ficus-indica* mucilage and its use as coagulant-flocculant aid for industrial wastewaters. International Journal of Biotechnology Research. 2013:38-45
- [19] V. V. A. P. O. Pagliano Giorgia. Integrated systems for biopolymers and bioenergy production from organic waste and by products: A review of microbial processes. Biotechnology for Biofuels. 2017;**10**(113):123-146
- [20] M. G. G. A. V. A. A. U. M. B. R. Nishi Leticia. *Cyanobacteria* removal by coagulation/flocculation with seeds of the natural coagulant *Moringa oleifera* Lam. Chemical Engineering Transactions. 2011:1129-1134
- [21] B.-D. L. F. E. T.-S. B. K. R. Medina-Torres L. Rheological properties of the mucilage gum (*Opuntia ficus-indica*). Food Hydrocolloids. 2000:417-424
- [22] R. H. Ospina O. Alternative home treatment of water for human consumption by means of phytochemicals. Journal of the Colombian School of Engineering. 2011;**84**(1):7-17
- [23] B. A. E. Daza Rina. Evaluation of the efficiency of bio-polymers derived from desertic plants as flocculation agents. Chemical Engineering Transactions. 2016:234-239

Artificial Neural Network-Genetic Algorithm Prediction of Heavy Metal Removal Using a Novel Plant-Based Biosorbent Banana Floret: Kinetic, Equilibrium, Thermodynamics and Desorption Studies

Clint Sutherland, Abeni Marcano and
Beverly Chittoo

Additional information is available at the end of the chapter

<http://dx.doi.org/10.5772/intechopen.74398>

Abstract

In this study, the biosorption performance of banana floret was assessed as a new biosorbent for the removal of Cu(II) ions (a model heavy metal) from aqueous solutions. Batch experiments were conducted to assess the effects of agitation, particle size, pH, temperature and initial concentration. Kinetic and equilibrium data were modeled, and mass transfer studies were conducted to elucidate the mechanisms of biosorption. Kinetic data were best simulated using the diffusion-chemisorption model while equilibrium data were best represented by the Sips isotherm. The dominant transport mechanism was attributed to intraparticle diffusion while the dominant attachment mechanism was chemical sorption. A predictive model was successfully developed using an artificial neural network (ANN) and optimized using a genetic algorithm (GA). The accuracy of the ANN-GA prediction was validated by laboratory experiments, which revealed a residual error of 1.3% and thus underscores the applicability of the model. This new biosorbent exhibited a remarkable affinity for the heavy metal ion and compared well to other reported biosorbents in the literature.

Keywords: banana floret, biosorption, heavy metal, artificial neural network, genetic algorithm

1. Introduction

Increased pollution resulting from excessive industrialization, urbanization, waste incineration and agricultural activities continues to magnify environmental contamination by heavy metals

[1]. Various technologies have been used for the removal of heavy metals including filtration, chemical precipitation, ion exchange, electrodeposition, membrane processes and adsorption using activated carbon [2]. Biosorption of heavy metals has attracted much attention recently due to its simplicity, efficiency, and availability of biomass and waste bioproducts [3]. Of keen interest are agricultural by-products such as peat [4], coconut shell [5], wood [6], banana trunk [7], rice husk [8], peanut shells [9], guava leaves [10] and banana stem [11]. A survey of the literature showed that no work had been reported on the use of banana floret as a biosorbent. In this study, Cu(II) is used as a model metal ion to assess the biosorptive potential of banana floret.

Kinetic and equilibrium studies are critical to determining the applicability of biosorbents as well as for the successful design of biosorption systems. These analyses provide an indication of sorption capacity, mechanisms as well as give some insight into the affinity of the biosorbent for the metal ion species [12]. Additionally, the development of predictive models can save time and improve efficiency in experimentation and enable the effectual upgrade to full-scale systems [13].

The objectives of this study are: (i) to determine the biosorption efficiency of banana floret as a new biosorbent; (ii) to elucidate the transport and attachment mechanisms of biosorption through batch kinetic, equilibrium, thermodynamic and desorption studies; and (iii) through single-variable kinetic and equilibrium analysis and ANN-GA modeling simulate batch process, which will enable process design and upscaling.

2. Materials and methods

2.1. Preparation of the biosorbent

Batch biosorption experiments were conducted using banana flower. The flower was first dried at 378 K for 24 h, washed and separated into three fractions which comprised the bract, the floret and the stem. The fractions were subsequently crushed and sieved into different sizes. The average particle size retained on a sieve was calculated as the geometric mean of the diameter openings in two adjacent sieves in the stack. The geometric mean size (GMS) is expressed as $(\text{diameter of upper sieve} \times \text{diameter of lower sieve})^{0.5}$ [14].

2.2. Determination of metal ions concentration

Stock solutions were prepared from analytical-grade copper(II) sulfate in distilled water (prepared by a Thermo Scientific Still of pH approximately 7 and conductivity $<5 \mu\text{S}/\text{cm}$). Cu(II) ions were analyzed by the cuprethol method using a Shimadzu UV-1800 Spectrophotometer and verified periodically using an Analytik-Jena contra 700 AAS.

2.3. SEM combined with EDS analysis

The biosorbent was characterized using a scanning electron microscope (SEM) (Hitachi S-3000 N) and an energy dispersive spectroscopy (EDS) analyzer (IXRF Systems) at a voltage of

20 kV. The SEM and EDS were used to investigate the changes in the surface microstructures and the elemental composition of the biosorbent before and after biosorption.

2.4. Biosorption kinetics

2.4.1. Kinetic studies

Batch biosorption studies were conducted using the parallel method according to EPA OPPTS method 835.1230 [15]. The study of metal uptake was done in duplicate at room temperature (300 ± 2 K) with an adsorbent mass 1.0 g/L and spiked with 50 mg/L of synthetic metal ion solution. Biosorbent masses were accurate to ± 0.001 g and solution volumes to ± 0.5 ml. Identical reaction mixtures were prepared for each time interval, agitated on a mechanical shaker and removed at predetermined time intervals [16]. The banana flower was first subjected to kinetic screening. Kinetic tests revealed the stem sorbed 14% more Cu(II) ions than the bract, while the floret sorbed 44% more than the stem. Consequently, a detailed analysis was performed on the banana floret and is reported in this study.

2.4.2. Adsorption yield

The ratio of adsorbed metal ion concentration to the initial metal ion concentration was calculated from Eq. (1).

$$\%Adsorption = \frac{C_0 - C_t}{M} * 100 \tag{1}$$

2.5. Equilibrium study

The effect of initial concentration was studied by equilibrating 1.0 g/L of adsorbent in synthetic Cu(II) solution of varying concentrations (within the range of 10–100 mg/L to ensure

Expression	Equation number
$RPE\% = \frac{1}{N} \sum_{i=1}^N \left[\frac{ (q_{e_i})_{pred} - (q_{e_i})_{exp} }{(q_{e_i})_{exp}} \right] * 100$	(3)
$MPSD = 100 \sqrt{\frac{1}{N-p} \sum_{i=1}^N \left[\frac{(q_{e_i})_{exp} - (q_{e_i})_{pred}}{(q_{e_i})_{exp}} \right]^2}$	(4)
$HYBRID = \frac{100}{N-p} \sum_{i=1}^N \left[\frac{\left((q_{e_i})_{exp} - (q_{e_i})_{pred} \right)^2}{(q_{e_i})_{pred}} \right]$	(5)
$R^2 = \frac{\sum_{i=1}^N \left((q_{e_i})_{exp} - q_{e_{exp, mean}} \right)^2 - \sum_{i=1}^N \left((q_{e_i})_{exp} - (q_{e_i})_{pred} \right)^2}{\sum_{i=1}^N \left((q_{e_i})_{exp} - (q_{e_i})_{pred} \right)^2}$	(6)
$MSE = \left(\frac{1}{N} \sum_{i=1}^N \left[(q_{e_i})_{exp} - (q_{e_i})_{pred} \right]^2 \right)$	(7)

Table 1. Error functions.

maximum sorption capacity was attained) in a shaking water bath (Julabo SW23) at temperatures varying from 300 ± 2 to 328 ± 2 K. The concentration of metal ions on the biosorbent was determined using the following mass balance equation:

$$q_e = \frac{(C_o - C_e)}{M} * V \quad (2)$$

2.6. Error analysis

The goodness of fit by the various models to the experimental data was evaluated using the coefficient of determination, R^2 , the Marquardt's percent standard deviation (MPSD), hybrid error function (HYBRID), mean square error (MSE) and relative percent error (RPE) and is presented in **Table 1**.

3. Results and discussion

3.1. Kinetic modeling

Kinetic simulation of banana floret biosorption was carried out using four models: Lagergren pseudo-first order (PFO) model; pseudo-second order (PSO) model; Weber and Morris intraparticle diffusion (ID) model; and the diffusion-chemisorption (DC) model.

In 1898, Lagergren developed a first-order rate equation which was subsequently described as pseudo-first order [17]. The linear and nonlinear forms are:

$$q_t = q_e(1 - \exp^{-K_{PFO}t}) \quad (8)$$

and

$$\log(q_e - q_t) = \log q_e - \frac{K_{PFO}}{2.303}t \quad (9)$$

The PSO equation is represented by Eqs. (10) and (11) [18]. The model is based on PSO chemical reaction kinetics [19].

$$q_t = \frac{K_{PSO}q_e^2t}{1 + K_{PSO}q_e t} \quad (10)$$

and

$$\frac{t}{q_t} = \frac{1}{K_{PSO}q_e^2} + \frac{t}{q_e} \quad (11)$$

Weber and Morris [20] proposed that the rate of ID varies proportionally with the half power of time and is expressed as Eq. (12). If the rate-limiting step is ID, a plot of solute adsorbed against the square root of time should yield a straight line passing through the origin [20].

$$q_t = K_{id} \left(t^{1/2} \right) + c \tag{12}$$

The DC kinetic model was developed to simulate sorption of heavy metals onto heterogeneous media [21]. It is based on the assumption that both diffusion and chemisorption control the biosorption process. Linear and nonlinear forms are as follows:

$$q_t = \frac{1}{\frac{1}{q_e} + \frac{t^{0.5-1}}{K_{DC}}} \tag{13}$$

and

$$\frac{t^{0.5}}{q_t} = \frac{1}{q_e} * t^{0.5} + \frac{1}{K_{DC}} \tag{14}$$

Assuming, a linear region as $t \rightarrow 0$, the initial rate is given as:

$$k_i = K_{DC}^2 / q_e \tag{15}$$

3.1.1. Linear regression

Table 2 shows the results of the linear regression analysis. The goodness of fit was assessed using error functions presented in **Table 1**. First, the experimental data were modeled using each of the kinetic models through linear regression. The highest coefficient of determination ($R^2 = 0.9981$) was produced by the PSO model. This was followed by the DC model ($R^2 = 0.9972$), PFO model ($R^2 = 0.9831$) and finally the ID model ($R^2 = 0.9435$). The equation parameters obtained from linear regression were subsequently used to construct the theoretical

Kinetic model	Linear plot	Nonlinear plot			
	R^2	RPE	MPSD	HYBRID	R^2
Linear regression					
PFO	0.9831	59.9038	75.6477	898.5153	0.8270
PSO	0.9981	6.7008	13.1281	21.2823	0.9743
ID	0.9435	4.8812	7.1356	7.4810	0.9864
DC	0.9972	1.6146	2.4843	0.9845	0.9981
Nonlinear regression					
PFO		11.4339	15.1570	34.5790	0.9380
PSO		6.2754	8.3444	10.3636	0.9813
ID		12.9165	17.8090	49.6369	0.9864
DC		1.6035	2.4244	0.9607	0.9981

Table 2. Results of linear and nonlinear regression analysis.

nonlinear curves, i.e. the form of the curve used for system design. These nonlinear plots were then compared to the primary experimental data using the error functions (RPE, MPSD, HYBRID, and R^2). The nonlinear R^2 values in **Table 2** show the correlation of the PSO model fell off significantly ($R^2 = 0.9743$) while that of the DC model and ID model improved. The other error functions also support this trend. This type of occurrence has been reported by Motulsky and Christopoulos [22], where the authors explicated that the transformation of experimental data to linear forms causes some assumptions of linear regression to be violated (e.g. distortion of the experimental error) and consequently the derived slope and intercept of the regression line are not the most accurate determinations of the parameters of a model.

3.1.2. Nonlinear regression

A more robust simulation was performed using nonlinear regression by the Levenberg-Marquardt algorithm. The results of this analysis were assessed using error functions which revealed that the DC model produced the highest R^2 and the lowest RPE, MPSD, and HYBRID values. **Figure 1a–d** shows the comparison of the experimental data to the nonlinear plots generated by both linear regression and nonlinear regression parameters. The accuracy of the DC model is confirmed by the

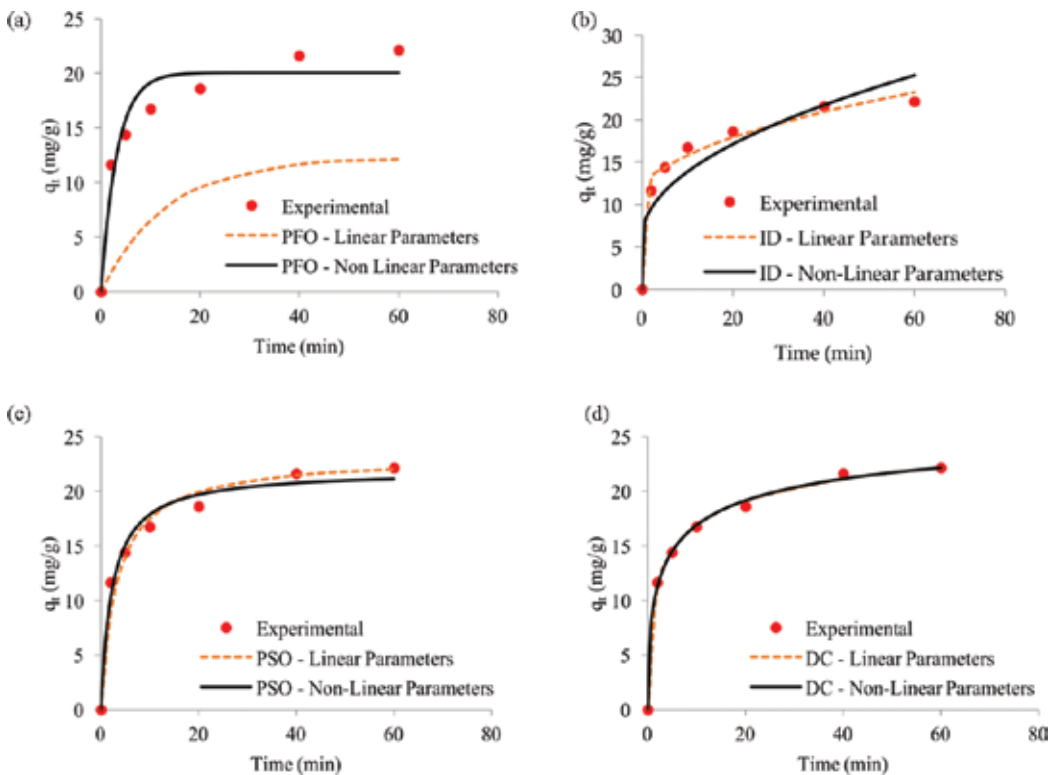


Figure 1. Comparison of experimental data to nonlinear kinetic curves by (a) PFO model, (b) ID model, (c) PSO model and (d) DC model.

superior simulation. What is most significant is the high precision of the DC model curves which demonstrates minimal violation as the data was transformed from linear to nonlinear forms.

3.2. Effect of mixing speed on biosorption

The DC model was used to assess the kinetic effect of mixing speed on the biosorption of Cu(II) onto banana floret and is presented in **Table 3**. The overall rate of biosorption increased with increasing agitation. This was expected as agitation promotes good contact between media and liquid and maintains a high-ion concentration gradient between the inner and outer regions of the particle. Further, the solvent film thickness, which surrounds the particle, reduces, and by extension, the resistance to film diffusion. This is supported by the significant increase in initial rate as agitation is increased.

3.3. Effect of pH on biosorption

To elucidate the impact of changing pH on biosorption, the pH was varied as presented in **Figure 2**. Maximum removal was observed at pH 5.3, followed by a significant decrease. **Figure 3** shows the results of the point of zero charge (pH_{PZC}) of the banana floret, which was found to be 6.2. At pH values far below the pH_{PZC} , functional groups on the surface of the biosorbent become highly protonated, which can result in reduced efficiency. At pH 6.0, there exist three species, Cu^{2+} in very small quantity and $Cu(OH)^+$ and $Cu(OH)_2$ in large quantities [23]. The reduction in sorption observed at pH 5.6 may indicate a preference by floret for the Cu^{2+} ions over that of the other species. The maximum biosorption at pH 5.3 (below pH_{PZC}) may in part be due to the greater preference of the higher valency Cu^{2+} ions over H^+ ions.

3.4. Effect of particle size on biosorption

The influence of particle size was studied and is also presented in **Table 3**. It is observed that as particle size decreased, both the overall rate and the initial rate increased. The reduction in

Operational conditions	Values	Overall rate, K_{DC} (mg/g-t ^{0.5})	Initial rate k_i (mg/g-t)
pH	3.2	6.4836	4.8743
	4.1	7.6858	4.1949
	5.3	13.3577	6.3379
	5.6	13.1258	9.7131
Agitation (RPM)	250	12.0172	5.0386
	350	13.3577	6.3379
	400	16.7028	9.8186
Particle, GMS (mm)	0.17	13.3873	6.3447
	0.35	11.2768	4.5407
	0.6	8.6429	3.0784

Table 3. DC model rate parameters for different operational conditions.

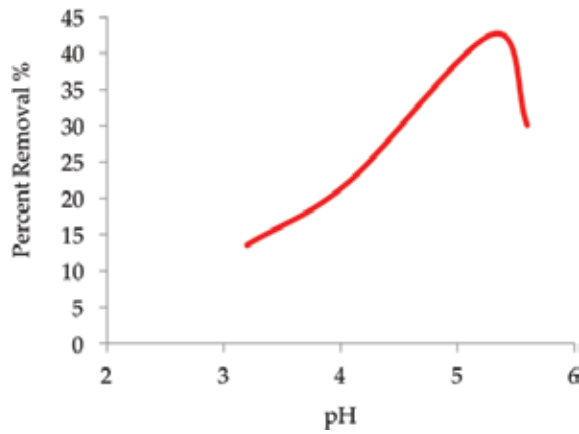


Figure 2. Effect of solution pH on Cu(II) uptake.

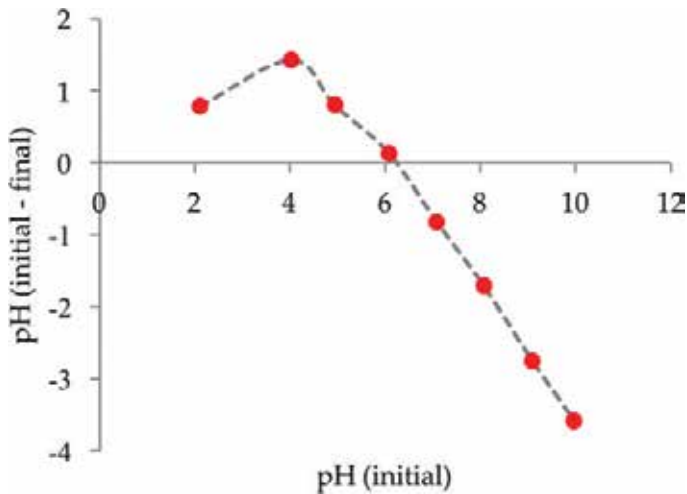


Figure 3. Point of zero charge of banana floret.

particle size is accompanied by an increase in surface area which can account for the increase in initial rate. Also, if the characteristics of the active sites on the surface of the biosorbent are the same as those within the pores, then this increase in overall rate with decreased particle size is expected.

3.5. Equilibrium modeling

The equilibrium capacity of banana floret for Cu(II) was assessed by nonlinear regression using two- and three-parameter equilibrium models, namely, the Langmuir isotherm, the Freundlich isotherm, the Redlich-Peterson isotherm and the Sips isotherm.

The Langmuir model (Eq. (16)) is a theoretical equilibrium isotherm originally developed to relate the amount of gas adsorbed on a surface to the pressure of the gas [24].

$$q_e = \frac{q_L K_L C_e}{1 + K_L C_e} \tag{16}$$

Firth as cited in [25], explained that the equation of the form $x = kc^{1/n}$ was first applied to adsorption of gases by De Saussure in 1814. Its application was further extended to solutions by Boedecker in 1859 [25]. In 1906, Freundlich described the adsorption isotherm mathematically as a special case for nonideal and reversible adsorption [26]. This equation is presented as:

$$q_e = K_F(C_e)^{1/n_F} \tag{17}$$

The Redlich-Peterson isotherm (Eq. (23)) is a hybrid isotherm that incorporates the features of the Langmuir and Freundlich isotherms [27]:

$$q_e = \frac{K_{RP} C_e}{1 + \alpha_{RP} C_e^{\beta_{RP}}} \tag{18}$$

The Sips isotherm (Eq. (19)) is also a combined form of the Langmuir and Freundlich isotherms [28]. The model was developed for predicting heterogeneous adsorption systems [29].

$$q_e = \frac{q_S (\alpha_S C_e)^{n_S}}{1 + (\alpha_S C_e)^{n_S}} \tag{19}$$

Table 4 shows that among the two-parameter models, the Langmuir isotherm best represented the equilibrium data. Approximately 34% increase in sorption capacity occurred as temperature was increased from 300 to 328 K. Hall et al. [30] postulated that the constant separation factor, R_L , may be used to further describe the nature of the adsorption process and to assess the suitability of the biosorbent for column applications.

$$R_L = \frac{1}{(1 + K_L C_o)} \tag{20}$$

The authors went on to explain that equilibrium conditions have an interesting effect on the shape of column breakthrough curves whereby for $0 < R_L < 1$ (favorable equilibrium) the curve of the mass transfer zone tends to attain a constant pattern and thus become relatively self-sharpening as it advances through the column. **Figure 4** presents a plot of R_L vs. C_o for varying reaction temperatures. In all cases, the value of R_L was between 0 and 1 indicating a favorable equilibrium and by extension confirms the applicability of banana floret for column application.

Equilibrium data are also useful for batch design whereby attainable levels of treatment can be explained. Therefore, the importance of challenging the experimental data against various models and obtaining an accurate simulation cannot be overemphasized. **Table 4** shows the results of the nonlinear regression of the Redlich-Peterson and the Sips model. The Sips model produced the highest R^2 among all tested equilibrium models (R^2 0.9947–0.9982). According to

Models	Solution temperature (K)			
	300.15	308.15	318.15	328.15
Langmuir				
q_L	33.37	34.42	39.98	44.86
K_L	0.0526	0.0521	0.0425	0.0402
R^2	0.9913	0.9900	0.9883	0.9929
Freundlich				
K_F	4.2153	4.3226	3.9603	4.1283
n_F	2.2753	2.2691	2.0508	1.9877
R^2	0.9575	0.9572	0.9607	0.9679
Redlich-Peterson				
K_{RP}	1.3514	1.3783	1.2902	1.3398
a_{RP}	0.0110	0.0106	0.0052	0.0037
g_{RP}	1.2948	1.3024	1.4153	1.4750
R^2	0.9962	0.9949	0.9937	0.9981
Sips				
q_s	28.06	28.86	32.12	37.43
a_s	0.0756	0.0749	0.0663	0.0585
n_s	1.4127	1.4226	1.4622	1.3098
R^2	0.9974	0.9962	0.9949	0.9982

Table 4. Biosorption isotherm constants for various temperatures.

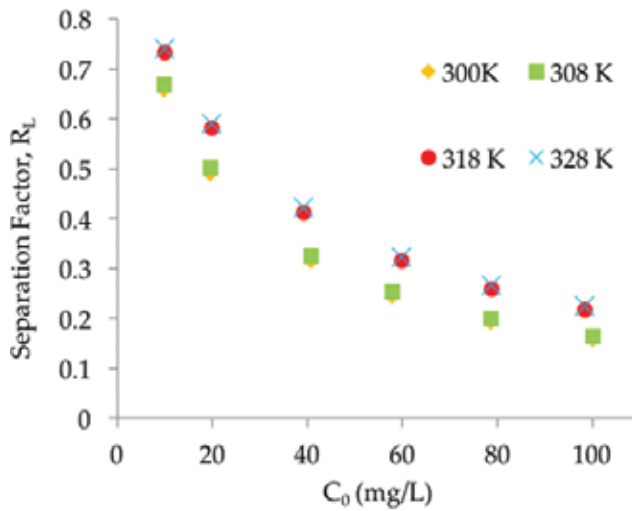


Figure 4. Variation in separation factor.

the Sips isotherm, banana floret exhibited a maximum adsorption capacity of 28.06 mg/g. This compared well with other biosorbents reported in the literature including peanut shells [31], Irish peat moss [32] and the fungal biomass *Cladosporium cladosporioides* [33] and banana stem [11], which exhibit capacities of 25.39, 17.6, 19.5 and 19.7 mg/g, respectively.

3.6. Thermodynamic studies

Thermodynamic effects were assessed at four different temperatures (300, 308, 318, and 328 K). Parameters such as standard Gibb’s free energy change (ΔG°), enthalpy change (ΔH°) and entropy change (ΔS°) were calculated using Eqs. (21) and (22) [34]:

$$\Delta G^\circ = -RT \ln K_d \tag{21}$$

The following form of the van’t Hoff equation was applied whereby K_d is the distribution coefficient under equilibrium conditions calculated from the relationship (q_e/C_e).

$$\ln(K_d) = \frac{\Delta S^\circ}{T} - \frac{\Delta H^\circ}{RT} \tag{22}$$

Table 5 presents the results of the thermodynamic analysis. The ΔG° values for the range of temperature and concentration were negative, indicating a spontaneous feasible reaction and varied from -12.39 to -7.75 kJ/mol. Values of ΔG° lower than -20 kJ/mol signify the involvement of physisorption in the biosorption process [35]. Oepen et al. as cited in [34], highlighted that the association of energy (ΔH°) are as follows: van der Waals interactions (4–8 kJ/mol); hydrophobic bonding (4 kJ/mol); hydrogen bonding (2–40 kJ/mol); charge transfer, ligand-exchange and ion bonding (40 kJ/mol); direct and induced ion-dipole and dipole-dipole interactions (2–29 kJ/mol). In this study, ΔH° ranged from 1.5 to 9.38 kJ/mol, and consequently, the involvement of one or all of these mechanisms of attachment cannot be discounted.

The negative values of ΔH° are indicative of an exothermic sorption process. The positive ΔS° reveals increasing randomness at the solid/liquid interface during sorption or structural changes among the active sites of the biosorbent. The values of activation energy, E_a , varied according to initial concentration and ranged from 3000 to 94,000 kJ/mol. As initial concentration increases, E_a

C_o (mg/L)	ΔH° (kJ/mol)	ΔS° (kJ/mol/K)	ΔG°				E_a (kJ/mol)	S^*
			300 K	308 K	318 K	328 K		
10	-5.1147	0.0529	-10.84	-11.19	-11.45	-12.39	93.6905	0.2073
20	-1.5114	0.0399	-10.51	-10.78	-11.06	-11.66	52.0972	0.1863
40	-3.6217	0.0459	-10.13	-10.54	-11.02	-11.42	26.0112	0.1867
60	-8.7953	0.0597	-9.16	-9.54	-10.15	-10.82	15.5156	0.2086
80	-8.6914	0.0565	-8.38	-8.66	-9.19	-9.96	10.2670	0.2364
100	-9.3850	0.0569	-7.75	-8.07	-8.75	-9.30	3.3152	0.1975

Table 5. Thermodynamic parameters.

decreases resulting in an increase in the number collision as well as an increase in reaction rate. Activation energy values between 5 and 20 kJ/mol infer physisorption is the predominant adsorption mechanism. Values greater than 20 kJ/mol and up to 40 kJ/mol generally indicate a diffusion-controlled process, and a higher value represents a reaction controlled by chemical process [36]. It can, therefore, be surmised that the mechanisms of biosorption of Cu(II) onto banana floret were significantly influenced by the initial Cu(II) concentration. The values of the sticking probability ($S^* < 1$) reveal that the process was favorable.

3.7. Development of a predictive model

3.7.1. Artificial neural network

In this study, a multilayer feed-forward backpropagation ANN model [37, 38] was developed for predicting the biosorption of copper onto banana floret. A total of 60 experimental data points was used to train and test the performance of the ANN. Each set contained four input variables comprising pH (3.2–5.6), particle size (GMS 0.17–0.06 mm), mixing speed (250–400 RPM), contact time (0–60 min), and one output variable, namely, the adsorbed concentration (4.06–23.28 mg/g). The dataset was divided into three parts, 70% for training the network, 15% for validation and 15% for testing the accuracy of the neural network model and its prediction.

The optimum architecture of the ANN was developed by first assessing the impact of 13 training backpropagation algorithms whereby the Levenberg-Marquardt algorithm produced the lowest MSE of 0.4030 and highest R^2 of 0.9938. The lowest MSE and highest R^2 within two training runs revealed the *Tansig* transfer function at the hidden layer and the *Tansig* transfer function at the outer layer were most optimal. A schematic representation of the architecture is shown in **Figure 5**. In this protocol, the number of neurons was varied from 2 to 20, and its

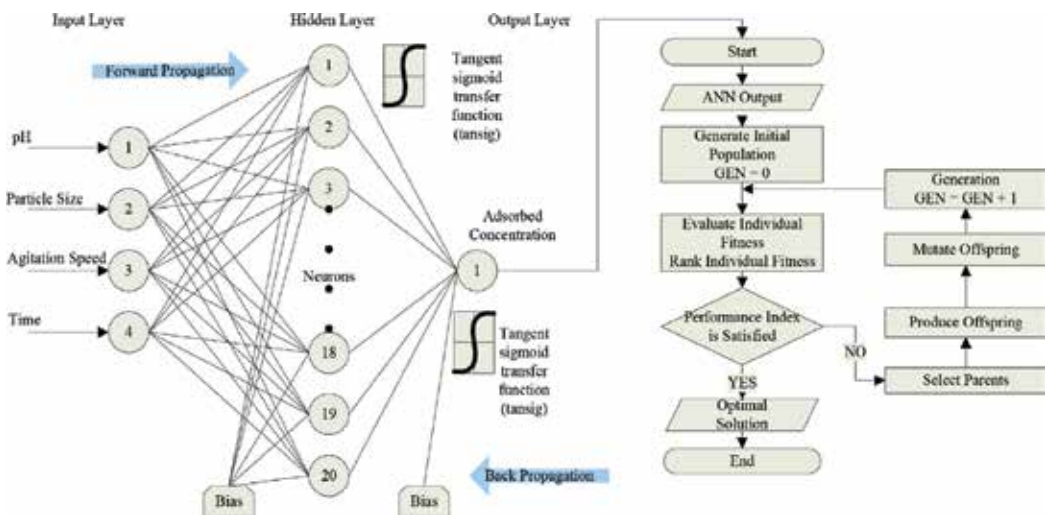


Figure 5. Optimized ANN-GA architecture.

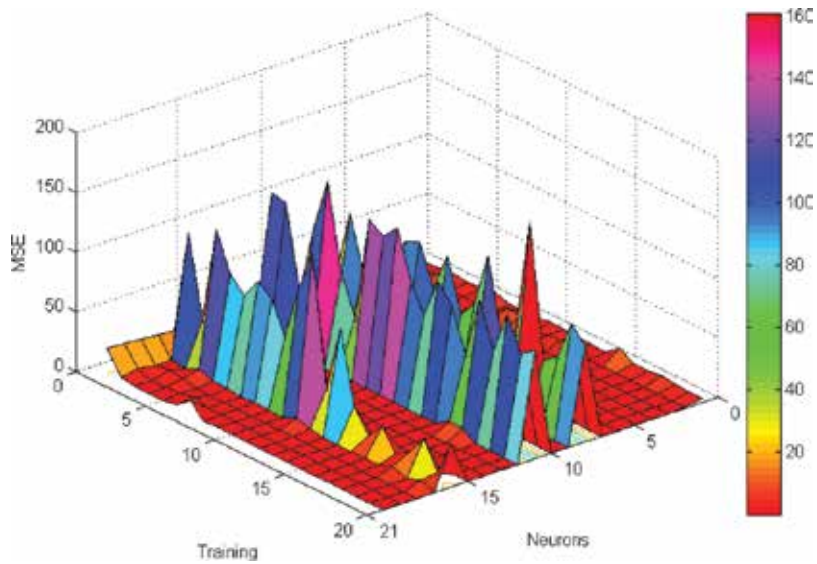


Figure 6. Effect of the number of neurons and training on ANN performance.

impact on performance assessed using the MSE as shown in **Figure 6**. The lowest MSE (0.0025) was obtained using 20 neurons. The figure also reveals fluctuations in MSE as the number of neurons increased. This may have resulted from the network being trapped into the local minima [39]. **Figure 7** shows a comparison of the ANN predicted data and the experimental data, which reveals a significantly high correlation ($R^2 = 0.9972$) and underscores the accuracy of the ANN prediction.

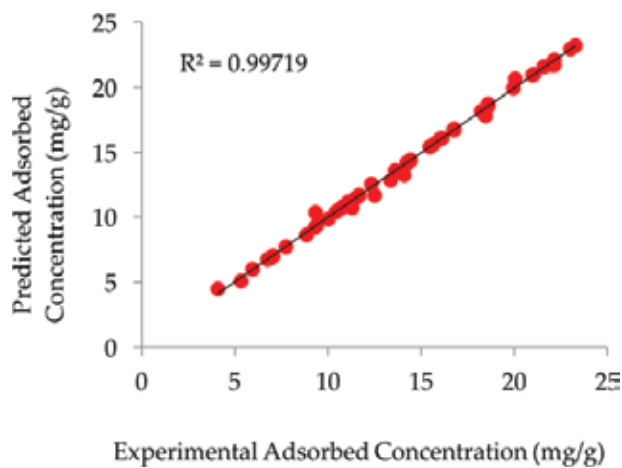


Figure 7. Comparison of experimental and ANN model prediction.

3.7.2. Formulation of empirical equation

The weights of the optimized ANN and the fitness function were used to develop an empirical expression for predicting biosorption kinetics without the ANN software using Eqs. (23), (24) and (25) [39].

$$F_i = \frac{2}{[1 + \exp(-2 * E_i)]} - 1 \quad (23)$$

where F_i is the *Tansig* transfer function used at the hidden layer. The input data are normalized in the range -1 to 1 using Eq. (24):

$$X_{norm} = 2 \left[\frac{X_i - X_{min}}{X_{max} - X_{min}} \right] - 1 \quad (24)$$

where X_i is the input or output variable X , and X_{min} and X_{max} are the minimum and maximum value of variable X . E_i is the weighted sum of the normalized input calculated whereby W_i represents the weights and bi is the biases and is defined as follows:

$$E_i = W_{i1} * t + W_{i2} * RPM + W_{i3} * d_p + W_{i4} * pH + bi \quad (25)$$

The predicted adsorbed concentration is therefore given by the following equation:

$$q_{t(\text{predicted})} = \frac{2}{1 + e^{(-2 * (-1.6177F1 - 0.5105F2 - 0.4558F3 + 2.5298F4 + 1.1608F5 + 0.6342F6 - 0.7647F7 + 1.0149F8 - 0.8711F9 + 0.7553F10 - 0.2475F11 - 0.4772F12 - 0.6349F13 - 0.3057F14 + 2.2585F15 - 0.0421F16 + 1.219F17 + 1.7408F18 + 0.1456F19 + 0.2931F20 - 1.0660))}} - 1 \quad (26)$$

3.7.3. Sensitivity analysis

A sensitivity analysis was carried out to determine the effect of each variable on the performance of the ANN model. Using the MSE and R^2 , an evaluation of the performance of various possible combinations of variables was investigated [40]. The variables were combined to form four groups as presented in Table 6. The input variables are defined as follows: $p1$ is time, $p2$ is agitation, $p3$ is particle size and $p4$ is solution pH. The table shows $p4$ (pH) to be the most influential parameter in the group of one variable, while $p1$ (time) and $p4$ (pH) were the most influential in the group of two variables, which produced the most significant improvement in the network. The greatest performance occurred with the inclusion of all four variables, which produced the lowest MSE (0.0025) and highest R^2 (0.9972). Consequently, it is resolved that pH and time have the greatest influence on the ANN structure.

3.8. Genetic algorithm (GA) optimization

Following the development of the ANN model, the GA technique was applied using the optimization toolbox of Matlab 2012a to determine the value of the operational parameters

No.	Combination	MSE	R ²
Group of one variable			
1	<i>p1</i>	11.6000	0.3264
2	<i>p2</i>	14.4100	0.1692
3	<i>p3</i>	34.9900	0.0052
4	<i>p4</i>	10.2250	0.4445
Group of two variables			
5	<i>p1 + p2</i>	8.3300	0.5329
6	<i>p1 + p3</i>	23.2000	0.2916
7	<i>p1 + p4</i>	0.1900	0.9052
8	<i>p2 + p3</i>	9.4400	0.1600
9	<i>p2 + p4</i>	7.6580	0.5476
10	<i>p3 + p4</i>	5.3254	0.5806
Group of three variables			
11	<i>p1 + p2 + p3</i>	74.2140	0.0062
12	<i>p1 + p2 + p4</i>	0.2770	0.8879
13	<i>p1 + p3 + p4</i>	1.0400	0.5184
14	<i>p2 + p3 + p4</i>	9.9110	0.5685
Group of four variables			
15	<i>p1 + p2 + p3 + p4</i>	0.0025	0.997202

Table 6. Performance evaluation of combinations of ANN input variables.

(pH, particle size, agitation and time) necessary for maximizing biosorption. The equation obtained from the ANN model was used as the objective function as follows [41]:

$$\text{Objective function} = \text{tansig}(LW * \text{tansig}(IW * [x(1); x(2); x(3); x(4)] + b1) + b2) \quad (27)$$

where *IW* and *b1* are the weight and bias of the hidden layer, and *LW* and *b2* are the weight and bias of output layer.

The optimized structure was achieved by a double vector population type, and the population size, population generation, crossover fraction and mutation rate were set to be 200, 100, 0.7 and 0.01, respectively. The selection, crossover and mutation operators were chosen as stochastic uniform, scattered and uniform, respectively. The fitness values versus generation are presented in **Figure 8**. The value of fitness reached to a minimum after approximately 30 generations. The ANN-GA optimization revealed that maximum removal could be obtained using pH 5.2, particle size 0.211 mm, agitation 388 rpm, and contact time 55 min. The model prediction of relative sorption capacity under these conditions was 23.25 mg/g. Laboratory experiments were subsequently conducted to validate these findings. The tests produced a

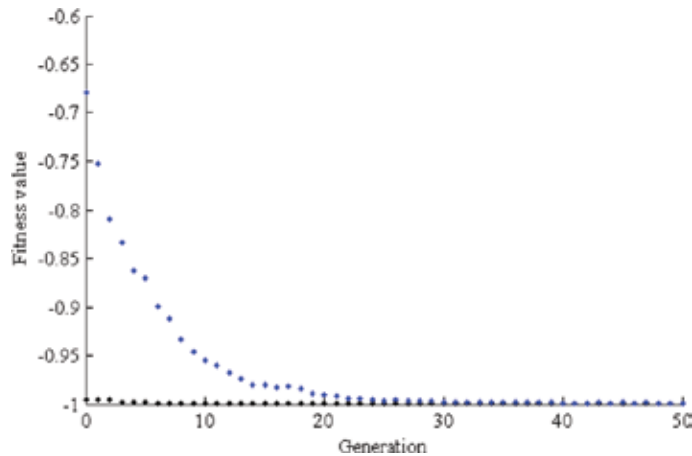


Figure 8. Fitness values versus generation.

relative sorption capacity of 22.95 mg/g, which revealed a residual error of 1.3% and therefore validate the ANN-GA structure.

3.9. Elucidation of mechanisms of biosorption

3.9.1. Biosorbent characteristics and performance

The surface morphology of floret biomass was observed by SEM before and after biosorption of Cu(II) ions (Figure 9a and b). Prior to biosorption, a rough irregular surface with a high amount of protuberance was observed. The protuberance on the biomass surface can be attributed to potassium and other salts deposition [42]. After biosorption, there was not a significant change in biomass surface morphology. However, a reduction in protuberance was observed. The EDS analysis (Figure 10a and b) reveals that banana floret contains mainly C, O and K with trace amounts of Mg, S, Si, P and Cl. After biosorption, the K, Mg and Cl peaks were removed. Similar results were reported for the biosorption of Cr³⁺ and Pb²⁺ using *Pistia stratiotes* biomass [43]. The authors explained that the adsorbate ions might have replaced some of the ions initially present in the cell wall matrix and created stronger cross-linking. The removal of K during Cu(II) biosorption may be attributed to ion exchange [44]. The appearance of a Cu peak after biosorption confirms that Cu(II) was successfully sorbed onto floret.

3.9.2. Desorption using various eluents

The desorption performance of a material can aid in assessing its reuse applicability, metal recovery potential and provide some valuable insight related to the mechanism of biosorption. The desorbing solutions selected were distilled water, 0.1 M EDTA, 0.1 M HCl and 0.1 M CaCl₂. The distilled water wash revealed only 1% of the Cu(II) was weakly bound by physical forces. The secondary ion exchange cation, Ca²⁺, recovered 11% of the sorbed ions after 60 min. The chelating agent, EDTA, known to form soluble complexes with metals ions [45] recovered

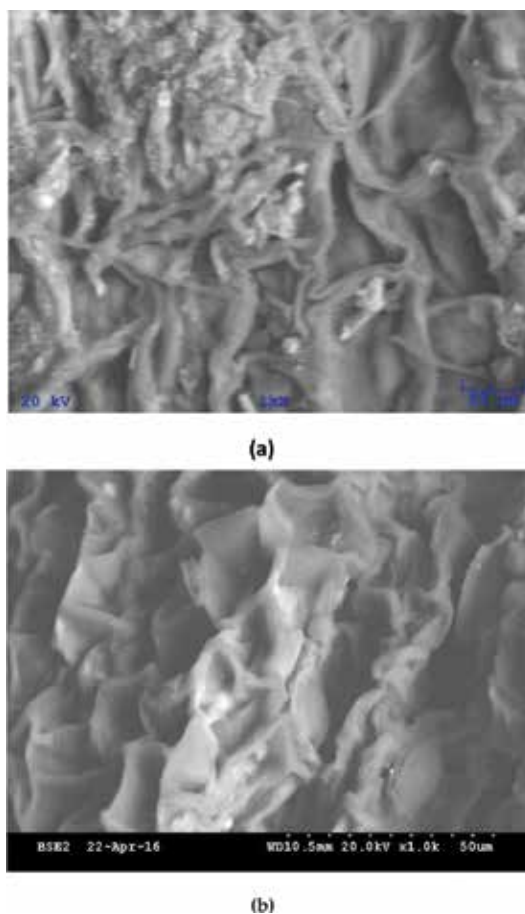


Figure 9. SEM micrograph of banana floret (a) before Cu(II) biosorption and (b) after Cu(II) biosorption.

60% of the sorbed ions. The harsh HCl wash, which is capable of destroying surface functional groups, released 87% of the sorbed ions after 60 min. Consequently, ion exchange and chemical bonding are confirmed attachment mechanisms of Cu(II) binding to banana floret.

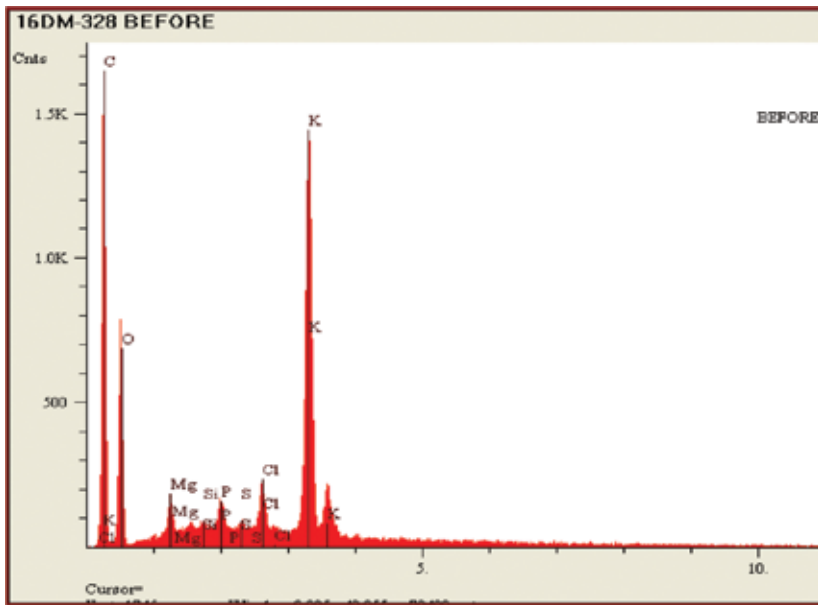
3.9.3. Mass transfer studies

Mass transfer studies were conducted using the external film diffusion model, the intraparticle diffusion model and the particle diffusion model.

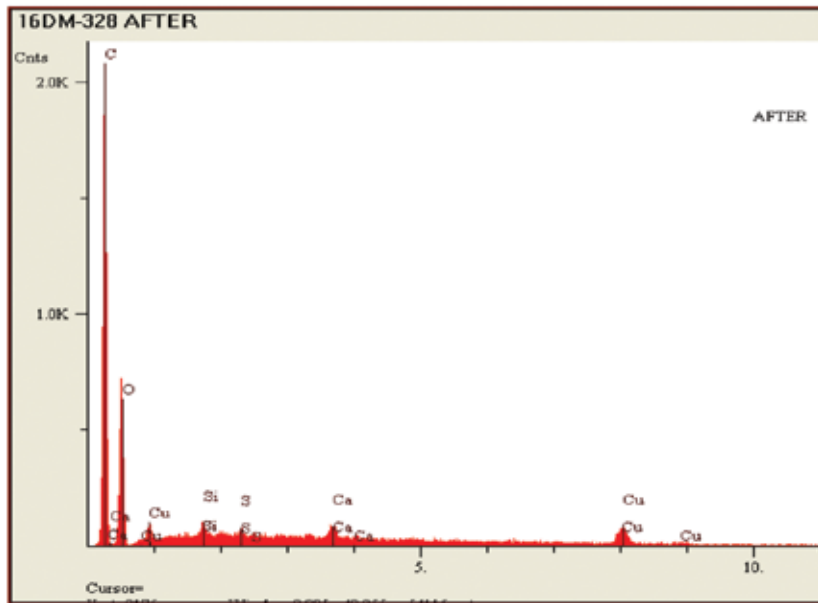
The external mass transfer model is expressed as [46]:

$$\frac{dq}{dt} = -k_f S_o (C - C_i) \quad (28)$$

Since C_i approaches zero and C approaches C_o , as $t \rightarrow 0$, Eq. (28) becomes:



(a)



(b)

Figure 10. EDS of banana floret (a) before Cu(II) biosorption and (b) after Cu(II) biosorption.

$$\left[\frac{d(C/C_o)}{dt} \right]_{t=0} = -k_f S_o \tag{29}$$

where

$$S_o = \frac{6m_s}{d_p \rho (1 - \epsilon_p)} \tag{30}$$

The particle diffusion is described by Boyd et al. [47]:

$$X(t) = 1 - \frac{6}{\pi^2} \sum_{Z=1}^{\infty} \frac{1}{Z^2} \exp \left[\frac{-Z^2 \pi^2 D_e t}{r^2} \right] \tag{31}$$

where $X(t)$ is the fractional attainment at time t , given by:

$$X(t) = \frac{q_t}{q_e} \tag{32}$$

Vermeulen's [48] approximation of Eq. (31) is given as:

$$X(t) = \left[1 - \exp \left[-\frac{\pi^2 D_e t}{r^2} \right] \right]^{\frac{1}{2}} \tag{33}$$

A linear plot of $\ln[1/1 - X^2(t)]$ vs. t enables D_e to be calculated [49]:

$$\ln \left[\frac{1}{1 - X^2(t)} \right] = \frac{\pi^2}{r^2} D_e t \tag{34}$$

The Biot number (Bi) is given by [50]:

$$Bi = \frac{k_f r}{D_e} \tag{35}$$

A plot of q_t versus $t^{0.5}$ in accordance with the Weber and Morris model for two sorbent sizes, namely, GMS 0.17 and 0.6 mm is shown in **Figure 11**. As the particle size decreased (which accompanies an increase in surface area and a reduction in pore length), the plots move further from the origin. Such deviation from the origin infers that intraparticle transport is not the only rate-limiting step [51].

The plot of 0.17 mm GMS reveals two distinct slopes. The first slope, which occurs within the first 30 min of the reaction, reveals the impact of intraparticle diffusion. Some researchers have

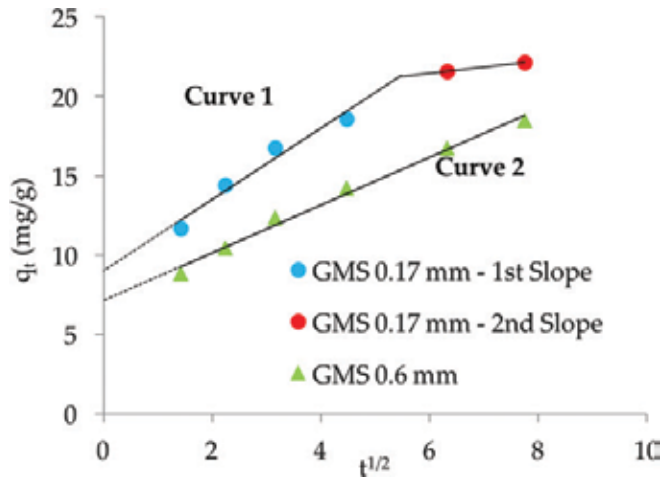


Figure 11. Kinetic plot of ID model for various particle size.

reported that the final slope corresponds to the slowing of the reaction, possibly due to a reduction in concentration gradient as the reaction approaches equilibrium [52, 53]. The plot of 0.6 mm GMS depicts the dominance of intraparticle diffusion for most of the reaction.

In order to explicate the degree of involvement of external and intraparticle diffusion, the resulting mass transfer coefficients obtained from the external and particle diffusion models were used to calculate the *Bi*. For *Bi* values <1.0, external mass transfer dominates while for *Bi* > 30, surface diffusion controls and for values between 1 and 30, both external and intraparticle mass transfer rates contribute [54]. The results presented in Table 7 confirm that within the range of particle sizes studied both external and intraparticle mass transfer rates contribute to the adsorption rate. Further, as particle size increased, particle diffusivity also increased while the film diffusion coefficient decreased.

3.10. Design of batch biosorption system from isotherm data

Laboratory-scale equilibrium studies are used to predict batch adsorber size and performance. Figure 12 shows the schematic of a single-stage batch adsorber with a solution volume of *V* (L) and the initial Cu(II) concentration, *C*₀ is reduced to *C*_{*t*} as the reaction proceeds. The Cu(II) loading on the adsorbent in the reactor of mass *M* (g) changes from *q*₀ to *q*_{*t*} with increased reaction time. The mass balance for the reactor is given by the following [55, 56]:

$$V(C_0 - C_t) = M(q_t - q_0) = Mq_t \tag{36}$$

The adsorption process at 300 K was best represented by the Sips isotherm, thus the mass balance under equilibrium condition (*C*_{*t*} → *C*_{*e*} and *q*_{*t*} → *q*_{*e*}) is arranged as follows:

$$\frac{M}{V} = \frac{C_0 - C_e}{q_e} = \frac{C_0 - C_e}{\frac{q_s(\alpha_s C_e)^{1/n_s}}{(1 + (\alpha_s C_e)^{1/n_s})}} \tag{37}$$

Figure 13 presents a series of plots of the predicted values of M (g) versus V (L) for 60, 70, 80 and 90% Cu(II) ion removal at the initial concentration of 50 mg/L and 300 K. As an example, the mass of adsorbent required for 60% Cu(II) removal from aqueous solution was 10 and 15 g,

GMS (mm)	k_f (cm/min)	R^2	D_e (cm ² /min)	R^2	Bi
0.17	6.44E-03	0.8332	5.40E-5	0.9751	10.1454
0.35	1.65E-02	0.8995	1.72E-04	0.9609	16.8203
0.6	2.14E-02	0.9241	4.35E-04	0.9573	14.7441

Table 7. Mass transfer coefficients and Bi for the biosorption of Cu(II).

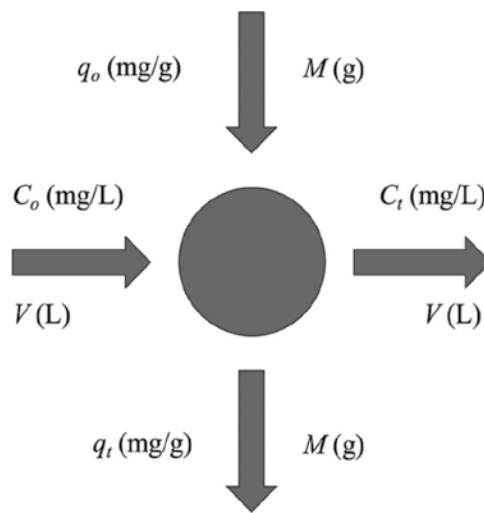


Figure 12. Design of single-stage batch system for Cu(II) biosorption.

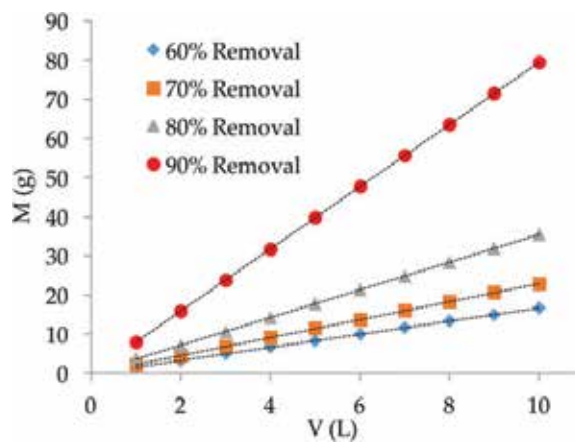


Figure 13. Biosorbent mass (M) versus volume of Cu(II) solution treated (V).

for Cu(II) solution volumes of 6 and 9 L, respectively. This evaluation becomes relevant for pilot-batch system design as well as large-scale batch applications.

4. Conclusion

The adsorption performance of banana floret was assessed as a new biosorbent for heavy metal removal. Cu(II) was used as a model heavy metal. Banana floret exhibited a maximum adsorption capacity of 28.06 mg/g which compares well to biosorbents reported in the literature. Operational parameters were varied and analyzed using a series of kinetic and equilibrium models. Nonlinear regression produced a more robust simulation of the kinetic data which best followed the DC model. Equilibrium data were best simulated using the three-parameter Sips isotherm. Mass transfer studies indicated that both film and intraparticle diffusion were responsible for the transport of Cu(II) to biosorption sites, while ion exchange and chemisorption were the most influential attachment mechanisms. A predictive model was successfully developed using ANN and optimized using GA. The accuracy of the ANN-GA prediction was validated by laboratory experiments, which revealed a residual error of 1.3% and therefore highlights the applicability of the model.

Nomenclature

a_s	Sips affinity constant
C	uniform concentration of the solute in the bulk of the liquid (mg/L) (Eq. 28)
C_e	equilibrium concentration in solution (mg/L)
C_i	concentration of the solute at the particle/liquid interface (mg/L) (Eq. 28)
C_o	initial metal ion concentration (mg/L)
C_t	concentration of metal ion at any time (mg/L)
d_p	average particle diameter (cm) (Eq. 30)
D_e	particle diffusion coefficient (cm ² /min)
g_{RP}	Redlich-Peterson exponent
k_i	DC initial rate (mg/g-t)
k_f	film mass transfer coefficient (cm/min)
K_{DC}	DC overall rate constant (mg/g-t ^{0.5})
K_{id}	ID rate constant (mg/g-t ^{0.5})

K_F	Freundlich constant related to adsorption affinity (mg/g)
K_L	Langmuir adsorption equilibrium constant (L/mg)
K_{PFO}	PFO rate constant (min^{-1})
K_{PSO}	PSO rate constant (g/mg-min)
K_{RP}	Redlich-Peterson equilibrium constant
m_s	mass of biosorbent particles per unit volume (g/cm^3) (Eq. 30)
M	biosorbent mass (g)
n_F	Freundlich constant related to heterogeneity
n_s	Sips index of heterogeneity
N	the number of experimental points
P	number of parameters in the regression model
q_e	equilibrium adsorption capacity (mg/g)
q_L	Langmuir monolayer sorption capacity (mg/g)
q_t	adsorption capacity at any time (mg/g)
R	universal gas constant, 8.314 J/K-mol
S_o	surface area for mass transfer (cm^{-1}) (Eq. 30)
t	reaction time (min)
T	absolute temperature in K
V	volume (L)
Greek symbols	
α_{RP}	Redlich-Peterson constant
ε_p	biosorbent porosity (Eq. 30)
ρ	true biosorbent solid phase density (g/cm^3) (Eq. 30)

Author details

Clint Sutherland*, Abeni Marcano and Beverly Chitto

*Address all correspondence to: clint.sutherland@utt.edu.tt

Project Management and Civil Infrastructure Systems, The University of Trinidad and Tobago, Trinidad and Tobago (WI)

References

- [1] Zahra N, Kalim I, Mahmood M, Naeem N. Perilous effects of heavy metals contamination on human health. *Pakistan Journal of Analytical & Environmental Chemistry*. 2017;**18**(1): 1-17. DOI: 10.21743/pjaec/2017.06.01
- [2] Low KS, Lee CK, Liew SC. Sorption of cadmium and lead from aqueous solutions by spent grain. *Process Biochemistry*. 2000;**36**(1):59-64. DOI: 10.1016/S0032-9592(00)00177-1
- [3] Kelly-Vargas K, Cerro-Lopez M, Reyna-Tellez S, Bandala ER, Sanchez-Salas JL. Biosorption of heavy metals in polluted water, using different waste fruit cortex. *Physics and Chemistry of the Earth, Parts A/B/C*. 2012;**37**:26-29. DOI: 10.1016/j.pce.2011.03.006
- [4] Lee SJ, Park JH, Ahn YT, Chung JW. Comparison of heavy metal adsorption by peat moss and peat moss-derived biochar produced under different carbonization conditions. *Water, Air, & Soil Pollution*. 2015;**226**(2):2106-2116. DOI: 10.1007/s11270-014-2275-4
- [5] Acheampong MA, Pereira JP, Meulepas RJ, Lens PN. Kinetics modelling of Cu(II) biosorption on to coconut shell and *Moringa oleifera* seeds from tropical regions. *Environmental Technology*. 2012;**33**(4):409-417. DOI: 10.1080/09593330.2011.576705
- [6] Ofomaja AE. Intraparticle diffusion process for lead (II) biosorption onto *Mansonia* wood sawdust. *Bioresource Technology*. 2010;**101**(15):5868-5876. DOI: 10.1016/j.biortech.2010.03.033
- [7] Yasim NS, Ismail ZS, Zaki SM, Azis MF. Adsorption of Cu, As, Pb and Zn by banana trunk. *Malaysian Journal of Analytical Sciences*. 2016;**20**(1):187-196. DOI: 10.17576/mjas-2016-2001-20
- [8] El-Said AG. Biosorption of Pb (II) ions from aqueous solutions onto rice husk and its ash. *Journal of American Science*. 2010;**6**(10):143-150
- [9] Ugwekar RP, Lakhawat GP. Recovery of heavy metal by adsorption using peanut hull. *Journal of Advanced Engineering Technology*. 2012;**3**:39-43
- [10] Ponnusami V, Vikram S, Srivastava SN. Guava (*Psidium guajava*) leaf powder: Novel adsorbent for removal of methylene blue from aqueous solutions. *Journal of Hazardous Materials*. 2008;**152**(1):276-286. DOI: 10.1016/j.jhazmat.2007.06.107
- [11] Hasanah AN, Rizkiana F, Rahayu D. Banana peels and stem (*Musa x paradisiaca* Linn.) as biosorbent of copper in textile industry wastewater. *Research Journal of Pharmaceutical, Biological and Chemical Sciences*. 2012;**3**:1171-1178
- [12] Sutherland C, Venkobachar C. Equilibrium modeling of Cu (II) biosorption onto untreated and treated forest macro-fungus *Fomes fasciatus*. *International Journal of Plant, Animal and Environment Sciences*. 2013;**3**:193-203. DOI: 10.21276/Ijpaes
- [13] Naja G, Diniz V, Volesky B. Predicting metal biosorption performance. In: STL Harrison, DE Rawlings, J. Peterson, editors. *Proceedings of the 16th International Biohydrometallurgy Symposium*; Compress Co.: Cape Town, South Africa; 2005. pp. 553-562
- [14] Pfost H, Headley V. Methods of determining and expressing particle size. *Feed Manufacturing Technology*. 1976:512-517

- [15] U.S. Environmental Protection Agency (USEPA). Fate, transport, and transformation test guidelines. Adsorption/desorption (batch equilibrium). Washington, DC; 2008. OPPTS 835.1230
- [16] Weber WJ, Miller CT. Modeling the sorption of hydrophobic contaminants by aquifer materials—I. Rates and equilibria. *Water Research*. 1988;**22**(4):457-464. DOI: 10.1016/0043-1354(88)90040-1
- [17] Ho YS, McKay G. A comparison of chemisorption kinetic models applied to pollutant removal on various sorbents. *Process Safety and Environmental Protection*. 1998;**76**(4): 332-340. DOI: 10.1205/095758298529696
- [18] Ho YS, McKay G. Sorption of dye from aqueous solution by peat. *Chemical Engineering Journal*. 1998;**70**(2):115-124. DOI: 10.1016/S0923-0467(98)00076-1
- [19] Ho YS, McKay G. Pseudo-second order model for sorption processes. *Process Biochemistry*. 1999;**34**(5):451-465. DOI: 10.1016/S0032-9592(98)00112-5
- [20] Weber WJ, Morris JC. Kinetics of adsorption on carbon from solution. *Journal of the Sanitary Engineering Division*. 1963;**89**(2):31-60
- [21] Sutherland C, Venkobachar C. A diffusion-chemisorption kinetic model for simulating biosorption using forest macro-fungus, *fomes fasciatus*. *International Research Journal of Plant Science*. 2010;**1**(4):107-117
- [22] Motulsky H, Christopoulos A. *Fitting Models to Biological Data using Linear and Nonlinear Regression: A Practical Guide to Curve Fitting*. New York: Oxford University Press; 2004. 19 p
- [23] Das B, Mondal NK, Bhaumik R, Roy P, Pal KC, Das CR. Removal of copper from aqueous solution using alluvial soil of Indian origin: equilibrium, kinetic and thermodynamic study. *Journal of Materials and Environmental Science*. 2013;**4**(4):392-408
- [24] Langmuir I. The adsorption of gases on plane surfaces of glass, mica and platinum. *Journal of the American Chemical Society*. 1918;**40**(9):1361-1403. DOI: 10.1021/ja02242a004
- [25] Swan E, Urquhart AR. Adsorption equations. *The Journal of Physical Chemistry*. 1927; **31**(2):251-276. DOI: 10.1021/j150272a008
- [26] Freundlich HM. Over the adsorption in solution. *The Journal of Physical Chemistry*. 1906; **57**:385-471
- [27] Redlich OJ, Peterson DL. A useful adsorption isotherm. *The Journal of Physical Chemistry*. 1959;**63**(6):1024-1026. DOI: 10.1021/j150576a611
- [28] Sips R. Combined form of Langmuir and Freundlich equations. *The Journal of Chemical Physics*. 1948;**16**(429):490-495
- [29] Günay A, Arslankaya E, Tosun I. Lead removal from aqueous solution by natural and pretreated clinoptilolite: Adsorption equilibrium and kinetics. *Journal of Hazardous Materials*. 2007;**146**(1):362-371. DOI: 10.1016/j.jhazmat.2006.12.034
- [30] Hall KR, Eagleton LC, Acrivos A, Vermeulen T. Pore-and solid-diffusion kinetics in fixed-bed adsorption under constant-pattern conditions. *Industrial & Engineering Chemistry Fundamentals*. 1966;**5**(2):212-223. DOI: 10.1021/i160018a011

- [31] Witek-Krowiak A, Szafran RG, Modelski S. Biosorption of heavy metals from aqueous solutions onto peanut shell as a low-cost biosorbent. *Desalination*. 2011;**265**(1):126-134. DOI: 10.1016/j.desal.2010.07.042
- [32] Gupta BS, Curran M, Hasan S, Ghosh TK. Adsorption characteristics of Cu and Ni on Irish peat moss. *Journal of Environmental Management*. 2009;**90**(2):954-960. DOI: 10.1016/j.jenvman.2008.02.012
- [33] Pethkar AV, Kulkarni SK, Paknikar KM. Comparative studies on metal biosorption by two strains of *Cladosporium cladosporioides*. *Bioresource Technology*. 2001;**80**(3):211-215. DOI: 10.1016/S0960-8524(01)00080-3
- [34] Delle Site A. Factors affecting sorption of organic compounds in natural sorbent/water systems and sorption coefficients for selected pollutants. A review. *Journal of Physical and Chemical Reference Data*. 2001;**30**(1):187-439. DOI: 10.1063/1.1347984
- [35] Kumar R, Rashid J, Barakat MA. Synthesis and characterization of a starch- AlOOH-FeS_2 nanocomposite for the adsorption of congo red dye from aqueous solution. *RSC Advances*. 2014;**4**(72):38334-38340. DOI: 10.1039/C4RA05183A
- [36] Anirudhan TS, Radhakrishnan PG. Thermodynamics and kinetics of adsorption of Cu(II) from aqueous solutions onto a new cation exchanger derived from tamarind fruit shell. *The Journal of Chemical Thermodynamics*. 2008;**40**(4):702-709. DOI: 10.1016/j.jct.2007.10.005
- [37] McCulloch WS, Pitts W. A logical calculus of the ideas immanent in nervous activity. *The Bulletin of Mathematical Biophysics*. 1943;**5**(4):115-133. DOI: 10.1007/BF02478259
- [38] Werbos PJ. Backpropagation through time: What it does and how to do it. *Proceedings of the IEEE*. 1990;**78**(10):1550-1560. DOI: 10.1109/5.58337
- [39] Shahryari Z, Sharifi A, Mohebbi A. Artificial neural network (ANN) approach for modeling and formulation of phenol adsorption onto activated carbon. *Journal of Engineering Thermophysics*. 2013;**22**(4):322-336. DOI: 10.1134/S181023281
- [40] Yetilmmezsoy K, Demirel S. Artificial neural network (ANN) approach for modeling of Pb (II) adsorption from aqueous solution by Antep pistachio (*Pistacia vera* L.) shells. *Journal of Hazardous Materials*. 2008;**153**(3):1288-1300. DOI: 10.1016/j.jhazmat.2007.09.092
- [41] Ghaedi AM, Ghaedi M, Pouranfard AR, Ansari A, Avazzadeh Z, Vafaei A, Tyagi I, Agarwal S, Gupta VK. Adsorption of triamterene on multi-walled and single-walled carbon nanotubes: Artificial neural network modeling and genetic algorithm optimization. *Journal of Molecular Liquids*. 2016;**216**:654-665. DOI: 10.1016/j.molliq.2016.01.068
- [42] Chen JP, Yang L. Chemical modification of *Sargassum* sp. for prevention of organic leaching and enhancement of uptake during metal biosorption. *Industrial & Engineering Chemistry Research*. 2005;**44**(26):9931-9942. DOI: 10.1021/ie050678t
- [43] Lima LK, Pelosi BT, Silva MG, Vieira MG. Lead and chromium biosorption by *Pistia stratiotes* biomass. *Chemical Engineering Transactions*. 2013;**32**:1045-1050. DOI: 10.3303/CET1332175

- [44] Vieira MG, de Almeida Neto AF, Da Silva MG, Carneiro CN, Melo Filho AA. Adsorption of lead and copper ions from aqueous effluents on rice husk ash in a dynamic system. *Brazilian Journal of Chemical Engineering*. 2014;**31**(2):519-529. DOI: 10.1590/0104-6632.20140312s00002103
- [45] Olusegun AO, Oluwafemi AS. Evaluation of chelating agents for the removal of heavy metals from contaminated soil. *Global Journal of Biochemistry and Biotechnology*. 2012; **1**(2):152-156
- [46] Mathews AP, Weber W. Effects of external mass transfer and intraparticle diffusion on adsorption rates in slurry reactors. *AIChE Symposium Series*. 1977;**73**(166):91-98
- [47] Boyd GE, Adamson AW, Myers LS Jr. The exchange adsorption of ions from aqueous solutions by organic zeolites. II. Kinetics. *Journal of the American Chemical Society*. 1947; **69**(11):2836-2848. DOI: 10.1021/ja01203a066
- [48] Vermeulen T. Theory for irreversible and constant-pattern solid diffusion. *Industrial & Engineering Chemistry*. 1953;**45**(8):1664-1670. DOI: 10.1021/ie50524a025
- [49] Lao-Luque C, Solé M, Gamisans X, Valderrama C, Dorado AD. Characterization of chromium (III) removal from aqueous solutions by an immature coal (leonardite). Toward a better understanding of the phenomena involved. *Clean Technologies and Environmental Policy*. 2014;**16**(1):127-136. DOI: 10.1007/s10098-013-0610-x
- [50] Do DD. *Adsorption Analysis: Equilibria and Kinetics: (With CD Containing Computer Matlab Programs)*. London: Imperial College Press; 1998. 555 p
- [51] Badmus MA, Audu TO, Anyata BU. Removal of lead ion from industrial wastewaters by activated carbon prepared from periwinkle shells (*Typanotonus fuscatus*). *Turkish Journal of Engineering and Environmental Sciences*. 2007;**31**(4):251-263
- [52] Wu J, Yu HQ. Biosorption of 2,4-dichlorophenol from aqueous solution by *Phanerochaete chrysosporium* biomass: Isotherms, kinetics and thermodynamics. *Journal of Hazardous Materials*. 2006;**137**(1):498-508. DOI: 10.1016/j.jhazmat.2006.02.026
- [53] Aksu Z, Kabasakal E. Batch adsorption of 2,4-dichlorophenoxy-acetic acid (2,4-D) from aqueous solution by granular activated carbon. *Separation and Purification Technology*. 2004;**35**(3):223-240. DOI: 10.1016/S1383-5866(03)00144-8
- [54] Pouloupoulos SG, Inglezakis VJ. *Adsorption, Ion Exchange and Catalysis: Design of Operations and Environmental Applications*. The Netherlands: Elsevier; 2006. 305 p. DOI: 10.1016/B978-044452783-7/50004-5
- [55] McKay G, Otterburn MS, Aga JA. Fuller's earth and fired clay as adsorbents for dyestuffs. *Water, Air, & Soil Pollution*. 1985;**24**(3):307-322. DOI: 10.1007/BF00161790
- [56] Deniz F. Dye removal by almond shell residues: Studies on biosorption performance and process design. *Materials Science and Engineering: C*. 2013;**33**(5):2821-2826. DOI: 10.1016/j.msec.2013.03.009



Edited by Murat Eyvaz and Ebubekir Yüksel

The need for fresh water is increasing with the rapid growth of the world's population. In countries and regions with available water resources, it is necessary to ensure the health and safety of the water supply. However, in countries and regions with limited freshwater resources, priority is given to water supply plans and projects, among which the desalination strategy stands out. In the desalination process, membrane and thermal processes are used to obtain fresh water from salty water that is in abundant amounts in the sea. This book will outline valuable scientific contributions to the new desalination and water treatment technologies to obtain high quality water with low negative environmental impacts and cost.

The editors would like to record their sincere thanks to the authors for their contributions.

Published in London, UK

© 2018 IntechOpen
© FOTOOSMEH / iStock

IntechOpen

